Design, Characterization, and Modeling of New Electrical Contact Material Systems Containing Carbon Nanoparticles

Dissertation

zur Erlangung des Grades
des Doktors der Ingenieurswissenschaften
der Naturwissenschaftlich-Technischen Fakultät
der Universität des Saarlandes

UNIVERSITÄT
DES
SAARLANDES

von
Bruno Martin Alderete Gomez

Saarbrücken
Dezember 2024

Printed with the support of the German Academic Exchange Service (DAAD).

Tag des Kolloquiums:	17.06.2025
Dekan:	Prof. Dr.-Ing. Dirk Bähre
Berichterstatter:	Prof. Dr.-Ing. Frank Mücklich Prof. Dr.-Ing. Hans-Georg Herrmann Prof. Dr. Martin Dienwiebel
Akad. Mitglied:	Dr.-Ing. Oliver Maurer
Vorsitz:	Prof. Dr. Roland bennewitz

TABLE OF CONTENTS

PREFACE i
ACKNOWLEDGMENTS iii
ABSTRACT v
ZUSAMMENFASSUNG vii
ABBREVIATIONS & SYMBOLS ix
1. MOTIVATION & INTRODUCTION 1
2. THEORETICAL FRAMEWORK 7
2.1. Electrical contacts 7
2.1.1. Fundamental theory 7
2.1.2. Slope analysis – dominant resistance & deformation mechanisms 11
2.1.3. Contact physics between real surfaces 13
2.2. Wear & degradation of electrical contacts 14
2.2.1. Wear in static connectors 15
2.2.2. Adhesive wear 16
2.2.3. Abrasive wear 18
2.2.4. Fretting wear 18
2.2.5. Erosive wear (electro-erosion) 21
2.2.6. Corrosion and atmospheric conditions 22
2.3. Lubrication in electrical systems 23
2.4. Carbon nanostructures 25
3. STATE OF THE ART 29
3.1. Current engineering solutions 29
3.1.1. Passivation 29
3.1.2. Surface modifications & lubrication 30
3.1.3. Coatings 31
3.1.4. Alloying 32
3.1.5. Composite materials 33
3.2. Carbon nanoparticle coatings 34
3.3. Carbon nanoparticle-reinforced composites 35
4. OBJECTIVES 39
5. INCLUDED ARTICLES 41
5.1. Outline 41

5.1.1. Setup 41
5.1.2. Materials 42
5.1.3. Coatings 43
5.1.4. Composites 45
ARTICLE I 49
ARTICLE II 65
ARTICLE III 95
ARTICLE IV 111
ARTICLE V 133
ARTICLE VI 175
ARTICLE VII 179
ARTICLE VIII 205
ARTICLE IX 237
ARTICLE X 259
ARTICLE XI 263
ARTICLE XII 283
ANNEX I 307
ARTICLE XIII 311
ARTICLE XIV 335
ARTICLE XV 375
6. SUMMARY & CONCLUSIONS 393
7. OUTLOOK 399
REFERENCES 401
LIST OF FIGURES I
LIST OF TABLES II
APPENDIX A III
A.1. Electricity III
A.1.1. Basic concepts III
A.1.2. Conductivity, resistivity, and resistance III
A.2. Ignition of the electrical arc while breaking VI
A.3. Carbon hybridization states VIII

PREFACE

This dissertation is the result of the work conducted between August 2020 and August 2024 at the Chair of Functional Materials (*Lehrstuhl für Funktionswerkstoffe – FuWe*), Saarland University, Germany.

The research was carried out within the framework of the German Academic Exchange Service (*DAAD*): Research Grant – Doctoral Programs in Germany 2020/21 (57507871) between August 2020 and July 2024.

Additional funding for the research was provided by the Roberto Rocca Education Program (*RREP*) between September 2021 and August 2024.

The results published in peer-reviewed scientific journals are appended to this dissertation. Due to copyright restrictions, some articles are appended in their **accepted manuscript** form rather than in the **journal-formatted version**. While these versions may differ in formatting, they retain the full scientific content and conclusions of the published articles.

Bruno Alderete
Saarbrücken, 2024

ACKNOWLEDGMENTS

First and foremost, I wish to extend my heartfelt thanks to my supervisor, Prof. Dr.-Ing. Frank Mücklich, for giving me the privilege of conducting my work at the Chair of Functional Materials (*Lehrstuhl für Funktionswerkstoffe – FuWe*) and for providing me with the freedom to pursue my work. His trust in my abilities and his guidance were invaluable to the completion of this thesis. I am very grateful for his support in creating an environment where I could develop my ideas and skills.

I am grateful and would like to acknowledge the German Academic Exchange Service (*Deutscher Akademischer Austauschdienst – DAAD*) for financially supporting my research from August 2020 until July 2024.

I would like to express my sincere gratitude to the Roberto Rocca Education Program (RREP) for their financial support from September 2021 until August 2024.

I am extremely indebted to Dr.-Ing Sebastian Suarez. I could have never asked for a better mentor, colleague, and friend with whom to carry out this work. From the very beginning, he has always been very forthcoming, supportive, and encouraging. His unwavering assistance, knowledge, and kindness have been the cornerstone of my doctoral journey. His passion for research, empathy, and approachable demeanor have been a source of constant motivation. Whether through insightful guidance or encouraging words, his commitment to fostering both my academic and personal growth has left a lasting impression. I am truly grateful to have had the privilege of learning and working by his side.

I am very thankful to all my co-authors for their invaluable contributions to the scientific publications that form the foundation of this thesis. Their expertise, feedback, and collaboration were instrumental in advancing this work. I also appreciate and acknowledge everyone who has contributed formally and informally through discussions, suggestions, and insights. These exchanges have greatly enriched my understanding and have been vital to shaping the direction of this research.

I am sincerely thankful to Dr.-Ing. U. Pranav Nayak and Dr.-Ing. Sebastian Suarez for thoroughly proofreading and providing valuable feedback on this thesis. Their meticulous attention to detail and their quick turnaround was vital in refining this work, and I am truly grateful for their time and dedication. Furthermore, I am extremely grateful to M.Ed. Carolin Schelske and M.Sc. Tobias Fox for proofreading and improving the German abstract of this thesis.

I am profoundly grateful to my former supervisor, Prof. Dr. Sonia Brühl, for introducing me to scientific research and inspiring me to pursue it as a career. Her encouragement and guidance during those early stages were pivotal in shaping my

passion for scientific research. I am especially thankful for her support in connecting me with valuable research internships, which provided me with crucial experience and laid the foundation for my journey towards this doctoral thesis.

I would like to extend my gratitude to my *FuWe* friends and colleagues. For over four years, you have created such a great collaborative and supportive work environment that has made this journey not only productive, but also very enjoyable. I treasure every light-hearted conversation, every "that's what she said" joke, and every (much needed) coffee that we have shared. These short – and oftentimes not so short – breaks proved to be the best and most efficient way to advance our work.

To my friends, I would like to extend a special thank you. Although life has driven us to different corners of the globe and we do not get to hang out and eat asado like we used to, I hold every single one near and dear to my heart. I can truly call myself a lucky person because I have such amazing friends.

My warmest thanks go to my majestic kitty. I want to thank her for being my comfort through it all. Her presence, the gentle nudge of her head, the soothing sound of her purring, and occasional mischief provided much-needed breaks from the stresses of life. When the world feels overwhelming, she is always there to remind me that everything will be alright. No matter how hard, stressful, or sad my day has been, a simple stroke of her soft fur brings a smile to my face.

I want to express my gratitude to my sister for her love and support. She is one of the coolest people I know, and I am truly privileged to have her as a sibling. I cannot wait to rock out with her at our next concert!

Words cannot fully express how thankful I am towards my parents for their endless love, encouragement, and sacrifice. I want to thank them for believing in me, for their unconditional support, and for being the best and coolest parents on the planet. Their unwavering faith and the values they have instilled in me have shaped me into the person I am today. It may be a cliché, but this achievement genuinely is as much theirs as it is mine, and I am forever indebted to them for everything they have done.

Last but certainly not least, I want to express my deepest gratitude to my wonderful girlfriend. I am extremely thankful and lucky to have her in my life. Her constant love, encouragement, and ability to not only tolerate, but accept my weirdness astounds me to this very day. Her brilliance, kindness, dedication, diligence, and commitment never cease to inspire me. I am incredibly grateful for the happiness she brings into my life, and I genuinely appreciate everything that she has done to help me keep moving forward. She is the motivation for me to want to be a better person. This achievement would not have been the same without her by my side.

ABSTRACT

As a consequence of the increased electrification of modern society, there is a greater need to ensure the reliability and durability of electrical contacts. This not only gives rise to more stringent performance requirements, but also places significant pressure on the demand for specific materials. Silver and copper are remarkable electrical conductors; however, these materials are not without shortcomings. In this regard, carbon nanostructures could play a pivotal role in enhancing their performance. This work focuses on the development, optimization, and characterization of carbon-containing electrical contact materials. In broad terms, the work can be divided into two areas: carbon nanostructure-based coatings for static connectors and carbon nanotube (CNT)-reinforced metal matrix composites for switching electrodes.

Thorough characterization of nanocarbon-based coatings has demonstrated that carbon black and CNT coatings show the most promising results based on their low impact on electrical conductivity and high wear protection, with the latter exhibiting superhydrophobic wetting behavior – thus potentially providing atmospheric protection. CNT-reinforced composites, on the other hand, present exceptional contact elasticity and reproducibility while reducing material requirements. Furthermore, the reinforcement phase improves electrode performance during switching, reducing unstable arcing, arc mobility, and molten pool duration without amorphization of the CNT.

ZUSAMMENFASSUNG

Die Elektrifizierung der modernen Gesellschaft führt dazu, dass die Zuverlässigkeit und Langlebigkeit von elektrischen Kontakten immer wichtiger werden. Für einige Materialien führt dies neben einem erheblichen Anstieg der Nachfrage auch zu erhöhten Anforderungen. Insbesondere Silber und Kupfer sind zwar bemerkenswerte elektrische Leiter, haben aber auch Nachteile. In dieser Hinsicht könnten Nanokohlenstoffe eine wichtige Rolle spielen. Diese Arbeit konzentriert sich deshalb auf Design, Optimierung und Charakterisierung von kohlenstoffhaltigen elektrischen Kontaktmaterialien. Die Arbeit lässt sich in zwei Bereiche unterteilen: Nanokohlenstoff-Beschichtungen für Steckverbinder und, mit Kohlenstoff-Nanoröhren (CNT) verstärkte Metallmatrix-Kompositwerkstoffe für Schaltelektroden.

Die Charakterisierung von Nanokohlenstoff-Beschichtungen zeigt, dass carbon black- und CNT-Beschichtungen aufgrund ihrer geringen Auswirkungen auf die elektrische Leitfähigkeit und ihres hohen Verschleißschutzes die vielversprechendsten Ergebnisse liefern. CNT-verstärkte Kompositwerkstoffe hingegen weisen eine außergewöhnliche Kontaktelastizität und Reproduzierbarkeit auf und reduzieren gleichzeitig den Materialbedarf. Darüber hinaus verbessert die verstärkende Phase die Elektrodenleistung während des Schaltens, indem sie die Lichtbogenentwicklung und -mobilität sowie die Dauer des Schmelzbades verringert, ohne dass die CNTs amorphisieren.

ABBREVIATIONS & SYMBOLS

Abbreviation	Definition
AM	Additive manufacturing
BEV	Battery electric vehicles
CA	Contact angle
CB	Carbon black
CLSM	Confocal laser scanning microscopy
CNC	Carbon nanocones
CND	Carbon nanodiamonds
CNH	Carbon nanohorns
CNO	Carbon nano-onions
CNP	Carbon nanoparticles
CNT	Carbon nanotubes
CO	Carbon onions
CoF	Coefficient of friction
CS	Current sweep
DC	Direct current
ECR	Electrical contact resistance
EDS	Energy dispersive X-ray spectroscopy
EPD	Electrophoretic deposition
EV	Electric vehicles
FIB	Focused ion beam
GF	Graphite flakes
GNP	Graphene nanoplatelets
GO	Graphene oxide
GW	Greenwood-Williamson model
HCT	Hertzian contact theory

HDT	Hexadecanethiol
HEV	Hybrid electric vehicles
HMMC	Hybrid metal matrix composites
HR-TEM	High resolution transmission electron microscopy
HIP	Hot isostatic pressing
HUP	Hot uniaxial pressing
ICEV	Internal combustion engine vehicles
IMP	Intermetallic phases
JG	Jackson-Green model
LOM	Light optical microscopy
MMC	Metal matrix composites
ODT	Octadecanethiol
OLC	Onion-like carbon
PFAS	Per- and polyfluoroalkyl substances
PM	Powder metallurgy
PFPE	Perfluoropolyether
PTFE	Polytetrafluoroethylene
rGO	Reduced graphene oxide
RMS	Root mean square
SEM	Scanning electron microscopy
SPS	Spark plasma sintering
XRD	X-ray diffraction

Symbol	Definition
°	Degrees
$2a$	a-spot diameter [m]
A	Cross section area [m]
A_c	Critical area [m^2]
a	Radius of circular Hertzian contact [m]
$at.\%$	Atomic percentage
α	Holm radius [m]
C	Critical yield stress coefficient
d_{cont}	Thickness of contaminant film [m]
δ	Total Hertzian contact deformation [m]
e_c	Charge of an electron [C]
E	Electric field [V/m]
E_m	Elastic modulus [Pa]
E_m*	Reduced elastic modulus [Pa]
η	Areal asperity density
η_c	Cleanliness factor (1 for clean surfaces)
F	Normal load [N]
F'	Distributed load along a linear trajectory (Hertz line contact) [N]
H	Material hardness [Pa]
I	Electrical current [A]
I_{min}	Minimum arc current [A]
J	Current density [A/m^2]
k	Constant
L	Length [m]
m_0	Spectral moment: mean square variance
m_2	Spectral moment: mean square slope
m_4	Spectral moment: mean square curvature

m_e	Mass of an electron [g]
n	n factor (exponent number for slope analysis)
n_e	Electron density [electron/m^3]
ω_c	Critical interference [m]
P_c	Critical load [N]
p_0	Maximum Hertzian contact pressure [Pa]
p_m	Median Hertzian contact pressure [Pa]
ψ	Plasticity index
Q	Joule heating [W]
R	Electrical resistance [Ω]
R_b	Bulk resistance [Ω]
R_c	Constriction resistance [Ω]
R_f	Film resistance [Ω]
R_s	Spreading resistance [Ω]
R_t	Total resistance [Ω]
r'	Combined contact radius [m]
r_a	Radius of individual hemispherical asperity [m]
ρ	Electrical resistivity [Ωm]
ρ_{cont}	Electrical resistivity of contaminant films [Ωm]
ρ_d	Electrical resistivity due to deformation [Ωm]
ρ_i	Electrical resistivity due to the incorporation of foreign atoms [Ωm]
ρ_m	Electrical resistivity of a pure material [Ωm]
ρ_p	Electrical resistivity of measurement probe [Ωm]
ρ_{Pf}	Electrical resistivity of plating material [Ωm]
ρ_t	Total electrical resistivity [Ωm]
S_q	RMS roughness [m]
S_y	Yield strength (based on the von Mises yield criterion) [Pa]
σ	Electrical conductivity [S/m]
σ_a	Standard deviation of asperity height [m]

σ_s	Standard deviation of surface height [m]
T	Temperature [K]
T_0	Ambient temperature [K]
T_b	Boiling temperature [K]
T_c	Contact temperature [K]
T_m	Melting temperature [K]
τ_e	Mean free time [s]
V	Electric potential or voltage [V]
V_c	Voltage drop between switching electrodes [V]
v	Poisson's ratio
v_d	Electron's drift velocity [m/s]
$wt.\%$	Weight percentage

Note: all units are shown in the international system of units without multiple or submultiple prefixes. The units used may differ from those shown in this table.

1. MOTIVATION & INTRODUCTION

The earliest known record of electricity is from ancient Egyptian texts dating back to 2750 B.C. These texts describe how the Egyptians were literally shocked by interacting with certain fish. The *Thunderers of the Nile* – or *Malapterurus electricus* – were a source of great wonder and intrigue to this ancient civilization, who regarded them as the "protectors" of all other fish [1]. It took over two millennia from the first recordings of electricity until the ancient Greek philosopher Thales of Miletus (circa 600 B.C.) observed that he could generate static electricity by rubbing items on amber, thus lifting lightweight objects such as feathers [2]. In the year 1600 A.D., a further two millennia after Thales discovered the electrostatic phenomenon, the English physician and physicist William Gilbert named the force exerted when items are rubbed together *electricus* – which translates to *of amber* from Latin – from the Greek term *elekron (λεκτρον)* [2]. A few years after Gilbert coined the term *electricus*, the English scientist Thomas Browne translated it into the word we still use to this day, electricity. The 18th and 19th century saw a plethora of pioneering experiments, inventions, and innovations, including the Watt steam engine, Volta's battery, and Faraday's electric dynamo power generator [3–5]. It was also during this period (1730) that Stephen Gray demonstrated that electrostatic charge can be transmitted, being among the first to experiment with electrical conduction [6].

Technological innovation and development have brought about numerous improvements in quality of life, and electrification is no exception. Increased energy consumption is strongly linked to this indicator [7], with global statistics highlighting an increased global demand for electricity. In 2022 and 2023, there was a 2.4% and 2.2% increase in global demand, respectively, with forecasts predicting an average annual growth of 3.4% through 2026 [8]. Access to electricity plays a crucial role in the standard of living of humanity, encompassing both essentials (such as healthcare and education) and mundane activities (such as entertainment and climate control) [9]. Moreover, interruptions in energy supply in a society that is extremely reliant on it leads to a number of adverse consequences, including health risks (e.g., carbon monoxide poisoning), higher carbon emissions, economic and financial losses, increased insecurity, and so forth; consequences which primarily affect at-risk populations [10]. This is particularly evident in developing nations, where access to reliable and clean sources of energy is a significant challenge. The United Nations has recognized the importance of energy access by including it in its Sustainable Development Goals for 2030 (7th goal) [11].

This highlights the significance of dependable, efficient, and sustainable electrical systems. The increased electrification not only results in a heightened demand for electrical components but also necessitates that these components be more durable and robust. Energy generation, electric mobility, and consumer electronics are among the primary drivers of elevated demand for electrical contact materials. For instance, electric vehicles (EVs) and low-carbon power generation technologies require a broader range of minerals and significantly larger quantities compared to conventional internal combustion engine vehicles (ICEVs) [12]. Green energy transition, in particular, is expected to significantly drive up the demand for copper from 28.3 million tons in 2020 to 40.9 million tons in 2040, according to research from CRU Group commissioned by the International Copper Association [13]. These trends have resulted in a transition from fuel-intensive to material-intensive energy systems.

One of the most significant aspects of the green transition is the electrification of transportation. Consequently, e-mobility is a particularly pertinent area of interest. The global stock of EVs, including both battery electric vehicles (BEVs) and hybrid electric vehicles (HEVs), has experienced a notable increase in recent years. In 2018, the global EV stock was approximately 5 million vehicles [14]. By 2023, this has increased to over 40 million, as shown in **Figure 1a** [15]. In the 1990s, the cost of a vehicle's on-board

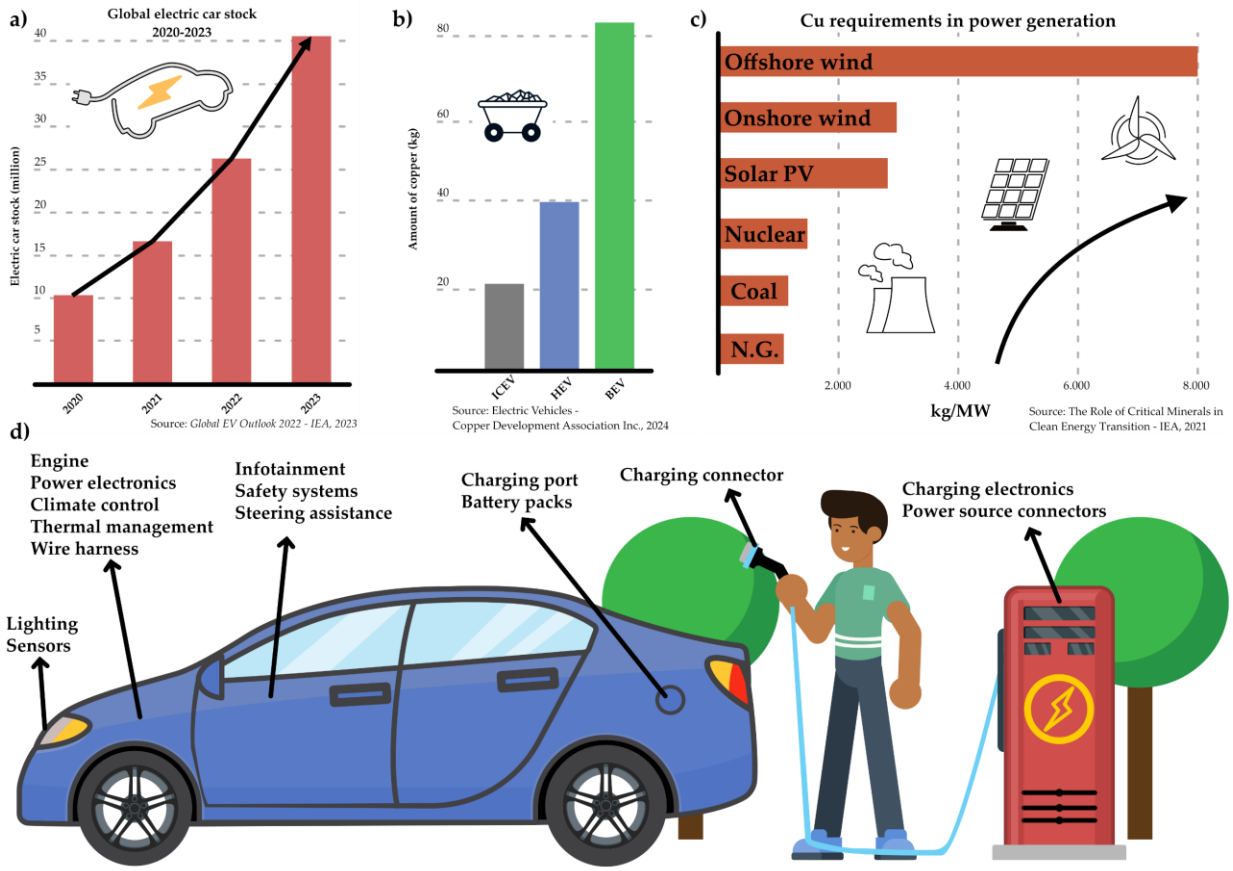

Figure 1: a) Global stock of electric vehicles between 2020 and 2023. Copper requirements in **b)** different passenger vehicle types and **c)** in power generation. **d)** Illustration of electrical systems in a BEVs and charging infrastructure.

electronics represented 15% of the total vehicle cost, this figure had increased to 40% in 2019 [16]. It is reasonable to presuppose that this number will continue to grow as EVs become more prevalent and developments in further automation and self-driving fleets become more commonplace. Current trends already show the increased demand for conductive materials, with HEVs requiring twice as much and BEVs up to four times as much compared to ICEVs (as shown in **Figure 1b)**. Similar trends are true in green energy generation, where renewable energy sources require exorbitant amounts of copper compared to conventional methods [12], as exhibited in **Figure 1c**.

The expansion of the electrical infrastructure is accompanied by an increased demand for contact materials. Conductive metals, such as silver and copper, are employed in a plethora of automotive applications, including wiring, switches, relays, conductive pastes, printed circuit boards, circuit-breakers, fuses, charging infrastructure, battery technology, and so forth [17–19], as illustrated in **Figure 1d**. Consequently, the development of lightweight, low-cost, energy and material efficient, durable, and eco-friendly electrical contacts is of the utmost importance. Considering each of these aspects individually:

- *Lightweight*: EVs have fewer moving parts compared to ICEVs and electric motors are lighter than internal combustion engines. However, EVs are generally heavier due to the significant weight of the battery packs. The weight of an EV is therefore linked to its range. The necessity for larger batteries to accommodate for longer ranges results in a substantial increase in the weight of the EV. Heavier vehicles raise concerns in a number of areas, including their performance, efficiency, effect on infrastructure, and safety. The weight of copper in ICEVs is estimated to be 23 kg. In a hybrid, plug-in hybrid, and battery EVs, these values increase to 40 kg, 60 kg, and 83 kg, respectively [18]. The number of connectors and electrical contacts in passenger vehicles is in the hundreds and thousands, respectively [20,21], with the number of these components expected to increase in line with the trend towards greater electrification. Consequently, even minor reductions in the weight of electrical contact materials can have a significant impact on the overall weight of a vehicle.

- *Low-cost*: silver is the metal with the highest conductivity [22]. However, this precious metal is considerably more costly than copper [23]. Therefore, it is of great importance to either reduce the quantity of silver required for specific applications or to extend the applicability of copper-based electrical contact materials.

- *Energy efficiency:* is a key consideration in certain applications, where in addition to minimal resistivity, the contact materials must be wear-resistant or chemically

stable. In these applications, noble metals such as silver and gold can be utilized; however, due to the costs associated, other metals such as copper can be used in combination with surface modifications. While certain techniques, such as protective coatings, metallic platings, and self-assembled monolayers may come at the cost of conductivity [24–31], improving the corrosion and wear resistance while minimizing resistivity gains is paramount. Furthermore, reducing the energy input required for component fabrication is highly advantageous [32].

- *Material efficiency:* in addition to lower energy consumption, material efficiency is closely linked to dematerialization. In this regard, it is of great interest to minimize the amount and variety of materials required to manufacture a component with the same – or improved – performance [32]. This results in a reduction in the quantity of virgin minerals required, while also facilitating a circular approach once the components reach their end-of-life [33,34].

- *Durable:* the concept of durability is inextricably linked to the principles of dematerialization and circular economy. Prolonging the duty life of components is a key objective in this regard. The enhanced durability of components results in a reduction in downtime, labor costs, replacement parts, among other expenses. The use of durable components not only reduces the frequency of replacements but also aligns with the principles of consumer-centricity, thereby enhancing the satisfaction and brand loyalty of the users.

- *Ecofriendly:* one of the most crucial aspects of sustainable electrical contact materials is the elimination of harmful substances. As previously stated, certain materials necessitate additional chemical treatments, coatings, reinforcing, and so forth. It is of utmost importance that additional techniques employed to minimize degradation do not harm the environment, those in contact, or present and future ecosystems. A prominent example is the substitution of harmful compounds, such as cadmium oxide in relay and contactor electrodes. Similarly, the use of per- and polyfluoroalkyl substances (PFAS) are currently being restricted due to their well-documented ecotoxicity [35,36].

Advanced contact materials have the potential to significantly enhance sustainability and operability, while also markedly improving quality of life, safety, and operational reliability. The automotive industry relies heavily on manual insertion of plugs during assembly. Many of these connections are in challenging-to-reach locations and require elevated insertion forces. The ZVEI (*Verband der Elektro- und Digitalindustrie*, or German Electro and Digital Industry Association) has reported that the primary cause of systematic failure in electrical contacts is the undesired disconnection of the contacts,

whereas the primary cause of accidental failure in electrical contacts is related to fretting wear [37]. Within the first 12 months of use, undesired disconnection and fretting wear account for 50% and 10.3% of failure, respectively, while within the first 36 months, these figures reach 58% and 8%. Systems that incorporate conductive lubricants can not only reduce wear, but also reduce insertion forces without compromising the all-important contact area required for proper electrical conductivity.

The failure of electrical components in automotive, aviation, and medical applications can have life-threatening consequences. The ADAC (*Allgemeiner Deutscher Automobil-Club*, or General German Automobile Club), reported that 10.5% of passenger vehicle breakdowns in 2023 were due to the failure of electrical systems, generators, lighting, and starter motors [38]. Furthermore, the primary cause of vehicle breakdowns was identified as battery-related issues, accounting for 44.1% of the causes. Additionally, 22.8% of incidents were attributed to motor, motor management, and sensor failures. Modern passenger vehicles and drivers are becoming increasingly reliant on the proper functioning of sensors – e.g., lane-changing sensors, cruise control distance sensor, and other advanced driver-assistance systems. This over-reliance significantly increases the necessity for the sensors and connectors to be trustworthy in order to ensure the safety of all road users. To further illustrate the severity of reliability in electrical components, it is necessary to discuss circuit breakers. These fundamental components are ubiquitous in both industrial and domestic settings, serving as essential safety devices for electrical systems. Circuit breakers are designed to protect devices from overcurrent, which could potentially lead to fires. However, ground fault circuit interrupters and residual current devices are fundamental to protecting humans from dangerous electrical discharges. Although electrical discharges from alternating currents are significantly more dangerous than direct current (DC) [39,40], the higher voltages used in EV battery packs and solar photovoltaic installations, for example, can be dangerous if safety measures are not implemented. If the switching component of these life-saving devices fails – due to the welding of the electrodes for example – it could cause severe harm or even death. Consequently, the design and characterization of electrical contact materials and components must be approached with utmost seriousness.

Accordingly, this work is focused on incorporating carbon nanoparticles into silver- and copper-based electrical contact materials (in the form of protective coatings and as reinforcement phases) with the objective of enhancing the contact materials' durability, applicability, and reliability. Design criteria, such as impact on conductivity, sustainability, industrial viability, user safety, etc., were kept at the forefront when selecting manufacturing techniques, processes, and materials/substances requirements.

2. THEORETICAL FRAMEWORK

This section is focused on the theoretical framework and development of concepts related to electrical contacts and electrical contact materials. For a brief description of basic electrical concepts, refer to APPENDIX A, *Section A.1*.

2.1. Electrical contacts

2.1.1. Fundamental theory

The functionality of electrical systems is contingent upon the efficacy and operational reliability of their electrical contacts. These components are designed to enable the flow of electrical current between different components. However, the efficiency and reliability of electrical contacts is considerably influenced by the selection of materials. Common metals employed in the fabrication of electrical contacts and their resistivity at 20 °C are shown in **Table 1**. This choice is vital, since other physical properties and material characteristics need to be taken into account when designing an electrical contact. Copper and its alloys are extensively used in a multitude of industrial and domestic applications due to their excellent conductivity, good mechanical properties, and relatively low cost [41]. Silver offers superior conductivity with improved anti-corrosive characteristics; however, this precious metal is significantly more expensive than copper. Therefore, silver is utilized in high-performance applications. Similarly, gold is exclusively employed in instances where corrosion resistance is of utmost importance due to the associated costs, as well as its higher resistivity compared to copper and silver. To overcome certain shortcomings of pure metallic conductors, it is standard practice to alloy, reinforce, process, or coat/plate the metals. Through alloying and reinforcements, metallic conductors can be made stronger, more ductile, wear, weld, or corrosion resistant. Likewise, post processing techniques seek to improve the mechanical properties (such as ductility, toughness, or strength) of the conductors, whereas coatings and platings primarily seek to maximize contact area, improve wear resistance, or corrosion resistance.

Table 1 – Electrical resistivity at 20 °C of commonly used metals [22].

Metal	Resistivity ($\times 10^{-8}$) /Ωm
Aluminum	2.65
Copper	1.65
Gold	2.19
Nickel	6.84
Platinum	10.6
Silver	1.59
Tin	11.6

Electrical resistance is not a material property, but rather a system characteristic. Factors that can influence electrical resistance are electrode geometry, applied load, surface finish, the presence of contaminants, etc. [22,42]. On a microscopic scale, all surfaces, regardless of how smooth they might appear to the naked eye, possess a certain roughness. This roughness is a result of topographic features, which can be brought upon due to processing techniques employed in the manufacturing process. Even mirror polished surfaces retain topographic minima and maxima. These features have a significant influence on the conduction of electrical current since the effective conduction paths between two microscopically rough surfaces are the sites where the topographic features of one surface meet the topographic features of the other surface. In other words, when two surfaces are pressed onto one another, there is an apparent contact area, which is the projected area of the smaller surface on the larger surface, and a real contact area, which is made up of the active conduction area, the quasi-metallic contacts (when insulating films are present), and the load bearing area. This phenomenon can be visualized by the illustration in **Figure 2a**. The real contact area between the two surfaces where the current flows through is the sum of all the individual sites where topographic features touch. Each of these sites are known as a-spots [22], and are schematically represented in **Figure 2b**. As this figure shows, the

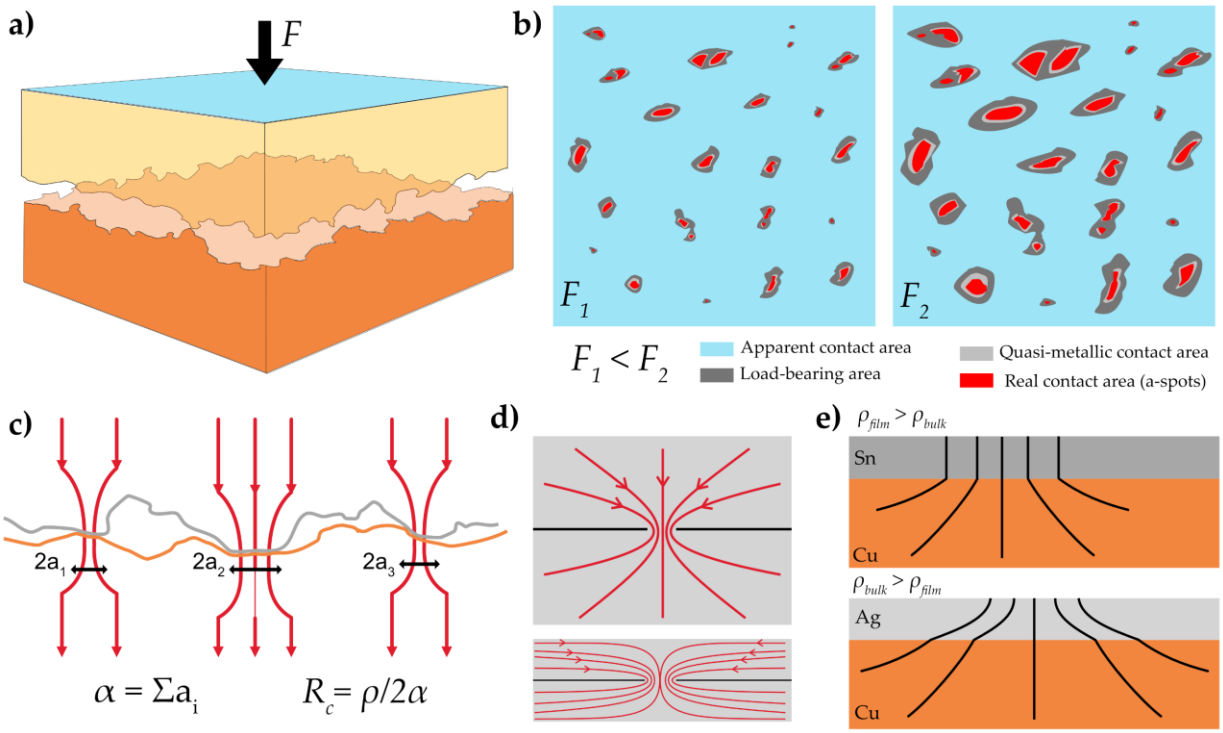

Figure 2: a) Schematic representation of two contacting surfaces. **b)** Top-down view of the apparent, load-bearing, quasi-metallic, and real contact area between two surfaces at different loads. **c)** Schematic representation of the current's constriction at a-spots and **d)** spreading resistance at an a-spot between two bulk conductors (top) and between two thin films (bottom). **e)** Visualization of constriction and spreading of the current due to differences in the film and bulk materials' resistivity. Subfigure **a)** was reused and adapted with permission from Gwidon W. Stachowiak and Andrew W. Batchelor, *Engineering Tribology* 2nd Edition, 2000, Butterworth-Heinemann, page 461, Figure 10.12 [43]. Subfigure **c)**, **d)**, and **e)** were reused and adapted with permission from Paul G. Slade, *Electrical Contacts: Principles and Applications* 2nd Edition, 2017, Taylor & Francis Group, page 5, Figure 1.1, page 19, Figure 1.15, and page 24, Figure 1.19, respectively [22].

real contact area (in red) is dependent on the normal load that is applied between the two surfaces. The light gray region highlights the quasi-metallic contacts established between the metal and the insulating film (e.g., oxide layers), whereas the dark gray region in the contact is the load-bearing area where conduction does not take place. Furthermore, the light blue area is the projected area of the two surfaces. Other parameters, apart from normal load, that can increase or decrease the size or number of a-spots are material hardness, roughness, and the presence of contaminant films. For example, harder materials do not easily deform; therefore, considerably higher normal loads are required to deform asperities and consequently increase the size of the a-spots.

The interface between electrodes is a critical region where electrons scatter. At the interface, the electrical circuit is microscopically open and closed in different regions, since not the entirety of the surface is in electrical contact. Therefore, the current flowing through a conductor, upon reaching the contacting region between two electrodes, is constricted and flows only through the a-spots – as shown in **Figure 2c**. Due to the reduction in the effective conduction area, the electrical resistance increases [22]. This is known as the constriction resistance R_c and was defined by Ragnar Holm as the quotient between the material's resistivity and the contact diameter [44]. The constriction resistance is shown in **Equation 1**, where α is known as the Holm radius and corresponds to the summation of the radius of each a-spot under the assumption of circular a-spots. Using Holm's radius, an equivalent circular real contact surface can be modeled to determine the constriction resistance of two rough surfaces in contact. Although **Equation 1** appears relatively simple, defining Holm's radius is not trivial since determining the radius of each individual a-spot is extremely complex. Therefore, the constriction resistance can be calculated using the materials' hardness H and the applied load F – as shown in **Equation 1**. η_c is an empirical factor that describes the cleanliness of the interface, taking a value of 1 for clean surfaces. Prior to and after constriction, in an isotropic conductor, the current spreads in the conductors. This is known as the spreading resistance R_s or the resistance of the bulk materials (visualized in **Figure 2d**) and can be approximated using Holm's equation shown in **Equation 2** [44]. This is an ideal resistance which occurs directly under the contact interface [45].

$$R_c = \frac{\rho}{2\alpha} = \rho\sqrt{\frac{\eta_c \pi H}{4F}} \qquad \textbf{Equation 1}$$

$$R_s = \frac{\rho}{4\alpha} \qquad \textbf{Equation 2}$$

$$R_t = R_c + R_f + R_b \qquad \textbf{Equation 3}$$

$$R_t = \frac{\rho_p + \rho_{Pf}}{2}\sqrt{\frac{\eta_c \pi H}{4F}} + \frac{\rho_{cont} d_{cont} H}{F} \qquad \textbf{Equation 4}$$

When surfaces in contact possess thin film, the current flowing through the a-spots undergoes localized constriction and spreading, known as the film resistance R_f – **Figure 2e**. The behavior of the current depends on the resistivity of the film. If the resistivity of the film ρ_{film} is higher than that of the bulk ρ_{bulk}, the current initially constricts followed by its spreading when flowing through the bulk. Conversely, if the resistivity of the bulk is higher than that of the film, the current spreads in both cases, however to a higher degree while flowing through the film. A prime example of the former is tin-plated copper, whereas the latter is the case in silver-plated copper. Therefore, the total electrical resistance R_t between two contacting surfaces can be defined as the sum of the constriction, film, and bulk resistances – R_c, R_f, and R_b, respectively – as presented in **Equation 3** [22]. In this case, the constriction resistance of the film can be determined similarly to **Equation 1**. The origin of the film resistance is not only associated with platings, but also with corrosion films, organic films, or other contaminant sources. Therefore, the resistance associated to these contamination films must also be taken into consideration. Accordingly, the total resistance of two contacting surfaces can be determined via **Equation 4**, where ρ_p is the resistivity of the material contacting the plated surface, ρ_{Pf} is the resistivity of the plating material, ρ_{cont} and d_{cont} are the resistivity and thickness of the contaminant film [22]. The first term in **Equation 4** represents the electrical resistance that arises from the contact between a perfectly clean plated material and probe, whereas the second term represents the electrical resistance originating from contaminant films. Furthermore, in the presence of contaminant, corrosion, or insulating films, the a-spots from **Figure 2b** are further divided into the quasi-metallic contact and the metallic contact [42], which are also considered in the second term in **Equation 4**.

Observing **Equation 4**, it is clear that the cleanliness of the contacting surfaces can have a significant impact on the total resistance of the system, particularly since the resistivity of these films are generally considerably higher than those of pure metals [22]. Consequently, minimizing contaminant films (e.g., organic contaminants) and/or insulating films (e.g., oxide films) is of utmost importance. From an engineering perspective, **Equation 4** is of significant importance. It presents the criteria for the proper design of an electrical contact. The numerator of the first term (excluding the cleanliness factor) is comprised of the materials' resistivity and other materials' characteristics. However, as shown in **Table 1**, material choice is generally limited since resistivity and other application-based requirements (such as chemical inertness, wear resistance, etc.) must be met. The denominators are solely governed by design choices and affect the degree to which the surfaces deform. Consequently, the designed load influences the real contact area and constriction resistance. Nonetheless, there are practical limitations to this selection. It is evident that higher normal loads will favor lower resistance values. However, opting for high loads is not always feasible since this will significantly increase the insertion and retraction forces required, in addition to

affecting wear rates. Lastly, the second term's numerator and the cleanliness factor can be manipulated through superficial treatments (e.g., laser texturing, passivation, plating, etc.). This design criterion can significantly influence the overall performance of the electrical connector and yields the most freedom to tailor the system for specific applications.

2.1.2. Slope analysis – dominant resistance & deformation mechanisms

Apart from the normal load F, all parameters in **Equation 4** can be considered constant. Therefore, for a given contact, **Equation 4** can be simplified into **Equation 5**, where k is a constant value that encompasses all resistivities, cleanliness factor, hardness values, and contaminant thickness, and n is an exponent. The latter can be experimentally calculated by performing a linear fitting of the load-dependent ECR curves when plotted in a double logarithmic axis, where the slope of the fitted curve corresponds to the n factor.

The significance of this n factor cannot be understated, since determining its value indicates not only the predominant resistance but also the predominant deformation mechanism for a specific loading range in the contacting system under consideration [22,44,46]. When the n factor takes values of -1/3 or -2/3, elastic deformation is predominant in the system, whereas plastic deformation is predominant when n takes a value of -1/2 or -1. Moreover, constriction resistance dominates the system when n takes a value of -1/3 or -1/2, whereas film resistance is the predominant source of resistance when n takes a value of -2/3 or -1. However, it should be noted that this analysis is strictly theoretical in nature. In practice, exponent deviations are to be expected since the method considers that the contacting bodies are flat, smooth, and clean. Furthermore, this methodology supposes that only one of the contacting bodies undergoes deformation, while only taking into consideration the loading phase of load-dependent ECR. In practice these assumptions cannot be guaranteed, thereby leading to n values that do not match with the theoretical values. Nonetheless, this methodology enables a quick and straightforward prediction of the predominant mechanisms at play in the system. An exemplary analysis is shown in **Figure 3**. In this example, a tin-plated copper electrode was contacted against a hemispherical hard-gold coated counter electrode and the load-dependent ECR between 1 N and 15 N was measured. As the shaded areas highlight, three distinct regions are discernable. Due to the aforementioned shortcomings, the slope values deviate from the theoretical values. Nonetheless, in the loading range between 1 N and 5 N (regions A and B), the n factor takes values that approach -1, whereas between 5 N and 15 N -1/3 (region C). In other words, the slope analysis indicates that film resistance and plastic deformation dominate the system below 5 N and that constriction resistance and elastic deformation dominate the system above 5 N. In this example, the hardness of the counter electrode is significantly higher than that of the tin-plated copper electrode. However, the n factor

$$R_t \cong \left(\frac{k}{F}\right)^n$$ **Equation 5**

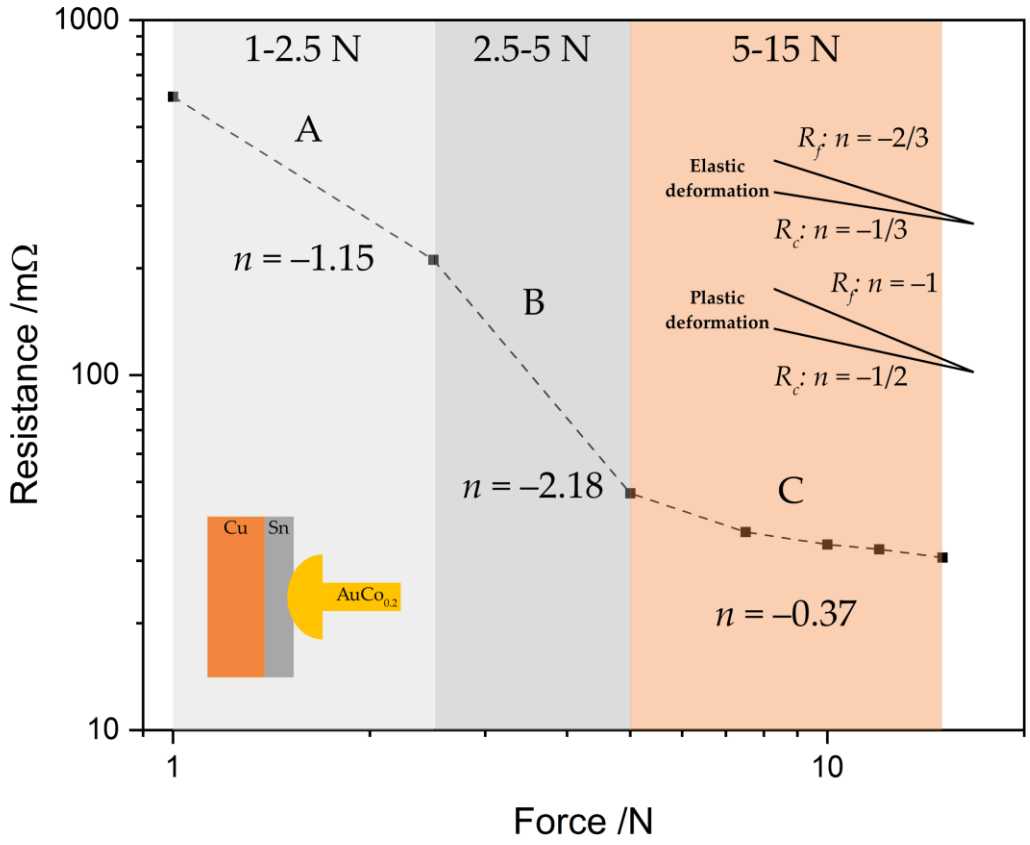

Figure 3: Exemplary slope analysis for a tin-plated copper electrode against a hemispherical hard gold coated counter electrode. The shaded areas highlight the different slopes and loading ranges. The slope of regions A and B approach -1, which corresponds to predominantly film resistance and plastic deformation, whereas the slope of region C approaches -1/3, which corresponds to predominantly constriction resistance and elastic deformation.

deviations can be attributed to the roughness present on both surfaces, in addition to the potential presence of contaminant films and hemispherical geometry of the counter electrode.

The simplification presented in **Equation 5** enables a quick approximation of the resistance as a function of material properties and normal load applied. This approximation was initially deduced by Holm to estimate the constriction resistance between two contacting spheres and an n factor equal to -1/3 [44]. The equation was subsequently generalized to incorporate film resistance when the n factor takes a value of -1 [22], as well as the predominant deformation mechanism [46]. As can be observed in the example presented in **Figure 3**, the n factor takes a value lower than -1 in regions A and B, which significantly deviates from the theoretical values for film resistance. As reported by Leidner et al. [47], n factor values below -1 can be attributed to, in part, the fact that the theoretical methodology was developed using Hertzian contact theory (HCT) which does not consider plastic deformation. Moreover, Leidner et al. discuss the

discontinuity of the contacting surfaces due to topographic features (contact between a-spots), the interaction between individual a-spots, localized stress concentration at the a-spots leading to their plastic deformation, the fact that the real contact area is significantly smaller than the apparent contact area, as well as the use of coatings and/or platings [47]; all components which contribute to the further deviation of the n factor.

2.1.3. Contact physics between real surfaces

A real surface, in the context of this theoretical framework, is a non-ideal surface. In other words, real surfaces are neither smooth nor undeformable. Although a mirror-polished surface – on a macroscopic level – may appear to be devoid of topographic features, this is certainly not the case on a microscopic level. These topographic features are responsible for generating the surfaces' roughness and can be qualitatively and quantitatively characterized through different parameters – e.g., the arithmetic roughness, root mean square (RMS) roughness, maximum height, skewness, among others [48]. It is the peaks – i.e., the topographic maxima – that initially establish the conduction paths through which the current flows (a-spots). Subsequently, as the contacting load increases, the asperities begin to deform thereby increasing the contacting area and thus reducing the constriction resistance. In this regard, the dimensions of the asperities play a crucial role in the contact mechanics between rough surfaces. On the one hand, larger asperities have a larger area for initial conduction; however, larger asperities require higher normal loads to reach plasticity. Smaller asperities, on the other hand, reach the onset of plasticity with significantly lower normal loads, thus flattening out and decreasing the current's constriction. Nonetheless, the initial contact sites are much smaller. The degree to which asperities deform, and the loads required to reach plasticity, will inevitably depend on the contacting materials' properties and characteristics – e.g., modulus of elasticity (E_m), Poisson's ratio (v), hardness (H), etc. All these interlinking conditions considerably complicate the analysis of real contacting surfaces.

In 1881, Heinrich Hertz published his work "On the contact of elastic solids" (translated from the original German title: *„Über die Berührung fester elastischer Körper"*) [49], where he analyzed the frictionless, elastic contact between non-conforming, ideal surfaces [50,51]. Hertz's model is applicable for point contacts (e.g., contact between two spheres, sphere-on-flat, or between two perpendicular cylinders) and line contacts (e.g., contact between two parallel cylinders). This theory enables a relatively straightforward way to determine the contact area between the two surfaces, the maximum and median contact pressure (known as Hertzian contact pressure), and the total (elastic) deformation that the bodies have endured at the specific load.

Although HCT is highly regarded, it presents several limitations due to the assumptions considered – i.e., only applicable for elastic deformation, localized contact

areas ignoring multi-point contacts, and neglects friction. Consequently, other mathematical models have been developed to overcome these shortcomings. Greenwood and Williamson expanded upon HCT by stochastically modelling the contact between rough surfaces [52,53]. Due to the presence of superficial roughness, the Greenwood-Williamson (GW) models the contact between multiple sphere-on-plane contacts. To simplify the model, the GW methodology considers one of the contacting surfaces to be perfectly smooth, whereas the other surface possesses a roughness equivalent to the real roughness of both contacting surfaces. Therefore, in the sphere-on-plane model, each sphere represents an asperity of the equivalent rough surfaces and the plane a perfectly smooth surface. Further assumptions for this model include: i) a random asperity distribution that can be modeled by a Gaussian distribution; ii) independently of asperity height, at their summit the radius of curvature is constant for all asperities; iii) asperities are mechanically independent; iv) only the asperities deform – i.e., elastic spheres against a rigid plane contact.

The GW model provides information on the elastic contact between rough surfaces; however, it does not provide sufficiently accurate information on the elasto-plastic regime. For such cases, complementary models should be employed, such as the Kogut-Etsion [54], Chang-Etsion-Bogy [55], Zhao-Maietta-Chang [56], Shankar-Mayuram [57], Lin-Lin [58], among other models [59]. The Jackson-Green model (JG) incorporates several spherical contact formulations, in addition to the fact that it is not dependent on limiting assumptions such as the hardness of the materials [60,61]. This model enables the calculation of the critical interference (ω_c), critical individual asperity contact force (P_c), and critical area of contact (A_c) in an elasto-plastic deformation regime. The contact condition itself is indicated by the plasticity index (ψ). Plasticity index values below 0.6 indicate that the system deforms purely elastically, whereas plasticity index values above 1 indicate that the system is in a plastic regime [60,61], with GW highlighting that for real surfaces the plasticity index ranges from 0.1 to 100 [52]. Accordingly, plasticity index values between 0.6 and 1 suggest the onset of plasticity in the system. The main considerations, assumptions, and equations for the GW and JG models are expanded upon in greater detail in ARTICLE V.

2.2. Wear & degradation of electrical contacts

The degradation of electrical contacts can be classified in several ways depending on the mechanisms at play. This section elaborates on the wear mechanisms on static electrical contacts, ways to minimize and/or prevent wear, atmospheric parameters that can degrade contact materials, and electro-erosion in switching contacts. Important tribological concepts are herein introduced, focusing specifically on those that are more relevant to electrical systems.

2.2.1. Wear in static connectors

Static connectors – such as plug-and-socket connectors – are designed to interconnect different components, thus enabling the conduction of current through the systems, typically consisting of a pin (also known as plug, jack, prong, or male terminal) and a socket (also known as receptacle, slot, rider, or female terminal) [22]. Other types of static connectors include flat-on-flat or round-on-flat pairs, busbar connectors, terminal block connectors, among others. These types of connectors are denominated as "static" since they are meant to remain in place upon connection with few disconnections and reconnections. However, wear still takes place during the insertion process, during maintenance, due to unforeseen disconnections, or as a consequence of vibrations, thermal cycling, etc. Several factors influence the extent of wear in static electrical contacts, including contact design (i.e., contact force, roughness, housing), material choice, and environmental conditions.

Wear is one of the three principal branches of tribology, along with friction and lubrication [43,50]. It is a phenomenon that arises from the interactions between contacting surfaces in relative motion to one another. Wear is generally an undesirable consequence of the tribological system which affects the durability of components due to the progressive removal of material. As wear intensifies, it entails other negative side effects, such as loss in efficiency, increased heat generation, reduction in contact area, etc. Irrespective of the wear mechanism at play, the strategy to minimize wear is the effective separation of the contacting surfaces through surface treatments or lubrication – i.e., liquid lubrication, greases, soft metal plating films, or solid lubrication.

Reducing wear in electrical contact is quite an undertaking, since we run into a bit of a paradox. On the one hand, to reduce friction and wear it is crucial to minimize the contact area. On the other hand, based on Holm's equation, a reduction in the contact area – and therefore a reduction of the a-spots – implies a reduction in the effective conduction area, which in turn increases the electrical resistance [22,44]. This dichotomy forces us to choose between prolonging the duty life of a connector by reducing wear and sacrificing conductivity or improving electrical performance and efficiency at the cost of increased degradation.

There are different types of wear, which depend on the mechanisms at play. The types and severity of wear depends on the materials in contact, characteristics of the contacting system, and operational conditions [43,50]. In general, the main types of wear in electrical systems can be classified as adhesive, abrasive, fretting, fatigue, corrosive, and erosive wear. Adhesive and abrasive wear are the primary wear mechanisms

caused by sliding motions. Fretting wear, on the other hand, is not caused by linear motion but rather by short oscillatory motions [22,43,50].

2.2.2. Adhesive wear

Adhesive wear occurs due to the interatomic interactions between the asperities in contact, creating localized adhesion caused by the contact load, temperature, pressure, or a combination thereof [62]. The formation of these localized micro-welds are – in part – responsible for the frictional forces that arise during relative motion. The adhesion of the contacting asperities is not intrinsically detrimental to the surface. However, as the surfaces sperate or move relative to one another, the localized adhesion points break – schematically represented in **Figure 4a** and **b**. This leads to the deterioration of the weaker surface, where material is chipped off, and material transfers towards the stronger surface through the adhered material. Adhesive wear is characterized by its high wear rates and considerable fluctuations that it produces in the coefficient of friction, which can severely damage the contacting surfaces or raising the coefficient of friction to a point where the motion does not take place (known as friction seizure) [43]. Furthermore, adhesive wear may also lead to the formation of debris particles from one or both surfaces. The debris particles may adhere onto the contacting surfaces or may remain loose. This is particularly troubling in electrical contacts, since these fine particles are prone to corrosion, which are generally poor conductors or insulations, thus worsening the electrical conductivity between the surfaces [22].

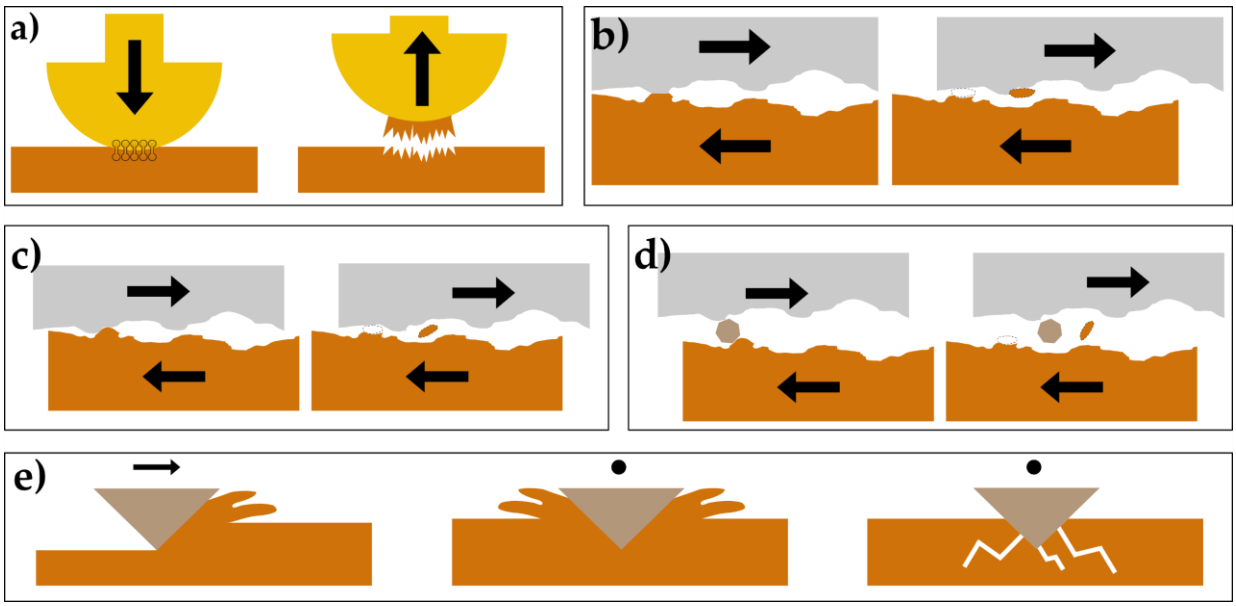

Figure 4. Schematic representation of **a)** static and **b)** dynamic adhesive wear, **c)** two-body and **d)** three-body abrasive wear. **e)** Schematic of different types of micro-cutting, micro-plowing, and micro-cracking (from left to right). The arrows indicate the direction in which each body is moving, whereas the dots indicate that the body is moving out of plane. Subfigures **a)** and **e)** were reused and adapted with permission from Gwidon W. Stachowiak and Andrew W. Batchelor, *Engineering Tribology* 2nd Edition, 2000, Butterworth-Heinemann, pages 484, Figure 11.1 and page 534, Figure 12.2, respectively [43].

Proper material selection is crucial to minimize adhesive wear, since material characteristics – such as hardness, ductility and chemical compatibility – play a pivotal role in the degree to which two asperities adhere [50]. Soft and ductile metals are more easily plastically deformed, which increases the area of contact between the surfaces. This is beneficial for electrical conductivity, but it also increases the potential for the surfaces to bond and adhere. Adhesion is stronger when the contacting bodies are the same metals, or metals with similar crystalline structure. However, dissimilar metals can also form strong adhesive bonds, the only requirement is that the two surfaces are in sufficient proximity in order to enable the free electrons to bond both solids [43]. Therefore, to reduce the likelihood of adhesion, the contact area should be relatively small, thus reducing the interatomic interactions between the surfaces. This is usually achieved by selecting hard materials, materials that do not easily deform (high elastic moduli), or materials with low chemical reactivity. Furthermore, oxide and passivation layers also tend to minimize adhesion by reducing chemical reactivity between the contacting surfaces [43,50]. For this reason, adhesive wear is more significant in vacuum conditions, since these layers do not naturally form. However, for electrical applications, material choice is limited due to the electrical requirements and oxide layers are generally detrimental towards their conductive properties. Moreover, minimizing contact area to reduce adhesive wear goes against Holm's equation for proper conduction of electricity. Therefore, alternative methods to reduce adhesive wear must be developed.

Other factors that influence adhesive wear include roughness, contact force, sliding speed, frictional forces, lubrication, and environmental conditions [22]. Nevertheless, the principle remains the same, minimizing interatomic interactions reduces the chances of adhesion, whereas conditions that promote these interactions will increase adhesive wear. The presence of oxide films is a factor that is of particular interest. Oxide films are generally non-conductive, which negatively impacts the conductivity of the contact. Therefore, it is generally sought after to remove the oxide films in order to improve electrical conductivity. Although the oxide films reduce chemical reactivity and consequently hinder adhesion, the removal of the oxide film caused by the sliding motion could lead to the formation of wear debris, which could promote severe abrasive wear while also enabling adhesive wear between the "clean" surfaces [22,42]. Likewise, other superficial contaminants (such as dust particles or organic contaminants) can effectively separate the two surfaces and consequently reduce the likelihood of adhesion, although it comes at the cost of increased electrical resistance and likelihood of abrasive wear.

2.2.3. Abrasive wear

Abrasive wear occurs when a hard body is pressed against a body of lower or equal hardness. The hard asperities indent onto the softer surface on account of the contact force, and as the surfaces move relative to one another material from the softer body is displaced or removed [22,43,50,62]. This type of wear can be classified into two subsections: two-body (**Figure 4c**) and three-body (**Figure 4d**) abrasive wear, with two-body abrasive wear generally resulting in more severely damaged surfaces. The former consists of a hard surface (asperity) displacing or removing material from a softer surface, whereas the latter involves the displacement or removal of material due to the presence of particles trapped between the contacting surfaces. These particles may originate either from external contaminants or due to wear debris stemming from detached or cracked asperities. Depending on the characteristics of the abrasive body, the mechanisms behind abrasive wear can be classified as micro-plowing (groove formed by displacing material), micro-cutting (removal of ductile material by the hard wedge), and micro-cracking (wear particles crack brittle material, which propagate resulting in the fragmentation of the material) – see **Figure 4e** [63]. As previously discussed for adhesive wear, abrasive wear can be minimized by proper material choice (e.g., selecting materials with similar hardness values), by contact design (contact force, sliding distance, etc.), or by effectively separating the contact through lubrication.

2.2.4. Fretting wear

Fretting wear, fretting corrosion, and fretting fatigue all refer to superficial damage incurred on contacting surfaces due to short-amplitude, oscillatory relative motion between the contacting bodies – schematically shown in **Figure 5** [22,42,44]. Although the line between reciprocating sliding wear and fretting is not clearly defined, it is generally accepted that fretting is the wear mechanism for sliding distances of up to 125 μm, with experimental evidence proving that amplitudes as small as 100 nm are enough to damage the surfaces [64]. These minor displacements – which can be caused by external vibrations, differences in thermal expansion coefficients, external mechanical perturbations, load relaxation, among others – degrade the contacting surfaces through conventional wear mechanisms (i.e., adhesive and abrasive wear). In addition, fretting wear degrades passivation and lubrications films, which in turn promotes corrosion of the contacting surfaces – hence the denomination of "fretting corrosion". Despite fretting's relatively small area of influence, it is a serious phenomenon which can severely affect the efficiency, reliability, and durability of electrical contacts. Moreover, since fretting wear is an undesirable and oftentimes unforeseen degradation mechanism, it is frequently overlooked. Therefore, in order to minimize its influence on the performance of electrical contacts, proper contact design

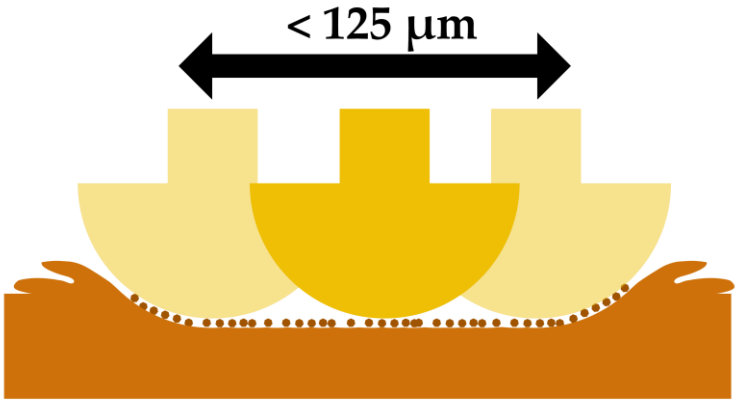

Figure 5. Schematic representation of fretting wear.

is pivotal. Fretting wear does not exclusively affect electrical connectors but is rather a pervasive phenomenon that affects plenty of components in a wide range of applications. However, the focus herein will be placed on the effect that fretting wear can cause on electrical connections, since it can lead to a deterioration in the contact area, thereby increasing contact resistance, and ultimately lead to failure of components [22,42]. This phenomenon can further increase electrical resistance since the debris formed during fretting (generally metal oxides) can act as an insulating barrier and accelerate abrasive wear in the contact [65].

The exact mechanisms via which fretting damages the surfaces in contact are disputed. A wide variety of explanations have been proposed since the first report of fretting wear/corrosion was brough to light in the early 1900's. The first theory on fretting corrosion was proposed by Tomlison [66], suggesting that as the two surfaces come into contact with one another, cohesive forces detach atoms and molecules. These detached atoms and molecules corrode upon detachment, hence causing fretting corrosion. Godfrey reported that fretting wear is caused by adhesive wear [67], where the debris that is generated due to adhesive wear corrodes. Feng and Rightmire [68], on the other hand, suggest a two-step model in which fretting wear is always initially caused by adhesive wear. After which, a transitional period takes place where the wear debris that is generated in the initial step are trapped between the contacting bodies and abrasive wear begins to dominate the system, eventually becoming the singular wear mechanism. Further possible explanations for fretting wear, corrosion, and fatigue have been proposed by Uhlig [69], Stowers and Rabinowicz [70], Oding and Ivanova [71], among others [72–77]. However, it is clear that during fretting: i) existing corrosion films are mechanically removed, thus exposing pristine metal to corrosion; ii) adhesive wear is prominent during fretting; iii) wear debris is generated, and this debris corrodes forming harder particles which increase abrasive wear [22,42].

The rate at which fretting wear degrades the surfaces depends on factors which can be classified into three main categories: 1) material properties, 2) contact conditions, and 3) environmental conditions [22,42]. Among the most important factors that influence fretting wear, duration, frequency, and amplitude (factors which can be classified under contact conditions) are the most noteworthy. The type of damage endured by electrical contacts due to fretting wear can be classified as *sticking*, *partial slip*, *gross slip*, and *reciprocating sliding* depending on the sliding amplitude. *Sticking* takes place at amplitudes below 1 μm, *partial slip* between 1 and 3 μm, *gross slip* between 10 and 100 μm, whereas *reciprocating sliding* is the denomination for all sliding motions with an amplitude greater than 100-200 μm [22]. However, by definition, *reciprocating sliding* is no longer considered fretting since the sliding distance exceeds the threshold for fretting. In a *sticking* regime, close to no superficial damage can be observed on the contacting surfaces; however, the low amplitude oscillations may lead to the generation of debris due to nucleation and propagation of fatigue cracks. A *partial slip* regime is characterized by a central sticking region, surrounded by a ring-shaped area where cracks may have formed, fatigue may have taken place, and debris have been generated. In a *gross slip* regime, the contacting surfaces slide across the entire contact area, resulting in the most severe form of fretting wear as a consequence of the removal of native oxide films (thus favoring adhesion). Moreover, a fifth regime denominated as *mixed slip* was also identified. A mixed slip regime involves an initial stage where gross slip dominates the system, followed by a stage where partial slip is the primary cause of wear [22].

Other prominent factors include the materials' susceptibility towards corrosion and adhesion, as well as the use of lubrication and atmospheric conditions (i.e., temperature and humidity). Elevated humidity levels, in particular, tend to accelerate the failure of electrical components subjected to fretting wear [22]. During fretting, the ECR of the system undergoes changes until ultimately reaching component failure. The evolution of ECR during fretting is characterized by three distinct domains:

1. Upon initiation of the oscillatory motion, the ECR will tend to decrease due to the removal or displacement of superficial contaminants and breakdown of corrosion films.
2. Subsequently, the resistance remains – to a certain extent – constant at a low value.
3. In the final step the electrical contacts degrade at an accelerated rate due to the increased generation and presence of wear debris, thereby substantially increasing the ECR due to the buildup of non-conductive metal oxides.

2.2.5. Erosive wear (electro-erosion)

Erosion is a wear mechanism that is characterized by the degradation of a surface due to the impact of hard particles. In erosive wear, the incident particles can be either in liquid or solid state. The degree to which a surface undergoes this type of wear depends on the angle and velocity of the impacting particles, as well as their relative hardness and size [43,62]. However, the focus of this section is to introduce the concept of electro-erosion (also referred to as arc erosion), particularly during break operations.

Electro-erosion is characteristic of switching electrical contacts – i.e., electromechanical contactors, relays, circuit breakers, etc. Due to the operational conditions of these components, the electrodes make (close) and break (open) the electrical circuit while energized, a process which is referred to as hot switching [78]. Essentially, electro-erosion is the localized material removal, material displacement, or superficial morphological and/or structural changes induced by the energy input originating from an electrical arc. These changes are brought upon the electrodes due to the bombardment of charged carriers as a consequence of the explosion of the molten bridges and subsequent ignition of the electrical arc. During the metallic vapor phase of the electrical arc, the electrons liberated from the cathode generate positive metal ions, causing the evaporation of anode material through electron bombardment [22]. In this instance, the positive metal vapor ions move towards the cathode. These ions recombine and condensate on the cathode's surface. The deposition of the ions on the cathode leads to a net cathode gain of material, whereas anode evaporation leads to anode loss of material [44]. However, after the electrical arc transitions from metallic vapor towards gaseous phase (process that only takes place if the arc's duration and length is sufficient to allow ambient gases to flow into the contact gap [22]), the ionized ambient gases erode the cathode, and to a minimal extent the anode, thus leading to an overall cathode loss of material and a net anode gain of material. This process is known as anodic to cathodic arc transition [79]. When the characteristic of the electrical arc allows anodic to cathodic arc transition, there is an instance known as net zero erosion where the material

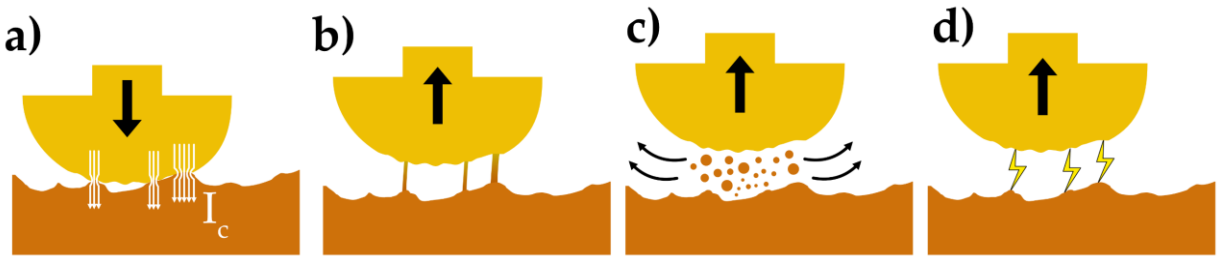

Figure 6. Schematic representation of the formation of the electrical arc during hot switching. **a)** Constriction of the current through the a-spots. **b)** As the moveable electrode retreats, the molten bridges are formed and drawn out. **c)** Molten bridges become unstable and rupture, emitting metallic vapor into the gap and increasing local pressure. **d)** The electrical arc ignites, eroding the electrodes through electron and ion bombardment.

that was deposited onto the cathode during the metallic vapor phase is eroded and the cathode has not gained nor loss material [80]. Net zero erosion depends on the amount of material that was transferred in the initial stages of the electrical arc; therefore, arc duration and electrode material influence when this point is reached. The mechanisms via which the electrical arc in a break operation ignites is schematically shown in **Figure 6** and explained in further detail in APPENDIX A, *Section A.2*.

2.2.6. Corrosion and atmospheric conditions

Corrosion is the result of an electrochemical reaction that occurs naturally over time. This reaction is associated with the transfer of electrons between two bodies or between one body and the surrounding environment, known as a redox (reduction-oxidation) reaction, whereby one component is the electron doner (oxidized body) and the other receives electrons (reduced body) [22,42,81–83]. An everyday example of corrosion is the oxidation of iron – commonly referred to as rusting. Although the process of corrosion occurs naturally, it can take quite some time to fully degrade the metals. However, certain atmospheric conditions can greatly accelerate the corrosion process. There are different types of corrosion that metals may endure, whereby the categorization depends on the mechanisms by which corrosion begins, propagates, and the volume that it affects. The most common types of corrosion that electrical contact materials are subjected to include atmospheric, dry, pore, galvanic, crevice, creep, dust, localized, pitting, and fretting corrosion [22,42,84].

The effect of corrosion in electrical components is not solely focused on their deterioration, but rather on the impact that corrosion (and corrosion byproducts) has on the electrical performance since metal oxide particles tend to present higher resistivities than their pure metallic counterparts [22]. The extent to which metals undergo corrosion varies considerably. For instance, copper and aluminum are highly susceptible to oxidation. However, once their surfaces have oxidized, this oxide layer serves to protect them from further corrosion (i.e., oxidic passivation). Similarly, zinc and nickel also form a corrosion passivation layer, which makes them suitable for use as protective platings. However, due to their lower electrical conductivity, these metals are not always viable. When corrosion resistance is required, but conductivity cannot be compromised, noble metals such as silver, gold, and platinum must be employed [22,42]. It should be noted, however, that the use of noble metals can rapidly and significantly increase the cost of the components. Therefore, in these cases, thin noble metal platings are common practice.

Although silver is considered a noble metal, it is not impervious to corrosion. It is true that silver does not oxidize; however, when in contact with sulfur-containing

atmospheres (particularly hydrogen sulfide – H_2S) silver undergoes a sulfidation process in which a thin silver sulfide (Ag_2S) film is formed on its surface (commonly referred to as tarnishing film) [31,85–87]. Copper, on the other hand, when exposed to oxygen, rapidly forms a native oxide layer (Cu_2O) on its surface which provides it with a certain degree of corrosion resistance [24,88,89]. However, when subjected to harsher environments (e.g., maritime environments), or when the native oxide layer is removed or punctured, copper contacts can sustain more severe corrosion forming its typical greenish patina film.

In practice, preventing corrosion is not realistic and unequivocally impossible due to the nature of the intended application. However, multiple widely adopted methods are typically employed to hinder and decelerate the deterioration of metals due to corrosion. The first strategy involves eliminating or minimizing environmental conditions that may accelerate corrosion, such as controlling temperature, humidity, contaminants, and pollutants [83]. If atmospheric control is not an option, protective coatings and platings are standard for a plethora of industrial applications, particularly the electrical contact industry [22]. As is the case with native oxide layers, platings and coatings minimize corrosion acting as a passivation layer and as protective barriers preventing the contact between the environment and the substate that is susceptible to corrosion. Furthermore, lubricants, self-assembled monolayers, alloying, and reinforcing are other alternatives used to inhibit corrosion [22,42].

2.3. Lubrication in electrical systems

Lubrication is the process of utilizing a substance (i.e., lubricant) at the interface between two contacting surfaces in relative motion with the prime objective of reducing friction and wear [22,42,43,50]. However, the use of lubricants can also contribute towards a reduction in heat generation and favoring its dissipation. Lubrication works by forming a layer (known as lubrication film) between the contacting surfaces that minimizes or prevents contact between both surfaces' asperities. Consequently, the coefficient of friction and wear will be significantly reduced, which in turn also reduces heat generation and the surfaces' degradation. Lubricants can also prevent the ingress of foreign particles and slow-down corrosion. Depending on the configuration, intended application, and contact requirements, different types of lubricants should be selected; namely, gaseous lubricants, liquid lubricants, lubricating greases, or solid lubricants. Good lubricants are those substances with low interfacial shear, thereby enabling relatively effortless movement of the contacting bodies [43,50].

When choosing a lubrication system, the specific requirements of the intended application must be considered since there is no "universal lubricant" that is

appropriate for all kinds of applications. Based on the concepts that have been discussed thus far, it is evident that the concept of lubrication (and therefore wear reduction) goes at odds with those of electrical conduction. On the one hand, for optimal electron conduction, it is highly sought after to increase the contact area. However, this comes at the cost of higher wear rates when relative motion is involved. Whereas, on the other hand, to properly reduce friction and wear, lubrication films seek to minimize the contact area. Therefore, the lubricant choice (or if lubrication is to be used altogether) in electrical systems is pivotal since an incorrectly lubricated contact can be severely affected in terms of its conductivity. This, in turn, may result in excess heat generation, higher energy requirements, arcing, the formation of insulating layers, and unforeseen component malfunctions or even failure. Nevertheless, a properly selected lubricant and its corresponding film thickness can provide the advantages of lubrication without the aforementioned drawbacks [90].

Liquid- and solid-based lubricants, as well as lubricating greases, are widely used in sliding and switching contacts, particularly in light-duty applications, with certain heavy-duty applications also utilizing lubricants [42]. However, the focus of this theoretical framework will be placed on solid lubrication. Two forms of solid lubrication exist and are used in the electrical contact industry. The first is solid lubrication through the utilization of soft metals (e.g., tin, silver, gold, and indium) [91]. Soft metal lubricants are typically employed in environments that are too hostile for other conventional lubricants (such as in vacuum or high-temperature environments), with the added advantage that these metals also present good conductive properties. The other alternative solid lubrication mechanism involves the use of solids with anisotropic mechanical properties, such as graphite [43]. Because of the anisotropic nature of these materials (also known as lamellar solids), low shear forces enable the material's planes (or lamella) to slide over one another, thereby considerably reducing friction and wear. However, one issue with solid lubrication is that if the lubricant is displaced from the contact site, it will no longer provide friction and wear reductions.

Solid lubricants are generally applied over electrical contacts as thin coatings or used as reinforcement phase in composite materials. The most widely adopted solid lubricants are graphite, molybdenum disulfide (MoS_2) and polytetrafluoroethylene (PTFE – or Teflon® by its brand name) [22,42,43,50,90]. PFAS (particularly Perfluoropolyether - PFPE), are also commonly used as lubricants despite the fact that they are dielectric compounds. Nevertheless, these lubricants exhibit low friction, chemical and thermal stability, and prevent the ingress of moisture and other external contaminants, thus environmentally insulating the contact. However, the use of PFAS is highly controversial and increasingly more regulated due to their ecotoxicity, health

concerns, and persistent nature (leading to them being dubbed "forever chemicals") [92,93].

Although the aforementioned solid lubricants can ensure low friction, these substances all fall short in high temperature applications, rapidly decomposing or oxidizing at temperature above 250, 260, 300, and 500 °C for PTFE, PFPE, MoS_2, and graphite, respectively [50]. Nonetheless, greases and liquid lubricants also show poor performance in high temperature environments due to the rapid degradation of their viscosity. In fact, solid lubrication generally extends the working range of certain components, enabling them to function at high temperatures and even in vacuum. Most notably, graphite presents the drawback that it requires the presence of moisture in order to ensure low friction, whereas MoS_2's ability to reduce friction is considerably affected by moisture. This further highlights the gravity of proper lubricant choice based on application, requirements, and environmental characteristics where the component will be utilized.

2.4. Carbon nanostructures

Carbon exhibits the particularity that it can form different carbon-carbon bonds depending on the electronic configuration [94]. This section will focus on sp^2-hybridized carbon nanostructures. Further information on sp^3 and *sp* electronic configuration can be found in APPENDIX A, *Section A.3*.

sp^2-hybridzed carbon structures present good mechanical properties due to the three strong *sigma* bonds, in addition to their exceptional transport properties provided by the highly mobile p_z-orbitals [94]. Accordingly, carbon allotropes presenting this electronic configuration are of scientific interest in the field of electrical contact materials. Despite the fact that chemically all sp^2-hybridized carbon allotropes are identical, these structures exhibit distinct properties and characteristics (mechanical, thermal, electrical, chemical, etc.) [94]. These discrepancies are linked to the structural, morphological, and dimensional differences between the allotropes [95]. The latter plays a particular role in the properties of carbon nanostructures – compared to bulk material – since nanostructure dimensionality influences the electronic density of states due to a quantum confinement phenomenon [96,97]. Irrespective of the differences in electronic density of states, these types of carbon allotropes tend to present promising behavior as solid lubricants and lubricant additives [98–121], thermal and electrical conductivity [122–161], hydrophobic wetting behavior [162–173], elastic properties [174–181], among others.

Carbon nanoparticles (CNP) are nano-scale structures consisting of carbon atoms that form strong carbon-carbon *sigma* bonds (schematically shown in **Figure 7**) – in addition to the attachment of functional groups or other foreign atoms that may originate from synthesis, functionalization, oxidation, etc. There is an abundance of CNP, including:

- ***Carbon black (CB)*** – are a type of carbon structure comprised of sp^2-hybridized parallelly layered planes. However, unlike graphite, these graphitic crystallite planes are not parallel to the adjacent planes [182,183]. CB has a high tendency to form agglomerates due to van der Waals forces, thus forming micro-sized particles (or aggregates) made up of primary CB particles (or nodules).
- ***Onion-like carbon (OLC), carbon nano-onions (CNO), or carbon onions (CO)*** – consist of concentric fullerene structures (i.e., nested closed spherical graphene shells) [184,185]. These types of structures are generally very small (< 10 nm), thus being considered zero-dimensional structures. OLC were first observed as the byproduct of CB synthesis, however, the most common synthesis route for OLC is via thermal annealing of carbon nanodiamonds (CND) [186]. Due to this synthesis method, OLC are sp^2-hybridized structures with a sp^3 core.
- ***Graphene-based CNP*** – are the most elemental sp^2-hybridized carbon nanostructure, forming the building blocks of all carbon allotropes with this electronic configuration [187,188]. Graphene planes can form:
  - ***Graphite (or graphite flakes – GF)*** – graphite consists of multiple parallelly stacked graphene planes [94,135,137,159]. Although graphite is not strictly speaking a "nanoparticle" due to its larger size, on account of graphite's extensive use in different industrial applications, these particles are included in this work as a benchmark.
  - ***Graphene nanoplatelets (GNP)*** – also known as few-layer-graphite, are stacked sp^2-hybridized (graphene) planes with thicknesses between 0.7 and 100 nm (two-dimensional nanostructure) [189]. These nanoparticles are an alternative to single-layered graphene since GNP are easier to mass synthesize coupled with their exceptional properties and low costs [190].
  - ***Graphene oxide (GO) and reduced graphene oxide (rGO)*** – these two structures can be obtained from graphite through processes such as chemical exfoliation, Hummer's, or Brodie's method [191–193]. Although GO and rGO are slightly lower quality than graphene and GNP, these two-dimensional structures present similar physical properties and are easier to cost-effectively synthesize in bulk [194].
- ***Carbon nanohorns (CNH) or nanocones (CNC)*** – are sp^2-hybridized tubular-shaped carbon nanostructures. These particles present horn-like tips, which

resemble capped single-walled carbon nanotubes with horn diameters and lengths between 2-5 nm and 40-50 nm, respectively [112,114]. These structures tend to form small agglomerates of up to 100 nm in size. Due to their size, these structures can be considered as quasi-zero-dimensional nanoparticles.

- ***Carbon nanotubes (CNT)*** – are one-dimensional, sp^2-hybridized, hollow, tubular-shaped carbon nanostructures. There are two main types of CNT, single-walled CNT and multi-walled CNT. Multi-walled CNT are made up of several concentric single-walled CNT with increasing diameter. Their diameter and length depend on the synthesis method, whereas the properties and behavior of the CNT depends strongly on their chirality [126–128].

A major challenge when working with CNP is their strong propensity to form agglomerates. Agglomeration takes place due to van der Waals interactions between adjacent nanoparticles or due to dipole-dipole forces [195,196]. This tendency towards agglomeration hinders the CNPs' intrinsic properties [126]. A further disadvantage of CNP agglomeration is that it leads to inhomogeneous dispersions, thereby affecting their effectiveness as reinforcement phase [197]. Large CNP agglomerates (along with the shape of the reinforcement phase) lead to a more heterogeneous distribution, thus generating composites with highly heterogeneous properties [198]. Accordingly, reducing CNP agglomerate sizes without structurally damaging the nanoparticles is

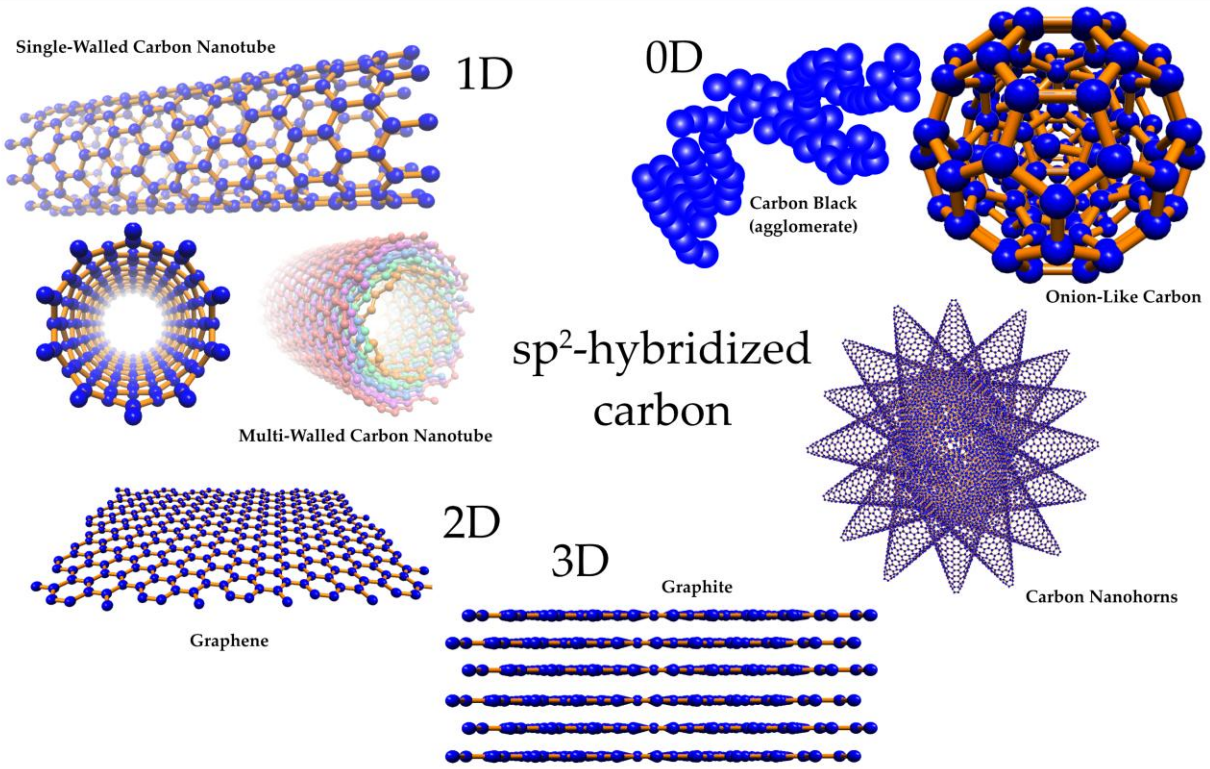

Figure 7. sp^2-hybridized carbon nanostructures, classified according to their dimensionality. 0D – Carbon black, onion-like carbon, carbon nanohorns. 1D – Single-walled and multi-walled carbon nanotubes. 2D – Graphene, few-layer graphite, graphene oxide, and graphene nanoplatelets. 3D – Graphite. Schemes made using *Nanotube Modeler*, © JCrystalSoft, Version 1.7.6 (www.jcrystal.com).

crucial to fully capitalize on their desired properties. This is generally achieved through mechanical milling, surface functionalization, or by employing dispersion techniques. Mechanical milling effectively de-agglomerates CNP, however it also affects their structural integrity [199–201]. Furthermore, functionalization involves dissociating carbon-carbon bonds or utilizing dangling bonds [202–204]. The dispersion route (homogenization and ultrasonication), on the other hand, have been proven effective at reducing agglomerate sizes without damaging the structure of carbon nanostructures [196].

3. STATE OF THE ART

This section provides a focused overview of specific concepts and advancements pertinent to the research herein presented. It is intended to complement the THEORETICAL FRAMEWORK by addressing practical and contextual aspects directly related to this work. While this section is concise, comprehensive discussions on the state of the art can be found in the introduction section of the appended articles, where the concepts are elaborated within the context of their respective studies.

3.1. Current engineering solutions

Overcoming the inherent limitations and obstacles that electrical contact materials encounter can be broadly classified into two principal categories. The first of these entails the introduction of superficial modifications to the surfaces in contact, whereas the second encompasses the modification of the bulk material itself. The former primarily focuses on the use of coatings, lubricants, or the passivation of the surface, whereas the latter mainly involves alloying or reinforcing of the bulk material [22,42,44].

3.1.1. Passivation

Depending on the properties and/or characteristics that are required of an electrical contact material, different superficial modification techniques can be utilized. Passivation is the process via which the chemical reactivity of a surface is inhibited, with the primary goal of preventing the surfaces' corrosion [205]. The most common form of passivation is the formation of native oxide layers, as is the case for copper and aluminum. However, passivation can also be induced using external substances. A prime example is the use of hexadecanethiol (HDT) and octadecanethiol (ODT) to protect silver surfaces from reacting with atmospheric sulfur, thereby preventing or

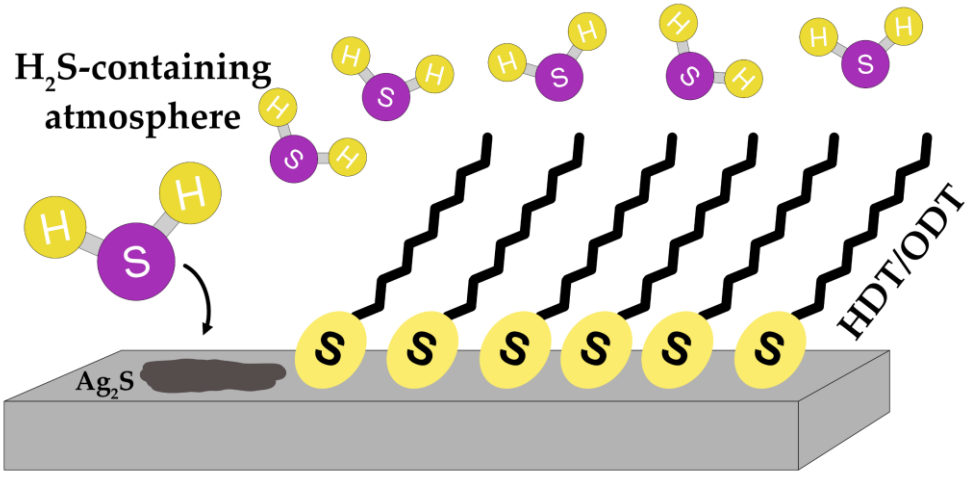

Figure 8. Schematic representation of HDT/ODT self-assembled monolayer on silver surface, protecting it from sulfidation. Without the passivation layer, silver reacts with atmospheric hydrogen sulfide to produce silver sulfide tarnishing film.

slowing down the formation of silver sulfide (Ag_2S) tarnishing films (schematically shown in **Figure 8**). HDT and ODT are alkanethiol compounds, comprised of unsaturated oil chains with sulfhydryl groups that have bonded with the carbon terminals, which saturate the silver surface. The HDT and ODT layers form covalent bonds with silver, thereby preventing the surface from reacting with atmospheric sulfur. Once these bonds saturate the surface, excess HDT and ODT cannot interact with silver, thus producing a very thin layer (in the nm range). Therefore, these layers are oftentimes referred to as self-assembled monolayers. Due to the efficacy, simplicity, and durability of the HDT and ODT layers at protecting silver surfaces, these substances are widely adopted – not only in the electrical connector industry, but also for cosmetic applications such as coin protection [28,86]. Although HDT and ODT can also protect copper surfaces from corrosion, due to the presence of its native oxide layer, it is not standard practice to utilize these substances.

3.1.2. Surface modifications & lubrication

Passivation deals with the mitigation of corrosion, however, tribological challenges cannot be addressed through this method (apart from soft metal coatings, for example). Engineering solutions to tribo-electrical challenges generally involve modifying the surfaces or incorporating lubrication. Surface modification techniques can range from simply polishing the surface to more complex techniques such as laser structuring processes [206–209]. The objective, however, remains the same – i.e., alter the surface's topography or characteristics (e.g., hardness, contact area, etc.) to better suit the application [206,208]. Conductive lubricants, on the other hand, seeks to minimize friction and wear, in addition to preventing the ingress of foreign particles and slow down corrosion while ensuring optimal conductivity (schematically shown in **Figure 9**). Albeit dielectric or insulating lubricants may also find applicability in switching electrodes (thus minimizing the likelihood of electrical arc ignition) and in multipolar

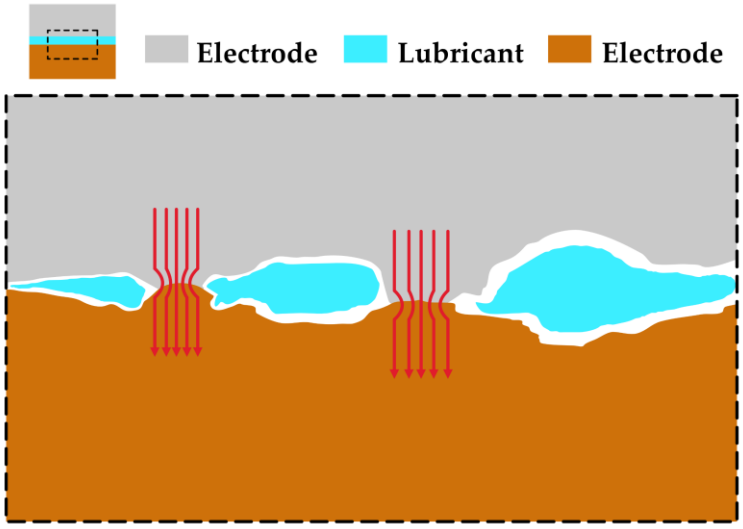

Figure 9. Scheme of lubrication between two electrodes and the constriction of the current at the a-spots.

connectors (thereby preventing short circuits between each pin). Many different types of lubricants are commercially available; however, lubricating greases are the most common. Prime examples include Nyogel® 760G (Nye Lubricants), Klüberlectric KR 44-102 (Klüber Lubrication), and Molykote® G-8101 (DuPont).

3.1.3. Coatings

Coatings are a standard practice in a plethora of industrial sectors [210–212]. This technological advancement is used to improve, prolong, or modify the performance of the substrate. In the electrical contact material sector, the main purpose of coatings include:

- Ensuring low electrical contact resistances, either by coating with a material that has higher conductivity or by plastic deformation, thus increasing the contact area.
- Protecting from atmospheric and operational conditions, thereby preventing or slowing down corrosion and wear.
- Reducing friction, minimizing connection and disconnection force required.
- Increasing thermal conductivity, thereby supporting thermal diffusivity, reducing thermal buildup, and lowering the likelihood of contact welding.

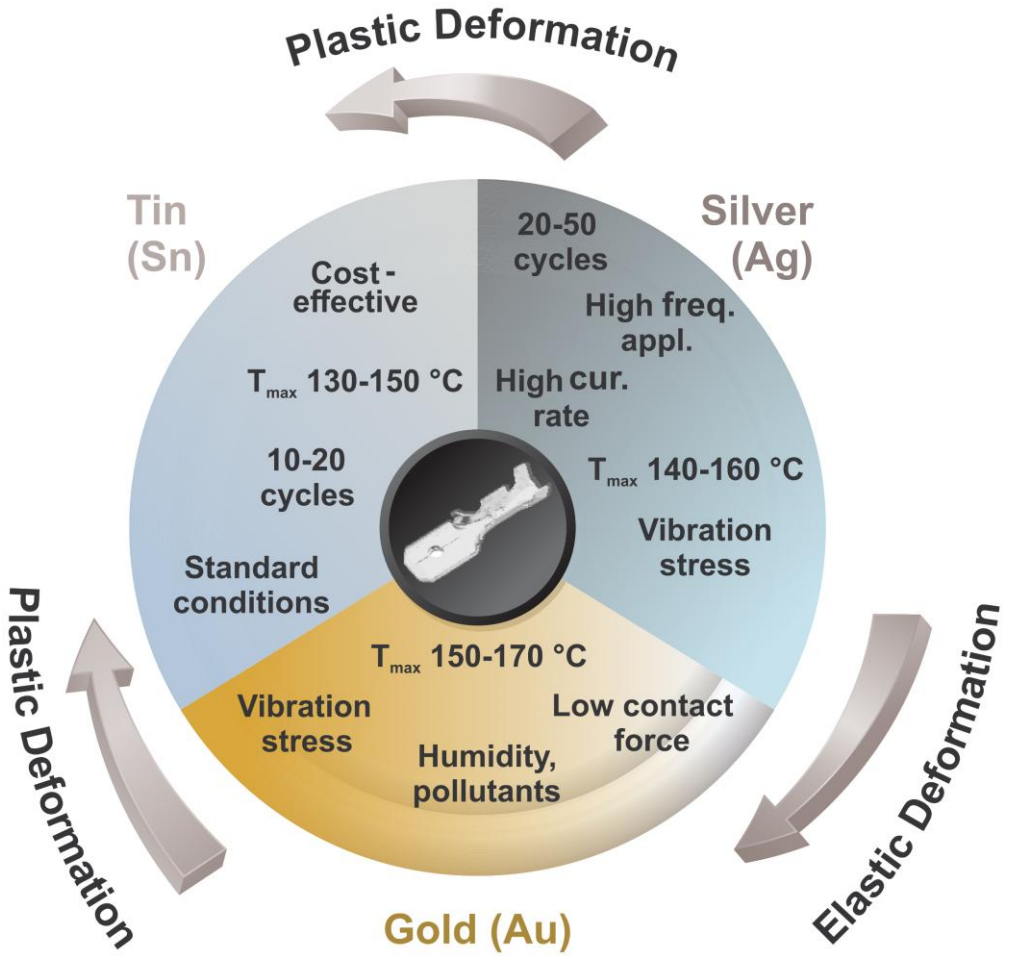

Figure 10. Selection criteria for plating material based on connector requirements [213].

Metallic platings are frequently used to satisfy these requirements [22,42]. Specifically in the case of copper connectors, tin and silver platings are commonly employed. Gold platings, on the other hand, are primarily used for low contacting forces – selection criteria for plating material illustrated in **Figure 10** [213]. Tin platings effectively protect the copper substrate from corrosive environments and ensure optimal electrical contact upon connection due to its softness. However, copper and tin tend to form intermetallic phases (IMP) [214,215]. These IMP are more corrosion-resistant than pure tin. However, they are brittle which can lead to cracking, thereby hindering their corrosion resistance. Nevertheless, the IMP are harder than tin and copper, which favors tribological performance of the contact. To prevent the formation of IMP, a nickel interlayer (diffusion inhibitor) may be deposited between the substrate and the tin plating. However, this comes at the cost of further processing and conductivity. Another alternative is plating copper with silver instead of tin. This improves the electrical performance while maintaining the relative chemical inertness of the surface, although silver platings are considerably more costly than tin platings. Nonetheless, for high performance applications, silver plated copper contacts are extensively used.

Similarly, bimetallic joints are extensively used due to the reduced material demand while harnessing the advantages from both materials [22,42]. Consequently, silver-copper bimetallic electrodes are a cost-effective alternative which ensure excellent conductivity, low tendency towards corrosion, and good mechanical properties. Depending on the manufacturing method, porosities and microstructural heterogeneities may be present at the interface. In addition, certain methods such as welding and brazing require filler materials [216].

3.1.4. Alloying

Copper is extensively alloyed, most notably with tin and zinc to form bronze and brass, respectively. Not only do bronze and brass have higher mechanical strength than pure copper, but these alloys also offer wear and corrosion resistance at a lower cost [41]. Other copper alloys include copper-silver for superior electrical conductivity and good mechanical properties, copper-beryllium for good thermal cycling performance, copper-chromium for high strength and arc resistance, copper tungsten for wear and arc resistance, copper-nickel and copper-silicon for corrosion resistance, among others [41]. However, it should be noted that the metals used to alloy copper generally possess higher electrical resistivities, which worsens the overall conductivity of the alloy. Therefore, when electrical performance is prioritized, pure copper remains the material of choice over its alloys.

Although the conductive properties of silver are not likely to improve via alloying, mechanical, tribological, and anticorrosive characteristics can be tailored for specific applications. Silver is generally alloyed with copper, zinc, nickel, palladium, platinum, and gold [217]. Silver-palladium and silver-gold alloys are used for improved tarnishing resistance while maintaining low resistances, whereas silver-platinum alloys enhance the mechanical properties and tarnishing resistance. However, these alloying components significantly increase the cost of the connector. Lower-cost alloys, such as silver-zinc and silver-nickel, are used to improve wear, arc erosion, weld and corrosion resistance, albeit at the cost of increased resistances – hence these alloys are mainly used for switching applications [22,218].

3.1.5. Composite materials

Composite materials are used for switching electrodes and sliding contacts. Composites for switching electrodes involve the use of metal oxides – such as cadmium, bismuth, indium, tin, and zinc oxide – as reinforcement phase in silver and copper matrices since these particles can significantly enhance electrode durability and reliability by improving their resistance to arc erosion and reducing their weldability (due to the elevated melting temperature of the reinforcement phases) [219–222]. Sliding contacts, on the other hand, utilizes lamella-type components – e.g., graphite, tungsten disulfide, and molybdenum sulfide – to impart solid lubrication into the system [22]. Although these composites are advantageous for certain applications, there are disadvantages associated with each approach. For example, silver-cadmium oxide composites exhibit remarkable arcing performance and weld resistance. Nevertheless, silver-cadmium oxide is no longer employed due to its toxicity and associated health risks [223], with it being replaced by silver-tin oxide. However, silver-tin oxide composites, over time, present higher electrical resistance due to poor wettability between silver and tin-oxide [222,224], in addition to the formation of layered tin oxide structures resulting from the energy input from the electrical arc, which further affects conductivity [225]. Moreover, incorporating other alloying components into silver-tin oxide composites (such as with indium) is oftentimes required to ease the oxidation of tin to prevent oxide-free regions (known as denuded zones) [226].

Graphite-based composites, on the other hand, provides the system with wear protection, friction reduction, and weld-resistance at the cost of increased electrical resistances [42,227–233]. Nonetheless, due to the anisotropic conductive properties of graphite, the relative orientation of the reinforcement phase is of utmost importance. Furthermore, the graphite content has been shown to increase erosion rate and the likelihood of arc reignition in silver-based composites [234]. Despite these challenges, silver-graphite and copper-graphite composites are commercially available. Examples

of silver-graphite composite electrical contact materials manufacturers include TE Connectivity Ltd., Doduco GmbH, Heraeus GmbH, Electrical Contacts Limited, and Hindustan Platinum Pvt. Ltd.

3.2. Carbon nanoparticle coatings

There is an abundance of coating techniques widely adopted in large-scale industrial applications, some examples include physical and chemical vapor deposition, sputtering, electroless plating, brushing, thermal evaporation, ion plating, among others [235,236]. However, manufacturing CNP-based coatings is commonly done through dispersion-based coating techniques, such as dip coating, spin coating, drop casting, spray coating, or electrocoating, due to their tendency towards agglomerating. By employing a dispersion-based coating technique, the agglomerates can be broken down prior to the deposition process. Within electrocoating processes, electrophoretic deposition (EPD) is a technique that has successfully produced high-quality CNP coatings over substrates from colloidal suspensions [237–242]. One of the key benefits of the methodology in question is its simplicity and straightforward nature, eliminating the necessity for costly or intricate equipment. EPD is a readily scalable technology, offering convenient integration as a final production step. Furthermore, EPD allows for straightforward control of coating thicknesses and deposition parameters, while enabling the coating of complex geometries. Moreover, the CNT coatings obtained via EPD comprises of a dispersed flat (transverse) CNT network, which has been previously reported to exhibit low CoF, as low as 0.09 [243,244].

These advantages cannot be understated since EPD outperforms other dispersion-based processes. For example, dip coating does not allow for a controlled deposition and is highly dependent on the wettability of the substrate with the colloid [245,246], spin coating is not applicable for large substrates while also not being material-efficient [247,248], and drop casting produces a heterogenous coatings due to Marangoni convection and the *coffee stain* effect [246,249–252]. The main disadvantages that EPD presents over other dispersion-based deposition techniques is that EPD requires charged particles and a stable colloid [253]. The former may be endogenous (i.e., the particles to be deposited possess a superficial charge) or the particles may be charged through the use of additives or via functionalization. Both these processes also aid in stabilizing the colloid by limiting interactions between the particles, since particle coagulation is detrimental to this deposition technique [253].

The production of CNP coatings via EPD consists of two simple steps: 1) the preparation of the CNP-containing colloid, and 2) the deposition of the nanostructures

on the substrate. The colloidal suspension is obtained via a two-step process that involves the breakdown of large CNP agglomerates through shear forces (homogenization), followed by the further breakdown of agglomerates through sonication [196]. Subsequently, two electrodes (one of which is the deposition electrode) are submerged in the colloidal suspension and connected to a DC power source and the deposition parameters are set – i.e., interelectrode distance, deposition time and voltage. An electric field is thereby generated between the electrodes, a force (electrophoresis) is imparted onto the charged particles (i.e., CNP), which move through the colloid towards the deposition electrode. Upon reaching the deposition electrode, the CNP deposit themselves on the substrate through particle coagulation [237].

The literature highlights the benefits of using CNP coatings produced via EPD in tribological systems. Due to the well-documented solid lubricity that the nanostructures provide the system, these coatings reduce friction, wear, and oxidation during sliding even under high contacting loads and with varying substrate roughness [254–263]. Furthermore, carbon-based coatings have the added advantage of being both thermally and electrically conductive [94,126,129,264,265]. In addition, these coatings may protect the base material from corrosive environments due to their hydrophobic nature, as well as maximizing contact area due to the elasticity of the carbon coatings [266].

3.3. Carbon nanoparticle-reinforced composites

Although there are numerous industrially viable methods to manufacture metal matrix composites (MMC), powder metallurgy (PM) is among the most commonly used. PM is a well-controlled process that produces near net-shape components. Other advantages of PM over other methods (such as stir casting, friction stir processing, infiltration, spray forming, diffusion bonding, etc. [267]) include: the possibility to manufacture complex geometries, no post-processing requirements, higher material efficiency, low costs and energy efficient method, simple alloying and reinforcing process, among others [268]. Moreover, PM-based manufacturing of electrical components is an industry-standard technique. This methodology is not only employed to manufacture pure metal electrodes, but also composite materials for switching applications (e.g., silver-tin oxide).

Manufacturing MMC via PM is relatively straightforward and consists of three steps: 1) CNP dispersal and mixture with metallic powder, 2) consolidation into green pellet, and 3) sintering. The dispersal of the CNP is the same two-step process previously described in *Section 3.2*, since the colloidal mixing route effectively disperses the CNP and achieves good reinforcement phase distribution without damaging the CNP [269–271]. Green pellet consolidation consists of uniaxial cold pressing the powder in a die,

obtaining a component with sufficient density to manipulate it [272]. The final step is of utmost importance for electrical applications, since the sintering step eliminates internal porosities. This process is crucial since internal porosities are detrimental to the mechanical and transport properties of the MMC [273]. Green pellet densification can be achieved through different methods, including conventional sintering, hot uniaxial pressing (HUP), hot isostatic pressing (HIP), spark plasma sintering (SPS), among others [272].

Conventional sintering – i.e., heating the green pellet below its melting point – is simple, cost-effective, and scalable. However, this process does not achieve high final densities and requires long processing times, which not only extends the duration of the whole process but also enables grain growth. HIP and SPS, on the other hand, are more costly, but these techniques have limited scalability. Therefore, HUP is the sintering method of choice, since in a single sintering step it produces components with high density and low porosity levels. Furthermore, with appropriate mold design, complex shapes can be mass produced, thus eliminating post-processing requirements. In addition, CNT reinforced nickel composites produced via this methodology have been previously reported to show good reinforcement phase distribution and improved mechanical properties [269].

Recent advancements in additively manufacturing (AM) techniques – i.e., powder bed fusion and direct energy deposition – have successfully manufactured dense MMC, primarily aluminum-based MMC [274–276]. The main advantage of AM-based routes is that the obtained microstructure is finer that in conventional methods, since conventional methods require prolonged sintering times at high temperatures, thereby leading to grain growth [277]. Furthermore, AM techniques enable the manufacturing of intricate and custom components, with a high degree of precision. However, carbon-reinforced MMC manufactured through laser-based AM techniques tend to affect the structure of the reinforcement phase. The carbon-based reinforcement absorbs the energy irradiated by the laser, leading to partial decomposition of the secondary phase. The partial decomposition leads to localized reactions between the reinforcement phase and the matrix, thus causing the formation of metallic carbides [277,278]. Although these effects can be limited by increasing the laser's scan speed. Despite the advantages discussed for AM techniques, this methodology possesses certain disadvantages which limit their wide-spread adoption. Some disadvantages include the requirement for post-processing to improve the surface's quality, high equipment costs, and crucially its limited scalability. Therefore, AM-based techniques, although feasible, fall outside the scope of this work.

Extensive research has been carried out to fully understand the advantages of reinforcing metallic matrices, primarily for aluminum and nickel matrices, with different CNP. The benefits of CNP-reinforced MMC include a reduction in the thermal expansion coefficient and enhanced thermal conductivity [279–282], improved mechanical properties (e.g., yield and tensile strength) [283–288], tailoring of the microstructure [284,286–290], incorporation of a solid lubricant within the bulk material (reducing friction and wear) [291–296], improvement in electrical conductivity in nickel matrices [297,298], and improved switching performance [299]. Moreover, the long-term switching performance of CNT-based electrodes, particularly for microelectromechanical systems, has been widely studied by McBride et al. [300–304], with the authors showing their promising potential in low force electrical contact applications.

Although many different CNP have been evaluated by researchers, CNT (particularly multi-walled CNT) have garnered the most attention [197,305–308]. Among the CNP herein discussed, a previous study by Reinert et al. has demonstrated that – at least in terms of solid lubricity – only CNT provide the system with efficient lubricity during reciprocal sliding tests (compared to OLC and CND) [291]. Consequently, manufacturing of carbon-based silver and copper MMC for electrical applications will be exclusively limited to the use of CNT as reinforcement phase. Using other carbon nanostructures as reinforcement phase falls outside the scope of this work.

4. OBJECTIVES

The central objective of this thesis is to harness the benefits from the different CNP, thereby improving the performance of silver- and copper-based electrical contact materials without negatively impacting the electrical properties of these materials. By incorporating CNP – in the form of coatings or as reinforcement phase – it was sought after to enhance the mechanical, tribological, and thermal properties, as well as improving the corrosion and erosive resistance. This is the cornerstone of this work, and it is always kept at the forefront when developing, processing, characterizing, and designing our CNP-based systems.

The research carried out and herein described is meant to be industrially viable. In other words, the methodology, materials, chemicals, and procedures employed should be simple, safe, sustainable, and scalable from laboratory levels up to industrial proportions.

The central objective can be divided into several contributing objectives, based on the specific way in which it is tackled. Accordingly, five targeted objectives can be defined.

1. **Characterization technique:**
   a. Are there standard ways to characterize the tribo-electrical performance of electrical contact materials?
   b. How can this methodology be improved, implemented, and standardized?

2. **Electrical characterization:**
   a. How does the sulfidation of silver contacts affect its electrical performance and can it be mitigated in-operando?
   b. How does CNP morphology and dimensionality affect the deposition rate on the substrate and what is the resulting topography?
   c. How do the CNP coatings affect the electrical performance of the substrate? What are the benefits and drawbacks of CNP coatings?
   d. How do bulk CNP powders perform when a direct current is applied between two electrodes? What influence does compressive normal loads (compaction) have on the electrical performance?
   e. How does real topography affect the contact area in electrical contact? Can the deformation mechanisms be modeled in a simple and accurate way?
   f. What is the influence of CNT reinforcement phase in metallic matrices and how does it affect the ECR?

g. How can the manufacturing process be optimized and can the same manufacturing methodology be employed to produce CNT-reinforced bimetallic electrodes?
h. Which are the benefits of incorporating the reinforcement phase in bimetallic electrodes?

3. **Mitigation of wear:**
   a. Which are the main causes of connector failure and can CNP coatings minimize them?
   b. Which CNP coating shows the most promising results? Which are the advantages and disadvantages of different CNP?
   c. Can CNP coatings provide wear protection while maintaining low and constant ECR? What is the long-term tribo-electrical performance of CNP coatings?

4. **Atmospheric protection:**
   a. Can CNP coatings protect the substrate from atmospheric conditions? Which CNP performs the best?
   b. How does CNP morphology and dimensionality, in addition to coating homogeneity and thickness, influence its wetting performance and atmospheric protection offered?

5. **Switching electrodes:**
   a. Are CNT-reinforced silver and copper electrodes a feasible alternative to reference and standard switching materials?
   b. What is the influence of the reinforcement phase on the characteristics of the electrical arc that is generated and how does the reinforcement phase's distribution affect the behavior of the electrical arc?
   c. Does the incorporation of CNT in the metallic matrix affect electro-erosion? What are the characteristics of the resulting electro-erosion craters?
   d. Is the reinforcement phase affected due to the arc's energy?

Addressing these five targeted objectives, and the different sub-objectives, are the aims of the publications herein included.

5. INCLUDED ARTICLES

The publications herein appended are divided into four classifications based on their subject matter: namely *setup*, *materials*, *coatings*, and *composites* (as illustrated in **Figure 11**). A brief description and the connection between the included articles are presented in the following sections. Furthermore, **Figure 12**, **Figure 13**, and **Figure 14** illustrate a schematic overview of the appended articles for the *materials*, *coatings*, and *composites* classification, respectively.

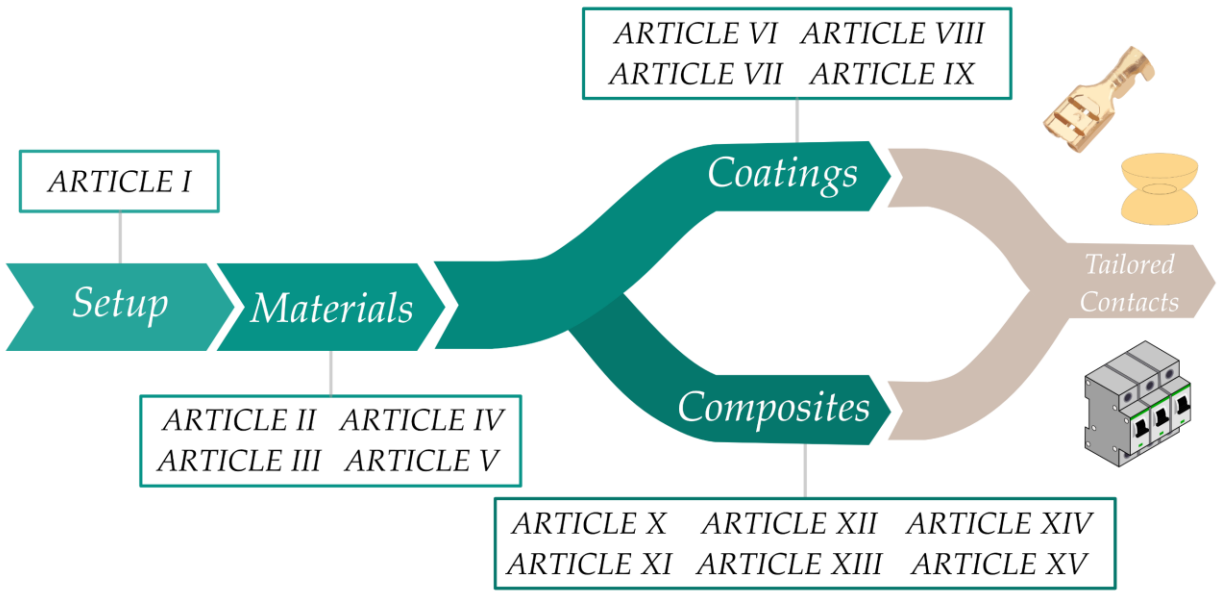

Figure 11. Schematic overview of the classifications for each appended article, followed by the perspective for future work (combining CNP-based coatings and composites).

5.1.Outline

5.1.1. Setup

ARTICLE I

This article details the construction, commissioning, and evaluates the precision of a custom tribo-electrical testing rig developed in order to attain an in-depth characterization of commercial and novel electrical contact materials. The new testing rig represents an improvement over a previous iteration, which incorporates the possibility of conducting higher load tests, controlling atmospheric conditions, conducting tribological experiments (i.e., fretting and scratch), and eliminating external factors that could impact the measurements. The setup described in this article serves as the foundation for the detailed characterization described in the subsequent articles.

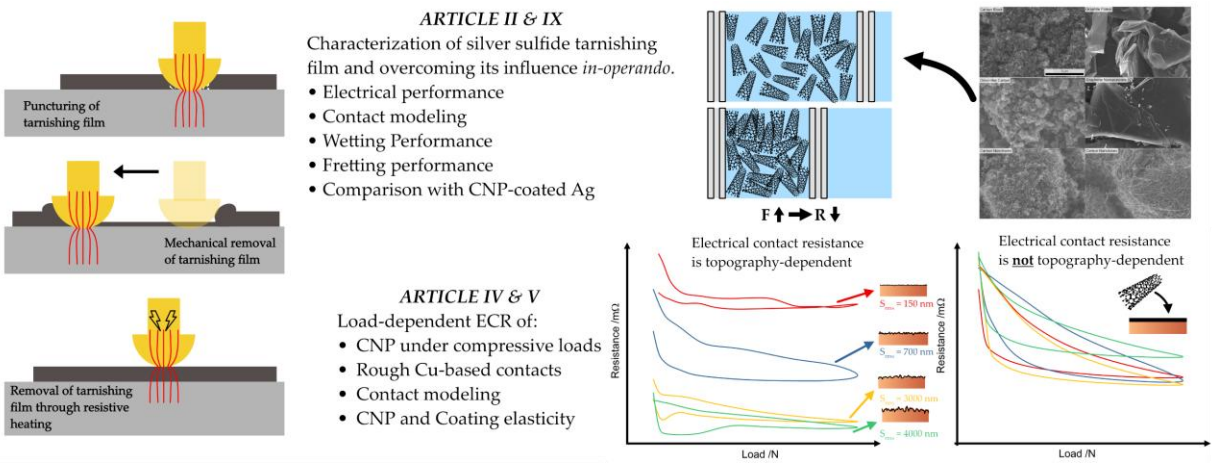

Figure 12. Schematic overview of appended articles for *materials* classification.

5.1.2. Materials

ARTICLE II

ARTICLE II evaluates three methods to overcome the influence of silver sulfide tarnishing films. A comparison of the tribo-electrical performance of tarnished and chemically cleaned samples was carried out. Among the proposed methods, puncturing the tarnishing film (applying a pressure of approximately 680 MPa) was found to be the most effective, reducing ECR to values that approach those of the chemically cleaned sample. Neither resistive heating nor mechanically scratching the tarnished surface resulted in an improvement in electrical performance. Moreover, scratch tests demonstrated that the tarnishing film reduces the CoF, yet it does not offer wear protection.

ARTICLE III

The objective of ARTICLE III is to evaluate the impact on CNP coatings on the ECR of copper substrates. In this article, potentiostatic EPD was used to produce the CNP coatings over oxygen-free copper substrates; CNP chosen based on their promising solid lubricity. After deposition, a comprehensive assessment was conducted on the resulting coatings, including their topography, porosity/compactness, adhesion, load-dependent ECR, and elasticity. The results indicate that CNT and CNH coatings exhibit the most promising results due to their lower resistance increment, favorable coating-substrate interface and coating adhesion, relatively compact coating, and elastic behavior.

ARTICLE IV

A substantial body of literature exists on the piezoresistive behavior of individual CNP, but no information was available on the performance of bulk CNP powders. Therefore, ARTICLE IV is devoted to an investigation of the characteristics of six different CNP and their piezoresistive performance. It demonstrates a robust correlation between nanostructure dimensionality and their propensity to form agglomerates with their electrical resistance. One- and two-dimensional CNP exhibited the lowest resistance values. However, quasi-zero-dimensional nanostructures demonstrated the largest relative reduction in electrical resistance during unidirectional loading.

ARTICLE V

The objective of ARTICLE V was to gather insight into the influence that different surface textures have on the electrical performance of copper-based electrical contact materials. In this study, smooth brass, bronze, and tin-plated copper samples were contacted against flat-headed copper electrodes that had been ground and polished to achieve a wide range of topographies. Load-dependent ECR was measured and numerical contact mechanics calculations were conducted. Moreover, due to the electrical performance and elasticity of the CNT coatings (discussed in ARTICLE III and ARTICLE IV), CNT coatings were deposited over the textured rivets to offset the influence of the generated topographies. It was observed that rougher surfaces exhibited lower ECR, particularly when contacting harder materials. This was attributed to the plastic deformation of the asperities. Furthermore, the proposed CNT coatings were found to effectively mitigate the influence of topography.

5.1.3. Coatings

ARTICLE VI

ARTICLE VI investigated the electrical performance of different CNP-coated copper substrates during fretting, as well as the characterization of fretting marks after 5,000 and 50,000 cycles. The CNP coatings initially exhibit a high ECR. However, after approximately 5-10% of the total fretting cycles, the coating adjusts due to the motion of the counter electrode, exhibiting ECR values that are similar to or lower than those of the copper reference. Furthermore, the ECR reaches a steady state value and remains relatively constant. The most significant reduction in worn area was observed for CB and CNT, with CNT additionally preventing oxidation during fretting.

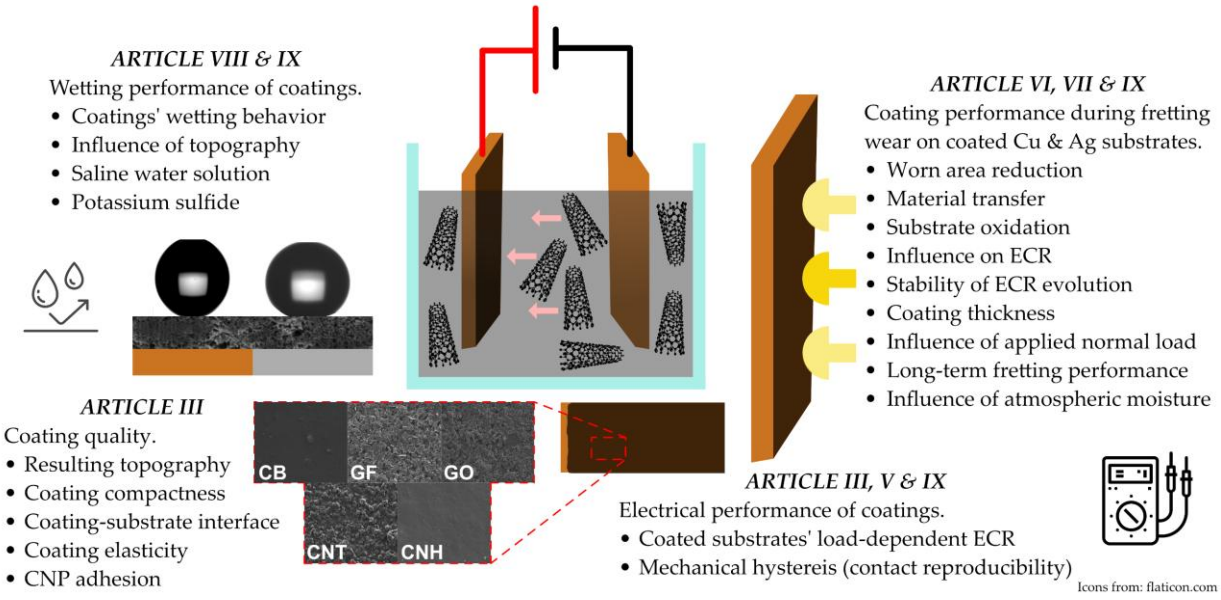

Figure 13. Schematic overview of appended articles for *coatings* classification.

ARTICLE VII

As a follow-up to ARTICLE VI, ARTICLE VII focused exclusively on the tribological performance of CNT coatings. Three CNT coatings with varying thicknesses were subjected to tribo-electrical characterization, with the objective of elucidating the influence of coating thickness, normal load during fretting, number of fretting cycles, and relative humidity. The results demonstrate that the coatings outperformed the copper reference during fretting. Thicker coatings enhanced wear protection, with relative worn area reduction reaching up to approximately 50% after 150,000 fretting cycles. The CNT coatings showed exceptionally low and stable ECR even after 500,000 fretting cycles, with thinner CNT coatings outperforming thicker coatings for prolonged fretting tests. Furthermore, CNT coatings offered wear protection even in low humidity environments.

ARTICLE VIII

Following the electrical and tribological characterization of the CNP in ARTICLE III, ARTICLE IV, ARTICLE VI, and ARTICLE VII, ARTICLE VIII examined the potential atmospheric protection offered by CNP coatings through the analysis of their wetting behavior. Sessile drop tests were conducted on CNP-coated copper platelets using purified and saline water. The CA was measured and correlated with the topographic features of the coatings. The GF, GO, and CNT coatings exhibited superhydrophobic wetting behavior, with the CB and CNH coatings demonstrating higher hydrophobicity than the uncoated copper reference. The thickness of the CNT coating did not influence the wetting behavior. However, given that the CNT coatings are highly heterogeneous due to CNT agglomeration, it is necessary to ensure that the coating thickness completely covers the substrate.

ARTICLE IX

With the knowledge acquired for copper in articles ARTICLE III-ARTICLE V and ARTICLE VI-ARTICLE VIII, CNP coatings were deposited over silver substrates. The electrical, tribological, and wetting performance of the coated silver samples was investigated in detail in ARTICLE IX. All CNP-coated samples demonstrated superior performance to the tarnished silver sample in load-dependent ECR, with CNT showing lower ECR at high normal loads. Furthermore, the CNH and CNT coatings exhibited comparable ECR during fretting to the reference sample, while simultaneously protecting from severe wear and reducing material transfer after 5,000 cycles. Even after five minutes, all samples showed a hydrophobic wetting behavior, with GF, CNH, and CNT coatings exhibiting higher water CA than the tarnished and reference samples. However, when the CA was measured with potassium sulfide, only the GF coating exhibited a stronger hydrophobicity than the reference and tarnished samples.

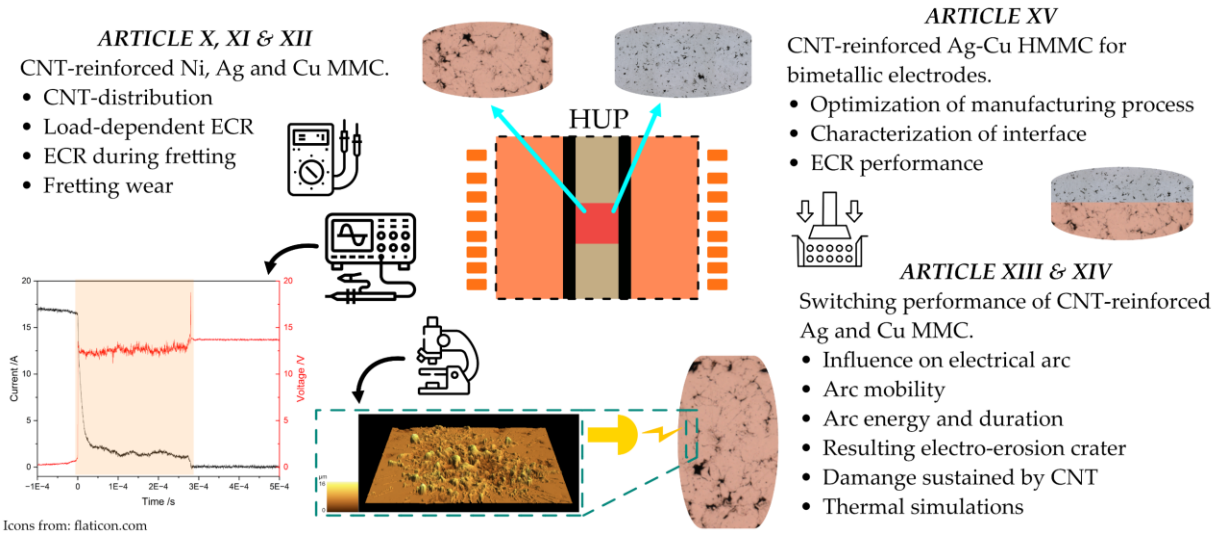

Figure 14. Schematic overview of appended articles for *composites* classification.

5.1.4. Composites

ARTICLE X

CNT-reinforced nickel MMC were produced via powder metallurgy. Current- and load-dependent ECR, as well as an analysis on the distribution of the reinforcement phase, of three different reinforcement concentrations were evaluated. The incorporation of the conductive CNT into the nickel matrix decreases the ECR compared to unreinforced nickel, in addition to improving the contact's elasticity. The findings from ARTICLE X highlight the potential of CNT-reinforced electrical contacts; albeit the results indicate that proper CNT dispersion and distribution is key to harness the desirable behavior from the reinforcement phase since large CNT clusters tend to increase ECR.

ARTICLE XI

Using the same procedure and parameters as in ARTICLE X, CNT-reinforced silver and copper MMC were produced at two different CNT concentrations (0.5 and 1 wt.%). The MMC were characterized, and their tribo-electrical performance was evaluated. Properly densified copper MMC were obtained from the sintering method, whereas the silver MMC did not achieve satisfactory density values (below 90%). The addition of CNT into the metallic matrix improved contact reproducibility, albeit at the cost of a slight gain in ECR. Furthermore, copper MMC rapidly reached steady state ECR during fretting test.

ARTICLE XII

ARTICLE XII expands upon the results from ARTICLE XI. The sintering process for silver MMC was improved on, thus obtaining relative densities above 90%. The morphology of the silver powder used generates considerable porosity prior to sintering, thus requiring longer holding times during HUP to properly close the internal pores. Load-dependent ECR and ECR evolution during fatigue cycles were measured on the dense MMC. Reinforced samples exhibited lower ECR and higher reproducibility than the harder reference samples. In fatigue tests, the MMC outperformed the reference samples, rapidly reaching steady-state ECR and maintaining low ECR throughout the 20 fatigue cycles measured.

ARTICLE XIII

Higher CNT concentration MMC were produces using the methodology from ARTICLE XI and ARTICLE XII with the objective of characterizing their performance under electro-erosion tests. ARTICLE XIII focuses on the characteristics of the electrical arc that is generated due to a single break operation under a pure ohmic load (automotive halogen lamps). All MMC exhibited similar arc characteristics as the reference materials, with copper MMC having the shortest arc duration and lowest arc energy. At least 2 wt.% of CNT is required in the MMC to prevent unstable arcing from taking place during hot switching. High speed video footage demonstrated that the addition of the reinforcement phase confines the arc, reducing its mobility.

ARTICLE XIV

Following the characterization of the electrical arcs in ARTICLE XIII, ARTICLE XIV aimed to analyze the damage produced on the electrodes due to the electrical arc. The resulting dimensionality of the electro-erosion craters and the structural integrity of the reinforcement phase was characterized, in addition to finite element method thermal simulations. ARTICLE XIV highlights CNT concentrations of up to 2 wt.% perform similarly – in terms of crater dimensionality, displaced volume, and roughness – to reference and standard materials. Furthermore, the thermal simulations showcase the fact that the reinforcement phase does not significantly affect the dimensions of the melting and boiling front. However, reinforcement concentrations of 2 and 3 wt.% significantly accelerate re-solidification of the molten material. Moreover, Raman spectroscopy demonstrated that the energy input originating from the electrical arc is not sufficient to significantly degrade the reinforcement phase.

ARTICLE XV	The objective of ARTICLE XV was to manufacture and electrically characterize bimetallic joints (hybrid metal matrix composites – HMMC) using the same methodologies from ARTICLE X-ARTICLE XIII. This manufacturing route presents the advantages that it enables a more precise control over the process, no filler material is required, the final component is near-net-shape, in addition to the fact that reinforcing the metals and batch production is possible. However, due to the proximity of the sintering temperature to the eutectic temperature of the silver-copper hybrid composite, the sintering temperatures were reduced to 550 °C. Furthermore, to minimize energy requirements, processing times, and copper's diffusion, the sintering times were reduced to 2.5 instead of 7.5 hours. Reinforcing the metallic powders with CNT resulted in HMMC with similar electrical performance as unreinforced sintered bimetallic joints, with the advantage that the CNT act as diffusion barriers, thus slowing down or even preventing the formation of Kirkendall voids.

ARTICLE I
Multipurpose Setup Used to Characterize Tribo-Electrical Properties of Electrical Contact Materials

Bruno Alderete[1,*], Rafael Puyol[2], Sebastian Slawik[1], Eric Espin[1], Frank Mücklich[1], Sebastian Suarez[1]

[1] Chair of Functional Materials, Saarland University, Campus D3.3, 66123 Saarbrücken, Germany
[2] ELEN, ICTEAM, UCLouvain, Place du Levant, 3 bte L5.03.02, 1348 Louvain-la-Neuve, Belgium

Method article
Published in "*MethodsX*" (2021)
Impact Factor: 1.6 (2023)

Accessible online at: doi.org/10.1016/j.mex.2021.101498

Own Contribution: Methodology; Software; Validation; Investigation; Data Curation; Writing – Original Draft; Visualization.

Cite this article as: B. Alderete, R. Puyol, S. Slawik, E. Espin, F. Mücklich, S. Suarez, Multipurpose setup used to characterize tribo-electrical properties of electrical contact materials, MethodsX 8 (2021) 101498. https://doi.org/10.1016/j.mex.2021.101498.

MethodsX 8 (2021) 101498

Contents lists available at ScienceDirect

MethodsX

journal homepage: www.elsevier.com/locate/mex

Method Article

Multipurpose setup used to characterize tribo-electrical properties of electrical contact materials

Bruno Alderete[a,*], Rafael Puyol[b], Sebastian Slawik[a], Eric Espin[a], Frank Mücklich[a], Sebastian Suarez[a]

[a] Chair of Functional Materials, Saarland University, Campus D3.3, Saarbrücken 66123, Germany
[b] ELEN, ICTEAM, UCLouvain, Place du Levant, 3 bte L5.03.02, Louvain-la-Neuve 1348, Belgium

A B S T R A C T

Electrical contacts are pervasively found on countless modern devices and systems. It is imperative that connecting components present adequate electrical, mechanical, and chemical characteristics to fulfill the crucial role that they play in the system. To develop an electrical contact material that is tailored for a specific application, different approaches are pursued (e.g., coatings, reinforced composites, alloyed metals, duplex systems, etc.). The manufacturing of electrical contact materials demand a thorough characterization of their electrical properties, mechanical properties, and their resistance to wear, as well as their resistance to atmospheric conditions. Accordingly, commissioning of a novel setup enables a more comprehensive study of the materials that are developed. Therefore, a complete understanding of the material's electrical and tribological characteristics are attained, allowing the production of a material that is compliant with the particular demands of the application for which it is intended. This multipurpose setup was built with higher precision stages and higher accuracy 3-axis force sensor, thus providing the following improvement over the preceding setup:

- Elevated load-bearing capacity (double), higher precision and stability.
- Tribo-electrical characterization (implementation of scratch and fretting tests).
- Environmental control (climate and external vibration).

A R T I C L E I N F O

Method name: Constant current method for automatic electrical contact resistance measurements
Keywords: Electrical contact resistance (ECR), Scratch test, Fretting test
Article history: Received 5 May 2021; Accepted 23 August 2021; Available online 24 August 2021

* Corresponding author.
E-mail address: bruno.alderete@uni-saarland.de (B. Alderete).

https://doi.org/10.1016/j.mex.2021.101498

Specifications table

Subject Area:	Materials Science
More specific subject area:	*Tribo-electrical characterization, Carbon-based metal reinforcement and coatings*
Method name:	*Constant current method for automatic electrical contact resistance measurements*
Name and reference of original method:	*R. Puyol and S. Suárez, "A contact resistance measurement setup for the study of novel contacts", IEEE URUCON, Montevideo, 2017, pp. 1-4.* doi:10.1109/URUCON.2017.8171881
Resource availability:	• https://www.physikinstrumente.store/eu/l-511.20sd00/ • https://www.physikinstrumente.store/eu/l-511.2asd00/ • https://www.physikinstrumente.store/eu/c-663.12/?c=7 • https://bit.ly/37ntbWP • https://bit.ly/3ysXWWv • https://bit.ly/2VxIv0C • https://bit.ly/3xs1nLy • https://github.com/me-systeme/gsv8pypi • https://de.tek.com/keithley-source-measure-units/keithley-smu-2400-standard-series-sourcemeter • https://de.tek.com/keithley-low-level-sensitive-and-specialty-instruments/keithley-nanovoltmeter-model-2182a • https://www.tek.com/keithley-accessories/test-fixtures-manual • https://github.com/royerlab/pipython • https://bit.ly/3rXHmLF • https://www.opta-gmbh.de/produkte/unterbauten/aktiver-unterbau.php • www.github.com/brunoalderete/tribo-electrical_testing_rig.git

Method details

Considering the most important characteristics that an electrical contact material should possess, the one at the forefront is the electrical contact resistance (ECR). Using metals that inherently have a low resistivity (such as silver, gold, copper, etc.) ensures that the energy loss throughout the electric circuit will be low. Therefore, when developing new electrical contact materials, it is crucial to quantify the electrical resistance that these materials pose to the flow of current under the contact situation that they will be subjected to. There are several methods to determine ECR, namely: four terminal sensing, three-wire sensing, and two terminal sensing (ohmmeter) under constant current method or constant voltage [1]. Of these methods, the four-probe method is the most common since it is not influenced by the resistance added by the connections and the wiring. In this study, four terminal sensing under constant current was chosen, due to its simplicity and effectiveness. As the name suggests, a constant DC electrical current is applied on the testing material, while the voltage drop is measured between two terminals. Through this measurement, and knowing the value of the applied current, the resistance is simply obtained by Ohm's law.

An efficient ECR measurement is crucial to obtain a complete understanding of the electrical properties of novel and commercially available electrical contacts. The acquisition of reliable ECR measurements is based on the repeatability and the precision of the equipment used. Therefore, the proper selection of the devices is vital. Accordingly, the customizations implemented to the preceding ECR testing rig focus on four key components: the force sensor, the linear stages, the piezoelectric stage, and the environmental control equipment. The selected force sensor not only broadens the range of measurement (by doubling the applicable normal load) but is also capable of measuring strain in three directions. Whereas the perpendicularly mounted linear stages enable the user to characterize the tribological behavior of the contact materials (e.g., connectors) by simulating insertion-removal cycles. Moreover, by implementing a piezoelectric stage, in-operation low-amplitude vibrations can be simulated (fretting) [2,3]. Finally, the incorporation of a climate control chamber and an active vibration dampening stage further expand the range of applications that can be simulated with the multipurpose rig. The former allows the manipulation of the ambient temperature and humidity (improving repeatability), whereas the latter mitigates external factors that may affect the measurements. Furthermore, through specific programming sequences, a wide variety of tests can be carried out, thus combining different normal loads, tangential motion, and ECR measurements.

Previous ECR setup

Determining the ECR of contact materials has been previously reported by Puyol et al., [4–6] where a setup was developed with the primary objective of determining low-level load-dependent ECR. This setup was able to quantify the ECR in the μΩ range with a measurement error below 10% for loads below 1 N, and below 1% for loads above 1 N. However, this setup is limited by the linear stage. Considering that the sample to be characterized is mounted on the stage, the system exclusively moves in a single direction. Additionally, the maximum applicable load is restricted by the force sensor's limit (10 N). Nonetheless, this device has proven crucial in conducting ECR of novel composite and coated materials, as well as conducting current sweeps with the help of additional equipment and software.

The setup is constituted by three sectors which work together to perform the measurements (motion and force control, electrical components, and software). The first sector consists of a linear stage (Physik Instrumente M-683.2U4, ultrasonic piezo stage, low-level self-locking, minimum incremental motion of 0.3 μm) and the uniaxial force sensor (ME-Systeme KD-24±10N, 0.1% accuracy). The former is used to control the motion of the sample towards and away from the counter electrode, whereas the latter is responsible for regulating the normal load that is applied. Independently, the setup is equipped with a current/voltage sourcing unit (Keithley 2400 SMU) and a nanovoltmeter (Keithley 2182a). These two components handle the electrical parameters of the setup. Finally, the software interface is implemented in LabView to control, observe and extract the parameters and information throughout the entire measurement process.

New multipurpose ECR setup

To expand upon the aforementioned method, and to acquire vital information on the tribo-electrical characteristics of the novel electrical contact materials (as well as commercially available electrical contact materials), it was sought to develop a new testing rig capable of conducting tribological tests, alongside electrical measurements. Consequently, the possibility for tangential motion (relative to the surface of the sample) was required. By incorporating the capability of lateral motion, scratch tests and reciprocating lateral motion cycles can be performed. The former focuses on the deformation/wear process that arises when the connector is used for the first time. Whereas the objective of the latter is to simulate the deformation that occurs under usual connecting-disconnecting cycles in traditional sliding electrical connectors; thus quantifying the degradation of the contact materials and the electrical characteristics after the initial connection-disconnection process. Moreover, the possibility to conduct high-frequency micro-vibrations was implemented by incorporating a piezoelectric stage. Through this device, naturally occurring vibrations inherent to the intended application of the connector are simulated (fretting test). Furthermore, a force sensor with a higher maximum load of 20 N was selected, in addition to the 3-axis sensing capabilities. Therefore, broadening the range of applicable loads of the setup. Finally, climate control was incorporated, by placing the setup within a climate test chamber, which can replicate in-operation conditions (temperature and humidity). To mitigate external factors from affecting the measurements, the rig was mounted on an active vibration dampening stage, which assures that the climate chamber's vibrations and external factors do not alter the ongoing experiments. The components equipped are summarized in Table 1.

The linear stage motors (M1 and M2) are mounted perpendicularly, relative to each other. M1 is responsible for motion perpendicular to the surface of the sample (normal load), whereas M2 moves parallel to the surface of the sample (tangential motion), as shown in Fig. 1. Both stages are controlled via an individual controller (M3). These two controllers are interconnected with one another via a daisy chain connection and communicate with the software via universal serial bus (USB). The stages move on account of a two-phase stepper motor, with a total of 52 mm travel range and a minimum incremental motion of 0.2 μm for M1 and 0.02 μm for M2. The higher precision of M2 is required to obtain a controlled frictional motion. Whereas the precision of M1 may be lower given that its objective is to control the normal load that is applied. M1 and M2 consist of spindle axis with high-level self-locking. Therefore, M1 increases the stability of the contact forces, granting higher

Table 1
Components required.

Use	Instrument	Manufacturer	Model	Precision	Quantity	Code
Motion	High-precision linear stage	PI	L-511.20SD00	0.2 µm	1	M1
Motion	High-precision linear stage with encoder	PI	L-511.2ASD00	0.02 µm	1	M2
Motion	Stage controller	PI	C-663.12 Mercury Step	-	2	M3
Motion	Piezoelectric stage	PI	P-750	1 nm	1	M4
Motion	Stage controller	PI	E-709.CHG		1	M5
Force	3-Axis force sensor	ME-Systeme	K3D60a±20N	0.1%	1	F1
Force	Amplifier	ME-Systeme	GSV-8 Sub D44HD	-	1	F2
Electric	Current/Voltage source	Keithley	2400 SMU	±(0.066% + 20 µA)	1	E1
Electric	Nanovoltmeter	Keithley	2182a	±(30 ppm + 4 ppm) at 100 mV range	1	E2
Electric	GPIB to USB adapter	Keithley	KUSB-488b	-	1	E3
Climate	Climate control chamber (temperature and relative humidity)	Vötsch Technik	LabEvent L C/150+10/5	±(0.3-0.5 K) ±(1-3% r.h) When controlling temperature and humidity	1	C1
Vibration	Active vibration dampening table	Opta	DMT 600	-	1	V1

force control precision compared to the previous setup's linear stage. The piezoelectric stage (M4) was mounted over the stages and connected to its controller (M5) via a Sub-D special socket 7W2. M5 communicates with the software via USB. M4 has a load capacity of 100 N, with 1 nm vertical accuracy, a maximum travel range of 75 µm, and a maximum frequency of 100 Hz.

The force sensor (F1) was mounted on a stationary column. It is connected to an amplifier (F2) which enhances the electrical signal from the force sensor and communicates it via USB to the software. The force sensor may operate at a maximum force of ±20 N (compressive and tensile stress) with an accuracy class of 0.1%. Although F1 and the force sensor from the preceding setup present the same accuracy class (0.1%), a high-accuracy factory calibration was selected, which guarantees measurement repeatability. Moreover, the 3-axis sensing capacity further improves the precision of F1 on account that when loading the device on more than one direction its precision is generally reduced, which is not the case in this force sensor. Regarding F2, the noise level is approximately 10 times lower than the amplifier used in the preceding setup. In other words, with F2 one more decimal number is reliably represented in the F1's measurement. The frequency at which F1 records a measurement can be varied. For force control, the frequency was set at 10 measurements per second. This frequency was chosen since it provides the most precise measurements (precision is load and frequency dependent), granting more precision in the force control. When acquiring the coefficient of friction (CoF), the measurement frequency was set at 100 Hz on account of dynamic process (scratch tests generally do not last for more than a few seconds). Therefore, a tradeoff between higher precision and a larger data pool was chosen.

The electric components are the same as described by Puyol et al. [4], current/voltage source (E1) and nanovoltmeter (E2). E1 is capable of sourcing current from 1 nA to 1.05 A, and voltage from 200 µV to 210 V from its rear control panel terminals. E2 may be programmed with five different measurement ranges from its front control panel terminal: 10 mV, 100 mV, 1 V, 10 V, and 100 V. E1 and E2 are connected to the computer independently via USB using a general purpose interface

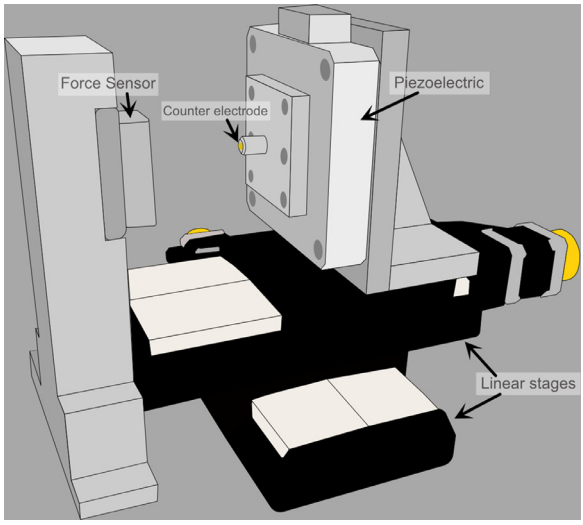

Fig. 1. Schematic representation of novel setup.

bus (GPIB) adapter (E3). An illustration of the setup and possible tests are shown in Fig. 2, whereas Fig. 3 shows a schematic representation of the setup connections. As illustrated in the latter, E1 and E2 have their respective positive terminals connected directly on the sample, whereas their negative terminals are connected on the counter electrode. The location of the positive and negative terminals is not of significance as long the same-sign terminals are connected on the same component. This is due to the fact that the absolute value of the resistance is recorded. To prevent introducing error in the measurements due to thermoelectric effects in the sample and/or conductors, E2 is configured to operate under current reversal mode.

To have a precise control over the atmospheric conditions during the tribo-electrical measurements, the setup is placed in a climate control chamber (LabEvent L C/150+10/5, Vötsch Technik). The chamber is equipped with a thermocouple and a wet bulb humidity sensor to measure the temperature and humidity while in operation, respectively. The thermocouple can be repositioned inside the climate chamber, allowing for a more precise temperature control while running experiments. C1 is able to control temperature between the ranges of 10 and 95°C ±(0.3-0.5 K) and relative humidity between 10 and 90% ±(1-3% r.h). The error for both parameters is based on an operation state where both are controlled simultaneously. Furthermore, the setup was mounted on an active vibration dampening stage (DMT 600, Opta GmbH) to mitigate the effects of external vibrations while operating. It is highlighted that both components (C1 and V1) are decoupled, thus the vibrations from C1 do not affect the ongoing experiments. The preceding setup does not account with atmospheric control or vibration dampening systems.

The sample is mounted directly on F1, whereas the counter electrode is mounted on M4. Therefore, an insulating Teflon platelet was placed between the counter electrode (where the negative terminals are connected) and M4. Similarly, a Teflon disk – in accordance with the specifications of the manufacturer – was placed between F1 and the sample (where the positive terminals are connected). A sample holder was designed, which was directly mounted on the Teflon disk. Consequently, depending on the weight of the sample holder and sample, the maximum range of F1 is slightly reduced. However, the reduction in maximum load capacity is negligible, below 1% of F1's capacity. The setup was configured in this manner to obtain better accuracy in the fretting tests. Considering that the maximum amplitude of M4 is 75 µm, the heavier weight of the sample holder-sample system would reduce the accuracy of the motion.

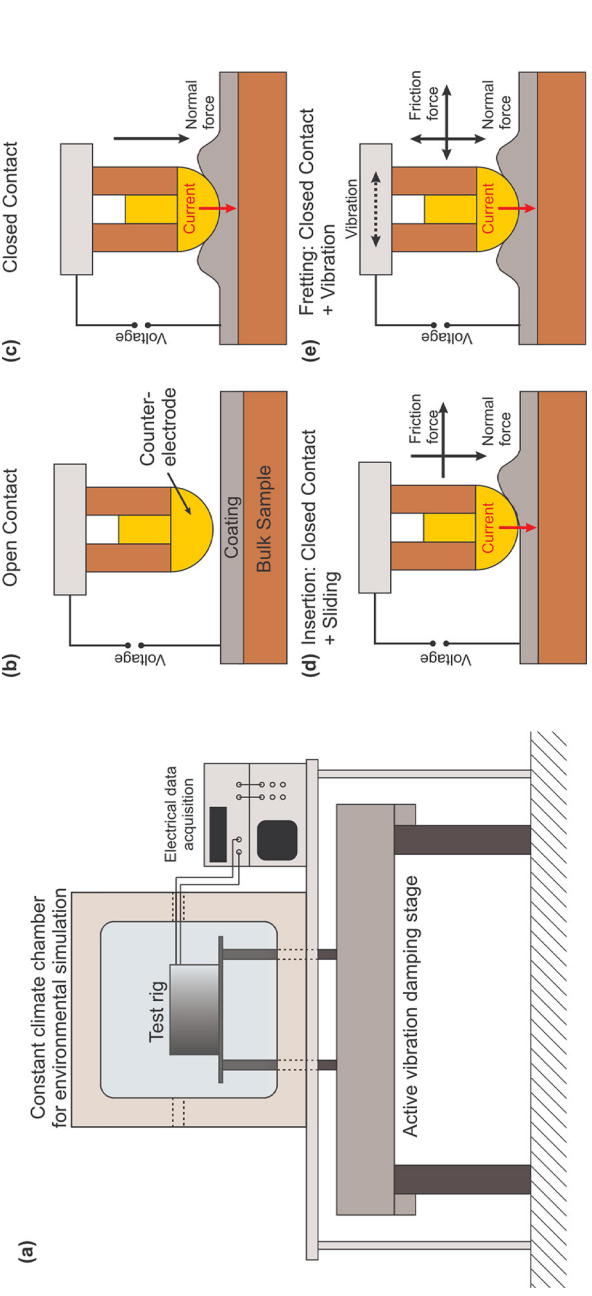

Fig. 2. Schematic representation of a) testing rig inside the climate test chamber and vibration dampening stage; b) open contact between sample and counter electrode; c) ECR measurement; d) ECR and scratch test; e) ECR and fretting test.

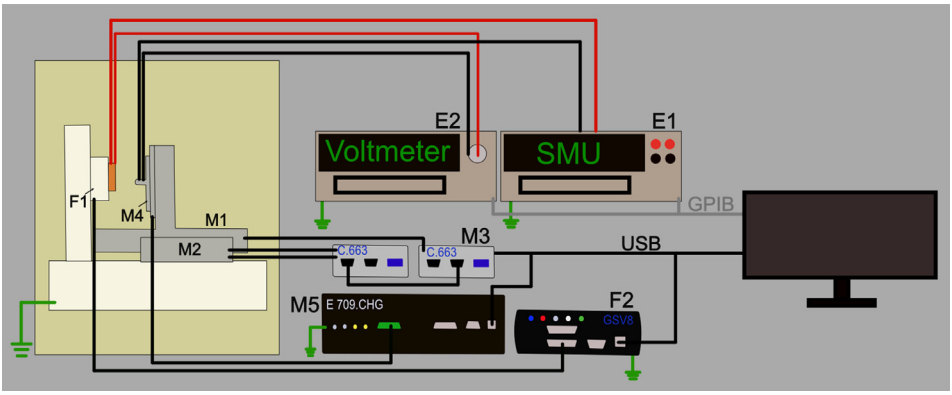

Fig. 3. Schematic representation of the component connections.

Programming and software

The programming for remote control of the setup was done exclusively in Python 3.8 on Windows OS. Through Python, different motion and reading sequences can be ordered. Certain packages must be installed beforehand, which are external to the original Python installation. Therefore, a virtual environment was created where all the necessary packages were installed. Two specific packages are provided by the manufacturer of the equipment (ME-Systeme and Physik Instrumente). In order to communicate with the motion stage controllers (M3 & M5), GCSDevice package were installed in the directory location where the scripts are saved. This package can be found in GitHub [7]. With this library wrapper, general command set (GCS) is used within Python to send commands to the positioner stages, as well as acquiring information (e.g., current position, movement speed, etc.) [8,9]. Likewise, communication between F1, F2 and Python requires several libraries that are specific for F2 [10]. For E1 and E2, no manufacturer-specific packages were available. However, the instruments support communication via different backend providers, of which different alternatives were scrutinized (e.g., NI-VISA, Keysight IO Libraries, and Pyvisa), opting for the latter. Using Pyvisa, communication between the software and E1 and E2 can be implemented using standard commands for programmable instruments (SCPI) [11,12]. Furthermore, packages such as pandas (to save the data), threading (to run multiple processes simultaneously), and time/datetime were imported. Once the initialization of the components, basic motions and data acquisition have been programmed, different test sequences can be programmed. The fact that different tests and test sequences can be programmed - tailored to the demands of the material that will be analyzed - is an advantage that this setup presents. The following table (Table 2) compiles the scripts and provides a brief summary of their capabilities. These scripts run independently and autonomously. After the user inputs the parameters, they do not require supervision. As an added advantage security steps were added to ensure the safety of the devices. An emergency stop button was installed in case manual power shut off is required. The data acquired by the programs (i.e., measurements taken) and the input parameters are recorded as comma separated values (csv files). All scripts are available in GitHub.

Method validation

The ECR of tin platted copper samples (Sn/Cu) was analyzed using both testing rigs. The objective was to validate the measurements acquired with the new rig compared to the previous setup. No commercially available devices were found that could be used to validate the results obtained. Therefore, considering the proposed improvements on the self-build previous setup, it was of interest to compare the results obtained with both rigs. Three different loading cycles were evaluated: low loads (0.25, 0.5, 0.75, 1 N), medium loads (1, 2.5, 5, 7.5, 10 N), and high loads (1, 5, 10, 15 N). The

Table 2
Obtained data and varying and fixed parameters of different Python scripts.

Program	Script name	Description
1	current_sweep.py	Takes ECR measurement by varying the applied current. E2 range and number of ECR measurements can be varied. The user can input the currents.
2	ecr.py	Takes ECR measurements by varying the normal load. The current, measurements per load, and E2 range can be varied. The user can input the loads desired.
3	scratch_ecr.py	Carries out a scratch test, followed by ECR measurements. The scratch load (and ECR load), and track length are set by the user. E2 range and number of ECR measurements can be varied. CoF and ECR are acquired.
4	fretting_ecr.py	Carries out fretting test, followed by ECR measurements. The fretting load, number of cycles, and amplitude are set by the user. E2 range and number of ECR measurements can be varied. ECR is acquired.
5	scratch_fretting.py	Carries out scratch test, followed by fretting. The user input and varying parameters are the same as program 3 and 4. CoF is acquired.
6	connection_ecr_disconnection.py	Simulates connection and disconnection cycles. A scratch test is performed, followed by ECR measurements and a scratch test returning to the starting position. The number of cycles, normal load, and scratch track are user input. E2 range and number of ECR measurements can be varied. CoF in both directions and ECR are acquired.

latter, however, was only measured using the new setup given the extended load ranges. Furthermore, the range of E2 was set at 0.1 V for medium and high loads, whereas it was set at 1 V for low loads to prevent the equipment from overflowing. It is important to highlight that the rig is not capable of changing the voltmeter's range within a single measurement cycle. The range can only be changed manually when the program starts. In this case, two different ranges were used to showcase the optimal accuracy of E2. As in many characterization techniques, one should have a previous idea about the order of magnitude of the variable that will be determined. It is known that low load measurements would grant higher ECR values than medium or high loads. Therefore, to prevent E2 from overflowing, a higher voltage range was selected. In actual measurements, where comparability between different measurement cycles is important, only one voltage range should be used. In all cycles, the current was set at 100 mA, so as to avoid any microstructural changes in the metallic sample (dry circuit testing) [13]. For each force, five measurements were taken and averaged, the results obtained are shown in Fig. 4. Observing Fig. 4 a, the ECR measurements for both setups are similar. The initial resistance at 0.25 N is slightly higher for the traditional setup. However, for 1 N the resistance is lower compared to the new setup. Despite some differences, the error for both systems are relatively low, and the ECR values follow the same tendency. Given the low contacting loads, the ECR values are relatively high, in the 1 Ω range. As Fig. 4 b depicts, similar tendencies are observed in both setups for medium load range. The initial ECR in the previous setup is significantly higher than in the proposed setup; however, the ECR sharply decreases for the second force. Similarly, the error observed in the new setup is elevated in the first two measurements (between 50 and 70 mΩ). However, for higher applied loads the error is reduced to below 10 mΩ (representing between 0.5% and 8% error of the current measurements). For higher normal loads the error observed decreases. ECR measurements for high normal loads, carried out with the proposed setup, are shown in Fig. 4 c. As observed, the error for the lower half of the measurements is relatively high, but is reduced for elevated normal loads. The tendency of this curve is similar to the one observed for medium normal loads, recording lower ECR throughout the cycles. The minimum ECR value recorded for 15, 10 and 5 N (in the unloading semi-cycle) are approximately 20 mΩ.

Additionally, ECR measurements were carried out at a constant normal load of 2 N varying the current in the following sequence: 30 μA, 0.1 mA, 0.3 mA, 1 mA, 3 mA, 10 mA, 100 mA, 300 mA, and 1

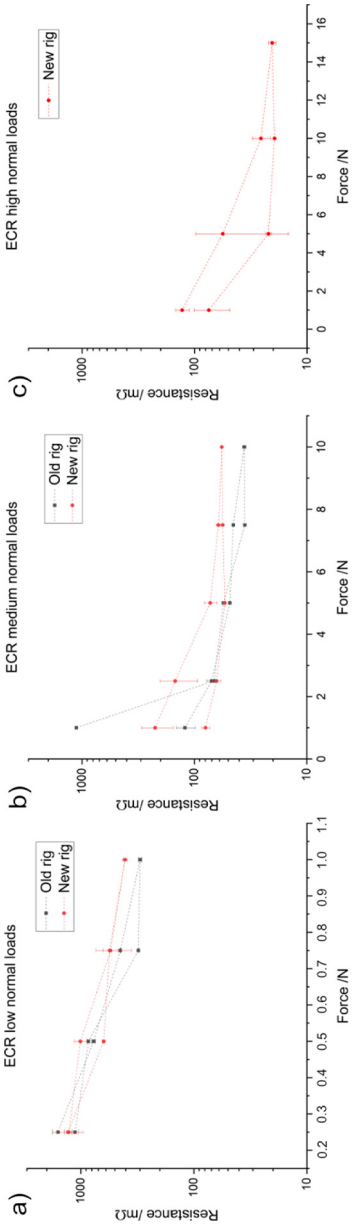

Fig. 4. ECR for a) low normal load range; b) medium normal load range; c) high normal load range.

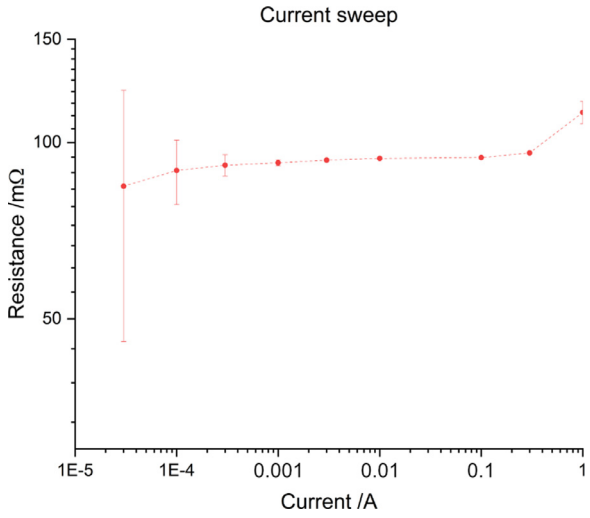

Fig. 5. ECR at constant normal load (2 N), varying current from 30 µA – 1 A.

A. Five ECR measurements were taken for each current. The average ECR appears constant throughout the sweep, as shown in Fig. 5. Given the low current used (30 µA and 0.1 mA), and the elevated range used in E2 (1 V), the error for these two measurements is more significant compared to measurements carried out at higher currents. This range was selected due to the fact that E2 would overflow if 100 mV range was used.

Additionally, scratch and fretting tests were conducted on Sn/Cu samples using the proposed setup. Scanning electron microscopy (SEM) micrographs using backscattered electron detector (BSE) of the scratch track and fretting mark are shown in Fig. 6. The scratch test was carried out at a normal load of 5 N for a total length of 10 mm with a sliding speed of 15 mm/s. Whereas the fretting test was carried out with an amplitude of 75 µm, a frequency of 9 Hz for 100 cycles. The rig was programmed in a way in which the normal load is actively compensated only during fretting tests. That is a consequence of the force sensor's data collection rate. During a scratch test, the force sensor constantly collects the registered force in the tangential and normal axis; this information is later used to determine the CoF. However, due to the short duration of the scratch test (generally below 1.5 s), the test does not last long enough for a proper normal load compensation. Therefore, to resolve this issue, an appropriate sample holder was designed (for each specific type of sample that will be measured). With this sample holder, one can ensure that the surface of the sample is perpendicular to the counter electrode at all times. During fretting, ECR, and indentations this problem does not arise since the CoF is not recorded. Therefore, the force sensor is used exclusively for normal load control.

Accuracy and uncertainty analysis

The resistance measurement was made using the traditional Kelvin method. The current was sourced by E1 and the voltage was measured with E2. Equipment manufacturers usually provide the uncertainty in the sourcing or measuring mode expressed by an uncertainty in the measurements, plus an uncertainty in the range. This numeric value is complemented by two more coefficients, which are expressed in the same way. That must be multiplied by the temperature exceedance from the permissible range to compensate for temperature effects [14]. Both E1 and E2 require temperature correction when working below 18°C or above 28°C. However, for this study, the temperature was kept between these ranges. Therefore, the correction factor was not required. The coefficients usually drift as time from calibration progresses. As a preventive measure the worst-case values were

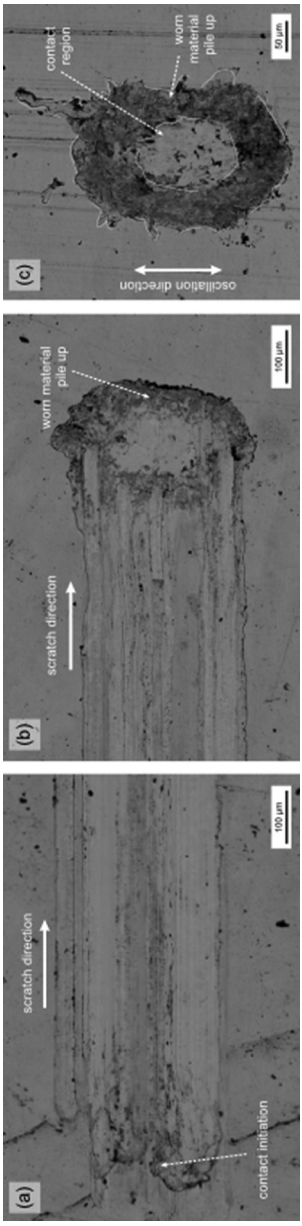

Fig. 6. SEM micrograph of a) beginning of scratch track; b) ending of scratch track; c) fretting mark.

Table 3
Calculated resistance standard deviation for different voltage ranges.

Keithley 2400 SMU range	Keithley 2128a range	σ
100 µA	10 mV	171.3 nΩ
100 µA	100 mV	170.6 nΩ
100 µA	1 V	170.4 nΩ

used. Consequently, a coefficient corresponding to a calibration of more than two years before the experiment was adopted.

Alternatively, the data (sourced or measured) can be interpreted as a random variable. The mean of the random variable is the value of the physical process we want to obtain, whereas the variance is composed by the addition of the range and measured uncertainty. Therefore, the variance is a function of the mean. Therefore, once the mean is set, the distribution is obtained. Furthermore, it was assumed that the uncertainty provided by the manufacturers corresponds to 3-sigmas. In other words, the measurements will fall within the uncertainty ranges provided 99.73% of the times.

To determine the resistance, two normally distributed random variables must be divided. However, this division yields another random variable with no finite moments and several different distributions, depending on the parameters. Nonetheless, several authors have proposed ways of approximating the distribution with a normal one and have also studied the conditions that make this approximation valid [15]. Therefore, the mean and standard deviation for the measured resistance can be determined from those of the voltage and current values through the following equations (Eq. 1 and Eq. 2):

$$\mu_R = \frac{\mu_V}{\mu_I} \tag{1}$$

$$\sigma_R = \mu_R \sqrt{\left(\frac{\sigma_V^2}{\mu_V^2} + \frac{\sigma_I^2}{\mu_I^2}\right)} \tag{2}$$

Kuethe et al. [16] has stipulated a condition that is sufficient for approximating the distribution of the resistance as a normal distribution. This condition is shown on Eq. 3. In this case, the condition is not difficult to satisfy, although for other applications it can be harder. Therefore, several authors have proposed alternative methods [17,18]. The mean and standard deviations for the optimal equipment ranges are shown in Table 3. It can be observed that all values satisfy the condition proposed by Kuethe et al.

$$\frac{\sigma_I}{\mu_I} \leq 0.1 \tag{3}$$

Both electrical devices have several ranges, many combinations of these provide suitable ranges for performing the measurements. Using the aforementioned equations, one can determine the range that minimizes uncertainty. Although several voltage ranges fall within the measurement range for a single current, the best choice is to use the largest current that is allowed by the voltage range (without overflowing). The part of the uncertainty related to the reading will be constant, but the fixed part related to the range will have a smaller impact if the measurand is closer to the upper limit of the range. Given the materials that will be analyzed with these setups, it is expected that the resistance will be in the range of 1 mΩ. Therefore, the uncertainty for all the combinations of voltage and current ranges when measuring 1 mΩ using the largest possible current per range is shown in Fig. 7. As the arrow indicates, there are three possible configurations with almost identical uncertainty levels, shown in Table 3, of which the latter range offers the lowest standard deviation. Furthermore, the lowest resistance can be measured using the 10 mV range, whereas the highest resistance can be measured with the 1 V range. Regarding the 100 mV range, it is the best choice when it is expected that the resistance will fluctuate in both directions.

Finally, the error present in the proposed setup while the stages control the normal load to the set value is shown in Fig. 8. For this plot, between 100 and 200 normal load measurements were

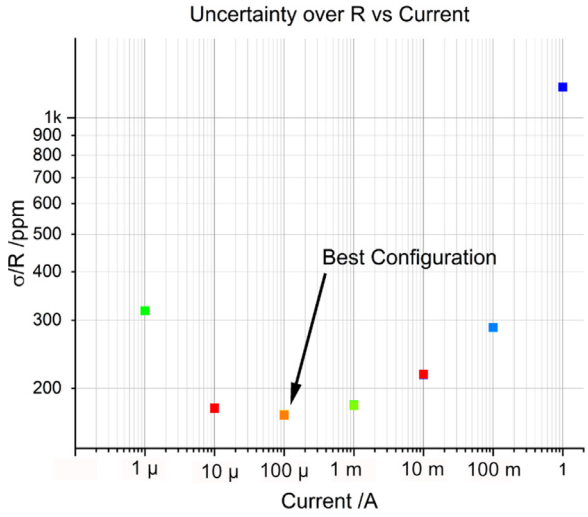

Fig. 7. Uncertainty on the measurements vs. current for the different configurations.

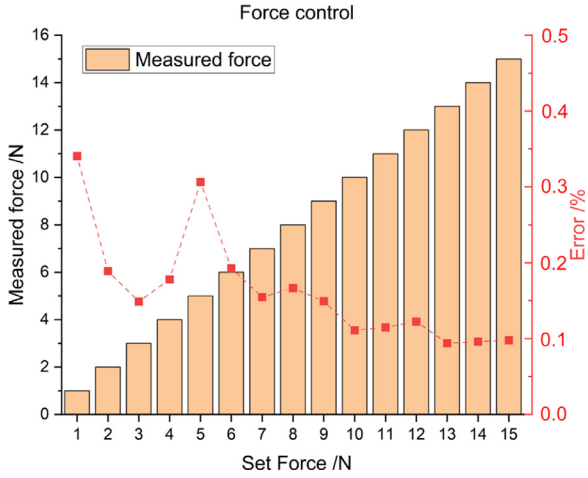

Fig. 8. Error while controlling normal load.

recorded while the stages controlled said force. As the graph depicts, the error never surpassed 0.35%, with values as low as 0.10% for higher normal loads.

Concluding remarks

This method article presents the added possibilities of a new multipurpose setup compared to the preceding. By implementing the additional motor stages and using a force sensor with a higher permissible load, the capabilities are extended; thus, achieving more in-depth information on the tribo-electrical characteristics of electrical contact materials. Additionally, the higher precision of the linear stages (along with the lower minimum incremental motion) allows a finer control of applied normal loads and precise lateral motions. The incorporation of the piezoelectric stage allows micro-oscillations that simulate in-operation fretting wear. As demonstrated in the method validation, the

ECR curves for the same force range are similar in magnitude when measured with both rigs; proving that the new setup effectively provides the resistance measurement. Moreover, the selection of high-precision linear stages and high-accuracy 3D force sensor is reflected upon the accuracy and uncertainty analysis. Therefore, rendering considerably precise measurements (regarding applied normal load, measurement of tangential load, and electrical measurements) with an offset from the set force as low as 0.1%. Furthermore, the atmospheric control chamber and active vibration dampening stage produce more reproduceable measurements, avoiding the influence of uncontrollable external factors on the measurements. The scripts developed and programming sequences were written in Python, all of which are open-source and available in GitHub.

Acknowledgement

B.A. wishes to acknowledge the support from the German Academic Exchange Service (DAAD). We acknowledge support by the Deutsche Forschungsgemeinschaft (DFG, German Research Foundation) and Saarland University within the funding program Open Access Publishing. The TÜV Saarland Stiftung is gratefully acknowledged for financially supporting the project. The authors gratefully acknowledge funding in the ZuMat project, supported by the State of Saarland from the European Regional Development Fund (Europäischen Fonds für Regionale Entwicklung, EFRE).

Declaration of Competing Interest

The authors declare that they have no known competing financial interests or personal relationships that could have appeared to influence the work reported in this paper.

References

[1] G.T. Meaden, Electrical Resistance of Metals, Springer US, 2013, doi:10.1007/978-1-4899-5717-7.
[2] A. Bouzera, E. Carvou, N. Ben Jemaa, R. El Abdi, L. Tristani, E.M. Zindine, Minimum fretting amplitude in medium force for connector coated material and pure metals, in: Electr. Contacts, Proc. Annu. Holm Conf. Electr. Contacts, 2010, pp. 101–107, doi:10.1109/HOLM.2010.5619557.
[3] D. Gagnon, M. Braunovic, J. Masounave, Effect of fretting slip amplitude on the friction behaviour of electrical contact materials, in: Electr. Contacts, Proc. Annu. Holm Conf. Electr. Contacts, 2005, pp. 186–195, doi:10.1109/HOLM.2005.1518243. vol. 2005.
[4] R. Puyol, S. Suarez, A Contact Resistance Measurement Setup for the Study of Novel Contacts, IEEE URUCON (2017) 1–4, doi:10.1109/URUCON.2017.8171881.
[5] K.E. Trinh, F. Mücklich, E. Ramos-Moore, The role of microstructure and surface topography in the electrical behavior of Sn-coated Cu contacts, in: 27th Int. Conf. Electr. Contacts, ICEC 2014 - Proc, 2014, pp. 243–248.
[6] K.E. Trinh, E. Ramos-Moore, I. Green, C. Pauly, M. Zamanzade, F. Mucklich, Topographical and Microstructural Effects of Laser Surface Texturing on Tin-Coated Copper Electrical Connectors under Load Cycling, IEEE Trans. Components, Packag. Manuf. Technol. 7 (4) (2017) 582–590, doi:10.1109/TCPMT.2017.2659224.
[7] Royerlab, "GCSDevice." www.github.com/royerlab/pipython (accessed Dec. 07, 2020).
[8] Physik Instrumente, in: C-663 Mercury Step Stepper Motor Controller User Manual, PI, Karlsruhe, 2020, p. 295.
[9] Physik Instrumente, in: PZ222E User Manual E-709 Digital Piezo Controller, 1 Channel, -30 to 130 V, PI, Karlsruhe, 2019, p. 269.
[10] ME-Systeme, "GSV8-Py." www.github.com/me-systeme/gsv8pypi (accessed Nov. 14, 2020).
[11] K. Instruments, Keithley 2400 User's manual, Cleveland (2011) [Online]. Available www.tek.com/keithley-source-measure-units/keithley-smu-2400-series-sourcemeter-manual/series-2400-sourcemeter .
[12] K. Instruments, Model 2182/2182A Nanovoltmeter User's Manual, Cleveland (2004) [Online]. Available: www.tek.com/product-support?series=Keithley Nanovoltmeter Model 2182A%0A.
[13] E.M. Bock, Low-Level Contact Resistance Characterization, AMP J. Technol. 3 (1993) 64–68.
[14] TektronixLow Level Measurements Handbook, Precision DC Current, Voltage and Resistance Measurements, 7th Editio, 2016 Beaverton.
[15] E. Díaz-Francés, F.J. Rubio, On the existence of a normal approximation to the distribution of the ratio of two independent normal random variables, Stat. Pap. 54 (2) (2013) 309–323, doi:10.1007/s00362-012-0429-2.
[16] D.O. Kuethe, A. Caprihan, H.M. Gach, I.J. Lowe, E. Fukushima, Imaging Obstructed Ventilation with NMR using Inert Fluorinated Gases, J. Appl. Physiol. 88 (2000) 2279–2286.
[17] G. Marsaglia, Ratios of Normal Variables and Ratios of Sums of Uniform Variables, J. Am. Stat. Assoc. 60 (309) (1965) 193–204, doi:10.1080/01621459.1965.10480783.
[18] J. Hayya, D. Armstrong, N. Gressis, A Note on the Ratio of Two Normally Distributed Variables, Manage. Sci. 21 (11) (1975) 1338–1341, doi:10.1287/mnsc.21.11.1338.

ARTICLE II
Tarnishing (Ag_2S) Layer on Silver-Plated Electrical Contacts: Its Influence on Electrical Contact Resistance

Bruno Alderete*, Frank Mücklich, Sebastian Suarez

Chair of Functional Materials, Saarland University, Campus D3.3, 66123 Saarbrücken, Germany

Research article
Published in "*IEEE Transactions on Components, Packaging and Manufacturing Technology*" (2023)
Impact Factor: 2.3 (2023)
Reproduced with permission from 'Institute of Electrical and Electronics Engineers - IEEE'
Accessible online at: doi.org/10.1109/TCPMT.2023.3238672

Own Contribution: Conceptualization; Methodology; Validation; Investigation; Data Curation; Writing – Original Draft; Visualization.

Cite this article as: B. Alderete, F. Mucklich, S. Suarez, Tarnishing (Ag2S) layer on silver-plated electrical contacts: its influence on electrical contact resistance, IEEE Trans Compon Packaging Manuf Technol 13 (2023) 45–58. https://doi.org/10.1109/TCPMT.2023.3238672.

Tarnishing (Ag_2S) Layer on Silver-Plated Electrical contacts: Its Influence on Electrical Contact Resistance

Bruno Alderete*, Frank Mücklich, and Sebastian Suarez

Chair of Functional Materials, Saarland University, Campus D3.3, 66123 Saarbrücken Germany

* Corresponding author: bruno.alderete@uni-saarland.de

***Abstract*:**

Silver is ubiquitously used in electrical contacts due to its exceptional electrical conductivity. Although silver does not oxidize, given time it does sulfurize under atmospheric conditions forming silver sulfide. This tarnishing film is often the cause of an electrical contact's malfunction or failure. In this research work we analyzed three alternate methods which could reduce the effect of the tarnishing film on the contact, therefore minimizing the chances of component malfunction. The alternatives analyzed included: puncturing through the tarnishing film, mechanical removal by scratch and fretting tests, and resistive heating removal by applying various currents. These methods were compared to chemically cleaned silver contacts used as reference. Careful analysis of the studied methods proved that normal loads above 5 N are enough to puncture the tarnishing film, thus reducing its effect on the contact material's conductivity. Furthermore, although mechanical removal is not a viable option, it proves that the silver sulfide film does not significantly affect the conductivity of the system when piled-up (as is the case with tin oxide in tin plated contacts). Finally, the resistance of tarnished contacts is considerably higher than the chemically cleaned contacts for loads at or below 5 N (over one order of magnitude).

Keywords: Electrical contact resistance, silver sulfide, tarnished silver.

I. INTRODUCTION

Among electrical contact materials, silver is one of the most sought-after due to its outstanding transport properties. For this reason, it is extensively used in a wide variety of applications, with considerable use in the automotive and aerospace industry. However, the cost associated with silver is its major drawback. Silver and copper are the two metals with the lowest resistivity: 1.59 x 10-8 Ω.m and 1.65 x 10-8 Ω.m at 20 °C, respectively [1]. These two elements present good mechanical properties, alongside the fact that they do not react with the atmosphere under normal conditions. Copper, on the one hand, is protected from further oxidation by an inherent

$$2Ag + S \rightarrow Ag_2S \quad (1)$$

copper oxide layer; however, this oxide layer is detrimental to its conductive properties. Silver, on the other hand, does not react with oxygen at ambient temperatures; therefore, it does not oxidize. Over time however, silver's prolonged exposure to the atmosphere causes a chemical reaction in which a silver sulfide film is formed on the material's surface (chemical reaction shown in (1)).

According to W. Aas et al. [2], between the year 2000 and 2015, Europe and North America have reduced their sulfur emissions by 40% and 50%, respectively. In this same time frame, the emissions of sulfur in Eastern Asia increased by up to 70% in the year 2005, with a 13% reduction between 2005 and 2015. Naturally, sulfur dioxide found in the air could provide a source of sulfur for the chemical reaction with silver to occur, consequently producing silver sulfide tarnish. Although, some studies suggest that sulfur dioxide does not react with silver at ambient temperatures [3], [4]. G.B. Fisher and C. DiMaggio suggest that sulfur dioxide first reacts with atomic oxygen on the silver surface, forming sulfur trioxide (SO_3) [3]. The oxygen atom acts as an intermediate binder between the silver surface and sulfur dioxide. Due to the geometry of this bond, the molecular distance between sulfur and silver is too large for them to react and form silver sulfide. R. Bauer [4], however, states that sulfur dioxide's reaction with silver is slow and can be discarded as originator of the silver sulfide tarnish.

Hydrogen sulfide on the other hand does react with silver under atmospheric conditions, forming the black tarnish on silver contacts [5]–[7]. As reported by Lilienfeld and White [5], hydrogen sulfide in the presence of moisture reacts with oxygen atoms or molecules on silver's surface. This reaction causes an oxidation of the hydrogen sulfide molecule, obtaining water and sulfur (2). The sulfur byproduct of hydrogen sulfide's oxidation immediately reacts with the silver atoms, thus producing silver sulfide. The chemical reaction which explains the tarnishing process is shown in (3). It is a necessity that both oxygen and moisture are present in the atmosphere for this reaction to take place. Otherwise, silver does not tarnish at normal temperatures and pressures. The presence of oxygen and moisture also guarantee that hydrogen is not a byproduct of the reaction between silver and silver sulfide.

Evidently, oxygen and moisture are always present in uncontrolled atmospheres. Therefore, for silver to tarnish, only hydrogen sulfide is required. According to Abdollahi et al. [8], ambient air has an estimated concentration of hydrogen sulfide that ranges from 0.11 to 0.33 ppb. In urban areas the concentrations of hydrogen sulfide can reach levels of up to 1 ppb, and in areas where

$$H_2S + {}^1/_2\, O_2 \rightarrow H_2O + S \quad (2)$$

$$2Ag + H_2S + {}^1/_2\, O_2 \rightarrow Ag_2S + H_2O \quad (3)$$

hydrogen sulfide is naturally produced or is released due to industrial activity, concentration spikes of over 90 ppb have been detected. Therefore, silver connectors that are operational in or around areas with such elevated hydrogen sulfide concentrations may suffer from excessive tarnishing. Consequently, these contacts are more prone to failure.

The influence of silver sulfide has been previously documented [9]–[12], among others. Although it must be noted that the resistance increase caused by the silver sulfide layer depends strongly on the Ag/S ratio [13]. Higher concentrations of sulfur increase the resistance of the film, with film resistivity ranging from 10^{-5} up to 10^4 Ω.m [9]. Depending on the temperature, silver sulfide tarnishing film comes in two allotropic crystalline structures [9], [14], [15]. Below 177 °C ($\beta - Ag_2S$) the conduction is in part by Ag^+ ions (ionic conduction) and in part electrons (electronic conduction). On the other hand, when working above this temperature ($\alpha - Ag_2S$) the conduction is predominantly electronic, with an abrupt decrease in resistivity at the transition temperature. The latter configuration of the silver sulfide crystal is an inorganic compound n-type semiconductor, whereas the former crystalline structure presents a quasi-metallic behavior [15]. The β structure has higher specific resistivity than the α structure, with high temperature dependance, whereas the resistivity of the α structure presents low temperature dependance [14].

Atmospheric and material parameters also affect the growth of Ag_2S, such as temperature, light exposure, roughness, etc. [12]. Temperature is specifically important since elevated temperatures promote chemical reactions, and thus the formation of the tarnishing film [16]. Ambien humidity and atmospheric gas composition play a crucial role in the growth of Ag_2S – particularly atmospheres containing sulfur and chlorine [17].

Many methods have been developed to prevent or delay the formation of the silver sulfide film. The most common method used to protect silver from sulfidation is the deposition of a protective coating, i.e., passivation [18]. These coatings can be of organic origin (such as lacquers, oils, waxes, etc.) or inorganic origins (such as metallic coatings). The latter are used more frequently due to ease of incorporation in industrial processes (common coating techniques: electrochemical deposition, immersion, chemical vapor deposition, and physical vapor deposition), and due to longer durability of the protective coating. Gay et al. [18] has categorized the inorganic coatings

into four primary classes: chromate conversion coatings, oxide coatings, tin coatings, and electrolytic silver alloy coatings. Chromate conversion is an outstanding protective coating, presenting the additional advantage that it does not alter the appearance of the substrate (important for the jewelry industry) [19]. However, due to the toxicity of hexavalent chromium, its use is no longer viable. Oxide coatings have also proven effective at protecting silver substrates. Oxides of elements from the third and fifth group of the periodic table – as well as silica, alumina, and zirconium oxide coatings – have been previously reported [18], [20]. However, the major drawback from this technique is that the oxide layers increase the electrical resistance of the substrate-coating system. An alternative is to deposit tin on silver's surface. Although tin has higher specific resistivity than silver (1.16×10^{-7} Ω.m at 20 °C) [1], tin is easily deformed. Therefore, when two contacting bodies are connected the tin plating deforms, thus allowing a better electrical contact while preventing silver from tarnishing. This method does however incorporate tin oxide into the system – which is a semiconductor – thus increasing the electrical resistance of the system. Furthermore, since tin deforms easily, after the first connection cycle the silver surface is exposed. This is beneficial for low electrical resistance, but in subsequent connection-disconnection cycles silver's surface will no longer be protected from atmospheric conditions. Therefore, tin coatings are only viable for storage of silver contacts, but not for operational contacts. Other elements can be used to protect from sulfidation, such as platinum or rhodium plating; however, these alternatives significantly increase costs. Finally, electrolytic silver alloy coatings have the primary objective of enhancing silver's resistance to hydrogen sulfide (e.g., Ag-Fe, Ag-Sn and Ag-Pt alloys).

An alternative method used to protect silver from sulfidation is through the formation of self-assembled monolayers of alkanethiols [6], [19], [21], [22]. Alkanethiols, such as hexadecanethiol and octadecanethiol (ODT), protect silver from reacting with atmospheric sulfur for long periods of time, as well as turning silver's surface hydrophobic. ODT is widely used as an anti-tarnishing film on silver connectors. It consists of long chains of unsaturated oils where the carbon terminal has bonded with sulfhydryl. As a consequence of these sulfhydryl bonds, ODT can bond to transition metals. The sulfur atoms in ODT form covalent bonds with silver, thus forming a dense monolayer on silver's surface. This method prevents silver from tarnishing by saturating the metal's surface with its own sulfur. Since the sulfhydryl reacts with silver, the tail of the ODT chain is left free to rotate, granting the possibility of the tails to be oriented in an up-standing position, or laying in a disordered fashion [21]. When the tails are ordered vertically, higher tarnish protection is attained. Although the monolayers are generally thin (in the nm range), the chemical composition and structure of this film does not favor the electrical conductivity of the

system. Therefore, it is of interest to analyze the electrical characteristics of silver sulfide to determine how adverse the tarnishing film really is. If there is a way to neglect the effects that the tarnishing layer incorporates into the system, then it would no longer be required to reapply ODT after it has naturally degraded. It could even be removed from manufacturing completely. This in turn would reduce or eliminate the need for contact maintenance, enhance durability, reliability, and efficiency of the contacts.

When working with soft metals – such as silver, gold, and tin – in sliding connector terminals, there is a pile-up effect of the metal at the end of the socket caused by the insertion of the pin. In the case of tin-plated connector terminals, the pile-up is comprised of a multilayer 'sandwich' of tin, tin oxide, tin. This multilayering is detrimental to the electrical transport properties of the connector terminal since the tin oxide layers are not conductive. This generates a barrier that hinders the flow of current; essentially obtaining a sort of capacitor where tin oxide behaves as the dielectric material. Although not as soft as tin, silver is also considered a soft metal; thus, it is of interest to analyze the effect that silver sulfide has on the electrical transport properties after connection-disconnection cycles. If the layer of silver sulfide does not significantly affect the transport properties of silver (unlike tin oxide), removal of the silver sulfide may be disregarded. Contrarily, if it is detrimental to its electrical properties, removal of this layer is crucial. Consequently, in this study we focus on four potential removal method that do not compromise the electrical properties of the connector. In other words, we will analyze a chemical removal method (which will be used as reference), two mechanical removal methods, and a resistive heating removal method of the sulfide layer. These methods consist of puncturing of the tarnish layer by applying elevated normal loads, scraping-off (or wiping off) the tarnish by simulating connection-disconnection cycles, and removing the tarnish by injecting elevated direct currents, respectively.

Comprehensive characterization of tarnished and cleaned contacts will be analyzed. This study will focus on imaging the surface of the contacts using confocal laser scanning microscopy (CLSM) and scanning electron microscopy (SEM). Moreover, energy dispersive x-ray spectroscopy (EDS) of the material's core, plating, and surface will be carried out to gather further information on the chemical composition of the connector material; as well as x-ray diffraction (XRD) to acquire information on the crystalline structure of the tarnishing film. Regarding tribo-electrical characterization, constant-current load-dependent electrical contact resistance (ECR) and constant-load current-dependent ECR will be carried out to determine the influence that the silver sulfide layer has on the resistance of the material. This analysis provides further information regarding whether the layer can be punctured (analyzed through the former),

or if elevated currents can remove the sulfide layer by resistive heating (analyzed through the latter). Scratch tests will be carried out to simulate connecting cycle conditions and the sulfide layer's effect on the ECR at the end of the scratch track. This will provide information on the influence of silver sulfide on the contact resistance when piled-up. Furthermore, the scratch tests will be used to determine if the insertion force is enough to remove the silver sulfide layer, reducing its effect on the resistance of the connector.

ECR measurements merit special focus on tarnished samples considering that an analysis of the curve slopes obtained provides insight on the force required to puncture the silver sulfide layer [23], [24]. This information proves useful since piercing through this layer should reduce the impact that it has on the flow of current, therefore improving the efficiency and reliability of the connector. It was established by Braunovic that the contact resistance (R_c) of a material is the sum of three factors [25]. These are: the material's bulk resistance (R_m), the constriction resistance (R_{const}) – consequence of the concentration of the flow of current on the a-spots – and the film resistance (R_f) – related to the resistance of the inherent superficial oxide films produce. Furthermore, Tamai et al. describes how to determine the predominant form of mechanical deformation that the material suffers (elastic or plastic) [24]. To do so, they propose that the resistance may be approximated to the applied normal load powered to a negative factor n. Depending on the value of this exponent, one may predict the predominant deformation mechanism. If n takes a value of -1/3 or -2/3, elastic deformation is predominant, whereas plastic deformation is predominant when n takes values of -1/2 or -1. However, these values are theoretical. It is important to consider that their study is limited to one contacting body – i.e., they only consider the deformation of a tin-plated brass contact – and relatively low normal loads [24]. The former consideration simplifies the analysis, but it must be addressed that this does not fully reflect reality since two bodies are in contact. Depending on the hardness of the contacting bodies, these exponents will be skewed from their theoretical values. In our study, the two contacting bodies are the sulfurized silver and a hard gold coated rivet (detailed rivet description in Section II, Sub-section B). Therefore, the practical values should not deviate much from the theoretical, since the rivet is harder than the softer silver contacts. Consequently, most of the deformation should occur on the silver contact, and to a lesser degree, on the counter electrode. Other factors that can cause the deviation of the exponents from the theoretical values were listed by Leidner et al. [26]. This analysis method can be further explained by (4) [1], where ρ_p, ρP_f, and ρ_{cont} are the resistivity of the probe, of the plated material, and of the contaminant film, respectively, η is a cleanliness factor, H is the hardness, and d_{cont} is the thickness of the

$$R_t = \frac{\rho_p + \rho P_f}{2}\left(\frac{\eta\pi H}{4F}\right)^{1/2} + \frac{\rho_{cont} d_{cont} H}{F} \quad (4)$$

contaminant film. The second term of (4) corresponds to the contaminant film, i.e., silver sulfide layer.

The parameters in (4) – apart from F – can be considered constants since the temperature variation is not significant enough to produce a change in the resistivity of the probe, the plated material, or the contamination film. Therefore, the equation can be simplified into: $Rt=(constant/F)^n$. The factor n can be calculated by performing a linear fit of the ECR curve when plotted in a doble logarithmic axis. Furthermore, the factor n can be used to determine the predominant type of resistance in the system. According to Holm and other authors – see [24], [27], [28] – the dominant resistance in the system can be determined by the slope analysis used to determine predominant deformation mechanism. For n values of -1/3 or -1/2 the authors established that constriction resistance is the predominant source of electrical resistance. Similarly, the film resistance is predominant in the system when n takes values of -2/3 or -1. However, it is important to point out that these values are purely theoretical. Consequently, these values are only possible when considering that only the sample studied is deformed (i.e., counter electrode not considered). Furthermore, surfaces must be clean and have no asperities, which is not the case in this study.

II. Materials and Methods

The material studied were flat, silver-plated copper electrical connectors. Focused ion beam (FIB) was used to mill a cross section of the Ag plating to determine its thickness. The plating shows an average thickness of 2.7 µm. The connectors studied are naturally tarnished due to prolonged storage, shown in Fig. 1a. As can be observed, the degree of sulfidation varies from region to region within the connector. CLSM (LEXT OLS4100, Olympus) with a laser wavelength of 405 nm was used to measure the roughness of the tarnished surface, resulting in a root mean square roughness of 267.3 ± 11.8 nm.

A cross section of a tarnished silver connector was embedded and metallographically prepared (ground with silica paper and polished to OPS). This cross section was visualized with SEM, micrograph shown in Fig. 1b. As anticipated, the silver sulfide film was not observable under SEM (FEI Helios NanoLab600 Dual Beam Setup using ETD detector). However, an EDS spectrum was taken in an area near the surface. This spectrum revealed the presence of silver

originating from the silver plating. A carbon peak appears on the superficial spectrum. This peak most likely stems from surface contamination. Sulfur was not detected in the EDS spectrum carried out near the surface. A subsequent EDS spectrum was carried out further into the material revealing its copper core. Silver was not detected as the scan progresses away from the surface.

Since the EDS spectra of the cross section carried out near the surface did not detect sulfur, an EDS scan of a tarnished connector's surface was carried out. Furthermore, an EDS mapping of the surface was carried out on the same region. The results are shown in Fig. 2a and Fig. 2b. The EDS spectrum of the surface (inset in Fig. 2a) detected multiple contaminants – including magnesium, sodium, oxygen, and carbon. However, these elements were detected in minimal quantities (below 1 wt.%), therefore their corresponding peaks were not indexed. Within the inset, a zoomed-in view of the sulfur peak detected is shown. The location of the sulfur peak is highlighted by the red rectangle. The EDS mapping of the surface provides supplementary information on the pervasive distribution of sulfur throughout the tarnish connector's surface (Fig. 2b).

XRD was carried out on a tarnished silver contact, spectrum shown in Fig. 2c. The spectrum was acquired using a copper x-ray source and a step size of 0.05° at room temperature. The measurement was done under grazing incidence to limit the penetration of the x-ray, therefore

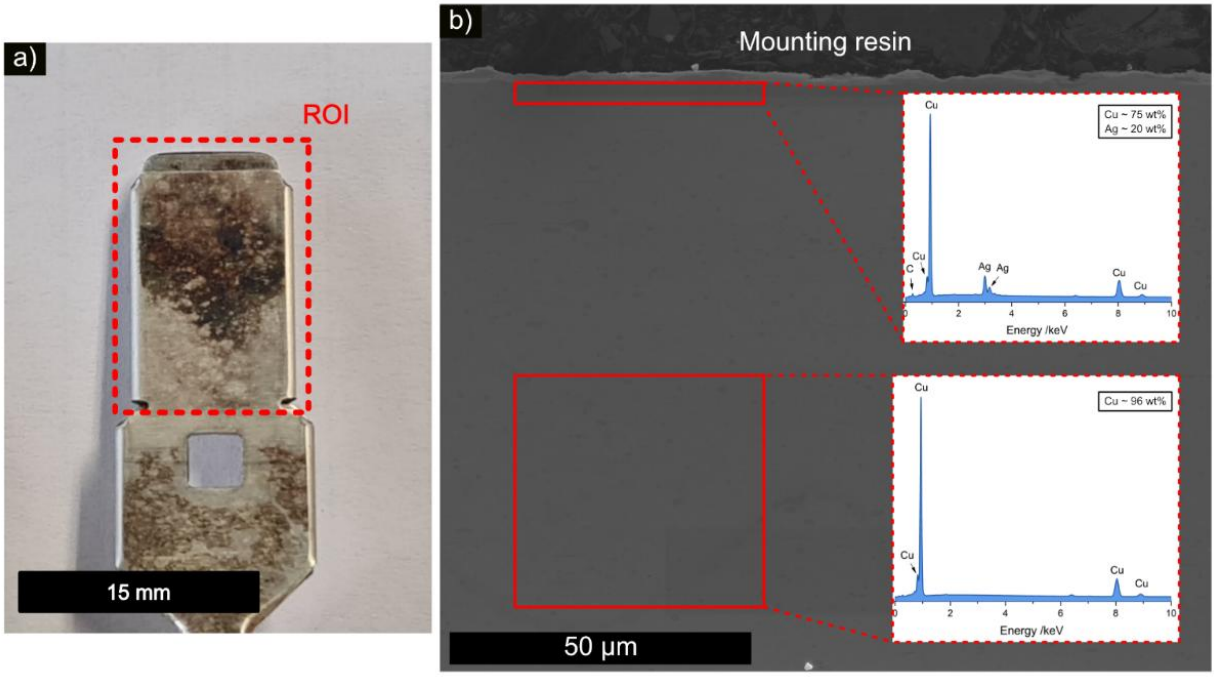

Fig. 1. a) Naturally tarnished contact. Red dashed lines show the region of interest in this study. As shown, the natural tarnishing phenomena varies significantly from region to region of the connector. The connector was stored under atmospheric conditions. b) Micrograph of tarnished connector's cross section with EDS spectra of its core and surface. The EDS spectrum at the top-right corresponds to the superficial scan of the cross section, whereas the spectrum at the bottom-right corresponds to the core's scan. The red squares highlight the region analyzed.

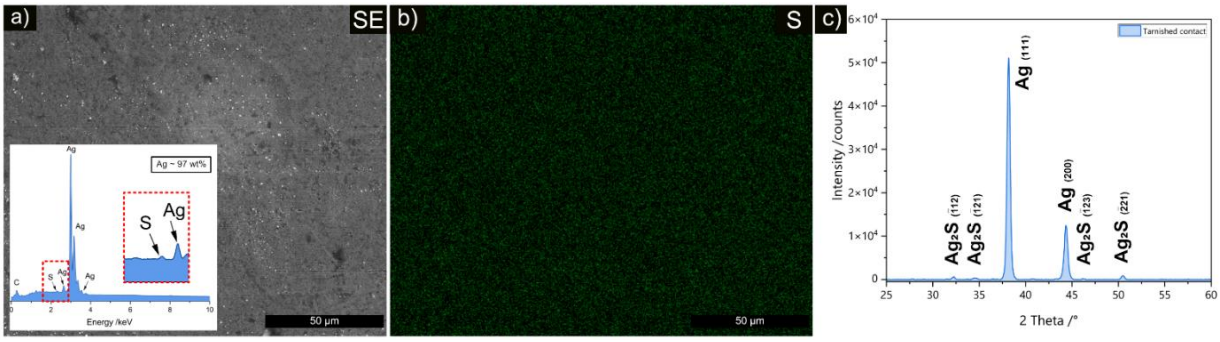

Fig. 2. a) EDS spectra of the tarnished connector's surface. Secondary electron micrograph of ROI. EDS spectrum was added as inset. The red rectangle shows a zoomed-in view of the sulfur peak detected. b) Sulfur signal detected in EDS mapping of surface. c) XRD spectrum of tarnished silver contact.

obtaining higher counts of the superficial silver sulfide tarnishing film. As Fig. 2c shows, silver and silver sulfide were detected. The cubic crystalline structure of silver can be observed by its characteristic peaks at 2θ values of 38.116 (111) and 44.277 (200); indexed using PDF number 00-004-0783 in [29]. Furthermore, silver sulfide in its monoclinic crystalline structure was detected as shown by the characteristic peaks at 2θ values of 31.52 ($\bar{1}12$), 34.385 ($\bar{1}21$), 46.208 ($\bar{1}23$), and 50.733 ($\bar{2}21$); indexed using PDF number 00-014-0072 in [29].

Microhardness measurements were conducted on the metallographic cross section of the connector using Dura Scan (Struers Inc., USA). Vickers hardness was measured on the copper base material using a load of 0.245 N. The load was applied onto the sample for a duration of 15 seconds, followed by imaging of the imprint using 40× magnification in a light optical microscope. Two sets of eight measurements were conducted and averaged. The core of the connector presented a hardness of $HV_{0.025} = 137 \pm 4$. Likewise, microhardness was measured at the surface of the connector's cross section with the aim of measuring the hardness of the Ag plating. The parameters of these measurements are identical to those of the base material, however, here Knoop indenter was utilized due to the thickness of the plating material [30]. Microhardness in vicinity of the connector's surface resulted in $HK_{0.025} = 143 \pm 6$.

A. Chemical Removal of Tarnishing Film

A chemical process was proposed to clean the tarnished surface of the samples [31]. The chosen technique chemically reduces the silver sulfide (see (1)), restoring the surface to its original, untarnished state. This method effectively removed all traces of silver sulfide without the need of material removal, as opposed to traditional mechanical cleaning procedures (grinding/polishing).

The procedure consists in lining the bottom of a beaker with aluminum foil (reducing agent) and placing the silver contact on top, making certain that both metals are in contact. The beaker

$$3Ag_2S + 2Al^0 \rightarrow 6Ag^0 + Al_2S_3 \quad (5)$$

$$Al^0 + 3Ag^+ \rightarrow Al^{3+} + 3Ag^0 \quad (6)$$

is then filled with 50 ml of water and 1.7 g of sodium bicarbonate – $NaHCO_3$ – ensuring that the contact material is fully covered. Using a hotplate, the solution was heated until boiling point, and continuing to heat the solution until the silver sulfide was reduced (approximately 10 min). Once the tarnish was reduced, the heating was switched off and, after the solution had cooled down, the contacts were removed. The contacts were first rinsed using deionized water, then submerged in isopropyl alcohol and placed in ultrasound bath (Bandelin Sonorex Super RK 514 BH, 33 kHz, 860 W) for 5 min. After ultrasound, the contacts were dried with compressed air (4 bar) and wrapped in aluminum foil to protect them from atmospheric conditions. If needed, the cleaning process can be repeated multiple times for samples that are severely tarnished.

The reduction of silver sulfide was produced by the reaction of this compound with aluminum. As shown in (5), silver sulfide is reduced to silver, whereas the sulfur and aluminum react to form aluminum sulfide (Al_2S_3). In this redox reaction, silver is reduced, while aluminum is oxidized, as shown in (6). After chemical removal of the tarnishing film, CLSM was used to measure the cleaned surface's roughness, resulting in a root mean square roughness of 271.8 ± 8.1 nm.

B. Puncture of Tarnishing Film

An alternative to chemically removing the tarnishing film is to pierce through the film by applying elevated contact forces. Since silver sulfide is considered soft, applying elevated normal loads can effectively puncture the tarnishing layer [1]. In this manner, the counter electrode would be able to break through the silver sulfide layer, establishing electrical contact with the silver surface. Consequently, this would reduce the contact resistance of the system. To evaluate this alternative, load dependent ECR measurements were carried out. Through these measurements it was possible to evaluate the contact resistance that the tarnished connectors present at different normal loads. Additionally, by analyzing the first semi-cycle of the measurement, the slope of the resistance-load curve can provide crucial information on the predominant electrical resistance mechanism, as previously described by Tamai et al. [24]. The direct current ECR of the silver connectors was measured using a testing rig as described by Puyol and Suarez [32]. In this setup, the sample was the electrode and a silver-nickel core ($AgNi_{0.15}$), hard gold coated rivet ($AuCo_{0.2}$) was used as counter electrode (Adam Bornbaum GmbH). The counter electrode had a curved head, with a diameter of curvature of 5 mm and a

hardness of 1.36 ± 0.01 GPa. The roughness of the rivet's tip was analyzed via CLSM, resulting in a root mean square roughness of 866.3 ± 51.6 nm.

By analyzing the ECR of the tarnished silver contacts, one can evaluate the effect that the silver sulfide layer has on the contact resistance at low contact loads, the load required to overcome this layer, and the contact resistance of the silver contact once the sulfide layer has been pierced. For this analysis, the current was set constant at 0.1 A (below the dry circuit conditions) [33], and the force was varied following the sequence: 0.5, 0.75, 1, 1.25, 1.5, 1.75, 2, 5, 6, 8, 9, and 10 N. In this loading range, a maximum Hertzian contact pressure of 314 MPa and 852 MPa are achieved at 0.5 and 10 N, respectively. These values were calculated using Hertzian contact theory for a sphere-on-plane contact [34], material properties extracted from [35]. The ECR measurements consisted of four total semi-cycles, two loading cycles and two unloading cycles. For each force, ten ECR measurements were taken and averaged, with the nanovoltmeter's range set at 1 V. Lower nanovoltmeter ranges caused saturation for normal loads below 1 N. In each measurement, the current was applied for 2 seconds. After a 1 second delay, the voltage drop was measured. There is a 1 second delay between consecutive ECR measurements. Therefore, any thermal effects that might occur due to the flow of current can be neglected. For comparative reasons these measurements were carried out on recently chemically cleaned and tarnished samples. The measurement cycles were taken at least 3 times per sample, with two samples of each type measured. Moreover, all measurements were taken under ambient temperature and humidity values between 20-22 °C and 21-25% r.h., respectively.

C. Removal of Tarnishing Film Through Resistive Heating

Removal of the tarnishing film through resistive heating involves circulating elevated currents through the sulfide layer. The objective is to determine if high enough currents can diminish or eliminate the effect of the silver sulfide layer, regarding electrical properties. Therefore, a constant load of 2 N was applied, and current-dependent ECR was measured following the sequence: 30 µA, 100 µA, 300 µA, 1 mA, 10 mA, 30 mA, 100 mA, 300 mA, and 1 A. Calculated in the same manner as for before, this load produced a maximum Hertzian contact pressure of 498.5 MPa. Five ECR measurements were taken per current level and averaged, with the nanovoltmeter's range set at 100 mV. As for load dependent ECR, hard gold coated rivets were used. The ECR measurement procedure is the same as in load dependent ECR. This analysis was carried out for recently chemically cleaned and tarnished samples. The ambient temperature and humidity values during the measurements were between 20-22 °C and 21-25% r.h., respectively.

D. Mechanical Removal of Tarnishing Film

Mechanical removal of the tarnishing film aims at simulating an initial connection-disconnection cycle. This is done by carrying out a scratch test on tarnished and chemically cleaned silver contacts. This analysis also provides information on the role that silver sulfide plays on piled-up material at the end of the connection track. This can be evaluated by measuring ECR after an initial scratch test (after simulating a connection cycle). Examining the difference in the ECR value at the same load in load dependent ECR (no piled-up material) and after the scratch tests (piled-up material), it can be determined if silver sulfide interlayers increase the electrical resistance, as is the case with tin oxide. This analysis was carried out using a testing rig as described by Alderete et al. [36]. Using this tribo-electrical testing rig, linear motions while in contact can be performed (scratch tests). The scratch tests can be performed under constant load with high accuracy. The setup also enables reciprocal motion of the counter electrode. Therefore, multiple scratches in two directions can be subsequently performed. The connection cycle simulation was done with a normal load of 5 N, a scratch length of 4 mm, and a scratch speed of 15 mm/s. The maximum Hertzian contact pressure achieved here is 676.5 MPa. After the initial connection cycle (first scratch test), ECR measurements were carried out using the same parameters and procedure as described in the subsection corresponding to puncturing of tarnishing film; a new rivet was used for each connection cycle simulation. After the ECR measurements a subsequent scratch test is carried out in the opposite direction, thus returning the counter electrode to its initial position (simulating a disconnecting cycle). The parameters of the second scratch test were identical to those of the first scratch. During each scratch test the coefficient of friction (CoF) was recorded. Tribo-electrical behavior was also studied via fretting tests. The fretting tests were carried out at a load of 2 N with an amplitude of 35 µm and a frequency of 8 Hz using the testing rig described in [36]. These tests were done for a total of 5,000 fretting cycles, with regular ECR measurements at set intervals of 100 cycles. Prior to the first set of fretting tests ECR was measured. Scratch tracks and fretting marks were micrographed using ETD detector and 5 keV (Thermo-Fisher Helios^{TM} G4 PFIB CXe DualBeam^{TM} FIB/SEM). EDS was carried out on fretting marks to qualitatively analyze the chemical composition after fretting cycles using 10 keV and 1.6 nA with an EDAX Octane Elite Super detector. The ambient temperature and humidity values during all measurements were between 20-22 °C and 21-25% r.h., respectively.

III. Results and Discussions

A. Load Dependent ECR

As previously discussed, load dependent ECR can provide crucial information on the load required to puncture the silver sulfide tarnishing layer. Therefore, in this section we aim to determine the specific load that must be applied on the tarnished connector to puncture this film, consequently achieving ECR values that approach that of the chemically cleaned reference. Furthermore, this analysis presents the evolution of the contact resistance. ECR measurements carried out on tarnished silver contacts are shown in Fig. 3a, whereas Fig. 3b shows ECR measurements on chemically cleaned silver contacts. In both cases two measurements cycles were carried out.

Focusing on Fig. 3a, it can be seen that the variation in the load dependent ECR is similar throughout the entirety of the measurement cycles. However, some mechanical deformation has occurred since the second, third and fourth semi-cycles present values lower than the first semi-cycle. For instance, at 5 N the resistance measured during the first semi-cycle is equal to 3.86 mΩ, whereas the resistance in the second cycle is 1.28 mΩ and 1.17 mΩ for the loading and unloading semi-cycles, respectively. Between the third and fourth semi-cycle, the resistance of the tarnished contact dropped by 8.6% approximately. This decrease in ECR could be a consequence of the puncturing of the tarnishing film after the first loading semi-cycle. Unexpectedly, the final value recorded (0.5 N of the fourth semi-cycle) was the only value that surpassed the initial contact resistance of the first semi-cycle; although the increase is minor, 39 mΩ against 32 mΩ. This could be explained by the decrease in the real contact area after both the silver contact and the gold rivet were mechanically deformed after the loading and unloading

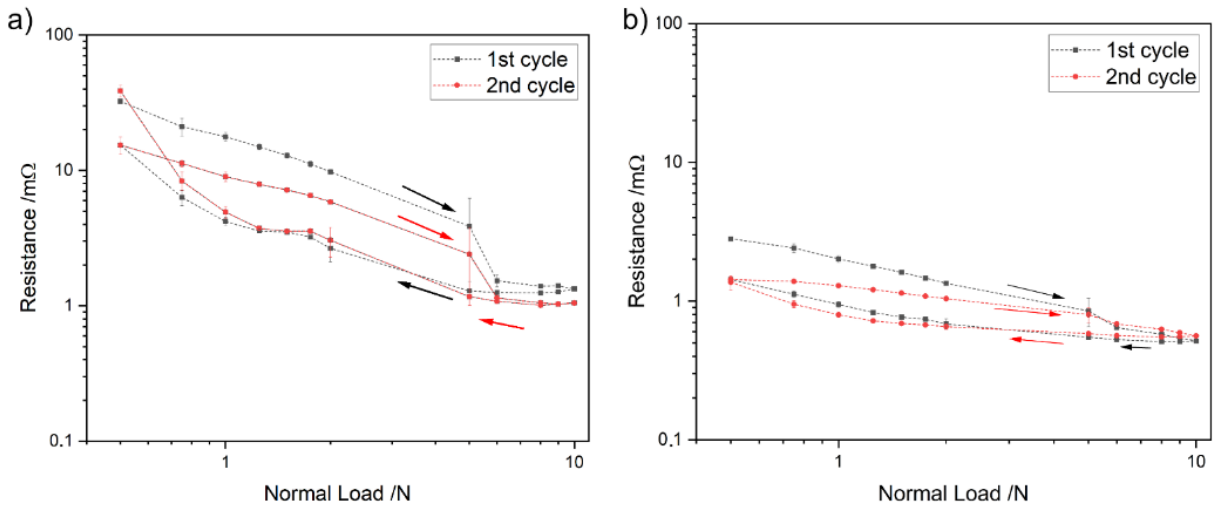

Fig. 3. Load dependent ECR of a) tarnished and b) chemically cleaned silver contacts. The first loading and unloading semi-cycles are displayed in black, whereas the second semi-cycles are shown in red. The arrows indicate the direction in which the semi-cycles progress.

cycles. Furthermore, the lowest resistances recorded were in the second cycle. At 9 N the resistance during the third and fourth semi-cycles was the same (approximately 1 mΩ), whereas at 8 N the resistance during the unloading semi-cycle was marginally below the resistance at the same force during the loading semi-cycle (1.05 mΩ and 1.01 mΩ respectively). Additionally, Fig. 3a shows a sharp decrease in ECR when transitioning from 5 N to 6 N. This sudden decrease can be attributed to the puncturing of the silver sulfide tarnishing layer. Therefore, when applying normal loads above 5 N (676.5 MPa) the resistance of this film can be neglected. Consequently, if the contact is designed in a way such that the system inherently demands contact loads above this critical load, the need for removal of the tarnishing layer is eliminated. 4 N is a relatively standard connection force; therefore, by marginally increasing the connection force to values above 5 N (676.5 MPa) the silver sulfide tarnishing layer can be rendered irrelevant.

It is interesting to observe that for both unloading semi-cycles (Fig. 3a), the resistance measurements follow the same tendency. From 10 N the resistance measured slightly decreases until 8 N. The resistance increases at a low rate continuously as the normal load is decreased from 8 N to 5 N. Between 5 N and 2 N a great change in resistance was observed: 1.2 mΩ at 5 N for the second and fourth semi-cycles and 2.7 mΩ and 3.0 mΩ at 2 N, respectively. Furthermore, both unloading semi-cycles show a plateau between 1.75 N and 1.25 N, with resistances between 3.6 mΩ and 3.7 mΩ. Below 1 N the resistance sharply increases in both cases, with the fourth semi-cycle presenting the highest resistance measured (38.7 mΩ). The significant increase is primarily a consequence of the reduced real contact area between the plastically deformed sample and electrode. As the normal load is gradually reduced, so does the real contact area (a-spots), thus resulting in a higher constriction resistance. Observing Fig. 3b, the highest ECR value recorded for the chemically cleaned silver contact was at 0.5 N in the first semi-cycle, 2.82 mΩ. As the normal load increases the resistance steadily decreases. For 5 N and 6 N a decrease in the curve's slope is observed. Above 6 N ECR values vary slightly, reaching a minimum value of 0.52 mΩ at 10 N. During the second semi-cycle (first unloading process), the change in ECR is marginal for loads above 5 N. A further reduction in normal load produces a significant increase in ECR from 0.55 mΩ at 5 N to 1.43 mΩ at 0.25 N. However, these values remain significantly lower than the value recorded at the start of the first semi-cycle. This variation at low normal loads is a consequence of the newly established contact loads after deformation has occurred in the silver contact and the counter electrode. As both bodies are deformed, the real and apparent contact areas become larger after the first cycle compared to the initial state before load was applied. Consequently, a larger contact area reduced the constriction resistance, and consequently the system's contact resistance. Regarding the second cycle, the initial ECR and final ECR values

at 0.5 N are approximately the same (1.43 mΩ and 1.37 mΩ for the third and fourth semi-cycles, respectively). This indicates that no further deformation was produced during the second measurement cycle. In other words, the real contact area was established during the first cycle. Consequently, the ECR values in the second, third, and fourth semi-cycles are always below the values observed in the first semi-cycle, as was the case for the tarnished silver contact. Furthermore, observing the evolution of both cycles, the major slope changes occur for the same normal loading conditions (i.e., same contact forces). It is interesting to highlight however, that the ECR values in the second cycle are higher than the ECR values of the first cycle for normal loads above 6 N. However, the difference in ECR is below 0.1 mΩ in all cases.

Comparing Fig. 3a and Fig. 3b, it can be seen that although the silver sulfide layer is punctured at normal loads above 5 N, the ECR of the tarnished silver contact does not reach resistances as low as the chemically cleaned contact. A significant drop in ECR is observed between 5 N and 6 N in the tarnished contact, which indicates the rupture of the silver sulfide film. However, some degree of silver sulfide must remain at the interface between the silver connector and the hard-gold counter electrode. Consequently, the ECR values above 6 N do not reach values below 1 mΩ (in the first cycle); whereas the chemically cleaned silver connector shows a resistance of approximately 0.5 mΩ under the same loading condition.

Roughness at the contacting sites after load dependent ECR was measured using CLSM in the tarnished and cleaned samples. The tarnished sample showed a roughness of 255.2 ± 4.5 nm, whereas the chemically cleaned sample showed a roughness of 280.2 ± 4.1 nm. Therefore, roughness of the sample does not significantly change after load dependent ECR. This means that the localized deformation that takes place on the silver contacts after a normal load of 10 N is not significant. This was also proven by carrying out a profile analysis on the contacting site using CLSM, where no change in surface profile was observed. Accordingly, the deformation that produces deficient contact at normal loads after the first loading cycle does not produce significant changes in topography and roughness. However, this deformation – primarily in the asperities – is significant enough to increase ECR at low normal loads.

Moreover, as evidenced by Fig. 1a, the extent of tarnishing film generated on the connector's surface varies from region to region. Therefore, the ECR measurements carried out in this study were conducted on different regions, ones with high degree of sulfurization as well as regions that appear lightly tarnished. No significant difference was measured between regions with different sulfurization degrees. However, it is believed that further atmospheric exposure will cause more widespread sulfurization, and thus change the overall degree of tarnishing.

B. Resistance-Load Curve Slope Analysis

As reported by Tamai et al. [23], [24] the slope of the ECR curves can be analyzed to obtain information on the type of electrical resistance that dominates in the system, as well as on the predominant deformation mechanism that the material undergoes. Therefore, this analysis is crucial for the tarnished silver contact. For this analysis only the first semi-cycle is studied since the subsequent semi-cycles evaluate the ECR after both bodies have been deformed. Moreover, as previously mentioned, the values obtained for the factor *n* may vary from the theoretical values. This is due to the surface finish of the silver connectors and the counter electrodes being a technical one. Furthermore, both the connector and counter electrode underwent deformation in the measurements carried out. Additionally, the value of the *n* factor is expected to deviate further from the theoretical values in the tarnished sample since the theoretical values were determined for clean samples.

The first loading semi-cycle of the ECR curve obtained for the tarnished sample is shown in Fig. 4a, whereas Fig. 4b shows the linear fitting of the regions of interest. There are three points in the evolution of the ECR curve where the slope drastically changes, with an additional point where the slope slightly changes. Therefore, a total of five areas can be analyzed. These are: 1) 0.5 to 0.75 N, 2) 0.75 to 2 N, 3) 2 to 5 N, 4) 5 to 6 N, and 5) 6 to 10 N. The second and third regions of interest could be fitted together; however, for a better analysis it is best to divide the regions. The regions of interest, slope, dominant resistance, and deformation mechanism of the tarnished sample are summarized in Table I. In this table, the theoretical values closest to the slope measured are shown. Analyzing the aforementioned table, it is determined that the main deformation mechanism in all regions studies is plastic deformation, except for the last region where the slope is approximately -1/3, corresponding to elastic deformation. This proves that the tarnishing film is in fact very soft. Therefore, when low normal loads are applied (0.5 N), this load is enough to produce plastic deformation. Throughout the entire loading range where the

TABLE I – Slope analysis of the first semi-cycle on the tarnished silver contact.

Region	Force range /N	Slope	Dominant resistance	Deformation mechanism
1	0.5 – 0.75	-1	Film	Plastic
2	0.75 – 2	-1	Film	Plastic
3	2 - 5	-1	Film	Plastic
4	5 - 6	-5	Film	Plastic
5	6 - 10	-0.3	Constriction	Elastic

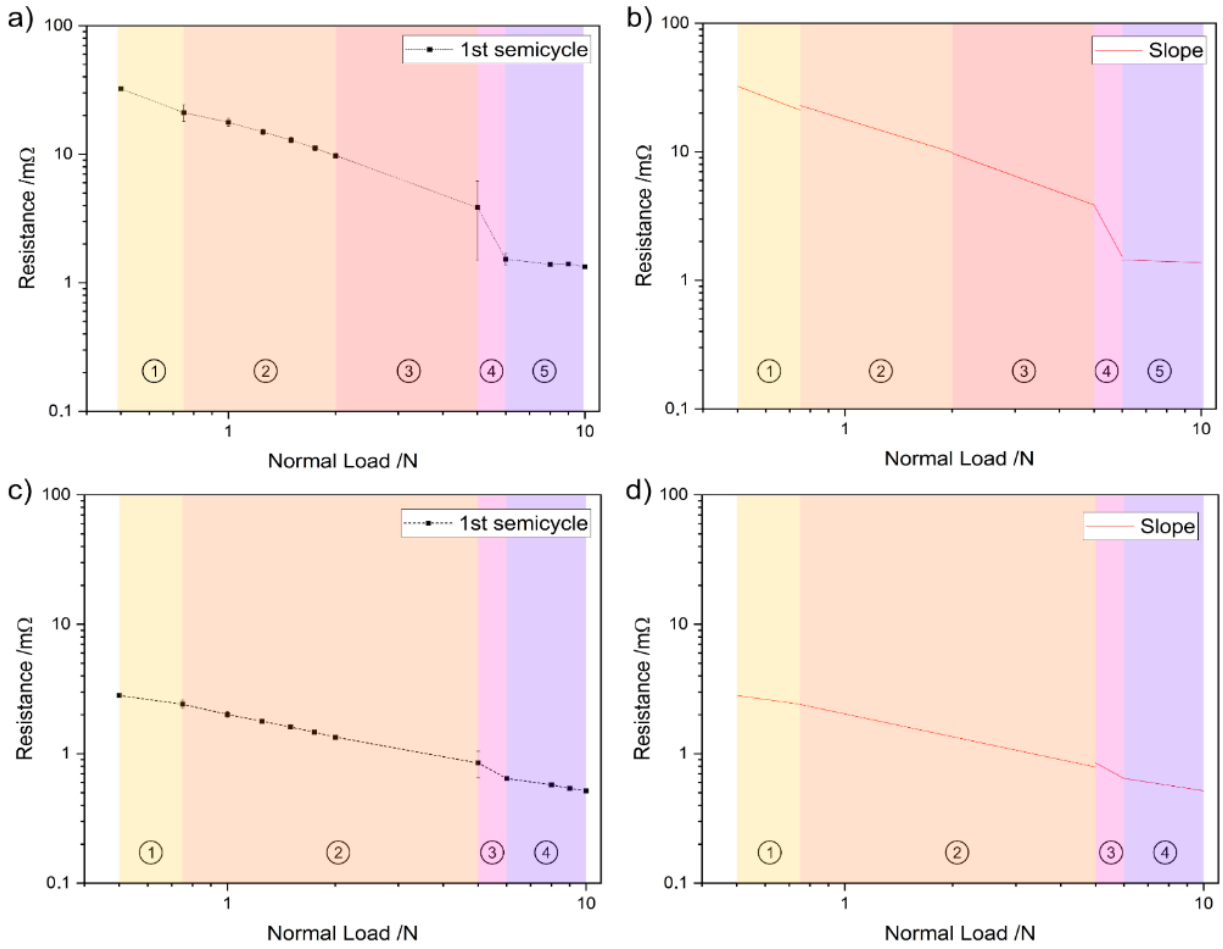

Fig. 4. Slope analysis of a) tarnished silver contact's loading semi-cycle and b) linear fit of loading ranges, c) cleaned silver contact's loading semi-cycle and d) linear fit of loading ranges. The shaded areas facilitate the differentiation between the regions analyzed.

tarnishing film influences the measurements (0.5-6 N) plastic deformation dominates. For loads above 6 N, elastic deformation dominates. This deformation mechanism takes place in the silver connector.

In the first three ranges analyzed the dominant resistance for the tarnished silver contact is the film resistance. Observing region 2 in Fig. 4a, it can be seen that the first load (0.75 N) slightly shifts the linear fitting of the region towards a more positive slope. Therefore, the slope of this regions is closer to -0.5 rather than -2/3. However, if this point is excluded from the linear fit, the slope of the region approaches -1. Consequently, in this region film resistance dominates. Dominant film resistance in these loading ranges was expected since below the critical load of 5 N the silver sulfide film was not punctured. Silver sulfide is a semiconductor with lower conductivity than that of silver. Therefore, the resistance in the film is higher than that of the substrate; thus causing a narrowing of the current as it flows through the film, followed by a subsequent spreading of the current when it reaches silver. After the silver sulfide film has been punctured (above 5 N) the film resistance is no longer dominating the overall resistance of the

system. This further proves that the sharp decrease in ECR between 5 N and 6 N is caused by the puncturing of the tarnishing film, which was observed in Fig. 3a. Furthermore, it appears that the onset of plasticity was reached within these forces. This can be evidenced by the change in slope between regions 3 and 4. Between these regions a significant change in slope can be observed; demonstrating the predominance of plastic deformation in the system. However, in region 5, the predominant deformation mechanism observed is elastic deformation, as evidenced by the *n* factor taking a value of -1/3. However, it is hypothesized that the silver contact is approaching plastic deformation as well for these load ranges.

Further proof can be observed in Fig. 3a by comparing the change in slope between the first and second loading cycle (at these regions of interest). If the sharp drop in the resistance-load curve was purely a consequence of puncturing the tarnishing film, this significant decrease in slope would only be visible in the first loading cycle. However, the change in slope is evidenced in both loading semi-cycles, demonstrating that plasticity plays a role in the slope analysis for these normal load ranges. Further analysis should be carried out at higher normal loads to verify if the predominant deformation mechanism of silver in this range, since CLSM did not reveal significant deformation after load dependent ECR. Nonetheless, plastic deformation is present in the asperities, evidenced by the drop in ECR as the load increases. As a consequence of the plastic deformation of the a-spots, the real contact area established approaches the apparent contact area. Therefore, due to the plastic deformation of the contact and the puncturing of the tarnishing film, the ECR decreases sharply (also evidenced by second cycle). As the normal load is further increased towards 10 N the dominant resistance type is constriction, no longer the film's resistance.

Correspondingly, the first loading semi-cycle of the ECR curves for the chemically cleaned silver contact is shown in Fig. 4c, whereas the linear fitting of the regions of interest are shown in Fig. 4d. In this sample, there are three points in which the slope of the ECR curve changes. However, contrarily to what was observed for the tarnished sample, the slope change is minor. Nonetheless, four regions are analyzed; these are: 1) 0.5 to 2 N, 2) 2 to 5 N, 3) 5 to 6 N, and 4) 6 to 10 N. The regions of interest, slope, dominant resistance, and deformation mechanism of the tarnished sample are summarized in Table II.

In this case, the analysis becomes more complex. Since there is no established contaminating film as the case before, the film resistance that dominates the system's resistance can be attributed to chemisorbed oxygen films by residue left behind after the cleaning process [27], or by organic contaminants found on the contact's surface. Therefore, Table II shows variation between constriction

TABLE II – Slope analysis of the first semi-cycle on the chemically cleaned silver contact.

Region	Force range /N	Slope	Dominant resistance	Deformation mechanism
1	0.5 – 0.75	-0.4	Constriction	Elastic
2	0.75 - 5	-0.6	Film	Elastic
3	5 - 6	-1.5	Film	Plastic
4	6 - 10	-0.5	Constriction	Plastic

and film resistance, as well as with the deformation mechanisms that the electrodes undergo. As was the case in the tarnished sample, it appears that plastic onset was reached in the 4-6 N range. This is also evidenced in the resistance-load curve (Fig. 3b), showing a change in slope between the second and third regions of interest. However, in this case, due to the lack of the tarnishing layer, the change in slope is less pronounced. Therefore, the decrease in slope is purely attributed to plastic deformation of the chemically cleaned sample. This change was evidenced in both loading semi-cycles. As opposed to the tarnished sample, in the 6-10 N range, the chemically cleaned sample experiences plastic deformation as predominant mechanism. Therefore, the fact that the slope for this range in the tarnished sample suggests elastic deformation may be influenced by the presence of the punctured tarnished film.

Mathematically, it would be correct to assign one slope for the entirety of the force range in the chemically cleaned sample, achieving a fitting with Pearson's r value of 0.999. However, in doing this, the actual physical phenomena taking place during load dependent ECR would not be correctly modeled. By separating into regions, the transition from elastic to plastic deformation can be accurately reported.

In the predominant resistance type, a transition from constriction, to film, and back to constriction was reported. At low loads, constriction resistance dominates. However, as the load increases, film resistance originating from chemisorbed and/or organic contaminants takes precedence. Nevertheless, once the load becomes significant enough to overcome these contaminant films (above 6 N), a transition back to constriction resistance is observed.

C. Current Dependent ECR

Current dependent ECR was carried out on tarnished and chemically cleaned silver contacts to determine whether resistive heating could diminish the effect that the silver sulfide film has on the contact resistance of the connector. The R-I curve is shown in Fig. 5. As can be observed the resistance measured when sourcing different currents does not vary significantly between the tarnished and chemically cleaned contacts. Both show a relatively high ECR value when sourcing

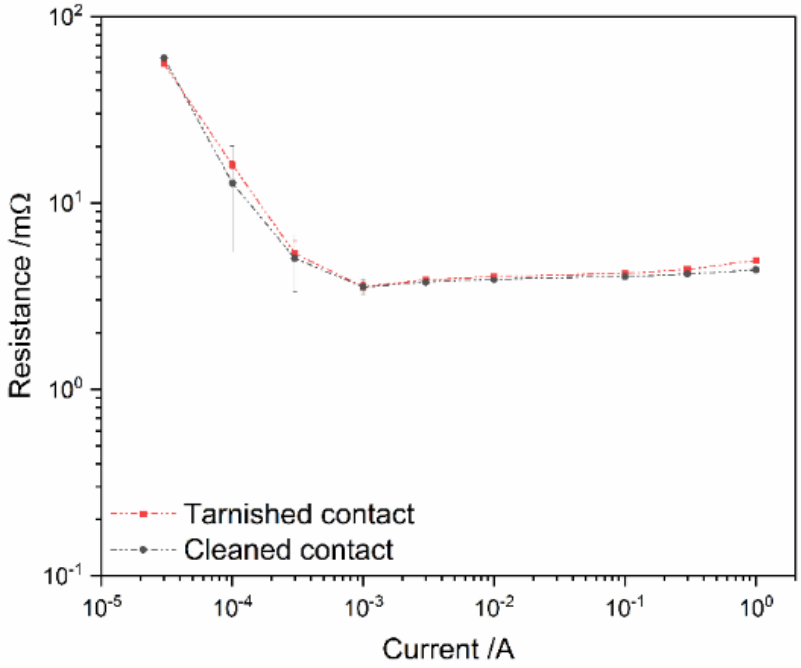

Fig. 5. Current dependent ECR measurements of tarnished (red) and cleaned (black) silver contact.

30 µA, approximately 60 mΩ. However, as the current is increased the resistance decreases. For current levels above 1 mA the resistance remains moderately constant at 4-5 mΩ. At low currents the cleaned contact shows marginally lower resistance than that of the tarnished contact, however the difference falls within the error values of the measurements. As Fig. 5 displays, current dependent ECR is not affected by the silver sulfide film. This is evidenced by the similar ECR values recorded for both samples throughout the measurements. Therefore, this test proves that when sourcing different direct currents – while loading below the critical load of 5 N – the silver sulfide film's effect on the connector's conductivity is negligible. Consequently, applying an elevated current to circumvent the tarnishing layer by resistive heating is not an effective method.

D. Scratch and Fretting Tests

Scratch tests seek to simulate connection and disconnection cycles; therefore, analyzing the ECR of the tarnished and cleaned connectors after they have been inserted for the first time. Moreover, the coefficient of friction (CoF) was measured during the connection and disconnection cycle. This value provides information on the influence of the tarnishing film on the insertion and removal force required. The CoF of the scratch tests is shown in Fig. 6a, whereas the ECR after the connection cycle is shown in Fig. 6b. In these figures, the tarnished connector is represented by the red markings and the chemically cleaned connector is represented by the black markings. The areas shaded in green represent the scratch cycles that simulate connection, whereas the blue-shaded areas represent the disconnection simulation. These simulation cycles

can be further differentiated by the sign of the CoF; positive represents connection and negative represents disconnection.

Observing the CoF of the scratch tests (Fig. 6a) it can be easily perceived that the tarnished connector opposes less resistance to the sliding motion of the scratch test. This is observed in both connection and disconnection cycles, with a CoF between 0.1 and 0.2 in all cases. The cleaned connector, however, shows higher CoF with values between 0.2 and 0.4. Therefore, it is concluded that although the silver sulfide film does not favor electrical conduction of the connectors, it acts as a solid lubricant reducing the CoF and potentially protecting the surface from wear. Furthermore, both connectors show higher CoF values in the disconnection cycles. In the tarnished sample, this is caused by the first scratch test, which partially removes the tarnish and, to a lesser extent, material plowing. Although, as evidenced by ECR after insertion, not enough tarnishing film is removed to restore conductivity to the system. Furthermore, it is

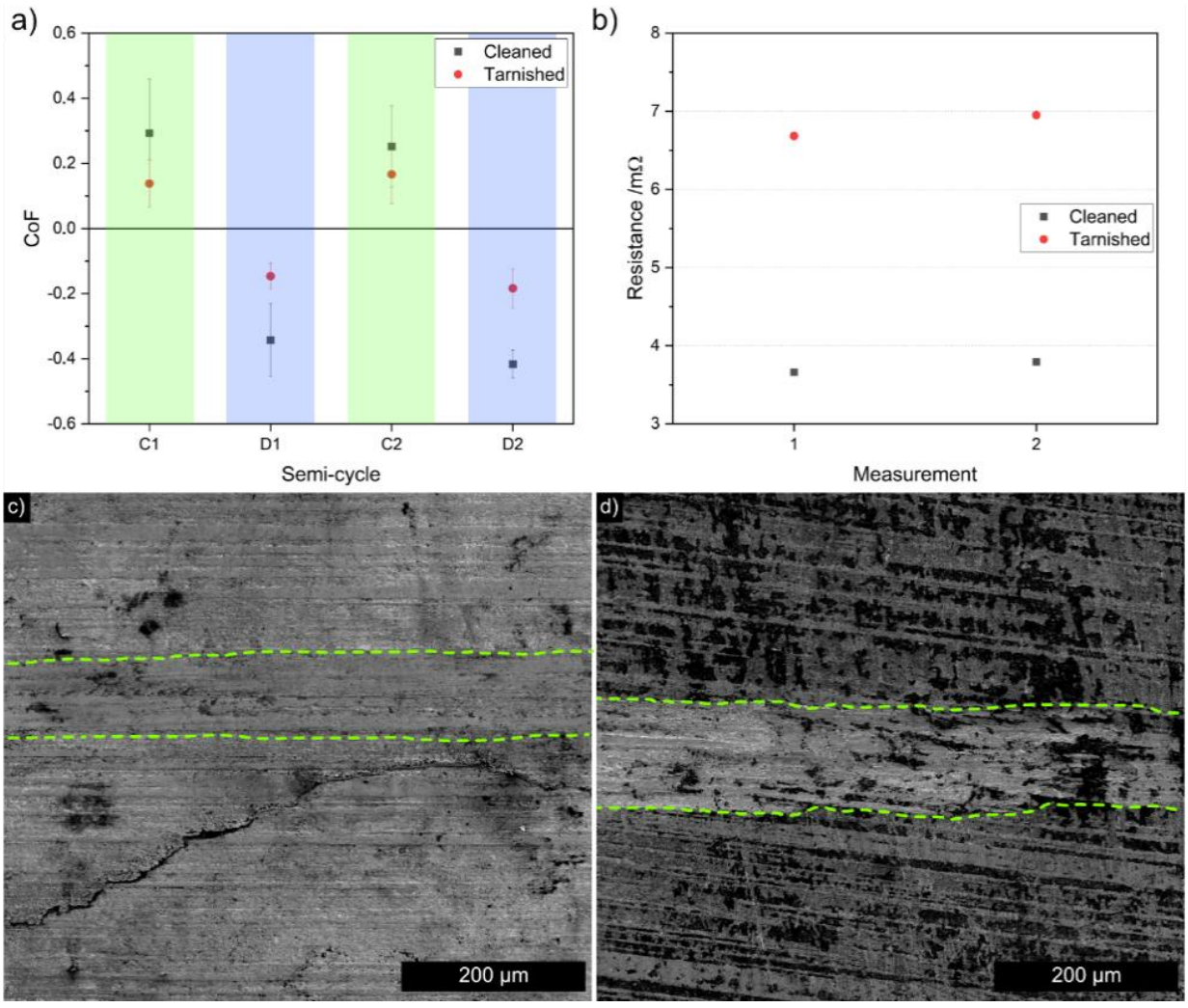

Fig. 6. a) CoF of tarnished (red) and cleaned (black). The areas highlighted in green correspond to the connection simulation, whereas the areas in blue simulate disconnection. b) ECR measurements after scratch test of tarnished (red) and cleaned (black) sample. c)-d) Scratch track after connection-disconnection simulation of tarnished and chemically cleaned silver connector, respectively. The green dashed lines help in delimiting the scratch tracks.

interesting to note that although the CoF of the tarnished contact increases during the disconnection cycle, the increase is marginal (approximately 0.02 in both disconnection cycles). For the cleaned contact however, the increase represents 0.05 for the first disconnection cycle and 0.15 for the second. In this case, material plowing plays a more important role due to the absence of the lubricating tarnishing film. Focusing on the ECR values recorded after the connection cycle (Fig. 6b) it is further witnessed how the silver sulfide film affects the conductivity of the connectors. The ECR values for the cleaned connector after connection are between 3.5 mΩ and 4 mΩ, whereas for the tarnished sample the values are between 6.5 mΩ and 7 mΩ. This shows that after subsequent connection and disconnection cycles, the resistance tends to increase to a minor degree; likely due to piled-up material at the end of the scratch track. However, a distinction must be made between the influence of piled-up material in the tarnished sample and in tin plated materials. Here, the gain in ECR is minor, therefore, the cause of this increase is not attributed to the silver-tarnish-silver 'sandwich', but rather to a deficient contact due to the geometry of the piled-up material when contacting with the counter electrode.

Although the overall values of the tarnished sample are relatively low, the tarnished connector poses almost double the resistance as the cleaned connector. This proves that even after insertion of the tarnished contact (connection cycle) the ECR is affected by this layer. Therefore, although the scratch tests were carried out at a relatively high normal load (at the critical load of 5 N), it was not sufficient to wipe the tarnish from the surface. The values observed for the tarnished connector are in correlation with the values observed in the loading cycle of the load dependent ECR tests at 5 N, see Fig. 3a. This confirms that the silver sulfide film does not affect the conductivity of the silver contact when piled-up. In other words, when silver sulfide is piled-up, there is no substantial gain in contact resistance. Therefore, although silver sulfide reduces the conductivity of silver electrical connectors, it is not as adverse as tin oxide is in tin plated electrical connectors. Regarding the cleaned connector, the resistance is low, but about 3 times higher than the values recorded at 5 N in the load dependent ECR tests, see Fig. 3b. This is likely due to a deficient contact between the counter electrode and the contact's surface on account of the piled-up material after the scratch test. The pile-up effect at the end of the scratch track reduces the real contact area of the electrical contact. SEM micrographs of the scratch tracks of the tarnished and chemically cleaned silver connector are shown in Fig. 6c and d, respectively. As the green-dashed lines illustrate, the scratch track of the tarnished contact (Fig. 6c) is more uniform after all four scratches were carried out (two simulating connection and two simulating disconnection). For the chemically cleaned contact (Fig. 6d) however, the scratch track shows more rugged boundaries between the edges of the scratch track and the unaffected surface of the

contact. This can be explained by the lubricant nature of the silver sulfide film. Recalling the CoF values of the tarnished sample (Fig. 6a), the wear protection of the silver sulfide film is evidenced in the micrograph of the scratch track. In addition to a uniform scratch track, the tarnished silver contact shows a thinner worn area compared to the cleaned contact. For the tarnished sample the mean track width is 91.5 µm ± 4.1 µm, whereas the mean track width for the cleaned sample is 116.0 µm ± 3.7 µm. The roughness within the scratch tracks was measured using CLSM. After the connection-disconnection simulations, the tarnished and chemically cleaned samples showed a root mean square roughness of 126.6 ± 22.3 nm and 183.3 ± 19.6 nm, respectively.

To understand the influence of piled-up material more accurately after the scratch track, shorter scratch tests of 1 mm were carried out. With shorter scratch tracks it is hypothesized that the influence of piled-up should be more significant since longer tracks allow for higher degree of material displacement (analogous to plowing). However, in shorter tracks the length of the scratch track is not significant enough for displacement to occur, and consequently, more of the tarnishing film should be interlaced between the silver substrate and the hard gold rivet. However, after multiple 1 mm scratch tracks and ECR measurements, no significant difference was observed compared to the longer 4 mm scratch tracks. Therefore, these measurements further confirm that silver sulfide does not significantly affect contact resistance when piled-up.

The lubricating properties of the silver sulfide film is of great interest. The fact that the sulfide layer reduces the CoF by about half explains the primary cause of failure in tarnished silver

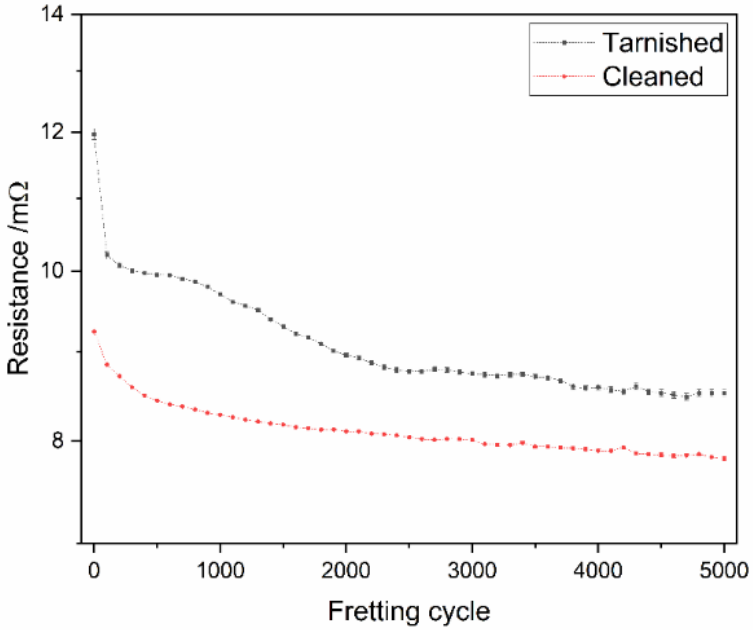

Fig. 7. Evolution of ECR during fretting tests, carried out on tarnished (black) and chemically cleaned (red) silver contact for 5,000 cycles. ECR measurements taken prior to fretting and every 100 cycles.

contacts. This highlights that the cause of connector failure is not the inadequate electrical connection (due to increased resistance), but rather due to connector disconnection – connector disconnection is the primary cause of electrical contact failure [37]. Since the CoF is halved when a connector tarnishes, external vibrations could more easily disconnect the connector. Therefore, it is of significant importance that the connector design allows higher normal loads, consequently puncturing the tarnishing film and thus reducing the likelihood of undesired disconnection.

For a more in-depth understanding of the influence of the tarnishing film on the tribo-electrical behavior of silver connectors, fretting tests were carried out on the tarnished and chemically cleaned samples, shown in Fig. 7. Both samples show the highest ECR value prior to fretting cycles. After the first 100 cycles, ECR sharply decreases. The reduction in resistance is more significant in the tarnished sample. This reduction is attributed to the rupture of superficial contaminant films in both samples. In the tarnished sample, however, part of the silver sulfide film is damaged, since the decrease is more prominent. However, in the tarnished sample, fretting a 2 N is not enough to penetrate the tarnishing film, since the ECR values of the tarnished sample are consistently higher than in the chemically cleaned sample. As the fretting cycles progress, the ECR gradually becomes lower in both samples. The ECR after the 5,000 cycles is approximately 30% and 15% lower than the ECR value prior to fretting for the tarnished and cleaned samples, respectively. These fretting tests further prove that the tarnishing film does not significantly impact the ECR of silver contacts when piled-up, as previously demonstrated by scratch tests.

SEM micrographs of the fretting marks on the tarnished and cleaned samples are shown in Fig. 8a and Fig. 8d, respectively. In these micrographs, a clear distinction can be made between tarnished and cleaned samples. That is, the fretting mark on the tarnished sample is significantly larger than that of the cleaned sample. These fretting marks were segmented using ImageJ (Fiji). After segmentation the worn area was measured, resulting in an approximate are of 35,817.62 μm^2 and 29,356.74 μm^2 for the tarnished and cleaned samples, respectively. Therefore, although the CoF recorded in the tarnished sample is considerably lower than that of the cleaned sample, the silver sulfide tarnishing layer does not offer wear protection. This behavior was not expected since the scratch tracks shown in Fig. 6c and Fig. 6d show more significant wear in the cleaned sample rather than on the tarnished sample.

EDS mappings were performed on the tarnished sample, shown in Fig. 8b and Fig. 8c. In the former, an overlay of the silver, copper and sulfur maps is shown. From this EDS map, sulfur can be seen remaining after 5,000 fretting cycles, primarily found in the grooves caused by the counter body. However, when gold is also mapped (Fig. 8c), sulfur can no longer be detected

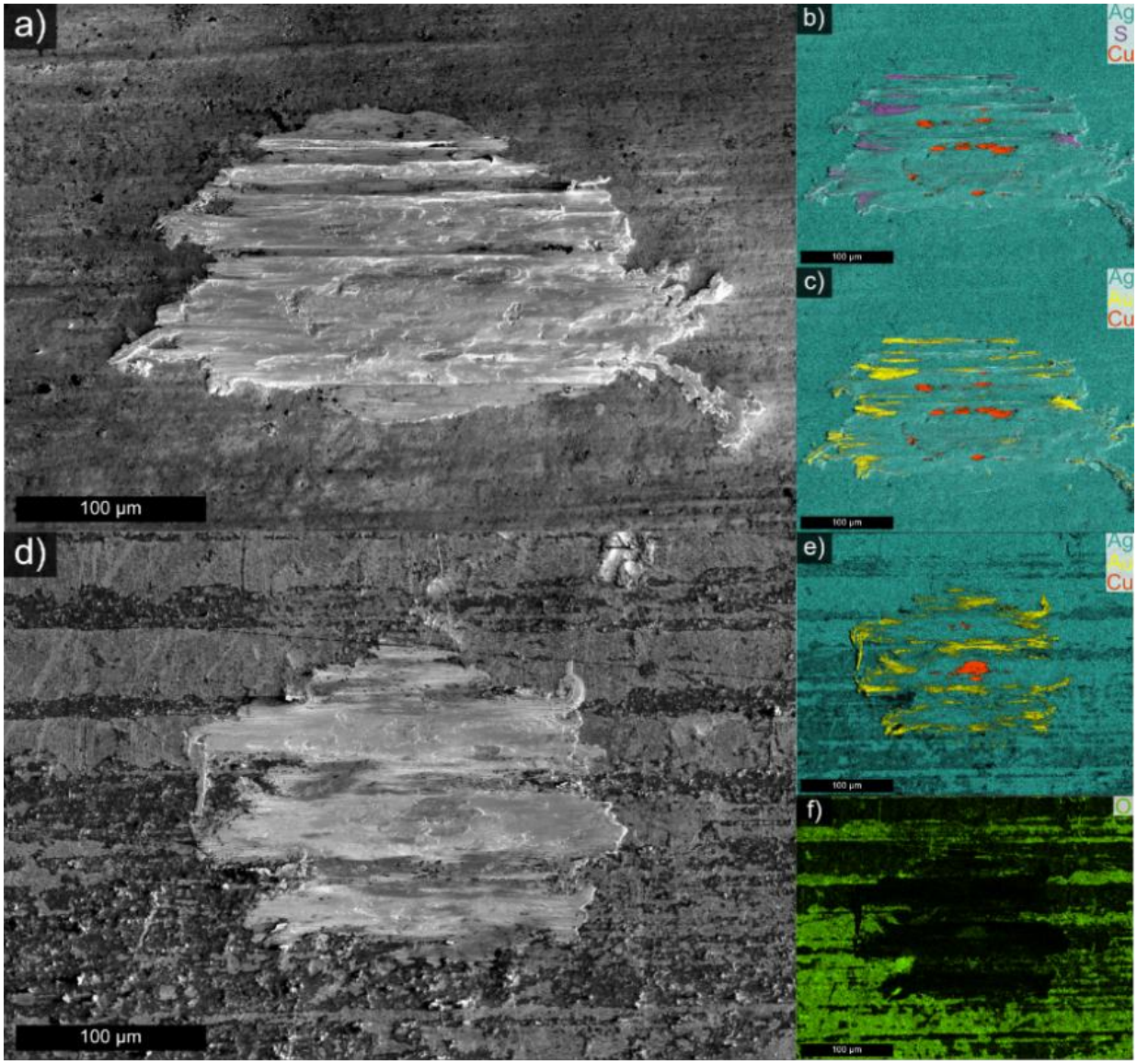

Fig. 8: a) SEM micrograph of tarnished sample. b)-c) Overlay of EDS mapping of silver, copper, gold, and sulfur. d) SEM micrograph of chemically cleaned sample. e) Overlay of EDS mapping of silver, gold, and copper. f) Oxygen EDS map.

since the transfer of gold from the rivet is also present in the grooves. Interestingly, copper maps reveal that the silver plating was sufficiently damaged, thus reaching the base material. Observing the EDS mappings of the cleaned sample (Fig. 8e and Fig. 8f), it can be seen that there was less significant gold transfer from the counter body. At the center of the fretting mark, a relatively large region reveals the copper base material. Although the overall worn area of the cleaned sample is smaller than in the tarnished sample (approximately 20% smaller), it appears as if the penetration at the center of the fretting mark was more significant, hence the strong copper signal in EDS mapping.

Sulfur was not detected in the chemically cleaned sample. However, residue left behind from the cleaning process was found (as evidenced in the SEM micrographs from Fig. 6d and Fig. 8d).

This residue presents large content of oxygen, as shown in Fig. 8f, and residual aluminum from the cleaning process.

Traces of magnesium was also detected in the EDS spectrum, potentially originating from sodium bicarbonate. However, the contaminants remaining from the cleaning process do not affect the silver connector when subjected to fretting, as evidence by the oxygen map. Nonetheless, adjustments should be made to the cleaning process to minimize the amount of residue left behind on the connector. Alternatively further cleaning should be employed, thus guaranteeing the lowest ECR possible.

IV. Conclusions

In this work, different methods aimed at minimizing the influence of silver sulfide tarnishing film on the electrical properties of silver-plated connectors were analyzed. From this study the following can be concluded:

- Silver sulfide's electrical resistance is higher than that of pure silver. Therefore, there is a constriction resistance when the current flows through the tarnishing film increasing the overall resistance of the system.
- The mechanical (scratch test simulating connection-disconnection) and resistive heating methods proposed did not diminish the effect of the tarnishing film as hypothesized. Regarding the later, the ECR values for tarnished and chemically cleaned samples were almost identical for all sourced currents. For the former, the tarnished sample displayed higher resistances than the cleaned samples (approximately double the value), however, the tarnishing film acts as solid lubricant, evidenced by lower CoF values.
- The tarnishing film does not incur additional contact resistance in the system when piled-up (end of scratch track), as is the case with tin oxide in tin plated electrical connectors. Increase in ECR was observed in both states as a consequence of inadequate contact between sample and counter electrode. Fretting tests results concur with scratch tests. After 5,000 fretting cycles ECR decreased 30% and 15% for tarnished and cleaned samples, respectively. However, the overall value of the tarnished sample remained higher than that of the cleaned sample. Therefore, the tarnishing film was not completely removed. Furthermore, the tarnishing film does not offer fretting wear protection, with the cleaned sample showing a fretting mark that is approximately 20% smaller than that of the tarnished sample.
- The silver sulfide film lubricates the surface, thus reducing friction caused by connection-disconnection cycles. Consequently, lower insertion and removal forces are required. Lower

removal forces aid undesirable disconnections, leading to malfunctions, loss in contact efficiency, and/or contact failure.

- The tarnishing film can be punctured by applying normal loads above 5 N (approximately 676.5 MPa). Above these normal loads the resistance resembles the values observed for the chemically cleaned silver contacts. Therefore, this method is suitable to diminish the effects of the tarnishing layer on ECR, thus eliminating the need of chemical removal.

ACKNOWLEDGEMENT

B. Alderete wishes to acknowledge the financial support from the German Academic Exchange Service (DAAD) and the Roberto Rocca Education Program (RREP). The TÜV Saarland Stiftung is gratefully acknowledged for financially supporting the project. The authors gratefully acknowledge funding in the ZuMat project, supported by the State of Saarland from the European Regional Development Fund (Europäischen Fonds für Regionale Entwicklung, EFRE). Funding for the PFIB/SEM instrument by German Research Foundation is greatly acknowledged (INST 256/510-1 FUGG).

REFERENCES

[1] P. G. Slade, *Electrical Contacts Principles and Applications*, Second Ed. Boca Raton: Taylor & Francis, 2014.

[2] W. Aas *et al.*, "Global and regional trends of atmospheric sulfur," *Sci Rep*, vol. 9, no. 1, pp. 1–11, 2019, doi: 10.1038/s41598-018-37304-0.

[3] D. A. Outka, R. J. Madix, G. B. Fisher, and C. DiMaggio, "Oxidation of sulfur dioxide on Ag(110): Vibrational study of the structure of intermediate complexes formed," *J Phys Chem*, vol. 90, no. 17, pp. 4057–4063, 1986, doi: 10.1021/j100408a044.

[4] R. Bauer, "Sulfide corrosion of silver contacts during satellite storage," *J Spacecr Rockets*, vol. 25, no. 6, pp. 439–441, 1988, doi: 10.2514/3.26025.

[5] S. Lilienfeld and C. E. White, "A Study of the Reaction Between Hydrogen Sulfide and Silver," *J Am Chem Soc*, vol. 52, no. 3, pp. 885–892, 1930, doi: 10.1021/ja01366a005.

[6] T. Ying, "An Advanced Anti-Tarnish Process for Silver Coins and Silverware—Monomolecular Octadecanethiol Protective Film," *Tribology Transactions*, vol. 64, no. 2, pp. 341–349, 2021, doi: 10.1080/10402004.2020.1842573.

[7] P. Patnaik, *Handbook of Inorganic Chemistry*. New York: MacGraw-Hill, 2002.

[8] M. Abdollahi and A. Hosseini, "Hydrogen Sulfide," in *Encyclopedia of Toxicology*, Third., P. Wexler, Ed. Academic Press, 2014, pp. 971–974. doi: 10.1016/B978-0-12-386454-3.00513-3.

[9] G. J. Russ, "Electrical Characteristics of Contacts Contaminated With Silver Sulfide Film," *IEEE Transactions on Parts, Materials and Packaging*, vol. 6, no. 4, pp. 129–137, 1970, doi: 10.1109/TPMP.1970.1136268.

[10] B. S. Hindin, "Silver Sulfide Corrosion Control using Corrosion Prevention Compounds," in *Corrosion*, 2006, p. NACE-06264.

[11] C. R. Denaburg, "Corrosion in Aerospace Electrical/Electronic Components in the Early Years of the Apollo Program, Kennedy Space Center, Florida," in *Corrosion*, 2000, p. NACE-00718.

[12] W. Schmitt, S. Franz, J. Heber, O. Lutz, and V. Behrens, "Formation of Silver Sulfide Layers and their Influence on the Electrical Characteristics of Contacts in the Field of Information Technology," in *ICEC*, 2008, pp. 489–494.

[13] C. Wagner, "Investigations on silver sulfide," *J Chem Phys*, vol. 21, no. 10, pp. 1819–1827, 1953, doi: 10.1063/1.1698670.

[14] M. H. Hebb, "Electrical conductivity of silver sulfide," *J Chem Phys*, vol. 20, no. 1, pp. 185–190, 1952, doi: 10.1063/1.1700165.

[15] K. Sahraoui, N. Benramdane, M. Khadraoui, R. Miloua, and C. Mathieu, “Characterization of Silver Sulphide Thin Films Prepared by Spray Pyrolysis Using a New Precursor Silver Chloride,” *Sensors & Transducers*, vol. 27, no. May, pp. 319–325, 2014.

[16] S. Zhang, M. Osterman, A. Shrivastava, R. Kang, and M. G. Pecht, “The Influence of H2S exposure on immersion-silver-finished pcbs under mixed-flow gas testing,” *IEEE Transactions on Device and Materials Reliability*, vol. 10, no. 1, pp. 71–81, Mar. 2010, doi: 10.1109/TDMR.2009.2033194.

[17] W. H. Abbott, “The Development and Performance Characteristics of Mixed Flowing Gas Test Environment,” *IEEE Transactions on Components, Hybrids, and Manufacturing Technology*, vol. 11, no. 1, pp. 22–35, 1988, doi: 10.1109/33.2959.

[18] P. A. Gay, P. Berçot, and J. Pagetti, “The protection of silver against atmospheric attack,” *Plating and Surface Finishing*, vol. 91, no. 5, pp. 71–73, 2004.

[19] C. H. Liang, C. J. Yang, N. B. Huang, and B. Wu, “Comparison of four antitarnishing self-assembled monolayers on silver coin,” *Surface Engineering*, vol. 27, no. 3, pp. 199–204, 2011, doi: 10.1179/026708410X12786785573599.

[20] M. Makela, P. Soininen, and S. Sneck, “US Patent No.: 8,883,258 B2,” 2014

[21] A. C. Phillips and A. Cowley, “Octadecanthiol for tarnish-resistant silver coatings,” *Modern Technologies in Space- and Ground-based Telescopes and Instrumentation II*, vol. 8450, p. 84503W, 2012, doi: 10.1117/12.925505.

[22] C. Liang, C. Yang, and N. Huang, “Tarnish protection of silver by octadecanethiol self-assembled monolayers prepared in aqueous micellar solution,” *Surf Coat Technol*, vol. 203, no. 8, pp. 1034–1044, 2009, doi: 10.1016/j.surfcoat.2008.09.034.

[23] T. Tamai, S. Sawada, and Y. Hattori, “Deformation of crystal structure and distribution of mechanical stress in tin-plated layer under contact loading,” *Electrical Contacts, Proceedings of the Annual Holm Conference on Electrical Contacts*, pp. 160–165, 2009, doi: 10.1109/HOLM.2009.5284406.

[24] T. Tamai, Y. Saitoh, S. Sawada, and Y. Hattori, “Peculiarities in characteristics between contact trace and contact resistance of tin plated contacts,” *Electrical Contacts, Proceedings of the Annual Holm Conference on Electrical Contacts*, vol. 00, no. c, pp. 337–343, 2008, doi: 10.1109/HOLM.2008.ECP.65.

[25] M. Braunovic, “Effect of connection design on the contact resistance of high power overlapping bolted joints,” *IEEE Transactions on Components and Packaging Technologies*, vol. 25, no. 4, pp. 642–650, 2002, doi: 10.1109/TCAPT.2003.809108.

[26] M. Leidner, H. Schmidt, M. Myers, and H. F. Schlaak, “A new simulation approach to characterizing the mechanical and electrical qualities of a connector contact,” *The European Physical Journal Applied Physics*, vol. 49, no. 22909, pp. 1–10, 2010, doi: 10.1051/epjap/2010002.

[27] R. Holm, *Electric Contacts Theory and Application*, Fourth Edi., vol. 13, no. April. Springer-Verlag Berlin Heidelberg, 1879. doi: 10.1007/978-3-662-06688-1.

[28] K. E. Trinh, F. Mücklich, and E. Ramos-Moore, “The role of microstructure and surface topography in the electrical behavior of Sn-coated Cu contacts,” *27th International Conference on Electrical Contacts, ICEC 2014 - Proceedings*, pp. 243–248, 2014.

[29] S. D. Gates-Rector and T. N. Blanton, “The Powder Diffraction File: A Quality Materials Characterization Database,” *Powder Diffr.*, vol. 34, no. 352–60, 2019.

[30] S. Balos *et al.*, “Knoop hardness optimal loading in measuring microhardness of maraging steel obtained by selective laser melting,” *Proc Inst Mech Eng C J Mech Eng Sci*, vol. 235, no. 10, pp. 1872–1877, May 2021, doi: 10.1177/0954406219841081.

[31] Philadelphia Museum of Art, “Finishing Techniques in Metalwork - Hands-Free Silver ‘Polishing,’” 2021. https://www.philamuseum.org/booklets/7_44_85_1.html?page=2 (accessed Jan. 18, 2021).

[32] R. Puyol and S. Suarez, “A Contact Resistance Measurement Setup for the Study of Novel Contacts,” *IEEE URUCON*, pp. 1–4, 2017, doi: 10.1109/URUCON.2017.8171881.

[33] Tektronix, *Low Level Measurements Handbook, Precision DC Current, Voltage and Resistance Measurements*, 7th Ed. Beaverton, 2016.

[34] K. L. Johnson, *Contact Mechanics*. Cambridge University Press, 1987.

[35] W. D. Jr. Callister, *Materials Science and Engineering: An Introduction*, 7 Ed., vol. 94. John Wiley & Sons, Ltd, 2006.

[36] B. Alderete, R. Puyol, S. Slawik, E. Espin, F. Mücklich, and S. Suarez, “Multipurpose setup used to characterize tribo-electrical properties of electrical contact materials,” *MethodsX*, vol. 8, 2021, doi: 10.1016/j.mex.2021.101498.

[37] Zentralverband Elektrotechnik- und Elektronikindustrie - ZVEI eV, *Ausfallraten für Bordnetz-Komponenten im Automobil - Erwartungswerte und Bedingungen*. 2021.

ARTICLE III
Characterization and Electrical Analysis of Carbon-Based Solid Lubricant Coatings

Bruno Alderete, Frank Mücklich, Sebastian Suarez*

Chair of Functional Materials, Saarland University, Campus D3.3, 66123 Saarbrücken, Germany

Research article
Published in "*Carbon Trends*" (2022)
Impact Factor: 3.1 (2023)

Accessible online at: doi.org/10.1016/j.cartre.2022.100156

Own Contribution: Conceptualization; Methodology; Validation; Investigation; Data Curation; Writing – Original Draft; Visualization.

Cite this article as: B. Alderete, F. Mücklich, S. Suarez, Characterization and electrical analysis of carbon-based solid lubricant coatings, Carbon Trends 7 (2022) 100156. https://doi.org/10.1016/j.cartre.2022.100156.

Carbon Trends 7 (2022) 100156

Contents lists available at ScienceDirect

Carbon Trends

journal homepage: www.elsevier.com/locate/cartre

Characterization and electrical analysis of carbon-based solid lubricant coatings

Bruno Alderete[a], Frank Mücklich[a], Sebastian Suarez[a,*]

[a] Chair of Functional Materials, Saarland University, Campus D3.3, 66123 Saarbrücken Germany

ARTICLE INFO

Article history:
Received 3 November 2021
Revised 18 January 2022
Accepted 18 January 2022

Keywords:
Carbon nanohorns
Carbon nanotubes
Electrical connector lubrication
Electrical contact resistance
Electrophoretic deposition
Graphene oxide
Graphite flakes

ABSTRACT

The use of electrical devices has skyrocketed over the past decades, increasing the demand for electrical connectors worldwide. Therefore, it is of utmost importance to produce more reliable, energy and material efficient, and durable electrical contact material systems; particularly in low-redundancy systems, such as in passenger vehicles. This work analyzes the potential use of carbon nanoparticle coatings applied via electrophoretic deposition over copper substrates to reduce wear, require lower insertion forces, and to protect the connectors from atmospheric conditions, while reducing the gain on the overall resistance of the system. Four carbon nanoparticles were considered due to their well-known solid-lubricating capabilities, namely: graphite flakes, graphene oxide, carbon nanotubes, and carbon nanohorns. Through a comprehensive characterization of the coatings, aspects like coating topography, compactness, thickness, elasticity, and electrical contact resistance were analyzed. Carbon nanotubes and nanohorns proved to have the highest potential. In addition to their previously documented outstanding solid-lubricity and environmental protection - after chemical modification of the coatings' surfaces - these nanoparticles showed low resistance values for loads above 4 N, i.e., below 400 mΩ. Moreover, the coatings produced were thin and homogeneous, with adequate mechanical stability, and elastic behavior.

1. Introduction

Over the past decades the use of electrical connectors has significantly increased. These components are ubiquitously found throughout a wide range of devices used in day-to-day life. Their use ranges from ordinary tasks (such as vacuum cleaning, water heating, etc.) up to applications where their correct performance is crucial for the safety of the users (e.g., navigation in passenger aircrafts, industrial machinery, among others). The rising trend in the consumption of electronic and smart devices - as well as the growing digitization of industrial processes - has spiked the demand for electrical components. Experts predict that the connector industry will register a 7% increase in compound annual growth rate between the years 2020 and 2026 (according to Global Market Insights Inc.), surpassing a total revenue of 61 billion Euro. This trend is not new, in the year 2000 alone connector sales were approximately 30 billion Euro [1]. Half of those sales were destined for the computer and telecommunication market, whereas 5 billion Euro in sales corresponded to the automotive industry. This scenario clearly highlights the importance of efficient, durable, and more reliable electrical connectors. The reliability of an electrical connector takes a more important role in low redundancy systems, such as in passenger vehicles. Here, most electrical circuits rely on only one connector to effectively open and close the circuit. Therefore, one electrical connector failing can potentially affect the entire system.

There are several atmospheric and tribological conditions that considerably reduce the duty life of electrical connectors. Regarding ambient conditions, contact materials react with agents present in the atmosphere, such as oxygen, sulfur, corrosive agents, acids, etc., depending on the application. Moreover, electrical connectors are subjected to wear during mating and un-mating cycles and fretting wear during normal operations. To reduce wear on the electrical connectors lubricant greases are applied on their surface. Greases are used since they do not easily wash off, therefore reducing the requirement of reapplication [2]. Using lubricant greases help prevent undesired reactions with atmospheric conditions, along with reducing wear, fretting, and the insertion force required. The greases also prevent the access of water in the contact. Connector lubricants consists of varying chemistry; they can

* Corresponding author at: Functional Materials, Dept. of Materials Science and Engineering, Functional Materials Institute - Saarland University, Campus D3.3, room 2.11, D66123 Saarbruecken, Germany.
E-mail address: s.suarez@mx.uni-saarland.de (S. Suarez).

https://doi.org/10.1016/j.cartre.2022.100156

be mineral or synthetic based oils with thickeners (e.g., polyurea-based thickeners). However, these lubricants increase the electrical resistance, therefore hindering their conductive properties. So far, this has been a favorable trade off since the greases extended their duty life.

Copper is among the most used metals for electrical connectors. It has the second lowest resistivity among metallic conductors (1.65 x 10^{-8} Ω.m at 20 °C) [2], being silver the best metallic conductor. Copper has adequate mechanical properties, and its surface is protected from oxidation as a consequence of a native oxide layer that is spontaneously formed on its surface. Although copper oxide is detrimental to its conductive properties, it effectively protects the metal from further degradation. Copper electrical connectors are generally plated with soft metals, such as gold, silver, or tin.

Carbon is a versatile element capable of forming different carbon-carbon bonds. Depending on the hybridization state, different allotropes are formed with varying properties [3,4]. In this work we explore alternative solutions to lubricating contacts so as to not compromise the electrical characteristics of the interfaces. Therefore, we propose carbon nanoparticle (CNP) coatings obtained via electrophoretic deposition on copper substrates. The CNP selected are graphite flakes (GF), graphene oxide (GO), carbon nanotubes (CNT), and carbon nanohorns (CNH). These CNP were chosen based on their well reported lubricant properties [5,6,7], with the added advantage of their exceptional transport properties due to the delocalized p_z orbital, characteristic of sp^2 carbon.

Graphite is a classical, well-known solid lubricant due to the weak interlayer interactions of the stacked hexagonal carbon structures. Therefore, graphite shows low shear strength when subjected to friction, describing its use as solid-state lubricant and its self-lubricating properties [8,9,10,11,12,13]. Due to its intrinsic lubricity, graphite has also been introduced as an additive in oils, commonly referred to as “nanofluids” [14,15]. Graphite additionally presents good transport properties, namely thermal and electrical conductivity. However, due to the stacking of the hexagonal layers it presents anisotropy. In-plane, the thermal and electrical conductivity are significantly lower than perpendicularly, relative to the surface of the individual graphite layers. Nonetheless, studies have shown that graphite presents 2000 to 4000 $W.m^{-1}.K^{-1}$ for large sized perfect structures, and electrical conductivity between 400 and 1250 $S.cm^{-1}$ [16,17,18]. Consequently, this allotrope was selected for two key reasons. Foremost, it is considered a benchmark since it is widely used as a solid lubricant. And more importantly, it presents good electrical properties. Furthermore, since graphite is a hydrophobic material, graphite coatings have promising applications as surface protection barriers [19].

Graphene oxide is a slightly lower quality material, with reduced physical properties compared to graphene [18,20–28]. GO can be obtained from graphite by chemical exfoliation (top-down method) [29]. Alternatively, GO can be obtained from graphite by Hummer’s method or Brodie’s method [30,31]. By undergoing an additional reduction step, reduced graphene oxide (rGO) can be obtained. This rGO still possesses some imperfections, but it is relatively similar to graphene regarding its physical properties. GO is not as conductive as rGO or graphene (the electrical conductivity of rGO is linked to the reduction agent and reduction times) as a consequence of the carbon-oxygen bonds [32]. Furthermore, the covalent bonds between oxygen and the functional groups in GO generate structural defects in the crystalline structure. These defects scatter the electrons, affecting GO’s electrical conductivity [23]. However, it is simpler to mass produce at a lower cost. GO is particularly interesting as a solid lubricant due to the oxygen bonds present in the lattice. As the oxygen bonds repel one another, they prevent the graphene sheets from re-stacking and thus forming graphite. This further decreases the shear forces during friction. Consequently, GO has been of great interest for applications as solid lubricant, self-lubricating solid, and as a lubricant additive [33,34,35]. Moreover, due to the oxygen present in GO, atmospheric protection may be affected due to an increased hydrophilic behavior. Nonetheless, studies have shown that the wetting behavior of GO can be altered by chemical modifications [36,37].

Carbon nanotubes have been of great interest to the research community in the past decades due to their outstanding intrinsic physical properties and their potential fields of application. These quasi-one-dimensional carbon structures - in their purest defect-free state - have the highest tensile strength of any material known, the highest thermal conductivity, and quasi-ballistic electronic conduction. The theoretical thermal conductivity of CNT was reported to be over 6000 $W.m^{-1}.K^{-1}$, whereas the electrical conductivity varies between 10^2 to 10^5 $S.cm^{-1}$ [38–46]. However, due to their geometry, CNT present anisotropy in their transport properties, showing better thermal and electrical conductivity in the axial direction compared to radial direction. Moreover, the excelling intrinsic properties of CNT are hindered by their tendency to form agglomerates (due to π-π interactions) [47,48]. Therefore, breaking up the CNT agglomerates without causing damage to the structure of the individual CNT is of utmost importance in order to maintain their properties. Previous reports have shown that CNT have promising applications as protective barriers from atmospheric conditions [49], as well as self-lubricating metal matrix composites and coatings [50–52]. Similarly to graphite, CNT have been used as additives to improve the lubricity of traditional oil-based lubricants [53–55]. In this work multi-walled CNT are used due to their simpler synthesis method, lower cost, and - most importantly - since statistically multi-walled CNT always have at least one conductive wall.

Single walled carbon nanohorns - also known as nanocones - are part of the sp^2 carbon family which have not received as much attention as the previously discussed CNP. CNH are nanoparticles with a tubular shape, similar to single-walled CNT [56–59]. However, CNH arrange themselves in horn-like endings, with tube diameters in the range of 2 to 5 nm and tube lengths between 40 and 50 nm. CNH present two important advantages over CNT, namely: 1) CNH synthesis does not require metallic catalyst, and 2) CNH can be produced on a large scale at room temperature. CNH are also differentiated from CNT because all CNH are semiconducting. Their conductive properties are closely linked to temperature and the adsorption of gases. As for all semiconductors, CNH show higher electrical conductivity at higher temperatures. Due to CNH morphology, they are of interest in solid lubrication applications and as oil-based lubricant additives [60]. Regarding the electron transport properties of CNH, a specific value was not found. However, one study has shown that incorporating CNH in organic aerogel composites has increased its electrical conductivity [61]. Moreover, it has been previously shown that CNH have a hydrophobic behavior [62]. Consequently, CNH coatings could potentially be used as protective barriers by manipulating their superficial characteristics, as previously shown for CNT.

Electrophoretic deposition (EPD) is a relatively straight forward method used to deposit CNP [49,63–70]. This method was selected due to its simplicity, easily controllable coating thicknesses, modest equipment requirements, and up-scalability. In essence, this technique requires the previous dispersion of the CNP in a suitable solvent. The electrodes are later immersed in the colloidal suspension and connected to a direct current power source. An electric field is generated, imparting electrophoresis on the CNP. The stability of the dispersion depends on the size of the CNP agglomerates. Therefore, mechanically breaking down the agglomerate size is crucial. Agglomerate size can be reduced through homogenization (shear force) and through sonication (ultrasound bath) [49,70]. Smaller particle sizes also promote more homogeneous coatings

and require weaker electric fields. The stability of the colloid is further improved by adding an additive to the solution. It has already been proven that triethylamine (henceforth TEA) improves the overall stability of the colloid, and assists the deposition process by giving the CNP a positive superficial charge (anodic deposition) [49,71].

A study carried out by Lloyd et al. has laid the foundation for graphite, graphene and CNT as electrical connector finishing layer [72]. Their study focused on the tribological and electrical behavior of thin coatings deposited by spray coating (and/or brushed) on Au, Ag and Sn surfaces. However, the normal loads applied for resistance measurements were low, 0.5 N for Au and 2 N for Ag and Sn. Within the scope of this work, we comprehensively analyze the potential use of four different CNP-based coatings obtained via EPD to increase the efficiency of electrical connectors. Additionally, these CNP have superior thermal conductivity, enhancing the dissipation of the heat that is produced in the electrical contact. Furthermore, depending on the resulting chemistry of the coating's surface, these can behave as near superhydrophobic surfaces [49]. The resulting coatings should lubricate the connector for mating and un-mating, protect the connector from ambient conditions, while minimizing the effect on the electrical conductivity of the system.

The coating's morphology was evaluated using scanning electron microscopy/focused ion beam (SEM/FIM) and confocal laser scanning microscopy (CLSM). From these techniques crucial information on the coating's topography, thickness, homogeneity, compactness, and interface was acquired. Additionally, the deposition rate of the CNP was qualitatively analyzed with the information acquired from FIB cross sections. SEM on the pristine nanoparticles was carried out, measuring their minimum, maximum, and mean particle/agglomerate size. Load-dependent electrical contact resistance (ECR), using a self-developed setup, was used to characterize the electrical properties of the coatings. Moreover, post-ECR CLSM measurements were carried out on the coated samples and the counter electrode. The two latter were the primary focus of this study since the electrical resistance and durability of the coatings plays a pivotal role in the efficiency and reliability of the connector.

2. Materials and method

The substrates used were laminated, flat pure-copper platelets (25 × 10 × 1) mm. These Cu platelets were ground (P1200 grit silicon carbide grinding paper) and polished at 6 µm, 3 µm, and 1 µm to obtain a mirror-polished surface before coating. Graphite flakes (Alfa Aesar, Germany) with a median size between 7 and 10 µm, 99.8% purity were used. The graphene oxide particles possess 51.25 wt% carbon, 43.99 wt% oxygen (Nanoinnova Technologies, Spain). The CNT used were chemical vapor deposition-grown multiwalled CNT (Graphene Supermarket, USA), with an outer diameter distribution between 50 and 85 nm, an as-received state length from 10 to 15 µm, and carbon purity over 94%. The single-walled CNH used were dahlia-type, produced by rapid condensation of carbon atoms without a catalyst by Carbonium SRL, Italy. The as-received high-purity CNH have a horn diameter between 3 and 5 nm, horn length between 30 and 50 nm, and a cluster diameter between 60 and 120 nm.

A schematic representation of the EPD setup is shown in **Fig. 1**. Due to the geometry of the electrodes (flat, rectangular platelets), the electric field is perpendicular to the parallel-mounted electrodes. A copper sample was used as a counter electrode. The power source used (Consort EV3020) operates under constant voltage (potentiostatic EPD). Therefore, to alter the strength of the electric field, the voltage must be manipulated. From previous studies [58], it was found that the optimal voltage level for EPD of CNP is 300 V. Due to the geometric constraints of the setup, the

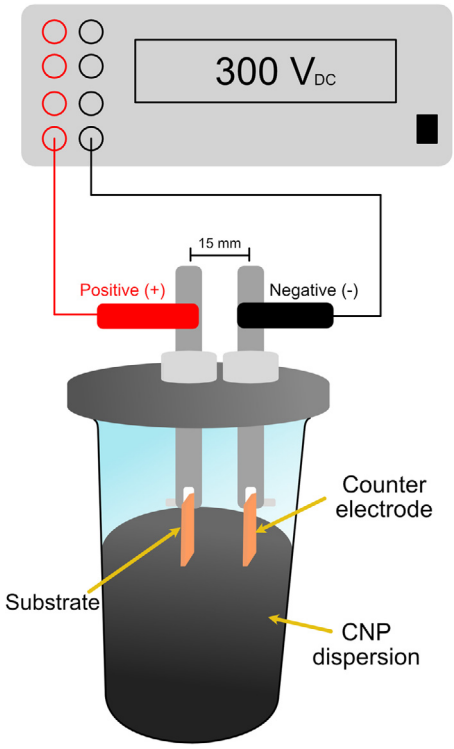

Fig. 1. Schematic representation of EPD setup.

minimum inter-electrode distance was 15 mm. Reducing the inter-electrode distance minimizes the distance the CNP must travel to reach the deposition electrode. Keeping this voltage and inter-electrode distance constant, the coating thickness is controlled by the duration of the deposition process. The deposition rate varies from nanoparticle to nanoparticle, depending on their conductivity. It is important that each CNP has enough time to fully coat the substrate during EPD. Therefore, the coatings obtained will be compact and without voids. This is highly desirable since uncoated regions lack wear and atmospheric protection. Furthermore, regarding ECR measurements, these regions will behave significantly different than completely coated regions.

The dispersion of the carbon nanoparticles consists of mixing them in a solvent, Isopropanol (IPA), and an additive. As previously mentioned, the role of the additive is to enhance the stability of the dispersion and provide a superficial charge to the nanoparticles. According to the additive used, the superficial charge of the nanoparticles varies, consequently changing the deposition electrode. In this study, TEA ($C_6H_{15}N$) was the additive used. The homogenization step begins once the solvent, additive, and nanoparticles have been added into a beaker. The homogenizer (IKA T25 digital Ultra-Turrax) breaks down the nanoparticle agglomerates using shear forces. To further separate the nanoparticles, the colloid is placed in an ultrasonic bath (Bandelin Sonorex Super RK 514 BH, 33 Hz, 860 W). The concentrations used and the dispersion times are described in detail in **Table 1**.

As previously mentioned, the deposition rate varies depending on the conductivity of each CNP. A common deposition time of 5 minutes was chosen for all CNP to achieve a uniform, homogeneous, and thin coating. Thick coatings would result in an additional barrier for electrical current. Therefore, thinner coatings are sought out, hence the benefits attained would outweigh the gain in ECR caused by the CNP coating. The produced coatings were characterized with SEM/FIB (FEI Helios NanoLab600 Dual Beam Setup) and Confocal Laser Scanning Microscopy (LEXT OLS4100, Olympus). The SEM micrographs were acquired using an acceleration voltage

Table 1
. Concentrations and dispersion times for each CNP colloid.

Nanoparticle	GF	GO	CNT	CNH
Nanoparticle concentration / mg/ml	0.2	0.5	0.2	0.05
IPA / ml	80			70
TEA / ml	10	10	5	5
Homogenizer / min	10	5	5	10
Homogenizer speed / rpm	7000			12000
Ultrasound / min	10			15

Table 2
. Mean particle/agglomerate size of pristine CNP.

Nanoparticle	GF	GO	CNT	CNH
Mean particle size	(7.1 ± 2.2) µm			(74 ± 18) nm
Agglomerate size		(5.0 ± 1.9) µm	(6.6 ± 4.2) µm	(264 ± 70) nm
Min. size	4.1 µm	2.2 µm	2.1 µm	Particle: 13 nm Agglomerate: 154 nm
Max. size	12.4 µm	7.8 µm	19.5 µm	Particle: 29 nm Agglomerate: 388 nm

of 5 kV and an electron beam current of 1.4 nA. The intensity maps and height profiles acquired with the CLSM were taken with 50× magnification and a laser wavelength of 405 nm. The profiles consist of a 3×3 stitching of the region of interest.

The four coatings and the substrate were electrically characterized via a self-developed ECR testing rig [73–75]. This rig can analyze load dependent ECR of the material via four-terminal method using a direct-current power source. Loading and unloading cycles from 0.25 up to 10 N can be measured. The power source used was a Keithley 2400 SMU, capable of sourcing between 1 nA and 1.05 A. This device can also source voltage, but for this method constant current was sourced, and the voltage drop between electrodes registered. The current was set at 100 mA to stay in the dry circuit conditions [76,77]. The voltage drop is measured using a Keithley 2182a nanovoltmeter. This device can be set at five different measurement ranges, i.e., 10 mV, 100 mV, 1 V, 10 V, and 100 V. Depending on the voltage range that is expected for the measurement, the instrument range must be selected accordingly. It is noteworthy that the lowest suitable range for the measurement must be chosen to minimize the uncertainty of the measurement [78].

One ECR measurement cycle was measured for each coating and the substrate. Each cycle consisted of one loading and one unloading semi-cycle. Ten ECR measurements are taken per load throughout the cycle. Depending on the voltage drop recorded, the range of the nanovoltmeter must be adjusted to prevent the device from overflowing. If the range is too low, the recorded value will be incorrect; whereas in selecting a range that is too high the uncertainty of the measurement increases [78]. The normal loads that constitute the cycles are: 0.5 N, 1 N, 2 N, 3 N, 4 N, 5 N, 6 N, 8 N, and 10 N. Two-cycle ECR measurements were taken using the same loads and current. This allowed an analysis on the deformation of the coatings.

In this setup, the coated sample was the electrode and a silver-nickel core ($AgNi_{0.15}$), hard gold coated rivet ($AuCo_{0.2}$) was used as counter electrode (Adam Bornbaum GmbH). The counter electrode had a curved head, with a mean curvature of 4 mm at its tip. The roughness of the rivet's tip was analyzed with CLSM with a laser wavelength of 405 nm and 20× objective. The root mean square roughness was S_q = 0.255 µm. For each coated sample, a new rivet was used. The same rivet was used for all subsequent measurements carried out on the same coating.

The pristine CNP were observed with SEM. Quantification on pristine CNP powders were carried out with ImageJ software on micrographs with a magnification of 2500×, except for the CNH where 50000× was used. The minimum, maximum and average particle/agglomerate sizes are summarized in **Table 2**. As this table shows, the mean GF particles size falls within the range provided by the manufacturer (7-10 µm). However, larger flakes up to 12.4 µm where observed. The GF observed were randomly distributed, without a specific orientation, showing multiple folded particles. On top of the larger GF particles, smaller GF were observed. GO showed large networks of agglomerated particles. A few significantly larger GO particles could be identified. The agglomerated GO particles interact with one another, making it difficult to differentiate one agglomerate from another. CNT showed varied agglomerate sizes. Agglomerates of 2.1 µm up to 19.5 µm were observed, with a mean size of 6.6 µm. The diameter of the CNT was also measured on a micrograph with 50000×. The mean CNT diameter measured was 45 nm with a standard deviation of 12 nm, in accordance with the values provided by the manufacturer. The CNH particles and clusters could both be measured. The mean CNH particle diameter measured was approximately 74 nm, whereas the mean cluster size was approximately 265 nm. CNH agglomerate sizes range from 154 nm up to 388 nm approximately. Regarding CNH particles, the smallest particle observed was 13 nm in diameter approximately, whereas the maximum particle diameter was 29 nm.

3. Results and discussion

3.1. Coating topographic characterization

SEM micrographs of the four coatings are shown in **Fig. 2**. From these micrographs one can obtain information on the different topographies obtained from each CNP coating. As **Fig. 2a** shows, GF are deposited with different orientations, with clusters of horizontally deposited GF and few vertically deposited GF. This leads to an uneven coating, with visible voids (some of which are highlighted in light green). This could potentially lead to a porous coating. The inset micrograph on the top right corner shows the pristine GF particles. As the inset illustrates, GF particles significantly vary in size and shape. It is interesting to highlight that GF do not form agglomerates. GO coating's topography is shown in **Fig. 2b**. This coating is similar to the GF coating, with an uneven surface and multiple voids (highlighted in light green). GO agglomerates can be seen throughout the surface, as well as large GO particles (shown by the yellow arrows). The particles deposited horizontally on the surface of the substrate will present a higher resistance, whereas the vertically deposited particles will conduct electrical current with lower resistance since in-plane conductivity is significantly higher. The top right inset shows a micrograph of pristine GO nanoparticles. In contrast to what was observed in graphite, GO does forms agglomerates. Bundles of GO particles are ubiquitous throughout the

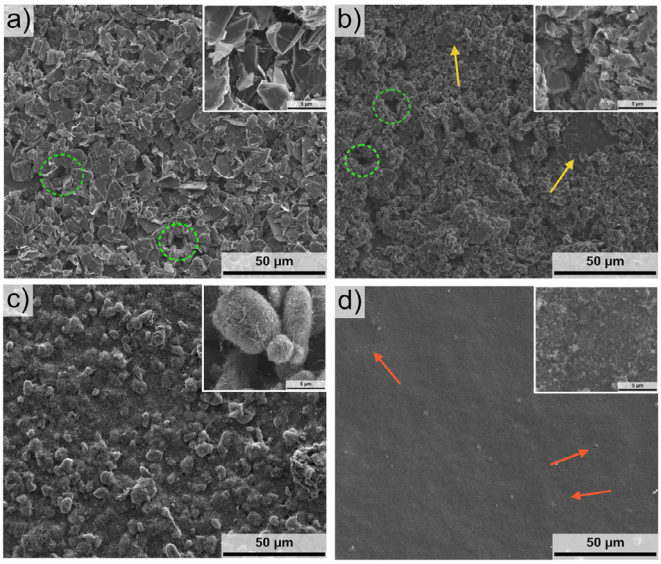

Fig. 2. Secondary electron micrographs of coating topography – a) GF, b) GO, c) CNT, and d) CNH. Light green circles highlight the presence of voids on the coatings' surface. The yellow arrows indicate the inclusion of larger GO particles. The red arrows indicate the presence of fissures on the CNH coating's surface. A micrograph of each pristine CNP is shown as an inset in the top right corner.

micrograph, making it difficult to identify individual GO particles. Nonetheless, individual larger GO particles can be distinguished among the GO bundles (lower left of the inset). The CNT coating, shown in **Fig. 2c**, presents a heterogeneous surface, with large CNT agglomerates scattered throughout its surface. Thicker regions can be seen where the agglomerates are present. The thinner regions correspond to small CNT agglomerates. However, the substrate cannot be seen suggesting that the entirety of the surface is coated. This is an advantage regarding wear and atmospheric protection, and consistency in contacting surfaces. Nonetheless, regions with larger CNT agglomerates could produce an increase in the electrical resistance. The inset at the top right shows a few pristine CNT agglomerates at higher magnification. In this inset the varying size of the agglomerates can be highlighted. Furthermore, the inset shows how the agglomerates tend to bundle, increasing the overall agglomerate size. Finally, **Fig. 2d** shows the SEM micrograph of the CNH coating. This figure shows a uniform surface with no topography. It does, however, present some small cracks (shown by the red arrows). These cracks may be a consequence of the elevated voltage used in EPD, and the drying of the coating after removal from the colloid [58]. These cracked surfaces jeopardize the transport properties and atmospheric protection characteristics of the coating. The inset in the top right shows the pristine CNH nanoparticles. Due to the dimensions of the CNH only larger agglomerates can be observed at this magnification. They are identifiable by the lighter shade in the SEM micrograph.

Observing the four surfaces, the CNH coating seems to be the most homogeneous and compact coating. Contrarily, the GF and GO coatings appear to be highly porous and heterogeneous. In the case of GF, the uneven coating can be explained by the large size of the particles. Relative to the GF coating, GO appears to be - to a moderate extent - more homogeneous. Although, several voids can be observed on its surface. Concerning the CNT coating, it is considered a heterogeneous coating. However, compared to GF and GO coatings, it appears to be a better alternative as voids cannot be observed. Nonetheless, the thickness of the coating changes significantly from region to region as a consequence of the larger agglomerates.

For further characterization of the coatings' topography, secondary electron images were acquired with the samples tilted to 52° relative to the electron beam. Their surfaces were additionally analyzed with CLSM, plotting their height profile. The height profile and SEM micrograph are shown in **Fig. 3**. The micrograph and height profile correspond to different regions in the coatings. The height profile and micrograph in **Fig. 3a** and **Fig. 3b**, respectively, correspond to the GF coating. These figures prove what the micrograph from **Fig. 2a** suggested; the coating produced by GF is highly irregular. The height profile of the GF coating shows that, on average, the height of the coating is in the range of 20 µm. This plot also shows that the coating has multiple voids and peaks scattered throughout the analyzed region. This can be seen by the distribution of blue and yellow/orange regions in the height profile. The peaks and valleys of the coating are also depicted in the tilted SEM micrograph. The valleys are found at an approximate height of 7 µm and the peaks at about 28 µm. **Fig. 3c** and **Fig. 3d** show the height profile and micrograph of the GO coating, respectively. Both figures show the irregularities and uneven nature of the coating. The irregularities are accentuated when compared to the GF coating. Although the SEM micrograph shows that the GO coating has many voids, it can be seen from the height profile that the voids are superficial. In other words, the voids are close to the surface of the coating. Furthermore, this coating has regions where the GO particles have been deposited higher than in other regions, as seen in the height profile (orange/red regions). The mean height of the coating is in the 20 µm range, with peaks as high as 35 µm and valleys around 10 µm. Observing the tilted micrograph, it can be seen that the higher regions in the coating correspond to GO agglomerates, but also due to large GO particles. These particles are significantly larger than the GO agglomerates, with sizes comparable to those of the GF particles. The height profile and micrograph of the CNT coating is shown in **Fig. 3e** and **Fig. 3f**, respectively. This coating highly contrasts with the previous two. The height profile shows that the mean height is approximately 10 µm with high peaks corresponding to the agglomerates (approximately 20 µm high). Both the height profile and the micrograph show that the coating does not present voids. The height difference on the coating's surface is solely a consequence of the large CNT agglomerates. These agglomerates produce the heterogeneity of the coating. Finally, **Fig. 3g** and **Fig. 3h** shows the height profile and micrograph of the CNH coating, respectively. These figures confirm that this coating is highly homogeneous, as suggested by the SEM micrograph from **Fig. 2d**. The average height of this coating is below 10 µm, with a few peaks reaching an approximate height of 14 µm. These peaks are seen as spots on the micrograph. These spots are a consequence of relatively large CNH agglomerates. The fissures observed on the SEM micrographs are not detected in the height profile. Therefore, the depth of the fissures can be neglected.

The height profiles acquired with CLSM provide additional information, complementing the information obtained from SEM microscopy. From **Fig. 3** we can establish that GF and GO produce irregular surfaces, being the former more heterogeneous than the latter. This statement contradicts what was initially hypothesized by observing the SEM micrographs in **Fig. 2**. The CNH coating is exceptionally homogeneous, with very few outlaying CNH agglomerates. The CNT coating stands in the middle showing heterogeneity, but to a lesser extent than GF and GO coatings. The tilted micrograph additionally allows the visualization of superficial voids. These are ubiquitously found in the GF and GO coatings, being more prominent in the former as demonstrated by the height profile.

3.2. Coating cross section

For an in-depth assessment of the compactness, thickness and coating-substrate interface, FIB cross sections on each of the coatings were carried out, shown in **Fig. 4**. In all cases, the substrate-

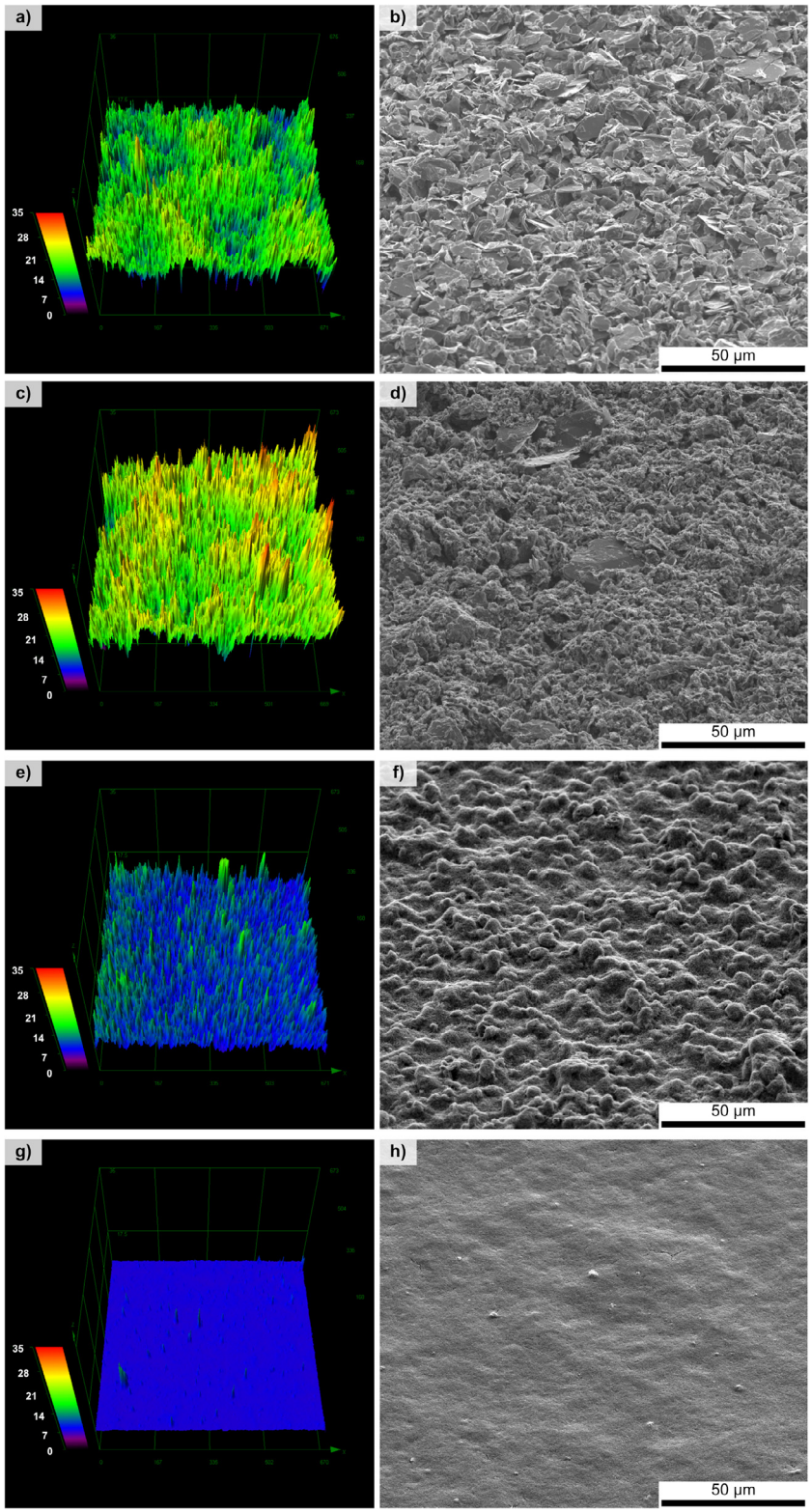

Fig. 3. CLSM height profile (left), secondary electron micrograph of coatings tilted at 52° relative to electron beam (right); a-b) GF, c-d) GO, e-f) CNT, and g-h) CNH. It is important to highlight that the height profile and SEM micrograph do not correspond to the same region of the coatings. The tilted SEM micrographs were taken on the same regions as the micrographs shown in Fig. 2.

coating interface is highlighted by a green line. Likewise, the surface of the coating is shown with a green dashed line.

The GF coating is shown in **Fig. 4a**. From the SEM image in **Fig. 2a**, the coating seemed highly heterogeneous. However, the cross section shows that the thickness of the coating does not vary significantly. This coating has an average thickness of 12.8 ± 0.9 µm. The uniformity of the coating is evidenced by the marginal standard deviation, accounting for only 7% variation in the overall thickness of the coating. This is in strong contrast from what one can infer from the SEM micrographs. The coating is relatively

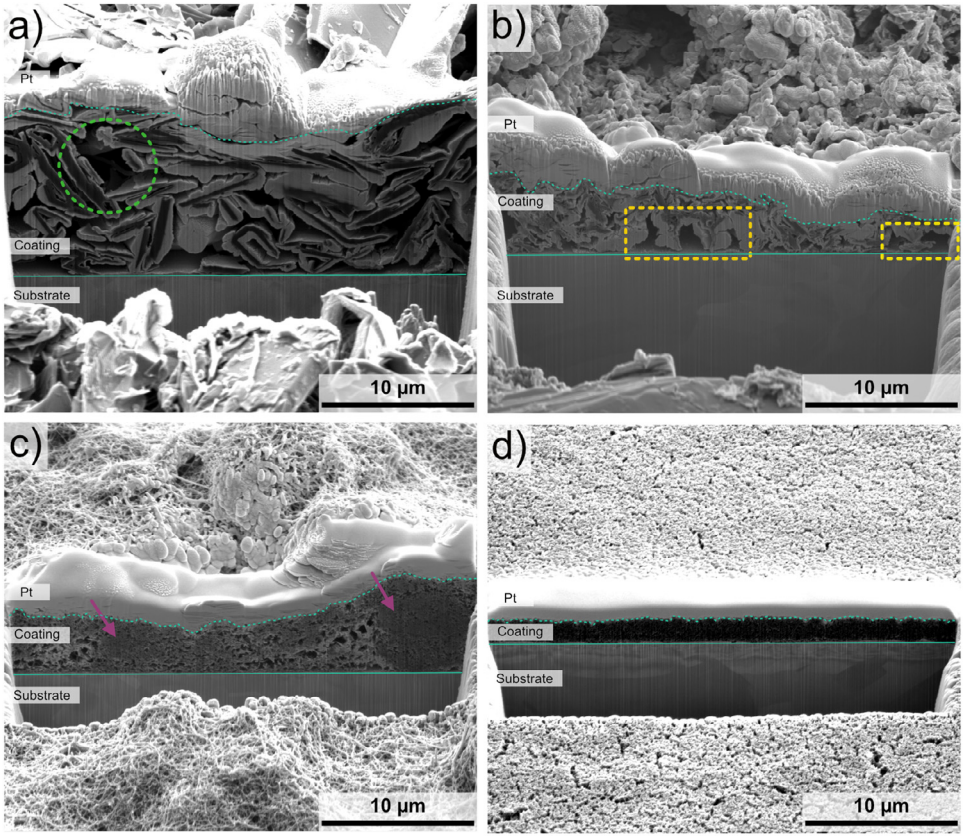

Fig. 4. FIB cross sections – a) GF, b) GO, c) CNT, and d) CNH. The green solid line indicates the substrate-coating interface. The green dashed line indicates the interface between the CNP coating and the protective Pt coating. The light green circle indicates a large void present in the GF coating. The violet arrows highlight compact regions in the CNT coating. The yellow squares highlight the porous interface between GO and the Cu substrate.

thick; however, this was expected since the particles are large in size. This cross section shows that the coating is not compact, with small voids (compared to the particle size). Larger voids are present in regions where the flakes were deposited in perpendicular direction relative to the previously deposited flake (highlighted in light green). The distance from the lowest point in the void, moving vertically towards the next GF, is approximately 4.1 µm. The maximum width of this void is approximately 5.8 µm. The different directions in which the flakes are deposited, as well as the presence of voids severely restricts the coating's ability to conduct electrical current. Therefore, the lack of compactness of this coating is undesirable for electrical applications. Nonetheless, this could be overcome by applying pressure during mating. Regarding atmospheric protection, the voids seen in the top-view micrograph do not appear as significant in the cross section. Although the superficial voids could allow atmospheric contaminants to penetrate. Nonetheless, the path towards the substrate is very intricate; no direct path is visible in this region of the coating. Concerning solid lubrication, the cross section shows some flakes that were deposited parallel to one another. This favors the solid-lubricating ability of graphite. Moreover, the interface between the graphite coating and the substrate raises concern. Only a few GF are in complete contact with the substrate, leaving large voids between the coating and the substrate. This is undesirable, as a weak bond between the coating and the substrate could facilitate the removal of the coating; thus, compromising the mechanical stability of the coating. However, this is beneficial for the lubricity of the system.

The GO coating is shown in **Fig. 4b**. Compared to the GF coating this coating seems more compact. Still large voids are present, especially near the coating-substrate interface. The GO coating is also thinner and more irregular, with an average thickness of 4.2 ± 1.2 µm. The standard deviation here represents a 27% variation in coating thickness in the region analyzed. This is a consequence of large GO agglomerates that significantly increase the thickness in some regions. This correlates with what was observed in SEM (**Fig. 2b**), since the topography of the coating appeared uneven throughout the coating. Many small voids are present within the core of the coating, with relatively larger voids near the substrate. As already stated, the presence of voids is highly unfavorable for electrical conduction, wear and atmospheric protection, and from a mechanical standpoint. The voids are non-conductive regions, which increase the overall electrical resistance of the coating. In addition, the presence of a porous network within the coating hinders the protection of the substrate from atmospheric conditions. This was inferred from the SEM micrographs, and now demonstrated by the ubiquitous presence of voids. Furthermore, the larger voids at the interface potentially reduce the coating's adhesion to the substrate (highlighted in yellow); consequently reducing the mechanical stability of the coating and facilitating its removal. These voids have a maximum width ranging from 1.0 to 3.2 µm. The left-most highlighted void has the largest vertical distance of approximately 3.3 µm.

The CNT coating's cross section is shown in **Fig. 4c**. This coating is comparatively more compact than the GF and GO coatings. A micro-porous network and some larger-sized voids can be seen. However, the voids are significantly smaller than in the previous two coatings. With the same deposition time, this coating results a bit thicker than the GO coating, but significantly thinner than the GF coating. It has an average thickness of 5.5 ± 1.5 µm. For the region analyzed, this coating also presents 27% variation in thickness. This was expected, since CNT tend to form large agglomerates, which were clearly visible in the SEM micrograph. The CNT coating presents dark regions where the coating appears very compact, with some identifiable small voids (shown by the violet ar-

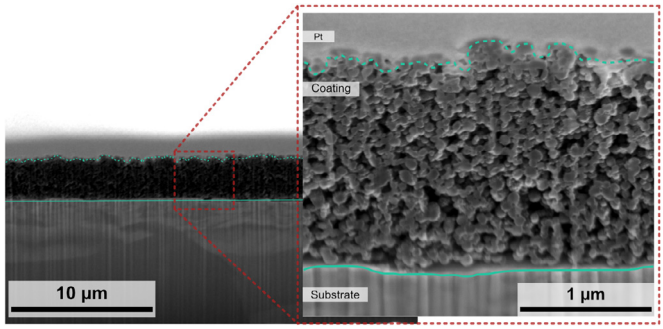

Fig. 5. Zoomed-in image showing the micro-porous network of the CNH coating. The green solid line highlights the substrate-coating interface, whereas the green dashed line highlights the interface between the CNH coating and the protective Pt coating.

rows). The small region highlighted (left arrow) has a maximum width of about 2.9 µm, whereas the larger region (right arrow) has a maximum width of 6.6 µm. These regions may be larger CNT agglomerates that were not broken apart during the dispersion process. Lighter regions represent areas with lower CNT density and larger voids. Nonetheless, this coating appears to be the most favorable for electrical current flow, atmospheric protection, and solid-state lubrication. Regarding the former, although many small voids are present, the CNT appear to have an adequate interconnection between the different regions of the coating. Consequently, this coating provides different pathways for electrons to be conducted from the electrode towards the substrate. Likewise, this is also an advantage for atmospheric protection since the lack of connection between voids blocks the flow of atmospheric contaminants towards the substrate. The larger voids observed in the lighter regions were measured. The average pore width is 0.55 µm. Although, they present a standard deviation of 0.25 µm, showing that within the larger voids there is significant variation in their dimensions. Moreover, this coating presents a seamless interface with the substrate. Some regions show voids at the interface; however, they are relatively small. Additionally, within the region with voids at the interface, CNT particles can be seen extending towards the substrate. This is of great interest since it promotes a better adhesion of the coating to the substrate.

Finally, the CNH coating's cross section is shown in **Fig. 4d**. As deduced from the SEM micrograph of the coating's surface (**Fig. 2d**), this coating is very thin, uniform, and compact. It has an average thickness of 1.8 µm with a standard deviation of 0.2 µm. The variation in thickness accounts for about 9% in the region analyzed, further proving the uniformity of the coating. The fissures that were observed on the coating's surface do not seem to extend within the coating (in the region analyzed), thus they do not affect the potential atmospheric protection of the coating. However, due to the thin nature of the coating, it is hard to visualize. Therefore, **Fig. 5** shows the coating at a larger magnification. In this image, the micro-porous network of the coating can be clearly observed. Observing this micrograph, many small voids can be identified. However, the CNH are connected to one another forming a complex structure of bonded particles, which in turn potentially enhances the coating's atmospheric protection behavior. Regarding the coating's electrical properties, the complex CNH network could hinder the electron transport properties. Nonetheless, there are multiple paths for the electrical current to flow towards the substrate due to the interconnected network of the CNH. Furthermore, as a consequence of the particle morphology, their potential as solid lubricants is of great interest. The voids present an average width of 0.12 µm with a standard deviation of 0.04 µm. From **Fig. 4d**, the CNH-substrate interface appears smooth and seamless.

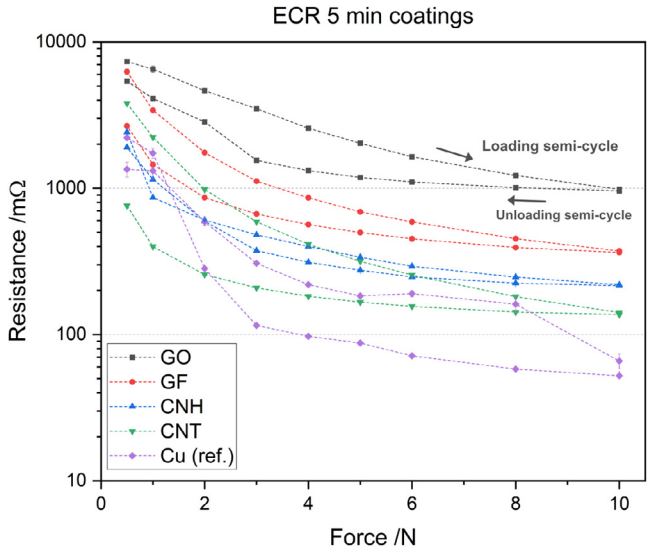

Fig. 6. Load-dependent ECR of coated and reference samples. The arrows indicate the direction in which the loading and unloading semi-cycles were carried out.

However, as **Fig. 5** shows, that is not the case. The voids found throughout the coating also extend to the interface, with few CNH particles in contact with the substrate. This has the potential to reduce the mechanical stability of the coating, allowing for an effortless removal of the coating after mating and un-mating cycles of a coated electrical contact.

All coatings were produced with a deposition time of five minutes. Considering the ratio between the mean particle/agglomerate size of the CNP (7.09, 5.01, 6.61, and 0.26 µm for GF, GO, CNT, and CNH, respectively) and the mean coating thickness (12.8, 4.24, 5.53, and 1.8 µm for GF, GO, CNT, and CNH, respectively), it can be stated that CNH has the highest deposition rate of all four nanoparticles. It is followed by GF; however, its deposition rate is significantly lower than CNH. GO and CNT have the lowest deposition rates. These nanoparticles have similar mean agglomerate sizes, and both produce coatings that are similar in thickness.

In addition to deposition time, voltage is also an important parameter. Since it is the electric field who imparts the electrophoretic force on the dispersed nanoparticles, which in turn is determined by the voltage applied; therefore, larger nanoparticles require larger voltages. Consequently, the small particle and cluster size of CNH (and by maintaining 300 V on all depositions) explains the higher deposition rate of CNH nanoparticles. This also justifies why GO and CNT have similar deposition rates, since these CNP have similar particle sizes. However, GF's deposition rate was not expected. Considering that GF are relatively large, it was anticipated that it would have the lowest deposition rate. Nonetheless, on account of the larger dimensions of the particles, thick coatings were expected.

3.4. Single-cycle electrical characterization

Load-dependent ECR values are shown in **Fig. 6**. The curves shown on the plot correspond to one measurement cycle (a loading semi-cycle and an unloading semi-cycle). The arrows indicate the loading and unloading directions. As a consequence of the values recorded, the nanovoltmeter was used with a range of 1 V to measure the four coatings, whereas 0.1 V was used for the copper reference sample (to minimize uncertainty in this measurements) [78]. All semi-cycles show the same tendency, i.e., higher ECR for lower loads, which is expected. This is a consequence of the compression of the coatings. As the normal load increases, the coat-

ings are compacted by the counter electrode, thus filling the voids within the coatings, and therefore improving the connectivity of the nanoparticles. Furthermore, as the load increases the round-headed counter electrode's apparent contact area also increases; consequently increasing the real contact area as well. In addition - due to the elastic behavior of the coatings - as the counter electrode compresses the coatings, it is immersed. This immersion of the rivet further increases the contact area. As the coatings are compacted - and the apparent contact area increases - so does the real contact area. The real contact area increases as the asperities (a-spots) of the electrodes come into electrical contacts. The elasticity of the coating increases the real contact area, approximating it to the apparent contact area. This is highly sought-after since it reduces the constriction resistance of the system by augmenting the a-spots that are in electrical contact.

As the figure shows, there is a clear hierarchy in the resistance of the coatings and substrate. As expected, the copper substrate has the lowest resistance at 10 N with a value of 52 mΩ. The substrate is followed by the CNT, CNH, GF, and GO coatings with 141 mΩ, 219 mΩ, 373 mΩ, and 985 mΩ at 10 N, respectively. This hierarchy was expected since GO and GF present high anisotropy in their transport properties. As the FIB cross sections shown in **Fig. 4a** and **Fig. 4b** these nanoparticles are randomly deposited, presenting different particle orientations. Ideally, the GF and GO particles should be deposited vertically. In that case these coatings would conduct the electrons in-plane, direction in which their electrical conductivity is higher. Nonetheless, within the randomly distributed coating, some particles were deposited in a more-or-less vertical direction, improving the electrical properties of the coating in these regions. However, this is more prominent in the GF coating. Since GF particles are larger, it is crucial that there is interconnectivity between the particles, considering that the voids generated within the coating are consequently also larger. Particularly for the GO coating, the oxygen atoms present in the structure due to the synthesis method hinder the nanoparticle's electrical properties. In addition to this particle's anisotropy, oxygen atoms act as scattering sites for the electrons; therefore, the electrical resistance increases. Moreover, the interface between the GO coating and the substrate affects its electrical properties. Among the four coatings analyzed, GO presents the weakest interface (shown by the porous interface in the FIB cross, **Fig. 4b**). Consequently, higher contact forces must be applied to achieve an adequate electrical contact between the counter electrode, coating, and substrate. The GF coating also presents a weak interface, however, not as significantly as GO. Voids present at the interface in the GO coating represent up to 70% of the coating's thickness. Whereas the dimension of the voids located at the interface in the GF coating are insignificant relative to the thickness of the coating (accounting for less than 15% of the coating thickness). Moreover, both coatings show elastic behavior since the ECR curves follow nearly the same tendency in the loading and unloading semi-cycle. It is interesting to point out that although the GF coating is more than twice as thick as the GO coating, the thickness does not play as a significant role as previously hypothesized. It was initially believed that thinner coatings would present lower ECR, however, these two coatings prove that the orientation of the nanoparticles is of greater importance than overall thickness (for these specific CNP).

The behavior of the CNH coating was unexpected, showing the second-best electrical behavior of the analyzed coatings. Due to the morphology of the particles (dahlia-shaped particle constituted of single-walled CNT with horn-shaped caps at their ends and semiconducting behavior) and it being a semiconducting CNP, it was not expected that it would show ECR values similar to that of the CNT coating. However, it was expected that the CNT coating would have lower resistance among the four CNP. Since multi-walled CNT were used, these nanoparticles always behave as metallic conductors. Nonetheless, for low contact forces in the loading semi-cycle, the CNT coating shows higher ECR values than CNH (3.8 Ω against 2.5 Ω). The CNH coating has a highly elastic behavior. Its ECR curve is very narrow, with the final value being similar to the initial value (1.9 Ω and 2.4 Ω, respectively). On the other hand, after the unloading semi-cycle the CNT coating presents significantly lower resistance than the CNH coating (0.76 Ω). These two coatings also present the advantage that they are relatively thin (especially the CNH coating). Thin coatings require lower normal loads for the counter electrode to reach the substrate, compacting the coating and reducing the film resistance. The compacting process allows for a better contacting area between the counter electrode, coating, and substrate, improving the real contact area and thus reducing the constriction resistance. Therefore, the resistance of the entire system is not significantly elevated. At maximum load (10 N), the resistance difference between the CNT and CNH coating is 80 mΩ (approximately 140 mΩ and 220 mΩ, respectively). Although these resistances seem low, they are extremely high compared to the values of the copper substrate. The substrate has an ECR of approximately 60 mΩ at 10 N. The CNT coating has more than double the resistance, whereas the CNH coating almost quadruple that resistance. However, these values are still relatively low considering that copper is one of the metals with the best electrical conductivity. This makes it is difficult to enhance copper's intrinsic electrical properties. Any additional layer added to this outstanding conductor significantly affects the conductivity of the pure metal. Nonetheless, at low normal loads the ECR values recorded for the copper substrate are comparable to the resistances of the coatings. This is because low normal loads do not puncture the native oxide layer that is formed on its surface. After puncturing this oxide layer however, the resistance of the substrate rapidly decreases. At 0.5 and 1 N the substrate shows the lowest resistance out of all the samples (approximately 1.5 Ω), when only considering the loading semi-cycle. However, the values do not differ significantly from the initial values of the CNH coating (about 2 Ω). At 2 N the resistance of the substrate is identical to that of the CNH coating. For the subsequent loads the resistance continues decreasing, reaching the lowest value at 10 N. As a consequence of the lower range used for the substrate's measurement (0.1 V), the measurements have a lower uncertainty. Therefore, at 10 N the value corresponding to the loading semi-cycle differs slightly from the value corresponding to the unloading semi-cycle. This difference detected may be caused by plastic flow of the substrate at this load. On the substrate, the ECR at low loads in the unloading semi-cycle is higher than the corresponding values during the loading semi-cycle. This is a consequence of the deficient contact between the copper sample and the counter electrode when unloading. As the load increases, the surface of the copper was deformed by the round counter electrode. During the unloading semi-cycle, as the load is gradually reduced, the real contact area decreases at a higher rate (fewer a-spots are in contact) due to the deformation that has occurred during the loading semi-cycle. With the normal load below 2 N the real contacting area is small, causing the ECR values to be comparable to the CNH coating. The same phenomenon was observed for the CNH coating, showing higher ECR at 0.5 N in the unloading semi-cycle than in the loading semi-cycle. This is a consequence of the thin nature of the coating. Due to the thickness of the GF, GO, and CNT coating, the resistance in the unloading semi-cycle is always lower than in the loading semi-cycle. Thus, enhancing the electrical contact between the coatings and the counter electrode even at low loads.

3.5. Post single-cycle ECR coating characterization

After carrying out the ECR measurements, the rivets and the coatings were observed under CLSM. The parameters of the CLSM

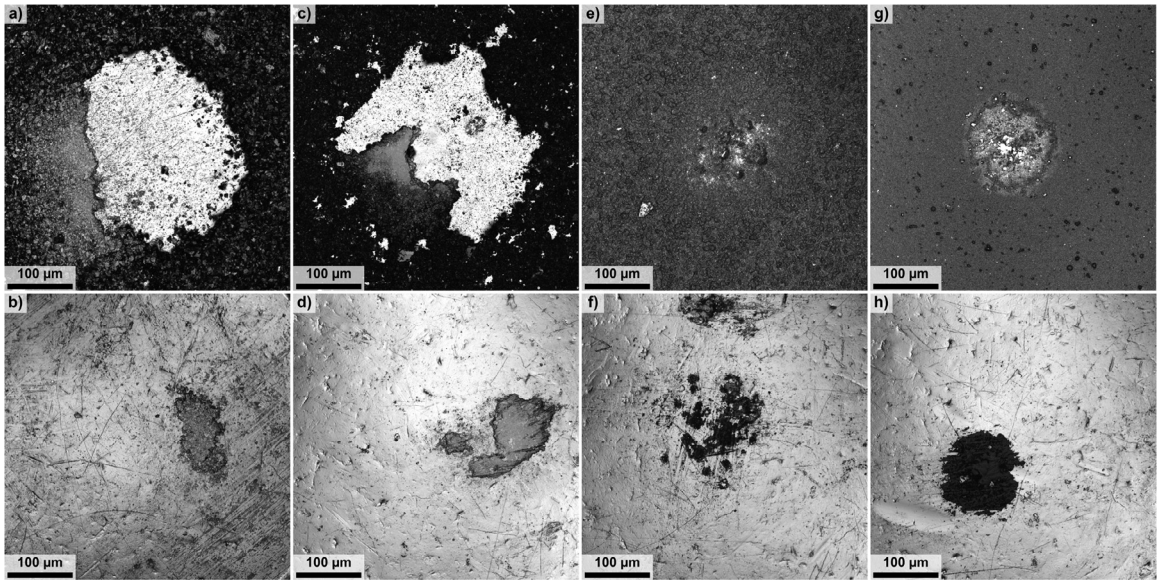

Fig. 7. CLSM intensity profile of CNP coating (top) and Au rivet (bottom); a-b) GF, c-d) GO, e-f) CNT, and g-h) CNH after one ECR measurement cycle.

are identical to those described in *Section 2*. Before observing the rivets under CLSM they were wiped with paper cloth and later cleaned with compressed air. The images are shown in **Fig. 7a-h**. The GF coating and the rivet's surfaces after ECR are shown **Fig. 7a** and **Fig. 7b**, respectively. The GF coating was partially removed after the electrical measurements. Part of the removed coating was deposited on the rivet itself. Graphite was also found remaining on the paper used to wipe the rivet before observing under the microscope. Although, the coating was not entirely removed. The mark left behind by the indenting counter electrode was circumscribed; the resulting circle had a diameter of approximately 470 µm. Similarly, the coating that was deposited on the rivet after the measurements was circumscribed resulting in a diameter of approximately 235 µm. The GO coating and rivet after ECR are shown in **Fig. 7c** and **Fig. 7d**, respectively. This coating was also partially removed after the ECR measurements, in similar manner as the GF coating. Moreover, the counter electrode was also partially coated. The diameter of the circumscribed mark left behind by the indenting counter electrode is approximately 460 µm. Regarding the coated rivet, it has a diameter of approximately 275 µm. GO particles were cleaned away when wiping the rivet before observing under CLSM. Observing the CNT coating and rivet, **Fig. 7e** and **Fig. 7f** respectively, it can be seen that the mark left correlates perfectly to the deposition on the rivet. The mark and deposition have an approximate diameter of 250 µm. The coating's surface shows that part of the CNT were removed, but to a lesser extent compared to the previous coatings. In the mark we can also see darker regions, which correspond to CNT agglomerates that remain in the indented area. Likewise, the image of the rivet shows areas with high concentration of CNT and areas without CNT. These images coincide, i.e., the intensity map of the coating shows CNT agglomerates in regions where the rivet does not show CNT particles. Likewise, the rivet shows regions with CNT deposited where the coating shows partial removal of the coating. No traces of CNT particles were observed when wiping the rivet after the measurement cycle. Finally, the CNH coating and rivet are shown in **Fig. 7g** and **Fig. 7h**. The intensity map of the coating shows partial removal of the nanoparticles on the outer 'ring' of the indented area, showing little to no CNH particles in the center of the circumference. The diameter of the interaction zone is approximately 220 µm, whereas the deposited CNH particles in the rivet has a diameter of approximately 200 µm. A clear correlation between the indented region in the coating and the CNH deposition in the rivet can be observed. As for CNT, no traces of CNH particles were observed after wiping the rivet.

The different interaction zones of the indenting counter electrode are interesting. They provide information on the compression that the coatings have undergone, but also on the mechanical stability of the coatings. Observing the intensity maps of the GF and GO coatings - **Fig. 7a** and **Fig. 7c**, respectively - it is evident that the coating was removed at a higher rate than in the case of CNT and CNH, **Fig. 7e** and **Fig. 7g**. As described in *Section 3.2*, the GF and GO coatings have a very weak interface with the substrate. The interface presents multiple large voids which hinder the adhesion of the coating to the substrate. Consequently, the coating is easily removed by the indenting counter electrode. Comparing the areas where the GF and GO coatings were removed with the areas on the rivet where the respective CNP were deposited, the latter is in the range of half of the former (470 µm to 235 µm and 460 µm to 275 µm, respectively). This shows that the coating area removed is higher than that deposited on the rivet. Additionally, these two coatings left behind CNP residue on the rivet, which was wiped away after the ECR measurements. This further demonstrates the fragility of these two coatings due to lack of adhesion with the substrate. The higher amount of CNP removed can be attributed to weaker adhesion to the substrate, compared to the adhesion between CNP. Consequently, when retracting the counter electrode, the CNP deposited on the counter electrode remove the CNP in the vicinity of the contact area. The CNT and CNH coatings, on the other hand, show a similar behavior regarding the diameter of the circumscribed area affected in the coating and deposited nanoparticle on the rivet's surface (250 µm in both cases for CNT and 220 µm to 200 µm for CNH). As the FIB cross sections from *Section 3.2* demonstrated, these two coatings present a better interface. That is, the coating-substrate interfaces are seamless (especially compared to the GF and GO). Therefore, the mechanical stability of the coating is superior. This is the reason why the area affected in the coatings matches the area affected in the rivets. The interaction between the CNP and the substrate is stable enough to prevent additional CNP removal when retracting the counter electrode.

3.6. Dual-cycle electrical characterization

Multiple loading and unloading semi-cycles provide useful information on the elasticity of the proposed coatings. An advantage

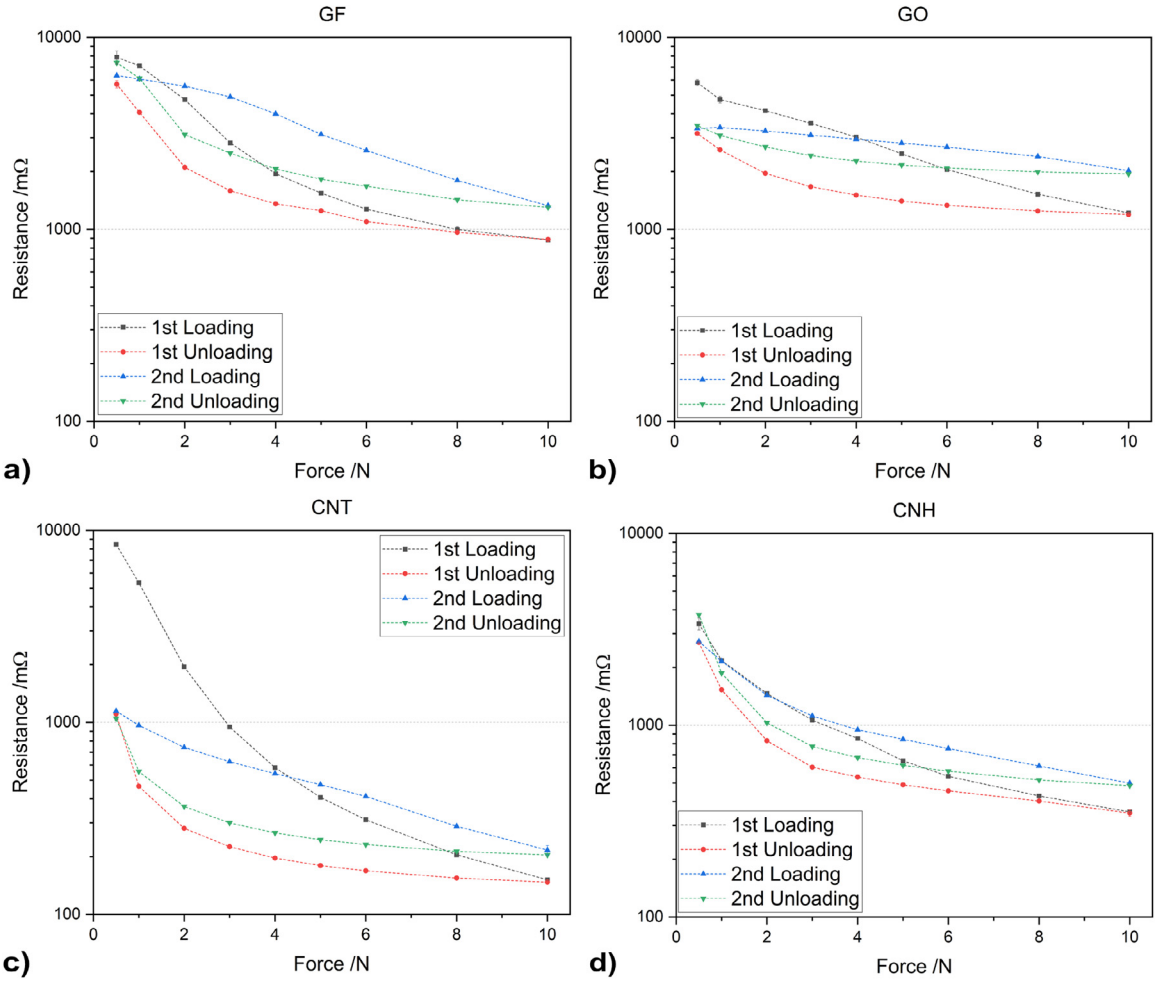

Fig. 8. Load-dependent ECR of coated samples over two cycles of a) GF, b) GO, c) CNT, and d) CNH. The gray line depicts the ECR values on the first loading semi-cycle, whereas the red line shows the first unloading semi-cycle. The blue and green line depict the ECR values of the second loading and unloading semi-cycles, respectively.

of CNP coatings is the ability of the coatings to return, to a certain degree, to their original form after the load has been removed. This elastic restitution of the coatings ensures repeatability in the contacting area after the first mating and un-mating cycle. Furthermore, this behavior improves the contacting area, consequently reducing the constriction resistance. Two-cycle ECR measurements were carried out on the four coatings produced. The ECR curves are shown in **Fig. 8**. As the figure shows, the coatings behave similarly on both measurement cycles. The most elastic coating measured was the CNH coating, since the curve corresponding to the first cycle is nearly the same for the second cycle. The least elastic coating measured was the CNT coating, showing high ECR values initially (for low loads in the first loading cycle). However, as the measurement cycle progresses, the resistance decreases and remains relatively low. The GF and GO behave in a similar manner. These coatings are not as elastic as the CNH coating, but these also do not show a significant decrease after the first loading cycle like the CNT coating. Between GF and GO, GO shows slightly more elasticity than GF. This is due to the inherent high flexibility and mechanical strength of the graphene nanoparticles. Furthermore, as observed in *Section 3.2*, GO particles form large networks. When loading on these GO clusters they will deform, copying the curved shape of the counter electrode. Contrarily, GF particles do not form clusters or agglomerates. In addition, GF particles are randomly oriented when deposited. Graphite interlayers interact weakly with one another. Therefore, when loading on a GF particle - displacing the particle from its original position - there is no restitution force. Consequently, the elasticity of the coating is relatively low.

The elasticity of the CNH coating can be attributed to two key factors, i.e., the compactness of the coating and intrinsic properties of the nanoparticle. The latter refers to the fact that CNH particles, when compressing a nanohorn axially, are capable of absorbing energy. When the compressing force is removed, the energy absorbed returns the nanohorn to its original shape. This property fundamentally guarantees an elastic coating. Although the CNH coating presents a porous network, the voids are small in dimensions. Therefore, when applying a normal load on the coating, the force does not significantly compact the coating; thus, the coating behaves elastically since the displacement is marginal.

Although the CNT coating does not show an elastic behavior in the first loading semi-cycle, in the subsequent semi-cycles it behaves moderately elastic. Nonetheless, this coating shows the lowest ECR values. All measurements taken after the first loading semi-cycle above 1 N normal load show an ECR value below 1000 mΩ. The minimum resistance value for this coating was observed at 10 N in the first unloading semi-cycle, with a resistance of approximately 150 mΩ. However, this coating also shows the highest initial ECR value in the first loading semi-cycle at 0.5 N, with an approximate value of 8460 mΩ. The initial high values of ECR may be a consequence of the large CNT agglomerates. Due to the geometry of CNT, when compressed radially, the electrostatic forces restitute the original shape of the CNT when the load is re-

Table 3
. Summary of key findings.

	GF	GO	CNT	CNH
Topography	Very low homogeneity	Low homogeneity	Mild homogeneity	High homogeneity
Compactness	High porosity	Moderately high porosity	Mild porosity	High compactness
Mean thickness /μm	12.8 ± 0.9	4.2 ± 1.2	5.5 ± 1.5	1.8 ± 0.2
Coating-substrate interface	Weak	Weak	Moderate	Seamless
Deposition rate	Moderate	Low	Low	Very high
ECR at 10 N /mΩ	373	985	141	219
Elastic restitution	Moderate	Moderate	(Initially) Low	Very high

moved. However, CNT agglomerates are formed by weakly-bonded CNT. Thus, the first loading semi-cycle breaks apart the CNT agglomerates, producing smaller agglomerates. Therefore, in the subsequent semi-cycles the resistance of the system is different from the first semi-cycle since the contacting surfaces are not the same.

In all cases, for high normal loads, the resistance of the system in the first cycle is higher than in the second cycle. This is a consequence of the deformation of the substrate. In the first loading semi-cycle, the substrate is mirror polished. As the load increases, the counter electrode penetrates the CNP coatings reaching the substrate. Consequently, the hard gold rivet indents the surface of the substrate deforming it. On the second cycle the counter electrode contacts the deformed surface. This should decrease the constriction resistance, approximating the real contact area to the apparent contact area. However, if that were the case, the resistance should decrease instead. The increase in electrical resistance in the second cycle (compared to the first unloading semi-cycle) may be a consequence of a deficient contact between the electrodes. For the analyzed coatings, the resistance values at 10 N in the first cycle is between 60% and 70% of the ECR values - at the same load - in the second cycle. Furthermore, the unloading semi-cycles show the lowest average resistance values throughout the entire semi-cycles. This behavior is a consequence of the coating. When unloading, the contact area between the counter electrode and the sample is gradually decreases. However, as the load on the coatings decreases, the CNP gradually return - approximately - to their initial positions, mimicking the geometry of the counter electrode. Therefore, as the load decreases the decrease in contact area is compensated by the coating, improving the electrical contact between the counter electrode and the coated sample.

The following table (**Table 3**) summarizes the key findings of this work. Through this study, it was determined that CNH coatings produce the most homogeneous topographies, followed by CNT, then GO, and GF the most heterogeneous topographies. Regarding compactness, CNH produce highly compact coatings, followed by CNT, then GO, with GF producing the most porous coatings. CNT and CNH coatings present adequate adhesion compared to GO and GF coatings, which show weak interactions with the substrate. The highest deposition rate was observed for CNH. GF follows, although with a much lower deposition rate. GO and CNT show similar deposition rates, the lowest out of the CNP in question. CNT present the lowest ECR at 10 N, followed by CNH and GF. GO shows the highest ECR at 10 N, with values close to 1000 mΩ. GF and GO coatings behave moderately elastic in multi-cycle ECR measurements. CNT showed the least elastic behavior, however after the first semi-cycle the elasticity moderately increased. CNH showed the highest elasticity out of the four CNP.

4. Conclusions

Four different CNP were deposited on copper substrates via EPD. Load-dependent ECR measurements showed that, for normal loads above 4 N, the resistance of the systems was always below 1 Ω, except for coatings produced with GO. The oxygen atoms present in GO act as scatter sites for the electros, hindering this coatings conductivity. Additionally, oxygen generates lattice defects in the graphene structure which further compromise the conductivity. CNT and CNH coatings proved the most favorable coatings. At 10 N the CNT and CNH coatings showed the lowest and second lowest ECR, respectively. Furthermore, although the CNT coating did not show an elastic behavior for the first loading semi-cycle, it did behave elastically for subsequent semi-cycles. On the other hand, the CNH coating shows a clear elastic behavior throughout both measurement cycles. Additionally, these coatings' interfaces with the substrate are seamless, thus guaranteeing a better adhesion and mechanical stability. Finally, these two coatings produce thin and uniform - in the case of CNH - coatings. Accordingly, these two CNP coatings have the potential application of protecting and lubricating electrical connectors for the following reasons:

- Both CNT and CNH have been proven effective as solid-state lubricants.
- They produce relatively compact coatings and have a hydrophobic behavior for atmospheric protection by manipulating their surface chemistry.
- Both CNT and CNH have high thermal conduction coefficients, thus dissipating the heat produced by Joule's effect.
- Above 4 N normal load, CNT and CNH showed ECR values below 400 mΩ.

In future works, it is of interest to analyze the ideal coating thicknesses (i.e., EPD duration) for the different CNP based on the ECR values measured. Moreover, tribological testing on the coatings produces is of interest. Fretting and scratch tests would help quantify the lubricating behavior of the CNP coatings and their adhesion, respectively. Additionally, different copper alloys are of interest, thus obtaining a wider understanding on how the substrate influences the deposition rate, adhesion, and electrical behavior of the systems. Furthermore, substituting GO with rGO can be a promising alternative for electrical contact applications. The absence of oxygen and fewer lattice defects in the graphene structure should improve the ECR of the coating. In addition, sessile drop tests are of interest; therefore analyzing the wetting behavior of the different CNP coatings.

Declaration of Competing Interest

The authors declare that they have no known competing financial interests or personal relationships that could have appeared to influence the work reported in this paper.

Acknowledgements

B. Alderete wishes to acknowledge the support from the German Academic Exchange Service (DAAD). The authors gratefully acknowledge funding in the ZuMat project, supported by the State of Saarland from the European Regional Development Fund (Europäischen Fonds für Regionale Entwicklung, EFRE).

References

[1] P. van Dijk, Critical aspects of electrical connector contacts, in: Proc. 21st Int. Conf. Electr. Contacts, Zurich, 2002.
[2] P.G. Slade (Ed.), Electrical Contacts Pinrciples and Applications, Second Edi, Taylor & Francis, Boca Raton, 2014.
[3] E.H.L. Falcao, F. Wudl, Carbon allotropes: beyond graphite and diamond, J. Chem. Technol. Biotechnol 82 (2007) 524–531, doi:10.1002/jctb.1693.
[4] A. Hirsch, The era of carbon allotropes, Nat. Mater. 9 (2010) 868–871, doi:10.1038/nmat2885.
[5] B. Zhmud, B. Pasalskiy, Nanomaterials in lubricants: An industrial perspective on current research, Lubricants 1 (2013) 95–101, doi:10.3390/lubricants1040095.
[6] Y. Chen, P. Renner, H. Liang, Dispersion of nanoparticles in lubricating oil: a critical review, Lubricants 7 (2019), doi:10.3390/lubricants7010007.
[7] W. Dai, B. Kheireddin, H. Gao, H. Liang, Roles of nanoparticles in oil lubrication, Tribol. Int. 102 (2016) 88–98, doi:10.1016/j.triboint.2016.05.020.
[8] W. Bollman, J. Spreadborough, Action of Graphite as a Lubricant, Nature 186 (1960) 29–30, doi:10.1038/186029a0.
[9] H. Wang, Graphite solid lubrication materials, in: Q.J. Wang, Z.-W. Chung (Eds.), Encycl. Tribol., Springer US, Boston, MA, 2013, pp. 1550–1555, doi:10.1007/978-0-387-92897-5_1261.
[10] T.W. Scharf, S.V. Prasad, Solid lubricants: A review, J. Mater. Sci. 48 (2013) 511–531, doi:10.1007/s10853-012-7038-2.
[11] H.E. Sliney, Solid Lubrificants, 1991. https://ntrs.nasa.gov/api/citations/19910013083/downloads/19910013083.pdf.
[12] F.J. Clauss, Solid Lubricants and Self-Lubricating Solids, Academic Press, New York and London, 1972.
[13] E.R. Braithwaite, Solid Lubricants and Surfaces, Pergamon Press Ltd.g, Oxford, 1964.
[14] C.-G. Lee, Y.-J. Hwang, Y.-M. Choi, J.-K. Lee, C. Choi, J.-M. Oh, A study on the tribological characteristics of graphite nano lubricants, Int. J. Precis. Eng. Manuf. 10 (2009) 85–90, doi:10.1007/s12541-009-0013-4.
[15] Z.J. Zhang, D. Simionesie, C. Schaschke, Graphite and hybrid nanomaterials as lubricant additives, Lubricants 2 (2014) 44–65, doi:10.3390/lubricants2020044.
[16] G. Fugallo, A. Cepellotti, L. Paulatto, M. Lazzeri, N. Marzari, F. Mauri, Thermal conductivity of graphene and graphite: Collective excitations and mean free paths, Nano Lett 14 (2014) 6109–6114, doi:10.1021/nl502059f.
[17] E. Planes, L. Flandin, N. Alberola, Polymer composites bipolar plates for PEMFCs, Energy Procedia 20 (2012) 311–323, doi:10.1016/j.egypro.2012.03.031.
[18] W. Park, J. Hu, L.A. Jauregui, X. Ruan, Y.P. Chen, Electrical and thermal conductivities of reduced graphene oxide/polystyrene composites, Appl. Phys. Lett. 104 (2014), doi:10.1063/1.4869026.
[19] A. Kozbial, F. Zhou, Z. Li, H. Liu, L. Li, Are Graphitic Surfaces Hydrophobic? Acc. Chem. Res. 49 (2016) 2765–2773, doi:10.1021/acs.accounts.6b00447.
[20] K.S. Novoselov, V.I. Fal'Ko, L. Colombo, P.R. Gellert, M.G. Schwab, K. Kim, A roadmap for graphene, Nature 490 (2012) 192–200, doi:10.1038/nature11458.
[21] C.N.R. Rao, K. Biswas, K.S. Subrahmanyam, A. Govindaraj, Graphene, the new nanocarbon, J. Mater. Chem. 19 (2009) 2457–2469, doi:10.1039/b815239j.
[22] A.K. Geim, Graphene : Status and Prospects, Science 324 (80) (2009) 1530–1535, doi:10.1126/science.1158877.
[23] D.G. Papageorgiou, I.A. Kinloch, R.J. Young, Mechanical properties of graphene and graphene-based nanocomposites, Prog. Mater. Sci. 90 (2017) 75–127, doi:10.1016/j.pmatsci.2017.07.004.
[24] I.N. Kholmanov, C.W. Magnuson, A.E. Aliev, H. Li, B. Zhang, J.W. Suk, L.L. Zhang, E. Peng, S.H. Mousavi, A.B. Khanikaev, R. Piner, G. Shvets, R.S. Ruoff, Improved electrical conductivity of graphene films integrated with metal nanowires, Nano Lett 12 (2012) 5679–5683, doi:10.1021/nl302870x.
[25] D. Berman, A. Erdemir, A.V. Sumant, Graphene: A new emerging lubricant, Mater. Today. 17 (2014) 31–42, doi:10.1016/j.mattod.2013.12.003.
[26] L. Liu, M. Zhou, L. Jin, L. Li, Y. Mo, G. Su, X. Li, H. Zhu, Y. Tian, Recent advances in friction and lubrication of graphene and other 2D materials: Mechanisms and applications, Friction 7 (2019) 199–216, doi:10.1007/s40544-019-0268-4.
[27] R.K. Singh, R. Kumar, D.P. Singh, Graphene oxide: Strategies for synthesis, reduction and frontier applications, RSC Adv 6 (2016) 64993–65011, doi:10.1039/c6ra07626b.
[28] Y. Zhu, S. Murali, W. Cai, X. Li, J.W. Suk, J.R. Potts, R.S. Ruoff, Graphene and graphene oxide: Synthesis, properties, and applications, Adv. Mater. 22 (2010) 3906–3924, doi:10.1002/adma.201001068.
[29] M.S.A. Bhuyan, M.N. Uddin, M.M. Islam, F.A. Bipasha, S.S. Hossain, Synthesis of graphene, Int. Nano Lett. 6 (2016) 65–83, doi:10.1007/s40089-015-0176-1.
[30] C. Botas, P. Álvarez, P. Blanco, M. Granda, C. Blanco, R. Santamaría, L.J. Romasanta, R. Verdejo, M.A. López-Manchado, R. Menéndez, Graphene materials with different structures prepared from the same graphite by the Hummers and Brodie methods, Carbon N. Y. 65 (2013) 156–164, doi:10.1016/j.carbon.2013.08.009.
[31] N.I. Zaaba, K.L. Foo, U. Hashim, S.J. Tan, W.W. Liu, C.H. Voon, Synthesis of Graphene Oxide using Modified Hummers Method: Solvent Influence, Procedia Eng 184 (2017) 469–477, doi:10.1016/j.proeng.2017.04.118.
[32] V.B. Mohan, R. Brown, K. Jayaraman, D. Bhattacharyya, Characterisation of reduced graphene oxide: Effects of reduction variables on electrical conductivity, Mater. Sci. Eng. B Solid-State Mater. Adv. Technol. 193 (2015) 49–60, doi:10.1016/j.mseb.2014.11.002.
[33] H. Liang, Y. Bu, J. Zhang, Z. Cao, A. Liang, Graphene oxide film as solid lubricant, ACS Appl. Mater. Interfaces. 5 (2013) 6369–6375, doi:10.1021/am401495y.
[34] A. Senatore, V. D'Agostino, V. Petrone, P. Ciambelli, M. Sarno, Graphene oxide nanosheets as effective friction modifier for oil lubricant: materials, methods, and tribological results, ISRN Tribol. 2013 (2013) 1–9, doi:10.5402/2013/425809.
[35] P. Wu, X. Chen, C. Zhang, J. Zhang, J. Luo, J. Zhang, Modified graphene as novel lubricating additive with high dispersion stability in oil, Friction 9 (2021) 143–154, doi:10.1007/s40544-019-0359-2.
[36] G. Wang, B. Wang, J. Park, J. Yang, X. Shen, J. Yao, Synthesis of enhanced hydrophilic and hydrophobic graphene oxide nanosheets by a solvothermal method, Carbon N. Y. 47 (2009) 68–72, doi:10.1016/j.carbon.2008.09.002.
[37] L. Xu, J. Teng, L. Li, H.D. Huang, J.Z. Xu, Y. Li, P.G. Ren, G.J. Zhong, Z.M. Li, Hydrophobic graphene oxide as a promising barrier of water vapor for regenerated cellulose nanocomposite films, ACS Omega 4 (2019) 509–517, doi:10.1021/acsomega.8b02866.
[38] R. Saito, G. Dresselhaus, M.S. Dresselhaus, Physical Properties of Carbon Nanotubes, Imperial College Press, London, 1998, doi:10.1142/p080.
[39] M.S. Dresselhaus, G. Dresselhaus, R. Saito, Physics of carbon nanotubes, Carbon N. Y. 33 (1995) 883–891, doi:10.1016/0008-6223(95)00017-8.
[40] V.N. Popov, Carbon nanotubes: properties and application, Mater. Sci. Eng. R Reports. 43 (2004) 61–102, doi:10.1016/j.mser.2003.10.001.
[41] T.W. Ebbesen, Carbon nanotubes, Chem. Eng. News. 79 (2001) 11.
[42] S. Nasir, M.Z. Hussein, Z. Zainal, N.A. Yusof, Carbon-based nanomaterials/allotropes: a glimpse of their synthesis, properties and some applications, Materials (Basel) 11 (2018) 1–24, doi:10.3390/ma11020295.
[43] N. Saifuddin, A.Z. Raziah, A.R. Junizah, Carbon nanotubes: A review on structure and their interaction with proteins, J. Chem. 2013 18 (2013), doi:10.1155/2013/676815.
[44] M. Moniruzzaman, K.I. Winey, Polymer nanocomposites containing carbon nanotubes, Macromolecules 39 (2006) 5194–5205, doi:10.1021/ma060733p.
[45] C. Li, E.T. Thostenson, T.W. Chou, Sensors and actuators based on carbon nanotubes and their composites: a review, Compos. Sci. Technol 68 (2008) 1227–1249, doi:10.1016/j.compscitech.2008.01.006.
[46] P. Kim, L. Shi, A. Majumdar, P.L. McEuen, Thermal transport measurements of individual multiwalled nanotubes, Phys. Rev. Lett. 87 (2001) 215502-1-215502-4, doi:10.1103/PhysRevLett.87.215502.
[47] J. Klinovaja, M.J. Schmidt, B. Braunecker, D. Loss, Carbon nanotubes in electric and magnetic fields, Phys. Rev. B - Condens. Matter Mater. Phys 84 (2011), doi:10.1103/PhysRevB.84.085452.
[48] E.M. Pérez, N. Martín, π-π Interactions in carbon nanostructures, Chem. Soc. Rev. 44 (2015) 6425–6433, doi:10.1039/c5cs00578g.
[49] B. Alderete, T. MacLucas, D. Espin, S.P. Brühl, F. Mücklich, S. Suarez, Near superhydrophobic carbon nanotube coatings obtained via electrophoretic deposition on low-alloy steels, Adv. Eng. Mater. (2021), doi:10.1002/adem.202001448.
[50] L. Reinert, F. Lasserre, C. Gachot, P. Grützmacher, T. MacLucas, N. Souza, F. Mücklich, S. Suarez, Long-lasting solid lubrication by CNT-coated patterned surfaces, Sci. Rep. 7 (2017) 1–13, doi:10.1038/srep42873.
[51] L. Reinert, S. Suarez, A. Rosenkranz, Tribo-mechanisms of carbon nanotubes: friction and wear behavior of CNT-reinforced nickel matrix composites and CNT-coated bulk nickel, Lubricants 4 (2016) 11, doi:10.3390/lubricants4020011.
[52] L. Reinert, I. Green, S. Gimmler, B. Lechthaler, F. Mücklich, S. Suàrez, Tribological behavior of self-lubricating carbon nanoparticle reinforced metal matrix composites, Wear 408-409 (2018) 72–85, doi:10.1016/j.wear.2018.05.003.
[53] J.A.C. Cornelio, P.A. Cuervo, L.M. Hoyos-Palacio, J. Lara-Romero, A. Toro, Tribological properties of carbon nanotubes as lubricant additive in oil and water for a wheel-rail system, J. Mater. Res. Technol. 5 (2016) 68–76, doi:10.1016/j.jmrt.2015.10.006.
[54] F. Dassenoy, L. Joly-Pottuz, J.M. Martin, T. Mieno, in: V.N. Popov, P. Lambin (Eds.), Carbon Nanotubes as Advanced Lubricant Additives, Carbon Nanotub, Springer Netherlands, 2006, pp. 237–238.
[55] J. Kaluzny, A. Merkisz-Guranowska, M. Giersig, K. Kempa, Lubricating performance of carbon nanotubes in internal combustion engines - engine test results for CNT enriched oil, Int. J. Automot. Technol 18 (2017) 1047–1059 https://doi.org/10.1007/s12239−017−0102−9.
[56] N. Karousis, I. Suarez-Martinez, C.P. Ewels, N. Tagmatarchis, Structure, properties, functionalization, and applications of carbon nanohorns, Chem. Rev. 116 (2016) 4850–4883, doi:10.1021/acs.chemrev.5b00611.
[57] S. Zhu, G. Xu, Single-walled carbon nanohorns and their applications, Nanoscale 2 (2010) 2538–2549, doi:10.1039/c0nr00387e.
[58] T. MacLucas, S. Suarez, On the solid lubricity of electrophoretically deposited carbon nanohorn coatings, Lubricants 7 (2019), doi:10.3390/lubricants7080062.
[59] M. Yudasaka, S. Iijima, V.H. Crespi, Single-wall carbon nanohorns and nanocones, Top. Appl. Phys. 111 (2008) 605–629, doi:10.1007/978-3-540-72865-8_19.
[60] D. Maharaj, B. Bhushan, S. Iijima, Effect of carbon nanohorns on nanofriction and wear reduction in dry and liquid environments, J. Colloid Interface Sci. 400 (2013) 147–160, doi:10.1016/j.jcis.2013.03.008.
[61] Y. Tao, D. Noguchi, C.M. Yang, H. Kanoh, H. Tanaka, M. Yudasaka, S. Iijima, K. Kaneko, Conductive and mesoporous single-wall carbon nanohorn/organic aerogel composites, Langmuir 23 (2007) 9155–9157, doi:10.1021/la701660w.
[62] P. Karfa, S. De, K.C. Majhi, R. Madhuri, P.K. Sharma, Functionalization of carbon nanostructures, in: D.L. Andrews, R.H. Lipson, T. Nann (Eds.), Compr. Nanosci. Nanotechonlogy, Second, Academic Press, 2019, pp. 123–144, doi:10.1016/B978-0-12-803581-8.11225-1.
[63] A.R. Boccaccini, J. Cho, J.A. Roether, B.J.C. Thomas, E.Jane Minay, M.S.P. Shaffer, Electrophoretic deposition of carbon nanotubes, Carbon N. Y. 44 (2006) 3149–3160, doi:10.1016/j.carbon.2006.06.021.

[64] J.H. Dickerson, A.R. Boccaccini, Electrophoretic Deposition of Nanomaterials, 2nd Ed., 2011, doi:10.1007/978-1-4614-4605-7.
[65] P. Sarkar, P.S. Nicholson, Electrophoretic deposition (EPD): mechanisms, kinetics, and application to ceramics, J. Am. Ceram. Soc. 79 (1996) 1987–2002, doi:10.1111/j.1151-2916.1996.tb08929.x.
[66] H.C. Hamaker, Formation of a Deposit by Electrophoresis, Trans. Faraday Soc 30 (1940) 279–287.
[67] M. Farrokhi-Rad, T. Shahrabi, Electrophoretic deposition of titania nanoparticles: sticking parameter determination by an in situ study of the EPD kinetics, J. Am. Ceram. Soc. 95 (2012) 3434–3440, doi:10.1111/j.1551-2916.2012.05402.x.
[68] M. Atiq Ur Rehman, Q. Chen, A. Braem, M.S.P. Shaffer, A.R. Boccaccini, Electrophoretic deposition of carbon nanotubes: recent progress and remaining challenges, Int. Mater. Rev. 0 (2020) 1–30, doi:10.1080/09506608.2020.1831299.
[69] Y. Ma, J. Han, M. Wang, X. Chen, S. Jia, Electrophoretic deposition of graphene-based materials: a review of materials and their applications, J. Mater. 4 (2018) 108–120, doi:10.1016/j.jmat.2018.02.004.
[70] L. Reinert, M. Zeiger, S. Suarez, V. Presser, F. Mücklich, Dispersion analysis of carbon nanotubes, carbon onions, and nanodiamonds for their application as reinforcement phase in nickel metal matrix composites, RSC Adv 5 (2015) 95149–95159, doi:10.1039/c5ra14310a.
[71] M.F. De Riccardis, D. Carbone, A. Rizzo, A novel method for preparing and characterizing alcoholic EPD suspensions, J. Colloid Interface Sci. 307 (2007) 109–115, doi:10.1016/j.jcis.2006.10.037.
[72] A. Loyd, J. Hemond, R. Martens, A preliminary investigation of graphite, graphene and carbon nanotubes (CNT's) as solid state lubricants, Electr. Contacts, in: Proc. Annu. Holm Conf. Electr. Contacts, 2011, pp. 22–30, doi:10.1109/HOLM.2011.6034776.
[73] R. Puyol, S. Suarez, A contact resistance measurement setup for the study of novel contacts, IEEE URUCON (2017) 1–4, doi:10.1109/URUCON.2017.8171881.
[74] K.E. Trinh, E. Ramos-Moore, I. Green, C. Pauly, M. Zamanzade, F. Mucklich, Topographical and microstructural effects of laser surface texturing on tin-coated copper electrical connectors under load cycling, IEEE Trans. Components, Packag. Manuf. Technol 7 (2017) 582–590, doi:10.1109/TCPMT.2017.2659224.
[75] K.E. Trinh, F. Mücklich, E. Ramos-Moore, The role of microstructure and surface topography in the electrical behavior of Sn-coated Cu contacts, in: 27th Int. Conf. Electr. Contacts, ICEC 2014 - Proc., 2014, pp. 243–248.
[76] TektronixLow Level Measurements Handbook, Precision DC Current, 7th Editio, Voltage and Resistance Measurements, Beaverton, 2016 https://download.tek.com/document/LowLevelHandbook_7Ed.pdf.
[77] E.M. Bock, Low-level contact resistance characterization, AMP J. Technol. 3 (1993) 64–68.
[78] B. Alderete, R. Puyol, S. Slawik, E. Espin, F. Mücklich, S. Suarez, Multipurpose setup used to characterize tribo-electrical properties of electrical contact materials, MethodsX 8 (2021) 101498, doi:10.1016/j.mex.2021.101498.

ARTICLE IV

Evaluating the Effect of Unidirectional Loading on the Piezoresistive Characteristics of Carbon Nanoparticles

Bruno Alderete*, Frank Mücklich, Sebastian Suarez

Chair of Functional Materials, Saarland University, Campus D3.3, 66123 Saarbrücken, Germany

Research article
Published in "*Scientific Reports*" (2024)
Impact Factor: 3.8 (2023)

Accessible online at: doi.org/10.1038/s41598-024-59673-5

Own Contribution: Conceptualization; Methodology; Formal Analysis; Validation; Investigation; Data Curation; Writing – Original Draft; Visualization.

Cite this article as: B. Alderete, F. Mücklich, S. Suarez, Evaluating the effect of unidirectional loading on the piezoresistive characteristics of carbon nanoparticles, Sci Rep 14 (2024) 9247. https://doi.org/10.1038/s41598-024-59673-5.

scientific reports

Check for updates

OPEN

Evaluating the effect of unidirectional loading on the piezoresistive characteristics of carbon nanoparticles

Bruno Alderete✉, Frank Mücklich & Sebastian Suarez

The piezoresistive effect of materials can be adopted for a plethora of sensing applications, including force sensors, structural health monitoring, motion detection in fabrics and wearable, etc. Although metals are the most widely adopted material for sensors due to their reliability and affordability, they are significantly affected by temperature. This work examines the piezoresistive performance of carbon nanoparticle (CNP) bulk powders and discusses their potential applications based on strain-induced changes in their resistance and displacement. The experimental results are correlated with the characteristics of the nanoparticles, namely, dimensionality and structure. This report comprehensively characterizes the piezoresistive behavior of carbon black (CB), onion-like carbon (OLC), carbon nanohorns (CNH), carbon nanotubes (CNT), dispersed carbon nanotubes (CNT-D), graphite flakes (GF), and graphene nanoplatelets (GNP). The characterization includes assessment of the ohmic range, load-dependent electrical resistance and displacement tracking, a modified gauge factor for bulk powders, and morphological evaluation of the CNP. Two-dimensional nanostructures exhibit promising results for low loads due to their constant compression-to-displacement relationship. Additionally, GF could also be used for high load applications. OLC's compression-to-displacement relationship fluctuates, however, for high load it tends to stabilize. CNH could be applicable for both low and high loading conditions since its compression-to-displacement relationship fluctuates in the mid-load range. CB and CNT show the most promising results, as demonstrated by their linear load-resistance curves (logarithmic scale) and constant compression-to-displacement relationship. The dispersion process for CNT is unnecessary, as smaller agglomerates cause fluctuations in their compression-to-displacement relationship with negligible influence on its electrical performance.

Keywords Carbon black, Carbon nanohorns, Carbon nanotubes, Graphene nanoplatelets, Graphite flakes, Onion-like carbon

The piezoelectric effect is the phenomenon of electrical charge concentration in materials when a force is applied[1]. This effect finds a plethora of applications since it can be exploited for sensors and actuators. Similarly, the piezoresistive effect is the change in a material's electrical resistance caused by its dimensional changes, which can originate from external forces or thermal expansion[2]. Piezoresistance has a wide range of applications, and recent innovations in materials science have expanded the potential uses of piezoresistive sensors. These include structural health monitoring, motion detection in fabrics and wearables, and human–machine interfaces, among others[3,4]. The most commonly used materials for their piezoresistive behavior are metals and metal alloys, semiconductors, piezoceramics (such as perovskite and tetragonal/rhombohedral crystals), and conductive polymeric composites. However, as previously alluded, the piezoresistance behavior of these materials is highly dependent on temperature, thus requiring temperature compensation[3]. Carbon-based strain sensors are particularly attractive due to their temperature independence, which is a substantial advantage over conventional piezoresistive materials. This eliminates the need for additional dedicated electronics to compensate for thermal impact. The thermal stability of carbon nanoparticles (CNP) is not only sought after because they eliminate this requirement,

Chair of Functional Materials, Saarland University, Campus D3.3, 66123 Saarbrücken, Germany. ✉email: bruno.alderete@uni-saarland.de

but they can a withstand extreme temperatures (high and low), as well as thermal fluctuations[4]. This characteristic makes CNP a promising material for sensor applications.

Multiple researchers have studied the piezoresistive performance of CNP, however, their studies focus on individual nanostructures or incorporate CNP within composite materials[4–14]. However, there is a lack of literature analyzing the behavior and performance of CNP bulk powders. Due to the versatility of the carbon atom, it is capable of forming different carbon–carbon bonds. Thus, carbon can form different allotropes, which depending on the hybridization state, changes their properties[15,16]. Accordingly, in this study we sought out to evaluate the piezoresistive behavior of different carbon archetypical structures: i.e., quasi-zero-dimensional (fullerene-type), one-dimensional (nanotube-type), and two-dimensional (graphene-type) nanostructures. Therefore, the CNP evaluated in this study are carbon black (CB), onion-like carbon (OLC), carbon nanohorns (CNH), carbon nanotubes (CNT), graphite flakes (GF), and graphene nanoplatelets (GNP). Certain CNP tend to form agglomerates due to Van der Waals interactions. Therefore, to evaluate the effect of CNP agglomeration on its piezoresistance, the as-received CNT were dispersed to reduce the size of CNT agglomerates (henceforth CNT-D).

The electrical properties of CNP have garnered much attention from the research community, leading to a profusion of applications for these unique nanostructures. Applications range from the aforementioned sensing and actuating purposes to applications such as printed electronics and their incorporation as reinforcement phase in polymeric matrices[17–19]. Additionally, the transport properties of CNP make them suitable for electronic bridging and as terminal interconnection media in micro- and nano-electromechanical systems. Moreover, the piezoresistive behavior of CNP can be utilized to determine the effective contact load in electrical connectors. This is typically calculated through simplified modelling (e.g., finite element method). By placing a CNP interlayer between two connectors the contact load can be rapidly and easily determined by measuring the contact resistance (using Holm's contact resistance equation). Therefore, understanding the piezoresistive behavior and determining the electrical resistance of CNP is of considerable interest in the field of sensors, electronics, and materials science.

In our previous work, different CNP have been used as protective coatings due to their hydrophobic behavior[20,21], as topography offsetting interfaces due to their elasticity[22], as well as for wear protection[23–27]. Moreover, CNP-containing composites have been studied for tribological and electrical applications[28–33]. However, in these studies, electrical characterization of the coating material or reinforcement phase was always in conjunction with the substrate or matrix material, respectively. Therefore, it is of significant interest to understand the electrical performance solely of the CNP. Thereupon, the objective of this work is to analyze the piezoresistive performance of the CNP under unidirectional compressive stress across a wide loading range. The results will determine the repeatability and reliability of the CNP, as well as identify the loading ranges with the best performance. This will enable the selection of the appropriate CNP for specific applications – such as wearable technology, strain sensors, etc. The six CNP analyzed were selected based on their mechanical and electrical properties, their geometry, their versatility, and their potential to be used as a straightforward piezoresistive medium. A non-conductive vessel was designed to contain the CNP between two electrodes and electrically characterized by load-dependent and current-dependent electrical resistance measurements under atmospheric conditions. The former aims to evaluate the piezoresistive behavior of the CNP, whereas the latter the ohmicity of the CNP[34]. The gauge factor (K from Eq. 1)[2] represents the ratio between the change in electrical resistance of a piezoresistive material and the mechanical strain that the piezoresistive material has undergone. However, the CNP in this work are mainly subjected to compaction and to a lesser extent to mechanical strain due to the porous nature of the bulk powders. Therefore, an analogous relationship (K_b factor) is proposed and discussed.

$$K = \frac{\Delta R/R_0}{\varepsilon}, \quad where\ \varepsilon = \frac{\Delta X}{X_0} \tag{1}$$

This work aims to analyze the piezoresistive behavior of bulk powder CNP with varying dimensionality, morphology, and chemistry. The characteristics of the CNP are subsequently correlated with their piezoresistive behavior and an adapted gauge factor is proposed to better predict their performance. This analysis is crucial since there is limited literature available that evaluates the influence of external compression on the conductivity of bulk CNP powders[35–37]. This work expands on the literature by correlating the change in electrical resistance with the strain—i.e., CNP displacement—and nanostructure dimensionality and morphology. In addition, with the aforementioned modified gauge factor it is possible to estimate the piezoresistive performance of the CNP without the need for experimental measurements.

Materials and methods

In this study, six different CNP were analyzed (CB, OLC, CNH, CNT, GF, and GNP). The CB particles (Orion, Luxembourg) possess over 96% carbon, 0.2–1.3 wt.% hydrogen, 0.2–0.5 wt.% oxygen, 0–0.7 wt.% nitrogen, and 0.1–1 wt.% sulfur, with a mean particle size between 10 nm up to 500 nm, approximately. The OLC were synthesized from carbon nanodiamonds (NaBond Technologies Co., China),—carbon purity greater than 98%, with individual diameters ranging from 4 to 8 nm—by annealing the nanodiamonds in a graphite crucible in a vacuum furnace (between 1×10^{-4} and 1×10^{-3} mbar) with a tungsten heater (three hour holding time at 1700 °C with a heating rate of 10 °C)[38]. The single-walled CNH used were dahlia-type, produced by rapid condensation of carbon atoms without a catalyst (Carbonium SRL, Italy). The as-received high-purity CNH have a horn diameter between 3 and 5 nm, horn lengths between 30 and 50 nm, and a cluster diameter between 60 and 120 nm. The CNT used were chemical vapor deposition-grown multi-walled CNT (Graphene Supermarket, USA), with an outer diameter distribution between 50 and 85 nm, an as-received state length from 10 to 15 µm, and carbon purity over 94%. Dispersed CNT were analyzed with the aim of evaluating the influence of agglomerate size on the piezoresistive behavior of CNT. CNT agglomerate size was reduced by dispersing the as-received CNT in ethylene glycol (EG)

at a concentration of 0.2 mg_{CNT}/ml_{EG}, followed by 5 min of homogenization (Ultra-Turrax T-25, IKA, Germany) at 7.5 krpm and 10 min in an ultrasound bath. This colloid was then placed inside a ventilated furnace at 150 °C for 48 h. GF (Alfa Aesar, Germany) with a median size between 7 and 10 µm, 99.8% purity were used. The GNP used consist of 3–8 graphene monolayers, with lateral dimensions between 2 and 8 µm, a carbon purity greater than 98 wt.% and a moisture content below 1 wt.% (Graphene Supermarket, USA). For morphological analysis, the different CNP were micrographed by electron microscopy (Helios™ G4 PFIB CXe DualBeam™ Super, Thermo-Fisher Scientific, The Netherlands) using Through-the-Lens detectors at an acceleration voltage of 5 kV and a current of 0.1 nA. In addition, the as-received CNP were micrographed by high resolution transmission electron microscopy (HR-TEM) to better analyze their morphology and dimensionality. The HR-TEM (JEOL ARM200, Japan) micrographs were acquired at 200 kV and are shown in Fig. 1. As the figure shows, three distinct dimensionalities can be observed. CB, OLC, and CNH (Fig. 1c–e) are quasi-zero-dimensional nanostructures, whereas the CNT (Fig. 1b) are one-dimensional nanostructures. Furthermore, GNP and GF (the latter of which cannot be micrographed by TEM due to the particle's thickness) are two-dimensional carbon nanostructures. For the purposes of this study, and based on its performance, GF is considered a two-dimensional particle, despite it being dimensionally larger.

Electrical testing was performed using a custom tribo-electrical testing rig[39]. In order to measure the electrical resistance of the CNP, a few modifications were required, primarily the design of an appropriate vessel for the CNP. The vessel is a 20 mm long cylinder, with an outer diameter of 23 mm and an inner diameter of 12.7 mm. The cylinder is made of a non-conductive polymer. The ends of the vessel were capped with two aluminum disks; these disks are the contacting electrodes in the testing rig. The aluminum disks were ground (P1200 grit silicon carbide grinding paper) and polished (6 µm, 3 µm, 1 µm, and 0.25 µm) to obtain a mirror polished surface. After polishing, the disks were coated with $Au_{80}Pd_{20}$ via plasma-assisted PVD to reduce the influence of aluminum corrosion and to improve the electrical connection prior to electrical resistance measurements. The coating was performed using argon plasma at 2×10^{-2} mbar and a current between 20 and 25 mA. A total of 3 deposition cycles were carried out on all contacting electrodes, each of 2 min duration, for a total of 6 min. The roughness of the resulting coated aluminum caps was measured via confocal laser scanning microscopy (LEXT OLS4100, Olympus, Japan) and showed a root mean square roughness of $S_{rms} = 0.03$ µm. In the modified setup, one of the

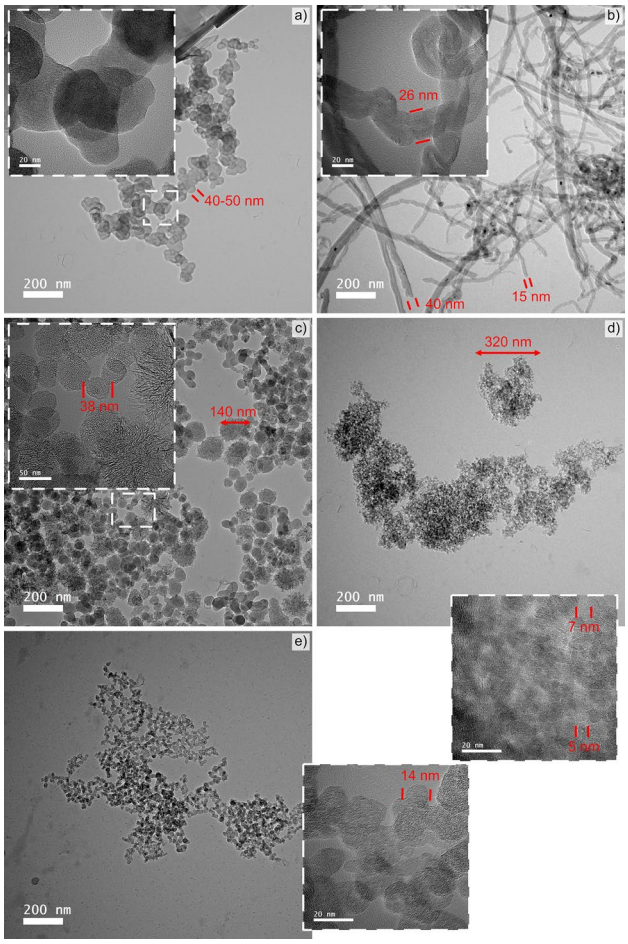

Figure 1. HR-TEM micrographs of (**a**) GNP, (**b**) CNT, (**c**) CNH, (**d**) OLC, and (**e**) CB acquired at ×50,000. Insets show magnified view of the different CNP.

electrodes is mounted directly onto the testing rig. The other electrode is fixed onto the end of the plastic vessel via four grub screws. The electrode/vessel system was then mounted onto the sample holder of the testing rig using conductive double-sided adhesive copper foil (Plano GmbH, Germany).

For piezoresistance measurements, the vessels were filled with 100 mg of CNP. The setup is then mounted onto the testing rig for electrical characterization. A schematic representation of the electrical resistance measurements is shown in Fig. 2a, b. The uncompressed, porous nanoparticles are depicted in Fig. 2a, whereas Fig. 2b depicts the improved interconnectivity between the nanoparticles as the load increases. Figure 2c is a schematic of the aluminum vessel caps.

Piezoresistance of the CNP was measured via load-dependent electrical resistance between 0.25 N and 10 N (corresponding to pressures ranging from 2 kPa up to 80.3 kPa). At each load, a current of 0.05 mA_{DC} was supplied using a Keithley 2400 SMU source. The normal load was held constant during resistance measurements with an error consistently below 0.05 N (i.e., 0.4 kPa). The voltage drop between the parallel aluminum vessel caps was measured ten times per load using a Keithley 2182a nanovoltmeter. The displacement between each established load was measured using a high-precision linear stage (precision of 0.2 µm[39]) by acquiring the current position of the stage once each load was established. Further electrical analysis was carried out through current-dependent electrical resistance measurements (henceforth, current sweep) with the aim of evaluating the ohmic behavior—or lack thereof—of the CNP in question. Voltage drop was measured ten times and averaged at a constant normal load of 2 N (i.e., 16 kPa) sourcing currents between 1 μA_{DC} up to 10 mA_{DC}. In both experiments, at least four tests were done per CNP with the bulk particles compacted prior to resistance measurements to achieve reliable and reproducible results. Therefore, the initial state of the CNP does not affect subsequent tests. During electrical tests, the ambient temperature and humidity were kept constant at 23 ± 2 °C and 57% ± 3% r.h., respectively.

Moreover, the dominant deformation mechanism that the CNP underwent was evaluated by the methodology proposed by Tamai et al.[40]. For this analysis, the load-dependent resistance curves were plotted in double logarithmic scale and the resistance curves linearly fitted. The slope of the fitted curve corresponds to the n factor in Eq. (2), where R_t is the total resistance, F is the force applied, and the numerator is a constant value that incorporates resistivity and hardness of the materials in question, as well as the influence of any surface contaminants present[41].

$$R_t = \left(\frac{Constant}{F}\right)^n \tag{2}$$

When the exponent (slope of the fitted line) takes a value of − 1/3 or − 2/3 the methodology suggests that elastic deformation is predominant in the system. Conversely, if the n factor takes a value of − 1/2 or − 1, plastic deformation is dominant. Similarly, the methodology proposed by Tamai et al. can also be used to predict the main source of electrical resistance in the system. When the n factor takes a value of − 1/3 or − 1/2, the constriction resistance is dominant in the system, whereas film resistance dominates for values of − 2/3 or − 1. It is important to note, however, that this analysis is highly theoretical in nature and applicable to a single deforming body. The purpose of this methodology is to verify the applicability of the method and validate the elasticity of the CNP.

Results and discussions

Ohmic response

The ohmic behavior of the different CNP was evaluated by performing current sweep tests. This experiment consists of contacting at a constant normal load and measuring the change in electrical resistance as different current levels are applied, thus providing information on the direct proportionality between the sourced current and the voltage drop measured. The results from the current sweep for the different CNP are shown in Fig. 3. The shaded region in Fig. 3 highlights the ohmic regime of the CNP, which is largely consistent for all nanoparticles from 0.05 mA to 10 mA. At lower current levels the resistance tends to increase, although the increase in resistance for currents below 0.05 mA depends on the particular CNP. The current is flowing through the CNP; therefore, the percolation path is established. However, the high resistance values observed for the CNP at low

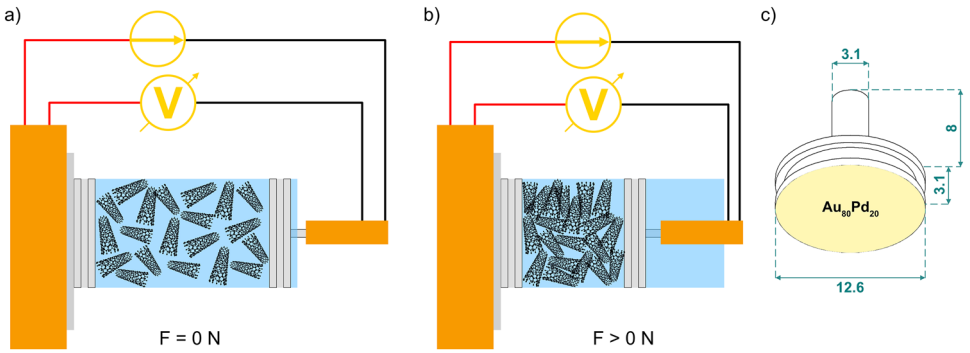

Figure 2. Schematic representation of piezoresistance measurements (**a**) prior to and (**b**) post compression. (**c**) $Au_{80}Pd_{20}$ coated aluminum vessel caps (electrodes).

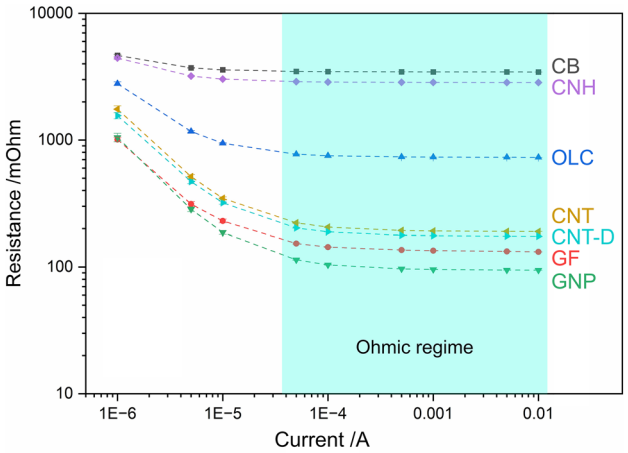

Figure 3. Results from current sweep of CNP at 2 N (i.e., 16 kPa). The shaded region from 0.05 to 10 mA highlights the ohmic regime.

currents suggest that there is significant tortuosity in the system. Tortuosity refers to the ease or difficulty with which transport, in this case electrons, take place in a porous medium. The high tortuosity within the vessel is a consequence of the relatively low normal loads used, which inadequately compacts the CNP. Insufficient compaction results in a more complex conduction path, thus increasing tortuosity and electrical resistance. However, at the same normal load (2 N), higher currents facilitate electron conduction through the porous media without requiring additional compression to fill the voids. At lower current levels, one- and two-dimensional nanostructures (i.e., CNT, CNT-D, GF, and GNP) exhibit a significant increase of approximately one order of magnitude, whereas CB and CNH maintain consistent values throughout the entire range of currents analyzed. OLC displays an intermediate behavior, with resistance increasing below 0.05 mA, albeit to a lesser extent than one- and two-dimensional nanostructures. In other words, CB and CNH show a resistance difference of 35% and 56% respectively between 0.001 mA and 10 mA, OLC a difference of 281%, whereas CNT, CNT-D, GF, and GNP show a difference of 823%, 792%, 668%, and 1010%, respectively. This difference is likely due to a higher potential barrier caused by the poor arrangement of the particles at 2 N[42,43]. The insufficient compaction implies that voids are not filled and causes a reduction in the contact zones. Specifically for the case of OLC, due to their synthesis method (thermal annealing of nanodiamond), a non-conductive sp^3 core remains, which could influence their transport[44,45].

Observing the ohmic region of the CNP, at a constant normal load of 2 N (i.e., 16 kPa), the CNP arrange themselves in a clear hierarchical order. The two CNP with the highest ohmicity (CB and CNH) also exhibit the highest absolute resistance, with values ranging between 4,000 and 5,000 mΩ. In contrast, OLC shows a narrower ohmic range with an approximate resistance value of 700 mΩ. One- and two-dimensional nanostructures, on the other hand, show a similar ohmic range to OLC. However, these CNP show resistance values below 200 mΩ. The high absolute resistance of CB, CNH, and OLC can be associated with the morphology of the nanoparticles. Both CB and OLC nanoparticles can be classified as quasi-zero-dimensional nanostructures (refer to Fig. 1d, e). The former is a combination of fullerenic, amorphous, and graphitic carbon[46], whereas the latter is comprised of concentric fullerenes with increasing diameters[47]. The classification of CNH is more difficult. Due to their closed cage structure, they can be classified as a subset of fullerenes with a high aspect ratio, or as a short single-walled CNT because of the similar chemistry between the two nanoparticles, as well as their elongated shape[48]. However, CNHs' behavior during current sweep tests aligns more closely with zero-dimensional nanostructures.

The nanostructures with the lowest absolute resistance (i.e., CNT, CNT-D, GF, and GNP) are not fullerene-type nanostructures, but rather one- and two-dimensional. The results from the current sweep tests indicate that the two-dimensional structures have lower electrical resistance than one-dimensional (further discussed in "Appraisal of all CNPs' piezoresistance"). Few-layer graphene exhibits the lowest resistance (below 100 mΩ), whereas as-received CNT show approximately twice the resistance in their ohmic regime. Comparing the ohmic response and absolute resistance values of as-received and dispersed CNT does not show significant differences. Therefore, for the purpose of this study, CNT agglomerate size is not as significant as initially predicted regarding CNTs' transport characteristics.

The lack of ohmicity by the two-dimensional nanostructures (i.e., GF and GNP) in the low current range can be explained by the anisotropic behavior of these particles. The in-plane (basal plane, or *ab* direction) conductivity of GF and GNP is orders of magnitude higher than in the transversal direction (*c* direction)[49]. Accordingly, considering the movement of electrons within the vessel between the aluminum caps, it is highly desirable that the GF and GNP particles align themselves perpendicular to the surface of the aluminum caps rather than in a parallel manner. However, as will be discussed in "Piezoresistance", the GF and GNP arrange themselves in an aleatory fashion within the vessel; nonetheless, after a certain load is reached, the flat nanoparticles take a predominant orientation which is transverse to the electron flow. GNP, in particular, tend to arrange themselves for the most part in a parallel fashion since the nanoplatelets lack the mechanical rigidity that GF presents. Consequently, for low currents, a capacitive effect is dominant in GNP, and to a lesser extent in GF. Thereupon,

the equivalent circuit is not purely resistive, but rather a combination of resistive-capacitive (R–C circuit). The capacitive component in GNP and GF arises from the distance between individual graphene layers, causing a potential barrier[42,43]. As shown in Fig. 3, this potential barrier is more significant for lower currents. Since this work pertains to direct current, the capacitive component of the two-dimensional CNP functions as an open circuit. As the current increases, the electrical resistance of these CNP decreases without the need for further compaction due to the reduced relevance of the dielectric (i.e., gap between graphene layers). It is worth noting that graphene and graphite are metal-like (zero band gap) conductors. Therefore, the ohmic behavior for current above 0.05 mA is observed in Fig. 3 as the capacitance takes a less dominant role (due to higher currents enabling the potential barrier to be overcome). The conductive properties of CNT and CNT-D, on the other hand, are highly reliant on the chirality of the tubes. Statistically, multi-walled CNT—such as the ones used in this study—always have at least one tube that behaves as a metallic conductor[50]. Therefore, the absence of ohmic behavior in CNT and CNT-D can be attributed to their semiconductive properties at low currents, rather than a capacitive effect, as is the case with GF and GNP. As the current levels increase, the energy required for electrons to move towards a metallic tube within the same multi-walled CNT—i.e., interlayer potential barrier—becomes more easily available thus shifting from a semiconductive dominant system towards a metallic-conductive system. Therefore, as the current increases, the individual CNT's resistance drops and shows an ohmic behavior. The interlayer potential barrier of multi-walled CNT is approximately 10 meV[51]. Therefore, at room temperature, where approximately 25 meV of thermal energy is available, interlayer coupling should be generated. Nonetheless, the presence of CNT agglomerates in CNT and CNT-D may increase the potential barrier, necessitating additional energy input (i.e., higher currents) to overcome it.

Piezoresistance

The piezoresistive behavior of the CNP was analyzed by measuring their electrical resistance under different loads. During the test, the nanoparticle powders were compacted by the electrodes while the voltage drop between them was measured; thus, recording the electrical resistance as a function of compaction (i.e., normal load). To minimize uncertainty in the measurements and reduce instrumental error, load-dependent electrical resistance tests were divided into two sets of loads: low loads (red plot) ranging from 0.25 N up to 2 N and high loads (black plot) ranging from 2 N up to 10 N. The current used for the measurements was 0.05 mA, ensuring that the resistance values are within the ohmic regime of the CNP tested (as shown in Fig. 3). This is not trivial since this indicates that Holm's contact resistance equation ($R_C = \rho/2a$) is valid[52]. In other words, the resistivity in the system can be estimated based on the area of a flat circular contact of radius a and the electrical resistance measured. Due to the ohmic behavior of the system at 0.05 mA and the relatively large pressure applied on the CNP, the Sharvin resistance ($R_S = C/{a_c}^2$) plays a minor role in the resistance measured[53], where a_c is the constriction radius and the constant C depends solely on the electronic properties of the conductor. The reported resistance values correspond to the sum of the Holm (Drude diffusion[54]) and Sharvin (Knudsen diffusion[55]) resistance. However, the main contribution is from the former.

This section discusses the load-resistance curves and CNP displacement. It is important to note that the y-axis in the load-resistance curves is plotted on a logarithmic scale. Therefore, when referring to linear behavior this should be taken into consideration. The repeatability, stability, and low error of the resistance values at different normal loads is highlighted in Figs. S1, S2, and S3. These figures display four electrical resistance measurements for quasi-zero-dimensional, one-dimensional, and two-dimensional nanostructures, respectively.

Carbon black

The results from load dependent electrical resistance for CB are shown in Fig. 4. Irrespective of the loading range, CB exhibits a relatively linear relationship between the applied load and the resistance—see Fig. 4a. In the lower loading range, CB exhibits the largest reduction in resistance. At 2 N the resistance of this nanostructure is only approximately 40% of the resistance measured at 0.25 N. However, at 10 N, CB's resistance further decreases to approximately 20% of the resistance recorded at 0.25 N. The scanning electron microscope (SEM) micrograph shown in Fig. 4d highlights considerable CB agglomeration, with the magnified micrograph (Fig. 4e) depicting porous networks caused by the clustering of agglomerates. This supports the electrical performance observed in Fig. 4a. In the low loading range, most of the voids formed by large adjacent CB agglomerates are closed, thus causing a considerable decrease in resistance during initial compaction. This behavior is further supported by the TEM micrograph (see Fig. 1e), which shows that the agglomerates formed by CB are not highly compact. In the high loading range, however, increasing the normal load is not as effective at reducing resistance since now the multiple conductive paths have been established within the vessel due to CB and CB agglomerate compaction.

The bar graphs shown in Fig. 4b, c depict the displacement recorded in the three load increments analyzed, which were 0.25 N and 0.5 N in the lower loading ranges and 0.5 N and 1 N in the higher loading ranges. These two graphs demonstrate the reliability of CB in terms of the compression-to-displacement relationship. In all three load increments, the displacement remains relatively constant. For an increment of 0.25 N, the CB mass within the vessel was displaced by approximately 0.02 mm. The displacement value increased to approximately 0.03 mm and 0.05 mm for increments of 0.5 N and 1 N, respectively. The initial slight variations in displacement observed are supported by the TEM and SEM micrographs (Figs. 1e and 4d, e) since the compaction of large voids is required before the initial loads can be established and maintained. Therefore, CB demonstrates promising results due to its consistency in its compression-to-displacement relationship in the mid-to-high loading range after the voids formed due to agglomeration are filled, showing slight fluctuations at low loads.

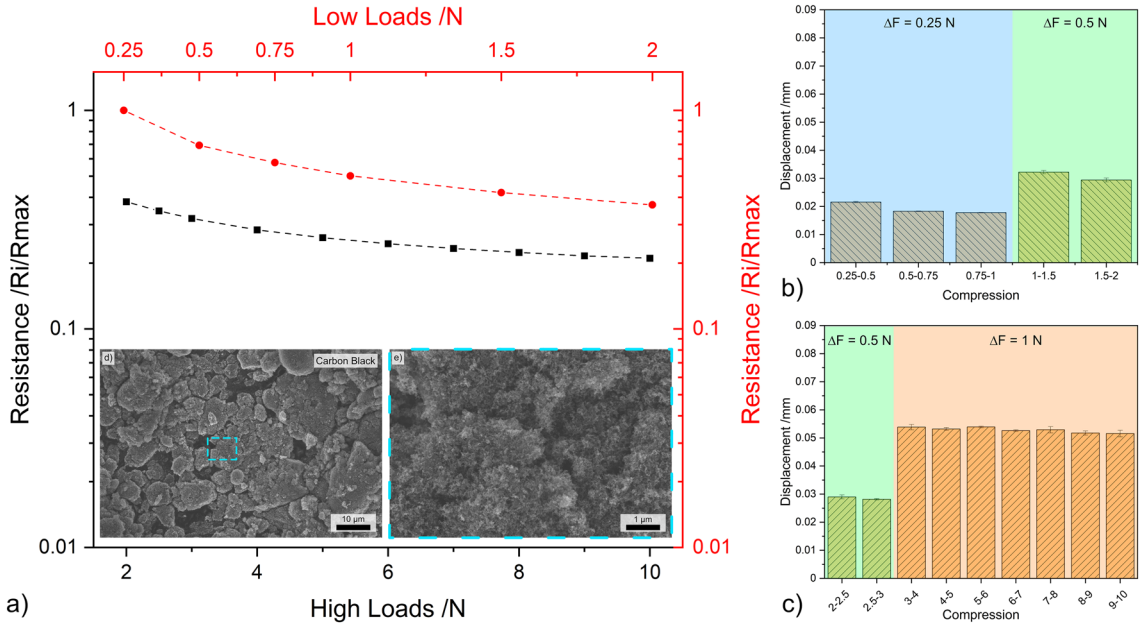

Figure 4. (**a**) Load dependent electrical resistance at low and high loads of CB. (**b**) and (**c**) Show the displacement for different compression levels at low and high loads, respectively. (**d,e**) SEM micrographs of CB (inset in load-resistance curves).

Onion-like carbon

The piezoresistance curve for OLC in the lower loading range, shown in Fig. 5a, exhibits behavior similar to that observed in CB, with a sharp reduction in resistance as the load increases. In the high loading range, the resistance decreases as the normal load increases, but to a lesser extent. This similarity in performance is a consequence of the porous network observed in the micrographs—see Fig. 5d, e. The spherical morphology of OLC tends to favor the formation of voids between adjacent agglomerates as demonstrated in the magnified micrograph (Fig. 5e). Consequently, as the load increases in the lower loading range the particles accommodate the deformation by moving into the voids, thus filling them, and thus increasing connectivity. The SEM micrographs highlight the tendency of the OLC to form agglomerates in the µm-range. However, recalling the HR-TEM micrograph (Fig. 1d) OLC bulk powders form a more massive aggregate than the CB powder (Fig. 1e), with the

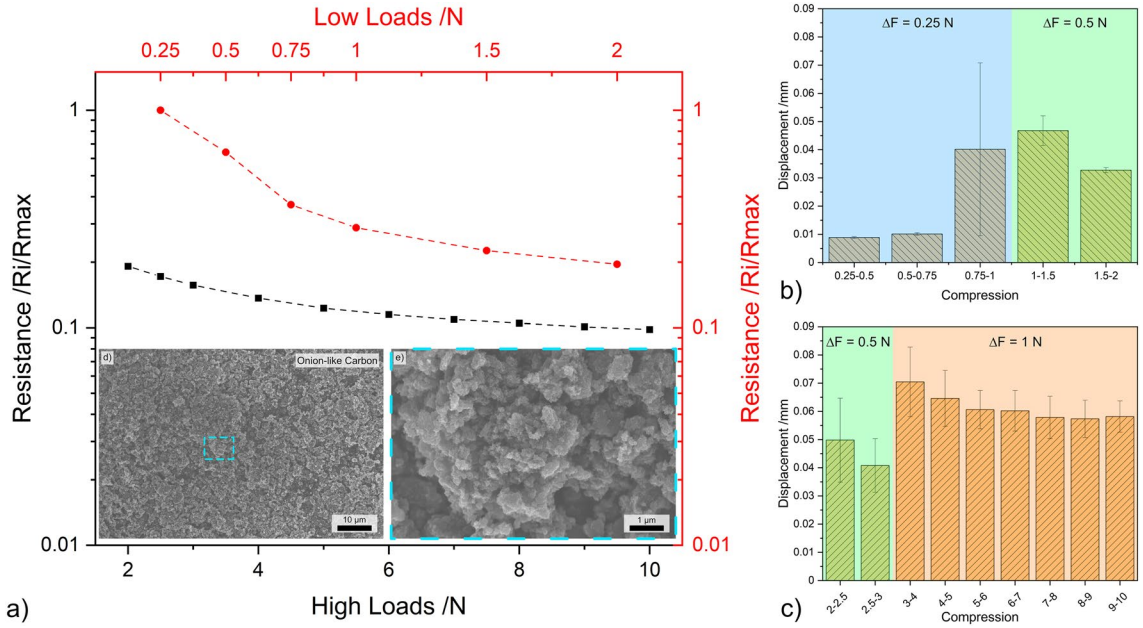

Figure 5. (**a**) Load dependent electrical resistance at low and high loads of OLC. (**b**) and (**c**) The displacement for different compression levels at low and high loads, respectively. (**d,e**) SEM micrographs of OLC (inset in load-resistance curves).

latter showing more scattered CB agglomerates rather than a cohesive mass. This is a key distinction between OLC and CB, which affects the piezoresistive performance of the bulk powders. Due to OLC's morphology and cohesive behavior, these nanostructures tend to show high elasticity. Therefore, the considerably lower resistance values measured are not only a consequence of void compaction, but also due to the compression of the OLC themselves. Furthermore, the magnified TEM micrograph in Fig. 1d illustrates the enhanced inter-particle connectivity within the OLC agglomerates. This improved interconnectivity accounts for the 20% resistance observed at 2 N and the 10% resistance observed at 10 N, both in comparison to the resistance at 0.25 N. It is worth noting that while CB and OLC are both quasi-zero-dimensional carbon nanostructures, the differences in their piezoresistive behavior is significantly influenced by intra-particle interactions and particle interactions within the powder's agglomerates.

The compression-to-displacement relationship in OLC is not linear, showing multiple fluctuations within the same load increments—see Fig. 5b, c. The displacement varies from approximately 0.01 mm to 0.04 mm at increments of 0.25 N, and fluctuates between 0.03 and 0.05 mm at increments of 0.5 N. For increments of 1 N, the displacement stabilizes above 6 N at 0.06 mm per 1 N. The variability in compression-to-displacement highlights the elasticity of OLC. The observed variations between 0.75 and 3 N suggest the onset of particle accommodation. Below 0.75 N, the displacement is caused by compaction and filling of the voids, whereas for loads above 3 N the displacement is due to the elastic deformation of OLC. Between 0.75 and 3 N, the compression-to-displacement results indicate a hybrid state where the displacement is caused by OLC adjustment and where elastic deformation begins. Therefore, compaction of the voids does not play such a crucial role, but rather the compression of the concentric fullerenes at higher loads. This behavior is desirable for electrical performance since it improves interconnectivity when compacted. However, the use of this nanoparticle for its piezoresistive performance must be limited to high load applications, preferably above 6 N. This is because, for lower loads, obtaining consistent and reproducible piezoresistive measurements is difficult (see Fig. S1). This inconsistency hinders the tracking of particle displacement, or normal load applied, by directly measuring the electrical resistance of the resistance, and vice versa.

Carbon nanohorns

CNH exhibit exceptional linearity in both low and high loading ranges, as shown in Fig. 6a. This performance is highly desirable in applications that utilize piezoresistance as a working principle. The resistance at 2 N is approximately 35% of the initial resistance, decreasing to 10% at 10 N. The micrographs in Fig. 6d, e reveal that the CNH form large agglomerates, which create a complex porous network within the vessel. The TEM micrograph shown in Fig. 1c, reveals that the size of the CNH agglomerates are significantly smaller than those observed for the other zero-dimensional nanostructures. As a result, the agglomerates can adjust and compact as the load increases, making it easier to fill the voids. However, the consistency in the load-resistance curves is due to the remarkable elasticity of the nanohorns. This elastic behavior of the nanohorns can be attributed to the CNT-like horns, which are capable of deforming under compressive loads, thus inverting the cone from tip to base[48]. Therefore, after the CNH have filled all voids resulting from compressive loads, the cone structures

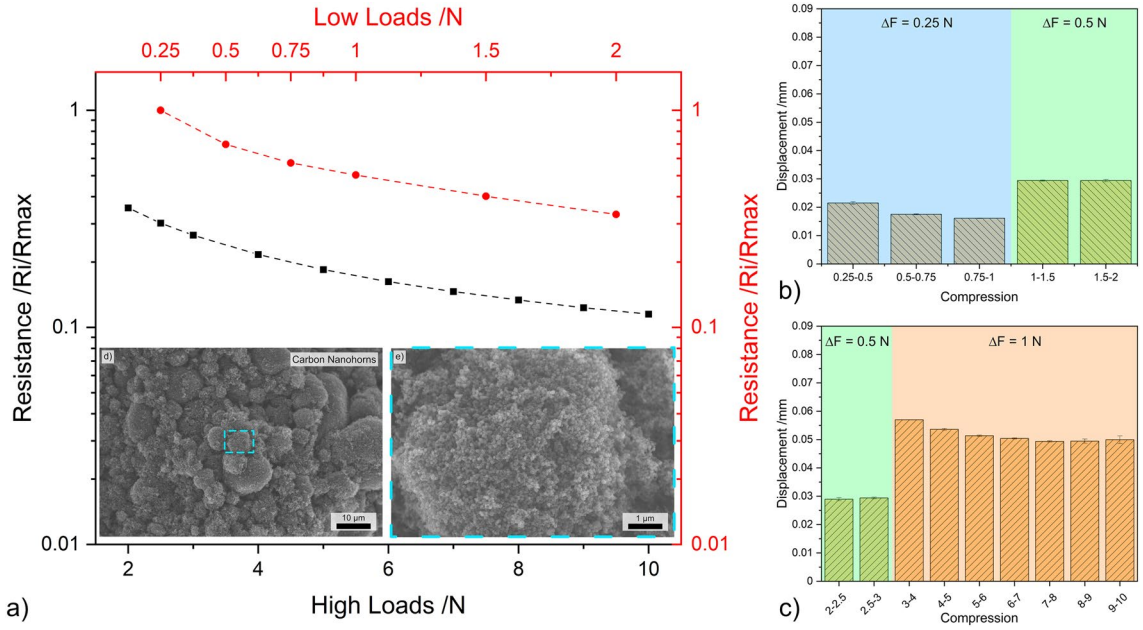

Figure 6. (**a**) Load dependent electrical resistance at low and high loads of CNH. (**b,c**) Show the displacement for different compression levels at low and high loads, respectively. (**d,e**) SEM micrographs of CNH (inset in load-resistance curves).

absorb the energy through mechanical deformation. This improves particle interconnectivity and enhances the conductive paths for electron mobility.

The compression-to-displacement relationship (Fig. 6b, c) indicates consistent results. Minor displacement variations were observed for increments of 0.25 N, but the value stabilizes after initial voids are closed. For increments of 1 N, the CNH bulk within the vessel is displaced by approximately 0.05 mm. This value was achieved for loads above 5 N; below 5 N, the displacement approaches 0.06 mm. For increments of 0.25 N and 0.5 N the displacement is approximately 0.02 mm and 0.03 mm, respectively. Thus, CNH demonstrate a wide range of applicability. The load-resistance curve of these nanoparticles exhibits exceptional linearity, and their compression-to-displacement relationship yields consistent results for both low and high loads.

Carbon nanotubes

The CNT in their agglomerated state demonstrate a linear load-resistance relationship, as shown in Fig. 7a. Unlike the zero-dimensional nanostructures, there are no sharp reductions in electrical resistance. At 2 N, CNT show approximately 55% of the initial resistance, and the percentage drops to approximately 35% at 10 N, thus showing the smallest percentual reduction among the CNP analyzed. The electrical performance is not negatively impacted by the large voids formed due to CNT agglomerates, as shown in the micrograph in Fig. 7d. However, the magnified micrograph (Fig. 7e) reveals that individual CNT and small CNT bundles bridge the gaps between agglomerates, which is a distinctive characteristic of CNT. Therefore, in this case, the voids formed by two nanoparticle agglomerates do not significantly affect the electrical performance, as is the case in zero-dimensional nanoparticles (CB, OLC, and CNH). Additionally, the lack of a sharp reduction in the load-resistance curves indicates that the maximum inter-tube distance for tunneling (1.8 nm) was already achieved at 0.25 N[42]. To achieve a distance of 1.8 nm, low compression is necessary. This is because the equilibrium distance between two single-walled CNT is 3.4 Å[56,57]. As a result, even at low loads, tunneling or coupling is activated between adjacent CNT, allowing electrons to move from one tube to another.

The compression-to-displacement relationship of CNT (shown in Fig. 7b, c) is similar to that of CB (Fig. 4b, c). There are almost no fluctuations within each interval. Initially, CNT are displaced by approximately 0.02 mm. This value increases to approximately 0.03 mm and 0.06 mm for 0.5 N and 1 N increments, respectively. Due to the abundant presence of CNT agglomerates, it was expected that considerable displacements would occur initially. However, the large network of agglomerate within the vessel causes large-scale voids which require compaction prior to establishing the initial load. Therefore, once a force 0.25 N is reached, most of the large voids within the vessel have already been filled by the compaction and rearrangement of CNT agglomerates. As a result, the resistance at 0.25 N is exceptionally low and does not exhibit any measurable abrupt changes. Furthermore, since most CNT are in their agglomerated form, the minimum distance for electron coupling is already fulfilled (within each agglomerate). Therefore, the external load is only necessary to establish a contact between adjacent agglomerates, which occurs at low loads.

Dispersed carbon nanotubes

CNT have a strong tendency to form agglomerates due to Van der Waals interactions. Therefore, the as-received nanoparticles have a high degree of agglomeration which could negatively affect the piezoresistive performance of

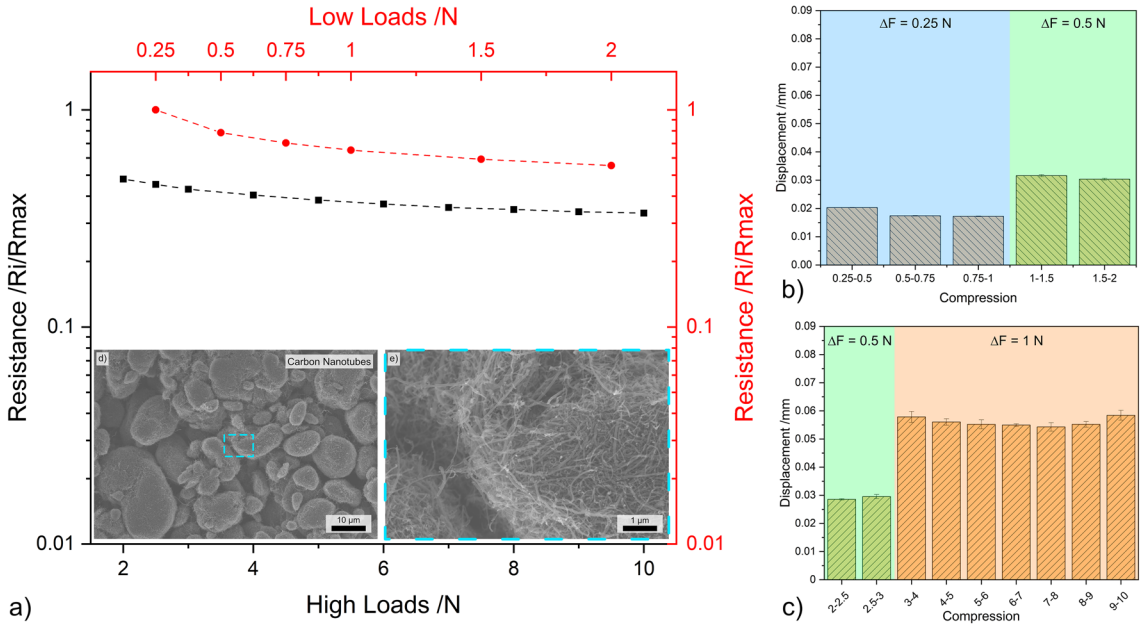

Figure 7. (**a**) Load dependent electrical resistance at low and high loads of CNT. (**b,c**) The displacement for different compression levels at low and high loads, respectively. (**d,e**) SEM micrographs of CNT (inset in load-resistance curves).

the nanoparticles. Therefore, it is important to analyze the influence of the agglomerate size on the piezoresistive behavior of the CNP since the electrostatic interactions within the agglomerates are significant. After dispersion, the CNT will re-agglomerate as the solvent evaporates. However, the overall agglomerate size will be smaller than in their as-received state[38,58]. The electrical performance of CNT-D is shown in Fig. 8a. As previously mentioned in "Ohmic response" (see Fig. 3), the similarity in electrical performance between CNT (Fig. 7a) and CNT-D (Fig. 8a) was not expected as it was hypothesized that the presence of larger CNT agglomerates would hinder the electrical performance of the as-received CNT. The resistance at 2 N and 10 N is approximately 50% and 30% of the initial resistance at 0.25 N, respectively. The micrographs (Fig. 8d, e) show that although the dispersion process was effective in breaking up large CNT agglomerates, multiple agglomerates remain, albeit to a much lesser extent (quasi-buckypaper). Prolonging the dispersion process would undoubtedly further minimize the presence of CNT agglomerates; however, prolonged sonication damages the structural integrity of the CNT[38,58]. Therefore, this is not a viable option as structural damage would reduce the desirable mechanical and transport properties of the CNT. However, despite the fact that CNT agglomerates are still found within the vessel, there is a large amount of disentangled CNT as shown in the micrographs.

The compression-to-displacement relationship for CNT-D (shown in Fig. 8b. c) is very different from that of CNT. In the as-received state, negligible fluctuations were observed between the different load increments. After dispersion, however, the compression-to-displacement relationship resembles that of CNH. In the 0.25 N and 0.5 N increments the displacement values tend to decrease, ranging from approximately 0.035 mm to 0.025 mm and 0.04 mm to 0.03 mm, respectively. The displacement measured at 1 N increment is initially high at approximately 0.06 mm and gradually decreases to about 0.05 mm. As previously discussed, the gradual reduction in the displacement as the normal load increases is due to particle elasticity. This behavior was also observed for the zero-dimensional particles (i.e., OLC, CNH, and to a lesser extent CB). Elastic behavior was more prominent in CNT-D since the compression acts upon small CNT clusters rather than on larger agglomerates. The compressive forces caused elastic deformation of the multi-walled CNT instead of the compacting of agglomerated CNT bundles. The displacement did not stabilize in the analyzed loading ranges, indicating that higher loads are necessary to establish a consistent compression-to-displacement relationship. Therefore, CNT-D is suitable for very high-load applications. However, for lower load applications, it is not necessary to reduce the size of agglomerate, since smaller agglomerates cause the fluctuation of the compression-to-displacement relationship and the piezoresistive behavior was not significantly affected by the presence of larger agglomerate sizes.

Graphite flakes

The load-resistance curves for GF (shown in Fig. 9a) contrast those observed for zero- and one-dimensional nanostructures in the fact that the resistance of GF does not decrease as significantly in the lower loading ranges, but rather in the higher ranges. At 2 N the resistance of GF decreases to approximately 80% the resistance at 0.25 N, with the value decreasing to about 30% at 10 N, thus showing the opposite behavior compared to zero-dimensional nanostructures (Figs. 4, 5, 6) where the predominant drop in resistance was recorded in the lower loading range. As opposed to zero- and one-dimensional nanostructures, GF does not form agglomerates. GF particles are large, with voids formed between adjacent flakes (see Fig. 9d, e). The micrographs demonstrate a

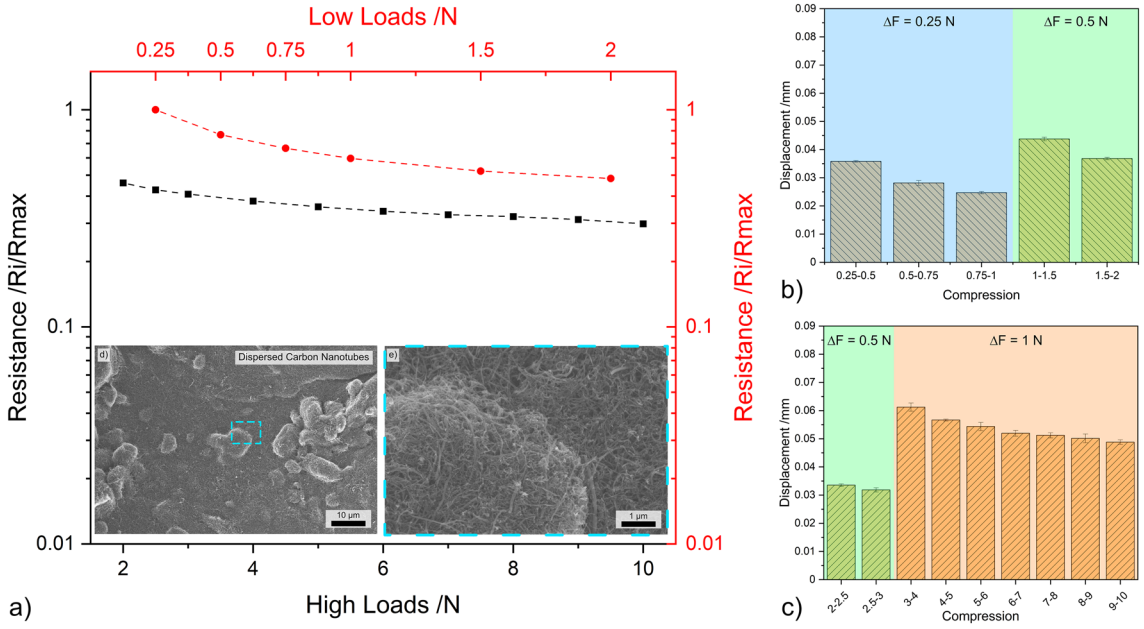

Figure 8. (**a**) Load dependent electrical resistance at low and high loads of CNT-D. (**b,c**) The displacement for different compression levels at low and high loads, respectively. (**d,e**) SEM micrographs of CNT-D (inset in load-resistance curves).

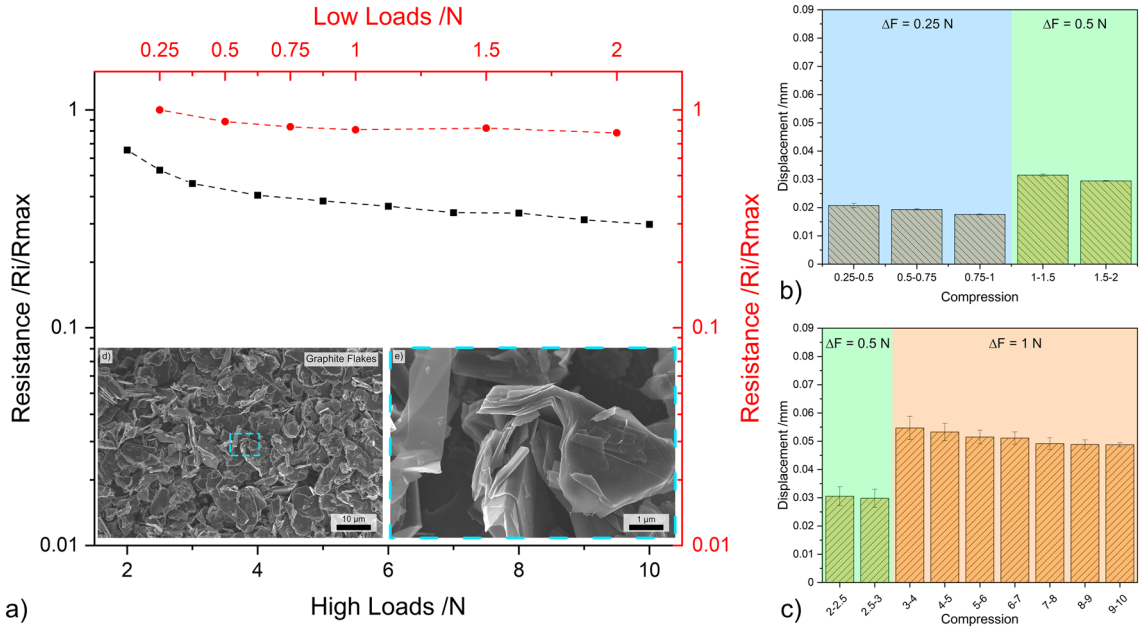

Figure 9. (**a**) Load dependent electrical resistance at low and high loads of GF. (**b,c**) The displacement for different compression levels at low and high loads, respectively. (**d,e**) SEM micrographs of GF (inset in load-resistance curves).

certain degree of GF interconnectivity. However, the large and irregular shape of these particles requires higher loads to close the voids, which increases compaction within the vessel and improves flake interconnectivity. Additionally, the compaction of flakes oriented parallel to the surface of the electrodes promotes the reduction of the inter-graphene layer potential barrier. Reducing the potential barrier establishes more conduction paths, which in turn reduces the resistance of the bulk GF flakes by eliminating capacitive barriers—which act as open circuits since the tests were conducted with direct current.

Similarly to zero-dimensional nanostructures (excluding OLC) and as-received CNT, GF also exhibits relatively stable compression-to-displacement relationship (Fig. 9b, c), demonstrating the reproducibility of the recorded results (see Fig. S3). Due to the lack of GF agglomerates, the displacement recorded for load increments of 0.25 N is more consistent than that of zero- and one-dimensional nanostructures, at approximately 0.02 mm. Similarly, displacements of 0.03 mm were recorded at increments of 0.5 N. However, slight variations were observed at increments of 1 N, with displacement values of approximately 0.05 mm showing higher standard deviation. However, as the compression increases beyond 7 N, the error tends to decrease while the displacement values remain constant. This behavior is also supported by the load-resistance curves in the high loading range, which show linear load-resistance curves as the compression-to-displacement relationship remains constant.

Graphene nanoplatelets

The piezoresistive behavior of GNP is shown in Fig. 10a. This nanoparticle shows a considerable reduction in resistance for the lower loading range, at 2 N reducing to approximately 40% the resistance measured at 0.25 N. In the higher loading range, it gradually reduces in a linear fashion to approximately 25% of the initial resistance (due to the rearrangement of the GNP—analogous to granular flow[59]), resembling the piezoresistive performance of one-dimensional nanostructures. As shown in Fig. 10d, e, the majority of the nanoplatelets align horizontally, in contrast to the observations in GF. This explains the higher initial reduction in resistance. The linear behavior in the higher loading range suggests that the voids have already been filled by GNP and the gradual reduction in resistance can be attributed to the compaction of individual nanoplatelets and nanoplatelet clusters. Furthermore, the thinner GNP are mechanically weaker than the thicker GF. Consequently, GNP require lower external pressure to orient the nanoplatelets parallel to the surfaces applying the load. Additionally, the micrographs illustrate individual nanoplatelets stacked in a disorderly manner, rather than GNP agglomerates. The magnified micrograph (Fig. 10e) reveals the presence of impurities (bright spots scattered throughout the nanoplatelet). These particles are likely a result of the synthesis process. Although the synthesis process details are unknown, it is reasonable to assume that the impurity particles are amorphous carbon. The impurities are deposited on the few-layer graphene platelets and are also found free-standing between them. However, the presence of amorphous carbon does not hinder the electrical performance of GNP, as it exhibits similar behavior to GF (see Fig. 9a).

The compression-to-displacement graphs (Fig. 10b, c) for GNP resemble those from GF in terms of values, but also in the fact that the displacement varies slightly for the load increments. For 0.25 N and 0.5 N increment the displacement is approximately 0.02 and 0.03 mm, respectively. The 1 N increment shows the most variation, ranging from approximately 0.06 mm down to 0.04 mm. Although the displacement values are not constant for the 1 N increments, the standard deviation in all measurements is negligible, thus suggesting the reproducibility

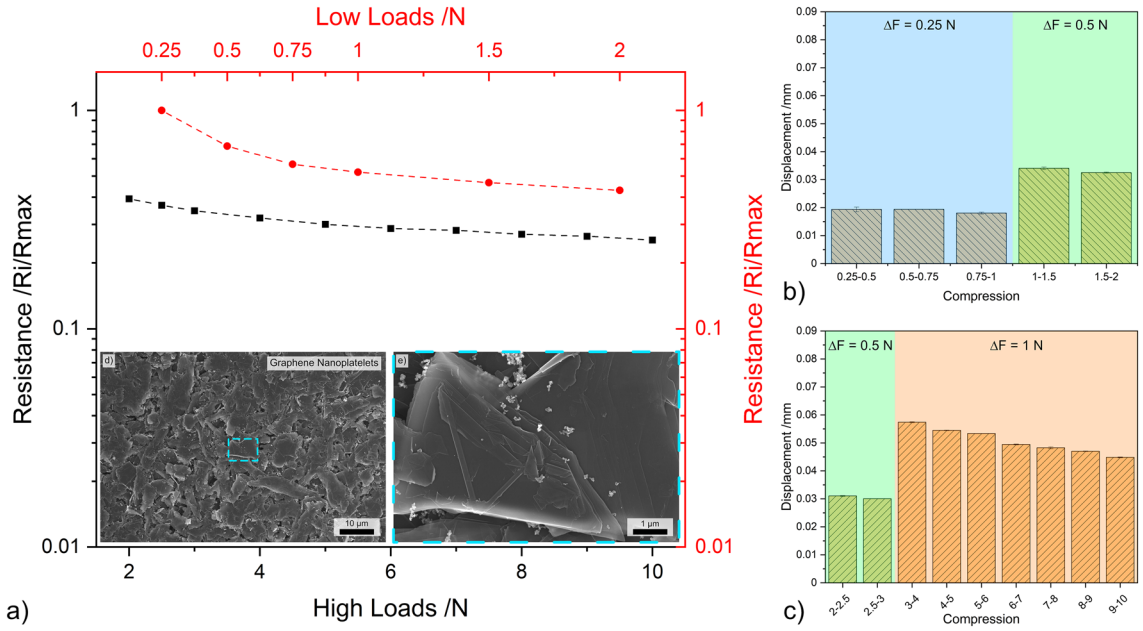

Figure 10. (**a**) Load dependent electrical resistance at low and high loads of GNP. (**b,c**) The displacement for different compression levels at low and high loads, respectively. (**d,e**) SEM micrographs of GNP (inset in load-resistance curves).

of the results. In contrast to GF and OLC, GNPs' displacement does not reach a stable value in the loading range analyzed, similarly to CNT-D. Therefore, the use of GNP for its piezoresistive behavior should be limited to low loads to ensure consistent results. GNP could be used for high load applications, however higher loads than those in the scope of this study are required.

K_b factor

The gauge factor, as shown in Eq. (1), is a useful tool for evaluating the sensitivity of strain sensors. A high gauge factor indicates an increased output signal. However, by definition, it is not directly applicable to the systems evaluated in this study because it is not possible to measure the undeformed length and resistance of the bulk mass within the vessel. The gauge factor equation was adjusted in consideration of the fact that compressive stress is applied to an aggregate of nanostructures, rather than a single nanostructure (see Eq. 3). In the modified equation proposed, R_x is the resistance value measured, $R_{0.25}$ is the initial resistance measured at 0.25 N, ΔD is the displacement difference, ΔD_{max} is the displacement difference between 0.25 N and 10 N, ΔF is the load difference, and F_{max} is the maximum load. Therefore, the bulk powder gauge factor (henceforth K_b) evaluates the linearity of the load-resistance curves (when plotted in a logarithmic scale), the consistency in the compression-to-displacement relationship and incorporates the loading range. The K_b factor values for each CNP are shown in Table 1 as the average for each load increment.

$$K_b = \frac{R_x/R_{0.25}}{\Delta D/\Delta D_{max}} \cdot \frac{\Delta F}{F_{max}} \tag{3}$$

The K_b factor proposed for bulk powders under unidirectional compressive stress assesses the reproducibility of the piezoresistive performance of the powders. The K_b factor values indicate the poor performance of OLC for low loading ranges (i.e., 0.25 N increments). However, for mid-to-high loading ranges, the performance

CNP	0.25 N	0.5 N	1 N
CB	0.41 ± 0.02	0.33 ± 0.02	0.25 ± 0.02
OLC	2.18 ± 1.50	0.51 ± 0.11	0.42 ± 0.01
CNH	0.42 ± 0.01	0.29 ± 0.04	0.16 ± 0.02
CNT	0.56 ± 0.02	0.49 ± 0.05	0.38 ± 0.02
CNT-D	0.35 ± 0.02	0.38 ± 0.01	0.38 ± 0.03
GF	0.41 ± 0.01	0.40 ± 0.09	0.26 ± 0.01
GNP	0.42 ± 0.04	0.34 ± 0.02	0.30 ± 0.01

Table 1. K_b factor for all CNP based on the load increments.

improves with slight variations not only in the K_b factor values, but also verified by the load-resistance curves and compression-to-displacement relationship (see Fig. 5). Moreover, the K_b factor for CB, CNH, CNT, and GNP decreases as the load increments increase, whereas GF remains constant for the first two load increments and CNT-D remain constant throughout. The fluctuations in K_b for the zero-dimensional nanostructures and CNT can be attributed to their tendency to form agglomerates. As a result, these structures must be displaced to fill the voids formed between agglomerates, which increases both the initial ΔD and ΔD_{max}, causing the K_b factor to vary between loading increments. For GNP, on the other hand, the adjusting and subsequent stacking of the graphene structures may be responsible for larger initial displacements, which could affect the K_b factor values. In contrast, GF are more mechanically rigid, requiring higher loads for the rearrangement of the large flakes. As a result, the K_b factor values remain relatively constant for increments of 0.25 N and 0.5 N, whereas it slightly decreases for 1 N increments (see Fig. 9). The K_b factor for CNT-D remains exceptionally stable for the three load increments evaluated due to the low agglomerate state of the nanotubes. It should be noted that the K_b factor for CNT in the high loading ranges is the same as the values observed for CNT-D. This suggests that larger CNT agglomerates perform similarly to smaller agglomerates at sufficiently high loads. This validates that voids in bulk powders with larger CNT agglomerates were effectively compacted at higher loads, and further loading will have the same effect regardless of the agglomerate state of the CNT.

Therefore, the K_b factor can be used as a general guide to rapidly assess the reproducibility and reliability of a specific CNPs' piezoresistive performance for different load increments. However, to comprehensively understand the behavior, it is crucial to analyze the load-resistance curves and the compression-to-displacement relationship.

Appraisal of all CNPs' piezoresistance

The absolute and normalized load-dependent electrical resistance values for both loading ranges (plotted in double logarithmic scale to highlight the linear load-resistance relationship) are shown in Fig. 11. This plot summarizes and expands upon the individual discussions for each CNP. Throughout the entire loading range, the same hierarchical order and groupings observed in Fig. 3 are maintained. This ordering of the CNP coincides with the particles' dimensionality, which dominates their quantum mechanical electronic properties. In other words, the electronic properties of the CNP are highly dependent on their electronic density of states[60]. As the dimensionality of the nanostructures changes, so does their electron distribution. Based on Fig. 11a and Fig. 3, it is evident that the zero-dimensional nanoparticles (CB, OLC, and CNH) exhibit the highest electrical resistance due to strict electron motion confinement in low dimensions due to quantum confinement effects, which results in a discrete free-electron density of states[60,61]. On the other hand, one-dimensional structures (CNT and CNT-D) display continuous spikes in free-electron density of states. The resistance observed for CNT and CNT-D in Fig. 11a is significantly lower than that observed for zero-dimensional nanostructures. In contrast, the two-dimensional structures (GF and GNP) have the highest free-electron density of states among the CNP analyzed. In this case, the staircase-like energy distribution more closely resembles the free-electron density of states of a bulk material, where the electron density of states is proportional to the square root of the energy. One-dimensional and two-dimensional structures, however, have anisotropic transport characteristics. Therefore, the electron density of states in the axial direction (in one-dimensional structures) and in the *ab* direction (in two-dimensional structures) varies significantly from the transversal direction (axial direction and *c* direction in one-dimensional and two-dimensional structures, respectively), thus affecting their transport characteristics.

Although two-dimensional structures exhibit a capacitive component due to the potential barrier between adjacent graphene layers, these nanoparticles demonstrate the lowest resistance. However, as discussed in "Ohmic response"and shown in Fig. 3, the current used in load-dependent resistance measurements (0.05 mA) is high enough to overcome the potential barrier. GF, in particular, exhibits a clear slope change before and after 2 N. The change may be caused by the rearrangement of vertical flakes; however, due to the mechanical rigidity of this structure, this is unlikely. The change is more likely due to the compaction of flakes that are parallel to the surface of the aluminum caps. In this case, as the load increases, the dielectric separation (interplanar distance in the *c* direction, which is 0.671 nm in the undeformed state[49]) decreases, minimizing the capacitive component's

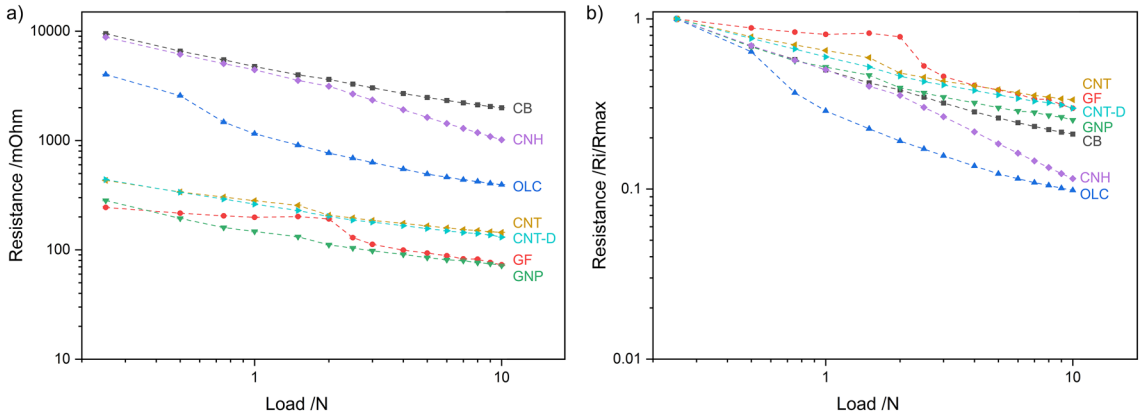

Figure 11. (**a**) Absolute and (**b**) normalized load dependent electrical resistance for the entire loading range. Note: the curves were plotted in double logarithmic scale.

relevance in the circuit. As a result, for sufficiently high normal loads and/or currents, the electrical circuit becomes purely resistive with a minimal capacitive component, following Ohm's law (see Fig. 3).

After normalizing the data from Fig. 11a, a different hierarchy is established, as shown in Fig. 11b. The normalized values at 10 N highlight the overall change in resistance as the load increases. In this case, the one- and two-dimensional nanostructures, which exhibit the lowest absolute electrical resistance, also show the smallest resistance change from start to finish. After normalization, CB is grouped with the one- and two-dimensional nanostructures, despite having the highest absolute resistance. This quasi-zero-dimensional structure exhibits exceptional linearity in its piezoresistance. The other quasi-zero-dimensional nanostructures (i.e., OLC and CNH) initially have very high resistances of approximately 4 and 10 Ω, respectively. However, the resistance of these CNP drops considerably as the load increases, with both experiencing a reduction of approximately one order of magnitude. The comparison between the absolute and normalized resistance is important because it highlights the sensitivity of the piezoresistive behavior. Counterintuitively, higher resistances are more desirable because they require measurement equipment with lower resolutions. Additionally, higher slopes in load-resistance curves are also sought after because they imply higher responsiveness. According to these criteria, OLC and CNH are the most promising CNP. However, when considering the compression-to-displacement graphs from Figs. 5b, c and 6b, c, it is evident that stable displacement value per 1 N increment require loads above 6 N. The CNP with stable compression-to-displacement graphs (i.e., CB, GF to a certain extent, GNP for low loads, and CNT) do not exhibit as significant reduction in resistance during compression. Therefore, instrumentation with higher precision is necessary to accurately measure electrical resistance. CB may be a promising alternative due to its relatively high absolute resistance (in the ohm range) and a steeper load-resistance curve compared to one- and two-dimensional nanostructures (i.e., GF, GNP, CNT, and CNT-D).

Moreover, the methodology proposed by Tamai et al. to determine the predominant deformation mechanism in contacting surfaces was analogously employed in this study[40]. This evaluation was carried out to determine the validity of the methodology in conductive powders. The full range load-resistance curves (Fig. 11a) were linearly fitted to obtain the corresponding slope values, which are presented in Table 2. As shown in Table 2, the slope values coincide, to a certain extent, with the theoretical values corresponding to a predominance of elastic deformation (i.e., – 1/3 and – 2/3). Therefore, the slope analysis confirms that all CNP underwent elastic deformation within the vessel for the entire of the loading range evaluated. Furthermore, most of the resistance of the nanostructures originates predominantly from constriction resistance (slope ≈ – 1/3) except for OLC and CNH where film resistance dominates the system (slope ≈ – 2/3). Although CB is also a zero-dimensional nanostructures, film resistance is not the dominant resistance type, which could be due to the content of graphitic carbon present in this structure. Graphitic carbon may occupy the interstices within each nanoparticle, forming percolation paths that aid the motion of electrons within and between CB particles. Consequently, constriction resistance is more dominant. The other zero-dimensional nanostructures, however, are not as interconnected as CB but rather form individual clusters, contributing to an increased electrical resistance, which corresponds to the film resistance in this analogy. Therefore, constriction resistance is not as dominant in these CNP. Although this methodology is purely theoretical and idealized by nature, the experimental results demonstrated here confirm its validity and applicability—considering the parameters and assumptions outlined in this work.

Conclusions

This study experimentally determined and discussed the piezoresistive performance of bulk carbon nanoparticles. Ohmic response, load-dependent contact resistance, and particle morphology were comprehensively characterized. The potential applicability of CNP due to their piezoresistive behavior is highlighted. It is shown that the morphology of the nanostructures plays a crucial role in their piezoresistive performance. Quasi-zero-dimensional nanostructures exhibit the highest absolute electrical resistance, as observed in CB and CNH. One-dimensional nanostructures, such as CNT and CNT-D, exhibit significantly lower electrical resistance than the zero-dimensional structures by approximately one order of magnitude, whereas two-dimensional structures present slightly lower electrical resistance than one-dimensional nanoparticles. OLC, in particular, fall between zero- and one-dimensional CNP in terms of electrical resistance.

The resistance of OLC decreases in a linear manner as the load increases (when plotted in a logarithmic scale), however the displacement fluctuates at low loads. Accordingly, the use of this nanoparticle for its piezoresistive performance must be limited to high load applications (above 6 N under the conditions of this study). Likewise,

CNP	Slope	Dominant resistance type
CB	– 0.38 ± 0.01	Constriction
OLC	– 0.63 ± 0.04	Film
CNH	– 0.62 ± 0.01	Film
CNT	– 0.29 ± 0.01	Constriction
CNT-D	– 0.32 ± 0.01	Constriction
GF	– 0.38 ± 0.03	Constriction
GNP	– 0.35 ± 0.01	Constriction

Table 2. Slope value of linear fitting of load dependent resistance curves (plotted in double logarithmic scale), R-squared of linear fit between 0.94 and 0.99.

GNP also exhibit exceptional linearity. However, the compression-to-displacement relationship varies significantly for loads above 3 N. Therefore, the use of this nanoparticle should be limited to low load and relatively high current applications so as to minimize the resistance caused by capacitances (interlayer gap). GF on the other hand, should be limited to low and high load applications due to fluctuations in its compression-to-displacement relationship in mid-range loads. In relative terms, CNH presents the largest resistance reduction within the loading range (along with OLC), decreasing in a relatively linear manner as the load increases. Its compression-to-displacement relationship is exceptionally constant with minor fluctuations in the mid-range loads. Therefore, as with GF, its application should be limited to low and high load requirements. However, CNH possesses a larger ohmic range, albeit its electrical resistance is significantly higher. CB shows very promising results due to its consistency in its compression-to-displacement relationship in the mid-to-high loading range after the voids formed due to agglomeration are filled. The load-resistance curves are linear, and CB has a significant resistance reduction between 0.25 and 10 N. Moreover, CNT performed exceptionally well, having consistent compression-to-displacement relationship, linear load-resistance curves, and adequate overall resistance reduction. The latter is a significant advantage since instrumentation with lower resistance precision are required. Smaller agglomerate sizes did not benefit their piezoresistive performance. CNT-D's electrical performance marginally improved compared to CNT. Its compression-to-displacement relationship, on the other hand, fluctuates throughout the entire loading range evaluated, tending to stabilize for high loads. Therefore, CNT-D should be utilized in very high load applications. Conversely, the reduction of agglomerate sizes (through dispersion) can be neglected since CNT in their agglomerated state are suitable for low, mid, and high load applications. Moreover, one- and two-dimensional nanostructures show relatively low electrical resistance at 10 N. Therefore, for sufficiently high loads, nanoparticle aggregates could be used as interconnection media between two terminals.

The results presented demonstrate the auspicious piezoresistive behavior of carbon nanostructures, emphasizing the importance of proper CNP selection based on intended applications. However, further research is necessary to gain a comprehensive understanding of their performance, efficiency, reliability, and limitations. Therefore, it is important to study the influence of atmospheric conditions (i.e., temperature and primarily humidity) and particle size, as well as loading conditions that exceed the ranges from this study. Additionally, while the measurements reported here showed exceptional repeatability, it is necessary to evaluate the CNPs' performance in successive loading and unloading cycles in more detail.

Data availability

The data required to support the present findings are present in the manuscript and supplementary information.

Received: 8 February 2024; Accepted: 13 April 2024
Published online: 22 April 2024

References

1. Arnau, A. & Soares, D. Fundamentals of piezoelectricity. In *Piezoelectric Transducers and Applications*. 1–38 https://doi.org/10.1007/978-3-540-77508-9_1 (Springer, 2009).
2. Doll, J. C. & Pruitt, B. L. Piezoresistance fundamentals. In *Piezoresistor Design and Applications*. 21–49 https://doi.org/10.1007/978-1-4614-8517-9_2 (Springer, 2013).
3. Fiorillo, A. S., Critello, C. D. & Pullano, A. S. Theory, technology and applications of piezoresistive sensors: A review. *Sens. Actuators A Phys*. **281**, 156–175 https://doi.org/10.1016/j.sna.2018.07.006 (2018).
4. Wang, X., Lim, E. G., Hoettges, K. & Song, P. A review of carbon nanotubes, graphene and nanodiamond based strain sensor in harsh environments. *C (Basel)* **9**, 108 (2023).
5. Zhao, J., Zhang, G. Y. & Shi, D. X. Review of graphene-based strain sensors. *Chin. Phys. B* https://doi.org/10.1088/1674-1056/22/5/057701 (2013).
6. Obitayo, W. & Liu, T. A review: Carbon nanotube-based piezoresistive strain sensors. *J. Sens.* https://doi.org/10.1155/2012/652438 (2012).
7. Jiang, M. J., Dang, Z. M., Xu, H. P., Yao, S. H. & Bai, J. Effect of aspect ratio of multiwall carbon nanotubes on resistance-pressure sensitivity of rubber nanocomposites. *Appl. Phys. Lett.* **91**, 13 (2007).
8. Jiang, M. J., Dang, Z. M. & Xu, H. P. Giant dielectric constant and resistance-pressure sensitivity in carbon nanotubes/rubber nanocomposites with low percolation threshold. *Appl. Phys. Lett.* **90**, 15 (2007).
9. Chen, L., Chen, G. & Lu, L. Piezoresistive behavior study on finger-sensing silicone rubber/graphite nanosheet nanocomposites. *Adv. Funct. Mater.* **17**, 898–904 (2007).
10. Dang, Z. M. *et al.* Supersensitive linear piezoresistive property in carbon nanotubessilicone rubber nanocomposites. *J. Appl. Phys.* **104**, 15 (2008).
11. Tao, L. Q. *et al.* Graphene-paper pressure sensor for detecting human motions. *ACS Nano* **11**, 8790–8795 (2017).
12. Yamada, T. *et al.* A stretchable carbon nanotube strain sensor for human-motion detection. *Nat. Nanotechnol.* **6**, 296–301 (2011).
13. Monteiro, A. O., Cachim, P. B. & Costa, P. M. F. J. Self-sensing piezoresistive cement composite loaded with carbon black particles. *Cem. Concr. Compos.* **81**, 59–65 (2017).
14. Li, H., Xiao, H. & Ou, J. Electrical property of cement-based composites filled with carbon black under long-term wet and loading condition. *Compos. Sci. Technol.* **68**, 2114–2119 (2008).
15. Falcao, E. H. & Wudl, F. Carbon allotropes: Beyond graphite and diamond. *J. Chem. Technol. Biotechnol.* **82**, 524–531 (2007).
16. Hirsch, A. The era of carbon allotropes. *Nat. Mater.* **9**, 868–871 (2010).
17. Wang, P. *et al.* Beyond color: The new carbon ink. *Adv. Mater.* https://doi.org/10.1002/adma.202005890 (2021).
18. Yin, G. *et al.* A carbon nanotube/polymer strain sensor with linear and anti-symmetric piezoresistivity. *J. Compos. Mater.* **45**, 1315–1323 (2011).
19. Huang, K. *et al.* Ultrasensitive MWCNT/PDMS composite strain sensor fabricated by laser ablation process. *Compos. Sci. Technol.* **192**, 13 (2020).
20. Alderete, B., Lößlein, S. M., Bucio Tejeda, D., Mücklich, F. & Suarez, S. Feasibility of carbon nanoparticle coatings as protective barriers for copper-wetting assessment. *Langmuir* **38**, 15209–15219 (2022).
21. Alderete, B. *et al.* Near superhydrophobic carbon nanotube coatings obtained via electrophoretic deposition on low-alloy steels. *Adv. Eng. Mater.* **23**, 2001448 (2021).

22. Alderete, B., Nayak, U. P., Mücklich, F. & Suarez, S. Influence of topography on electrical contact resistance of copper-based materials. *Surf. Topogr.* **11**, 025027 (2023).
23. Alderete, B., Mücklich, F. & Suarez, S. Wear reduction via CNT coatings in electrical contacts subjected to fretting. *Tribol. Lett.* **71**, 54 (2023).
24. Alderete, B., Suarez, S., Tejeda, D. B. & Mücklich, F. Fretting and electrical contact resistance characteristics of carbon nanoparticle-coated Cu electrical contacts. In *2022 IEEE 67th Holm Conference on Electrical Contacts* (*HLM*). 1–8 https://doi.org/10.1109/HLM54538.2022.9969836 (IEEE, 2022).
25. MacLucas, T. & Suarez, S. On the solid lubricity of electrophoretically deposited carbon nanohorn coatings. *Lubricants* **7**, 62 (2019).
26. MacLucas, T., Schütz, S., Suarez, S. & Mücklich, F. Surface protection of austenitic steels by carbon nanotube coatings. *Surf. Topogr.* **6**, 014005 (2018).
27. Alderete, B., Mücklich, F. & Suarez, S. Characterization and electrical analysis of carbon-based solid lubricant coatings. *Carbon Trends* **7**, 100156 (2022).
28. Reinert, L., Varenberg, M., Mücklich, F. & Suárez, S. Dry friction and wear of self-lubricating carbon-nanotube-containing surfaces. *Wear* **406–407**, 33–42 (2018).
29. Reinert, L. *et al.* Long-lasting solid lubrication by CNT-coated patterned surfaces. *Sci. Rep.* **7**, 42873 (2017).
30. Alderete, B., Mücklich, F. & Suarez, S. Electrical characterization of carbon nanotube reinforced silver and copper composites for switching contacts. *J. Compos. Sci.* **7**, 284 (2023).
31. Suarez, S., Alderete, B., Puyol, R. & Mücklich, F. Load-dependent electrical contact resistance of carbon nanotube-reinforced metal matrix composites. In *2022 IEEE 67th Holm Conference on Electrical Contacts* (*HLM*). 1–6 https://doi.org/10.1109/HLM54538.2022.9969801 (IEEE, 2022).
32. Suarez, S., Puyol, R., Schafer, C. & Mucklich, F. Carbon nanotube-reinforced metal matrix composites as novel electrodes for low-voltage switching applications: A surface degradation analysis. In *2019 IEEE Holm Conference on Electrical Contacts.* 135–141 https://doi.org/10.1109/HOLM.2019.8923921 (IEEE, 2019).
33. Suárez, S., Rosenkranz, A., Gachot, C. & Mücklich, F. Enhanced tribological properties of MWCNT/Ni bulk composites—Influence of processing on friction and wear behaviour. *Carbon N. Y.* **66**, 164–171 (2014).
34. Sharma, S., Sharma, A., Cho, Y. K. & Madou, M. Increased graphitization in electrospun single suspended carbon nanowires integrated with carbon-MEMS and carbon-NEMS platforms. *ACS Appl. Mater. Interfaces* **4**, 34–39 (2012).
35. Marinho, B., Ghislandi, M., Tkalya, E., Koning, C. E. & de With, G. Electrical conductivity of compacts of graphene, multi-wall carbon nanotubes, carbon black, and graphite powder. *Powder Technol.* **221**, 351–358 (2012).
36. Sánchez-González, J., Macías-García, A., Alexandre-Franco, M. F. & Gómez-Serrano, V. Electrical conductivity of carbon blacks under compression. *Carbon N. Y.* **43**, 741–747 (2005).
37. Rani, A., Nam, S.-W., Oh, K.-A. & Park, M. Electrical conductivity of chemically reduced graphene powders under compression. *Carbon Lett.* **11**, 90–95 (2010).
38. Reinert, L., Zeiger, M., Suárez, S., Presser, V. & Mücklich, F. Dispersion analysis of carbon nanotubes, carbon onions, and nanodiamonds for their application as reinforcement phase in nickel metal matrix composites. *RSC Adv.* **5**, 95149–95159 (2015).
39. Alderete, B. *et al.* Multipurpose setup used to characterize tribo-electrical properties of electrical contact materials. *MethodsX* **8**, 101498 (2021).
40. Tamai, T., Saitoh, Y., Sawada, S. & Hattori, Y. Peculiarities characteristics between contact trace and contact resistance of tin plated contacts. In *2008 Proceedings of the 54th IEEE Holm Conference on Electrical Contacts*. 337–343 (IEEE, 2008).
41. Alderete, B., Mucklich, F. & Suarez, S. Tarnishing (Ag2S) layer on silver-plated electrical contacts: Its influence on electrical contact resistance. *IEEE Trans. Compon. Packag. Manuf. Technol.* **13**, 45–58 (2023).
42. Li, C., Thostenson, E. T. & Chou, T. W. Dominant role of tunneling resistance in the electrical conductivity of carbon nanotube-based composites. *Appl. Phys. Lett.* **91**, 91–94 (2007).
43. Saito, R., Matsuo, R., Kimura, T., Dresselhaus, G. & Dresselhaus, M. S. Anomalous potential barrier of double-wall carbon nanotube. *Chem. Phys. Lett.* **348**, 187–193 (2001).
44. Zeiger, M., Jäckel, N., Aslan, M., Weingarth, D. & Presser, V. Understanding structure and porosity of nanodiamond-derived carbon onions. *Carbon N. Y.* **84**, 584–598 (2015).
45. Suarez, S. *et al.* In-situ nanodiamond to carbon onion transformation in metal matrix composites. *Carbon N. Y.* **129**, 631–636 (2018).
46. Vander Wal, R. L., Tomasek, A. J., Pamphlet, M. I., Taylor, C. D. & Thompson, W. K. Analysis of HRTEM images for carbon nanostructure quantification. *J. Nanopart. Res.* *6*, 555–568 (2004).
47. Bobrowska, D. M., Olejnik, P., Echegoyen, L. & Plonska-Brzezinska, M. E. Onion-like carbon nanostructures: An overview of bio-applications. *Curr. Med. Chem.* **26**, 6896–6914 (2018).
48. Karousis, N., Suarez-Martinez, I., Ewels, C. P. & Tagmatarchis, N. Structure, properties, functionalization, and applications of carbon nanohorns. *Chem. Rev.* **116**, 4850–4883. https://doi.org/10.1021/acs.chemrev.5b00611 (2016).
49. Pierson, H. O. *Handbook of Carbon, Graphite, Diamond and Fullerenes: Properties, Processing and Applications* (Noyes Publications, 1993).
50. Robertson, J. *et al.* Use of carbon nanotubes for VLSI interconnects. *Diam. Relat. Mater.* **18**, 957–962 (2009).
51. Bandaru, P. R. Electrical properties and applications of carbon nanotube structures. *J. Nanosci. Nanotechnol.* **7**, 1239–1267 (2007).
52. Holm, R. *Electric Contacts*. https://doi.org/10.1007/978-3-662-06688-1 (Springer, 1967).
53. Slade, P. G. *Electrical Contacts*. https://doi.org/10.1201/b15640 (CRC Press, 2014).
54. Ibach, H. & Lüth, H. "Free" electrons in solids. In *Solid-State Physics*. 135–158 https://doi.org/10.1007/978-3-540-93804-0_6 (Springer, 2009).
55. de Jong, M. J. M. Transition from Sharvin to Drude resistance in high-mobility wires. *Phys. Rev. B* **49**, 7778–7781 (1994).
56. Zhao, J., Jiang, J. W., Jia, Y., Guo, W. & Rabczuk, T. A theoretical analysis of cohesive energy between carbon nanotubes, graphene and substrates. *Carbon N. Y.* **57**, 108–119 (2013).
57. Chang, T. Torsional behavior of chiral single-walled carbon nanotubes is loading direction dependent. *Appl. Phys. Lett.* **90**, 20 (2007).
58. Hilding, J., Grulke, E. A., George Zhang, Z. & Lockwood, F. Dispersion of carbon nanotubes in liquids. *J. Dispers. Sci. Technol.* **24**, 1–41 (2003).
59. Campbell, C. S. Granular material flows—An overview. *Powder Technol.* **162**, 208–229 (2006).
60. Grundmann, M. *Nanostructures*. 461–487 https://doi.org/10.1007/978-3-319-23880-7_14 (2016).
61. Sumanth Kumar, D., Jai Kumar, B. & Mahesh, H. M. Quantum nanostructures (QDs): An overview. In *Synthesis of Inorganic Nanomaterials*. 59–88 https://doi.org/10.1016/B978-0-08-101975-7.00003-8 (Elsevier, 2018).

Acknowledgements

B. Alderete wishes to acknowledge the support from the German Academic Exchange Service (DAAD) and the Roberto Rocca Education Program (RREP). The authors wish to thank J. Schmauch for the acquisition of HR-TEM micrographs and M.A. Guitar for proofreading the manuscript. The authors gratefully acknowledge funding in the ZuMat project, supported by the State of Saarland from the European Regional Development

Fund (Europäischen Fonds für Regionale Entwicklung, EFRE). Funding for the PFIB/SEM instrument by German Research Foundation is greatly acknowledged (INST 256/510-1 FUGG).

Author contributions

Conceptualization, B.Alderete and S.Suarez; Data curation, B.Alderete; Formal analysis, B.Alderete; Funding acquisition, F.Mücklich and S.Suarez; Investigation, B.Alderete; Methodology, B.Alderete and S.Suarez; Project administration, F.Mücklich and S.Suarez; Resources, F.Mücklich; Supervision, S.Suarez; Validation, B.Alderete; Visualization, B.Alderete; Writing—original draft, B.Alderete; Writing—review & editing, S.Suarez.

Funding

Open Access funding enabled and organized by Projekt DEAL.

Competing interests

The authors declare no competing interests.

Additional information

Supplementary Information The online version contains supplementary material available at https://doi.org/10.1038/s41598-024-59673-5.

Correspondence and requests for materials should be addressed to B.A.

Reprints and permissions information is available at www.nature.com/reprints.

Publisher's note Springer Nature remains neutral with regard to jurisdictional claims in published maps and institutional affiliations.

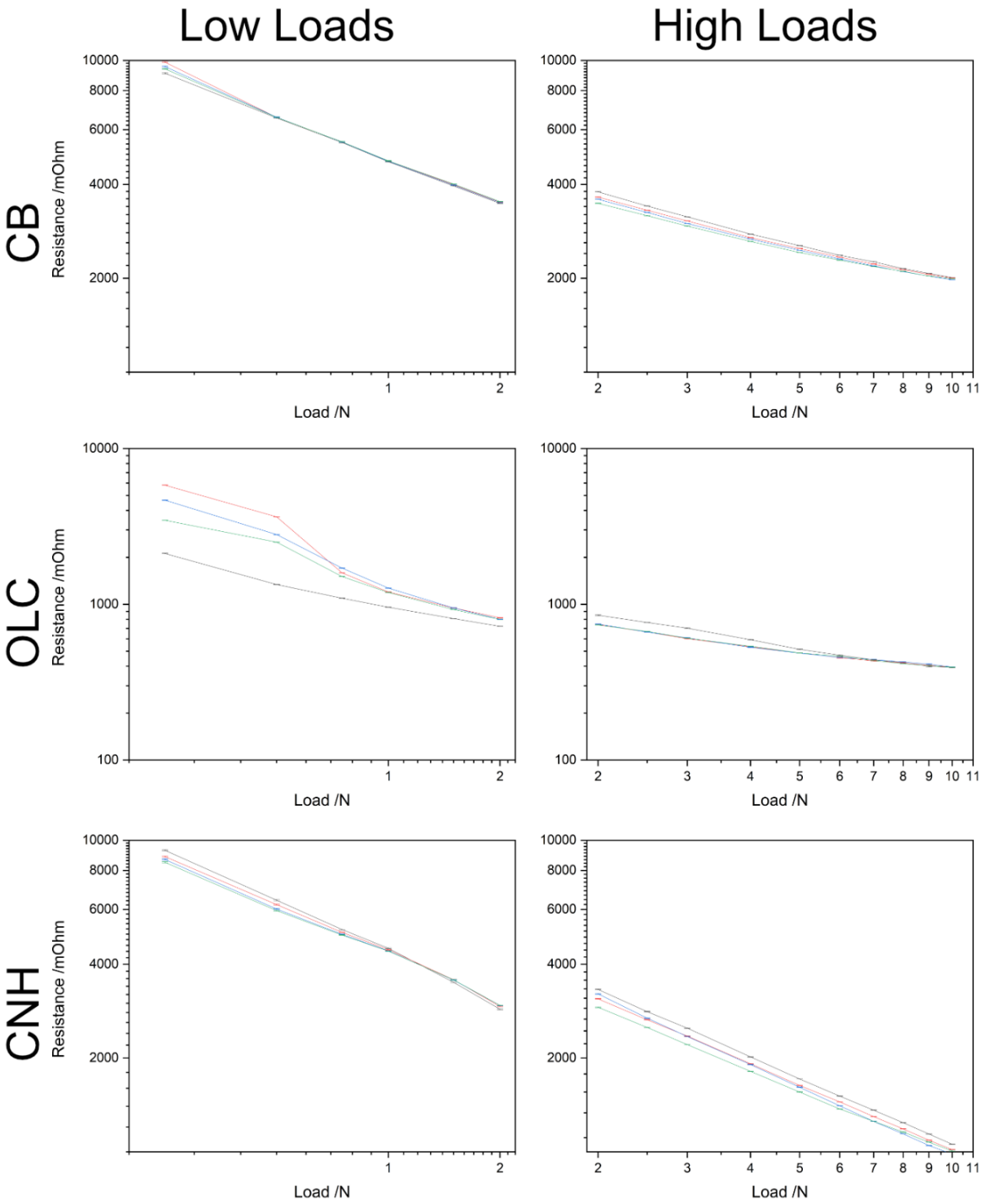

Figure S1: Multiple resistance curves of quasi-zero-dimensional CNP for low and high loading range highlighting the repeatability of the results.

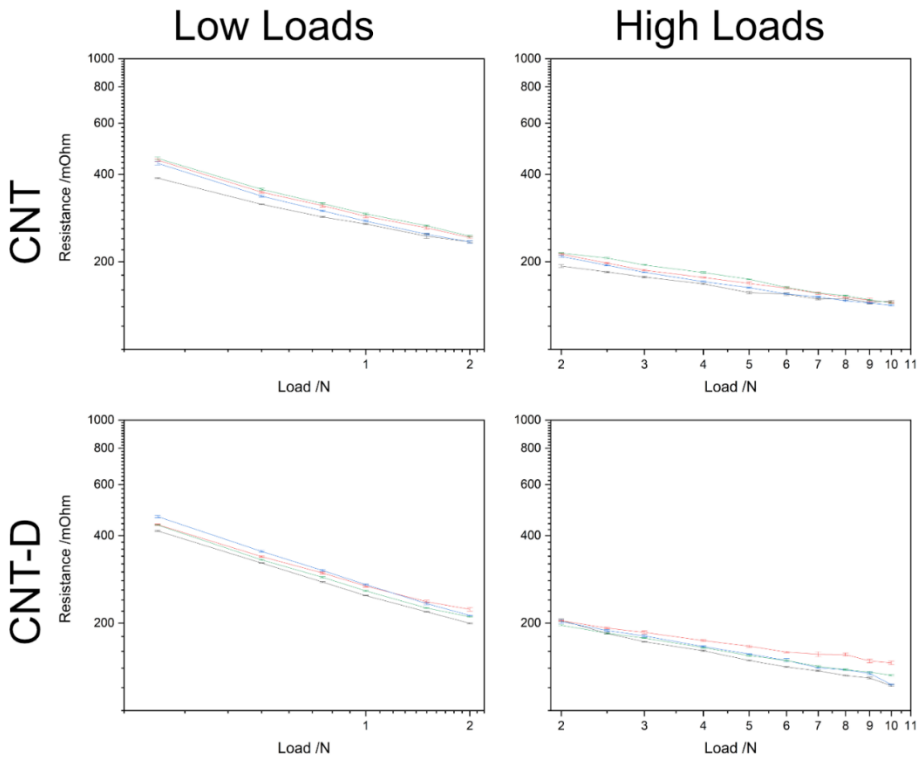

Figure S2: Multiple resistance curves of one-dimensional CNP for low and high loading range highlighting the repeatability of the results.

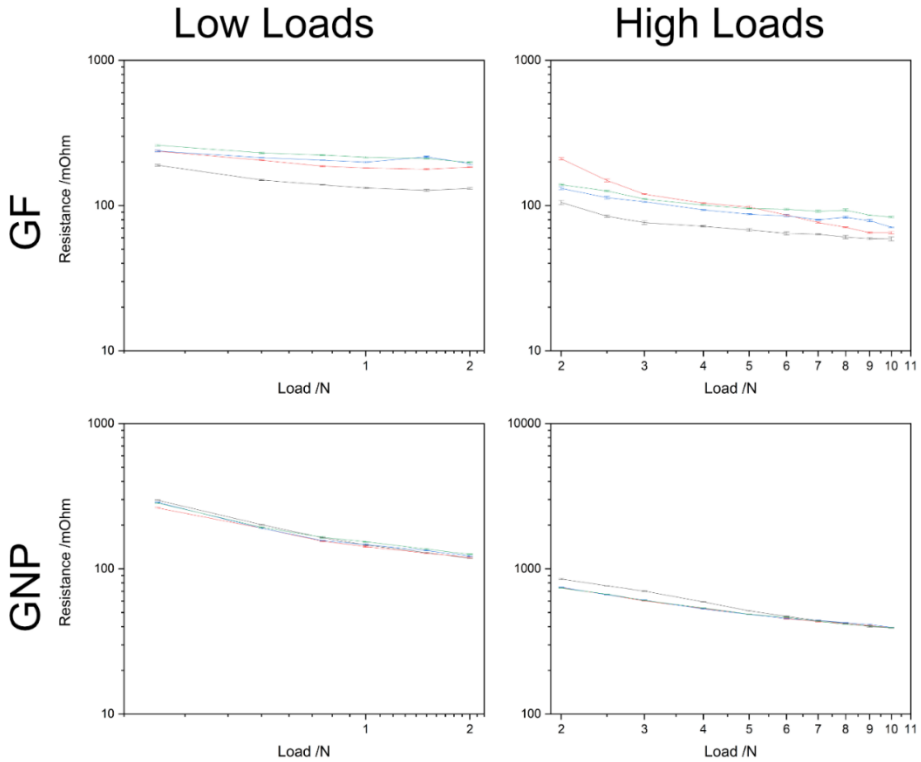

Figure S3: Multiple resistance curves of two-dimensional CNP for low and high loading range highlighting the repeatability of the results.

ARTICLE V
Influence of Topography on Electrical Contact Resistance of Copper-Based Materials

Bruno Alderete*, U. Pranav Nayak, Frank Mücklich, Sebastian Suarez

Chair of Functional Materials, Saarland University, Campus D3.3, 66123 Saarbrücken, Germany

Research article
Published in "*Surface Topography: Metrology and Properties*" (2023)
Impact Factor: 2.0 (2023)
Reproduced with permission from Institute of Physics Publishing
Accessible online at: doi.org/10.1088/2051-672X/acdfea

Own Contribution: Conceptualization; Methodology; Investigation; Formal Analysis; Validation; Writing – Original Draft; Visualization.

Cite this article as: B. Alderete, U.P. Nayak, F. Mücklich, S. Suarez, Influence of topography on electrical contact resistance of copper-based materials, Surf Topogr 11 (2023) 025027. https://doi.org/10.1088/2051-672x/acdfea.

Influence of topography on electrical contact resistance of copper-based materials

Bruno Alderete*, U. Pranav Nayak, Frank Mücklich, Sebastian Suarez
Chair of Functional Materials, Saarland University, Campus D3.3, Saarbrücken 66123, Germany
* Corresponding author: bruno.alderete@uni-saarland.de

Abstract

The design of an electrical contact is crucial to ensure optimal performance, reliability, and efficiency of connectors. One key aspect is the surface quality of the contacting bodies – among other factors such as material selection, contact geometry, etc. In this work, we evaluated the influence on electrical contact resistance (ECR) of a smooth copper-based surface (brass, bronze, and tin-plated copper) when contacted against surfaces with different degrees of roughness. Furthermore, a carbon nanotube (CNT) coating was proposed with the goal of mitigating the topography-induced influence of the textured counter electrodes. The electrodes and counter electrodes were thoroughly characterized to understand the contacting mechanisms through numerical modeling, – namely, Greenwood-Williamson and Jackson-Green models – as well as using a practical-oriented slope analysis. Load-dependent ECR measurements were carried out to quantify the effect of roughness on contact resistance. When contacting against brass and bronze, a clear correlation between roughness and ECR can be established, with higher roughness equating to lower ECR. In tin-plated copper, on the other hand, this hierarchy is not as well defined due to the ease with which the tin plating deforms, thus enabling the penetration of outstanding asperities and consequently establishing a better electrical contact. CNT-coated counter electrodes showed promising results, partially confirming the hypothesis proposed. However, unforeseen topography-related interactions with the CNT coating produced exceptions in the ECR measurements. Nonetheless, for most cases studied the coating did mitigate the influence of roughness.

Keywords: carbon nanotubes, contact mechanics, electrical contact design, electrophoretic deposition, rough surfaces.

1. Introduction

When designing an electrical contact, multiple requirements must be satisfied for optimal contact performance. However, as there is no perfect electrical contact material, tradeoffs must

be made depending on the specific application of the contact in question. Design choices such as material, geometry, surface finish, etc. are pivotal for optimal contact performance. Focusing on material selection, mechanical properties, wear, and corrosion resistance, and particularly transport properties play an important role not only in performance, but also on durability, maintenance requirements, and reliability.

Understanding the various parameters that affect electrical contact resistance (ECR) of metals is crucial for optimal contact design. However, when analyzing these parameters, it is important to consider practical applications. Although laboratory conditions help to understand the different phenomena at play, these conditions cannot always be met in industrial manufacturing processes. Unequivocally, laboratory conditions do not always reflect real-world applications, where technical contact surfaces are subjected to harsh mechanical and environmental conditions. Accordingly, it is of interest to conduct a quantitative and qualitative analysis of the influence of surface topography on the ECR of flat contacting bodies. Therefore, more accurately understanding the behavior of realistic contacting surfaces.

By studying the loading phase of load dependent ECR, information on the predominant deformation mechanisms can be acquired, as reported by Tamai et al. [1,2]. This analysis is based on the total resistance (R_t) of a contact, shown in **Equation 1**. In this equation, ρ_p, ρP_f, and ρ_{cont} are the resistivity of the probe, of the plated material, and of the contaminant film, respectively, η_c is a cleanliness factor (an empirical coefficient that takes a value of 1 for clean interfaces), H is the hardness, F is the load, and d_{cont} is the thickness of the contamination film. The second term from **Equation 1** corresponds to the contamination films present in the contacts [3,4]. All parameters in **Equation 1** are material or system properties, therefore, they are constant throughout all measurements. Although ρ_p, ρP_f, and ρ_{cont} are temperature dependent, these can be considered constant since the temperature does not change sufficiently to have a significant impact on the materials' resistivity during experimentation. Therefore, the only parameter that varies is the applied load F. Consequently, **Equation 1** can be simplified and expressed as shown in **Equation 2**, where k is a constant value that encompasses the fixed values and n is an exponent that can be approximated by the slope value of load dependent ECR when plotted in a double logarithmic scale.

It is important to consider, however, that this analysis should not be overinterpreted due to its

$$R_t = \frac{\rho_p + \rho P_p}{2}\left(\frac{\eta_c \pi H}{4F}\right)^{1/2} + \frac{\rho_{cont} d_{cont} H}{F} \qquad \textbf{Equation 1}$$

$$R_t = \left(\frac{k}{F}\right)^n \qquad \textbf{Equation 2}$$

theoretical nature. This theoretical framework was established for flat, smooth, and clean surfaces, as well as the consideration that only one surface undergoes deformation. Therefore, exponent deviation from theoretical values is expected. Nonetheless, this analysis could prove useful to predict the deformation that takes place in the system in a quick and straight forward manner. Further deviation from theoretical values were listed by Leidner et al. [5]. Depending on the value of *n*, the deformation mechanism of the system can be predicted. When *n* takes a value of -1/3 or -2/3, elastic deformation is predominant in the system, whereas plastic deformation is predominant when *n* is equal to -1/2 or -1 [6].

In contacting surfaces, the ECR is the sum of three components, as shown in **Equation 3**. This equation states that the total resistance of a system is the sum of the constriction resistance (caused by the concentration of current in the contacting sites, i.e., a-spots), the film resistance (consequence of residual films on the contacting surfaces), and the resistance of the bulk material, R_c, R_f, and R_b, respectively [3]. The bulk resistance R_b is constant (separated into R_{b1} and R_{b2} for cases when two different materials are in contact), determined by the material choice, whereas the constriction and film resistance vary significantly depending on surface finish, oxidation state, and contact cleanliness. Constriction resistance is the primary focus of this study since the concentration of current flow is strongly linked to the number of asperities in contact, as defined by Holm in **Equation 4** [7], where a is the radius of the circular contact area and ρ is the conductivity of the contacting materials. Constriction resistance is size dependent, with different validities depending on if the contact size is larger than or smaller than the mean free path of electrons [8]. In the former case Holm resistance is valid, whereas Sharvin resistance is valid for smaller contact areas. In this study, we will focus solely on Holm resistance. As expressed in **Equation 4**, with higher number of a-spots in contact, the real contact area approaches the apparent contact area. Consequently, the constriction resistance is reduced due to a higher number of contacting sites.

Therefrom, the slope analysis can provide insight into the predominant resistance type: constriction or film resistance [2,6,7,9]. When *n* takes a value of -1/3 or -1/2 it was established that the constriction resistance dominates the system. Film resistance, on the other hand, dominates when the exponent *n* takes values of -2/3 or -1. As with the deformation mechanism analysis, the actual values will deviate from these theoretical values. Furthermore, more than one deformation mechanism taking place simultaneously can cause an intermediate value.

$$R_t = R_c + R_f + R_{b1} + R_{b2} \qquad \textbf{Equation 3}$$

$$R_C = \frac{\rho}{2 \cdot a} \qquad \textbf{Equation 4}$$

The contact between two rough surfaces can be modeled by determining an equivalent roughness. In other words, the system can be simplified by assuming that one surface is perfectly smooth and undeformable, whereas the other surface possesses a roughness that is equivalent to the actual roughness of both surfaces [10]. Furthermore, if it is considered that the asperities have a rounded peak (or summit), then the contacting system can be evaluated as a sphere-on-plane. To properly simulate the contact situation, the correct mathematical model should be selected. In fully elastic contact between two smooth bodies, Hertzian contact theory can be used to determine the contact radius of individual asperities, as well as their mean and maximum contact pressure [11]. In rough surfaces, as the asperities begin to deform, it is intuitive to believe that the real contact area grows as the load increases. Consequently, the contacting pressure should reduce due to the larger area in which the load is distributed, in addition to new smaller contacting sites also encounter the surface. At a given load, the contact pressure should remain constant as the asperities deform, however, with increasing loads the contact pressure also increases. Therefore, the contacting area does not depend on the contact pressure, but rather on the applied load, as proven by Greenwood and Williamson [12].

A major limitation in Hertzian theory is that the contacting surfaces must be perfectly smooth, since this model considers a round body contacting a flat body. Greenwood and Williamson (GW) expand Hertzian contact by stochastically modeling the contacting systems involving roughness more accurately. Consequently, the GW model extends the analysis from a single asperity to a more realistic representation with multiple sphere-on-plane contacts. The GW model considers the following assumptions [10,13]:

1. The asperity distribution is random and can be modeled by a Gaussian distribution.
2. At their peaks, asperities have a constant radius of curvature which is independent of their individual height.
3. As asperities deform, these do not interfere with adjacent asperities, i.e., asperities are mechanically independent.
4. The bulk material does not deform as the asperities are loaded onto its surface (elastic sphere against a rigid plane).

Prior to applying the GW model, statistical parameters such as the radius of curvature of the individual asperities (r), the areal asperity density (η), and the standard deviation of the surface height (σ_s) must be calculated [14]. Physically, r is the mean radius of each asperity, η is the number of asperities per unit of area – and σ_s is the deviation in height of each asperity with respect to the mean value (i.e., the datum line). These parameters can be determined by using the spectral moments, as described by McCool [13]. As with Hertzian contact theory, GW model is

applicable and widely accepted for purely elastic contact situations. However, this model is not sufficiently accurate in the elasto-plastic regime. In this case, other models which extend the range of applicability of the GW model must be employed. A plethora of researchers have sought out to improve upon the GW model, while others derived their own models for plastic deformation, such as: Kogut-Etsion [15], Chang-Etsion-Bogy [16], Zhao-Maietta-Chang [17], Shankar-Mayuram [18], and Jackson-Green model (JG) [19,20], among others [21]. The JG model presents the added advantage that it is not dependent on limiting assumptions – e.g., the hardness of the material [14]. To establish in which regime our system is functioning, the plasticity index (ψ) must be calculated [12,14,20]. If the plasticity index takes a value below 0.6, it means that our system deforms purely elastically. When ψ takes values above 0.6, it indicates that the onset of plasticity has begun, whereas for ψ values above 1 the system is in plastic regime. Based on the ψ value acquired, the correct model must be chosen since the results vary from model to model [20]. The ψ can also qualitatively describe the amount of plastic deformation that the asperities of the rough surface undergo [21].

In many industrial operations, having thorough control of the manufacturing process can be resource-intensive, costly, and time consuming. However, for specific applications a certain surface finish, post process, etc. may be required. Therefore, in this study we go one step further by proposing a carbon nanotube (CNT) coating on the textured counter electrodes. The aim of this coating is to potentially compensate the influence of the generated topographies. Accordingly, the counter electrodes will be coated via electrophoretic deposition (EPD) [22,23]. It is hypothesized that due to the restitutional forces present in the multi-walled CNT, any influence in ECR developed by the existing topographies, could be neutralized. Along with the intrinsic elastic restitution of the individual CNT, interaction between CNT and CNT agglomerates could further promote restitution. Additionally, CNT are electrically conductive particles, thereby having a limited effect on the overall ECR of the system [22]. Therefore, sufficiently thick CNT coatings may be capable of limiting any undesirable topography-induced effects. These nanoparticle coatings also have the added advantage of providing wear protection due to their outstanding solid lubricity [24], as well as atmospheric protection because of their intrinsic hydrophobic wetting behavior [23,25]. Consequently, this simple, cost-effective, and quick post process could be implemented at the last stages of a manufacturing process. This could not only eliminate secondary finishing processes and quality control processes, but also incorporate the aforementioned benefits.

Copper and copper-based materials are extensively used in diverse applications due to their outstanding transport properties, as well as good mechanical properties and corrosion resistance. The focus of this study is on electrical applications. Therefore, brass, bronze, and tin-plated

copper (SnCu) will be investigated. These materials were chosen based on their extensive use in electrical applications, such as: connectors, relays, brackets, sockets, conductive springs, bus bars, etc. Round, flat-headed copper rivets (counter electrodes) will be ground and polished to different grit and particle sizes, thus generating different topographies. The textured counter electrodes will contact the polished electrodes and this system will be electrically and topographically characterized. Furthermore, the contacting situation of the system will be modeled and evaluated.

Previous research carried out by Zhai et al. have reported a power law relationship between normal load and conductance between rough aluminum alloy surfaces [26,27], with the exponent being closely linked to the topographic characteristics of the surfaces. Furthermore, numerical and theoretical investigations conducted by Wang et al. have also reported this power-law relationship [28]. Within the scope of this work, we aim to evaluate the influence of different stochastic counter electrode topographies (i.e., textures generated by grinding and polishing) against smooth brass, bronze, and tin-plated copper electrical contacts with loads ranging from 0.25 N up to 10 N. The electrodes and counter electrodes will be characterized via confocal laser scanning microscopy (CLSM) to attain information on the resulting roughness. Load-dependent ECR will be carried out to assess the influence of topography on the contacting system's electrical behavior. Furthermore, slope analysis on the loading phase of load dependent ECR, as well as numerical contact mechanics simulations will be calculated to gain insight into the contacting situation in our system – via GW and JG model. EPD will be used to coat the textured counter electrodes, which will be subsequently characterized via load dependent ECR. Furthermore, focused ion beam (FIB) cross sections will be carried out on the coated counter electrodes to measure the resulting coating thickness, evaluate coating compactness, as well as the coating-rivet interface.

2. Materials and methods

2.1. Material characterization

2.1.1. Electrodes

To evaluate the influence of counter electrode topography on electrical contacts, three different materials were studied – i.e., brass ($CuZn_{37}$), bronze ($CuSn_6$), and tin-plated copper (tinned Cu-Ni-Si alloy, Stol 76M C19005) – henceforth SnCu. Laminated brass and bronze platelets were used – (25 × 10 × 1) mm. The tin-plated copper samples were obtained from commercially available strip material (KMD Group, Germany). These Cu strips were plated by a galvanization process. The SnCu samples were characterized in an as-received state. The brass and bronze samples, on the other hand, were ground (P1200 grit silicon carbide grinding paper)

and polished with 6 µm, 3 µm, 1 µm diamond suspension, and oxide particle suspension to obtain a mirror-polished surface. The roughness of the materials was measured via CLSM (LEXT OLS4100, Olympus) with a laser wavelength of 405 nm. To obtain a larger field of view with high magnification, 3×3 stitching at 20× was carried out. After polishing, the brass and bronze samples presented a root mean square (rms) roughness between 10-30 nm. On the other hand, the as-received SnCu samples presented a rms roughness of 220 ± 20 nm.

A FIB cross section (FEI Helios NanoLab600 Dual Beam Setup) on a SnCu sample was carried out to measure the plating thickness, shown in **Figure 1**. In the cross section, the Cu base material and Sn plating can be observed, as well as the protective Pt deposition. The Sn plating has a mean thickness of 2.2 ± 0.1 µm. A magnified region at the center of the cross section is shown where intermetallic phases (IMP) can be more easily identified in the micrograph acquired with the ion beam. These IMP are highlighted in **Figure 1** by the white dashed line. The thickness of the IMP varies significantly from region to region, showing an average thickness of 0.7 ± 0.1 µm. The formation of the IMP occurs naturally over time due to aging.

Microhardness measurements were carried out using Struers Dura Scan 50 microhardness tester (Struers Inc., USA) with a load of 0.98 N. The load was applied onto the sample for a duration of 15 seconds and the resulting imprint was imaged via light optical microscopy using

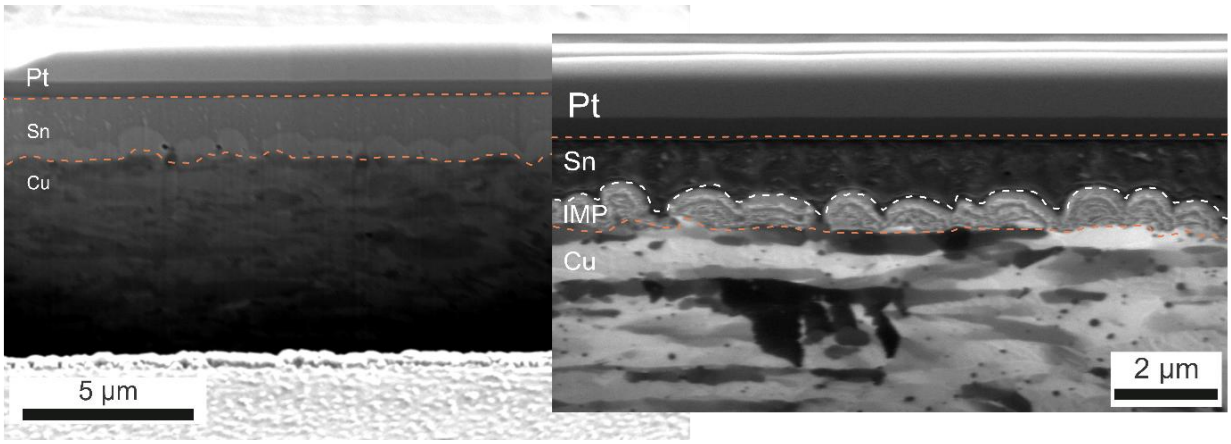

Figure 1: Cross section of SnCu showing Cu base material, Sn plating, and intermetallic phases formed between Cu and Sn. The inset shows a magnified micrograph of the cross section acquired with ion beam to achieve better contrast between the Sn plating, the IMP, and the Cu base material.

Table 1 - Vickers microhardness of copper, brass, bronze, and tin-plated copper.

Material	**$HV_{0.1}$**
Copper	83 ± 2
Brass	88 ± 3
Bronze	174 ± 2
SnCu	95 ± 5

40× magnification. The resulting hardness of brass, bronze, and SnCu is shown in **Table 1**. The hardness of Cu was also measured to illustrate how the alloying and plating elements affect the hardness of this metal. It is important to consider that the hardness of SnCu is the composition of the hardness of the Sn plating and the Cu base material.

Although the load is relatively low, the penetration of the indenter is over three times greater than the mean thickness of the plating, thus proving that the measured hardness is influenced by the base material. To show the influence of the base material on its hardness, microhardness measurements at higher load were carried out on SnCu samples. At a load of 9.8 N, SnCu showed an average hardness of $HV_1 = 111 \pm 7$, resulting in a penetration depth of approximately 18.5 µm. With triple the penetration depth, a small increase of approximately 16 HV compared to the measurements carried out at 0.98 N was recorded. The hardness values at this higher load also surpass the values obtained for the pure Cu sample by about 30 HV. This increase in hardness at higher loads is caused by the Sn plating.

At an attempt to decrease the influence of the base material on the plating's hardness, Knoop microhardness was measured. However, these measurements were consistent with Vickers microhardness in SnCu samples under identical loading conditions.

2.1.2. Counter electrodes - rivets

The counter electrodes used were flat-headed Cu rivets, with a diameter of 5 mm. These rivets were ground and polished down to 1 µm polishing suspension. Further polishing was attempted using oxide particle suspension; however, this process oxidized the surface of the polished counter electrodes. Consequently, this process was eliminated, opting for 1 µm as the smoothest topography. Once all rivets were polished, a set of rivets were re-polished to a specific grit/grain size – i.e., 6 µm, P600, and P320 – thus obtaining four different topographies starting from the same surface condition. A 3D view of these topographies, rms roughness values, and a linear profile scan of the rivets is shown in **Figure 2**. The roughness profile is the mean of a 300 µm width scan at the center of each counter electrode. This profile scan is important since it depicts the asperity distribution of each counter electrode. It is especially useful in highlighting the difference between P600 and P320. Although the rms roughness of P600 is approximately 75% that of P320, the profile scan shows large-scale peaks and valleys present in the latter, whereas the irregularities in P600 are smoother and less pronounced. Observing 1 µm and 6 µm counter electrodes, the rms roughness difference is significant, with the 1 µm sample representing only about 20% that of the 6 µm sample. The profile scans of the 6 µm sample shows many asperities throughout the scan. The 1 µm sample, on the other hand, is predominantly flat.

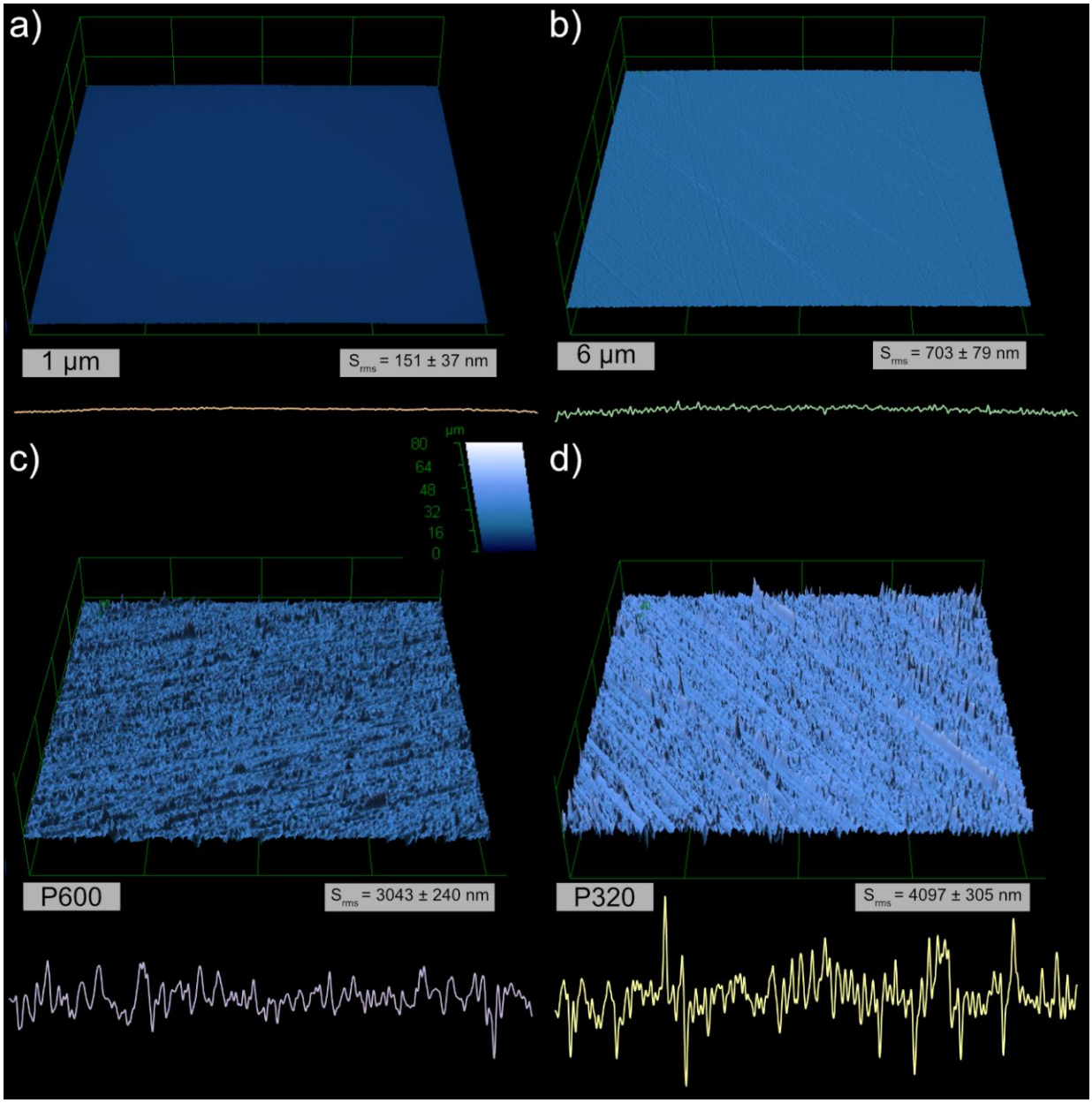

Figure 2: 3D view of rivet topography generated and linear profile of **a)** 1 µm, **b)** 6 µm, **c)** P600, and **d)** P320 with average rms roughness.

Table 2- S-ratio and $R_{\Delta q}$ of topographies produced.

	S-ratio	$R_{\Delta q}$ /°
1µm	1.020	5.6 ± 1.7
6µm	1.275	30.8 ± 3.4
P600	4.092	163.1 ± 40.7
P320	4.883	193.4 ± 51.5

Another key parameter that can be measured using CLSM is the roughness ratio (S-ratio). This parameter provides crucial information on the increase in the ratio between real and apparent contact area (S-ratio = real contact area / apparent contact area). For our analysis, these values are considered merely qualitatively, therefore aiding in comprehending the differences in contact

situation between the four produced topographies. The S-ratio for each rivet is shown in **Table 2**. Moreover, the root mean square gradient ($R_{\Delta q}$) was also determined using CLSM measurements. This surface parameter provides insight into the slope of the asperities present in the textured rivets, shown in **Table 2**. Higher $R_{\Delta q}$ values imply steeper asperity flanks, whereas smooth surfaces should present values that approach zero. As evidenced in the topographies generated, as the grit size increases so does the asperity flank slope. As with rms roughness and S-ratio, a grouping of the 1 µm with 6 µm and P600 with P320 is observed, albeit the former shows a higher deviation from one another.

Vickers microhardness using a load of 0.98 N of three as-received rivets were measured in six different points, resulting in an average hardness of $HV_{0.1} = 154 \pm 5$. In this work, the increase in hardness due to the grinding/polishing processes are neglected.

Prior to EPD, the colloid must be prepared. In this work, isopropyl alcohol was used as solvent (80 ml), with 8 mg of CNT dispersed (0.1 $mg_{CNT}/ml_{solvent}$) [22,23]. Before dispersion, 5 ml of triethylamine were added to the solvent. This additive presents the advantage that it does not influence the chemistry of the resulting coatings. It was added to aid in the deposition process by promoting CNT dispersion. Furthermore, this additive gives the CNT a surface charge, therefore resulting in an anodic deposition [23,25]. Each counter electrode was coated via potentiostatic EPD at 300 V_{DC}. The interelectrode distance for the deposition process was set at 10 mm, for a duration of 4 minutes.

2.2. Electrical characterization

The topographical influence on ECR was analyzed via load dependent ECR. For this analysis, the samples and the counter electrodes were mounted on a self-developed four-probe tribo-electrical testing rig [29]. Each ECR measurement consisted of one loading and one unloading semi-cycle. The loads used were 0.25, 0.5, 0.75, 1, 1.5, 2, 2.5, 3, 4, 5, 6, 7, 8, 9, and 10 N. These loads were selected since they cover a wide range of application-relevant contacting loads. Special emphasis was placed on the lower loading ranges, since here the deformation mechanisms of the asperities play a larger role. A direct current of 10 mA was sourced, recording the voltage drop between the electrodes using a nanovoltmeter range of 0.1 V. This current and voltage range were chosen to accurately measure the differences in ECR as a consequence of the contacting surfaces' topography. When measuring at a lower current level, the topographical features are more influential on the resistance measured. Contrarily, at higher current levels the influence of the topography on ECR could be outweighed, thus reducing the accuracy of the measurements. Furthermore, with 10 mA_{DC} the measurements are carried out under dry circuit conditions, thus ensuring that no microstructural changes that could affect the results take place

due to Joule heating during the measurements [30]. All ECR measurements were carried out at an ambient temperature and relative humidity between 19-24 °C and 40-50%, respectively. Each measurement was taken at least 5 times to ensure reproducibility and fidelity. Prior to ECR measurements, the samples and counter electrodes were cleaned in ultrasound (Bandelin Sonorex Super RK 514 BH, 33 kHz, 860 W) in isopropyl alcohol for 5 minutes.

Load dependent ECR measurements using CNT-coated counter electrodes were carried out using the same parameters and conditions as with uncoated counter electrodes. In these measurements, however, the nanovoltmeter's range was set to 1 V to prevent the device from saturation when measuring higher voltage drops.

2.3. Contact mechanics

The contact situation of the different systems is of significant importance to better understand the frictional, electrical, and thermal behavior of the contacting pairs. This deeper understanding can, in turn, enable the prediction of behavior in different systems by extrapolating the data from this study. Therefore, the contacting situations were evaluated via two methods: 1) via a slope analysis method, as described by Tamai et al. [1,2,6], and 2) via the calculation of the plasticity index, followed by GW or JG model, accordingly [10,12–14,19,20]. The former allows a fast and simple method to predict deformation and conduction mechanisms, whereas the latter is a more robust statistical method that models the contacting surfaces.

In these calculations, the material properties will be those provided by the manufacturer. For the counter electrodes, no specifications were provided. Therefore, it is considered that the material properties of the counter electrodes are those of bulk copper. Furthermore, it is also considered that these material properties do not change after grinding and polishing (i.e., deformation induced changes are disregarded).

2.3.1. Slope analysis

The slope analysis method requires the plotting of the loading semi-cycle of load dependent ECR in a double logarithmic scale. The different ECR values are then linearly fitted, thus acquiring the slope of the fitted line. The slope can be then interpreted as the exponent n from **Equation 2**. Based on the value obtained, the dominant deformation mechanism can be determined, as well as the dominant resistance type. In this work, this analysis will be contrasted with the numerical approach to evaluate the accuracy of this method despite the aforementioned shortcomings and complexity of the analyzed system.

2.3.2. Numerical approach

The theoretical calculations to understand the contacting mechanisms during load dependent ECR cannot be carried out by Hertzian theory due to the plastic deformation that the rough electrodes undergo. Therefore, modeling via GW and JG model are implemented. Modeling procedure and parameters are thoroughly explained in **Appendix I**.

3. Results and discussions

3.1. Load dependent ECR

To understand the influence of counter electrode topography on contact resistance, load dependent ECR measurements were carried out. The results are shown in **Figure 3**. These plots show the full measurement cycle – i.e., loading and unloading – in double logarithmic scale. Visualizing the beginning of the loading phase allows a better depiction of the behavior of the electrode-counter electrode system at low normal loads, whereas the unloading phase provides information on the electrical behavior after the system has undergone deformation.

A clear correlation can be observed between topography and ECR based on the measurements conducted on brass samples, shown in **Figure 3a**. In other words, as counter electrode roughness increases, the contact resistance decreases. This relationship can be observed for all roughness values in hierarchical order. The average resistance of the system is highest when measured with the 1 µm electrode, followed by 6 µm, P600, with the lowest average resistance recorded with P320. This behavior can be explained by the S-ratio of the counter electrodes shown in **Table 2**. As the topography generated on the rivets increases, so does the ratio between apparent and real contact area. Therefore, when measuring ECR with rivets with higher topography, the approximate real contact area is over 4 times higher in the case of P320 rivet. This reduced the contact resistance since there are more contacting sites between the two surfaces. In turn, having a higher number of contacting sites reduces the concentration of current between electrode and counter electrode. Consequently, constriction resistance is less meaningful. A higher roughness also facilitates the piercing of contaminant films due to the outstanding asperities exerting a higher local contact pressure [9]. This also causes an earlier onset of plasticity. Furthermore, counter electrodes presenting higher roughness are more likely to puncture contaminant and oxide films present on the surface of the electrode – as well as on the rivets itself – thus causing a reduction in film resistance. These deductions concur with **Equation 3** and **Equation 4**. A gradual increase in the normal load enables more asperities to puncture superficial films, thus diminishing the influence of film resistance. Moreover, as the load increases, two key processes promote the reduction of constriction resistance. These are: 1) the deformation of asperities, thus

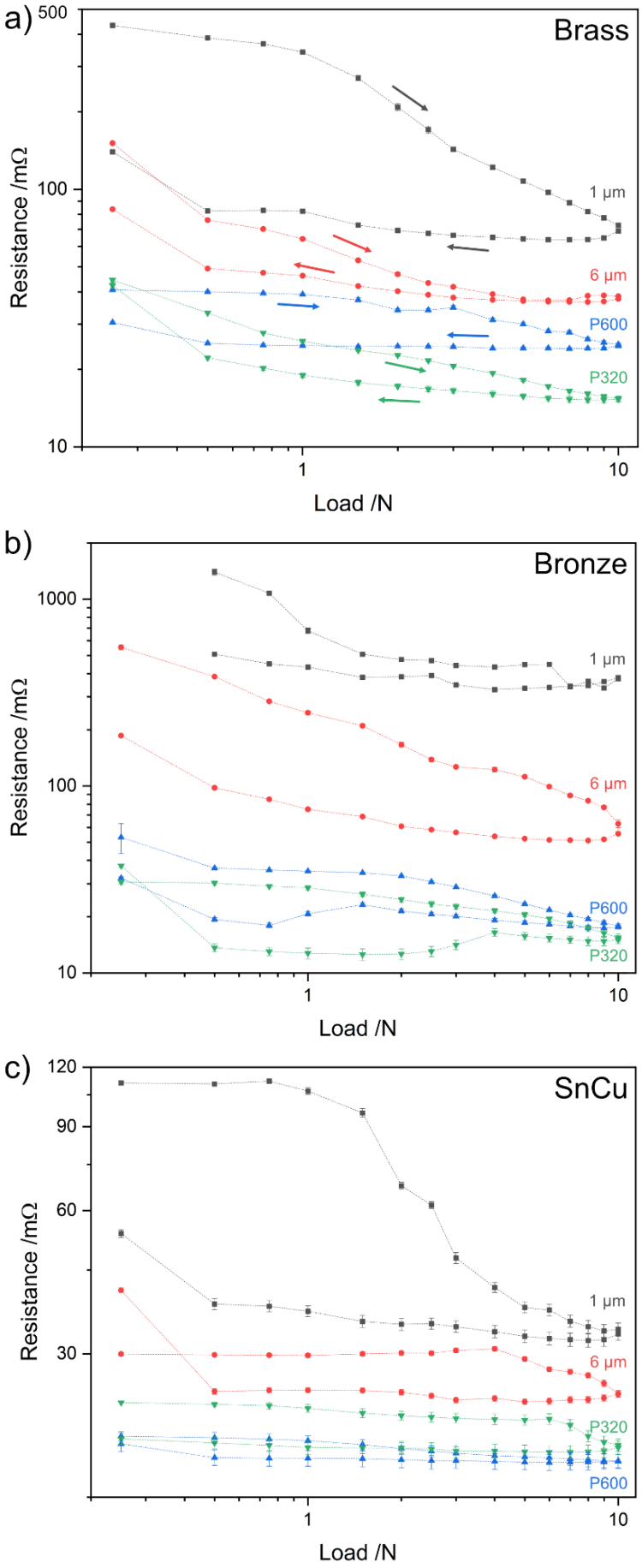

Figure 3: Load dependent ECR measurements. **a)** Brass, **b)** Bronze, and **c)** SnCu. Note: the y-axes are plotted with different ranges. Note: error in all measurements below 7%.

increasing the real contact area; 2) due to the deformation of dimensionally larger asperities, smaller asperities also come into contact with the other surface, thus further increasing the real contact area. In 6 μm, P600, and P320, as the load surpasses 8 N (5 N in the case of 6 μm) ECR values remain, to a certain degree, constant. This ECR value is equal to the bulk materials' resistance, as well as the minimum value of film and constriction resistance for these systems. Higher normal loads would not significantly reduce ECR since at this point the bulk materials' resistance is controlling the system. In addition, asperities may have reached their plastic limit. Since they can no longer plastically deform, the contact area can no longer increase, thus the constriction resistance will remain constant. In these three systems, different 'minima' are reached, thus implying different film and constriction resistances. These minimum ECR values are topography-dependent since the bulk resistance remains constant throughout. Contrarily, all systems would present the same ECR at 10 N.

The 1 μm rivet's behavior, however, differs from the others in two major ways. On the one hand, the absolute resistance reduction in the system is larger than when measuring with the other rivets – decreasing from approximately 430 mΩ at 0.25 N to approximately 70 mΩ at 10 N, an 83% decrease. In the same loading ranges, the other 6 μm, P600, and P320 rivets presented an ECR decrease of approximately 75%, 40%, and 67%, respectively. However, at low normal loads the 1 μm rivet's ECR changes slowly, showing a somewhat constant resistance until 1 N, with a sharp decrease above this load. The other difference seen when measuring with the 1 μm counter electrode is that the ECR value does not appear to have stabilized at high normal loads. In this system, higher normal loads could potentially further decrease the constriction and film resistance components. Among these two components, constriction resistance is believed to play a more decisive role due to the size of the asperities in 1 μm rivets – see **Table A2**. As a consequence of the smaller asperity dimensions, a higher number of asperities need to come into contact with brass' surface to significantly reduce constriction resistance. Furthermore, the smaller asperity size generates higher localized pressure on brass' surface, therefore, superficial films can be punctured at lower normal loads.

Observing the unloading semi-cycle, it is interesting to point out that the resistance remains relatively constant throughout the entire semi-cycle. Minor fluctuations in ECR are observed at loads below 2 N, more noticeably when measured with P320. In all cases, the highest change in ECR during unloading is observed when reaching 0.25 N. This suggests that some degree of plastic deformation took place in the asperities during the loading semi-cycle, thus causing an inadequate contact at such low normal loads between the electrodes as a consequence of less and smaller contact spots.

ECR curves for bronze are shown in **Figure 3b**. Immediately, a significant difference can be noticed compared to brass, however, the hierarchical order observed with brass is also observed here. The ECR when measured with 1 µm and 6 µm is considerably higher, with 1 µm measurements in the range of 500-1000 mΩ. However, this was expected since the conductivity of bronze is lower than that of brass and copper. According to the manufacturer, these bronze samples possess an electrical conductivity of 16% IACS. Bronze's conductivity is less than 60% that of brass, which presents an electrical conductivity of 28% IACS according to its manufacturer. Consequently, measurements carried out with 1 µm rivets saturated the nanovoltmeter at low normal loads. Therefore, the measurements carried out at 0.25 N could not be acquired with the device's range set at 0.1 V. It was opted to discard these measurements instead of increasing the voltage range of the nanovoltmeter to maintain the same uncertainty ranges in all measurements. However, when considering a linear extrapolation, it can be assumed that the ECR value at 0.25 N would exceed 1100 mΩ.

Although bronze is less conductive than brass and copper, it is significantly harder – see **Table 1**. Therefore, when measuring with 1 µm rivets, the small-sized asperities deform at lower normal loads when contacting the harder bronze surface compared to the softer brass surface. Consequently, a constant ECR value was reached from 7 N onward. In this system, due to the hardness of the bronze sample, constriction resistance is quickly reduced due to the extensive deformation of the asperities that are pressed against the harder surface. Observing **Figure 3b**, a sharp decrease in ECR can be observed above normal loads of 1 N, as was the case in brass. Therefore, it is deduced that below this normal load, asperities do not significantly deform (enough to reduce the constriction of current) and/or superficial contaminant films are not punctured. However, due to the small dimensions of the asperities, it is believed that constriction resistance dominates below 1 N.

Contrarily to the measurements on brass, 6 µm, P600, and P320 measurements do not reach their minimum constriction resistance against bronze – evidenced in **Figure 3b**. The larger-sized asperities produced by the grinding and polishing processes can be further deformed by the harder surface. Therefore, even at normal loads of 10 N, further deformation can take place on textured rivets. This was not observed in the 1 µm rivet due to the small size of the asperities. These quickly deform as the load increases, reaching their plastic flow limit at around 7 N. When measuring with P600 and P320 rivets, the loading semi-cycle shows a clear downward tendency. A further increase in normal load could generate more severe plastic deformation, thus producing additional reduction in constriction resistance.

ECR values obtained coincide with the predictions based on the S-ratio. In other words, P600 and P320 show significantly lower ECR values than 6 µm rivets, with the latter showing

significantly lower ECR than 1 μm rivets. This was expected based on the increased real contact area produced by the topography generated on the counter electrodes. However, this behavior was not observed when measuring against brass. Because of the higher hardness of bronze, the increased deformation further enhances the real contact area and confirms the predictions based on the S-ratio. Consequently, a considerable difference in ECR is observed when comparing 1 μm rivets with P600 and P320 rivets – over two orders of magnitude. On the other hand, in brass, this difference approached one order of magnitude. Therefore, when working with hard and relatively low conductive materials, generating a strong topography on the softer electrode is of utmost importance to ensure minimal electrical resistance.

The high degree of asperity deformation can be evidenced by the behavior of P600 and P320 rivets in the unloading semi-cycle. ECR slowly increases as the load decreases. However, after a certain point – 2.5 N for P600 and 4 N for P320 – the resistance takes a dip and then sharply increases at 0.25 N. It is unclear as to why the resistance decreases. One hypothesis would be that lower asperities that did not plastically deform return to their original position, thus ensuring adequate electrical contact with the substrate. The resistance reduces since oxide and contaminant films were punctured during loading. However, plastically deformed asperities would inadequately contact bronze's surface, thus increasing the constriction resistance. Another possible explanation could be that during unloading, rearrangement of the deformed asperities at low loads temporarily enhances the contact between the two surfaces until the load is sufficiently low (at 0.25 N) and the contact is exacerbated.

Among the samples in question, SnCu presents the lowest ECR, shown in **Figure 3c**. Measurements with 1 μm rivets results in ECR values slightly over 100 mΩ and with P600 as low as 20 mΩ at 0.25 N. Again, the S-ratio pairing of P600 and P320 is observed in SnCu. However, in these measurements P600 showed lower resistance than P320. Although SnCu presents similar hardness values to copper and brass (see **Table 1**), it should be recalled that this is a compound hardness comprised of the tin plating and the copper base metal. The relative softness of tin is the primary reason as to why it is so extensively used as plating material. In this system, the tin plating is easily deformed by the asperities of the copper counter electrode, thus quickly reaching a steady contact area. Therefore, the similarities in S-ratio and rms roughness of P600 and P320 rivets results in similar ECR values. Throughout the entire measurement cycle the difference in ECR values between these two rivets falls below 4 mΩ (17% difference). Therefore, although the same hierarchical order observed with brass and bronze is not strictly valid here, it remains somewhat true to state that a higher degree of roughness leads to lower ECR values. Nonetheless, with materials that present higher electrical conductivity, the reduction in ECR with increased roughness is not as crucial as with less conductive materials – e.g., bronze.

As the normal load increases, the asperities of the counter electrodes penetrate through the tin plating. Once the asperities reach the base material, the asperities begin to deform. This occurs at approximately 7 N for P600 and P320 rivets, as evidenced by the decrease in ECR in **Figure 3c**. The same can be observed in 1 µm and 6 µm rivets at approximately 2 N and 4 N, respectively. However, in this case, asperities do not reach the base material since the tin plating is thicker than the outstanding height of the asperities. In these rivets, deformation occurs at lower loads because of the smaller size of the asperities – higher contact pressure – and due to the tin plating undergoing compression. This occurs faster in 1 µm rivets, thus reaching the constant ECR values at approximately 8 N.

The tin plating presents the added benefit of improving electrical connectivity during unloading. P600 and P320 rivets show similar ECR values during loading and unloading. When unloading these asperities in contact not only remain in contact with the copper base material, but also with the tin plating – as illustrated in **Figure 4**. Therefore, even after deformation took place, ECR values remain low at low normal loads. This was not the case with rivets with lower roughness. As seen in **Figure 3c**, at 0.25 N in the unloading semi-cycle, ECR sharply increases in both 1 µm and 6 µm rivets.

Comparing the results shown in **Figure 3** (load dependent ECR) and **Table 2** (s-ratio and roughness of textured counter electrodes), the data tends towards the fact that there is an upper limit on the influence of roughness on the ECR. The tendency is clearer when contacting against harder surfaces (i.e., bronze and SnCu – see **Table 1**). In these cases, the softer asperities of the textured counter electrodes are more easily deformed when pressed against harder surfaces, thus

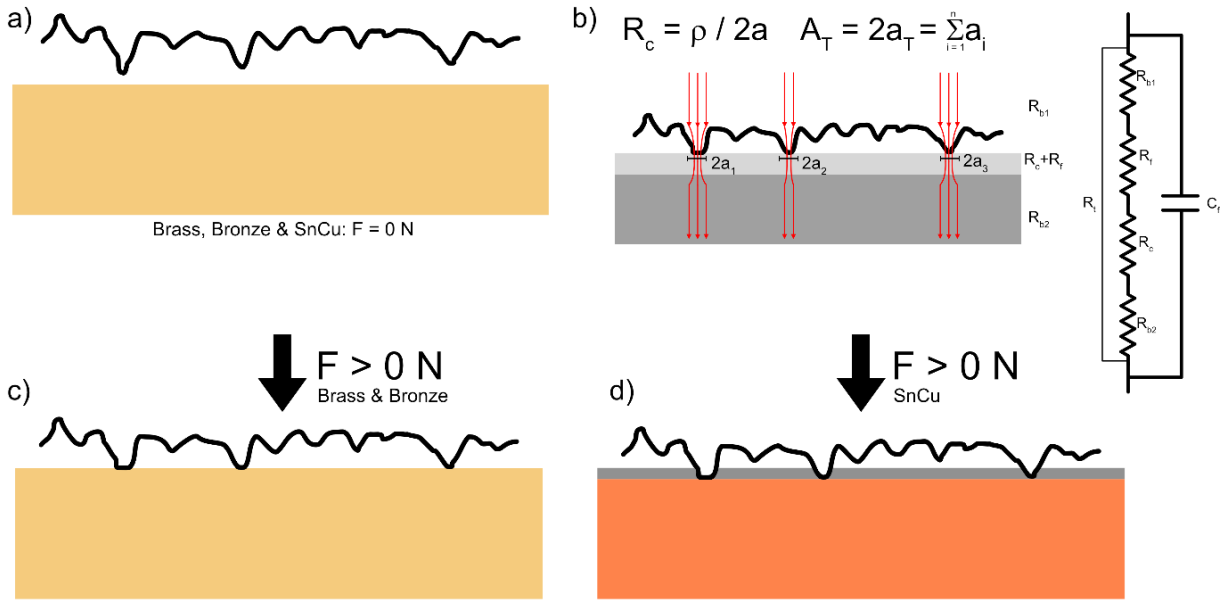

Figure 4: Schematic representation of contacting situation at a) F = 0 N, c) F > 0 N in brass and bronze, d) F > 0 N in SnCu against a textured counter electrode. b) Shows the equivalent circuit of **Equation 3** (total resistance) and a schematic representation of **Equation 4** (constriction resistance).

resulting in the onset of plasticity at lower loads. Consequently, the maximum plastic deformation of the asperities is reached faster and well within the loading range analyzed. In the case of SnCu specifically, the presence of the soft tin plating further aids in rapidly reaching steady state ECR due to the softness of the tin plating, coupled with the deformation of the asperities in the counter electrode with higher roughness values. When contacting against smooth surfaces with similar hardness values (i.e., brass), on the other hand, the tendency is not as clear. Here, the onset of plasticity of the asperities requires higher loads, since the similar hardness values of both materials causes mutual deformation. In other words, the smooth brass surface deforms the counter electrode's asperities at the same time as the asperities imprint on the smooth brass surface.

3.2. Resistance-load curve slope analysis and numerical analysis

3.2.1. Brass

Due to the aforementioned complexities of the system in question, different contacting counter electrodes group themselves in different force ranges – as evidenced in **Table 3**. For 1 μm and 6 μm, three different groups were identified, whereas two ranges were identified for P600 and P320. Although, the boundary differs among the different counter electrodes.

In 1 μm, the slope analysis indicates that the asperities deform elastically in the first two force ranges from 0.25 N up to 3 N. As the load increases beyond 3 N, the plastic deformation indicated by this analysis is attributed to asperity deformation. The dominant resistance type alternates between constriction and film between the analyzed ranges. Initially, at loads below 1 N, the constriction resistance could be caused by small contacting sites between the electrodes. As the load increases and the contacting surfaces increases, film resistance is more dominant in the contact between the asperities and the electrode. This transition can be easily observed in the loading phase of the 1 μm counter electrode in **Figure 3a**. At loads above 3 N, the oxide films are punctured (on both surfaces), thus constriction resistance dominates once again.

The 6 μm counter electrode is also classified in three ranges. However, as opposed to the 1 μm counter electrode, the first range lies between 0.25 and 0.5 N. Here, plastic deformation of the oxide film and film resistance dominates the system. In the second range, from 0.5 to 6 N, constriction resistance is dominant due to the puncturing of the oxide layers and the establishing of the contact area, evidenced by the change in slope in **Figure 3a**. The predominant deformation mechanism according to the slope analysis indicates elastic deformation. Likewise, in P600 and P320 counter electrodes, constriction resistance and elastic deformation dominate the system in both of their respective ranges. The change in slope observed in **Figure 3a** is not significant

Table 3 - Slope analysis of brass sample in loading phase of load dependent ECR.

Topography	Range	Force range /N	Slope	Dominant resistance	Deformation mechanism
1 µm	1	0.25-1	0.16	Constriction	Elastic
	2	1-3	0.76	Film	
	3	3-10	0.56	Constriction	Plastic
6 µm	1	0.25-0.5	0.99	Film	Plastic
	2	0.5-6	0.31	Constriction	Elastic
	3	6-10	0.11		
P600	1	0.25-3	0.07	Constriction	Elastic
	2	3-10	0.27		
P320	1	0.28-0.75	0.44	Constriction	Elastic
	2	0.75-10	0.22		

enough to produce a change in deformation mechanism according to this analysis.

The results from numerical modeling in brass electrodes are shown in **Table 4**. These values were calculated using **Equation A5** through **Equation A11** inputting the parameters from **Table A1** and **Table A2**, as well as the spectral moments calculated using **Equation A1**, **Equation A2**, and **Equation A3**.

The physical meaning of each GW parameter is shown in **Figure A1**. Observing the values from **Table 4**, it is logical that the standard deviation of surface and asperity heights (σ_s and σ_a, respectively) increases as the grit size/suspension particle size increases. Evidently, a coarser grinding/polishing medium will produce a rougher surface which, in turn, will generate a larger standard deviation of asperities related to the datum line (dashed line in **Figure A1**) – i.e., the mean roughness value. This parameter also helps to quantify the degree to which the roughness increases as the texturing method changes. In other words, it is interesting to note how σ_s and σ_a more than doubles between 1 µm and 6 µm, with it representing more than fivefold and sixfold increase in P600 and P320, respectively, with respect to the 6 µm. This behavior was not reflected

Table 4 - Greenwood and Williamson, and Jackson and Green parameters of brass.

Model	Parameters	1 µm	6 µm	P600	P320
GW	σ_s /µm	0.287	0.785	3.120	5.231
	σ_a /µm	0.275	0.726	2.716	4.935
	η /µm^{-2}	0.103	0.112	0.127	0.140
	r /µm	2.366	0.574	0.099	0.080
JG	ψ	29.40	96.87	551.05	678.46
	ω_c /nm	0.319	0.078	0.013	0.012
	P_c /nN	745.10	43.87	1.30	0.84
	A_c /nm^2	2372.80	139.66	4.12	2.68

when measuring the roughness ratio – see **Table 2**. The individual asperity radius values obtained also correlate with the texture produced. A rougher surface can be more accurately modeled by a higher number of smaller circular features, rather than by fewer larger ones. This can be understood easier with the aid of **Figure A1**, where the finer surface is modeled by seven large circular features, as opposed to the coarser surface being modeled by multiple smaller circular features. Accordingly, the rougher surfaces have a mean individual asperity radius below 100 nm, whereas in the finer topographies r is in the μm range. The remaining GW parameter, the areal asperity density, is unexpected. It was hypothesized that rougher surfaces would have a higher number of asperities per μm^2. In other words, a higher density of asperities per μm^2. Although that is the case, the difference is marginal.

The JG parameters, along with the plasticity index for the different topographies is also shown in **Table 4**. A considerable difference can be observed when comparing the plasticity index values obtained with the varying topographies. Finer topographies generate lower plasticity index values, thus implying lower degrees of plastic deformation. Contrarily, rougher surfaces present considerably higher plasticity indices (surpassing 670 for P320) suggesting significant plastic deformation. As suggested by Greenwood and Williamson [12], the plasticity index of real surfaces should fall within the range of 0.1 and 100. Furthermore, Jackson and Green have demonstrated the correlation between increasing plasticity index values with the reduction of yield strength [20]. Since the material properties of the counter electrodes remains constant throughout our numerical analysis, with only the surface parameters (i.e., topography) changing, it is unsurprising that there is such a drastic change in plasticity index values between the counter electrodes analyzed.

Taking note of the JG parameters, it is evident that smoother topographies possess a higher load bearing capacity as opposed to rougher surfaces. The 1 μm surface presents a critical load that is one, two, and three orders of magnitude higher than that of the 6 μm, P600, and P320, respectively. This behavior can be explained by the standard deviation of asperity height. Rougher surfaces present a higher σ_a value, which physically represents the height of outstanding asperities. Contrarily, a finer topography – with lower σ_a values – represents a more homogeneous surface, as shown by the linear profile scans in **Figure 2**. Therefore, the applied normal load is evenly distributed among a higher number of asperities. Although the finer topographies have smaller asperity diameters at their summit, the load is distributed throughout the higher number of asperities in contact with the other surface. Consequently, the critical load is smaller for rougher surfaces since the applied load is concentrated on the higher outstanding asperities (bottom left surface in **Figure A1**). This appears to contradict with the values obtained from the areal asperity density (η from the GW parameters). However, a clear distinction should be made

between η and the real number of asperities in the actual contacting surfaces. Furthermore, the number of asperities alone is not enough, but the overall height of the asperities. More homogeneous surfaces will have a higher number of simultaneously contacting asperities, which can in turn better distribute the load, rather than heterogeneous surfaces where few asperities bear the load. Similarly, the critical area also considerably decreases as roughness increases. Moreover, the critical interference indicates that finer topographies must deform to a higher degree to reach the onset of plasticity. In other words, the small 1 µm asperities must deform more than 0.3 nm in order to transition from elastic to plastic deformation, whereas rougher surfaces require lower magnitudes of deformation to transition from elastic to plastic. Again, this emphasizes the load bearing capacity of finer topographies on account of the improved load distribution.

From the numerical analysis, it can be seen that all the counter electrodes plastically deform. This contradicts the results from the slope analysis, with this method implying that the rougher counter electrodes only underwent elastic deformation. However, as evidenced by the plasticity index and the critical values calculated with the JG model, this is clearly not the case. Plastic deformation was also expected in all cases when observing the unloading semi-cycle of load dependent ECR (**Figure 3a**). As theorized, the complexity of the systems in question, coupled with the idealized surface requirements in the slope analysis, hinder this method's ability to accurately model the deformation, and thereupon, the transport mechanisms at play in our system. Albeit, in systems where the contacting surfaces fulfil more closely with the requirements, this model can be accurately used, thus simplifying the analysis [6,9].

3.2.2. Bronze

As was the case with brass (see section 3.2.1), 1 µm and 6 µm are also be divided into three distinct force ranges. In bronze, however, P600 and P320 can also divided into three ranges as opposed to two, as shown in **Table 5**.

Regardless of the topography that was generated, the slope analysis indicates elastic deformation for their respective second force range. The change in slope is observed at 1.5 N in 1 µm and 6 µm counter electrodes, although the change is not as significant as in brass. Moreover, P600 and P320 show small changes in slope throughout the entire loading semi-cycle (see **Figure 3b**). Complementary numerical modeling is required to gain further insight into the deformation mechanism taking place in the system.

Different resistance types dominate the identified ranges in 1 µm and 6 µm. Initially, film resistance dominates the 1 µm system for loads below 1.5 N. This film deforms plastically, with it being punctured between 1.5 and 2 N – detected by slope change (see **Figure 3b**). Beyond this

Table 5 – Slope analysis of bronze sample in loading phase of load dependent ECR.

Topography	Range	Force range /N	Slope	Dominant resistance	Deformation mechanism
1 µm	1	0.5-1.5	1.06	Film	Plastic
	2	1.5-6	0.12	Constriction	Elastic
	3	7-10	0.25		
6 µm	1	0.25-1.5	0.57	Constriction	Plastic
	2	1.5-4	0.74	Film	Elastic
	3	4-10	0.65		
P600	1	0.25-0.5	0.54	Constriction	Plastic
	2	0.5-2	0.06		Elastic
	3	2-10	0.39		
P320	1	0.25-0.5	0.05	Constriction	Elastic
	2	0.5-2	0.20		
	3	2-10	0.44		

load, the oxide films on the electrode and counter electrode are punctured. Consequently, constriction resistance dominates at and above 1.5 N. Inversely, constriction resistance dominates below 1.5 N and film resistance above 1.5 N in the 6 µm system. However, this behavior is counterintuitive due to the higher contact pressure above 1.5 N. Therefore, it is believed that the high contact pressure will puncture the oxide film, thus guaranteeing that constriction resistance dominates the system. In this regard, the slope analysis' shortcomings are exposed. P600 and P320, on the other hand, show constriction resistance dominating the system throughout the entire loading range. This is likely the case due to the larger radius of the individual asperities, thus establishing a larger contact area even at lower normal loads.

The GW and JG parameters calculated via the numerical analysis for bronze electrodes are shown in **Table 6**. As with brass, the standard deviation of surface and asperity heights correlate with the method employed to texture the counter electrodes. In other words, as the roughness of

Table 6 – Greenwood and Williamson, and Jackson and Green parameters of bronze.

Model	Parameters	1 µm	6 µm	P600	P320
GW	σ_s /µm	0.266	0.778	3.045	4.256
	σ_a /µm	0.256	0.719	2.781	3.974
	η /µm-2	0.105	0.112	0.153	0.156
	r /µm	2.624	0.577	0.102	0.081
JG	ψ	27.99	99.94	468.6	626.85
	ω_c /nm	0.327	0.072	0.013	0.010
	P_c /nN	841.31	40.73	1.26	0.81
	A_c /nm^2	2695.35	130.73	4.05	2.58

the produced surface increases, so does σ_s and σ_a. Furthermore, the mean individual asperity radius also complies with the expected behavior. The areal density of asperities increases as the roughness of the counter electrode increases. However, the rise in η is not as significant as initially expected. All the GW parameters of bronze resemble that of the brass counter electrode. This is unsurprising since both alloys present similar mechanical properties.

The JG parameters of bronze follow the same tendencies as with brass. In all the analyzed topographies the critical parameters decrease as the roughness increases. Likewise, the plasticity index increases with roughness, presenting similar values as when contacting against brass. Although bronze is significantly harder than brass, more severe plastic deformation of the textured counter electrodes is not observed, as proven by the JG parameters. This is due to the model's independence on the material's hardness [14]. When comparing the plasticity index values obtained for brass and bronze, it was expected – based on the unloading semi-cycle from **Figure 3b** – that the textured rivets would deform to a higher degree when contacting against bronze due to the higher hardness value. However, the plasticity index does not reflect this behavior.

3.2.3. SnCu

The slope analysis on SnCu poses the additional challenge of the plating material, thus inducing more complexity into the system and consequently less applicability of this analysis. The slope values obtained are exceptionally low – see **Table 7**. Consequently, in the majority of the ranges analyzed, the -1/3 *n* factor was attributed even though the determined slope value is actually closer to zero. Therefore, the deformation mechanisms and resistance type shown in **Table 7** should not be regarded; albeit the values are reported here to emphasize the deficiency of this method. In this system, the numerical analysis is of utmost importance.

Table 7 - Slope analysis of SnCu sample in loading phase of load dependent ECR. The low slope values emphasize the deficiency of this method.

Topography	Range	Force range /N	Slope	Dominant resistance	Deformation mechanism
1 µm	**1**	0.25-1.5	0.03	Constriction	Elastic
	2	1.5-5	0.78	Film	
	3	5-10	0.18		Plastic
6 µm	**1**	0.25-4	0.00	Constriction	Elastic
	2	4-10	0.21		
P600	**1**	0.25-6	0.03	Constriction	Elastic
	2	6-10	0.26		
P320	**1**	0.25-10	0.04	Constriction	Elastic

Nonetheless, observing **Figure 3c**, the resistance remains constant throughout the loading semi-cycle until a certain critical load. Once the critical load is surpassed, the resistance drops. In the 1 µm counter electrode, the critical load is at 1.5 N, with a sharp decrease in resistance thereafter. This critical load value is 4 N and 6 N for 6 µm and P600 counter electrodes, respectively. For the P320 counter electrode, this phenomenon is not observed. Therefore, as the roughness of the counter electrode increases, so does the critical load for resistance drop. A higher roughness means that outstanding asperities can penetrate the tin plating at lower loads. Consequently, the critical load increases with roughness, as seen in **Figure 3c**. This phenomenon is schematically shown in **Figure 4**. This behavior is unique to this electrode since the plating material is significantly softer than the base material.

The GW and JG parameters calculated for SnCu are shown in **Table 8**. Initially, the σ_s and σ_a of the 1 µm counter electrode stand out, showing double the value compared to the previous electrodes. This is unsurprising since these values correlate to the equivalent surfaces of the GW model (see **Figure A1**). Recalling CLSM measurements, SnCu's surface was not polished, therefore these commercially available material presents higher roughness than polished brass and bronze – i.e., SnCu presents a roughness that is one order of magnitude higher than that of brass and bronze. Nonetheless, as the roughness increases, the σ_s and σ_a resemble more those of the copper alloys. This is because the roughness of the SnCu electrode is more prominent against finer rivets. In coarser-textured rivets, 200 nm is negligible compared to over 3000 and 4000 nm in P600 and P320, respectively. This behavior can be observed in all the GW parameters calculated for SnCu.

In SnCu, finer topographies show higher plasticity indices than when contacting against brass and bronze. However, as roughness increases the difference is not as significant (e.g., P600 and P320). This is a consequence of the soft tin plating. Since the JG parameters are calculated based on the GW parameters, which are a combination of the surface parameters and material properties

Table 8 - Greenwood and Williamson, and Jackson and Green parameters of SnCu.

Model	Parameters	1 µm	6 µm	P600	P320
GW	σ_s /µm	0.510	0.891	3.076	4.278
	σ_a /µm	0.488	0.831	2.813	3.997
	η /µm^{-2}	0.075	0.107	0.153	0.156
	r /µm	1.752	0.561	0.101	0.081
JG	ψ	50.70	116.99	505.79	674.54
	ω_c /nm	0.190	0.061	0.011	0.009
	P_c /nN	322.14	33.01	1.08	0.69
	A_c /nm^2	1044.68	107.36	3.51	2.24

of the contacting materials, the tin plating influences the value of the plasticity index. Therefore, the higher plasticity index is not solely because the asperities of the counter electrode deform, but rather a combination of the asperities and the tin plating deforming. For higher roughness values, the outstanding asperities more easily penetrate the tin plating, thus reaching the copper base material. Subsequently, the deformation of the asperities takes precedence over the tin plating's deformation. Similarly, the critical parameters in finer surfaces are smaller than when contacting against brass and bronze but tend to approach those values in rougher surfaces. In this case again, the numerical approach contrasts with the deformation mechanism resulting from the slope analysis. All textured counter electrodes deform plastically during load dependent ECR measurements.

3.3. Load-dependent ECR with coated counter electrodes

ECR measurements carried out with CNT-coated rivets are shown in **Figure 5**. As can be seen, the hypothesis proposed is, in part, ratified. In other words, the CNT coating does diminish the influence of counter electrode topography on ECR measurements. However, this was not the case in all the topographies generated, as evidenced by **Figure 5a** and **Figure 5c**. In both cases, the behavior of one textured surface varies. Nonetheless, comparing **Figure 5** to **Figure 3**, it is clear that the topographical influence is not as significant, since in **Figure 3** the topography has a stronger effect on ECR. Albeit the overall contact resistance of the system increases considerably. When measuring with uncoated rivets, ECR values range from 20 to 500 mΩ, from 10 to 1000 mΩ, and from 20 to 120 mΩ in brass, bronze, and SnCu, respectively. On the other hand, when measuring with coated rivets, ECR values range from 100 to 100,000 mΩ in brass and SnCu, and between 1,000 to 100,000 mΩ in bronze. In other words, approximately two orders of magnitude higher in all cases.

The ECR behavior of brass when measuring with CNT-coated rivets can be seen in **Figure 5a**. In these measurements, 1 µm stands out, whereas 6 µm, P600 and P320 show similar behavior. ECR initially is similar to that at the end of the measurement, which establishes the elastic restitution of the coating due to van der Waals interactions between CNT. Therefore, CNT coatings generate reproducible measurements. If the behavior of the coated 1 µm rivet is compared to that of the uncoated rivet (**Figure 3a**), it can be seen that the ECR evolution during the loading semi-cycles are similar. Furthermore, ECR values at 10 N are also in the same range, i.e., approximately 100 mΩ. Nonetheless, in the case of the coated rivet, the initial ECR values are approximately one order of magnitude higher. This initial behavior is logical, since the low normal loads applied are not sufficient to compact the porous CNT coatings [22,23]. As the load increases, the CNT coating adjusts and compacts. This process fills the voids within the coating.

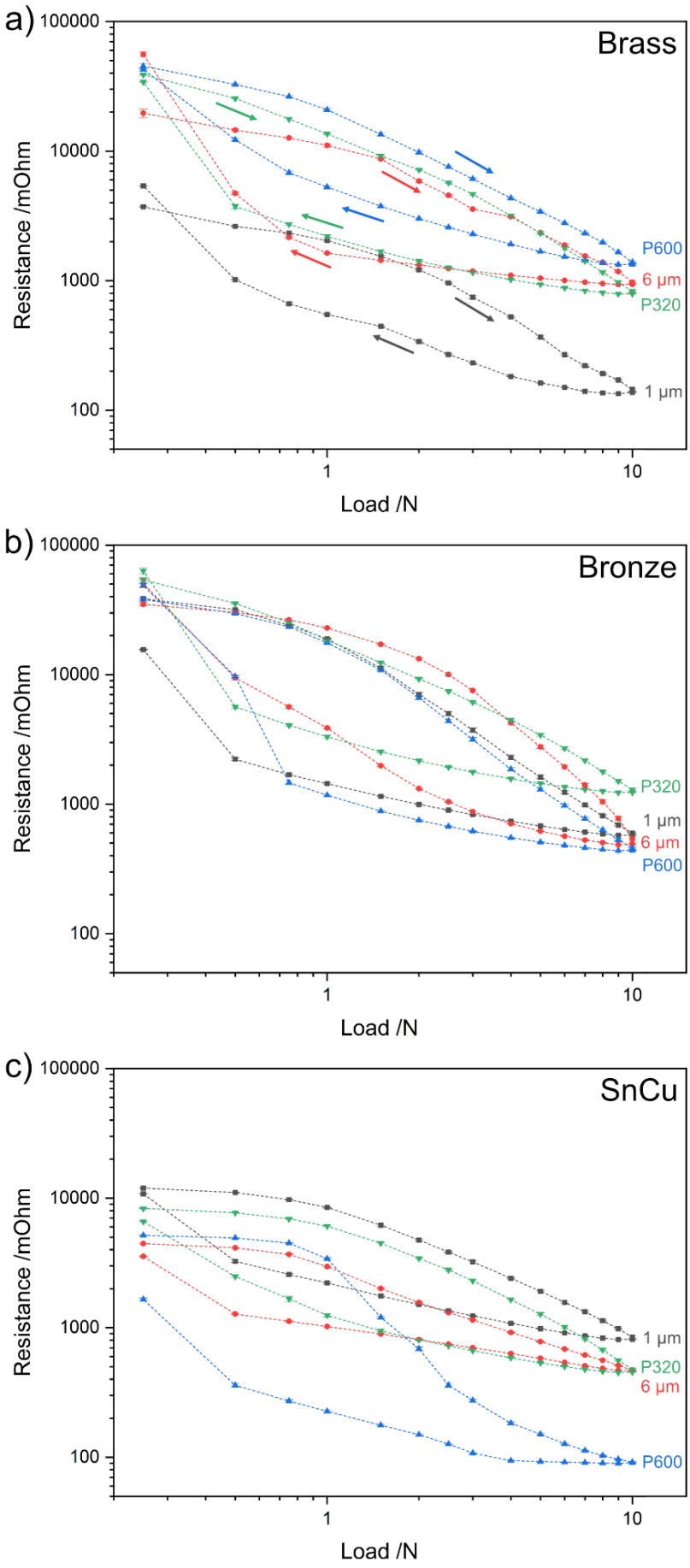

Figure 5: Load dependent ECR measurements with CNT-coated counter electrodes. a) Brass, b) bronze, and c) SnCu. Note: error in all measurements below 8%.

Consequently, the connectivity between the individual CNT and CNT agglomerates improves, which is reflected in the ECR's evolution. The increased connectivity equates to a reduction in ECR as the load increases due to the formation of a percolative path. When loading with 10 N, the ECR value is approximately two orders of magnitude lower than when loading with 0.25 N. This can be observed in all cases, not just when measuring with the coated 1 µm counter electrode. With the other counter electrodes, however, the initial value is about one order of magnitude higher than that of the 1 µm rivet. Therefore, the two-order-of-magnitude reduction reported still corresponds to a higher overall ECR values of around 1,000 mΩ.

Observing the unloading semi-cycles, similar tendencies can be observed. Contrasting to the behavior shown in **Figure 3a**, ECR values steadily increase as the load decreases, whereas the values remain fairly constant when measuring with uncoated rivets. This is a consequence of two key distinctions:

1. As the load decreases the CNT coating decompacts. Therefore, the improved connectivity established between adjacent CNT and CNT agglomerates cease, thus increasing the resistance of the system. This phenomenon is a consequence of the aforementioned restitutive behavior of the CNT.
2. The CNT coating decreases the contact pressure that is applied onto the electrode. Since CNT – to a certain extent – uniformly cover the surface of the counter electrode, outstanding asperities do not individually contact the electrode, but rather the entire CNT-coated surface. Asperities do come into contact first, but the load is distributed onto the CNT that fill the topographical valleys. Consequently, the contact pressure is lower, and therefore the electrodes do not undergo significant deformation, which is the case when measuring with uncoated rivets. This is a negative side effect of the CNT coatings. In this case, deformation is a positive outcome since it ensures an adequate contacting surface, and thus lower ECR values. This can be validated by observing the unloading semi-cycles reported in **Figure 3**.

It is unclear as to why the coated 1 µm rivet shows dissimilar behavior to the others. A potential explanation for this behavior could be that due to the almost negligible roughness (approximately 150 nm), the CNT and CNT agglomerates are more compacted than in counter electrodes with higher roughness. Therefore, even at lower loads, a higher degree of connectivity can be established between adjacent CNT and CNT agglomerates, thus ensuring higher electrical conductivity within the coating and towards the conductive substrate. Additionally, the CNT coating's compactness – generated by the low roughness – promotes a real contact area that approaches that of the apparent contact area. This improved contacting situation further lowers

ECR values. Although the roughness of the 6 μm counter electrode is relatively low, it is still over four times higher than that of the 1 μm rivet. Therefore, this counter electrode shows similar characteristics as P600 and P320.

With the bronze electrode, shown in **Figure 5b**, the hypothesis is validated. In all cases, load dependent ECR shows similar evolution throughout both loading and unloading semi-cycles. Again, the elastic-restitutive behavior of the CNT coating can be highlighted by the similarity between ECR values at the start and at the end of the measurements. As with brass, the ECR when measuring with coated rivets shows similarities to the measurements done with uncoated 1 μm rivets. However, the starting ECR value is over one order of magnitude higher. As previously discussed, this is due to the porous nature of the coating and the lack of compression provided by the low contacting loads. Nonetheless, as the load increases, all coated counter electrodes show a steady decrease in ECR until reaching approximately 1,000 mΩ at 10 N. As observed with brass, the unloading semi-cycle in bronze also shows increased ECR values as the load decreases. The justification for this behavior is the same as with brass.

Observing the behavior of SnCu (**Figure 5c**), we can again see that one counter electrode does not behave like the rest, in this case P600. The other textured rivets show similar behavior, thus partially backing the hypothesis considered in this study. As with the previous electrodes, coated measurements on SnCu show the restitutive behavior of CNT, with reproducible results at the cost of higher overall ECR values (of approximately two orders of magnitude). This electrode, however, shows an interesting behavior during the unloading semi-cycle. In contrast to brass and bronze, ECR does not significantly change as the load decreases. The resistance does increase, but at a lower rate. This is due to the soft tin plating that characterizes this electrode. In this system, the outstanding asperities could, to a minor degree, deform the tin plating regardless of the CNT coating. Therefore, as the load is removed, the coated asperities remain in contact with the electrode. Consequently, the decompacting of the CNT coating is not as significant as in the harder electrodes. This phenomenon does play a role in the increased ECR values, but at considerably lower loads – e.g., below 0.5 N. Furthermore, from ECR measurements conducted with coated rivets, and comparing with the behavior when measuring with uncoated rivets (**Figure 3c**), it can be stated that deformation takes place in this system, however, it is not substantial. This can be corroborated by comparing ECR values at 10 N when measuring with the uncoated and coated rivets. If considerable deformation were to take place in this system, ECR values should be more akin.

It is unclear why the P600 system behaves drastically different than the P320 counter electrode, whereas the latter behaves similarly to the finer textured rivets. The higher resistance presented by 1 μm, 6 μm, and P320 could be caused by inadequate contact between the coated

rivets and the electrode. Similarly, improved contact between the P600 rivet could be established between the electrodes, thus reducing the overall ECR. However, this information cannot be extracted from load dependent ECR.

To further understand the behavior of the coated counter electrodes, FIB cross sections were carried out on one rivet per topography. The goal is to not only measure the coating thickness, but also to observe how the CNT arrange themselves when deposited over different topographies and evaluate the interfacial interactions between CNT and substrate.

The coated 1 µm rivet is shown in **Figure 6**. Observing the micrograph in **Figure 6a**, CNT agglomerates can be observed scattered pervasively through the rivet's surface. In our previous work [25], the area fraction of CNT agglomerate was determined by image analysis, resulting in a CNT-agglomerate area fraction of around 44%. The FIB cross section shown in **Figure 6b** reveals an irregular, porous coating. This is characteristic of carbon nanoparticle coatings, as thoroughly explained in our previous studies [22,23]. Due to the fine topography generated, a seamless coating-base material interface can be observed. Nonetheless, some small voids, as well as larger void networks – highlighted by the violet arrows – can be observed at or near the interface. For optimal electron transport, these voids should be closed by applying relatively high normal loads, thus improving the electrical connection between CNT and CNT agglomerates with the base material. The cross section also reveals a significant variation in coating thickness. The CNT agglomerate (to the left of **Figure 6b**) presents a considerable coating thickness of approximately 6 µm, whereas CNT and smaller CNT agglomerates show a fine, even coating with an approximate thickness of 0.6 µm. This variation is reflected in the standard deviation of the coating thickness measured in the cross section, shown at the bottom left of **Figure 6b**.

SEM micrographs of the coated 6 µm rivet are shown in **Figure 7a** and **Figure 7b**. As with

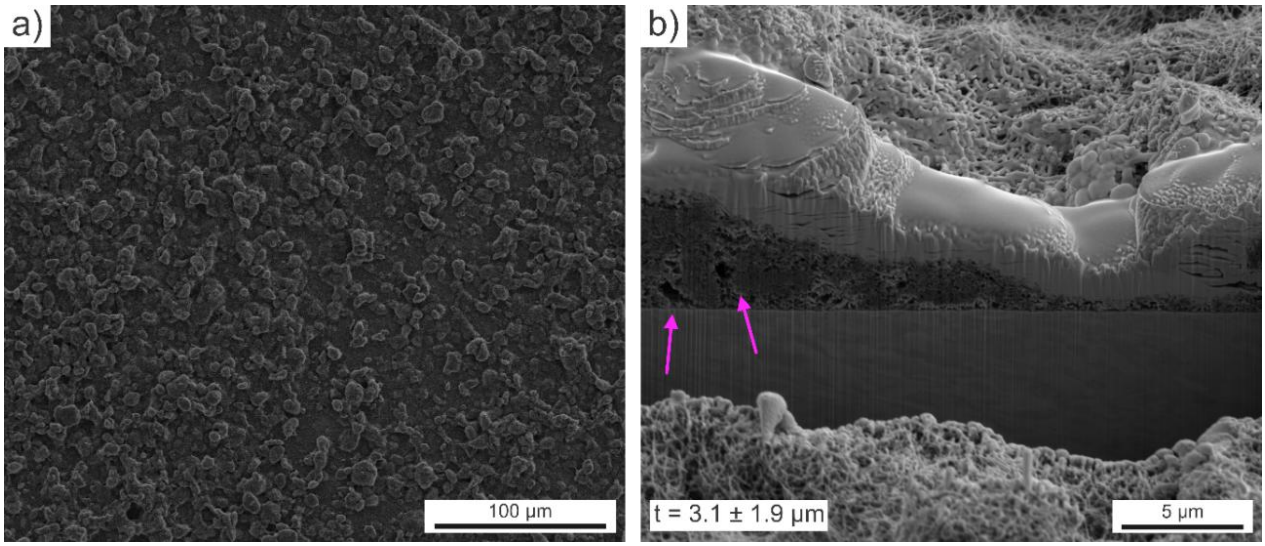

Figure 6: a) SEM micrograph and **b)** FIB cross section of CNT-coated 1 µm rivet. Violet arrows highlight voids in the coating. *t* is the mean coating thickness measured in the cross section.

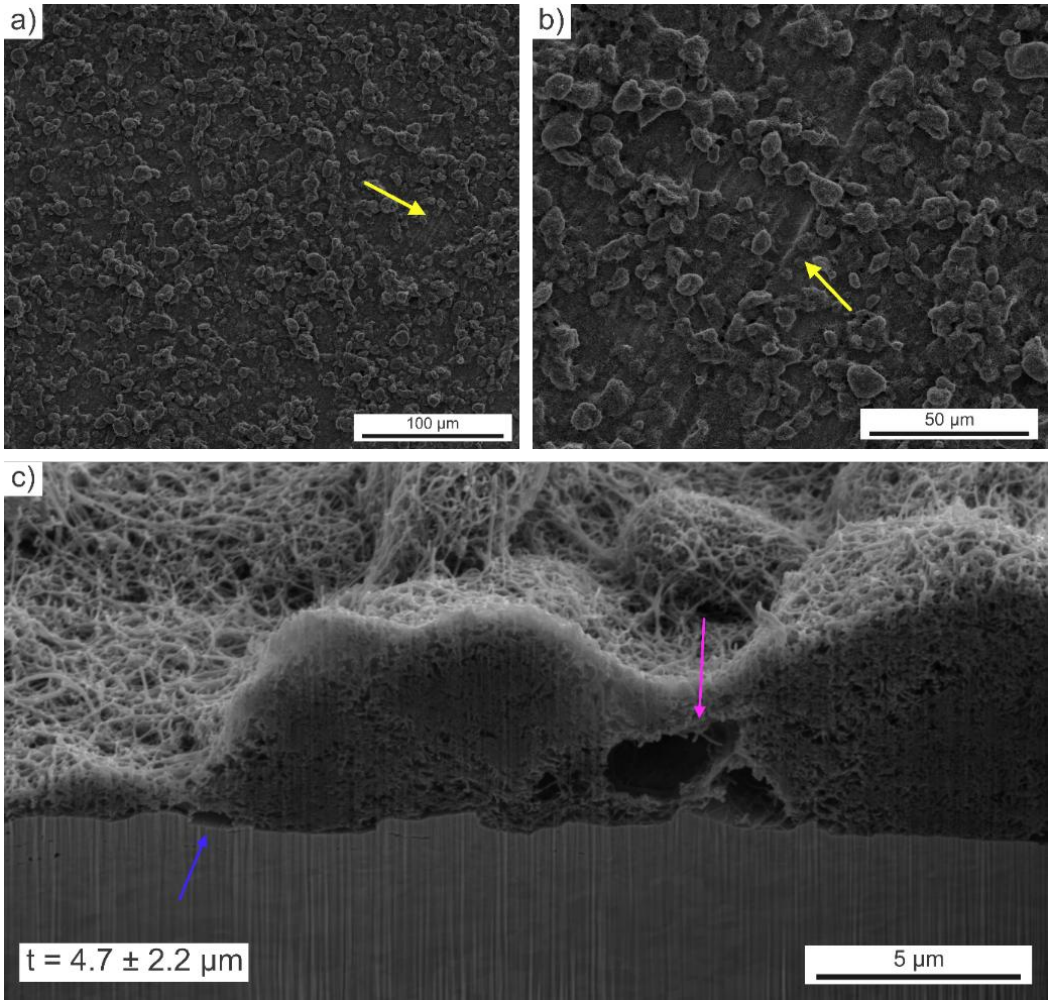

Figure 7: a) SEM micrograph, **b)** magnified view of coated surface, and **c)** FIB cross section of CNT-coated 6 µm rivet. Yellow arrows highlight topographic features on the surface. Violet arrows highlight voids in the CNT-coating, whereas blue arrows highlight topography-related voids. *t* is the mean coating thickness measured in the cross section.

the 1 µm rivet, CNT agglomerates are observed throughout the surface. However, in this counter electrode, some topographic features can be observed despite the CNT coating – as highlighted by the yellow arrows. In **Figure 7a**, a micrograph at lower magnification shows that topographic features are scarce. However, as evidenced by **Figure 7b**, these deep grooves are of significant dimensions. These can be caused by larger, hard particles trapped between the rivets and the polishing cloth. Nonetheless, few scratches were observed, with most of the coating showing a relatively homogeneous coating. Observing the FIB cross section (**Figure 7c**), the same as with the 1 µm counter electrode can be stated. Large CNT agglomerates generate considerably thicker regions in the coatings. Voids are present within the coating, highlighted by the violet arrow. In contrast with the 1 µm rivet, the topography generated on the rivet affects the coating-base material interface. The rougher rivet's surface generates voids at the interface, shown by the blue arrow. It is crucial that the interfacial voids, as well as the voids within the coating, are compacted to improve the electrical conductivity between the CNT and the base material and the CNT interconnectivity.

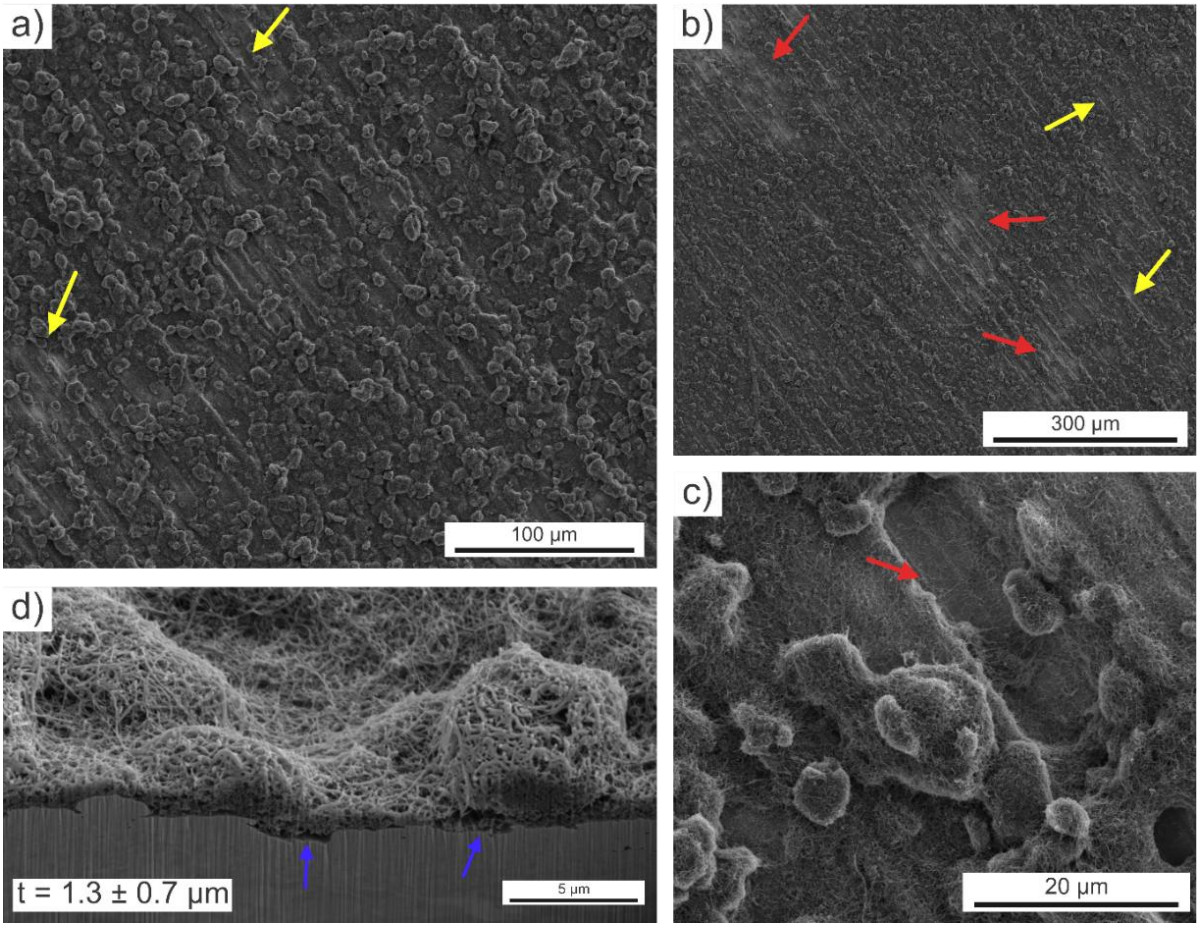

Figure 8: a) SEM micrograph of CNT-coated P600 rivet. b) Shows a general overview of the coated surface, whereas c) shows a magnified view of a groove present on the coated rivet. d) FIB cross section of CNT-coated P600 rivet. This coating does not show significant voids; however, blue arrows highlight topographic-related voids. *t* is the mean coating thickness measured in the cross section. Yellow arrows highlight topographic features on the surface, whereas red arrows point towards regions that were not satisfactorily coated.

The P600 rivet shows a highly heterogenous surface. Observing **Figure 8a**, **b**, and **c**, large topographic features can be observed (yellow arrows), as well as light regions where the copper substrate can be identified (red arrows). A magnified view of a groove is shown in **Figure 8c**, which depicts smaller CNT agglomerates deposited within the scratch, although, copper is exposed regardless. This could explain why the coated P600 rivet performed better than the other counter electrodes when measuring load dependent ECR on SnCu. The exposed topographic features can deform the tin plating, thus augmenting the real contact area and consequently reducing constriction resistance. Furthermore, the inadequate CNT coating enables lower ECR values, since it is more likely that copper can directly contact the electrode without CNT presenting an electrical barrier. The FIB cross section (**Figure 8d**) also strongly contrasts with the previous counter electrodes. A considerably thinner coating is revealed, with smaller overall agglomerates. However, it should be stated that a FIB cross section is a very localized technique. Therefore, different regions could present significantly higher thicknesses. Nonetheless, the region observed shows an average thickness of approximately 1 µm. The smaller CNT

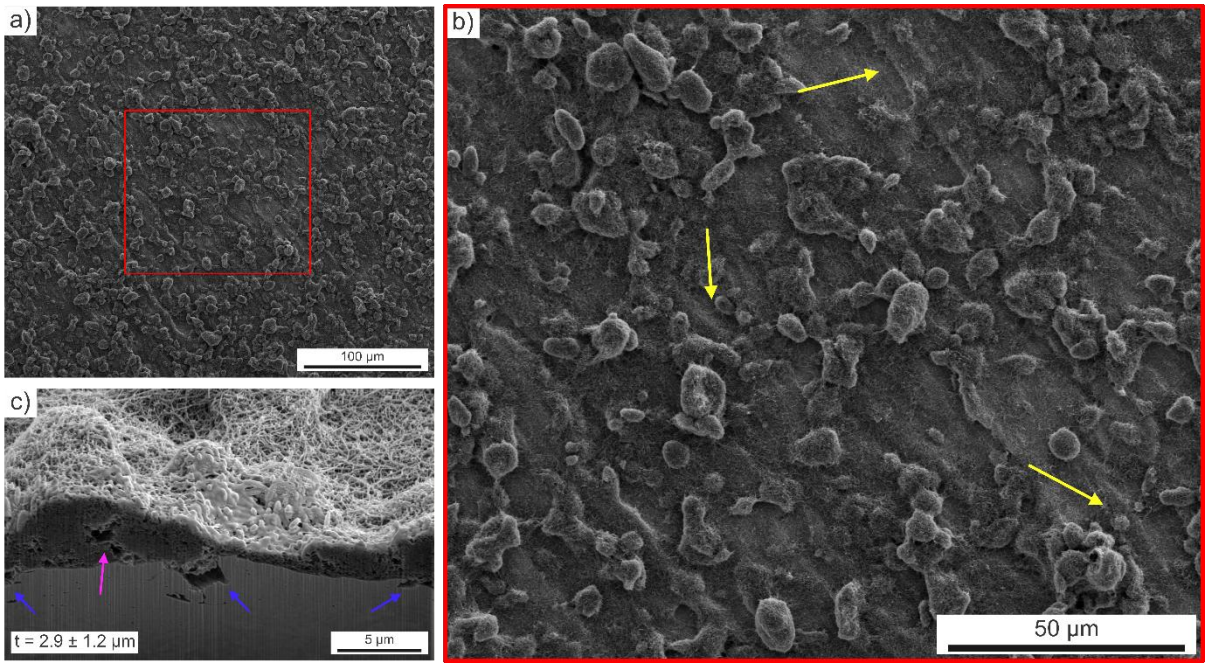

Figure 9: a) SEM micrograph of CNT-coated P320 rivet. **b)** Magnified view of coated surface with yellow arrows highlighting topographic features. **c)** FIB cross section of CNT-coated P320. Violet arrow highlights voids in the coating, whereas blue arrow highlights topography-related voids. *t* is the mean coating thickness measured in the cross section.

agglomerates also prevent the formation of voids within the coating. However, the roughness of the substrate does enable voids at the CNT-substrate interface, as highlighted by the blue arrows.

The SEM micrographs and FIB cross section of the CNT-coated P320 counter electrode are shown in **Figure 9**. From **Figure 9a** and **Figure 9b**, CNT agglomerates can be observed scattered pervasively through the rivet's surface. Fewer topographic features are observed on the coated P320 rivet as opposed to the P600 – highlighted by the yellow arrows in **Figure 9b**. The key distinction between these two coatings is the thickness achieved. As **Figure 9c** shows, the average thickness measured in the cross section is almost threefold that of the P600 coating. Therefore, the thicker CNT coating covers the topographic features from the rougher rivet. This explains the behavior of P600 and P320. The thickness of the P320 coating is the reason why this rivet shows similar ECR values as 1 µm and 6 µm, whereas the deficient CNT coating over the P600 rivet allows better conductivity between the electrodes. Albeit the thicker CNT coating over P320 allows for large voids to form within the coating, as shown in by the violet arrow in the FIB cross section. Although EPD allows for complex geometries to be seamlessly coated, some interfacial voids were observed, as highlighted by the blue arrows. These voids are a consequence of large topographical variations, and the fact that larger CNT agglomerates may not be able to arrange themselves in these valleys; thus, generating cavities. However, as normal load is applied, porosities within the coating as well as larger interfacial ones will be occupied by CNT as the coating compacts. This is the case with larger voids as, for example, at the center of the cross section. Smaller cavities, such as the one at the right of **Figure 9c**, are too small and will

most likely not be filled by CNT under standard loading conditions. Therefore, these voids pose a challenge for electron transfer from the coating onto the substrate. Nonetheless, load dependent ECR measurements (**Figure 5**) imply that these cavities are not detrimental towards system conductivity. In the P320 rivet, thicknesses of over 5 μm were measured, with the mean coating thickness being approximately 2.9 ± 1.2 μm. The mean value is certainly skewed by the thin regions at the center of the cross section with an average thickness of merely 0.8 μm.

4. Conclusions

In this work, four different topographies were generated onto flat-headed copper electrodes. These textured electrodes were then contacted against smooth brass, bronze, and tin-plated copper surfaces. A set of textured counter electrodes were coated with CNT via EPD with the goal of limiting the influence that topography has on ECR. Electrical characterization and contact mechanics modeling were carried out. From this study, the following key conclusions can be drawn:

- The ECR of brass, bronze, and SnCu is strongly linked to the roughness of the counter electrode. As the roughness increases, the contact resistance decreases. This can be explained by the geometric enlargement (S-ratio). As the roughness increases, so does the contact area between the electrodes. Therefore, as established by **Equation 4**, with constant resistivity the resistance can only decrease if the contact area increases.
- The role of topography in electrical resistance is more significant in harder materials. Comparing the behavior of brass and bronze to SnCu, the roughness of the surface had a stronger impact on the former. Whereas in the latter, as roughness increased, its effect on ECR tends to decrease due to the deformation of the softer plating material. This can be evidenced by the ECR values of P600 and P320 shown in **Figure 3c**.
- Asperity deformation takes place during the load dependent ECR measurements. This can be verified by two key observations:
  i. The reduction in ECR as the load increases. This implies that there is an augment in the contact area, which can only be a consequence of asperity deformation.
  ii. Observing the unloading semi-cycle, ECR values do not significantly decrease as the load is reduced. Therefore, even though the normal load is gradually lowered, there is still adequate electrical contact between the electrodes. This is explained by the plastic deformation of the asperities during the loading semi-cycle.
- All systems, regardless of roughness, showed a plasticity index of at least 30, thus implying plastic deformation throughout. Finer topographies reach the onset of plasticity at a lower normal load as opposed to rougher surfaces. Nonetheless, plastic deformation is guaranteed

during load dependent ECR. These conclusions from the numerical analysis comply with the observations from load dependent ECR, contradicting the results from the slope analysis.

- When measuring ECR with coated counter electrodes, the topographical influence can – to a certain degree – be mitigated. This was the case with bronze samples, but also with 6 µm, P600, and P320 in brass, as well as with 1 µm, 6 µm, and P320 in SnCu. In CNT-coated counter electrodes, the crucial factor governing its ECR is how well the coating is compacted as the normal load changes, as well as the CNT-copper interface. With higher degrees of compaction, improved electrical connectivity is established between adjacent CNT and CNT-agglomerates, thus reducing the contact resistance of the system. Furthermore, a seamless interface is desirable since interfacial porosity requires a higher normal load to compact CNT and CNT agglomerates. Moreover, synergy between texture and CNT coating is crucial, as shown by brass-1 µm and SnCu-P600. This synergy supports lower ECR values regardless of the additional nanocarbon layer.

Acknowledgement

B. Alderete wishes to acknowledge the support from the German Academic Exchange Service (DAAD) and the Roberto Rocca Education Program (RREP). The TÜV Saarland Stiftung is gratefully acknowledged for financially supporting the project. The authors gratefully acknowledge funding in the ZuMat project, supported by the State of Saarland from the European Regional Development Fund (Europäischen Fonds für Regionale Entwicklung, EFRE).

Author contributions (CRediT)

Bruno Alderete: Conceptualization, Methodology, Investigation, Formal analysis, Validation, Writing - Original Draft, Visualization.

U. Pranav Nayak: Formal analysis, Validation, Visualization.

Frank Mücklich: Supervision, Project administration.

Sebastián Suárez: Conceptualization, Methodology, Visualization, Writing - Review & Editing, Project administration, Supervision.

Conflicts of interest or competing interests

The authors declare no conflict of interest.

Data and code availability

The datasets generated during and/or analyzed during the current study are available from the corresponding author on reasonable request.

Supplementary information

Not applicable

Ethical approval

Not applicable

References:

[1] Tamai T, Sawada S and Hattori Y 2009 Deformation of crystal structure and distribution of mechanical stress in tin-plated layer under contact loading *Electrical Contacts, Proceedings of the Annual Holm Conference on Electrical Contacts* 160–5

[2] Tamai T, Saitoh Y, Sawada S and Hattori Y 2008 Peculiarities in characteristics between contact trace and contact resistance of tin plated contacts *Electrical Contacts, Proceedings of the Annual Holm Conference on Electrical Contacts* **00** 337–43

[3] Slade P G 2014 *Electrical Contacts Principles and Applications* ed P G Slade (Boca Raton: Taylor & Francis)

[4] Biele L, Schaaf P and Schmid F 2022 Influence of contact pressure on the specific electrical contact resistance of copper *IEEE Trans Compon Packaging Manuf Technol*

[5] Leidner M, Schmidt H, Myers M and Schlaak H F 2010 A new simulation approach to characterizing the mechanical and electrical qualities of a connector contact *The European Physical Journal Applied Physics* **49** 1–10

[6] Alderete B, Mucklich F and Suarez S 2023 Tarnishing (Ag2S) layer on silver-plated electrical contacts: its influence on electrical contact resistance *IEEE Trans Compon Packaging Manuf Technol* **13** 45–58

[7] Holm R 1967 *Electric Contacts - Theory and application* (Berlin, Heidelberg: Springer Berlin Heidelberg)

[8] Mikrajuddin A, Shi F G, Kim H K and Okuyama K 1999 Size-dependent electrical constriction resistance for contacts of arbitrary size: from Sharvin to Holm limits *Mater Sci Semicond Process* **2** 321–7

[9] Trinh K E, Mücklich F and Ramos-Moore E 2014 The role of microstructure and surface topography in the electrical behavior of Sn-coated Cu contacts *27th International Conference on Electrical Contacts, ICEC 2014 - Proceedings* 243–8

[10] Greenwood J A and Tripp J H 1970 The contact of two normally flat rough surfaces *Proceedings of the Institute of Mechanical Engineers* **185** 625–33

[11] Fischer-Cripps A C 2007 *Introduction to Contact Mechanics* ed F F Ling (New South Wales: Springer)

[12] Greenwood J A and Williamson J B P 1966 Contact of nominally flat surfaces *Proceedings of the Royal Society of London* **295** 300–19

[13] McCool J I 1987 Relating Profile Instrument Measurements to the Functional Performance of Rough Surfaces *J Tribol* **109** 264–70

[14] Reinert L, Green I, Gimmler S, Lechthaler B, Mücklich F and Suàrez S 2018 Tribological behavior of self-lubricating carbon nanoparticle reinforced metal matrix composites *Wear* **408–409** 72–85

[15] Kogut L and Etsion I 2002 Elastic-plastic contact analysis of a sphere and a rigid flat *J Appl Mech* **69** 657–62

[16] Chang W R, Etsion I and Bogy D B 1987 An Elastic-Plastic Model for the Contact of Rough Surfaces *J Tribol* **109** 257–63

[17] Zhao Y, Maietta D M and Chang L 2000 An Asperity Microcontact Model Incorporating the Transition From Elastic Deformation to Fully Plastic Flow *J Tribol* **122** 86–93

[18] Shankar S and Mayuram M M 2008 A finite element based study on the elastic-plastic transition behavior in a hemisphere in contact with a rigid flat *J Tribol* **130**

[19] Jackson R L and Green I 2011 On the modeling of elastic contact between rough surfaces *Tribology Transactions* **54** 300–14

[20] Jackson R L and Green I 2006 A statistical model of elasto-plastic asperity contact between rough surfaces *Tribol Int* **39** 906–14

[21] Ghaednia H, Wang X, Saha S, Xu Y, Sharma A and Jackson R L 2017 A Review of Elastic-Plastic Contact Mechanics *Appl Mech Rev* **69**

[22] Alderete B, Mücklich F and Suarez S 2022 Characterization and electrical analysis of carbon-based solid lubricant coatings *Carbon Trends* **7**

[23] Alderete B, MacLucas T, Espin D, Brühl S P, Mücklich F and Suarez S 2021 Near Superhydrophobic Carbon Nanotube Coatings Obtained via Electrophoretic Deposition on Low-Alloy Steels *Adv Eng Mater* **23**

[24] Alderete B, Suarez S, Tejeda D B and Mücklich F 2022 Fretting and Electrical Contact Resistance Characteristics of Carbon Nanoparticle-Coated Cu Electrical Contacts *2022 IEEE 67th Holm Conference on Electrical Contacts (HLM)* (IEEE) pp 1–8

[25] Alderete B, Lößlein S M, Bucio Tejeda D, Mücklich F and Suarez S 2022 Feasibility of Carbon Nanoparticle Coatings as Protective Barriers for Copper─Wetting Assessment *Langmuir*
[26] Zhai C, Hanaor D, Proust G, Brassart L and Gan Y 2016 Interfacial electro-mechanical behaviour at rough surfaces *Extreme Mech Lett* **9** 422–9
[27] Zhai C, Hanaor D, Proust G and Gan Y 2017 Stress-Dependent Electrical Contact Resistance at Fractal Rough Surfaces *J Eng Mech* **143**
[28] Wang X, Zhai C and Gan Y 2021 Stress-dependent electrical impedance behaviours at fractal rough interfaces *Surf Topogr* **9**
[29] Alderete B, Puyol R, Slawik S, Espin E, Mücklich F and Suarez S 2021 Multipurpose setup used to characterize tribo-electrical properties of electrical contact materials *MethodsX* **8**
[30] Tektronix 2016 *Low Level Measurements Handbook, Precision DC Current, Voltage and Resistance Measurements* (Beaverton)
[31] Maaboudallah F, Najah M and Atalla N 2022 A Review on the Contact Mechanics Modeling of Rough Surfaces in the Elastic Regime: Fundamentals, Theories, and Numerical Implementations *Tribology of Machine Elements - Fundamentals and Applications* (IntechOpen)
[32] Green I 2005 Poisson ratio effects and critical values in spherical and cylindrical hertzian contacts *Int. Journal of Applied Mechanics and Engineering* **10** 451–62
[33] Varney P and Green I 2016 Rough Surface Contact of Curved Conformal Surfaces: An Application to Rotor-Stator Rub *J Tribol* **138**
[34] Jackson R L and Green I 2005 A finite element study of elasto-plastic hemispherical contact against a rigid flat *J Tribol* **127** 343–54
[35] Freund L B and Suresh S 2004 *Thin Film Materials: Stress, Defect Formation and Surface Evolution* (Cambridge: Cambridge University Press)
[36] Callister W D Jr 2006 *Materials Science and Engineering: An Introduction* vol 94 (John Wiley & Sons, Ltd)

A. **Appendix I**

a. Numerical Calculations

Hertzian contact theory is only applicable when the smooth contacting bodies undergo pure elastic deformation. Since plastic deformation takes place on the textured electrodes the plasticity index must be determined. Consequently, statistical surface parameters must be calculated using the spectral moments of the electrode and counter electrode surfaces. These can be obtained from surface topography measurements acquired using CLSM. With the spectral moments, further calculations can be executed as described by Jackson and Green [14,19,31]. The spectral moments can be calculated using the following formulas:

$$m_0 = \frac{1}{N}\sum_{n=1}^{N}(z)_n^2 \qquad \textbf{Equation A1}$$

$$m_2 = \frac{1}{N}\sum_{n=1}^{N}\left(\frac{dz}{dx}\right)_n^2 \qquad \textbf{Equation A2}$$

$$m_4 = \frac{1}{N}\sum_{n=1}^{N}\left(\frac{d^2z}{dx^2}\right)_n^2 \qquad \textbf{Equation A3}$$

where N is the total number of data points collected from the surfaces and z is the height of the surfaces relative to their mean values. These formulas (**Equation A1**, **Equation A2**, and

Equation A3) are for two dimensions, with the three dimensional information split into individual rows, as explained by Jackson and Green [19,20,32]. Reinert et al. further explains the 3D expansion from a 2D data set [14]. The authors calculate the arithmetic average of the moments (m_0) and harmonic averaged moments (m_2 and m_4) in the principal directions defined by m_2 maxima and minima. A set of two orthogonal directions which produce maximum and minimum values of m_2 and m_0, followed by the harmonic average of these two values. In that same direction, $m_{4(1)}$, $m_{4(2)}$, $m_{0(1)}$, and $m_{0(2)}$ are calculated (irrespective of their maximum and minimum values). With these values, m_4 and m_0 are then calculated by harmonic averaging and arithmetic averaging, respectively [14].

Once the spectral moments have been calculated, the standard deviation of the surface height, the areal asperity density, and the radius of curvature can be calculated as described by McCool et al. [13,19]. These are shown in **Figure A1** and can be calculated as:

$$\sigma_s = \sqrt{m_0} \qquad \textbf{Equation A4}$$

$$\eta = \left(\frac{m_4}{m_2}\right)\left(\frac{1}{6\pi\sqrt{3}}\right) \qquad \textbf{Equation A5}$$

$$r = 0.375 \cdot \sqrt{\frac{\pi}{m_4}} \qquad \textbf{Equation A6}$$

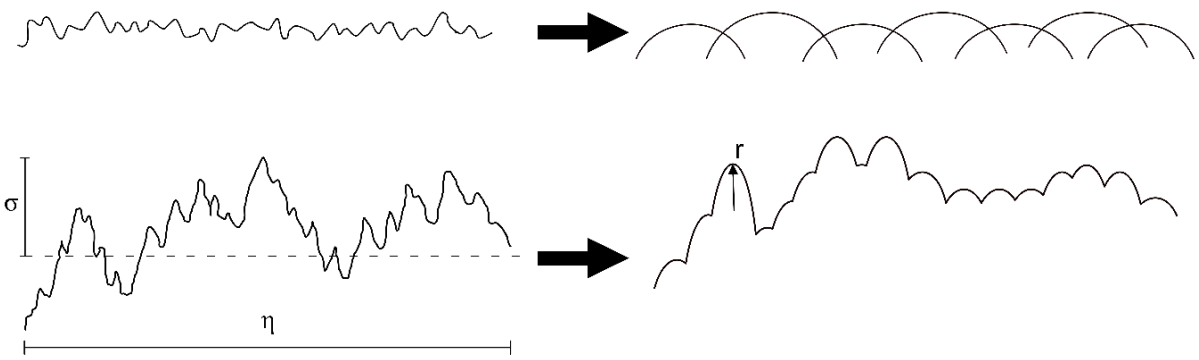

Figure A1: Schematic representation of GW parameters.

With the McCool parameters calculated using **Equation A4**, **Equation A5**, and **Equation A6**, the standard deviation of asperity heights (σ_a) can be calculated using **Equation A7** [33].

$$\sigma_a = \sqrt{\sigma_s^2 - \frac{3.717 \times 10^{-4}}{\eta^2 \cdot r^2}} \qquad \textbf{Equation A7}$$

Furthermore, the critical interference, as derived by Jackson and Green [32,34], can be calculated with **Equation A8**:

$$\omega_C = \left(\frac{\pi \cdot C \cdot S_y}{2 \cdot E'}\right)^2 \cdot r' \qquad \textbf{Equation A8}$$

where $C = 1.295 \exp(0.736v)$, with v being the Poisson's ratio of the material that deforms first (i.e., the textured rivets), S_y is the yield strength of the deforming material based on a von Mises yield criterion (i.e., material hardness divided by the adapted Tabor's relation), E' is the combined elastic modulus of the materials in contact, and r' is the combined radius of curvature between the materials in contact. For these calculations we assume that deformation takes place at the asperities – i.e., following the considerations of GW model. In other words, elastic sphere against a rigid plane.

Finally, with the standard deviation of asperity height and the critical interference, the plasticity index can be calculated with **Equation A9** [20,33].

$$\psi = \sqrt{\frac{\sigma_a}{\omega_{C,r}}} \qquad \textbf{Equation A9}$$

Moreover, the individual asperity contact force (P_c) and area of contact (A_c) can also be calculated according to Jackson and Green [20] using **Equation A10** and **Equation A11**.

$$P_C = \frac{\left(\pi \cdot C \cdot S_y\right)^3}{6 \cdot E'^2} \cdot r'^2 \qquad \textbf{Equation A10}$$

$$A_C = \pi^3 \cdot \left(\frac{C \cdot S_y \cdot r'}{2 \cdot E'}\right)^2 \qquad \textbf{Equation A11}$$

Since all parameters are derived from the spectral moments – i.e., from CLSM surface analysis – the resolution of image acquisition is of utmost importance, as previously reported by Jackson and Green [19]. Surface information was acquired at a resolution of 1024×1024, however, due to computational limitations the actual analyzed area corresponds to a 999×999 matrix by removing information from the outer perimeter.

Table A1 – Material properties for contact mechanics calculations.

	Copper	**Brass**	**Bronze**	**SnCu**
Modulus of elasticity /Pa	1.15E11	1.10E11	1.18E11	1.35E11
Poisson's ratio	0.34 *	0.35 **	0.34 **	0.325 *

* Values from [35].

** Values from [36].

The material properties used for all calculations are summarized in **Table A1**. The modulus of elasticity values for copper was obtained from Slade [3], whereas the values for brass, bronze,

and tin-plated Cu were obtained from the specifications of the manufacturers. For SnCu, the Poisson ratio of tin was used. Since the asperities were produced by grinding and polishing, the asperity radius can be considered half the particle size obtained with the grinding paper and polishing suspensions – shown in **Table A2**.

Table A2 – Theoretical asperity radius according to grinding and polishing particle size.

	1 µm	**6 µm**	**P600**	**P320**
Asperity radius /m	5E-07	3E-06	1.29E-05	2.31E-05

B. Appendix II

R_t	Total resistance
R_c	Constriction resistance
R_b	Bulk material's resistance
R_f	Resistance of the contaminant film
ρ_p	Resistivity of probe
ρ_{Pf}	Resistivity of plated material
ρ_{cont}	Resistivity of contamination film
η_c	Cleanliness factor
H	Hardness
F	Normal load
a	Radius of circular contact area
r	Individual asperity radius
η	Areal asperity density
σ_s	Standard deviation of surface heights
σ_a	Standard deviation of asperity heights
ψ	Plasticity index
ω_c	Critical interference
P_c	Critical load
A_c	Critical area
m_0	Square of root mean square surface height
m_2	Mean square slope
m_4	Mean square curvature
N	Total number of data points collected from surface
z	Height of the surface relative to its mean value
v	Poisson's ratio
S_y	Yield strength (based on a von Misses yield criterion)
E'	Combined elastic modulus
r'	Combined contact radius
t	CNT coating thickness

ARTICLE VI
Fretting and Electrical Contact Resistance Characteristics of Carbon Nanoparticle-Coated Cu Electrical Contact

Bruno Alderete[1,*], Sebastian Suarez[1], Diana Bucio Tejeda[2], Frank Mücklich[1,3]

[1] Chair of Functional Materials, Saarland University, Campus D3.3, 66123 Saarbrücken, Germany

[2] International Laboratory of Environmental Electron Devices (LAIDEA), ENES Morelia Universidad Nacional Autónoma de México, Mexico

[3] Materials Engineering Center Saarland (MECS), Campus D3.3, 66123 Saarbrücken, Germany

Research article

Published in "*Proceedings of the 2022 IEEE 67th Holm Conference on Electrical Contacts (HLM)*" (2022)

Impact Factor: NA

Reproduced with permission from 'Institute of Electrical and Electronics Engineers - IEEE'

Accessible online at: doi.org/10.1109/HLM54538.2022.9969836

Own Contribution: Conceptualization; Methodology; Validation; Investigation; Data Curation; Writing – Original Draft; Visualization.

Cite this article as: B. Alderete, S. Suarez, D.B. Tejeda, F. Mücklich, Fretting and Electrical Contact Resistance Characteristics of Carbon Nanoparticle-Coated Cu Electrical Contacts, in: 2022 IEEE 67th Holm Conference on Electrical Contacts (HLM), IEEE, 2022: pp. 1–8. https://doi.org/10.1109/HLM54538.2022.9969836.

ARTICLE VII
Wear Reduction via CNT Coatings in Electrical Contacts Subjected to Fretting

Bruno Alderete*, Frank Mücklich, Sebastian Suarez

Chair of Functional Materials, Saarland University, Campus D3.3, 66123 Saarbrücken, Germany

Research article
Published in "*Tribology Letters*" (2023)
Impact Factor: 2.9 (2023)

Accessible online at: doi.org/10.1007/s11249-023-01724-5

Own Contribution: Conceptualization; Methodology; Validation; Investigation; Data Curation; Writing – Original Draft; Visualization.

Cite this article as: B. Alderete, F. Mücklich, S. Suarez, Wear Reduction via CNT Coatings in Electrical Contacts Subjected to Fretting, Tribol Lett 71 (2023) 54. https://doi.org/10.1007/s11249-023-01724-5.

Tribology Letters (2023) 71:54
https://doi.org/10.1007/s11249-023-01724-5

ORIGINAL PAPER

Wear Reduction via CNT Coatings in Electrical Contacts Subjected to Fretting

Bruno Alderete[1] · **Frank Mücklich**[1] · **Sebastian Suarez**[1]

Received: 24 January 2023 / Accepted: 22 March 2023

Abstract

Carbon nanotubes (CNT) are of great interest to the research community due to their outstanding mechanical, transport, and optical properties. These nanoparticles have also shown exceptional lubricating capabilities, which coupled with their electrical conductivity show promising results as solid lubricants in electrical contacts. In this study, three different CNT coatings were deposited over copper platelets via electrophoretic deposition and subsequently tribo-electrically characterized including electrical contact resistance evolution during fretting wear, wear protection, chemical analysis of fretting marks, as well as influence of CNT coating thickness, duration and normal load applied during fretting, and atmospheric humidity. Thicker CNT coatings show improved wear protection while retaining similar electrical behavior as uncoated copper, or even improving its electrical contact resistance. Moreover, the compaction of the porous CNT coating is crucial for optimal electrical performance at low humidity. For longer fretting tests (150,000 and 500,000 cycles), the coatings are displaced thus affecting the wear protection offered. However, the coatings stabilize and reduce ECR compared to uncoated samples. Furthermore, thicker CNT coatings can bear higher loads during fretting due to the increased lubricant reservoir, with carbonaceous tribofilm remaining at the contacting interface after 5,000 fretting cycles regardless of normal load.

Graphical Abstract

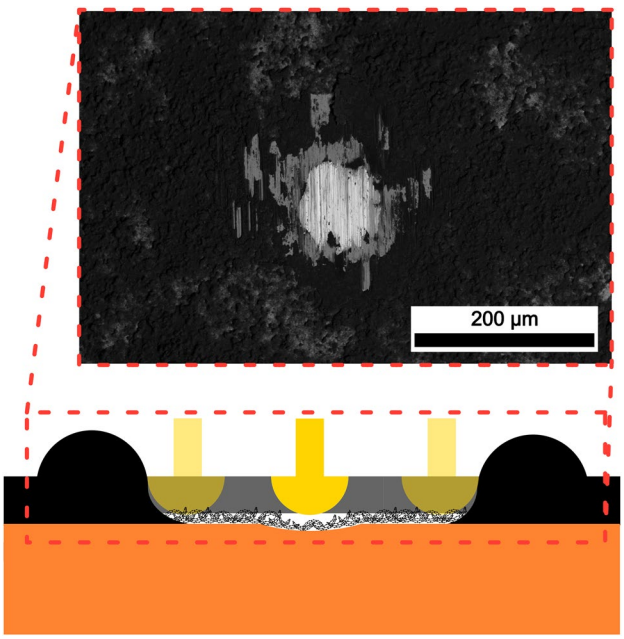

Keywords Carbon nanotubes · Electrical contact resistance · Fretting wear · Wear reduction

Extended author information available on the last page of the article

Published online: 09 April 2023

1 Introduction

Copper is widely used in electrical contacts due to its outstanding electrical conductivity, its moderate mechanical properties, its formability, along with its rapid passivation on account of its thin native oxide layer which is spontaneously formed when in contact with ambient conditions, and its low cost when compared with other contact materials—e.g., silver, gold, and platinum. As societal trends further move towards a more electrified future, it is crucial that more reliable, efficient, cost-effective, and more versatile electrical contacting systems are designed and developed [1–3]. In turn, this can not only increase material efficiency and reduce maintenance requirements in the systems, but also improve the overall sustainability of the electrical device.

Fretting wear is a phenomenon that can severely impact the duty life and optimal operation of electrical contacts. This does not only affect when in-operation, but also affects the reproducibility of a stable connection in separable contacts. Fretting occurs when two contacting bodies are in relative motion with one another. This motion is highly localized and of oscillatory nature [4, 5], with amplitudes typically ranging from a couple of micrometers up to 100 µm in electrical applications [5, 6]; however, fretting has also been studied in the nanoscale via techniques such as scanning probe microscopy [7]. Although fretting wear is not exclusive to electrical contacts, since all systems subjected to oscillatory motion can be affected, in this study we will focus on this specific application. The root of fretting wear cannot always be eliminated since it could be caused by mechanical vibrations intrinsic to the application—such as vibrations originating from an engine. Nonetheless, other sources such as dissimilar thermal expansion coefficient, mechanical shock, or electromagnetically induced vibrations can be—to a certain extent—mitigated by proper system and contact design [5, 8]. Environmental conditions can also impact fretting wear. Relative humidity in particular can affect the time it takes for electrical contact resistance (ECR) to stabilize while an electrical contact is subjected to fretting wear [5].

This wear mechanism degrades the contacting materials and entraps debris at the contacting sites, thus generating a considerable increase in electrical contact resistance [9]. When dealing with materials that form superficial films—e.g., copper and tin—the breakdown of these layers can be detrimental to the electrical behavior, but also in terms of wear resistance. Although the breakdown of copper oxide should increase the conductivity between the contacting bodies, the accumulation of debris could potentially hinder the electrical contact between the electrodes. Furthermore, the debris trapped at the contacting interface could act as third bodies, thus transitioning to severe abrasive wear.

As with other wear mechanisms, the effects of fretting wear can be minimized by proper lubrication of the contacting surfaces. In electrical applications, however, lubrication hinders the electron transport between the surfaces since it is an additional barrier. Furthermore, with some exceptions, most traditional lubricants possess high electrical resistivity, thus, imposing a significant increase in ECR. Consequently, liquid lubricants are not favored for electrical applications, hence opting for lubricant greases or solid lubricant alternatives. However, solid lubricants are not traditionally favored for fretting wear since these tend to be easily displaced, thus rapidly leaving the surface exposed to wear.

At an attempt to determine a more suitable solid lubricant alternative, four different carbon nanoparticles (CNP) coatings were investigated and tribo-electrically characterized [10]. From this study, we concluded that carbon black and carbon nanotubes (CNT) showed the most promising results based on their exceptional ECR behavior, as well as wear and oxidation protection, with CNT showing better results in general. Therefore, it is of interest to expand upon these results to further understand the lubricating capabilities of CNT coatings.

Carbon is a versatile element which is capable of forming different carbon–carbon bonds. The different bonds change the hybridization state of the carbon atoms, which in turn changes the properties of the formed allotrope [11–13]. The lubricating capabilities of allotropes such as onion-like carbon, carbon nanohorns, and CNT have been previously studied and reported [14–18]. However, for the specific application of electrical contacts, the conductivity of the carbon allotrope is of utmost importance. Therefore, CNT are a promising alternative since these CNP have not only been found to be exceptional solid lubricants, but these nanoparticles are also outstanding conductors [19–24], with a longer mean free path than copper and quasi-ballistic electron transport properties in metallic CNT [25–28]. This is important to keep in mind, since depending on the chirality of the CNT, these nanoparticles can behave as a metallic conductor or as a semiconductor [29–31]. Consequently, in this study, multi-walled carbon nanotubes (MWCNT) are used since they are easier to manufacture—compared to single-walled carbon nanotubes (SWCNT)—while having similar current carrying capacity as metallic SWCNT [32]. Furthermore, MWCNT present the added advantage that they conduct electricity as a zero band gap conductor since they always possess at least one metallic tube [33, 34].

Conventional solid lubricants, such as graphite and MoS_2, have specific humidity requirements in order to appropriately lubricate the contacting site. The former requires high atmospheric humidity—lower friction and wear at higher relative humidity—whereas the latter presents lower friction and wear at lower relative humidity [35, 36]. This humidity-dependent behavior has been widely reported for graphite.

Multiple models have been proposed—e.g., Savage, Rowe and Bryant, Bollmann and Spreadborough, among others—however, authors agree that graphite is not an intrinsically good lubricant, but rather requires ambient moisture to become one [37–42]. However, it is now understood that water's role in graphite's lubricity is not physiosorbed but rather dissociative chemisorption, thus leading to the formation of H and OH ions [37, 43]. Moreover, recent work by Morstein et al. suggest an extended adsorption model due to the tribo-induced formation of turbostratic carbon [38]. This structural transition enables graphite to lubricate even at high loads and low humidity.

A review article from Kumar et al. has summarized the temperature range of applications of different solid lubricants [44]. In their study, the authors have placed graphite and other carbon materials—such as diamond-like carbon and CNT—in similar working ranges. Therefore, it is of great interest to evaluate the influence of atmospheric moisture on the wear protection offered by CNT coatings. It is hypothesized that humidity will not have a significant influence on the lubricating capabilities of this CNP due to the sp^2-hybridization state of CNT, coupled with the large aspect ratio of the tubes themselves (1-dimensional material) [45]. Therefore, it was hypothesized that CNT lubricate by rolling on the surface, thus acting like a roll bearing [15, 46, 47]. However, if that were the case, friction would be significantly lower than what is usually reported [14, 46]. New research by MacLucas et al. has demonstrated that the main lubrication mechanism active in CNT is sliding rather than rolling [48].

Within the scope of this work, CNT will be deposited via electrophoretic deposition (EPD) over copper substrates [13, 49, 50], followed by tribo-electrical characterization via fretting tests and ECR measurements [10]. The fretting tests were carried out at constant normal load, with periodic ECR measurements at set intervals (static ECR) to track the evolution of ECR as fretting tests progress. Three different coating thicknesses were evaluated, as well as four different normal loads to gather insight into their respective influences on wear and electrical behavior. Fretting tests were also conducted at low relative humidity to analyze the potential use of CNT coatings as lubricants even in the absence of atmospheric moisture. The resulting fretting marks were subsequently characterized via confocal laser scanning microscopy (CLSM) to determine the affected area, as well as scanning electron microscopy (SEM) to micrograph the fretting mark. Furthermore, chemical analysis via energy dispersive X-ray spectroscopy (EDS) was conducted to acquire information on the oxidation state of the fretting mark, as well as to quantitatively assess material transfer from the counter electrode onto the coated electrode, done by the acquisition of elemental mappings.

2 Materials and Method

The substrates used were laminated, flat, oxygen-free, pure-copper platelets (25 × 10 × 1) mm (Wieland Electric GmbH, Germany). These copper platelets were ground (P1200 grit silicon carbide grinding paper) and polished at 6, 3, and 1 µm to obtain a mirror-polished surface before coating; thus achieving a root mean square roughness between 10 and 20 nm. The CNT used were chemical vapor deposition (CVD)-grown MWCNT (Graphene Supermarket, USA). The outer diameter of the CNT have a distribution between 50 and 85 nm, an as-received state length from 10 to 15 µm, and a carbon purity above 94%.

Potentiostatic EPD was carried out at a set voltage of 300 V, with an inter-electrode distance of 15 mm. The dispersion parameters and deposition process were thoroughly explained in Alderete et al. [10, 13, 49, 50]. Three different CNT coatings were produced, where the only parameter that was varied was the deposition time—i.e., the coating thickness [10, 13]. Therefore, a total of four samples were analyzed, namely: an uncoated copper reference sample, and three CNT-coated samples with deposition times of 3, 4, and 5 min (henceforth CNT3, CNT4, and CNT5, respectively).

After coating the samples were tribo-electrically characterized via a custom multipurpose testing rig [51]. This setup allows an ample combination of tribological and electrical characterization. In this work, we focus specifically on conducting fretting wear tests with periodic ECR measurements at set intervals (static ECR) to evaluate the influence of CNT coating thickness, normal load applied, as well as ambient humidity and test duration. Since this report follows up on previous work [10], it is of interest to maintain the same fretting parameters to ensure comparability. Contrarily, changing a parameter might influence the results. For example, it was reported by Park et al. that varying the amplitude of fretting tests affects the resulting dynamic ECR [52]. The authors also analyze different permutations of frequency and amplitude and show the resulting fretting mark, as well as

Table 1 Summary of tribo-electrical testing parameters

Measurement	Load/N	Fretting cycles /10^3 cycles	Intervals /10^3 cycles	Relative humidity
1	0.5	5	0.1	30–40%
2	1			
3	2.5			
4	5			
5	1			15%
6		150	1	30–40%
7		500		

reporting the time it takes for ECR to stabilize with the different parameter combinations [52]. Therefore, in our study, fretting tests were conducted with an amplitude of 35 µm and an oscillation frequency of 8 Hz, matching those of our previous work [10].

ECR measurements were conducted using the four-probe method sourcing a direct current of 100 mA using a Keithley 2400 SMU. This current level was chosen to stay under dry-circuit conditions [53]. The voltage drop was measured using a Keithley 2182a nanovoltmeter with a voltage range of 1 V. The contacting counter electrode for fretting and ECR measurements was a silver-nickel core ($AgNi_{0.15}$) hard-gold-coated ($AuCo_{0.2}$) rivet (Adam Bornbaum GmbH). These rivets have a curved head, with a mean diameter of curvature of 4 mm and a root mean square roughness of 0.25 µm. The hard-gold coating has an average thickness of 6.47 ± 0.18 µm. In the loading ranges evaluated in this study (0.5–5 N), a maximum Hertzian contact pressure between 314 and 676.5 MPa is achieved. All atmospheric tribo-electrical tests were carried out at ambient conditions, i.e., temperature and humidity ranging from 20 to 25 °C and 30–40% r.h., respectively. The low humidity tribo-electrical measurements were conducted using a climate test chamber set at 20 °C and 15% r.h. Seven different fretting conditions per sample were evaluated, summarized in Table 1. Ten ECR measurements were carried out before fretting as well as at each cycle interval and then averaged, with each fretting test being reiterated at least three times. A new rivet was used for every measurement.

After tribo-electrical testing the fretting marks were imaged with SEM (using ETD detector and 5 keV acceleration voltage) and chemically analyzed via EDS (ThermoFisher Helios™ G4 PFIB CXe DualBeam™ FIB/SEM equipped with an EDS detector EDAX Octane Elite Super). EDS scans were carried out using an acceleration voltage of 15 keV, thus acquiring a 2-dimensional chemical distribution map. Topographical and wear analyses were carried out by imaging via CLSM (LEXT OLS4100, Olympus) using a laser wavelength of 405 nm. A larger field of view at higher resolution was attained by stitching a 2×2 or 3×3 grid (depending on wear track size) at $50 \times$ with a 20% overlap. With the information acquired via CLSM scans coating thickness, worn area, and roughness after fretting can be obtained.

A 5×2 grid at $50 \times$ was stitched in the CLSM to measure coating thickness. The coatings have an average thickness of 1.27 ± 0.12 µm, 1.62 ± 0.11 µm, and 1.77 ± 0.01 µm for CNT3, CNT4, and CNT5, , respectively.

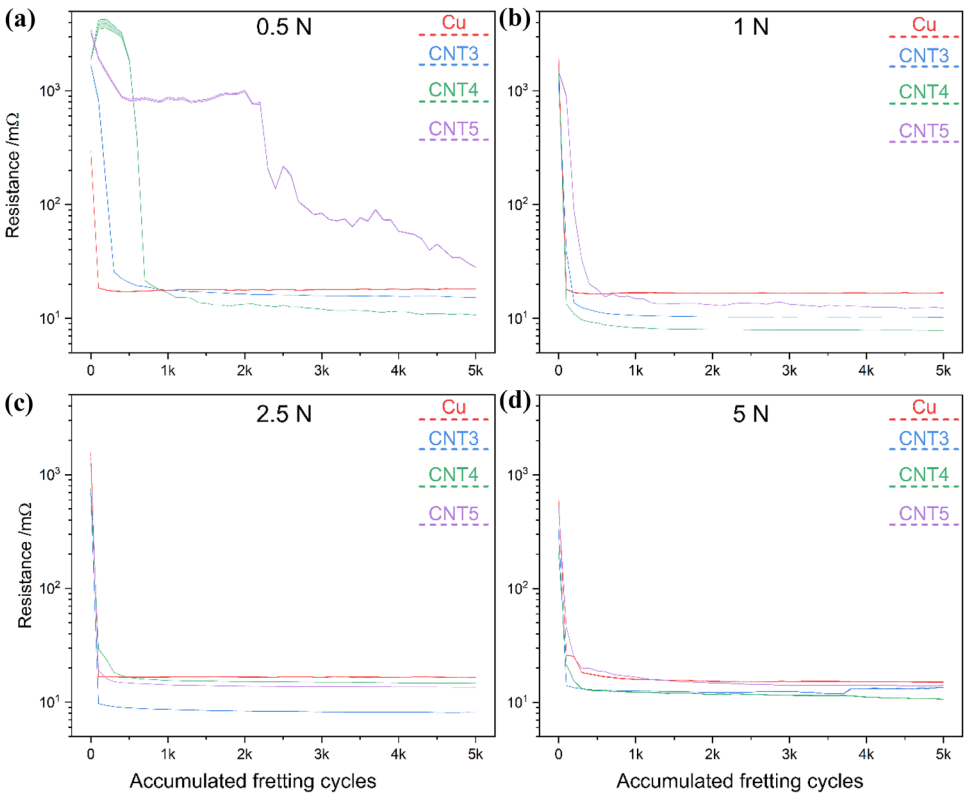

Fig. 1 ECR measurements of CNT-coated samples for a total of 5 k fretting cycles at **a** 0.5 N, **b** 1 N, **c** 2.5 N, and **d** 5 N. The line plot indicates the tendency of the ECR evolution during static ECR measurements

3 Results and Discussions

3.1 Electrical Behavior

3.1.1 Influence of Normal Load

The ECR evolution based on the analyzed normal loads are shown in Fig. 1. These fretting tests were all carried out for a total of 5 k cycles with periodic ECR measurements every 100 cycles. It is noteworthy to highlight that these measurements are highly reproducible, with very low error—standard deviation of the measurements are plotted in all ECR curves, however these cannot be appreciated due to the thickness of the line itself. Furthermore, it should be noted that since static ECR was measured, the line plot shows the ECR tendency and not the actual behavior. Observing the plots from Fig. 1 it can be seen that the behavior of the uncoated copper substrate is consistent regardless of normal load. The ECR value of the reference prior to fretting are high, however, after the first 100 fretting cycles the ECR value sharply decreases to approximately 20 mΩ and remains constant throughout the measurement. The behavior is unexpected, since the breakdown and reformation of the oxide layer should cause fluctuations in the resistance between intervals. However, due to the short period of time between consecutive ECR measurements—it takes approximately 20 s for the setup to complete 100 cycles—the thickness of the reformed oxide layer could not be sufficient to affect the resistance. This behavior could also be associated with the number of a-spots being established and remaining constant throughout the fretting cycles, consequently presenting constant ECR.

Focusing on the tests done at 0.5 N, CNT5 stands out from the rest. This coating presents an initial reduction in ECR during the first hundred cycles caused by the compaction and adjustment of the coating during fretting. The ECR remains constant for the following couple thousand cycles, followed by a progressive reduction in ECR. The sudden reduction at around 2 k cycles could be due to (1) the breakdown of a large CNT agglomerate at the contacting site, or (2) the displacement of a significant portion of the CNT coating. Based on the observed behavior, the former seems more likely. Following the fretting-induced breakdown of the CNT agglomerate, smaller agglomerates are subsequently displaced from the fretting mark; thus explaining the progressive reduction in the following fretting cycles.

Initially, CNT4 shows similar behavior as CNT5. However, after 500 cycles the ECR sharply falls to values that approach that of the uncoated reference. As the fretting cycles progress, a small reduction in ECR is observed, with values falling below that of the copper reference and reaching values of approximately 10 mΩ. CNT3 behaves akin to the uncoated reference, with ECR values falling below 30 mΩ after a few hundred cycles. After 1 k cycles, CNT3 presents lower ECR than the uncoated reference, however, the resistance is still higher than that of CNT4.

When increasing the normal load, the ECR behavior tends to not vary as considerably as with low normal loads—i.e., 0.5 N. In the tests carried out at 1 N, 2.5 N, and 5 N, ECR values quickly fall below 30 mΩ and outperform the uncoated reference within the first 1 k cycles. CNT5 shows improved performance compared to the uncoated reference sample, however, the thinner three- and four-minute coatings consistently outperform the thickest coating.

The normal load during fretting does not have an observable influence on the ECR of an electrical contact. This was evidenced by the uncoated reference sample, and corroborated with the coated samples from normal loads above 0.5 N. The considerable deviation in the coated samples at 0.5 N is a consequence of inadequate electrical contact in the system. At low loads, the coating is not sufficiently compacted, thus presenting a porous network that hinders electron transport from the counter electrode towards the substrate. Furthermore, thicker coatings require more fretting cycles to breakdown the larger CNT agglomerates, thus initially presenting higher ECR values. When contacting at

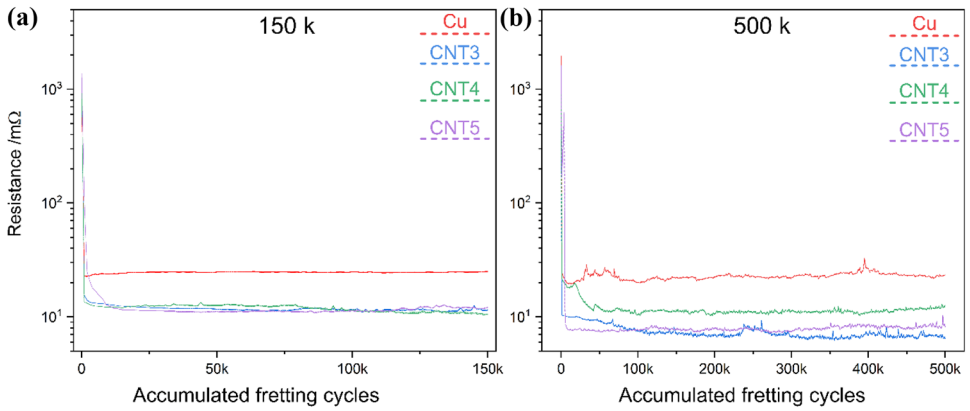

Fig. 2 ECR measurements of CNT-coated samples at 1 N for a total of **a** 150 k and **b** 500 k fretting cycles. The line plot indicates the tendency of the ECR evolution during static ECR measurements

higher normal loads, these elevated contact pressures, coupled with the oscillatory motion, enable the breakdown of these agglomerates at a much faster rate. Consequently, the resistance values stabilize reaching a steady state with fewer fretting cycles.

It is, therefore, crucial that thin coatings are employed in electrical contacts that operate at low normal loads. Contrarily, undesired energy loss will take place at the contact interface, thus lowering its efficiency. When the contact operates at higher normal loads, on the other hand, the coating thickness is irrelevant. However, to optimize material efficiency, a three-minute CNT coating is sufficient from an electrical perspective.

3.1.2 Endurance Test

The electrical behavior of the samples at 1 N for longer fretting durations is shown in Fig. 2. As was the case for 5 k cycles (Fig. 1) the ECR value of the uncoated reference tends to stabilize at approximately 20 mΩ. In the case of the 500 k-cycle test slight fluctuations are observed. Regardless of the variation observed, the value does not vary past 30 mΩ—values which correlate with those measured in the 150 k-cycle test.

In the longer fretting tests the coatings show a considerable improvement in terms of contact resistance. Regardless of coating thickness, the ECR values are half of that of the uncoated sample, or even lower. It was initially believed that longer fretting tests could be more severely influenced by the breakdown and subsequent reformation of the oxide layer. However, this is proven otherwise since the ECR values of the uncoated reference resemble those of the references in the shorter fretting tests. Nonetheless, the presence of a thin copper oxide layer that forms between ECR intervals cannot be disregarded. These tests are conducted with intervals that last over four times more than the shorter tests, however, the duration is still relatively short. Therefore, a complete reformation of the oxide layer is unlikely since the spontaneous formation of Cu_2O takes considerably longer [54].

Furthermore, as opposed to what was observed for shorter fretting tests (Fig. 1), the thickness of the coating does not have a significant influence on the electrical behavior of the coated samples. The five-minute CNT coating performs on par with the thinner coatings, all outperforming the uncoated reference. It seems that the carbonaceous tribofilm formed enhances the electron transport at the interface.

3.1.3 Influence of Ambient Humidity

The influence of humidity on the electrical behavior of metals when subjected to fretting wear has already been analyzed by Timsit and Antler (in Slade) [5]. In their work, the authors report that at lower ambient humidity, copper

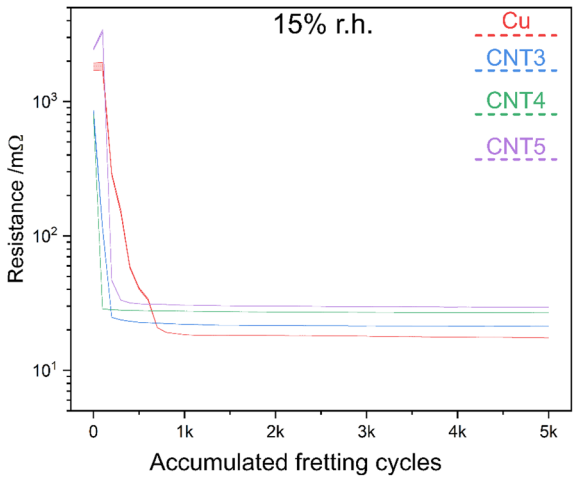

Fig. 3 ECR measurements of CNT-coated samples for a total of 5 k fretting cycles at a constant temperature and humidity (20 °C and 15% r.h., respectively). The line plot indicates the tendency of the ECR evolution during static ECR measurements

electrical contacts show an improved duration when subjected to fretting wear. In other words, the copper contact requires considerably more fretting cycles to reach the ECR threshold of failure proposed by the authors. Therefore, it could be foreseen that the uncoated copper shows higher ECR values at lower fretting cycles, stabilizing after 700–800 cycles. After stabilization, the copper reference shows ECR values that resemble the measurements carried out at ambient conditions (see Fig. 3). The coated samples, on the other hand, reach a steady state rather quickly, after around 300 cycles. However, the steady state values of the coated samples are of interest since now the uncoated reference outperforms the coated samples. Under these conditions thicker coatings promote higher ECR values. Although the increase is marginal, the tendency is clear. This behavior was not expected since it has been previously reported that metallic SWCNT show the opposite behavior—i.e., resistance increases as relative humidity increases [55–57]. Since MWCNT always have a conductive tube, it was expected that resistance would decrease at lower humidity. However, this humidity-dependent behavior was reported for humidity sensing devices. In our analysis a more complex scenario is taking place due to the addition of tribological testing.

The worsened electrical behavior of the coated samples could be associated to a tribologically induced degradation of the CNT, however, this is unlikely on account of the longer fretting tests carried out (see Fig. 2). As witnessed in the 150 and 500 k cycle tests, the ECR of the coated samples outperform the uncoated reference despite the greater stresses incurred onto the CNT. Therefore, it is implausible that at 15% r.h. and 5 k fretting cycles more severe wear took place in the CNT rather than in 150 k and 500 k cycles.

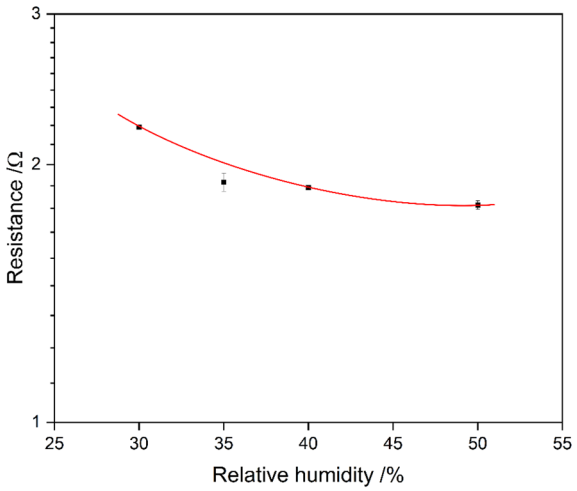

Fig. 4 ECR of CNT4 at different humidity with second order polynomial fitting (r-square = 0.991)

To confirm the tribological-independence of the ECR gain, static-constant-load ECR measurements at 1 N were carried out with the same instrumental parameters as with the tribo-electrical tests. Four different ambient humidity conditions were evaluated (i.e., 30, 35, 40, and 50%), measured at five different points in CNT4 with twenty measurements per point—giving a total of 100 ECR measurements per r.h. These values were then averaged and plotted, shown in Fig. 4. As the graph illustrates, it is clear that higher r.h. promotes lower ECR values. Therefore, the electrical behavior observed in Fig. 3 is not caused by the tribological tests but rather is inherent to our coating systems. Although the literature suggests that CNT should show the inverse behavior, it is important to highlight that our system differs significantly from those previously studied—i.e., studies on resistive CNT-based humidity sensors. In a study by Lee et al. they used SWCNT networks analyzing the electrical response of metallic and semiconducting CNT [56], whereas Ling et al. worked with thin SWCNT networks with thicknesses below 1 µm [57]. On the other hand, highly dispersed and aligned MWCNT have been used by Tsai et al. as sensor interconnections [55]. The CNT coatings dealt with in this study differentiate themselves from those previous studies in the following ways:

- The coatings are made up of a composition of individual CNT and CNT agglomerates, with a mean agglomerate area fraction of approximately 43% [50].
- The coatings are highly porous, thus requiring pressure from the counter electrode to compact and adjust internally to reduce ECR by increasing the amount of parallel percolation paths—see focused ion beam cross sections in [13].

The latter is believed to play a crucial role in the humidity-dependent behavior of the CNT coatings. It is hypothesized that ambient humidity promotes lower ECR values since moist air is a better electrical conductor than dry air. Therefore, the dry air found in the porous network of the CNT coatings influences the ECR behavior, possibly explaining the electrical behavior of the CNT-coated samples from Fig. 3.

Another phenomenon that could influence the electrical behavior at higher atmospheric humidity is that of electrowetting [58]. The contact angle of a water droplet can be modified in the presence of an electric field [58, 59], causing the droplet to become more hydrophilic (flatten out) when a voltage is applied and showing its most hydrophobic state in the absence of an electric field. Although the voltages that the authors report are significantly higher than the voltages recorded in our ECR measurements, this flattening effect could improve the contact between individual CNT and CNT agglomerates by bridging the voids in the coating even further—in addition to compaction due to the normal load applied—thus improving the system's conductivity at higher humidity levels. Furthermore, the small dimensions of the CNT and CNT agglomerates, coupled with their curvature, could potentially intensify this effect by concentration the electric field thus causing the flattening of moisture droplets even at low voltages. Moreover, the small dimension of moisture droplets—as opposed to macro-sized droplets—would require lower voltages to change its wetting behavior.

Therefore, although there is an increase in ECR at low humidity, these coatings could still be beneficial in applications where the ambient humidity varies over time. For specific applications operating for prolonged periods of time at low humidity, on the other hand, the negative influence on the electrical behavior of the CNT coatings is counterproductive, thus promoting loss in contact efficiency. However, it should be noted that 15% r.h. is a low atmospheric value, with higher typical values in central Europe [60, 61]. The wear protection offered should be carefully analyzed to evaluate if the wear reduction offered at low ambient humidity could outweigh the gain in ECR.

3.2 Wear Protection

3.2.1 Influence of Normal Load

SEM micrographs of the fretting marks for each sample at each load are shown in Fig. 5, with the red dashed line highlighting regions where severe wear took place, i.e., gross slip [62]. Only regions where gross slip took place are considered for the relative worn area calculations. Observing the

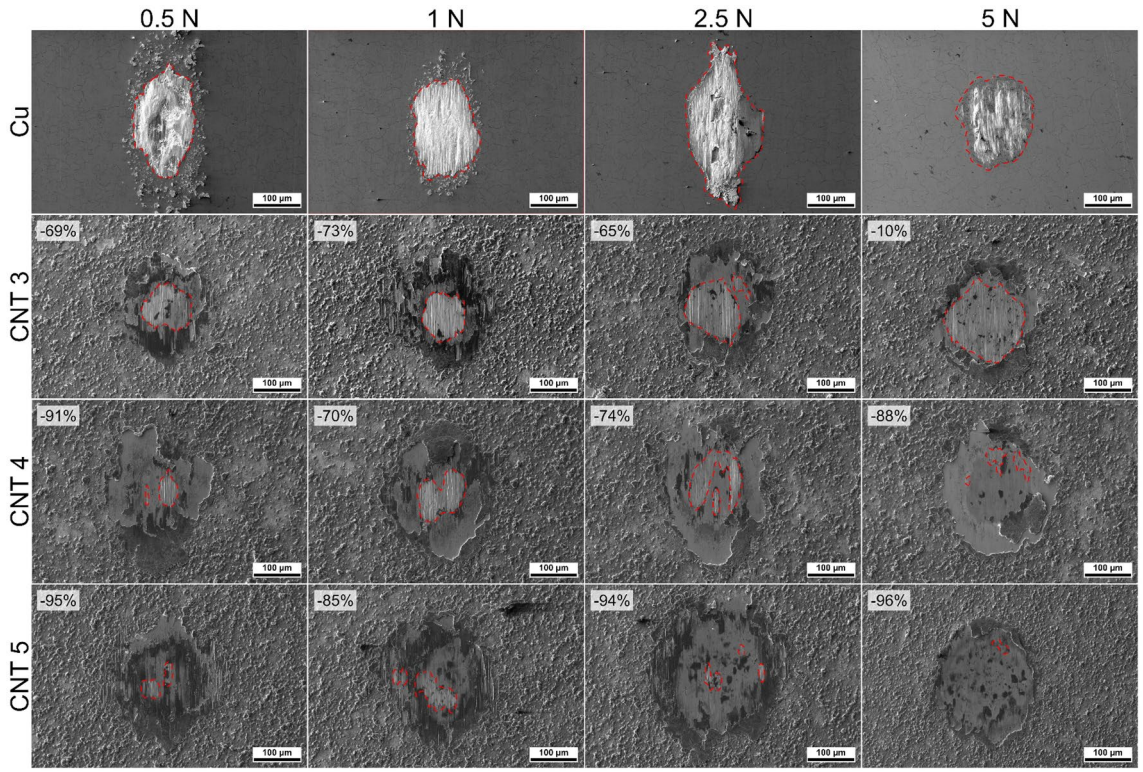

Fig. 5 SEM micrographs of fretting marks after 5 k fretting cycles. The red dashed lines highlight the areas where severe wear is observed (gross slip). The number at the top left corner of each CNT-coated sample exhibits the reduction in worn area relative to the respective uncoated copper sample

load-dependent behavior of the uncoated copper sample, two aspects stand out: (1) the wear track tends to decrease in size as the load increases, with the 5 N fretting mark showing the smallest worn area, and (2) formation of debris surrounding the fretting mark is only observed for load below 2.5 N. The latter is of concern from a tribological standpoint since debris can be trapped at the contacting site, thus causing third-body abrasion. This phenomenon, coupled with adhesive wear, could further promote the transition from mild to severe wear [63]. The lack of loose debris formation at 5 N exemplifies this behavior. Since debris are not prominent in this fretting mark, the only wear mechanism active is adhesive wear and two-body abrasive wear. The latter, however, is not as dominant in the system due to the soft radius of curvature of the counter electrode. Therefore, in this case, three-body abrasive wear due to debris formation is more detrimental rather than two-body abrasion. Although debris pile up can be observed at 2.5 N, these particles are located at the ends of the fretting tracks. Therefore, the particles are displaced onto the upper and lower limits of the oscillatory motion, thus reducing the likelihood of third-body abrasion. The geometry of the counter electrode also explains the smaller worn area at higher normal loads. The non-conformal contact established between the bodies implies a considerably higher contact pressure at the tip of the rivet, which, in turn drastically increases frictional forces. Furthermore, metallic oxides generally have higher shear strength than the unoxidized metal. Therefore, according to Tabor's theory [36], higher shear strength also causes higher friction. Higher friction restricts, to a certain extent, the displacement of the counter electrode over the copper surface. Consequently, the load is more concentrated on the central part of the amplitude of motion, thus causing smaller worn areas.

The fretting marks of the CNT-coated substrate look notably different compared to their uncoated counterparts. The wear tracks are smaller, as evidenced by the relative worn area reduction at the top left corner of each micrograph. Although coating displacement is observed, with the micrographs showing exposed regions of the substrate as well as clusters of CNT agglomerates surrounding the fretting mark. The degree to which the coating is displaced varies from sample to sample; however, it was observed for all coatings. Nonetheless, coating displacement does not appear to affect the wear protection offered by the CNT coating. Certain fretting marks showing severe displacement, and even coating removal such as CNT4 at 2.5 N still offer considerable wear protection compared to the uncoated reference, with a worn

area that is over 70% smaller than the copper sample at 2.5 N—areas measured from CLSM scans.

At and below 2.5 N CNT3 shows considerable wear protection, with a worn area that is between 60 and 70% smaller compared to their uncoated counterparts. At 5 N, however, there is a marginal reduction of the worn area at only 10%, approximately. Nonetheless, the damage incurred at 5 N in the coated sample does not appear as severe as the uncoated sample.

CNT4 and CNT5 show exceptional wear protection. In all cases a reduction in the worn area of at least 70% can be observed, regardless of normal load and state of the coating—i.e., coating damage and/or displacement/piling up. For these two coatings, fretting at 5 N does not incur considerable damage onto the substrate's surface, showing partial slip rather than gross slip as in the uncoated reference. In fact, CNT4 and CNT5 at 5 N show the least amount of damage after 5 k cycles. This is attributed to the lack of debris formation, as well as CNT clusters that remain at and around the contact site after the fretting cycles, evidenced by the black regions in the SEM micrographs—and later verified by EDS mappings. This is especially true for all measurements carried out on the CNT5 sample. Due to the considerably thicker coating, an abundance of CNT remains at the contacting interface, thus granting greater wear protection throughout the measurement cycles.

Furthermore, the electrical behavior of CNT5 at 0.5 N is reasonable observing the SEM micrograph (see Fig. 1a). This image shows a significant amount of CNT remaining at the contacting site. Although this is extremely desirable from a solid-lubrication perspective, it is important to note that CNT are not as conductive as the metallic electrodes—despite the fact that individual CNT demonstrate exceptional electron transportability.

With sufficiently thick CNT coatings, the wear protection offered is independent of the normal load during fretting. Some variations are observed; however, this is intrinsic to the heterogeneity of the coatings themselves [13]. Contrarily, the thinner CNT3 coating shows a substantial increase in worn area at 5 N, resembling the uncoated sample. At lower loads, some wear protection is offered, however, it is not as significant as in the thicker coatings. Consequently, a coating thickness threshold is established, with a requirement of at least 1.5 to 1.6 µm to observe consistent and load-independent wear protection.

From a tribological standpoint, thicker CNT coatings are more desirable since they offer a larger lubricant reservoir. As evidenced by the micrographs from Fig. 5, thicker CNT coatings provide a more significant wear protection, with CNT remaining at the contact site after tribological testing. However, when taking into account the purpose of these coatings, thicker coatings may be counterproductive.

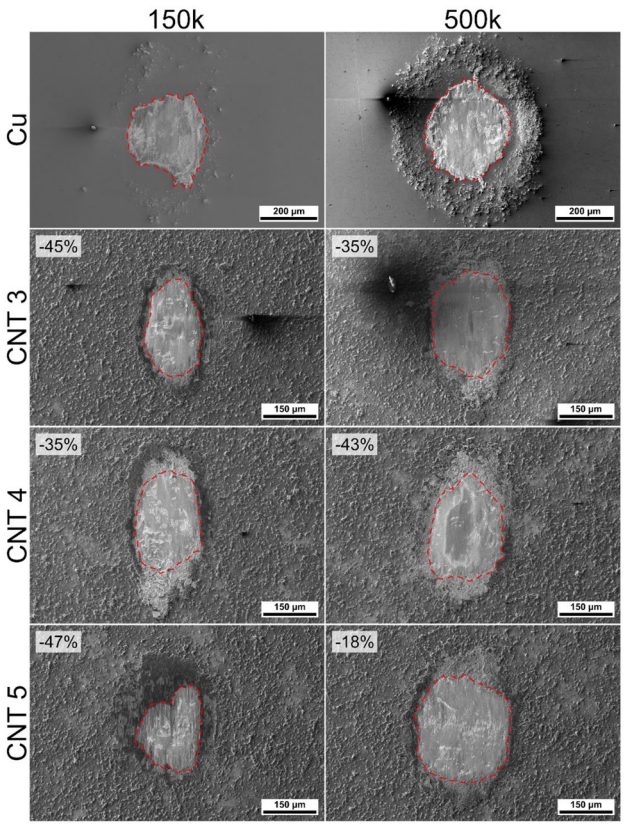

Fig. 6 SEM micrographs of fretting marks after 150 and 500 k fretting cycles. The red dashed lines highlight the areas where severe wear is observed (gross slip). The number at the top left corner of each CNT-coated sample exhibits the reduction in worn area relative to the respective uncoated copper sample. Note that the magnification of the uncoated samples is smaller than the magnification of the coated samples

In other words, for electrical applications, thicker coatings have a more significant impact on the conductivity of the system. Therefore, a tradeoff must be considered, where a balance between wear protection and admissible ECR gain must be weighed.

3.2.2 Endurance Test

The SEM micrographs resulting from the 150 and 500 k fretting cycles tests on the coated and uncoated samples are shown in Fig. 6. As expected, the uncoated samples show substantial wear after 500 k cycles. Since these tests were carried out at 1 N—and based on the behavior of the substrate after 5 k cycles—it was also expected that debris would gather around the fretting mark. However, the amount of debris observed around the 500 k cycles is significant. After 150 k cycles, on the other hand, a negligible amount of debris is observed, especially when compared to the 500 k cycles measurement. These tracks are significantly larger than the 1 N tracks after 5 k cycles, with the 150 k

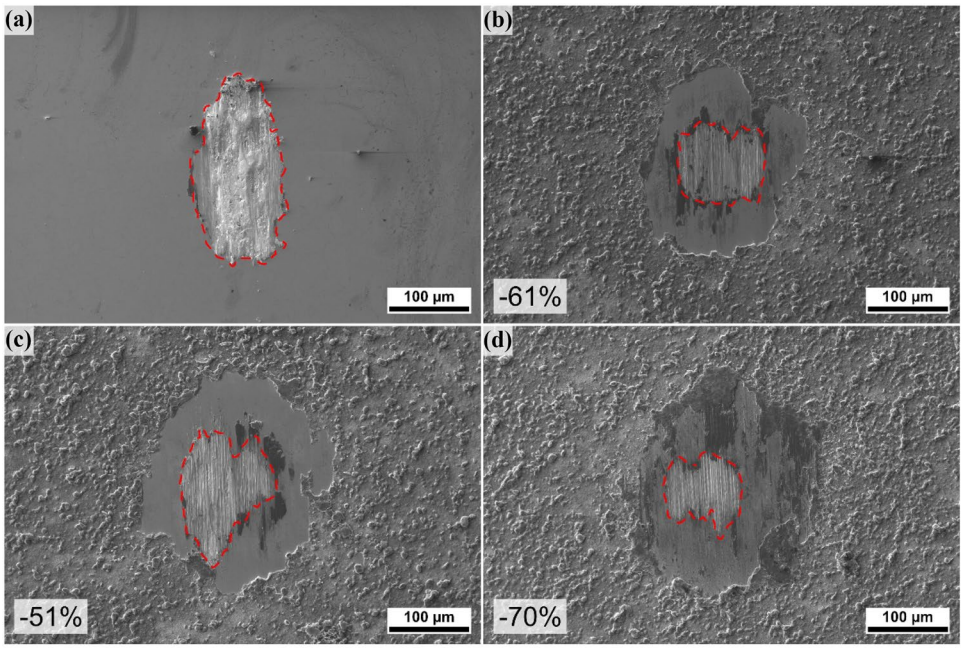

Fig. 7 SEM micrographs of fretting marks after 5 k fretting cycles at 20 °C and 15% r.h. **a** Uncoated copper, **b** CNT3, **c** CNT4, and **d** CNT5. The red dashed lines highlight the areas where severe wear is observed (gross slip). The number at the bottom left corner of each CNT-coated sample exhibits the reduction in worn area relative to the respective uncoated copper sample

cycles track being double the size and the 500 k cycles track three-fold the size of the 5 k track. For this reason, the magnification of the micrograph had to be reduced. The same can be stated about the CNT-coated samples, with these representing an even larger multiple compared to their 5 k counterpart.

The micrographs of the CNT-coated samples reveal that CNT are not as effective in reducing wear after prolonged fretting cycles, showing gross slip regardless of coating thickness. Although all coatings show a reduction in worn area, the degree to which the coatings reduce wear is not as significant as was the case in shorter fretting cycles. This is because the CNT are displaced from the contact site, thus eliminating the possibility of reducing wear. Therefore, for prolonged fretting cycles, the wear reduction capability of CNT is irrespective of the coating thickness since the nanoparticles are displaced from the contacting interface altogether.

Even though the coatings do not perform as exceptionally well for prolonged fretting cycles in terms of wear protection, they do improve the electrical behavior of the system—see Fig. 2. Therefore, their potential use for electrical systems should not be discarded. All three coatings outperform the uncoated reference, with low and stable ECR throughout the entire measurement. Although wear protection is sparse, the electrical advantage is beneficial.

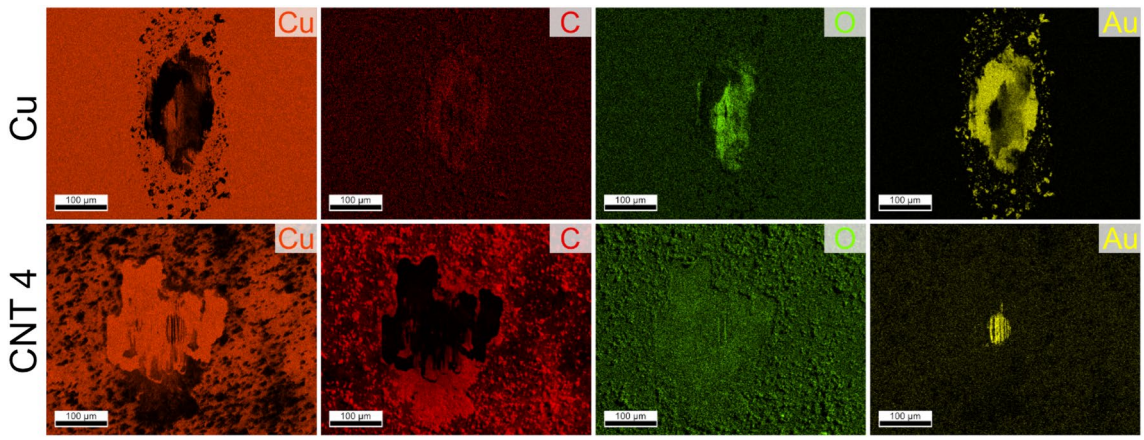

Fig. 8 EDS maps of uncoated copper and CNT4 showing copper, carbon, oxygen, and gold after 5 k fretting cycles at 0.5 N. EDS maps of all fretting marks are available in the Online Resources

3.2.3 Influence of Ambient Humidity

The SEM micrographs of the fretting tests carried out at low humidity are shown in Fig. 7. The worn area of the uncoated reference after 5 k cycles at 1 N from Fig. 5 is comparable with the size of the reference at 15% r.h. However, in the case of the coated samples, all coatings show an increase in worn area as a consequence of the lower atmospheric humidity. The increase in relative worn area is linked to the coating thickness, with thicker coatings showing worse wear protection compared to thinner coatings. Therefore, it is established that CNT, similarly to graphite, requires moisture to reduce wear. As the tubes degrade as a consequence of severe stress, they start to break apart into individual graphite and graphene sheets. The tubes' degradation into graphite-like structures justifies the more severe wear observed in the SEM micrographs [64]. For this function, MWCNT are better suited than SWCNT since MWCNT require higher pressures to break their bonds and degrade the tubes into graphitic structures. Furthermore, the degradation of MWCNT—as opposed to SWCNT—would provide a more ample source of graphitic structures, thus improving lubricity to a certain extent. Consequently, the MWCNT employed in this study continue demonstrating wear protection at low humidity levels after 5 k fretting cycles, with worn area reductions of at least 50% compared to the reference sample.

3.3 Chemical Analysis

EDS was carried out to qualitatively determine the chemical composition of the fretting marks. The resulting EDS maps of the fretting marks conducted at 0.5 N and 5 k cycles for the copper reference and CNT4 are shown in Fig. 8. Although EDS maps for all conditions and samples were acquired, only these two fretting marks will be discussed in this section since similar behavior was observed throughout the remaining fretting marks. EDS maps of all samples analyzed at 0.5 N, 1 N, 2.5 N, and 5 N are shown in Online Resource 1, 2, 3, and 4, respectively. Online resource 5 shows the EDS maps of fretting marks after tests at 15% r.h. of all samples, whereas Online Resources 6 and 7 show the fretting marks after 150 k and 500 k, respectively.

A key takeaway from the EDS maps of the uncoated copper sample is that oxidation takes place during fretting, as evidenced by the spike in oxygen intensity at the center of the wear track. Furthermore, it is of interest to highlight the extent to which gold was transferred from the counter electrode towards the copper sample. As evidenced, almost the entirety of the fretting mark contains gold. In addition, the debris observed in the SEM micrographs (Fig. 5) is purely made up of gold, as proven by both the copper and gold intensity maps. This implies that material is supplied to the copper sample rather than material being purely removed by fretting. The transfer of gold is promoted by the harder counterpart—i.e., the oxide layer—since dissimilar hardness between the contacting surfaces fosters material transfer from the softer onto the harder surface [5, 6]. The removal of the softer material and its deposition onto the harder material is caused by the sliding motion, where asperity junctions are stronger than the weaker metal. Moreover, the continuous breakdown of the re-formed oxide film due to fretting wear further favors the adhesion of gold onto the copper surface [6]. As fretting cycles progress, gold continuously adheres to the copper sample and is subsequently removed from the wear track, resulting in gold debris surrounding the contacting site. Nonetheless, recalling the SEM micrographs from Fig. 5, the formation of debris was only observed at normal loads below 2.5 N and for prolonged fretting cycles, primarily 500 k cycles.

The EDS map of CNT4 shows some decisive differences compared to the copper sample. Copper is more homogeneously distributed in the coated sample. Here, regions where copper is not detected is caused by the thickness of the coating which hinders the emitted x-ray from the base material from reaching the detector. Accordingly, carbon intensities are maximum in sites where copper is not detected, and vice versa. Another key difference is the degree of oxidation incurred onto the copper substrate during fretting. Observing the oxygen map closely, no spikes in intensities can be identified. Therefore, the oxygen detected is found either in the copper's surface—in the form of Cu_2O—or as functional groups bound to the nanotubes. The last distinction is the amount of gold that is transferred. Although EDS is a qualitative technique, the signal-to-noise ratio of gold in CNT4 shows that the maxima in gold are not as strong as is the case in the uncoated sample. Furthermore, the gold that is transferred onto the copper sample is concentrated at the center of the fretting mark. Moreover, gold debris is not formed in the CNT-coated sample as a consequence of the lubricity of the nanoparticles, thus reducing gold's adhesion. These distinctions between uncoated and CNT-coated samples are consistent throughout all fretting marks regardless of test parameters or coating thickness.

The carbon map of CNT4 also shows the presence of carbonaceous phase remaining in the contact area even after 5 k cycles regardless of coating displacement, thus explaining the reduction in worn area of the coated samples. This is the case in all CNT-coated samples, except for prolonged fretting cycles where the coating is entirely displaced from the contacting site (see Online Resources 6 and 7). This fact explains the milder wear protection offered by the coatings after 150 k and 500 k fretting cycles. As a consequence of the coating displacement, the coated samples show similar

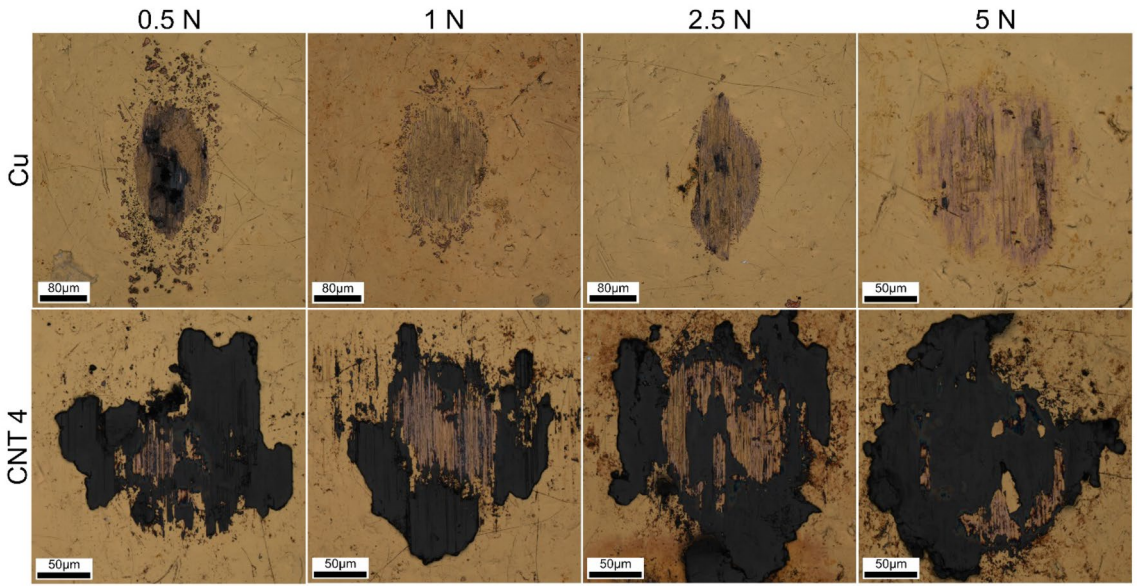

Fig. 9 CLSM light scan of counter electrode used against copper and CNT4 for the different loading conditions and 5 k fretting cycles. CLSM scans of all fretting marks are available in the Online Resources (including light, laser and height)

degrees of oxidation and gold transfer—as well as gold debris formation—as their uncoated counterparts.

3.4 Counter Electrode

CLSM scans of the counter electrode after fretting were carried out, with Fig. 9 showing the damage incurred under different loading conditions when contacting against uncoated copper and CNT4. For the light, laser, and height scan of all fretting marks refer to the Online Resources. CLSM scans of the counter electrodes used at 0.5 N, 1 N, 2.5 N, and 5 N are shown in Online Resources 8, 9, 10, and 11, respectively. The scans for counter electrodes used on fretting tests done at 15% r.h. are shown in Online Resource 12, with Online Resources 13 and 14 showing the counter electrodes after 150 k and 500 k fretting cycles, respectively.

As Fig. 9 shows, gold debris surrounds the fretting mark on the counter electrode that contacted the uncoated sample at 0.5 N as well as 1 N, concurring with the observations of the uncoated copper electrodes. Furthermore, the affected regions in the counter electrode dimensionally resemble the observations on the counter electrode, with higher loads showing smaller areas where gross slip took place. The CLSM scans also show that there is no material transfer from the uncoated electrode towards the counter electrode. The unidirectional transfer of material from the gold counter electrode towards the uncoated copper is due to the hardness difference between the contacting surfaces. In order for bidirectional material transfer to take place, the contacting surfaces should possess a hardness difference below 10% [5]. Since the hardness of the counter electrodes is 1.36 ± 0.01 GPa (measured via microhardness measurements on Struers Inc. Dura Scan with a load of 0.98 N), whereas—according to literature—copper oxide thin films have a hardness between 7.2 ± 0.2 GPa and 12.3 ± 0.5 GPa, depending on grain size [65]. Moreover, as the oxide layers are broken by the progression of fretting tests, the contact between the "clean" surfaces improves adhesion of the metallic surfaces due to the strengthening of the interfacial bonds between the contacting asperities [6].

The scans conducted on the coated samples are of considerable interest since these prove that carbon was transferred onto the counter electrodes. This is significant since the uncoated regions in the contacting site (shown in the micrographs in Figs. 5, 6, and 7) are not areas where the coating was removed, but rather there was a relocation of the coating from the copper substrate towards the gold rivet. This was seen in all the CNT coatings to varying degree; variations caused by inherent heterogeneity of the coatings. Nonetheless, carbon transfer was consistently observed on the counter electrodes regardless of coating thickness (see Online Resources 8–14).

Carbon transfer is not only load independent, but also humidity independent, with CNT being observed on the counter electrodes on all tests conducted at 15% r.h. (see Online Resource 12). Nonetheless, carbon transfer at lower humidity is not as prevalent as in tests carried out at ambient humidity. At low humidity only CNT5 shows prominent material transfer, with CNT3 and CNT4 showing marginal amounts of carbon transfer, where CNT3 shows slightly more material transfer than CNT4. This explains why the wear protection offered by CNT3 at 15% r.h. outperforms

CNT4 (see Fig. 7). Therefore, this confirms that wear protection is not strongly influenced by atmospheric humidity, but rather an aggregate of contact situation due to coating heterogeneity, amount of displaced coating, and amount of material transferred towards the counter electrode.

The counter electrodes used in the durability tests were also scanned via CLSM. In these cases, however, marginal traces of carbonaceous depositions can be observed; thus explaining why the wear protection offered by the coatings diminishes in these tests. For extended fretting tests, the prolonged shear stresses degrade the CNT and displace the carbon tribofilm from the contact site. The damaged CNT do not adhere to the counter electrode (see Online Resources 13 and 14), instead the graphitized particles are easily displaced from the contact site [10]. Consequently, wear protection is reduced with the bulk of transferred carbon being found at the ends of the fretting mark (as was observed in the fretting marks of the coated copper samples in Fig. 6).

4 Conclusions

In this work, three different CNT coatings were deposited over copper substrates. These coatings were tribo-electrically characterized to further understand the influence of coating thickness, the influence of normal load on fretting tests, and the wear reduction capabilities of CNT at low ambient humidity, taking into consideration the electrical behavior of the coated systems.

Thicker CNT coatings are not easily displaced by fretting at low normal loads, consequently, the ECR is higher than that of the uncoated copper. Nonetheless, for loads higher than 0.5 N this effect is negligible, albeit thicker coatings present higher ECR values than their thinner counterparts. From a tribological standpoint, thicker coatings promote smaller worn areas, with areal reductions between 80 and 90% in CNT5, for example. As expected, the wear protection offered by thinner coatings is reduced at higher normal loads. Therefore, the optimal coating thickness depends on the predominant objective, namely, electrical or tribological. Thinner coatings are preferred for applications where low ECR is crucial, with wear reduction being secondary. Whereas thicker coatings are required when improved tribological behavior is essential at the expense of conductivity.

For prolonged fretting cycles the CNT are displaced from the contacting site, with marginal carbon transfer towards the counter electrode. Consequently, the behavior of these coated samples resembles that of the uncoated. Therefore, in applications where prolonged fretting wear is expected these coatings do not contribute significant wear reduction. Nonetheless, if wear is not a key concern, low and stable ECR values were achieved for both 150 and 500 k fretting cycles, outperforming the uncoated reference samples.

At lower ambient humidity the wear protection of CNT is reduced, showing milder wear reduction compared to fretting tests carried out at ambient humidity. Furthermore, the electrical behavior also diminishes at lower humidity. The porous nature of the CNT coatings requires moderate contact pressures to enable compaction and readjustment of the coating. Contrarily, dry air located in the voids opposes a higher resistance than moist air, thus explaining the increased ECR at low humidity. Therefore, these coatings are not suitable for exclusive applications in low humidity. For applications where humidity fluctuates from ambient to below mean values (and vice versa), theses coatings show promising results as a versatile solid lubricant.

Supplementary Information The online version contains supplementary material available at https://doi.org/10.1007/s11249-023-01724-5.

Acknowledgements B. Alderete wishes to acknowledge the support from the German Academic Exchange Service (DAAD) and the Roberto Rocca Education Program (RREP). The TÜV Saarland Stiftung is gratefully acknowledged for financially supporting the project. The authors gratefully acknowledge funding in the ZuMat project, supported by the State of Saarland from the European Regional Development Fund (Europäischen Fonds für Regionale Entwicklung, EFRE). Funding for the PFIB/SEM instrument by German Research Foundation is greatly acknowledged (INST 256/510-1 FUGG).

Author Contributions Conceptualization: BA, SS; Methodology: BA, SS; Visualization: BA; Formal analysis and investigation: BA; Writing—original draft preparation: BA; Writing—review and editing: SS; Funding acquisition: FM, SS; Resources: FM; Supervision: FM, SS; Project Administration: FM, SS.

Funding Open Access funding enabled and organized by Projekt DEAL. The authors have not disclosed any funding.

Data availability Data available on request from the authors.

Declarations

Conflict of interest The authors have no relevant financial or non-financial interests to disclose.

References

1. Tsao, J.Y., Schubert, E.F., Fouquet, R., Lave, M.: The electrification of energy: long-term trends and opportunities. MRS Energy Sustain. (2018). https://doi.org/10.1557/mre.2018.6
2. Manzolli, J.A., Trovão, J.P., Antunes, C.H.: A review of electric bus vehicles research topics—Methods and trends. Renew Sustain Energy Rev (2022). https://doi.org/10.1016/j.rser.2022.112211
3. Zhou, E.M.T.: Electrification futures study: operational analysis of U.S. power systems with increased electrification and demand-side flexibility. Golden, Colorado (2021)
4. Varenberg, M., Etsion, I., Halperin, G.: Slip index: a new unified approach to fretting. Tribol Lett. **17**, 569–573 (2004). https://doi.org/10.1023/B:TRIL.0000044506.98760.f9
5. Slade, P.G.: Electrical contacts principles and applications. Taylor & Francis, Boca Raton (2014)
6. Hutchings, I.M., Shipway, P.: Tribology: Friction and wear of engineering materials. Butterworth-Heinemann (2017)
7. Varenberg, M., Etsion, I., Halperin, G.: Nanoscale fretting wear study by scanning probe microscopy. Tribol Lett. **18**, 493–498 (2005). https://doi.org/10.1007/s11249-005-3609-6
8. Antler, M., Drozdowicz, M.H.: Fretting corrosion of gold-plated connector contacts. Wear **74**, 27–50 (1981). https://doi.org/10.1016/0043-1648(81)90192-7
9. Trinh, K.E., Tsipenyuk, A., Varenberg, M., Rosenkranz, A., Souza, N., Mücklich, F.: Wear debris and electrical resistance in textured Sn-coated Cu contacts subjected to fretting. Wear **344–345**, 86–98 (2015). https://doi.org/10.1016/j.wear.2015.10.010
10. Alderete, B., Suarez, S., Tejeda, D.B., Mücklich, F.: Fretting and electrical contact resistance characteristics of carbon nanoparticle-coated Cu electrical contacts. In: 2022 IEEE 67th Holm Conference on Electrical Contacts (HLM). pp. 1–8. IEEE (2022)
11. Falcao, E.H.L., Wudl, F.: Carbon allotropes: beyond graphite and diamond. J. Chem. Technol. Biotechnol. **82**, 524–531 (2007). https://doi.org/10.1002/jctb.1693
12. Hirsch, A.: The era of carbon allotropes. Nat Mater. **9**, 868–871 (2010). https://doi.org/10.1038/nmat2885
13. Alderete, B., Mücklich, F., Suarez, S.: Characterization and electrical analysis of carbon-based solid lubricant coatings. Carbon Trends (2022). https://doi.org/10.1016/j.cartre.2022.100156
14. Reinert, L., Lasserre, F., Gachot, C., Grützmacher, P., MacLucas, T., Souza, N., Mücklich, F., Suarez, S.: Long-lasting solid lubrication by CNT-coated patterned surfaces. Sci Rep. **7**, 1–13 (2017). https://doi.org/10.1038/srep42873
15. Reinert, L., Green, I., Gimmler, S., Lechthaler, B., Mücklich, F., Suàrez, S.: Tribological behavior of self-lubricating carbon nanoparticle reinforced metal matrix composites. Wear **408–409**, 72–85 (2018). https://doi.org/10.1016/j.wear.2018.05.003
16. Reinert, L., Suarez, S., Rosenkranz, A.: Tribo-mechanisms of carbon nanotubes: friction and wear behavior of CNT-reinforced nickel matrix composites and CNT-coated bulk nickel. Lubricants. **4**, 11 (2016). https://doi.org/10.3390/lubricants4020011
17. MacLucas, T., Suarez, S.: On the solid lubricity of electrophoretically deposited carbon nanohorn coatings. Lubricants. **7**, 60 (2019). https://doi.org/10.3390/lubricants7080062
18. Zhmud, B., Pasalskiy, B.: Nanomaterials in lubricants: an industrial perspective on current research. Lubricants. **1**, 95–101 (2013). https://doi.org/10.3390/lubricants1040095
19. Saito, R., Dresselhaus, G., Dresselhaus, M.S.: Physical properties of carbon nanotubes. Imperial College Press, London (1998)
20. Dresselhaus, M.S., Dresselhaus, G., Saito, R.: Physics of carbon nanotubes. Carbon NY. **33**, 883–891 (1995). https://doi.org/10.1016/0008-6223(95)00017-8
21. Popov, V.N.: Carbon nanotubes: Properties and application. Mater. Sci. Eng. R. Rep. **43**, 61–102 (2004). https://doi.org/10.1016/j.mser.2003.10.001
22. Ebbesen, T.W.: Carbon nanotubes. Chem Eng News. **79**, 11 (2001)
23. Saifuddin, N., Raziah, A.Z., Junizah, A.R.: Carbon nanotubes: a review on structure and their interaction with proteins. J Chem. **2013**, 18 (2013). https://doi.org/10.1155/2013/676815
24. Nasir, S., Hussein, M.Z., Zainal, Z., Yusof, N.A.: Carbon-based nanomaterials/allotropes: a glimpse of their synthesis, properties and some applications. Materials. **11**, 1–24 (2018). https://doi.org/10.3390/ma11020295
25. Ando, T., Matsumura, H., Nakanishi, T.: Theory of ballistic transport in carbon nanotubes. Physica B. **323**, 44–50 (2002)
26. Svizhenko, A., Anantram, M.P., Govindan, T.R.: Ballistic transport and electrostatics in metallic carbon nanotubes. IEEE Trans Nanotechnol. **4**, 557–562 (2005). https://doi.org/10.1109/TNANO.2005.851409
27. Li, H.J., Lu, W.G., Li, J.J., Bai, X.D., Gu, C.Z.: Multichannel ballistic transport in multiwall carbon nanotubes. Phys Rev Lett. (2005). https://doi.org/10.1103/PhysRevLett.95.086601
28. van der Veen, M.H., Barbarin, Y., Kashiwagi, Y., Tokei, Z.: Electron mean-free path for CNT in vertical interconnects approaches Cu. In: 2014 IEEE International Interconnect Technology Conference/Advanced Metallization Conference, IITC/AMC 2014. pp. 181–184. IEEE Computer Society (2014)
29. Maiti, A., Svizhenko, A., Anantram, M.P.: Electronic transport through carbon nanotubes: effects of structural deformation and tube chirality. Phys Rev Lett. **88**, 4 (2002). https://doi.org/10.1103/PhysRevLett.88.126805
30. Yanagi, K., Udoguchi, H., Sagitani, S., Oshima, Y., Takenobu, T., Kataura, H., Ishida, T., Matsuda, K., Maniwa, Y.: Transport mechanisms in metallic and semiconducting single-wall carbon nanotube networks. ACS Nano **4**, 4027–4032 (2010). https://doi.org/10.1021/nn101177n
31. Krupke, R., Hennrich, F., Löhneysen, H.V., Kappes, M.M.: Separation of metallic from semiconducting single-walled carbon nanotubes. Science. **301**, 344–347 (2003). https://doi.org/10.1126/science.1086534
32. Li, H., Yin, W.Y., Banerjee, K., Mao, J.F.: Circuit modeling and performance analysis of multi-walled carbon nanotube interconnects. IEEE Trans Electron Devices. **55**, 1328–1337 (2008). https://doi.org/10.1109/TED.2008.922855
33. Robertson, J., Zhong, G., Hofmann, S., Bayer, B.C., Esconjauregui, C.S., Telg, H., Thomsen, C.: Use of carbon nanotubes for VLSI interconnects. Diam Relat Mater. **18**, 957–962 (2009). https://doi.org/10.1016/j.diamond.2009.02.008
34. Suarez, S.: Development of carbon nanotube-reinforced nickel matrix composites: processing, microstructure and physical properties (2014)
35. Berman, D., Erdemir, A., Sumant, A.V.: Graphene: a new emerging lubricant. Materials Today **17**, 31–42 (2014)
36. Scharf, T.W., Prasad, S. V.: Solid lubricants: a review (2013)
37. Chen, Z., He, X., Xiao, C., Kim, S.H.: Effect of humidity on friction and wear—a critical review (2018)
38. Morstein, C.E., Klemenz, A., Dienwiebel, M., Moseler, M.: Humidity-dependent lubrication of highly loaded contacts by graphite and a structural transition to turbostratic carbon. Nat Commun. (2022). https://doi.org/10.1038/s41467-022-33481-9
39. Lancaster, J.K.: A review of the influence of environmental humidity and water on friction, lubrication and wear. Tribol Int. **23**, 371–389 (1990). https://doi.org/10.1016/0301-679X(90)90053-R
40. de Wijn, A.S., Fasolino, A., Filippov, A.E., Urbakh, M.: Low friction and rotational dynamics of crystalline flakes in solid lubrication. EPL. (2011). https://doi.org/10.1209/0295-5075/95/66002

41. Langlade, C., Fayeulle, S., Olier, R.: New insights into adhesion and lubricating properties of graphite-based transfer films. Wear **172**, 85–92 (1994). https://doi.org/10.1016/0043-1648(94)90303-4
42. Ouyang, J.H., Li, Y.F., Zhang, Y.Z., Wang, Y.M., Wang, Y.J.: High-temperature solid lubricants and self-lubricating composites: a critical review (2022)
43. Lepage, J., Zaida, H.: Influence of the water vapour adsorption on the boundary conditions in tribology. Tribol Ser. **12**, 259–266 (1987). https://doi.org/10.1016/S0167-8922(08)71074-5
44. Kumar, R., Hussainova, I., Rahmani, R., Antonov, M.: Solid lubrication at high-temperatures—a review (2022)
45. Lijima, S.: Helical microtubules of graphitic carbon. Nature. **354**, 56–58 (1991)
46. Reinert, L., Schütz, S., Suárez, S., Mücklich, F.: Influence of surface roughness on the lubrication effect of carbon nanoparticle-coated steel surfaces. Tribol Lett. **66**, 1–11 (2018). https://doi.org/10.1007/s11249-018-1001-6
47. Greenberg, R., Halperin, G., Etsion, I., Tenne, R.: The effect of WS_2 nanoparticles on friction reduction in various lubrication regimes. Tribol Lett. **17**, 179–186 (2004). https://doi.org/10.1023/B:TRIL.0000032443.95697.1d
48. MacLucas, T., Klemenz, A., Grünewald, P., Presser, V., Mayrhofer, L., Moras, G., Suarez, S., Dienwiebel, M., Mücklich, F., Moseler, M.: Multiwall carbon nanotubes for solid lubrication of highly loaded contacts. ACS Appl Nano Mater. (2023). https://doi.org/10.1021/acsanm.2c04729
49. Alderete, B., MacLucas, T., Espin, D., Brühl, S.P., Mücklich, F., Suarez, S.: Near superhydrophobic carbon nanotube coatings obtained via electrophoretic deposition on low-alloy steels. Adv Eng Mater. (2021). https://doi.org/10.1002/adem.202001448
50. Alderete, B., Lößlein, S.M., Bucio Tejeda, D., Mücklich, F., Suarez, S.: Feasibility of carbon nanoparticle coatings as protective barriers for copper─wetting assessment. Langmuir (2022). https://doi.org/10.1021/acs.langmuir.2c02295
51. Alderete, B., Puyol, R., Slawik, S., Espin, E., Mücklich, F., Suarez, S.: Multipurpose setup used to characterize tribo-electrical properties of electrical contact materials. MethodsX. (2021). https://doi.org/10.1016/j.mex.2021.101498
52. Woo Park, Y., Sankara Narayanan, T.S.N., Yong Lee, K.: Effect of fretting amplitude and frequency on the fretting corrosion behaviour of tin plated contacts. Surf Coat Technol. **201**, 2181–2192 (2006). https://doi.org/10.1016/j.surfcoat.2006.03.031
53. Bock, E.M.: Low-level contact resistance characterization. AMP J Technol. **3**, 64–68 (1993)
54. Platzman, I., Brener, R., Haick, H., Tannenbaum, R.: Oxidation of polycrystalline copper thin films at ambient conditions. J. Phys. Chem. C **112**, 1101–1108 (2008). https://doi.org/10.1021/jp076981k
55. Tsai, J.T.H., Lu, C.C., Li, J.G.: Fabrication of humidity sensors by multi-walled carbon nanotubes. J Exp Nanosci. **5**, 302–309 (2010). https://doi.org/10.1080/17458080903513300
56. Lee, Y., Yoon, J., Kim, Y., Kim, D.M., Kim, D.H., Choi, S.J.: Humidity effects according to the type of carbon nanotubes. IEEE Access. **9**, 6810–6816 (2021). https://doi.org/10.1109/ACCESS.2020.3048173
57. Ling, Y., Gu, G., Liu, R., Lu, X., Kayastha, V., Jones, C.S., Shih, W.S., Janzen, D.C.: Investigation of the humidity-dependent conductance of single-walled carbon nanotube networks. J Appl Phys. (2013). https://doi.org/10.1063/1.4774075
58. Shamai, R., Andelman, D., Berge, B., Hayes, R.: Water, electricity, and between on electrowetting and its applications. Soft Matter **4**, 38–45 (2007). https://doi.org/10.1039/b714994h
59. Quinn, A., Sedev, R., Ralston, J.: Contact angle saturation in electrowetting. J. Phys. Chem. B **109**, 6268–6275 (2005). https://doi.org/10.1021/jp040478f
60. Frick, C., Steiner, H., Mazurkiewicz, A., Riediger, U., Rauthe, M., Reich, T., Gratzki, A.: Central European high-resolution gridded daily data sets (HYRAS): mean temperature and relative humidity. Meteorol. Z. **23**, 15–32 (2014). https://doi.org/10.1127/0941-2948/2014/0560
61. Sachindra, D.A., Nowosad, M.: Variations in relative humidity across Poland and its possible impacts on outdoor thermal comfort: an analysis based on hourly data from 1995 to 2020. Int. J. Climatol. **42**, 3861–3887 (2022). https://doi.org/10.1002/joc.7449
62. Vingsbo, O., Söderberg, S.: On fretting maps. Wear **126**, 131–147 (1988). https://doi.org/10.1016/0043-1648(88)90134-2
63. Varenberg, M., Halperin, G., Etsion, I.: Different aspects of the role of wear debris in fretting wear. Wear **252**, 902–910 (2002)
64. Reinert, L., Varenberg, M., Mücklich, F., Suárez, S.: Dry friction and wear of self-lubricating carbon-nanotube-containing surfaces. Wear **406–407**, 33–42 (2018). https://doi.org/10.1016/j.wear.2018.03.021
65. Jian, S.R., Chen, G.J., Hsu, W.M.: Mechanical properties of Cu2O thin films by nanoindentation. Materials. **6**, 4505–4513 (2013). https://doi.org/10.3390/ma6104505

Authors and Affiliations

Bruno Alderete[1] · Frank Mücklich[1] · Sebastian Suarez[1]

✉ Bruno Alderete
bruno.alderete@uni-saarland.de

[1] Chair of Functional Materials, Saarland University, Campus D3.3, 66123 Saarbrücken, Germany

Wear reduction via CNT coatings in electrical contacts subjected to fretting

Bruno Alderete*, Frank Mücklich, Sebastian Suarez
Chair Functional Materials, Saarland University, Campus D3.3, Saarbrücken 66123, Germany
* bruno.alderete@uni-saarland.de

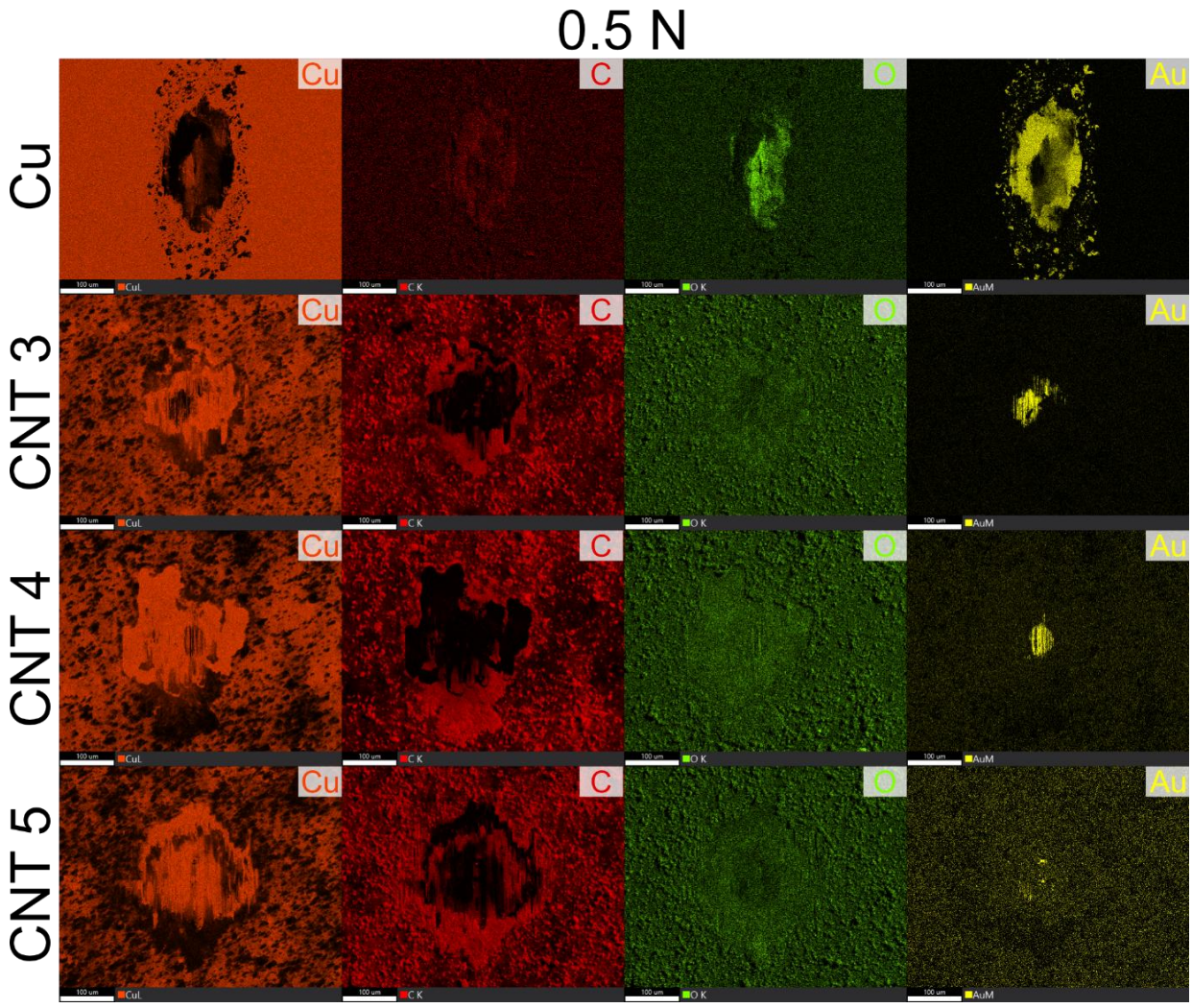

Online Resource 1: EDS maps showing copper, carbon, oxygen, and gold of all fretting marks carried out at 0.5 N after 5k cycles.

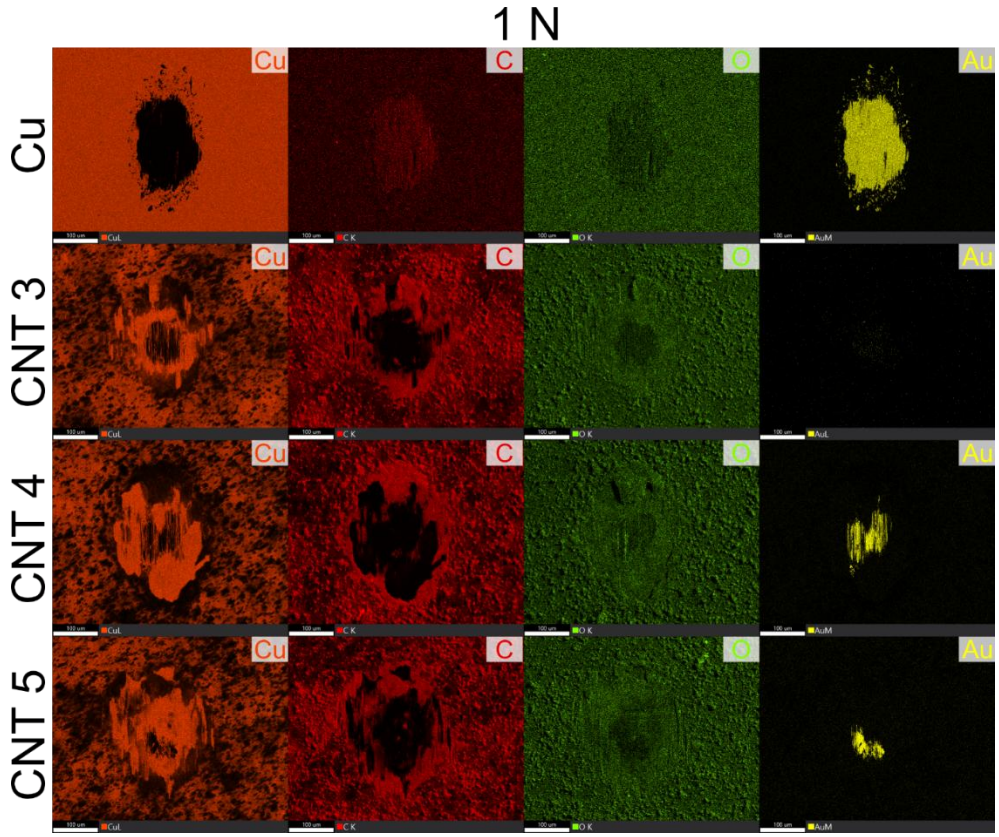

Online Resource 2: EDS maps showing copper, carbon, oxygen, and gold of all fretting marks carried out at 1 N after 5k cycles.

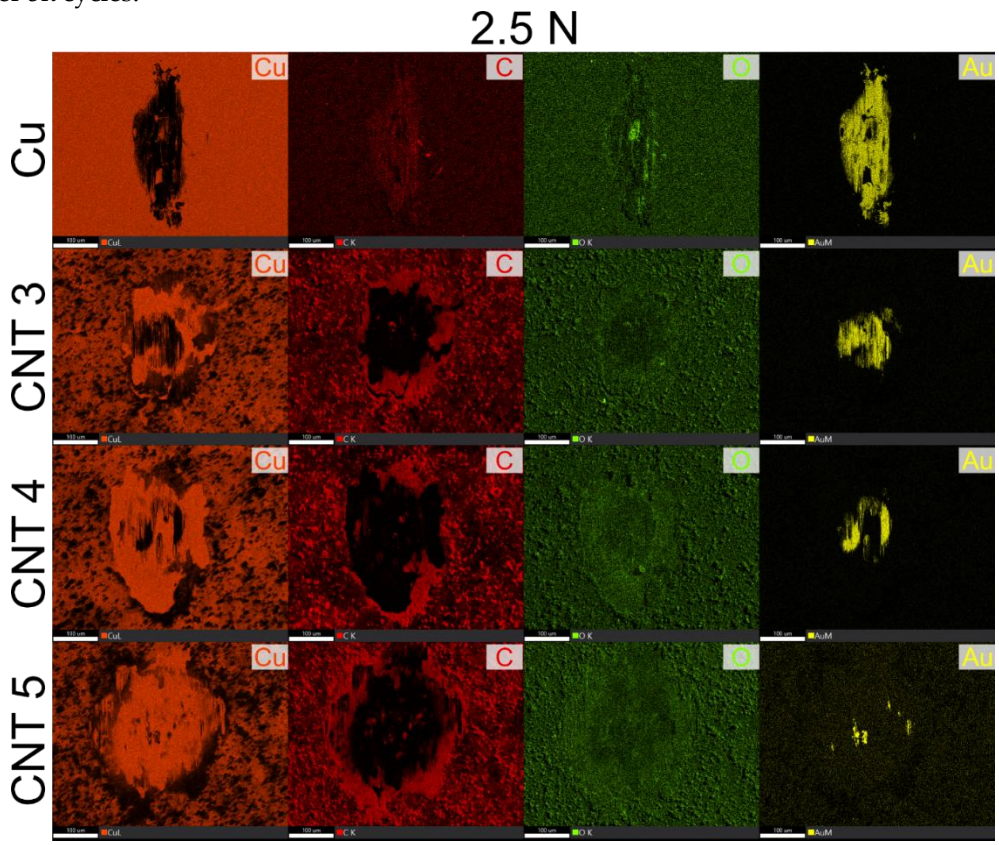

Online Resource 3: EDS maps showing copper, carbon, oxygen, and gold of all fretting marks carried out at 2.5 N after 5k cycles.

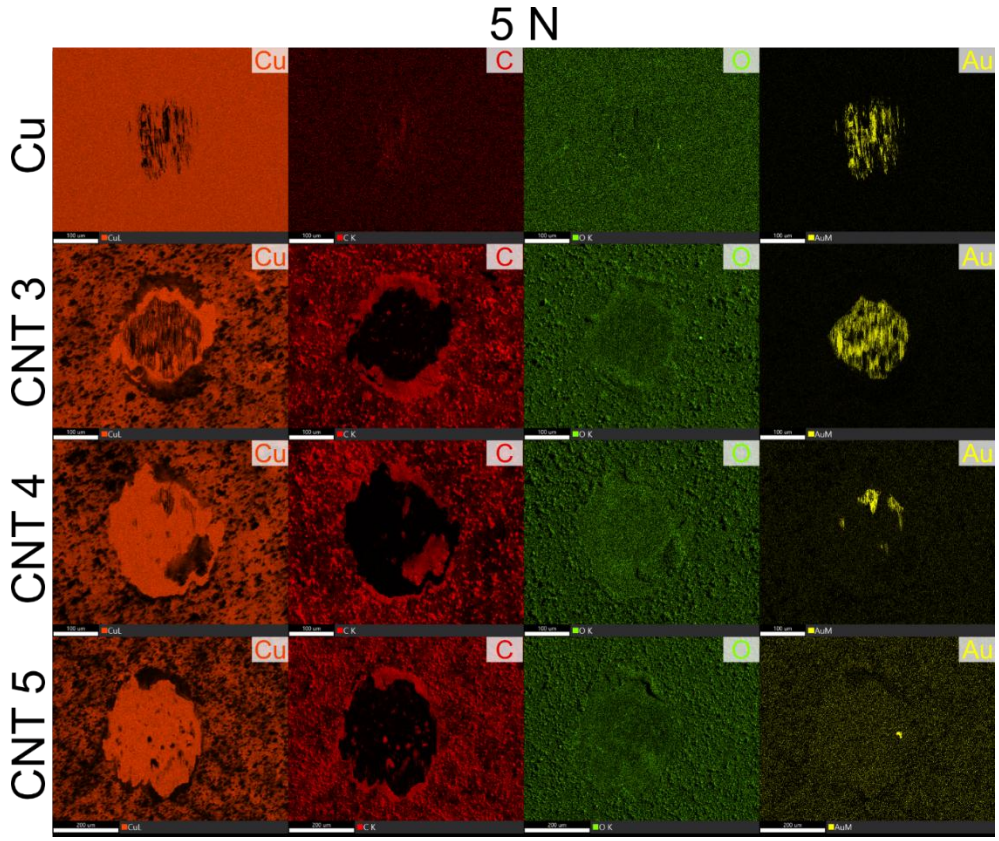

Online Resource 4: EDS maps showing copper, carbon, oxygen, and gold of all fretting marks carried out at 5 N after 5k cycles.

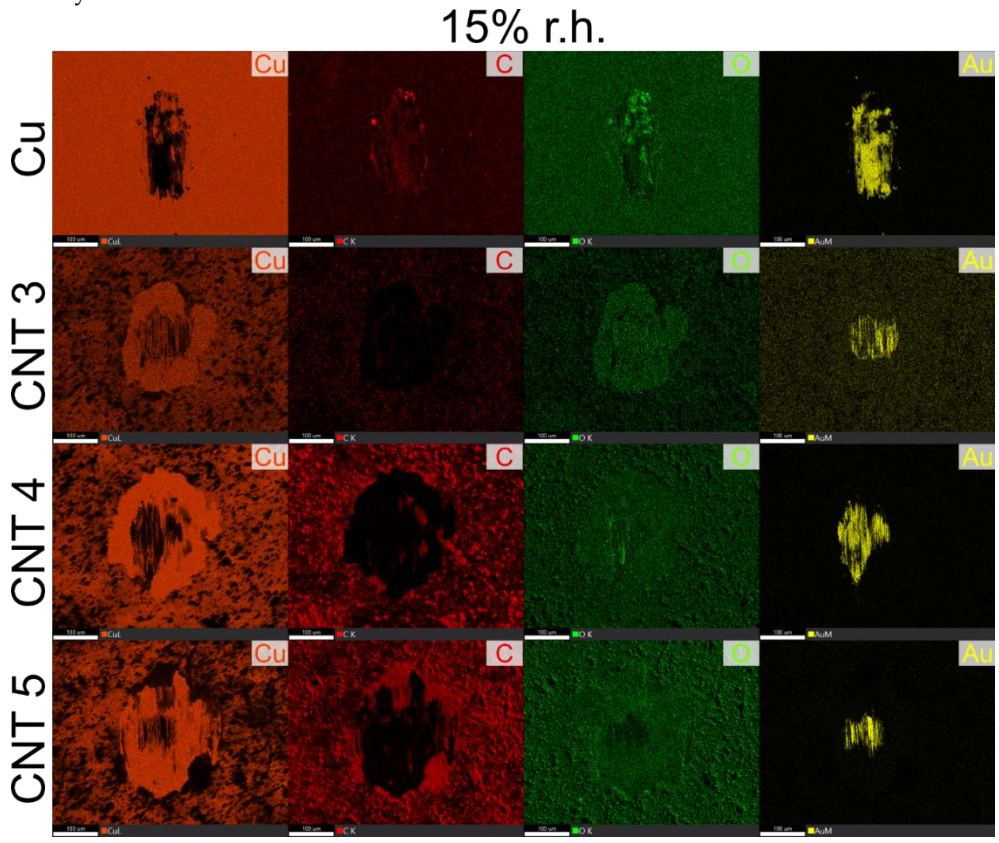

Online Resource 5: EDS maps showing copper, carbon, oxygen, and gold of all fretting marks carried out at 15% r.h. and 1 N after 5k cycles.

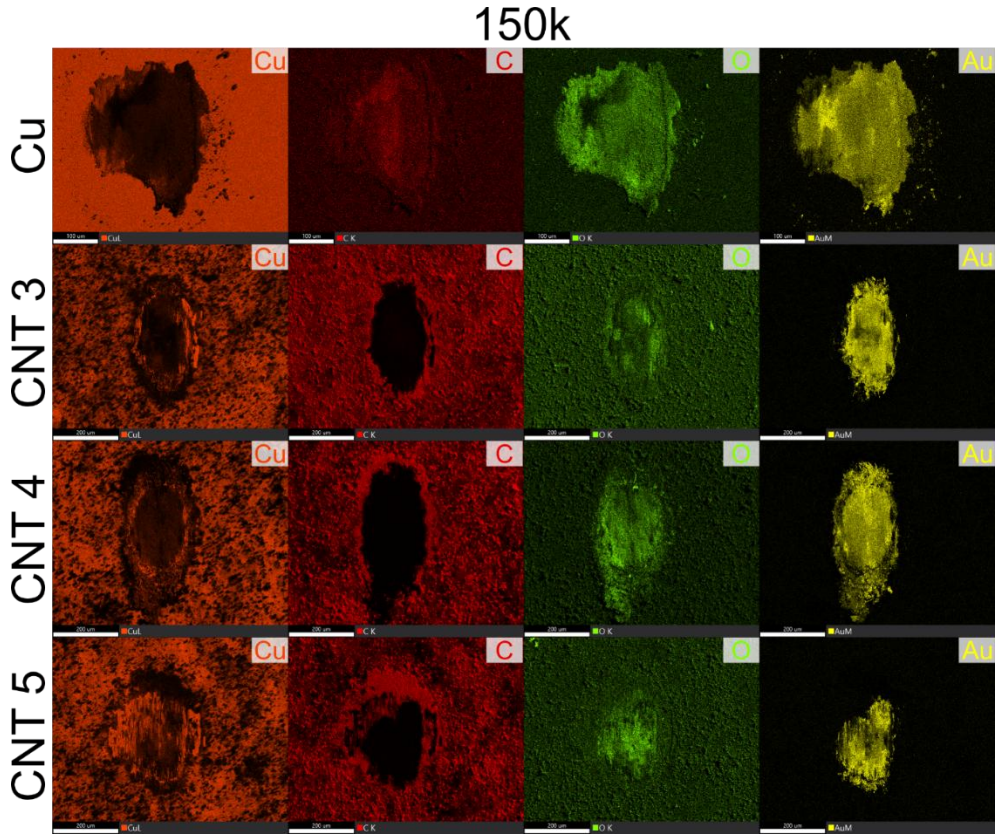

Online Resource 6: EDS maps showing copper, carbon, oxygen, and gold of all fretting marks carried out at 1 N after 150k cycles.

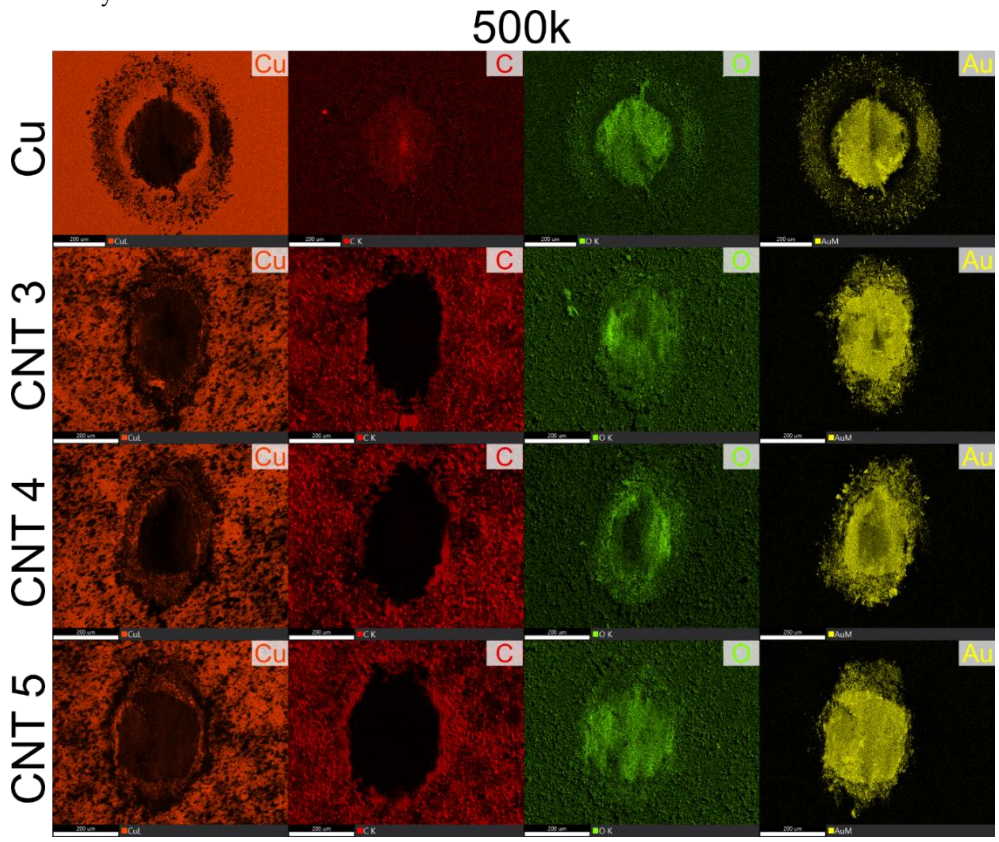

Online Resource 7: EDS maps showing copper, carbon, oxygen, and gold of all fretting marks carried out at 1 N after 500k cycles.

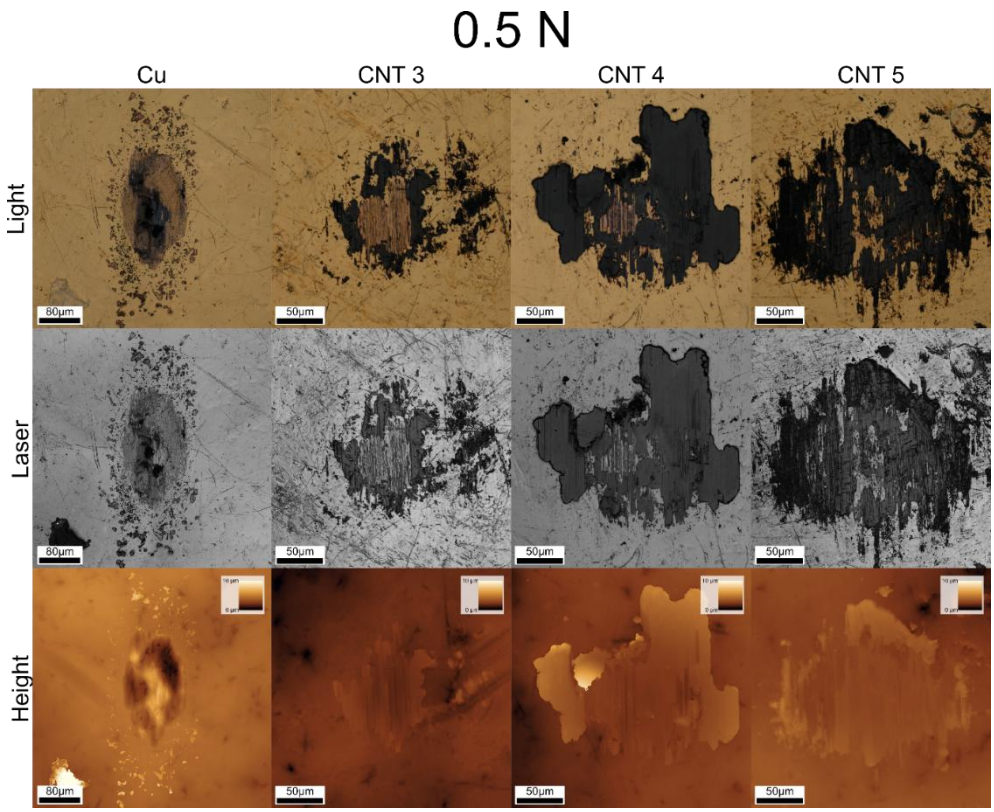

Online Resource 8: Light, laser, and height CLSM scan of counter electrodes used in 5k fretting cycles carried out at 0.5 N.

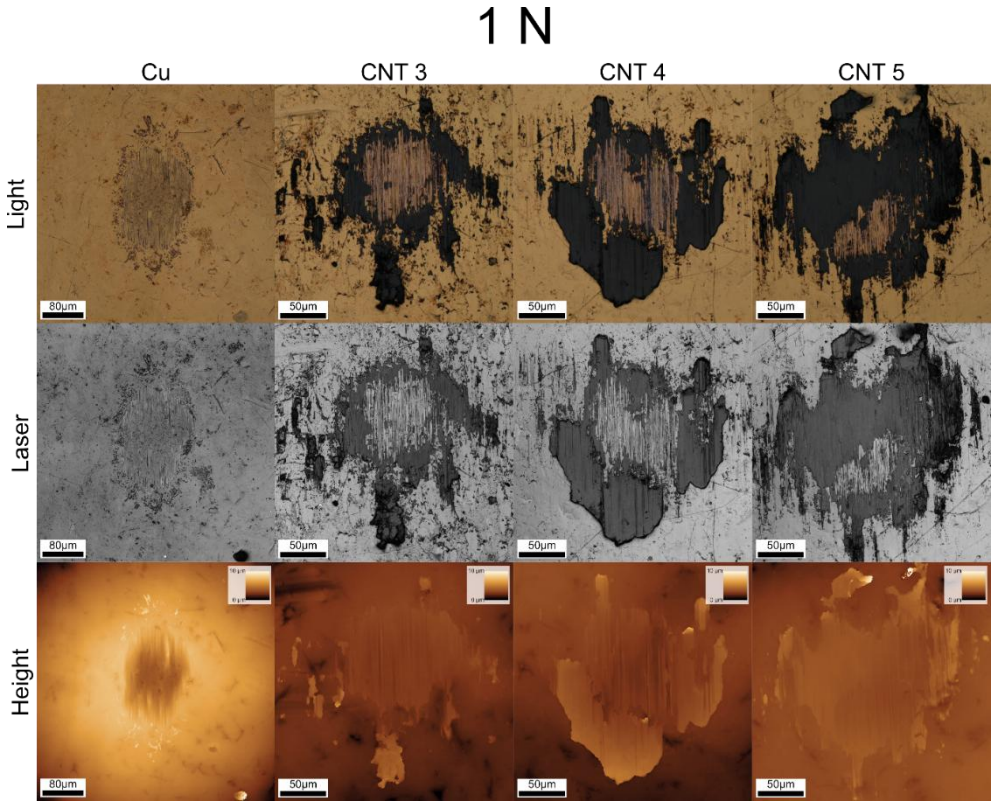

Online Resource 9: Light, laser, and height CLSM scan of counter electrodes used in 5k fretting cycles carried out at 1 N.

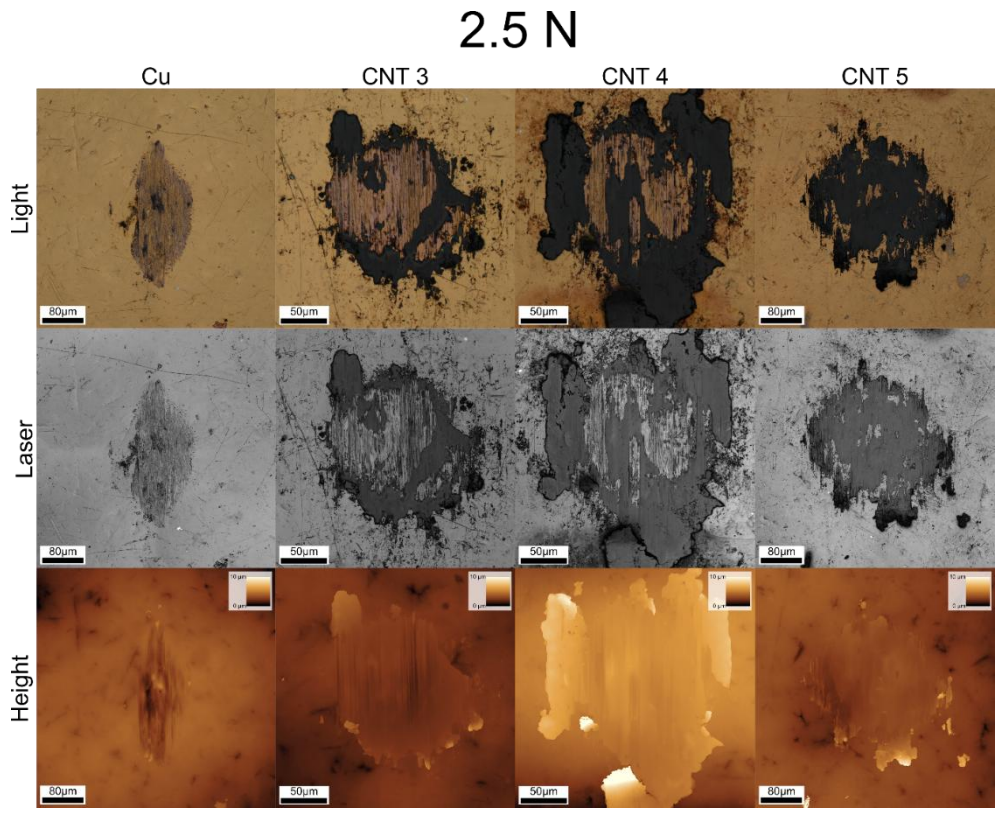

Online Resource 10: Light, laser, and height CLSM scan of counter electrodes used in 5k fretting cycles carried out at 2.5 N.

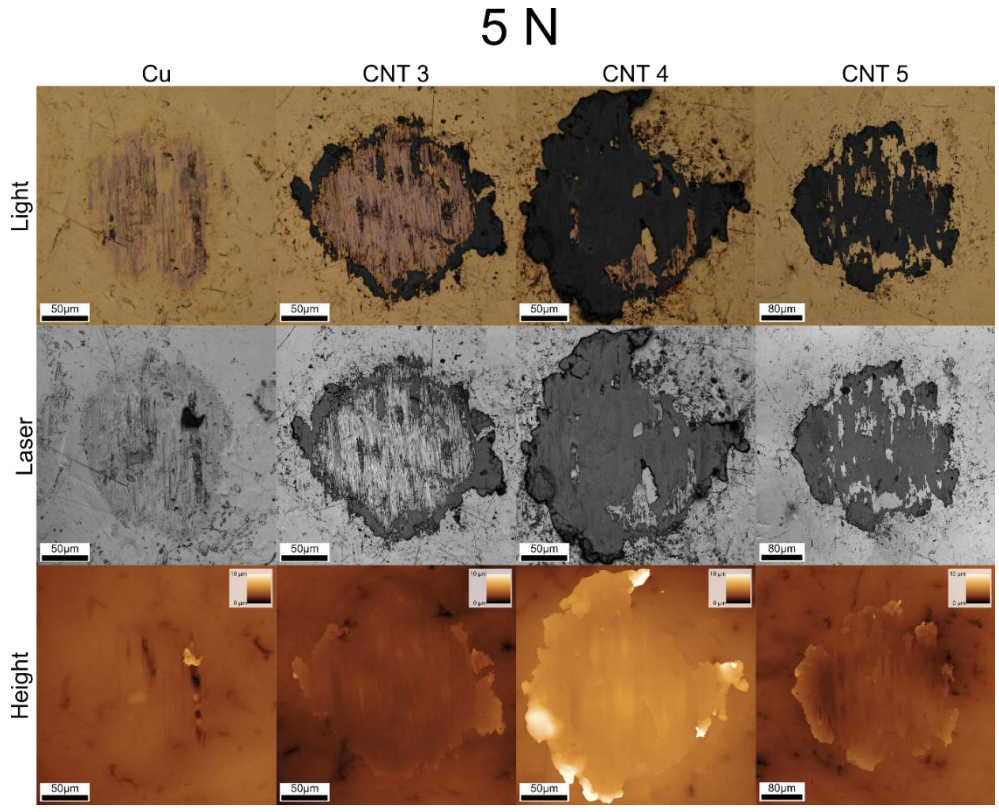

Online Resource 11: Light, laser, and height CLSM scan of counter electrodes used in 5k fretting cycles carried out at 5 N.

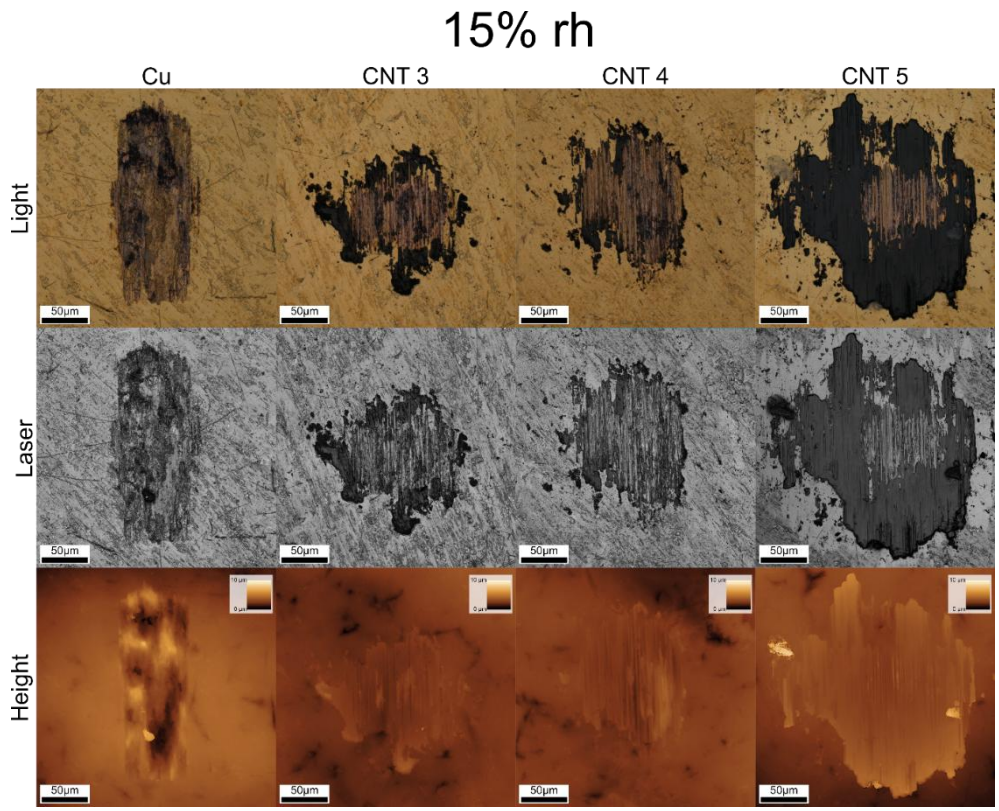

Online Resource 12: Light, laser, and height CLSM scan of counter electrodes used in 5k fretting cycles carried out at 15% r.h. and 1 N.

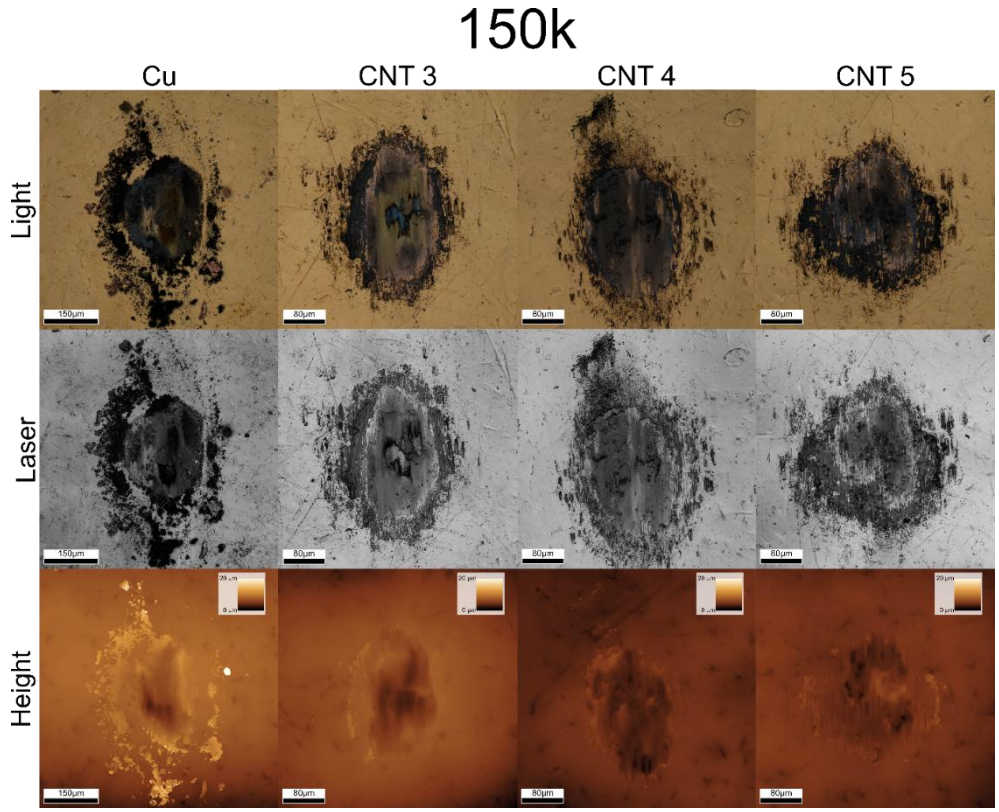

Online Resource 13: Light, laser, and height CLSM scan of counter electrodes used in 150k fretting cycles carried out at 1 N.

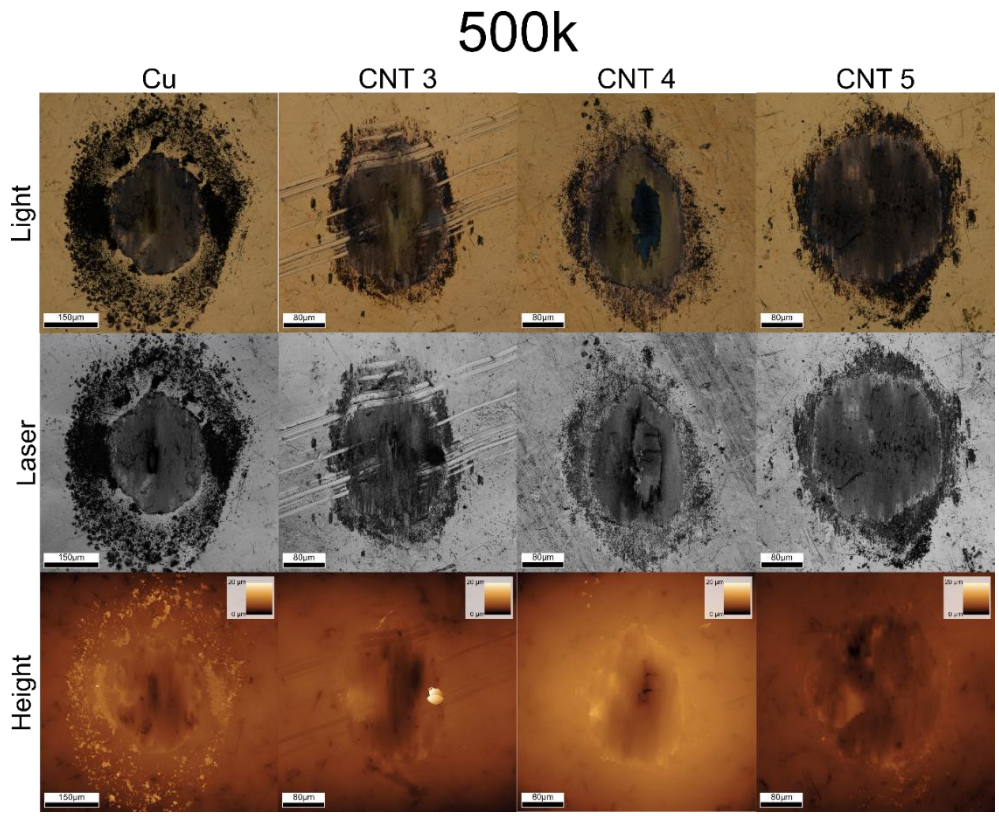

Online Resource 14: Light, laser, and height CLSM scan of counter electrodes used in 500k fretting cycles carried out at 1 N.

ARTICLE VIII
Feasibility of Carbon Nanoparticle Coatings as Protective Barriers for Copper – Wetting Assessment

Bruno Alderete[1,*], Sarah Marie Lößlein[1], Diana Bucio Tejeda[2], Frank Mücklich[1], Sebastian Suarez[1]

[1] Chair of Functional Materials, Saarland University, Campus D3.3, 66123 Saarbrücken, Germany
[2] International Laboratory of Environmental Electron Devices (LAIDEA), ENES Morelia Universidad Nacional Autónoma de México, Mexico

Research article
Published in "*Langmuir*" (2022)
Impact Factor: 3.7 (2023)
Reproduced with permission from 'American Chemical Society'
Accessible online at: doi.org/10.1021/acs.langmuir.2c02295

Own Contribution: Conceptualization; Methodology; Validation; Investigation; Data Curation; Writing – Original Draft; Visualization.

Cite this article as: B. Alderete, S.M. Lößlein, D. Bucio Tejeda, F. Mücklich, S. Suarez, Feasibility of Carbon Nanoparticle Coatings as Protective Barriers for Copper—Wetting Assessment, Langmuir 38 (2022) 15209–15219. https://doi.org/10.1021/acs.langmuir.2c02295.

Feasibility of carbon nanoparticle coatings as protective barriers for copper – wetting assessment

Bruno Alderete[*,†], *Sarah Marie Lößlein*[†], *Diana Bucio Tejeda*[‡], *Frank Mücklich*[†], *Sebastian Suarez*[†]

[†] Chair of Functional Materials, Saarland University, Campus D3.3, Saarbrücken 66123, Germany

[‡] International Laboratory of Environmental Electron Devices (LAIDEA), ENES Morelia UNAM, Antigua Carretera a Pátzcuaro 8701, Morelia 58190, Mexico

KEYWORDS: Electrophoretic deposition, hydrophobic nanocarbon coatings, sessile drop test, wetting behavior

ABSTRACT: Copper is extensively used in a wide range of industrial and daily-life applications, varying from heat exchangers to electrical wiring. Although it is protected from oxidation by its native oxide layer, when subjected to harsh environmental conditions – such as in coastal regions – this metal can rapidly degrade. Therefore, in this study we analyze the potential use of carbon nanoparticle coatings as protective barriers due to their intrinsic hydrophobic wetting behavior. The nanocarbon coatings were produced via electrophoretic deposition on Cu platelets and characterized via scanning electron microscopy, confocal laser scanning microscopy, and sessile drop test; the latter being the primary focus since it provides insight into the wetting behavior of the produced coatings. Among the measured coatings, graphite flakes, graphene oxide, and carbon nanotube coatings showed superhydrophobic behavior. Based on their wetting behavior, and specifically for electrical applications, carbon nanotube (CNT) coatings showed the most promising results since these coatings do not significantly impact the substrate's electrical conductivity. Although CNT agglomerates do not affect the wetting behavior of the attained coatings, the coating's thickness plays an important role. Therefore, to completely coat the substrate the CNT coating should be sufficiently thick – above approximately 1 µm.

INTRODUCTION

Copper and copper alloys are extensively used due to their outstanding transport properties. Accordingly, copper-based materials can be found in a plethora of industrial and daily-life applications, such as: heat exchangers, electrical and electronic devices, power generation and distribution, electrical contacts, etc. Although copper is protected from accelerated corrosion due to its native oxide layer (oxidic passivation), aggressive atmospheric conditions can significantly degrade the material, particularly when subjected to saline environments.[1–3] For electrical contacts specifically, the oxide layer is detrimental to the bulk material's conductive properties since Cu_2O is a well-known p-type semiconductor. Consequently, the system's overall resistance is augmented due to the increased film resistance.[4] This oxide layer forms spontaneously in normal atmospheric conditions, with Cu forming approximately 50% of the oxide layer after one hour of exposure.[5]

Due to the extensive use of copper-based materials, it is of utmost importance to effectively protect its surface from corrosive atmospheric conditions. Coatings (or platings in electrical applications) are a widespread method employed to protect and inhibit its surface from corrosion,[3,6–9] with many studies focused on the corrosion behavior of this metal.[10–13] Other approaches include atomic layer deposition, graphene-based coatings, and the production of superhydrophobic Cu surfaces, among others.[14–17] Research indicate an abondance of factors that influence the corrosion of copper and copper alloys, such as temperature (influencing the kinetics of the reaction), humidity, presence of organic matter (biofouling), and fundamentally the presence of chlorine ions (Cl^-), among others. Therefore, these materials must be capable of withstanding diverse atmospheric conditions that can accelerate their degradation. Carbon nanoparticles (CNP) can play a crucial role in minimizing – or potentially preventing – accelerated degradation since these nanocarbons can be used as protective barriers. Due to the hydrophobic nature of the CNP, coating the metallic substrates has the capability to prohibit the ingress of reactive agents and therefore insulating the metallic substrate from aggressive

atmospheric conditions. If we consider that tin is used exclusively as plating material to protect most copper electrical contacts, highly conductive CNP can potentially replace this plating process since previous studies have demonstrated that these coatings have a marginal influence on the system's conductivity while reducing physicochemical wear.[18]

In this work, we analyze the viability of electrophoretically deposited CNP coatings over Cu substrates aimed towards electrical applications. Although the focus of this work is on electrical contacts, the conclusions can be extrapolated to other applications. Electrophoretic deposition (EPD) was chosen due to its relative simplicity, easily controllable coating thicknesses, and modest equipment requirements.[18–27] The deposition process is explained in further detail in [18,27,28]. The parameters for the deposition process – as well as the selection of the CNP for this study – were chosen on the basis of their influence on the conductivity of the contacting material. It is crucial that the CNP coatings do not significantly impact the conductivity of the Cu substrate. Regarding the EPD parameters, the dominant parameter is the deposition time, which determines the coating thickness. Herewith, the coating should be sufficiently thick to effectively protect the surface from aggressive environments, but also have as marginal effect on conductivity as possible. Therefore, the deposition time should be selected accordingly. Graphite flakes (GF), graphene oxide (GO), carbon nanohorns (CNH), and carbon nanotubes (CNT) have been thoroughly characterized in a previous study,[18] highlighting their potential use as solid lubricant alternative in electrical contacts – primarily CNT and CNH. Moreover, these CNP are of particular interest in this study as a consequence of their hydrophobic behavior.[27,29–32] Apart from GO, all previous studies report hydrophobic behavior of these CNP. The presence of O may hinder GO's hydrophobicity. However, reports have shown that by manipulating the chemistry of GO, hydrophobicity can be achieved.[30,31] Furthermore, carbon black (CB) is included in this study because of its low cost, lubricating properties, and acceptable impact on the substrate's conductivity. Previous studies have sought to determine the efficacy of superhydrophobic surfaces to prevent or reduce the degradation of Cu. However, in these studies,

superhydrophobicity was achieved by depositing non-carbonous films.[14,33,34] Furthermore, diamond-like carbon has been previously implemented to produce hydrophobic surfaces.[35,36] Among the CNP chosen in this current work, CNT have received the most attention. However, previous studies of CNT for hydrophobic applications focused on low alloyed and stainless steel substrates.[27,28,37]

Within the scope of this work, we aim to examine the wetting behavior of the five CNP under different aqueous media – i.e., purified water and saline water solution. To determine the wetting behavior, sessile drop test was carried out to determine the contact angle (CA) between the CNP coatings and the aqueous media. This characterization method is fundamental to determine the efficacy of the coatings with respect to atmospheric protection. Additionally, the wetting behavior is not exclusively dependent on the surface's chemistry, but also the topography of the coatings plays a crucial role.[38,39] Therefore, scanning electron microscopy (SEM) images were acquired to observe the resulting coatings' topography. Furthermore, the thickness and roughness of the coatings was determined via confocal laser scanning microscopy (CLSM); therefore, establishing a relationship between these parameters and the coatings' wetting behavior.

EXPERIMENTAL SECTION

The substrates used were laminated, flat, oxygen-free, pure-copper (≥ 99.95% Cu) platelets with the following dimensions: (25 × 10 × 1) mm. These Cu platelets were ground using P1200 grit silicon carbide grinding paper, followed by a polishing sequence consisting of 6, 3, and 1 μm diamond suspensions; thus, obtaining a mirror-polished surface prior to EPD. The deposition procedure and parameters (except for deposition time) are the same as reported in[18,27]. A schematic representation of the EPD setup is shown in **Figure 1**, with the deposition parameters for each CNP shown in **Table 1**. The coating procedure is the same with all CNP, only the colloid concentrations and dispersion vary.[18] As previously reported,[27] proper selection of an additive for the EPD process is crucial. Correspondingly, triethylamine was used for this study; therefore, obtaining a hydrophobic surface that potentially will not significantly hinder the conductive

properties of the substrate. The main advantage of this additive is that it aids in coating deposition and in producing a hydrophobic surface. Furthermore, this additive completely evaporates after deposition – vapor pressure of triethylamine is 57.07 mmHg at 25 °C,[40] higher than that of the solvent (isopropyl alcohol vapor pressure: 45.4 mmHg at 25 °C).[41] This is important to consider since this additive does not alter the chemistry of the coating – as is the case with other additives such as magnesium nitrate hexahydrate[27,28] – and its influence on the wetting behavior of the produced coating can be neglected. After the desired coating duration has passed, the samples are removed from the colloid with the voltage source still on. This favors the structural integrity of coatings during removal from the colloid. By maintaining the voltage source, the electric field between the sample and counter electrode is still present during removal, which prevents the coating from damage as it is withdrawn from the colloid. Immediately after extraction, solvent and additive remaining in the coating begins to evaporate under atmospheric conditions. This process takes between 1 to 2 minutes. Once fully evaporated, the voltage source is switched off and the sample and counter electrode can be removed from the setup.

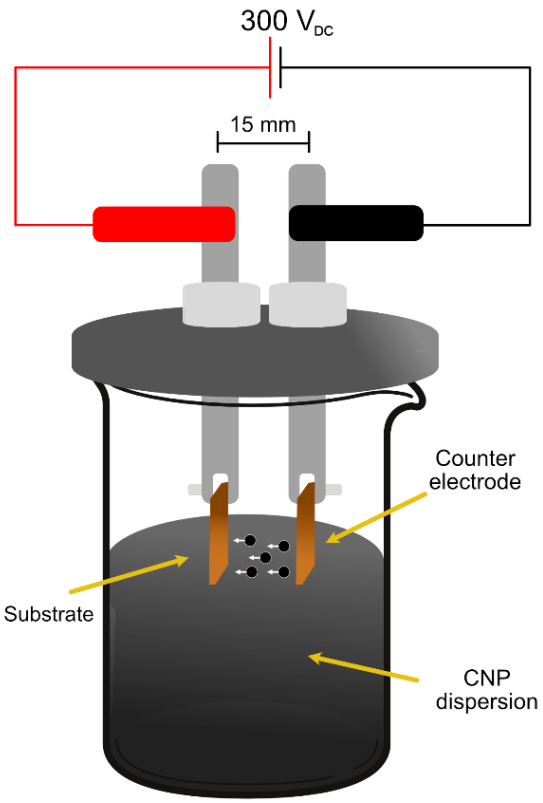

Figure 1: Schematic representation of EPD setup.

Table 1 – Concentrations and dispersion times for each CNP colloid.

CNP	**CNP Concentration / mg/ml**	**IPA /ml**	**TEA /ml**	**Homogenizer /min**	**Homogenizer speed /krpm**	**Ultrasound bath / min**
CB	0.4	80	10	10	7	10
GF	0.2					
GO	0.5			5	10	
CNH	0.05	70	5	10	12	15
CNT	0.2	80	10	5	7	10

As previously mentioned, five different CNP were deposited (CB, GF, GO, CNH, and CNT). The CB particles (Orion, Luxembourg) possess over 96% carbon, 0.2-1.3 wt.% hydrogen, 0.2-0.5 wt.% oxygen, 0-0.7 wt.% nitrogen, and 0.1-1 wt.% sulfur, with a mean particle size between 10 nm up to 500 nm, approximately. The GF (Alfa Aesar, Germany) have a mean size between 7-10 μm and 99.8% purity. Due to the size of the graphite flakes, these particles are not technically nanoparticles. However, these particles were chosen as benchmark, due to their hydrophobic behavior. For simplicity, GF will be included in the CNP nomenclature, but it is important to keep in mind that GF are not in the nanometer range. The GO particles possess 51.25 wt.% carbon, 43.99 wt.% oxygen (Nanoinnova Technologies, Spain). The particle size distribution ranges from 100 nm up to 800 nm, with GO flake agglomerates between 1-3 μm. According to the manufacturer, the average thickness of the GO flakes ranges from 0.7 to 1.2 nm. The single-walled CNH used were dahlia-type, produced by rapid condensation of carbon atoms without a catalyst (Carbonium SRL, Italy). The as-received high-purity CNH have a horn diameter between 3 and 5 nm, horn length between 30 and 50 nm, and a cluster diameter between 60 and 120 nm. The CNT used were chemical vapor deposition (CVD)-grown multiwalled CNT (Graphene Supermarket, USA). The outer diameter of the CNT have a distribution between 50-85 nm, an as-received state length from 10-15 μm, and a carbon purity above 94%.

The roughness of the substrates prior to coating was determined via CLSM (LEXT OLS4100, Olympus) working with a laser wavelength of 405 nm. To achieve larger field of view with higher

resolution, a 2×2 stitching at 50× with an overlap of 20% was carried out. The polished substrates present a root mean square (rms) roughness between 10-20 nm. Likewise, a 3×3 stitching was carried out to determine the coating thickness – done by acquiring the height profile at the interface between a coated and an uncoated region. The SEM micrographs were acquired using a FEI Helios NanoLab600 Dual Beam Setup using an acceleration voltage of 5 kV and a current of 1.4 nA.

The CA was measured via sessile drop test using a drop shape analyzer (Krüss – DSA100B, Germany). As previously mentioned, two different aqueous media were used: purified water (HPLC grade) and saline water solution (according to ASTM D1141-98). In CA measurements with purified water a 3 µl droplet was deposited with a microliter syringe (Hamilton Company, USA), whereas the saline solution was applied via a pipette – also 3 µl. The volume of 3 µl suppresses gravitational distortion of the drop's shape and at the same time covers a sufficiently large sample area to even out topographical or chemical inhomogeneities.[42,43] Furthermore, the CA was recorded by fitting the contour of the droplet using an elliptical shape within the ADVANCE^{TM} Software (Krüss, Germany). Three droplets were placed on each sample. The CA measurements were taken 5 seconds after depositing the droplets. All measurements were carried out with an ambient temperature and humidity in the range of 20-25 °C and 20-35% r.h., respectively.

RESULTS AND DISCUSSIONS

Coating Thickness and Topography. The coatings obtained via EPD differ depending on the CNP that has been dispersed. EPD-related parameters were kept constant in all deposition processes, i.e., potentiostatic deposition at 300 V and interelectrode distance between 13 and 15 mm. The only parameter that varied was the duration of the deposition process. Each CNP is deposited at different rates. This deposition rate is directly linked to particle size and the particle's conductivity. Larger sized particles tend to have lower deposition rates since the gravitational and drag forces that the particle must overcome during electrophoresis are more significant for

dimensionally bigger particles. To counteract these resistive forces, electrophoresis could be augmented by increasing the voltage and/or decreasing the distance that the particles must travel (decreasing interelectrode distance). However, in this study these two parameters were kept constant. By only varying the duration of the deposition process, repeatable and reliable coating thicknesses can be obtained. A summary of the chosen coatings can be found in **Table 2**. This table highlights the deposition time and coating thickness of each coating produced. Since the intended application of these coatings is aimed at electrical contacts, these coatings were chosen based on their influence on the electrical contact resistance (ECR) of the substrate. Nonetheless, as previously mentioned, the conclusions drawn from this analysis on wetting behavior can be extrapolated to non-electrical related applications. Considering that CB, GF, and GO have a higher impact on Cu's ECR,[18] only one coating of each CNP was analyzed to qualitatively assess their potential atmospheric protection. CNH and CNT, on the other hand, do not significantly increase the ECR of the substrate.[18] Therefore, it is of interest to analyze the influence of the coating's thickness on the wetting behavior of these two CNP. Consequently, four different coating thicknesses were analyzed.

Although all CNP (except for GO) tend to be intrinsically hydrophobic, topography plays a

Table 2 - Deposition times and coating thicknesses measured via CLSM.

CNP	Deposition time /min	Mean thickness /µm
CB	2	2.92 ± 0.06
GF	8	35.56 ± 0.45
GO	10	55.91 ± 0.61
CNH	5	1.99 ± 0.05
	8	3.35 ± 0.13
	10	3.51 ± 0.08
	15	5.29 ± 0.21
CNT	1	0.60 ± 0.01
	2	1.11 ± 0.07
	4	1.70 ± 0.03
	5	1.72 ± 0.03

Table 3 - Roughness of CNP coatings measured via CLSM.

CNP	S_{rms} /nm
CB-2	900.8 ± 56.9
GF-8	1,750.2 ± 49.5
GO-10	1,755.4 ± 62.1
CNH-5	205.4 ± 39.5
CNH-8	280.8 ± 22.2
CNH-10	340.0 ± 31.0
CNH-15	359.8 ± 38.1
CNT-1	1,004.2 ± 44.6
CNT-2	833.2 ± 52.5
CNT-4	961.0 ± 51.9
CNT-5	1,257.2 ± 31.6

crucial role in wetting behavior.[38,39] The influence of topography can be expressed through Cassie-Baxter and Wenzel wetting states. In the former, air is trapped in the valleys formed by the surface's topography, whereas in the latter the liquid fills the voids originating from topographic features. According to these models, the CA changes depending on which wetting state our system resembles. When analyzing the same sample under the different wetting states, higher CA values are expected in Cassie-Baxter rather than in Wenzel wetting state – due to increased wettability as a consequence of the infiltration of the droplet into the voids.[44] The higher CA is because in the Cassie-Baxter wetting state a composite state is formed between the solid (CNP coating) and the gas (air bubbles trapped in the topographic voids). Therefore, the roughness of the produced coating is of great significance and is accordingly shown in **Table 3**. The elevated roughness obtained for the GF and GO coatings stem from the topographic heterogeneity. The topography of these coatings is characterized by large voids (see reference [18]), producing the coatings with the roughest surface. In the GF coating, these voids are a consequence of the large particle size and due to aleatory stacking of the large flakes on the substrate. This not only produces voids on the coating's surface, but also within the coating itself.

This could potentially jeopardize the coating's wetting behavior, with the fluid infiltrating into the coating and thus achieving low CA. In the GO coating, however, the voids are primarily caused by GO agglomerates, and to a lesser extent due to large individual GO particles – since characterization on the as-received GO particles showed the presence of larger GO flakes among the agglomerated GO bundles.[18] These voids are also a cause of concern, similarly to the GF coating. However, these two coatings are thick. The elevated thickness of these coatings could produce complex pathways which the fluid may not be capable of navigating. Therefore, although initially the CA could decrease due to fluid infiltration, it is expected that after time the CA will stabilize at a specific value once the fluid can no longer penetrate the coatings. CB, on the other hand, shows a more homogeneous coating topography when compared to GF and GO – approximately half the roughness value. However, it is not as homogeneous as the CNH coatings. CNH shows a highly homogeneous coating, with low rms roughness values ranging from 200 to 400 nm. The actual roughness value of CNH coatings depends on the thickness of the coatings, with thicker coatings showing rougher surfaces and vice versa. The roughness of the CNH coatings is influenced by fissures that are pervasively found throughout the surface of this coating type. These fissures could be caused by changes in the dimensions of the CNH coating during drying and/or the elevated voltage used during EPD, as reported by MacLucas et al.[45] These fissures are observable under light microscopy. On the other hand, the CB coating also shows small fissures, however, these fissures are not as pervasive as in the CNH coating. Furthermore, the fissures are not observable with light microscopy in the CB coating. The presence of the fissures was identified solely using SEM. As is the case with the voids in the GF and GO coatings, the fissures could hinder the atmospheric protection that the CNH and CB coatings provide, thus exposing the substrate.

The roughness values of the CNT coatings shown in **Table 3** highlight that the topography of these coatings depend, to a slight degree, on the thickness of the coating. CNT coatings show higher roughness values as the coating thickness increases. The CNT coatings present mild

homogeneity (as reported in [18]) due to large CNT agglomerates that are unevenly deposited throughout the coated substrate. In general, the topography of the CNT coating tends to increase as the thickness of the coating increases – as was the case with the CNH coatings. However, CNT-1 showed higher rms roughness than CNT-2 and CNT4. Nonetheless, this increased roughness is not inherent to the coating itself, but rather to the heterogeneity of the coating. As a consequence of the short deposition time, the substrate is not completely coated. Therefore, when measuring roughness, the method considers a mixed system comprised of coated and uncoated regions, thus achieving a higher rms roughness. It is important to highlight that this was the case exclusively for CNT-1. The coatings with higher duration completely coated the substrate.

SEM micrographs of each CNP coatings were acquired and are shown in **Figure 2**. The homogeneity of the CB coating can be seen in the micrograph (**Figure 2a**). However, as the magnified micrograph shows, there are defects in the coating. It is unclear what the defects are, however, it is believed that these defects could be caused by CB particles being deposited at an accelerated rate in specific sites where the electric field peaks during EPD due to increased conductivity. Another possible explanation could be that a void was generated due to aleatory stacking of the CB particles. The defect itself is not a cause for concern, but rather the fissure observed around the defect. As is the case with the CNH coatings, fissures could compromise the atmospheric protection that this coating type could offer. From **Figure 2b** and **Figure 2c**, the heterogeneity of the GF and GO coatings can be observed, respectively. The homogeneity of the CNH-8 coating is observed in **Figure 2d**. However, a large network of fissures is observed throughout the coating's surface. Albeit focused ion beam cross sections of this coating did not show the fissures extending inward (see reference [18]). Nonetheless, the fissures might jeopardize the wetting behavior of the CNH coatings. The magnified micrograph shows a defect and a large fissure in higher detail. Observing the micrograph in **Figure 2e**, the CNT-5 coating appears highly heterogeneous due to the medium and large sized CNT agglomerates. However, this micrograph shows that – in regions where there are no CNT agglomerates – the CNT coating is

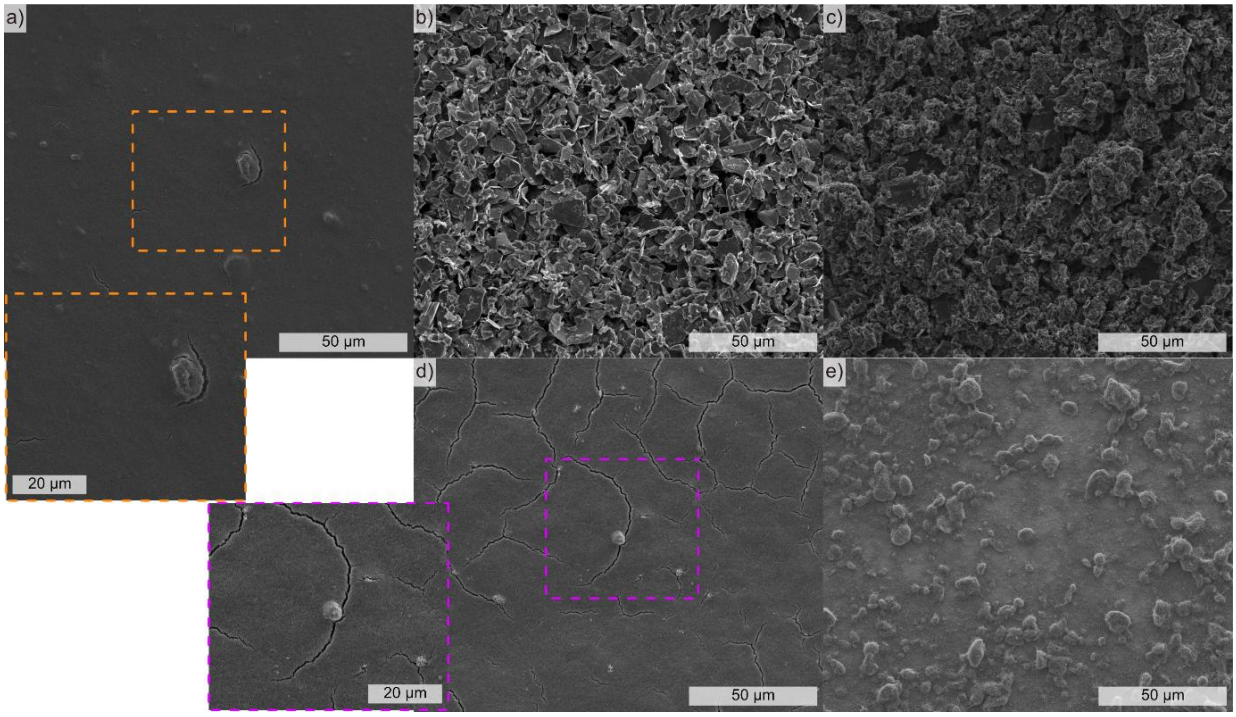

Figure 2: SEM micrograph of a) CB-2, b) GF-8, c) GO-10, d) CNH-8, and e) CNT-5 coatings. Higher magnification micrographs highlight defects and fissures in the CB and CNH coatings.

highly homogeneous. Therefore, this coating is classified as mildly homogeneous. This micrograph also proves that the substrate is fully coated by CNT, which is crucial to prevent atmospheric conditions from affecting the substrate.

Of the five CNP, CNT coating's topography is of interest since it is a consequence of the agglomerates. This means that the topography could be potentially reduced by increasing the CNT dispersion method, and thus further breaking down the CNT agglomerates prior to deposition. However, this does not necessarily mean that the coating will be better, since prolonged dispersion steps tend to damage the structural integrity of the CNT. The highly localized thermomechanical load applied by the ultrasound bath on the CNT tends to shorten the tubes, which favors their dispersion. However, this damage and change in the tube's aspect ratio diminishes the CNT's intrinsic desirable properties.[46,47] Therefore, although prolonged homogenization and sonication steps could produce a more homogeneous coatings, the damage incurred on the CNT could prove counterproductive.

Consequently, it is of interest to analyze the area fraction of CNT agglomerates that were deposited on the Cu substrate. The area fraction will depend on several conditions: e.g., colloid parameters (CNT concentration, additive used, etc.), CNT dispersion parameters (duration of homogenization and sonication), and EPD parameters. However, here we aim to obtain a qualitative analysis of the agglomerate area fraction. Therefore, the Trainable WEKA Segmentation plugin tool was used in ImageJ (Fiji).[48] Prior to WEKA segmentation, an SEM micrograph of the CNT coating must be opened with ImageJ and the image must be adjusted (contrast/brightness, noise removal, etc.). With the WEKA segmentation tool open, the tool must be 'trained' by marking and identifying the different constituents in the image: i.e., the agglomerates and the coating. This step can be repeated multiple times to improve the segmentation algorithm. Once the segmentation tool has been satisfactorily trained, the results can be extracted, and post processing filters can be applied to improve the fit of the segmentation tool. With the resulting segmented image, quantitative image analysis can be carried out to determine the area fraction of the CNT agglomerates. This process was done for three different SEM micrographs of the 5-minute CNT coating since here the agglomerates play a larger role on the roughness. The segmentation process resulted in an agglomerate area fraction of 43.4 ± 2.5 %. An overlay of the SEM micrograph and its resulting segmentation is shown in **Figure 3**. This figure shows the CNT agglomerates in red, whereas the green areas represent regions in the coating that are not constituted by agglomerates. Although the image shows areas where the segmentation tool is not accurate, it must be reiterated that this tool was used for a qualitative analysis. The 43.4% area fraction is the mean value obtained from three segmentation processes. However, this value should be considered merely as an estimate.

Purified Water. The CA of the coatings – as well as that of a polished Cu reference sample – using purified water are shown in **Figure 4**. The CA value of the Cu reference is 100° (hydrophobic surface), which correlates with theoretical values. These measurements were taken after a prolonged period of time after polishing since the CA of Cu varies significantly with

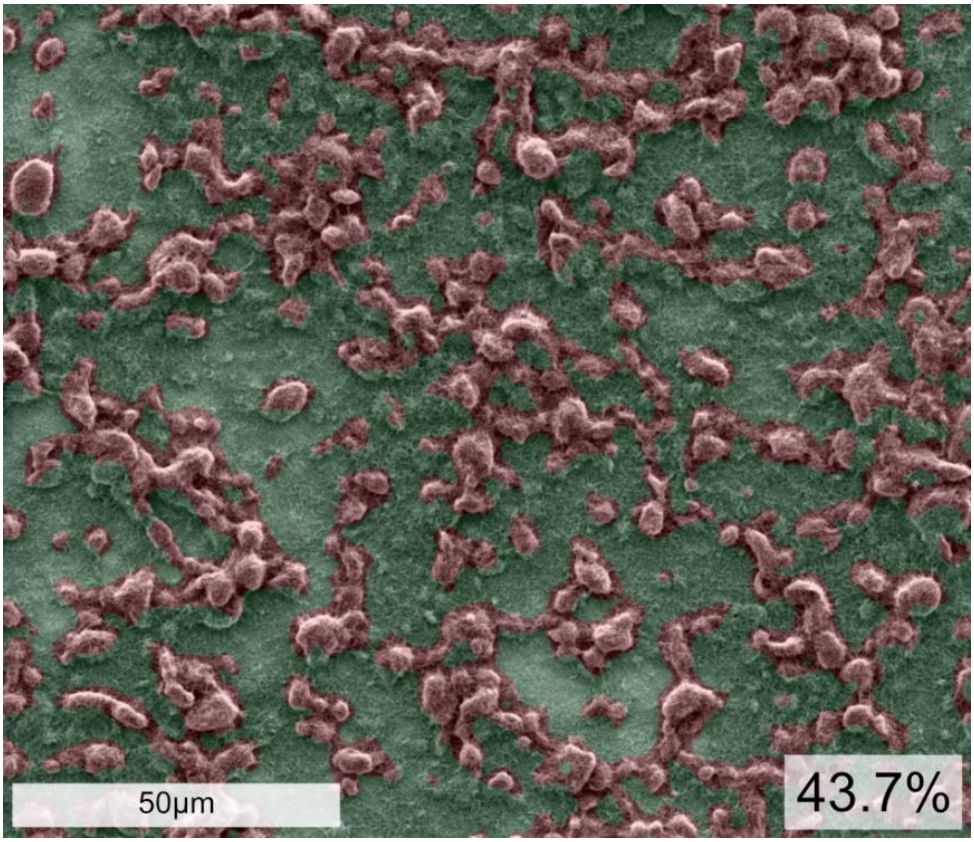

Figure 3: Overlay of SEM micrograph and segmented image obtained via Trainable WEKA Segmentation plugin in ImageJ. Red regions highlight the CNT agglomerates, whereas green highlights regions where the coating is not constituted by CNT agglomerates. This micrograph shows an approximate area fraction of CNT agglomerates of 43.7%.

time.[49] This phenomenon is a consequence of Cu surfaces' adsorption of hydrocarbons present in the atmosphere. Therefore, the analyzed and coated samples were left to 'age' for a prolonged period of time, thus achieving a stable CA value. This CA value is of interest since it represents a more realistic scenario, as well as allowing the analysis of the influence that the CNP coating have on the more hydrophobic Cu surface.

CB's wetting behavior is strongly related to the combustion process with which the nanoparticle is produced. A study carried out by Persiantseva et al.[50] showed that the CA of CB – produced using a gas turbine engine and a propane-butane fuel source – is between 60° and 80°, corresponding to hydrophilic particles. Here, however, higher CA values were measured, with these nanoparticles showing hydrophobic wetting behavior. This suggests that the CB particles used in our study were likely produced using diesel, kerosene, or wood as fuel source.[51]

This is an important fact to consider since the most common CB manufacturing process is in a combustion furnace using hydrocarbon fuel – a thermal-oxidative process [52] – which favors a more hydrophilic nanoparticle, as is the case in Persiantseva et al.[50] The variation in the wetting behavior of CB produced via these fuels was reported by Wei et al.,[51] with values from 65° up to values surpassing 100°. In our case, this coating achieved a marginally hydrophobic surface with average CA value of 93°. However, it is believed that a more hydrophobic surface can be achieved by producing a surface with fewer fissures and defects. Although these fissures are not as extensive as in the CNH coatings, they could potentially compromise the hydrophobicity of the CB coating.

As **Figure 4** depicts, CNH coatings form a CA corresponding to a hydrophobic surface (CA above 90° but below 150°). In these coatings, it is interesting to not that the thickness does not influence the wetting behavior. **Figure 4** (left) shows that the CA of CNH coatings ranges from approximately 110° to 120° irrespective of their thickness. Furthermore, the roughness of the CNH coatings is dependent on the thickness, with thicker coatings presenting higher roughness. However, the roughness of the coatings does not significantly influence the CA. Therefore, the CA of CNH coatings is determined by the intrinsic hydrophobic nature of these nanoparticles, with chemistry prevailing over topography. Along with topographical changes, defects and fissures present on the surface do not impact the wetting behavior of these coatings. Although these features can be seen pervasively throughout the CNH coatings, these are not detrimental towards the hydrophobicity of the coatings. This could be attributed to the complex micro-porous network of the coating – see reference [18]. However, it can be hypothesized that defect-free surfaces could potentially present near superhydrophobic or even superhydrophobic surfaces. Moreover, the lack of superhydrophobicity in CNH coatings can also be credited to the particle's morphology. The dahlia-type CNH particles have horn diameters between 3 to 5 nm with their ends capped. In other words, the ends of the horns are closed by a hemispherical honeycomb carbon structure. As a consequence of the small individual horn structure, the horn and their

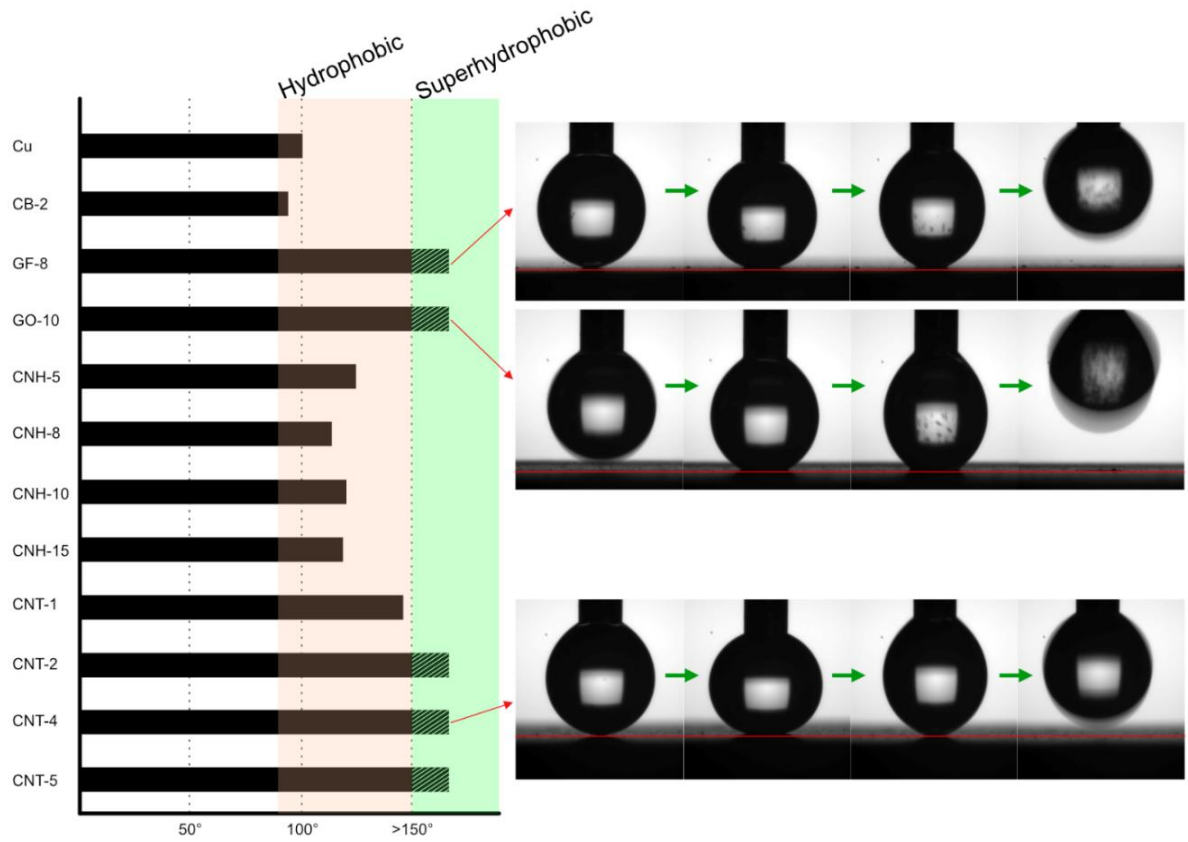

Figure 4: Left – CA with purified water of coatings and reference sample. Right – progression (from left to right) of water droplet contacting the coated surfaces, but unable to be deposited due to hydrophobicity. See supporting information for videos corresponding to wetting sequences. In all cases the baseline was highlighted by a red line. Left – classified contact angle (>90° hydrophobic, >150° superhydrophobic). Note that a CA value was not obtained for the superhydrophobic coatings, the bars are used to depict their wetting behavior.

cappings have a pronounced curvature. This strain-induced curvature delocalizes the high-mobility π orbitals, increasing the particle's reactivity on its external face while decreasing its reactivity on its internal face (known as pyramidization).[53] Therefore, pyramidization favors a more hydrophilic nanoparticle, thus explaining the lack of superhydrophobicity measured during sessile drop test in all CNH coatings.

On the other hand, GF and GO coatings showed superhydrophobic behavior. The hydrophobicity of GO was not expected due to the oxygen atoms present in this CNP, with a stronger hydrophilic behavior as the concentration of oxygen in the graphene structure increases.[54] Therefore, it was hypothesized that this CNP would have greater affinity towards water molecules. The superhydrophobic behavior of GF and GO are shown in **Figure 4** (right),

depicting the progression – from left to right – of the water droplet as it approaches (frames 1 and 2) and recedes (frames 3 and 4) from the surface. Although these two coatings performed exceptionally well, it is noteworthy to highlight that the coatings were affected by the measurements carried out – as witnessed by the third and fourth frame in the CA measurement progression. These two frames show that, although the droplet cannot be deposited onto the surface, part of the coating was removed and retained within the water droplet. However, no visible damage was observed on the samples' surface following the measurements. The partial removal of these coatings might be due to the water droplet's infiltration in the coating. These two coatings show many voids on their surfaces, allowing the water droplet to penetrate the surface of the coating. However, as was hypothesized, the complex void network within the coatings – and the coatings' relative thickness – prevents the water droplet from penetrating too deeply into the coatings. Consequently, these coatings produce a superhydrophobic surface. The CA observed for these coatings is reduced, since it is believed that these coatings are under a Wenzel wetting state; notwithstanding, superhydrophobicity was observed. The infiltration of GF and GO particles into the water droplet was observed immediately after the droplet encountered the coatings – refer to videos in supporting information. Within the droplet, these particles had an upward trajectory, indicating a convective flow of the particles. Convective flow is caused by a temperature gradient in the droplet, with higher temperatures at the top of the droplet (in contact with the syringe) and lower temperature in the coating-droplet contacting sites. The lower temperature is attributed to the exceptionally high thermal conductivity of the GF and GO particles. It is noteworthy that convective flow is more clearly observed in GO rather than in GF. This can be explained by particle size, since GF particles are larger, gravitational forces play a more important role. In the GO coating, GO agglomerates are retained within the droplet by the convective flow, which pushes the GO agglomerates within the droplet and in an upward motion. In the GF coating however, the GF particles are retained within the droplet and tend to move

upwards, followed by a downward motion once the droplet has completely receded from the coating's surface.

CNT coatings performed consistently hydrophobic. The 1-minute coating generated an average CA of approximately 145°, not quite reaching superhydrophobicity. However, the thicker CNT coatings all achieved superhydrophobic wetting behavior. In contrast with the GF and GO coatings, the CNT coatings were not damaged while measuring; this can be evidenced by the progression of the CA measurement shown in **Figure 4** (bottom right) – video available in supporting information. Moreover, although in the GF and GO coatings the droplet could not be deposited, slight adhesion was observed as the droplet contacted and receded from the coatings – evidenced in the second and third frame of the sequence shown in **Figure 4**. However, this was not the case with the CNT coatings. This adhesion – or lack thereof – is observed in the second and third sequence of the CA progression in **Figure 4**. Moreover, observing CNT-1, the conclusion can be drawn that at least 1 μm thickness is required in CNT coatings to achieve superhydrophobic wetting behavior. A previous study by Korczeniewski et al.[55] found that the diameter of the CNT agglomerates is crucial to control the wetting behavior of EPD-produced CNT coatings. The authors conclude that smaller CNT agglomerate diameters (measured via dynamic light scattering) and higher substrate roughness correlates to higher CA – with variations of up to 40°. Moreover, Shirtcliffe et al.[56] also reported increased CA in copper-based materials with increased roughness – with higher roughness surfaces transitioning from Wenzel wetting state towards Cassie-Baxter wetting state. This is a potential explanation as to why the CNT-1 coating does not reach superhydrophobicity. Since the thickness of CNT-1 is relatively thin – 0.6 μm – the roughness of the substrate could influence the wetting behavior of this coating. If it is considered that the CNT agglomerate size is constant throughout the four CNT coatings, then the relatively low roughness of the substrate – 10-20 nm – could cause a slight decrease in the CA of CNT-1. Moreover, uncoated regions show higher affinity towards water, causing further decrease in CA. Comparing the wetting behavior of the thicker CNT coatings, it is clear that the

thickness does not influence the CA – all coatings are superhydrophobic. However, it is of utmost importance that the coating is sufficiently thick to overcome the influence of the substrate and that the wetting behavior of the CNT dominates, as evidenced in the thinner CNT-1 coating. Contrarily, a substrate with higher roughness should be adopted to achieve higher CA, as reported by Korczeniewski et al.[55] and Shirtcliffe et al.[56] The strong hydrophobic tendencies of CNT is evidenced in CNT-1. However, the short deposition time did not allow a complete coating of the substrate. Therefore, the relative poorer performance in sessile drop test of CNT-1 can be considered to be strongly influenced by the wetting behavior of the substrate, and not exclusively due to the coating itself. Nonetheless, the intrinsic hydrophobic tendencies of the CNT significantly increases the CA of the surface from 100° in the Cu reference up to 145°. Although the heterogeneity and thinness of this coating does not allow for a superhydrophobic surface, the hydrophobicity of the substrate is not affected but rather improved by the presence of CNT.

To gain a better understanding of the impact of the coating time and the resulting thickness on the roughness ratio (S-ratio) and the wetting behavior, the S-ratio for each coating was measured and correlated with the results from the sessile drop tests (shown in **Figure 5a**). The physical meaning of the roughness ratio is the relationship between the apparent and real contact area (s-ratio = real contact area / apparent contact area). The different coatings arrange in different roughness ratio fields. CNH coatings depict an average S-ratio of 1.08 ± 0.02, whereas CNT coatings have an average S-ratio of 1.42 ± 0.03. In these coatings the roughness ratio appears to be independent of the deposition time and rather be determined by the particles used. GF and GO, on the other hand, show the highest S-ratio with values close to 3, with CB showing a roughness ratio value of approximately 1.4. Therefore, from this analysis it can be seen that the degree of roughness ratio induced by the CNP coatings is determined exclusively by the CNP that is used and appears to be independent of the deposition time/coating thickness.

Furthermore, observing **Figure 5a** it is concluded that the CNH coating thickness also does not have a significant influence on the roughness ratio. The same conclusion can be drawn from

the CNT coatings. In CNT-1, however, a difference can be observed. Nonetheless, as previously mentioned, the difference in roughness ratio (i.e., rms roughness) and lack of superhydrophobicity is solely a consequence of the inadequate coating type. In other words, 1-minute deposition time is no sufficient to fully coat the substrate, therefore obtaining a mixed state where the roughness and CA measured is a combination of that of the substrate in uncoated regions as well as the coating itself. For thicker CNT coatings, the interaction between water and the copper substrate is no longer a dominant but is rather overruled by the CNT-water interaction.

A more in-depth understanding of the influence of roughness on the wetting behavior of the coated samples can be attained by determining the CA of a perfectly smooth surface. That is, the CA of a surface with an S-ratio equal to 1. This value can be calculated by using Wenzel's equation which provides a relationship between the measured CA and the quotient between the roughness factor and the CA of a perfectly smooth surface.[57] Therefore, according to a Wenzel wetting state in hydrophobic surfaces, as the roughness factor increases, so does the measured CA. On the other hand, in hydrophilic surfaces, as the roughness factor increases, the measured CA decreases. Due to the high CA and low topography, CNH and CNT coatings continue showing hydrophobic wetting behavior when topographic features are not accounted for – highlighted by the blue shaded region in **Figure 5a**, which shows the area in the plot where the smooth-surface and measured CA are both in a hydrophobic wetting state. CB shows similar roughness values as CNT; however, its measured CA is significantly lower. Therefore, the calculated smooth CA is approximately 92.5° - marginally remaining in a hydrophobic wetting state. GF and GO also show low smooth-surface CA, with values of approximately 110°. However, it must be noted that the calculations were based on the assumption that the measured CA was 170° since the actual value could not be measured due to their superhydrophobic wetting behavior. This assumption, in addition to the high roughness values, generate the low CA in the calculations using Wenzel's equation. Nonetheless, these two nanoparticles remain in a hydrophobic wetting state. GF and GO show the largest topographic features among the studied

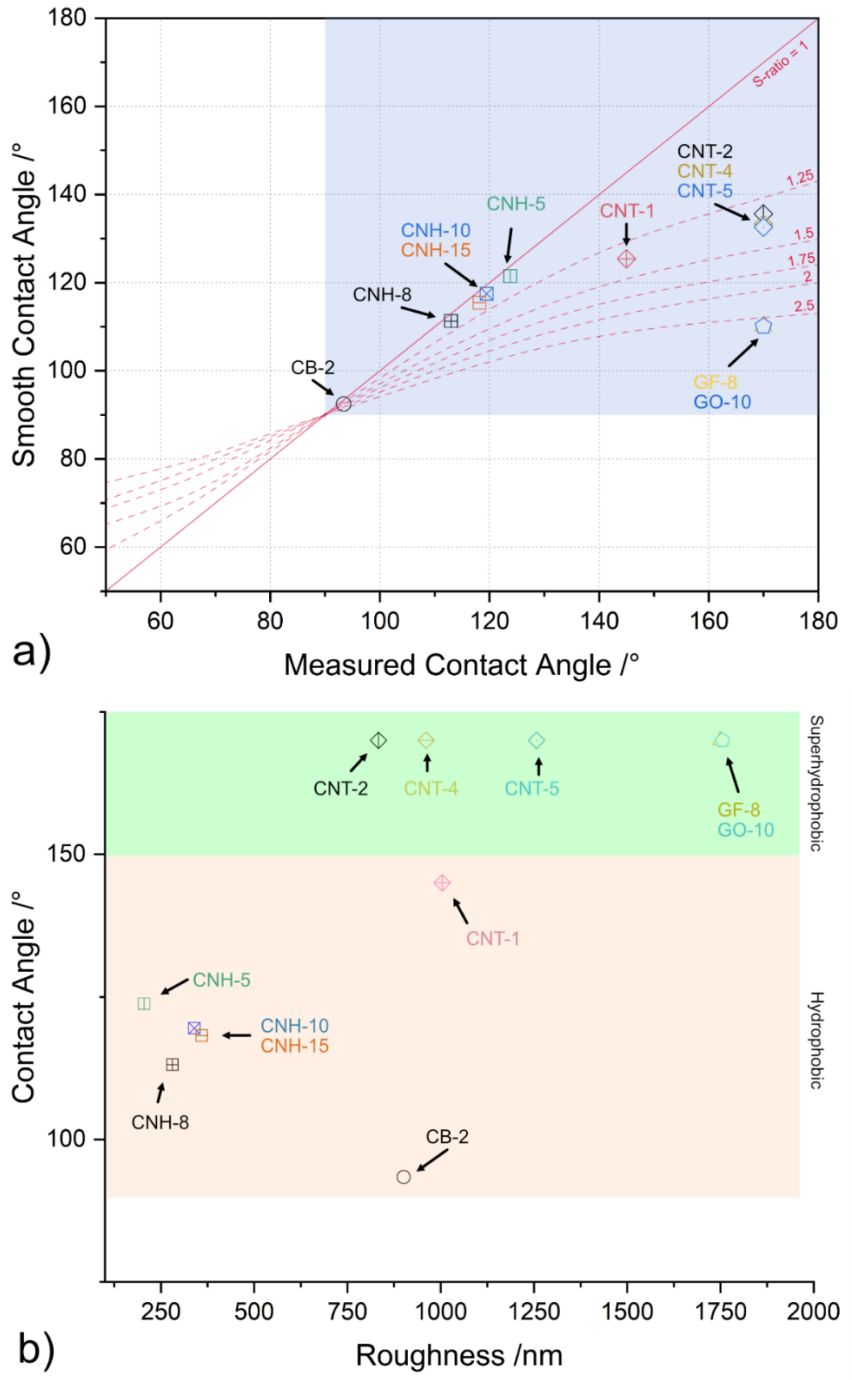

Figure 5: a) Plot of smooth-surface CA – calculated by Wenzel's equation – as a function of measured CA. The red lines show how the theoretical smooth-surface CA should vary as the S-ratio increases. The blue region highlights the area where the smooth and the measured CA are hydrophobic. **b)** Relation between static CA and roughness. Superhydrophobic coatings not showing surface wetting are categorized with a CA of 170°.

nanoparticle coatings. These high roughness values – paired with the morphology of the coatings observed in **Figure 2** – explain the superhydrophobic behavior of these nanoparticles, primarily of GO. As a consequence of the oxygen content in GO, it is hypothesized that the

superhydrophobic wetting behavior of this coating type is primarily attributed to the large topographic features.

As with the S-ratio, when plotting the CA as a function of roughness the coatings arrange themselves in different regions of the plot (**Figure 5b**). The CNH coatings all present similar roughness values – lowest among the studied coatings – and consistently produced hydrophobic surfaces. Observing the CNT coatings, apart from CNT-1, a clear correlation can be observed between coating thickness and increased roughness. As the deposition time increases, so does the roughness of the resulting coating. Although, as previously mentioned, the increased roughness of CNT-1 is a consequence of insufficient coating time; thus obtaining a rougher surface due to uncoated regions and CNT agglomerates deposited on the surface. GF and GO possess the highest roughness of the analyzed coatings. The CA as a function of roughness plot is of significance for the CB samples, since this plot shows that the lower CA of the CB coating can be attributed to chemical factors rather than to topographical. CB coating show similar roughness values as CNT coatings. Nonetheless, CB coating show a borderline hydrophobic wetting behavior, whereas CNT coatings show superhydrophobic wetting behavior. This suggests that CB is more strongly oxidized than CNT, resulting in higher affinity towards the water droplet and consequently reducing the measured CA. As when plotting the S-ratio, GF and GO are grouped due to their similar roughness values and superhydrophobic behavior. Both plots (from **Figure 5a** and **Figure 5b**) show similar information regarding the influence of the CNP morphology at the surface level, and the resulting wetting behavior.

Saline Water. As previously discussed, copper is extensively used in a wide range of applications and is especially susceptive to accelerate corrosion in environments with chlorine ions (e.g., in coastal regions). Therefore, the coating's wetting behavior analyzed with artificial salt water is of great importance. The CA measurements using this medium are shown in **Figure 6**. At first glance, the same tendencies as with purified water are observed. The CNP coatings that were superhydrophobic when measured with water remain superhydrophobic when

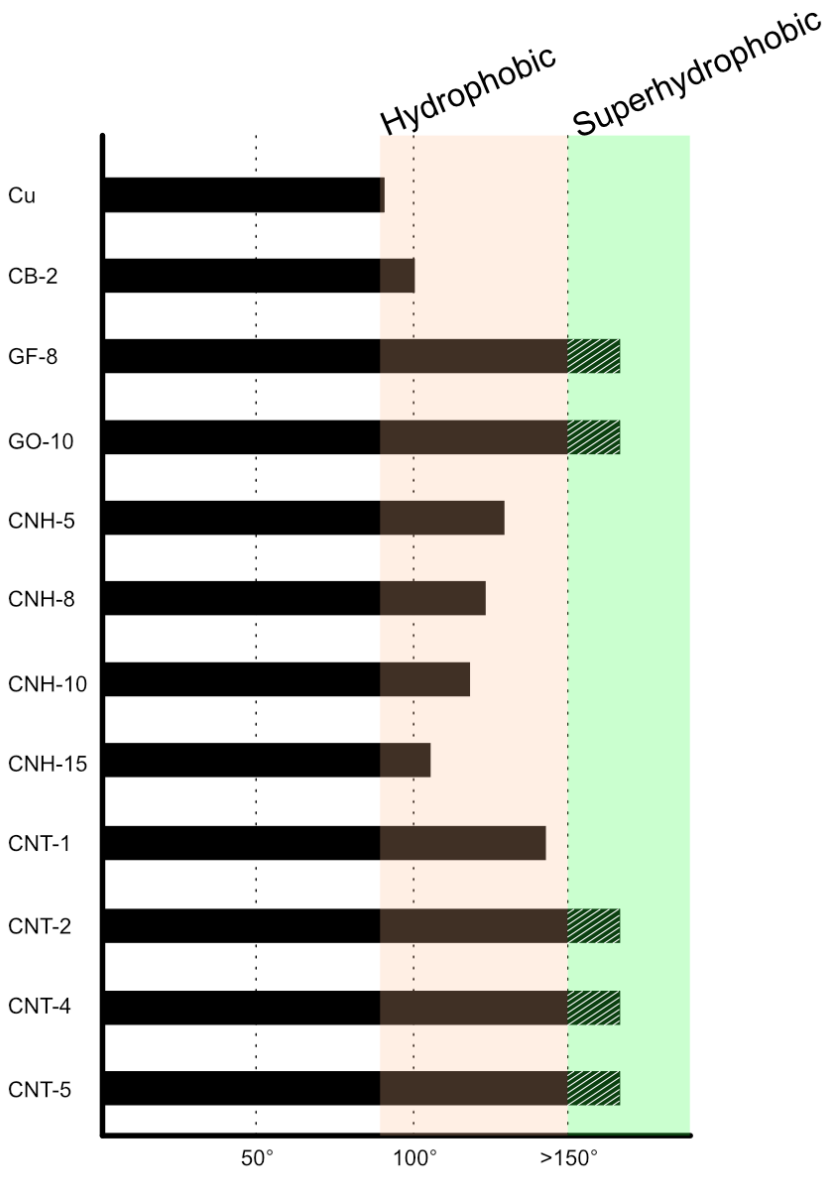

Figure 6: CA with saline water solution of CNP and reference sample. Note that a CA value was not obtained for the superhydrophobic coatings, the bars are used to depict their wetting behavior.

measured with saline water. Likewise, the coatings that presented hydrophobic wetting behavior remain hydrophobic. However, in this case, the Cu reference presents borderline hydrophobicity, with an average CA value of 90° as opposed to 100° when measuring with purified water. The salt molecules in the solution tend to interact with the Cu surface, thus reducing CA. This is also observed in CNH-10 and CNH15, however, the change in CA should not be overinterpreted since it could be a consequence of the coating's structural defects. The same can be stated about CNH-5 and CNH-8, which show slightly improved hydrophobicity.

For CB on the other hand, the slight increase in CA (approximately 93° and 100° when measured with purified water and saline water, respectively) can be attributed to the presence of Na^+ ions in the droplet. It has been previously reported by Powell et al.[58] that CB tends to increase its hydrophobicity when these ions were added in an aqueous media. This coincides with what was observed in our study. The authors also reported CB's tendency to floc in the presence of salt. However, this was not observed in our measurements while conducting sessile drop tests with saline water – since the saline water droplet did not damage the CB coating and there was no infiltration into the droplet.

The main conclusion from these measurements is that GF, GO, and thicker CNT coatings persistently produce superhydrophobic surfaces. Therefore, these coatings show promising applications as protective barriers from atmospheric moisture, as well as saline environments. Moreover, although superhydrophobicity was not achieved with CB and CNT-1 coatings, these coatings outperform the reference sample. Therefore, although the benefit might not be as significant, these two coatings could potentially delay degradation in Cu when subjected to saline environments. Likewise, CNH coatings remain consistently hydrophobic when measuring with this medium, thus their potential use cannot be discarded. Although, their potential protection would be inferior to GF, GO, and thicker CNT coatings.

CONCLUSIONS

In this work five different CNP coatings were produced via EPD on Cu substrates with the objective of analyzing their potential use as protective barriers from atmospheric conditions via sessile drop test. One CB, GF, and GO, and four CNT and CNH coatings were analyzed – as well as a Cu reference sample – chosen based on previous studies on their influence on the ECR of Cu samples. The following conclusions can be drawn from this study:

- CB and CNH showed defects and fissures on their surface which could jeopardize their wetting behavior. Nonetheless, both nanoparticles produce hydrophobic surfaces when measuring with both media.

- In the CNH coatings, thickness and roughness do not play an important role in the wetting behavior of the coatings. The chemical tendency of this nanoparticle outweighs these factors. However, pyramidization can be the justification for the lack of superhydrophobic CNH coatings.
- GF and GO coatings have high roughness with voids on their surface inherent to the geometry and particle interactions. However, these voids do no hinder the superhydrophobic wetting behavior of these CNP – irrelevant if the measurements were carried out with purified water or saline water. Do to their superhydrophobic wetting behavior, these two coatings could potentially be used as protective barriers in diverse atmospheric conditions.
- CNT coatings showed superhydrophobic wetting behavior when measured with both media – with the exception of the thin CNT-1 coating. The topography generated by the CNT agglomerates does not significantly influence the wetting behavior of the inherently hydrophobic nanotubes.
- As evidenced by CNT-1, it is crucial that the thickness of the CNT coating is enough to outweigh the influence of the substrate. In other words, a complete coating of the substrate is crucial to achieve superhydrophobic wetting behavior.
- CNT-2, CNT-4, and CNT-5 prove to be the most promising coatings as protective barriers in diverse atmospheric conditions for copper materials since these coatings show superhydrophobic wetting behavior. Specifically for copper electrical contacts, these coatings present the additional advantage that they do not significantly impact the ECR of the substrate.

ASSOCIATED CONTENT

Supporting Information

The following files are available free of charge.

- Video of contact angle measurement on superhydrophobic coatings (GF 8 min, GO 10 min, CNT 2 min, CNT 4 min, and CNT 5 min. (.avi & .wmv video files).

AUTHOR INFORMATION

Corresponding Author

* e-mail: bruno.alderete@uni-saarland.de

Author Contributions

All authors have given approval to the final version of the manuscript.

Notes

The authors declare no competing financial interest.

ACKNOWLEDGEMENT

B. Alderete wishes to acknowledge the financial support from the German Academic Exchange Service (DAAD) and the Roberto Rocca Education Program (RREP). S. M. Lößlein acknowledges the funding of the German Research Foundation (Deutsche Forschungsgemeinschaft, DFG, project number: 435334669. D. Bucio Tejeda acknowledges "Programa de iniciación a la investigación" (CNBBJ-UNAM-2020) for financially supporting her stay in Saarbrücken. The authors gratefully acknowledge funding in the ZuMat project, supported by the State of Saarland from the European Regional Development Fund (Europäischen Fonds für Regionale Entwicklung, EFRE).

REFERENCES

(1) Chavez, K. L.; Hess, D. W. A Novel Method of Etching Copper Oxide Using Acetic Acid. *J Electrochem Soc* **2001**, *148* (11), G640. https://doi.org/10.1149/1.1409400.

(2) Díaz León, J. J.; Fryauf, D. M.; Cormia, R. D.; Kobayashi, N. P. Study of the Formation of Native Oxide on Copper at Room Temperature. In *Low-Dimensional Materials and Devices 2016*; 2016; Vol. 9924, pp 99240O 1-7. https://doi.org/10.1117/12.2238745.

(3) Rice, D. W.; Peterson, P.; Rigby, E. B.; Phipps, P. B. P.; Cappell, R. J.; Tremoureux, R. Atmospheric Corrosion of Copper and Silver. *J Electrochem Soc* **1981**, *128* (2), 275–284. https://doi.org/10.1149/1.2127403.

(4) Park, J. H.; Natesan, K. Oxidation of Copper and Electronic Transport in Copper Oxides. *Oxidation of Metals* **1993**, *39* (5–6), 411–435. https://doi.org/10.1007/BF00664664.

(5) Platzman, I.; Brener, R.; Haick, H.; Tannenbaum, R. Oxidation of Polycrystalline Copper Thin Films at Ambient Conditions. *Journal of Physical Chemistry C* **2008**, *112* (4), 1101–1108. https://doi.org/10.1021/jp076981k.

(6) Fateh, A.; Aliofkhazraei, M.; Rezvanian, A. R. Review of Corrosive Environments for Copper and Its Corrosion Inhibitors. *Arabian Journal of Chemistry* **2020**, *13* (1), 481–544. https://doi.org/10.1016/j.arabjc.2017.05.021.

(7) Brusic, V.; Frisch, M. A.; Eldridge, B. N.; Novak, F. P.; Kaufman, F. B.; Rush, B. M.; Frankel, G. S. Copper Corrosion With and Without Inhibitors. *J Electrochem Soc* **1991**, *138* (8), 2253–2259. https://doi.org/https://doi.org/10.1149/1.2085957.

(8) Pareek, S.; Jain, D.; Behera, D.; Sharma, S.; Shrivastava, R. A Review on Inhibitors Alleviating Copper Corrosion in Hostile Simulated Sea-Water (3.5 Wt.% NaCl Solution). In *Materials Today: Proceedings*; Elsevier Ltd, 2021; Vol. 43, pp 3303–3308. https://doi.org/10.1016/j.matpr.2021.01.966.

(9) Yang, S.; Zhao, X.; Qi, Z.; Lu, Y. H.; Somorjai, G.; Yang, P.; Baskin, A.; Prendergast, D.; Salmeron, M. Chloride-Assisted Corrosion of Copper and Protection by Benzotriazole. *ACS Appl Mater Interfaces* **2022**, *14* (4), 6093–6101. https://doi.org/10.1021/acsami.1c15808.

(10) Birn, J.; Skalski, I. Overview of Copper and Aluminium Alloys. In *Corrosion behaviour and protection of copper and aluminium alloys in seawater*; Féron, D., Ed.; Woodhead Publishing Limited: Cambridge, 2007; pp 3–46.

(11) Ijsseling, F. P. General Guidelines for Corrosion Testing of Materials for Marine Applications - Literature Review on Sea Water as Test Environment. *British Corrosion Journal* **1989**, *24* (1), 53–78. https://doi.org/https://doi.org/10.1179/000705989798270388.

(12) Núñez, L.; Reguera, E.; Corvo, F.; González, E.; Vazquez, C. Corrosion of Copper in Seawater and Its Aerosols in a Tropical Island. *Corros Sci* **2005**, *47* (2), 461–484. https://doi.org/10.1016/j.corsci.2004.05.015.

(13) Cai, Y.; Xu, Y.; Zhao, Y.; Zhang, W.; Yao, J.; Wei, M.; Zhou, K.; Ma, X. Quantitative Understanding of the Environmental Effect on B10 Copper Alloy Corrosion in Seawater. *Metals (Basel)* **2021**, *11* (7), 1080. https://doi.org/10.3390/met11071080.

(14) Liu, T.; Yin, Y.; Chen, S.; Chang, X.; Cheng, S. Super-Hydrophobic Surfaces Improve Corrosion Resistance of Copper in Seawater. *Electrochim Acta* **2007**, *52* (11), 3709–3713. https://doi.org/10.1016/j.electacta.2006.10.059.

(15) Nakajima, A.; Hashimoto, K.; Watanabe, T. Recent Studies on Super-Hydrophobic Films. In *Molecular Materials and Functional Polymers*; Blau, W. J., Lianos, P., Schubert, U., Eds.; Springer: Vienna, 2001; pp 31–41. https://doi.org/https://doi.org/10.1007/978-3-7091-6276-7_3.

(16) Kirkland, N. T.; Schiller, T.; Medhekar, N.; Birbilis, N. Exploring Graphene as a Corrosion Protection Barrier. *Corros Sci* **2012**, *56*, 1–4. https://doi.org/10.1016/j.corsci.2011.12.003.

(17) Cremers, V.; Rampelberg, G.; Baert, K.; Abrahami, S.; Claes, N.; de Oliveira, T. M.; Terryn, H.; Bals, S.; Dendooven, J.; Detavernier, C. Corrosion Protection of Cu by Atomic Layer Deposition. *Journal of Vacuum Science & Technology A* **2019**, *37* (6), 060902. https://doi.org/10.1116/1.5116136.

(18) Alderete, B.; Mücklich, F.; Suarez, S. Characterization and Electrical Analysis of Carbon-Based Solid Lubricant Coatings. *Carbon Trends* **2022**, *7*. https://doi.org/10.1016/j.cartre.2022.100156.

(19) *Electrophoretic Deposition of Nanomaterials*, 1st ED.; Dickerson, J. H., Boccaccini, A. R., Eds.; Nanostructure Science and Technology; Springer US: New York, NY, 2012. https://doi.org/10.1007/978-1-4419-9730-2.

(20) Boccaccini, A. R.; Cho, J.; Roether, J. A.; Thomas, B. J. C.; Jane Minay, E.; Shaffer, M. S. P. Electrophoretic Deposition of Carbon Nanotubes. *Carbon N Y* **2006**, *44* (15), 3149–3160. https://doi.org/10.1016/j.carbon.2006.06.021.

(21) Atiq Ur Rehman, M.; Chen, Q.; Braem, A.; Shaffer, M. S. P.; Boccaccini, A. R. Electrophoretic Deposition of Carbon Nanotubes: Recent Progress and Remaining Challenges. *International Materials Reviews* **2020**, *0* (0), 1–30. https://doi.org/10.1080/09506608.2020.1831299.

(22) Sarkar, P.; Nicholson, P. S. Electrophoretic Deposition (EPD): Mechanisms, Kinetics, and Application to Ceramics. *Journal of the American Ceramic Society*. 1996, pp 1987–2002. https://doi.org/10.1111/j.1151-2916.1996.tb08929.x.

(23) Reinert, L.; Zeiger, M.; Suarez, S.; Presser, V.; Mücklich, F. Dispersion Analysis of Carbon Nanotubes, Carbon Onions, and Nanodiamonds for Their Application as Reinforcement Phase in Nickel Metal Matrix Composites. *RSC Adv* **2015**, *5* (115), 95149–95159. https://doi.org/10.1039/c5ra14310a.

(24) Ma, Y.; Han, J.; Wang, M.; Chen, X.; Jia, S. Electrophoretic Deposition of Graphene-Based Materials: A Review of Materials and Their Applications. *Journal of Materiomics* **2018**, *4* (2), 108–120. https://doi.org/10.1016/j.jmat.2018.02.004.

(25) Hamaker, H. C. Formation of a Deposit by Electrophoresis. *Trans. Faraday Soc.* **1940**, *35*, 279–287. https://doi.org/https://doi.org/10.1039/TF9403500279.

(26) Farrokhi-Rad, M.; Shahrabi, T. Electrophoretic Deposition of Titania Nanoparticles: Sticking Parameter Determination by an in Situ Study of the EPD Kinetics. *Journal of the American Ceramic Society* **2012**, *95* (11), 3434–3440. https://doi.org/10.1111/j.1551-2916.2012.05402.x.

(27) Alderete, B.; MacLucas, T.; Espin, D.; Brühl, S. P.; Mücklich, F.; Suarez, S. Near Superhydrophobic Carbon Nanotube Coatings Obtained via Electrophoretic Deposition on Low-Alloy Steels. *Adv Eng Mater* **2021**, *23* (5). https://doi.org/10.1002/adem.202001448.

(28) MacLucas, T.; Schütz, S.; Suarez, S.; Mücklich, F. Surface Protection of Austenitic Steels by Carbon Nanotube Coatings. *Surf Topogr* **2018**, *6* (1), 14005. https://doi.org/10.1088/2051-672X/aab145.

(29) Kozbial, A.; Zhou, F.; Li, Z.; Liu, H.; Li, L. Are Graphitic Surfaces Hydrophobic? *Acc Chem Res* **2016**, *49* (12), 2765–2773. https://doi.org/10.1021/acs.accounts.6b00447.

(30) Wang, G.; Wang, B.; Park, J.; Yang, J.; Shen, X.; Yao, J. Synthesis of Enhanced Hydrophilic and Hydrophobic Graphene Oxide Nanosheets by a Solvothermal Method. *Carbon N Y* **2009**, *47* (1), 68–72. https://doi.org/10.1016/j.carbon.2008.09.002.

(31) Xu, L.; Teng, J.; Li, L.; Huang, H. D.; Xu, J. Z.; Li, Y.; Ren, P. G.; Zhong, G. J.; Li, Z. M. Hydrophobic Graphene Oxide as a Promising Barrier of Water Vapor for Regenerated Cellulose Nanocomposite Films. *ACS Omega* **2019**, *4* (1), 509–517. https://doi.org/10.1021/acsomega.8b02866.

(32) Karfa, P.; De, S.; Majhi, K. C.; Madhuri, R.; Sharma, P. K. Functionalization of Carbon Nanostructures. In *Comprehensive Nanoscience and Nanotechonlogy*; Andrews, D. L., Lipson, R. H., Nann, T., Eds.; Academic Press, 2019; pp 123–144. https://doi.org/10.1016/B978-0-12-803581-8.11225-1.

(33) Vilaró, I.; Yagüe, J. L.; Borrós, S. Superhydrophobic Copper Surfaces with Anticorrosion Properties Fabricated by Solventless CVD Methods. *ACS Appl Mater Interfaces* **2017**, *9* (1), 1057–1065. https://doi.org/10.1021/acsami.6b12119.

(34) Wang, P.; Zhang, D.; Qiu, R.; Wan, Y.; Wu, J. Green Approach to Fabrication of a Super-Hydrophobic Film on Copper and the Consequent Corrosion Resistance. *Corros Sci* **2014**, *80*, 366–373. https://doi.org/10.1016/j.corsci.2013.11.055.

(35) Ji, H.; Côté, A.; Koshel, D.; Terreault, B.; Abel, G.; Ducharme, P.; Ross, G.; Savoie, S.; Gagné, M. Hydrophobic Fluorinated Carbon Coatings on Silicate Glaze and Aluminum. *Thin Solid Films* **2002**, *405* (1–2), 104–108. https://doi.org/https://doi.org/10.1016/S0040-6090(01)01707-2.

(36) Caschera, D.; Cortese, B.; Mezzi, A.; Brucale, M.; Ingo, G. M.; Gigli, G.; Padeletti, G. Ultra Hydrophobic/Superhydrophilic Modified Cotton Textiles through Functionalized Diamond-like Carbon Coatings for Self-Cleaning Applications. *Langmuir* **2013**, *29* (8), 2775–2783. https://doi.org/10.1021/la305032k.

(37) de Nicola, F.; Castrucci, P.; Scarselli, M.; Nanni, F.; Cacciotti, I.; de Crescenzi, M. Super-Hydrophobic Multi-Walled Carbon Nanotube Coatings for Stainless Steel. *Nanotechnology* **2015**, *26* (14), 145701. https://doi.org/10.1088/0957-4484/26/14/145701.

(38) Lößlein, S. M.; Mücklich, F.; Grützmacher, P. G. Topography versus Chemistry – How Can We Control Surface Wetting? *J Colloid Interface Sci* **2022**, *609*, 645–656. https://doi.org/10.1016/j.jcis.2021.11.071.

(39) Kavousanakis, M. E.; Chamakos, N. T.; Papathanasiou, A. G. Connection of Intrinsic Wettability and Surface Topography with the Apparent Wetting Behavior and Adhesion Properties. *Journal of Physical Chemistry C* **2015**, *119* (27), 15056–15066. https://doi.org/10.1021/acs.jpcc.5b00718.

(40) Hazardous Substances Data Bank (HSDB). *PubChem Annotation Record for TRIETHYLAMINE*. Natoinal Library of Medicine (US), National Center for Biotechnology Information. https://pubchem.ncbi.nlm.nih.gov/source/hsdb/896#section=Human-Health-Effects (accessed 2022-07-19).

(41) Hazardous Substances Data Bank (HSDB). *PubChem Annotation Record for ISOPROPANOL*. Natoinal Library of Medicine (US), National Center for Biotechnology Information. https://pubchem.ncbi.nlm.nih.gov/source/hsdb/116 (accessed 2022-07-20).

(42) Hans, M.; Müller, F.; Grandthyll, S.; Hüfner, S.; Mücklich, F. Anisotropic Wetting of Copper Alloys Induced by One-Step Laser Micro-Patterning. *Appl Surf Sci* **2012**, *263*, 416–422. https://doi.org/10.1016/j.apsusc.2012.09.071.

(43) Krainer, S.; Hirn, U. Contact Angle Measurement on Porous Substrates: Effect of Liquid Absorption and Drop Size. *Colloids Surf A Physicochem Eng Asp* **2021**, *619* (March), 126503. https://doi.org/10.1016/j.colsurfa.2021.126503.
(44) Murakami, D.; Jinnai, H.; Takahara, A. Wetting Transition from the Cassie-Baxter State to the Wenzel State on Textured Polymer Surfaces. *Langmuir* **2014**, *30* (8), 2061–2067. https://doi.org/10.1021/la4049067.
(45) MacLucas, T.; Suarez, S. On the Solid Lubricity of Electrophoretically Deposited Carbon Nanohorn Coatings. *Lubricants* **2019**, *7* (8), 60. https://doi.org/10.3390/lubricants7080062.
(46) Suarez, S.; Lasserre, F.; Prat, O.; Mücklich, F. Processing and Interfacial Reaction Evaluation in MWCNT/Ni Composites. *Physica Status Solidi (A) Applications and Materials Science* **2014**, *211* (7), 1555–1561. https://doi.org/10.1002/pssa.201431018.
(47) Simmons, T. J.; Hashim, D.; Vajtai, R.; Ajayan, P. M. Large Area-Aligned Arrays from Direct Deposition of Single-Wall Carbon Nanotube Inks. *J Am Chem Soc* **2007**, *129* (33), 10088–10089. https://doi.org/10.1021/ja073745e.
(48) Nayak, U. P.; Müller, M.; Britz, D.; Guitar, M. A.; Mücklich, F. Image Processing Using Open Source Tools and Their Implementation in the Analysis of Complex Microstructures. *Practical Metallography* **2021**, *58* (8), 484–506. https://doi.org/10.1515/pm-2021-0039.
(49) Korczeniewski, E.; Bryk, P.; Koter, S.; Kowalczyk, P.; Kujawski, W.; Kujawa, J.; Terzyk, A. P. Revisiting Wetting, Freezing, and Evaporation Mechanisms of Water on Copper. *ACS Appl Mater Interfaces* **2021**, *13* (31), 37893–37903. https://doi.org/10.1021/acsami.1c09733.
(50) Persiantseva, N. M.; Popovicheva, O. B.; Shonija, N. K. Wetting and Hydration of Insoluble Soot Particles in the Upper Troposphere. *Journal of Environmental Monitoring* **2004**, *6* (12), 939–945. https://doi.org/10.1039/b407770a.
(51) Wei, Y.; Zhang, Q.; Thompson, J. E. The Wetting Behavior of Fresh and Aged Soot Studied through Contact Angle Measurements. *Atmospheric and Climate Sciences* **2017**, *07* (01), 11–22. https://doi.org/10.4236/acs.2017.71002.
(52) Wang, M.-J.; Gray, C. A.; Reznek, S. A.; Mahmud, K.; Kutsovsky, Y. Carbon Black. In *Kirk-Othmer Encyclopedia of Chemical Technology*; John Wiley & Sons, Inc.: Hoboken, NJ, USA, 2003. https://doi.org/10.1002/0471238961.0301180204011414.a01.pub2.
(53) Haddon, R. C. Chemistry of the Fullerenes: The Manifestation of Strain in a Class of Continuous Aromatic Molecules. *Science (1979)* **1993**, *261* (5128), 1545–1550. https://doi.org/10.1126/science.261.5128.1545.
(54) Wei, N.; Lv, C.; Xu, Z. Wetting of Graphene Oxide: A Molecular Dynamics Study. *Langmuir* **2014**, *30* (12), 3572–3578. https://doi.org/10.1021/la500513x.
(55) Korczeniewski, E.; Zieba, M.; Zieba, W.; Kolanowska, A.; Bolibok, P.; Kowalczyk, P.; Wiertel-Pochopien, A.; Zawała, J.; Boncel, S.; Terzyk, A. P. Electrophoretic Deposition of Layer-by-Layer Unsheathed Carbon Nanotubes-a Step towards Steerable Surface Roughness and Wettability. *Materials* **2020**, *13* (3), 595. https://doi.org/10.3390/ma13030595.
(56) Shirtcliffe, N. J.; McHale, G.; Newton, M. I.; Perry, C. C. Wetting and Wetting Transitions on Copper-Based Super-Hydrophobic Surfaces. *Langmuir* **2005**, *21* (3), 937–943. https://doi.org/10.1021/la048630s.
(57) *Engineering Textiles: Integrating the Design and Manufacture of Textile Products*, Second Ed.; Elmogahzy, Y. E., Ed.; Woodhead Publishing, 2020.
(58) Powell, K. C.; Chauhan, A. Interfacial Tension and Surface Elasticity of Carbon Black (CB) Covered Oil–Water Interface. *Langmuir* **2014**, *30* (41), 12287–12296. https://doi.org/10.1021/la503049m.

ARTICLE IX
Comprehensive Study on Carbon-Coated Silver for Improved Tribo-Electrical and Wetting Performance

Bruno Alderete*, Frank Mücklich, Sebastian Suarez

Department of Materials Science and Engineering, Saarland University, Campus D3.3, 66123 Saarbrücken, Germany

Research article
Published in "*C – Journal of Carbon Research*" (2024)
Impact Factor: 3.9 (2023)

Accessible online at: doi.org/10.3390/c10010016

Own Contribution: Conceptualization; Data Curation; Methodology; Validation; Formal Analysis; Investigation; Data Curation; Writing – Original Draft; Visualization.

Cite this article as: B. Alderete, F. Mücklich, S. Suarez, Comprehensive Study on Carbon-Coated Silver for Improved Tribo-Electrical and Wetting Performance, C (Basel) 10 (2024) 16. https://doi.org/10.3390/c10010016.

C Journal of Carbon Research

MDPI

Article

Comprehensive Study on Carbon-Coated Silver for Improved Tribo-Electrical and Wetting Performance

Bruno Alderete *, Frank Mücklich and Sebastian Suarez

Department of Materials Science and Engineering, Saarland University, Campus D3.3, 66123 Saarbrücken, Germany; muecke@matsci.uni-sb.de (F.M.); s.suarez@mx.uni-saarland.de (S.S.)
* Correspondence: bruno.alderete@uni-saarland.de; Tel.: +49-681-3027-0544

Abstract: The rise in electrification has considerably increased the demand for high-efficiency and durable electrical contact materials. Carbon nanoparticles (CNP) are a promising coating material due to their intrinsic transport properties (thus minimizing the impact on conductivity), their proven solid lubricity (potentially improving tribological performance), and their hydrophobic wetting behavior (potentially providing atmospheric protection). In this study, carbon nanotube and nanohorn coatings are produced via electrophoretic deposition on silver-plated surfaces, followed by tribo-electrical and wetting characterization. The proposed coatings do not negatively affect the conductivity of the substrate, showing resistance values on par with the uncoated reference. Tribo-electrical characterization revealed that the coatings reduce adhesive wear during fretting tests while maintaining stable and constant electrical contact resistance. Furthermore, CNP-coated surfaces show a hydrophobic wetting behavior toward water, with graphite and carbon nanotube (CNT) coatings approaching super-hydrophobicity. Prolonged exposure to water droplets during sessile drop tests caused a reduction in contact angle (CA) measurement; however, CNT coatings' CA reduction after five minutes was only approximately 5°. Accordingly, CNP (specifically CNT) coatings show auspicious results for their application as wear and atmospheric protective barriers in electrical contacts.

Keywords: carbon nanotubes; carbon nanohorns; electrical contact resistance; graphite; tarnished silver

Citation: Alderete, B.; Mücklich, F.; Suarez, S. Comprehensive Study on Carbon-Coated Silver for Improved Tribo-Electrical and Wetting Performance. *C* **2024**, *10*, 16. https://doi.org/10.3390/c10010016

Academic Editor: Gil Goncalves

Received: 13 December 2023
Revised: 18 January 2024
Accepted: 1 February 2024
Published: 4 February 2024

1. Introduction

Silver is very reputed as an electrical contact material not only due to its extraordinary conductivity but also due to its chemical stability. A key component in silver's ubiquitous use in high-reliability connectors is that it does not oxidize. The lack of oxidation is advantageous since it precludes the formation of non-conductive or semi-conducting oxide films, as is the case with other commonly used contact materials (i.e., copper, tin, aluminum, etc.). Nonetheless, prolonged atmospheric exposure causes the formation of a semi-conductive silver sulfide (tarnishing) film—reaction shown in (1) [1–12]. Many methods have been developed to hinder or prevent this reaction, primarily in the form of protective coatings; however, alkanethiols have garnered the most widespread industrial adaptation [13–16]. The use of alkanethiols (e.g., hexadecanethiol and octadecanethiol, HDT and ODT, respectively) delays the formation of silver sulfide by saturating the silver surface with sulfhydryl groups. HDT and ODT consist of long chains of unsaturated oils where sulfhydryl groups bond with carbon terminals, thus allowing HDT and ODT to bond with transition metals. Sulfhydryl passivation forms Ag-S covalent bonds, forming a dense self-assembled monolayer, thus preventing atmospheric sulfur from reacting with the silver contact material by saturating the silver surface with the sulfur from the sulfhydryl groups [16]. However, the efficacy of these self-assembled monolayers is reliant on the orientation of the free-standing HDT or ODT tail. After the sulfhydryl group bonds with silver, the tail is free to rotate, allowing it to orient itself in an upstanding orderly position or lying on the silver surface in a disordered fashion. These monolayers are more efficient

at preventing silver from tarnishing when the tails are oriented in an upstanding position due to increased thiol bonds with the substrate [16].

$$2Ag + S \rightarrow Ag_2S \quad (1)$$

Carbon nanoparticles (CNP) present a viable alternative to other passivation techniques which cannot only improve on the shortcomings of these techniques but could also present added advantages. Carbon nanostructures have excellent transport properties, a characteristic of utmost importance when dealing with electrical contact material [17–22]. Furthermore, nanocarbons present the advantage of outstanding lubricating capabilities, with extensive use as solid lubricants and lubricant oil additives [23–32].

Previous work carried out by Loyd et al. delineated the lubricating capabilities of graphite, graphene, and CNT specifically for their implementation in low-voltage and low-current applications [33]. Moreover, previous studies on CNP coatings over copper substrates have shown favorable results in terms of tribological and electrical performance, as well as for atmospheric protection due to the hydrophobic tendency of the CNP [34–37]. Therefore, it is the objective of this study to evaluate the impact, drawbacks, and advantages of CNP coatings on silver substrates. The CNP chosen for this analysis are carbon nanotubes (CNT) and carbon nanohorns (CNH), nanostructures that have shown the most promising results on copper substrates with regards to their effect on the system's conductivity, as well as wear and atmospheric protection. However, since silver is used in demanding, high-reliability applications, and considering the significant financial investment that silver contacts incur, it is crucial to comprehensively understand the impact that CNP coatings could have on this outstanding conductor, as well as the benefits that could be gained from CNP-coated silver surfaces. In order to accurately appraise the feasibility of the proposed coatings, benchmarking samples were also evaluated. Accordingly, the CNT and CNH coatings were compared with a reference sample, a tarnished sample (i.e., a silver surface with a thin silver sulfide tarnishing film), and a sample coated with graphite flakes (GF). The proposed coatings were not only compared to a clean reference sample (optimal conductivity) but also to a tarnished sample (worsened conductivity) to gain complete insight into the performance of the CNT and CNH coatings within this conductivity spectrum. Furthermore, GF-coated samples serve as an industrially accepted benchmark (due to graphite's solid lubricity and conductivity), which will better reflect on the feasibility and applicability of the proposed coatings.

Prior to characterization, all samples were chemically cleaned. The cleaned samples were subsequently tarnished or coated. The tarnishing process is a chemical process that involves subjecting the silver surfaces to a saturated sulfur atmosphere, thus rapidly generating a silver sulfide film on the sample's surface. The coatings were produced via electrophoretic deposition (EPD). This method was chosen due to its simplicity, ease in controlling coating thicknesses, its ability to coat geometrically complex surfaces, as well as its scalability. All surfaces were tribo-electrically characterized via load-dependent electrical contact resistance (ECR) and static ECR development during fretting wear. Furthermore, roughness, coating thickness, and assessment of the fretting marks were carried out via confocal laser scanning microscopy (CLSM). The latter were additionally characterized via scanning electron microscopy (SEM) and energy dispersive X-ray spectroscopy (EDS) for extensive chemical analysis. Moreover, wetting behavior was characterized via sessile drop test using two different media: deionized water and a potassium sulfide-deionized water solution. These characterization techniques allow for an in-depth analysis of the impact on the system's conductivity, as well as the potential wear and atmospheric protection provided by the CNP coatings in relation to the reference, tarnished, and GF-coated samples.

2. Materials and Methods

2.1. Sample Preparation

Three CNP coatings were the subject of this study (namely, GF, CNT, and CNH). The GF (Alfa Aesar GmbH, Kandel, Germany) have a median size between 7 and 10 μm a

carbon purity of 99.8%. The CNT used were chemical vapor deposition-grown multi-walled CNT (Graphene Supermarket, New York, NY, USA). The as-received CNT have a length ranging from 10 to 15 μm, an outer diameter distribution between 50 and 85 nm, and a carbon purity over 94%. Furthermore, the CNH used are single-walled, dahlia-type nanostructures (Carbonium SRL, Brescia, Italy). These particles were produced without a catalyst by rapid condensation of carbon atoms, resulting in high carbon purity. Horn diameters range from 3 to 5 nm, with horn lengths from 30 to 50 nm and cluster diameters from 60 to 120 nm.

The substrates and reference material were silver-plated copper surfaces. A focused ion beam (FIB) cross-section was conducted (FEI Helios NanoLab600 Dual Beam Setup, Hillsboro, OR, USA) to determine the plating thickness. The cross-section revealed an average silver plating thickness of 4 μm, as well as a nickel interlayer between the silver and copper base material (see Figure S1). Due to the thinness of the silver plating, the samples were neither ground nor polished to avoid the removal of the plating material. Vickers hardness of the substrate was measured using a microhardness tester (Dura Scan 50, Struers Inc., Cleveland, OH, USA). A total of 35 indentations were carried out using a load of approximately 2 N and a holding time of 15 s. The imprints were optically observed using a 40× objective, resulting in an average hardness of 1.33 ± 0.04 GPa.

Accelerated corrosion (sulfidation) of the silver surfaces was carried out using the methodology proposed by Huo et al. [38]. This method consists of subjecting the silver surfaces to a saturated atmosphere of sulfur vapor. This methodology ensures a well-controlled and repeatable sulfur-rich atmosphere, which promotes and accelerates the formation of the silver sulfide tarnishing film. Therefore, an oversupply of sulfur powder (8 g) was placed in a ceramic container within a beaker. The vessel was covered with a watch glass and heated to 150 °C, thus evaporating the sulfur and saturating the atmosphere within the vessel. Thereupon the silver samples were placed inside the sulfur-rich atmosphere for 10 min. After the accelerated tarnishing process, the samples present a highly heterogeneous silver sulfide layer (see Figure S2). To ensure reproducibility, all tarnished samples used in this study were sulfurized simultaneously. Therefore, the degree to which the samples were tarnished did not significantly differ, thus guaranteeing similar behavior regardless of the sample that was used.

EPD was carried out at a constant voltage of 300 V (potentiostatic process) with an inter-electrode distance of 15 mm. Prior to the deposition process, the CNP must be dispersed in isopropyl alcohol by homogenization and ultrasound [35,36]. Triethylamine ($C_6H_{15}N$) was added to the colloid prior to dispersion. The use of this additive enhances the stability of the colloidal dispersion as well as providing the CNP with a superficial charge through the attachment of functional groups (i.e., positive charge, anodic deposition). The colloid, dispersion, and deposition parameters for all four sample types are detailed in Table S1 [35]. The four resulting coatings are a 10 min GF coating, a 5 min CNT coating, a 10 min CNT coating, and a 10 min CNH coating (henceforth GF10, CNT5, CNT10, and CNH10, respectively). To ensure consistent results, a fresh dispersion was prepared prior to each coating process. Consequently, the CNP's concentration and dispersion quality of the colloid can also be considered constant. Although the use of other solvents (e.g., ethylene glycol) results in a more stable dispersion [39], isopropyl alcohol was chosen due to its lower viscosity. A solvent with lower viscosity will minimize viscous drag in the colloid, which will consequently minimize the CNP's resistance toward electrophoresis, thus improving the deposition rate. Moreover, the lower vapor pressure of isopropyl alcohol guarantees fast and efficient drying of the coated samples after removal from the colloid.

Prior to EPD and accelerated tarnishing, the silver platelets were chemically cleaned to remove any passivating elements that were added (e.g., octadecanethiol) as a final step in the manufacturing process. The cleaning process consists of reducing the silver sulfide layer formed during passivation [40,41]. Removing any potential passivation elements on the samples' surface ensures that maximum electrophoresis is achieved during EPD and that the accelerated tarnishing process is effective without requiring excessive exposure

times. After chemical cleaning, the samples were thoroughly rinsed with deionized water, followed by ultrasonication in isopropyl alcohol for 5 min, thus removing potential residue from the cleaning process.

2.2. Characterization Techniques

The substrate, tarnished, and coated samples were micrographed via CLSM (OLS4100, Olympus, Tokyo, Japan). CLSM micrographs were acquired using 20× and 50× magnification and a laser wavelength of 405 nm. These micrographs were used to analyze the roughness of the samples (shown in Table 1) and coating thicknesses (shown in Table 2), as well as to qualitatively evaluate fretting marks on both electrodes. Furthermore, fretting marks were also micrographed via SEM (Helios^{TM} G4 PFIB CXe DualBeam^{TM} Super FIB/SEM equipped with an energy dispersive X-ray spectroscopy detector EDAX Octane Elite Super, Thermo-Fisher Scientific, Eindhoven, The Netherlands) using ion conversion and electron (ICE) detector with an acceleration voltage of 5 kV. The same instrument was used to carry out chemical composition maps of the wear marks via EDS at an acceleration voltage of 15 kV. With this technique, a qualitative analysis of material transfer can be conducted. Furthermore, it can be used to determine if the wear resulting from the fretting tests was severe enough to reach the copper base material.

Table 1. Root mean squared roughness of samples, measured using CLSM.

Surface	Roughness/µm
Reference	0.26 ± 0.03
Tarnished	0.40 ± 0.04
GF10	1.40 ± 0.12
CNT5	0.91 ± 0.16
CNT10	0.62 ± 0.02
CNH10	0.51 ± 0.01

As the results from Table 2 show, the resulting coating thicknesses are relatively thin. Previous studies evaluating CNP-coated copper substrates using the same deposition technique produced considerably thicker coatings [35,37,42,43]. It was hypothesized that residue left behind by the chemical cleaning process might affect the conductivity of the silver samples, thus reducing the deposition rate of CNP onto their surfaces. To rule this possibility out, an as-received silver sample was coated—without prior cleaning—using the same parameters. The resulting coating thickness measured coincided with the samples that were chemically cleaned. The high roughness present in the silver samples could also play a role in the thinness of the coatings (260 nm against 10–20 nm in mirror-polished copper) since the electric field generated during EPD is concentrated at the asperities. The field's concentration can thus disrupt and diminish the deposition rate of the CNP. However, this is unlikely to be the cause since it has been previously studied and reported that EPD has the capability to coat geometrically complex surfaces [44–46].

Table 2. Coating thicknesses measured via CLSM.

Coating	Thickness/µm
GF10	0.34 ± 0.10
CNT5	0.14 ± 0.04
CNT10	0.41 ± 0.05
CNH10	0.32 ± 0.08

Wetting behavior was characterized by measuring the contact angle (CA) via sessile drop test using a drop shape analyzer (Krüss—DSA100B, Hamburg, Germany). A 3 µL droplet of deionized water and potassium sulfide (K_2S) was placed onto the surfaces via a pipette. The volume of 3 µL suppresses gravitation distortion of the droplet's shape

and, at the same time, covers a sufficiently large area on the sample's surface to even out topographical or chemical inhomogeneities [47,48]. The potassium sulfide solution consists of dissolving the compound in deionized water at a concentration of 3 wt.% at 23 °C (according to factory standard LK2070). Once each droplet was settled onto the sample's surface, the CA was recorded by fitting its contour using an elliptical shape within the ADVANCE Software (version 1.14.3, Krüss, Germany). At least two droplets were measured per sample, measuring CA after 10, 30, 60, and 300 s. Measuring at different time intervals provides insight into the dynamic, time-resolved wetting performance of the surfaces in question and its reliance on the liquid media used during sessile drop test. All CA measurements were carried out at temperatures and humidity ranging from 19–20 °C and 24–26% RH, respectively.

Tribo-electrical characterization of the reference, tarnished, and CNP-coated samples was conducted using a custom testing rig [49]. Characterization was divided into two experimental methodologies: i.e., load-dependent ECR and ECR evolution during fretting test. Load-dependent ECR consisted of one loading and unloading cycle sourcing 100 mA_{DC} and measuring voltage drop between the electrodes (loading cycle: 0.5, 1, 2, 3, 4, 5, 6, 7, 8, 9, 10 N). This current level was chosen so that the measurement process does not cause microstructural modification of the contacting surfaces, thus affecting subsequent measurements (i.e., dry circuit conditions) [50]. In this loading range, a maximum Hertzian contact pressure of 230 and 623 MPa were achieved for 0.5 and 10 N, respectively. These values were determined using Hertzian contact theory for sphere-on-plane contact [51,52]. Fretting tests were carried out at a load of 1 N (maximum Hertzian contact pressure of 289 MPa), with an amplitude of 35 µm and an oscillation frequency of 8 Hz. A total of 5000 fretting cycles were conducted with periodic galvanostatic (100 mA_{DC}) ECR measurements carried out every 100 cycles (static ECR). All tribo-electrical tests were carried out using a Keithley 2400 source and a Keithley 2182a nanovoltmeter with a range of 0.1 V (Cleveland, OH, USA). In all cases, the voltage drop was recorded ten times and averaged, with each test being repeated at least three times to ensure reproducibility. Tribo-electrical characterization was conducted under ambient conditions, i.e., 21 ± 1 °C and 35 ± 5% RH. Since humidity plays an important role in the conductivity of CNT [44,53–56], all electrical measurements for each coating type were conducted on the same day. Therefore, errors in the measurements due to changes in atmospheric conditions were minimized.

The counter electrodes used for tribo-electrical characterization are silver-nickel core ($AgNi_{0.15}$) and hard-gold-coated ($AuCo_{0.2}$) rivets (Adam Bornbaum GmbH, Neuhausen, Germany). The hard-gold coating has an average thickness of 6.47 ± 0.18 µm. The rivets have a hemispherical head, with a mean radius of curvature at its tip of 4 mm, a root mean squared roughness of 0.26 µm (measured via CLSM), and a hardness of 1.38 ± 0.01 GPa (measured via Vickers microhardness). A new rivet was used for each measurement.

3. Results and Discussion

3.1. Load-Dependent ECR

Electrical characterization is an important component when considering coatings for electrical contacts since these layers play a pivotal role in the conductivity and overall efficiency of the connector. A key aspect that can be tailored during connector design is the contact load. Therefore, load-dependent ECR curves of the materials used provide crucial information for connector and connector housing design. The ECR curves for the reference, tarnished, and coated samples are shown in Figure 1. Immediately, it is clear that the tarnished sample stands out from the reference and coated samples. Throughout the loading range, the tarnished sample consistently shows ECR values above 20 mΩ, whereas the reference and coated samples show ECR values between 11 and 20 mΩ. It is interesting to highlight the variability in the ECR of the tarnished sample in the loading semi-cycle, whereas the ECR values are constant in the unloading semi-cycle. Between 0.5 N and 2 N, there is a sharp reduction in ECR. This is due to the puncturing of the silver sulfide tarnishing film by the counter electrode's asperities [41,57]. However, as loads gradually

increase (above 2 N), so does the ECR. The counter electrode's geometry plays a role in this observation. As the load increases, the apparent contact diameter increases on account of the hemispherical shape of the rivets used. As the apparent contact area increases, so do the contacting sites between the counter electrode and the less-conductive (semi-conductive) tarnishing film, increasing the quasi-metallic contact [57,58]. The newly formed quasi-metallic contacts between the rivet's lower asperities and the tarnished sample increase the predominance of the film resistance, thus playing a more crucial role in the overall electrical resistance of the system. For sufficiently high loads (from 4 N), however, the resistance of the film takes a less dominant role due to the puncturing of the film and well-established metallic contact between the counter electrode and the silver surface beneath the silver sulfide film. This results in the constant ECR measured from 4 N (in the loading semi-cycle) until the end of the measurement cycle. This behavior in the tarnished sample is solely caused by the puncturing of the tarnishing film since the sharp reduction in ECR is characteristic of this sample, with the clean silver sample not presenting this behavior. In other words, the asperities in contact with the silver sulfide film undergo additional constriction of the current, which is eased as the film is punctured by the individual asperities (between 0.5 and 2 N). The additional constriction of the current is a consequence of the higher resistivity of the tarnishing film compared with the resistivity of the bulk material. Between 2 N and 4 N, new quasi-metallic contacts are established between lower asperities and the tarnishing film, once again increasing constriction resistance's dominance in the system. For loads above 4 N, most of the asperities have punctured the film, resulting in lower constriction resistance due to the current flowing from the counter electrode's asperities toward the silver bulk material. Moreover, the current level used to measure ECR is sufficiently high to overcome the loss of ohmicity produced by not only the tarnishing film but also other contaminant films and the CNP coatings (current-dependent ECR curves shown in Figure S3).

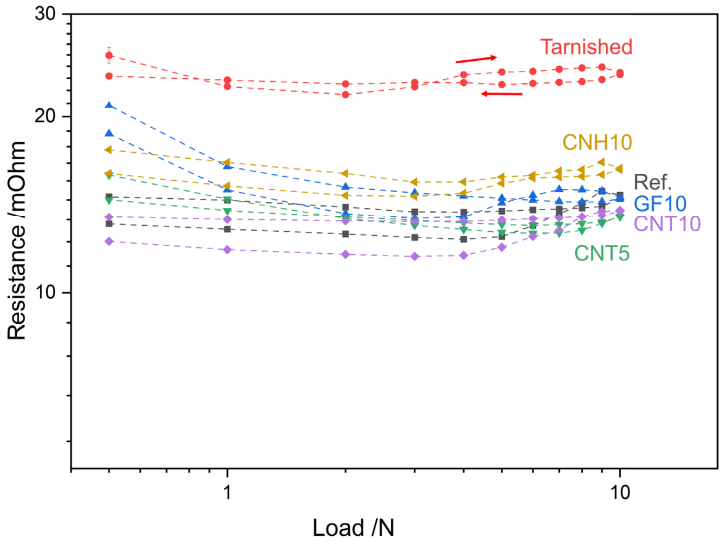

Figure 1. Load-dependent ECR of reference, tarnished, and coated samples. The arrows indicate the direction in which the loading and unloading semi-cycles progress.

The CNH coating shows the highest resistance among the coated samples, with the only exception being the GF coating at low loads. However, at 10 N, the ECR of CNH10 is only 2 mΩ higher than the reference sample at the same load. Therefore, the CNH coating does not significantly impact the electrical performance of the silver substrate. Nonetheless, the CNH coating is considerably thin (approximately 0.32 µm). Moreover, the CNH coating shows the most similarity in terms of ECR values between loading and unloading semi-cycle. This is due to the high elasticity of the coating, thus showing low electrical hysteresis. In this regard, the use of CNH coatings for electrical contacts could

promote reproducible contact areas irrespective of the normal load applied while also mitigating topographic factors [48]. The high elasticity observed in CNH coatings is due to two factors: (1) the nanoparticles' morphology and (2) the microporous network obtained by EPD. The former allows the CNT-like horns to deform inward from tip to base when undergoing compressive stress, thus enabling this nanostructure to return to its original shape after removing the compressive load (elastic restitution) [59]. This characteristic of the CNH justifies the low electrical hysteresis observed. The latter is a characteristic of the coatings obtained. The CNH coatings do not present large voids (as is the case with other CNP coatings) but rather a complex microporous network (see coating cross-section in [35]). This allows the voids to be rapidly closed during compaction with minimal CNH readjustment required, thus explaining the relatively constant ECR values measured during loading and unloading.

GF produces the thickest CNP coating; nonetheless, the resistance values are not severely impacted by the coating for loads above 1 N. Although the ECR values for the GF-coated sample are higher than the reference, the ECR coincide at 9 and 10 N. The CNT-coated samples, on the other hand, show exceptional electrical performance. The thinner CNT coating shows marginally higher ECR values than the reference sample; however, past 5 N CNT5 shows lower ECR. The thicker CNT coating outperformed the reference sample for the entire loading range, highlighting the promising potential of this coating type. The improved performance can be explained by two aspects: (1) the conductivity and (2) the elasticity of the CNT. These two aspects combined increase the real contact area between the counter electrode and the sample. The increased conductivity of the nanotubes, in conjunction with their elasticity, enables more pathways for electron motion between the two electrodes. In other words, although the apparent contact area may be the same, the highly elastic CNT coating increases the real contact area between the electrodes, thus reducing the ECR. Since CNT5 is thinner than CNT10, this phenomenon does not occur initially, thus requiring higher loads to establish an adequate electrical contact between the nanotubes and the counter electrode. Furthermore, the CNT tend to adhere to the counter electrode after loading, which also promotes lower electrical hysteresis and overall ECR (CLSM micrographs of counter electrodes post-ECR are shown in Figure S4).

3.2. ECR Evolution during Fretting Test

Tribo-electrical characterization aims to determine the effectiveness of the proposed coatings at reducing wear with negligible influence on ECR. Consequently, tracking the evolution of ECR as fretting cycles progress is of utmost importance. The results are shown in Figure 2. The plot depicts that irrespective of the sample type, all samples showed higher ECR initially and a slight reduction as fretting cycles progressed. However, this was to be expected since prior to fretting, the ECR is a combination of the film resistance (contaminant film, tarnishing film, or the coating itself), constriction resistance, and bulk material resistance. After the fretting test begins, contaminant films are constantly being broken down. Therefore, the resistance after the initial fretting cycles is primarily due to constriction resistance and the bulk material's resistance. Particularly in the case of the coated samples, the CNP are displaced due to the fretting motion, which reduces the amount of CNP present at the contacting site, thus marginally reducing ECR [42,43]. It is noteworthy to highlight, however, that the ECR values after the first few hundred fretting cycles are highly stable for all samples. In other words, there are no abrupt fluctuations in ECR due to fretting. This could be related to the fact that silver and gold do not form oxide films (as opposed to other metals, e.g., copper). It could also be related to the generation of a stable conductive carbonaceous tribofilm, which stabilizes the interface. Figure 2 exhibits that two distinct groupings took place. Namely, the tarnished and GF-coated samples present higher ECR during fretting than the reference, CNT, and CNH-coated samples. As was the case with load-dependent ECR (Figure 1), both CNT coatings outperformed the reference sample. CNT5 initially has a slightly higher ECR than the reference sample. However, after the first one hundred fretting cycles, it quickly falls below the values

observed in the reference sample. CNT10, on the other hand, has a lower ECR throughout the measurement. The CNH coating, nonetheless, also outperformed the reference sample during fretting tests with an electrical performance similar to that of CNT5, albeit this could be caused by the heterogeneous nature of the EPD coatings and should not be over-interpreted.

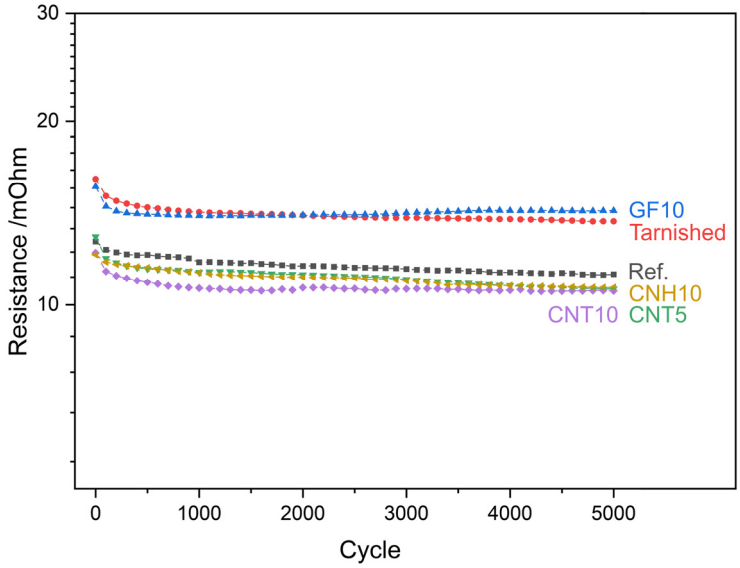

Figure 2. Evolution of ECR as fretting cycles progress of reference, tarnished, and coated samples. Note: error in all ECR measurements below ±0.2 mΩ.

Post-fretting micrographs of the marks left behind on the samples and counter electrodes are shown in Figure 3. In the reference sample, a considerable amount of material was transferred from the counter electrode toward the sample (Figure 3a), whereas marginal amounts of silver were transferred toward the counter electrode (Figure 3b). Silver debris is found primarily in the perimeter of the fretting marks and, to a minor extent, within the gross slip regions in the center of the fretting mark [60]. Gold is only observed adhered onto the sample's surface without gold debris surrounding the fretting marks. Bidirectional material transfer was expected during wear tests since the silver sample and the hard-gold counter electrode have similar hardness values (less than 10% difference—1.33 and 1.38 GPa, respectively) [60]. The tarnished sample fretting mark (Figure 3c,d) strongly contrasts the wear track observed in the reference sample. Although both fretting marks are approximately the same size, the mark on the tarnished sample does not have adhered gold. Furthermore, the counter electrode that contacted the tarnished sample shows minimal silver debris particles. The lack of material transfer can be explained by the lubricating capacity of the silver sulfide tarnishing film, albeit the lubricating capacity of the tarnishing film does not significantly reduce worn area [41]. Nonetheless, the presence of the tarnishing film strongly reduces gross slip, with both the sample and the counter electrode showing minimal wear. Furthermore, black particles observed in the counter electrode are silver sulfide particles that adhered during tribological testing.

The micrographs of the GF-coated sample (Figure 3e,f) depict that considerable gross slip took place in the central region of the fretting mark (in both the sample and the counter electrode). This is likely due to the ease of GF displacement and the detachment of the GF coating. Nonetheless, as shown in Figure 3f, large amounts of detached GF particles adhered to the counter electrode (lower-right region of the fretting mark in Figure 3e,f). Consequently, minimal amounts of GF remain within the fretting mark, therefore reducing this coating's capacity to reduce wear. CNT and CNH-coated samples' fretting marks (Figure 3g–i) highly contrast with GF-coated samples. These coatings do not show significant displacement or detachment. Consequently, after 5000 fretting cycles, there are regions

within the fretting marks that still have CNP which provide protection from wear (regions highlighted by cyan ovals in CLSM micrographs). Consequently, the CNPs within the fretting mark protect from wear, as proven by the enclosed region in the counter electrodes (i.e., regions where partial slip or no damage took place). Moreover, traces of CNT and CNH adhered to the counter electrode, further promoting wear protection. However, the amounts of transferred CNT and CNH are negligible compared to the quantity of GF that was transferred.

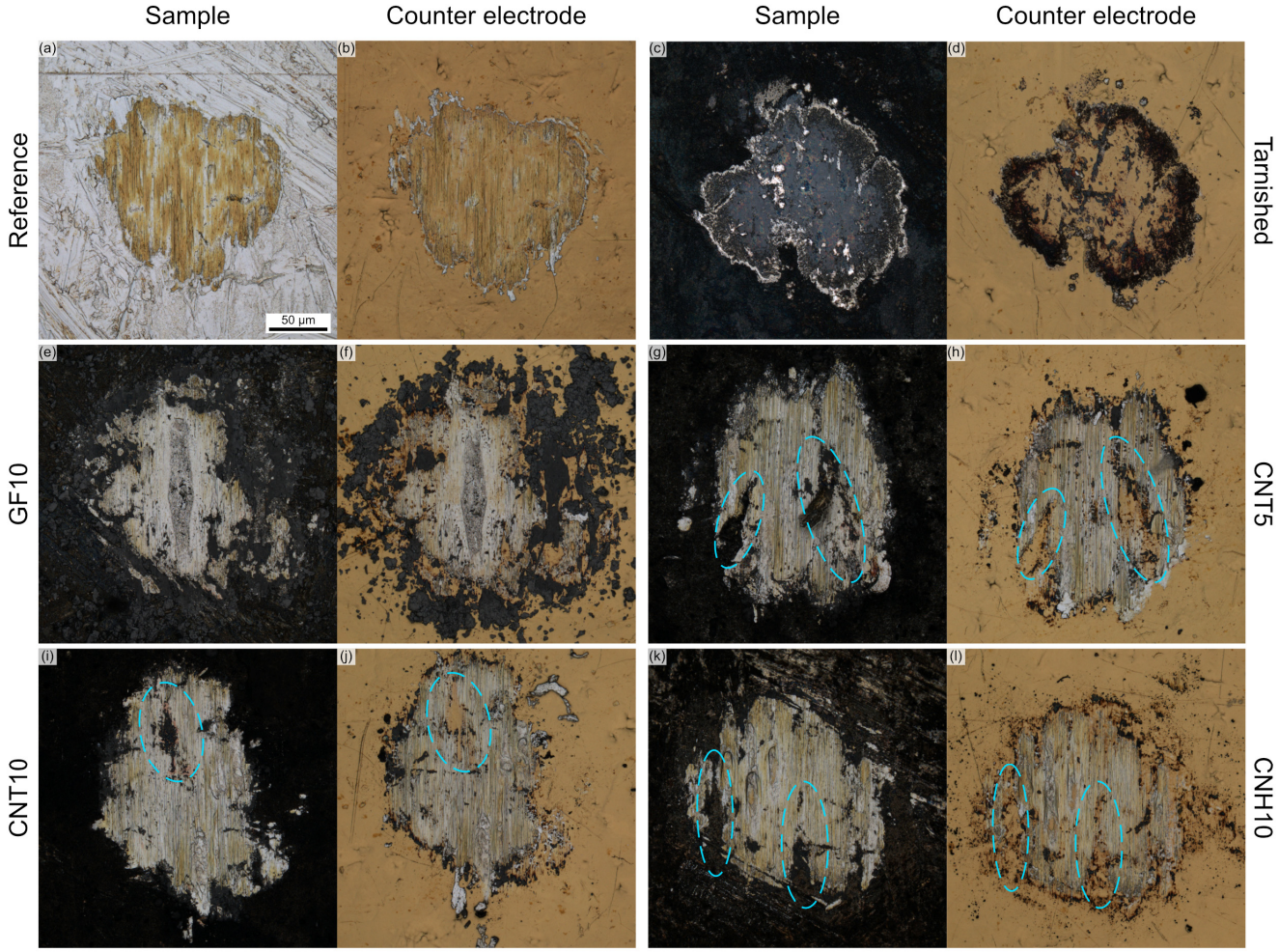

Figure 3. CLSM micrograph after 5000 fretting cycles of reference (**a**) sample and (**b**) counter electrode, tarnished (**c**) sample and (**d**) counter electrode, GF10 (**e**) sample and (**f**) counter electrode, CNT5 (**g**) sample and (**h**) counter electrode, CNT10 (**i**) sample and (**j**) counter electrode, and CNH10 (**k**) sample and (**l**) counter electrode. Cyan dashed line highlights regions in the sample where CNP remain within the fretting mark and their corresponding region in the counter electrode where only partial slip took place rather than gross slip.

A key distinction between the reference sample and the CNP-coated samples is the permutation of the dominant transfer electrode. In other words, the former shows that gold was predominantly transferred from the counter electrode toward the silver sample, whereas the latter shows that silver was predominantly transferred from the sample toward the counter electrode. Silver was not transferred in the form of debris (there are minimal amounts of silver debris present in the CNP-coated samples), but rather, silver adhered to the gold counter electrode. The material transfer observed during fretting is caused by adhesive wear, in other words, cold welding. After initial wear, contaminant films are removed from both surfaces (silver and gold). As fretting cycles progress, the elimination of the contaminant films enables the adhesion of the two metals [61]. However, the presence

of carbon in the coated samples reduces the microscopic temperature of the asperities in the silver sample due to the outstanding thermal conductivity of the CNP. Furthermore, the carbon coating effectively separates the two contacting surfaces, reducing the likelihood of metal-metal contact but rather generating a contacting site constituted of metal-carbon-metal. Therefore, it is reasonable to infer that the permutation of the deposition electrode is caused by the increased temperature in the counter electrode and a consequent reduction on the silver surfaces. This hypothesis is further supported by the lack of material transfer observed in the tarnished sample (Figure 3c,d). Since the silver sulfide tarnishing film lubricates the contact site, gold adhesion did not take place in the silver sample, whereas small silver debris particles can be seen in the counter electrode's micrographs surrounding the fretting mark.

To further analyze the mechanism behind material transfer, EDS mappings were carried out. The EDS maps are shown in Figure 4, with the corresponding secondary electron micrograph shown in Figure S5 and the sulfur EDS map of the tarnished sample shown in Figure S6. The EDS maps confirm that gold was transferred from the counter electrode towards the CNP-coated silver samples. Although EDS is a qualitative technique, it is accurate to state that the presence of the CNP coatings reduces the amount of gold transferred onto the samples due to the lack of gold signal detected within the fretting marks in spots where carbon and/or silver signals are stronger. Furthermore, the EDS maps of the tarnished sample (Figure 4b) also confirm that the lubricating capacity of the silver sulfide layer prevents the adhesion of gold. Moreover, the EDS maps prove that after 5000 fretting cycles, the base material was not reached in any of the samples analyzed. Although copper was detected within the fretting mark in the CNT5 sample (Figure 4d), the areas enclosed by the white dashed lines showcase that the plating material's thickness throughout the samples is heterogeneous. Consequently, there are regions (unaffected by fretting wear) where the copper base material was detected via EDS. Therefore, the copper detected within the fretting mark in CNT5 cannot be attributed to a lack of wear protection from the coating but rather heterogeneity in the plating process.

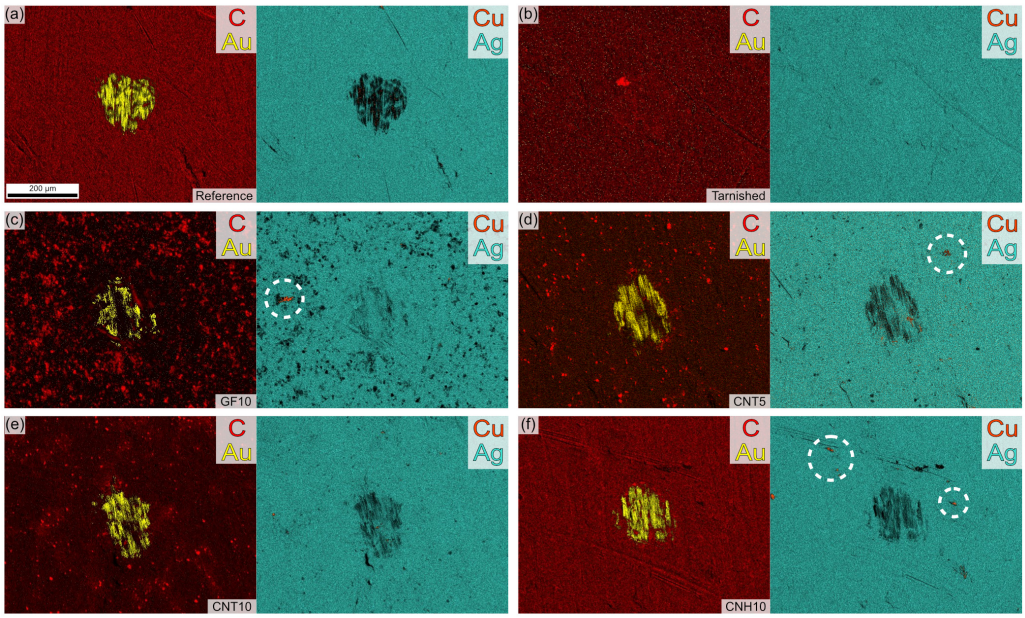

Figure 4. EDS elemental maps of (**a**) reference, (**b**) tarnished, (**c**) GF10, (**d**) CNT5, (**e**) CNT10, and (**f**) CNH10 samples. The left image shows an overlay of carbon (red) and gold (yellow), whereas the right image shows an overlay of silver (turquoise) and copper (orange). The regions enclosed by the dashed lines are regions unaffected by fretting wear where the copper base material was detected.

3.3. Wetting Behavior

Water contact angle measurements were carried out to evaluate the wetting behavior of the reference, tarnished, and CNP-coated surfaces (Figure 5). All surfaces show a hydrophobic wetting behavior within five minutes of placing the water droplet. Nonetheless, the reference sample shows a marginally hydrophobic behavior, with stable CA values of approximately 100° within the first minute. After five minutes, however, the CA decreases to approximately 92°, thus showing borderline hydrophobicity. The tarnished sample initially shows a higher CA; however, the value quickly decreases as time passes, reaching 90° after five minutes. GF and CNT show a strong hydrophobic behavior, approaching superhydrophobic wetting behavior after prolonged droplet exposure. CNH also shows high CA values; however, its performance does not reach as high CA as GF and CNT. The slightly stronger affinity toward water from CNH can be caused by the particle's morphology. Due to the dahlia-type nanostructures, the nanohorns have a strong strain-induced curvature, which delocalizes the high mobility π orbitals, thus increasing this nanostructure's reactivity and consequently affecting its wetting behavior [62]. Nonetheless, CNH coatings produced via EPD generate a coating with a complex microporous network [35]. Therefore, despite the reactivity of the CNH, coating morphology prevents the penetration of the water droplet, consequently producing a surface-droplet interface that resembles a Cassie-Baxter wetting state. Based on a previous study, thicker CNH coatings do not significantly impact its wetting behavior [43]. Therefore, even for thin CNH coatings, the microporous network is quickly established and is effective at preventing droplet infiltration.

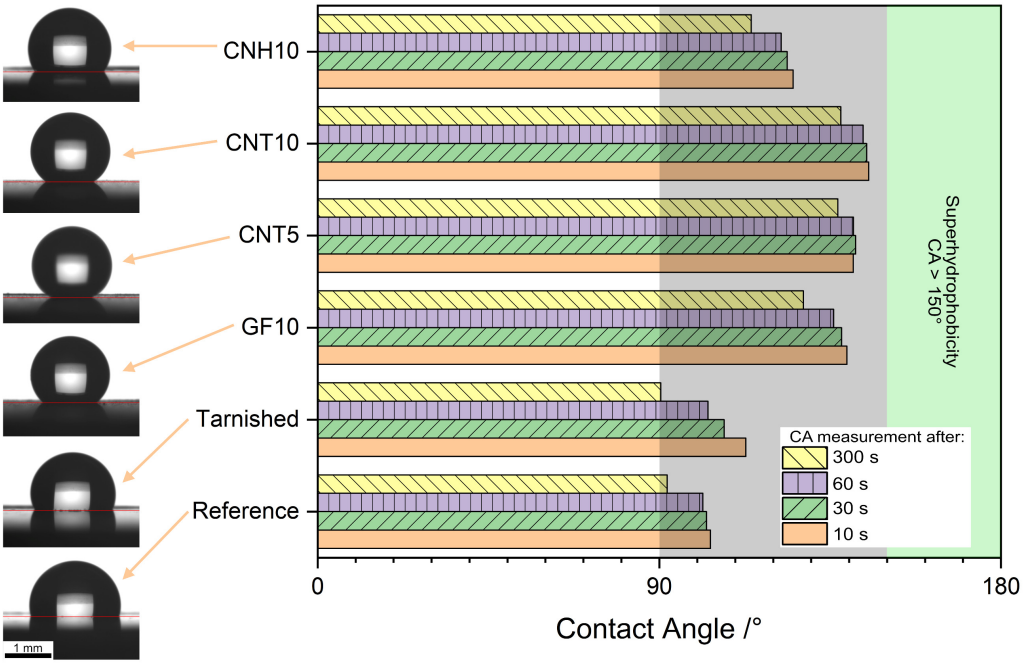

Figure 5. Water contact angle measurements 10 s (orange), 30 s (green), 60 s (violet), and 300 s (yellow) after placing the droplets onto the surfaces. To the left, the macrographs of a droplet on each surface and the baseline (red) are shown. The shaded regions highlight the surfaces with hydrophobic (gray) and superhydrophobic (green) wetting behavior.

GF shows near-superhydrophobic wetting behavior; however, after five minutes, the CA decreases by approximately 10°. This reduction indicates that the water droplet is slowly infiltrating the coating, primarily due to pores on the surface of the coating. Notwithstanding, the complexity of the porous network within the coating retains the hydrophobic wetting behavior of the GF-coated surface, resembling the performance observed for the CNH-coated surface. On the other hand, both CNT coatings show, to a certain extent, stable

CA values within the timeframe evaluated. After five minutes of setting the droplet onto the CNT surfaces, the CA decreases by approximately 5° as opposed to over 10° in the GF- and CNH-coated surfaces. This performance highlights the hydrophobic nature of the nanotubes, with thicker coatings showing a tendency toward marginally higher CA. Therefore, prolonging the deposition process (and thus obtaining a thicker coating) could promote super-hydrophobicity in the CNT-coated surfaces. Moreover, a smoother substrate could further increase the CA, improving hydrophobicity [63]. Additionally, Korczeniewski et al. previously reported that larger CNT agglomerate reduces CA, however, prolonging dispersion times (homogenization and ultrasound) negatively impacts the structure of the nanotubes [39,64]. The damage incurred by the CNT (in the form of dangling bonds, among other structural defects) could prove counterproductive by increasing the nanostructure's reactivity, thus reducing its CA.

Based on the wetting behavior observed with water droplets, it was of interest to evaluate the effectiveness of the coatings with a harsher medium (i.e., potassium sulfide). As was done with deionized water, 3 µL of the potassium sulfide solution was pipetted onto the six surfaces (CA results shown in Figure 6). However, the CNP-coated surfaces did not prevent the infiltration of the solution. The droplet rapidly penetrated the coatings and dispersed over the surfaces, producing CA below 40°. The GF showed an improved performance compared to the reference and tarnished samples. After 10 s, GF showed a CA of approximately 60°. However, the CA rapidly decreased to approximately 50° after 60 S and below 40° after 5 min. Nonetheless, this is a higher CA of 10–20° after five minutes of exposure to the highly aggressive potassium sulfide solution.

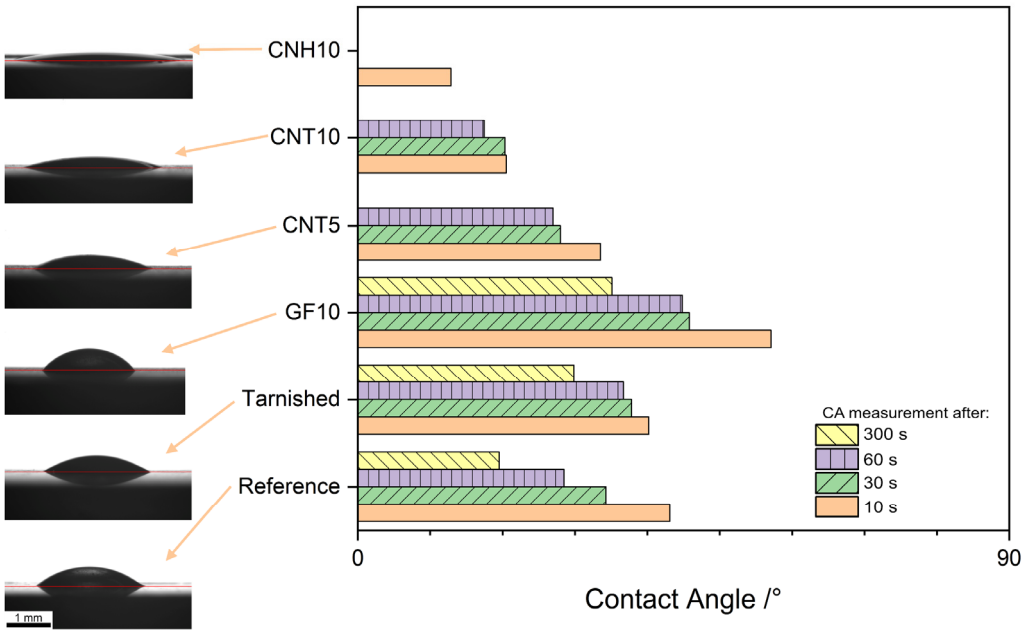

Figure 6. Contact angle measurements 10 s (orange), 30 s (green), 60 s (violet), and 300 s (yellow) after placing a 3 µL droplet of K_2S 3 wt.% solution onto the surfaces. To the left, the macrographs of a droplet on each surface and the baseline (red) are shown. Due to the hydrophilic wetting behavior, it was not possible to measure CA after 300 s in CNT5 and CNT10. Only CA after 10 s could be measured in CNH10.

Although the wetting results obtained when measuring CA with potassium sulfide do not suggest a favorable outcome, it should be noted that the solution is an extreme case used to analyze the potential protection offered by the carbon coatings. In other words, this is an accelerated method used to simulate prolonged exposure to sulfur-rich atmospheres. As previously studied, nanocarbon coatings show exceptional wetting behavior when measuring CA with other media than water (i.e., salt water) [43]. Therefore, the results

from the potassium sulfide tests should be used to fully dismiss the potential use cases of carbon coatings, particularly GF.

4. Conclusions

In this work, silver-plated electrical connectors were coated with CNT and CNH. The tribo-electrical and wetting performance of these coatings was compared to reference, tarnished (corroded), and GF-coated samples. Load-dependent electrical contact resistance proves that the presence of thin CNP films does not hinder the efficiency of the connectors. CNT-coated samples showed exceptional electrical performance, with similar ECR values to that of the reference sample throughout the entirety of the loading ranges analyzed. Although CNH and GF presented slightly higher ECR values than the reference, these two coatings did not increase the resistance as significantly as the corrosion film (silver sulfide tarnishing film). Likewise, the tarnished sample showed poor electrical performance during fretting wear tests. The tarnishing film, however, protects the silver surface from severe wear, minimizing adhesive wear and gross slip. The CNP-coated surfaces reduced material transfer during fretting while maintaining consistently low ECR. However, coating displacement hinders wear protection (primarily affecting GF coatings). Certain regions of the CNT and CNH-coated samples (and counter electrode) were protected from severe fretting wear due to the presence of these nanostructures within the contacting site after 5000 fretting cycles. Moreover, the CNP-coated surfaces exhibit a hydrophobic (near-superhydrophobic in the case of GF and CNT) wetting behavior in sessile drop tests measured using deionized water, outperforming the tarnished and reference samples. Prolonged water droplet exposures tend to decrease the CA measured; however, the reduction in CA for the CNT-coated samples is significantly lower than in the other surfaces studied. Moreover, the CA measurements with potassium sulfide indicated that although CNT and CNH do not offer significant protection, GF coatings did show higher CA than the reference and tarnished samples, even after five minutes of exposure. Nonetheless, it should be reiterated that the medium used (i.e., potassium sulfide) is extremely aggressive and was chosen based on the fact that this solution would simulate prolonged exposure to sulfur-rich atmospheres.

This study features the exceptional characteristics of nanocarbon coatings and their potential benefits for the electrical contact industry. However, further studies are required to improve on the aspects presented in this work. Namely, improving wear and atmospheric protection without impacting electrical performance. The former may be improved by evaluating different EPD additives that improve coating adhesion (e.g., magnesium nitrate), thus reducing coating displacement during wear tests. The latter, on the other hand, may benefit from chemical alterations of the CNP (e.g., CNP decoration), consequently tailoring the reactivity of the nanostructures for specific atmospheric conditions.

Supplementary Materials: The following supporting information can be downloaded at: https://www.mdpi.com/article/10.3390/c10010016/s1, Figure S1: FIB cross section of silver-plated copper electrical contact. The platinum layer was deposited using the SEM with the purpose of protecting the sample and to minimize the curtaining effect during ion milling; Figure S2: Silver sample (a) before and (b) after being subjected to sulfur-rich atmosphere. Highlighted regions show SEM micrographs of the surface before and after the accelerated tarnishing process; Table S1: Colloid, dispersion, and EPD parameters; Figure S3: Current-dependent ECR of references, tarnished, and coated samples; Figure S4: CLSM micrograph of counter electrodes after ECR measurements of (a) reference, (b) tarnished, (c) GF10, (d) CNT5, (e) CNT10, and (f) CNH10 sample; Figure S5: Secondary electron micrograph of fretting marks after 5000 cycles of (a) reference sample, (b) tarnished sample, (c) GF10, (d) CNT5, (e) CNT10, and (f) CNH10. Micrographs (a) and (b) were acquired at 15 kV due to the presence of surface contaminants, whereas the rest were acquired at 5 kV acceleration voltage; Figure S6: EDS map of the fretting mark after 5000 cycles in the tarnished sample showing the signal for sulfur.

Author Contributions: Conceptualization, B.A. and S.S.; Data curation, B.A.; Formal analysis, B.A.; Funding acquisition, F.M. and S.S.; Investigation, B.A.; Methodology, B.A. and S.S.; Project administration, F.M. and S.S.; Resources, F.M.; Supervision, S.S.; Validation, B.A.; Visualization, B.A.; Writing—original draft, B.A.; Writing—review and editing, S.S. All authors have read and agreed to the published version of the manuscript.

Funding: This research received no external funding.

Data Availability Statement: Data available upon reasonable request from the corresponding author.

Acknowledgments: B. Alderete wishes to acknowledge the support from the German Academic Exchange Service (DAAD) and the Roberto Rocca Education Program (RREP). The authors gratefully acknowledge funding in the ZuMat project, supported by the State of Saarland from the European Regional Development Fund (Europäischen Fonds für Regionale Entwicklung, EFRE). Funding for the PFIB/SEM instrument by the German Research Foundation is greatly acknowledged (INST 256/510-1 FUGG).

Conflicts of Interest: The authors declare no conflict of interest.

References

1. Outka, D.A.; Madix, R.J.; Fisher, G.B.; DiMaggio, C. Oxidation of Sulfur Dioxide on Silver (110): Vibrational Study of the Structure of Intermediate Complexes Formed. *J. Phys. Chem.* **1986**, *90*, 4051–4057. [CrossRef]
2. Bauer, R. Sulfide Corrosion of Silver Contacts during Satellite Storage. *J. Spacecr. Rocket.* **1988**, *25*, 439–440. [CrossRef]
3. Lilienfeld, S.; White, C.E. A Study of the Reaction between Hydrogen Sulfide and Silver. *J. Am. Chem. Soc.* **1930**, *52*, 885–892. [CrossRef]
4. Russ, G. Electrical Characteristics of Contacts Contaminated with Silver Sulfide Film. *IEEE Trans. Parts Mater. Packag.* **1970**, *6*, 129–137. [CrossRef]
5. Hindin, B.S. Silver Sulfide Corrosion Control Using Corrosion Prevention Compounds. In Proceedings of the CORROSION 2006, San Diego, CA, USA, 12–16 March 2006; p. NACE-06264.
6. Denaburg, C.R. Corrosion in Aerospace Electrical/Electronic Components in the Early Years of the Apollo Program, Kennedy Space Center, Florida. In Proceedings of the CORROSION 2000, Orlando, FL, USA, 26–31 March 2000; p. NACE-00718.
7. Schmitt, W.; Franz, S.; Heber, J.; Lutz, O.; Behrens, V. Formation of Silver Sulfide Layers and Their Influence on the Electrical Characteristics of Contacts in the Field of Information Technology. In Proceedings of the ICEC, Innsbruck, Austria, 19–22 August 2008; pp. 489–494.
8. Wagner, C. Investigations on Silver Sulfide. *J. Chem. Phys.* **1953**, *21*, 1819–1827. [CrossRef]
9. Hebb, M.H. Electrical Conductivity of Silver Sulfide. *J. Chem. Phys.* **1952**, *20*, 185–190. [CrossRef]
10. Sahraoui, K.; Benramdane, N.; Khadraoui, M.; Miloua, R.; Mathieu, C. Characterization of Silver Sulphide Thin Films Prepared by Spray Pyrolysis Using a New Precursor Silver Chloride. *Sens. Transducers* **2014**, *27*, 319–325.
11. Zhang, S.; Osterman, M.; Shrivastava, A.; Kang, R.; Pecht, M.G. The Influence of H2S Exposure on Immersion-Silver-Finished PCBs under Mixed-Flow Gas Testing. *IEEE Trans. Device Mater. Reliab.* **2010**, *10*, 71–81. [CrossRef]
12. Abbott, W.H. The Development and Performance Characteristics of Mixed Flowing Gas Test Environment. *IEEE Trans. Compon. Hybrids Manuf. Technol.* **1988**, *11*, 22–35. [CrossRef]
13. Ying, T. An Advanced Anti-Tarnish Process for Silver Coins and Silverware—Monomolecular Octadecanethiol Protective Film. *Tribol. Trans.* **2021**, *64*, 341–349. [CrossRef]
14. Liang, C.; Yang, C.; Huang, N. Tarnish Protection of Silver by Octadecanethiol Self-Assembled Monolayers Prepared in Aqueous Micellar Solution. *Surf. Coat. Technol.* **2009**, *203*, 1034–1044. [CrossRef]
15. Liang, C.H.; Yang, C.J.; Huang, N.B.; Wu, B. Comparison of Four Antitarnishing Self-Assembled Monolayers on Silver Coin. *Surf. Eng.* **2011**, *27*, 199–204. [CrossRef]
16. Phillips, A.C.; Cowley, A. Octadecanthiol for Tarnish-Resistant Silver Coatings. In Proceedings of the Modern Technologies in Space- and Ground-Based Telescopes and Instrumentation II, Amsterdam, The Netherlands, 1–6 July 2012; Navarro, R., Cunningham, C.R., Prieto, E., Eds.; Volume 8450, p. 84503W.
17. Planes, E.; Flandin, L.; Alberola, N. Polymer Composites Bipolar Plates for PEMFCs. *Energy Procedia* **2012**, *20*, 311–323. [CrossRef]
18. Saito, R.; Dresselhaus, G.; Dresselhaus, M.S. *Physical Properties of Carbon Nanotubes*; Imperial College Press: London, UK, 1998; ISBN 978-1-86094-093-4.
19. Dresselhaus, M.S.; Dresselhaus, G.; Saito, R. Physics of Carbon Nanotubes. *Carbon* **1995**, *33*, 883–891. [CrossRef]
20. Popov, V. Carbon Nanotubes: Properties and Application. *Mater. Sci. Eng. R Rep.* **2004**, *43*, 61–102. [CrossRef]
21. Ebbesen, T.W. Carbon Nanotubes. *Annu. Rev. Mater. Sci.* **1994**, *24*, 235–264. [CrossRef]
22. Nasir, S.; Hussein, M.; Zainal, Z.; Yusof, N. Carbon-Based Nanomaterials/Allotropes: A Glimpse of Their Synthesis, Properties and Some Applications. *Materials* **2018**, *11*, 295. [CrossRef] [PubMed]
23. Lee, C.-G.; Hwang, Y.-J.; Choi, Y.-M.; Lee, J.-K.; Choi, C.; Oh, J.-M. A Study on the Tribological Characteristics of Graphite Nano Lubricants. *Int. J. Precis. Eng. Manuf.* **2009**, *10*, 85–90. [CrossRef]

24. Zhang, Z.; Simionesie, D.; Schaschke, C. Graphite and Hybrid Nanomaterials as Lubricant Additives. *Lubricants* **2014**, *2*, 44–65. [CrossRef]
25. Cornelio, J.A.C.; Cuervo, P.A.; Hoyos-Palacio, L.M.; Lara-Romero, J.; Toro, A. Tribological Properties of Carbon Nanotubes as Lubricant Additive in Oil and Water for a Wheel–Rail System. *J. Mater. Res. Technol.* **2016**, *5*, 68–76. [CrossRef]
26. Dassenoy, F.; Joly-Pottuz, L.; Martin, J.M.; Mieno, T. Carbon Nanotubes as Advanced Lubricant Additives. In *Carbon Nanotubes*; Popov, V.N., Lambin, P., Eds.; Kluwer Academic Publishers: Dordrecht, The Netherlands, 2006; pp. 237–238.
27. Kałużny, J.; Merkisz-Guranowska, A.; Giersig, M.; Kempa, K. Lubricating Performance of Carbon Nanotubes in Internal Combustion Engines—Engine Test Results for CNT Enriched Oil. *Int. J. Automot. Technol.* **2017**, *18*, 1047–1059. [CrossRef]
28. Maharaj, D.; Bhushan, B.; Iijima, S. Effect of Carbon Nanohorns on Nanofriction and Wear Reduction in Dry and Liquid Environments. *J. Colloid. Interface Sci.* **2013**, *400*, 147–160. [CrossRef]
29. Sethi, S.; Dhinojwala, A. Superhydrophobic Conductive Carbon Nanotube Coatings for Steel. *Langmuir* **2009**, *25*, 4311–4313. [CrossRef]
30. Rahman, M.M.; Islam, M.; Roy, R.; Younis, H.; AlNahyan, M.; Younes, H. Carbon Nanomaterial-Based Lubricants: Review of Recent Developments. *Lubricants* **2022**, *10*, 281. [CrossRef]
31. De Nicola, F.; Castrucci, P.; Scarselli, M.; Nanni, F.; Cacciotti, I.; Crescenzi, M. De Super-Hydrophobic Multi-Walled Carbon Nanotube Coatings for Stainless Steel. *Nanotechnology* **2015**, *26*, 145701. [CrossRef] [PubMed]
32. Chen, X.; Li, J. Superlubricity of Carbon Nanostructures. *Carbon* **2020**, *158*, 1–23. [CrossRef]
33. Loyd, A.; Hemond, J.; Martens, R. A Preliminary Investigation of Graphite, Graphene and Carbon Nanotubes (CNT's) as Solid State Lubricants. In Proceedings of the 2011 IEEE 57th Holm Conference on Electrical Contacts (Holm), Minneapolis, MN, USA, 11–14 September 2011; IEEE: Piscataway, NJ, USA, 2011; pp. 1–9.
34. Reinert, L.; Varenberg, M.; Mücklich, F.; Suárez, S. Dry Friction and Wear of Self-Lubricating Carbon-Nanotube-Containing Surfaces. *Wear* **2018**, *406–407*, 33–42. [CrossRef]
35. Alderete, B.; Mücklich, F.; Suarez, S. Characterization and Electrical Analysis of Carbon-Based Solid Lubricant Coatings. *Carbon Trends* **2022**, *7*, 100156. [CrossRef]
36. Alderete, B.; MacLucas, T.; Espin, D.; Brühl, S.P.; Mücklich, F.; Suarez, S. Near Superhydrophobic Carbon Nanotube Coatings Obtained via Electrophoretic Deposition on Low-Alloy Steels. *Adv. Eng. Mater.* **2021**, *23*, 2001448. [CrossRef]
37. Alderete, B.; Lößlein, S.M.; Bucio Tejeda, D.; Mücklich, F.; Suarez, S. Feasibility of Carbon Nanoparticle Coatings as Protective Barriers for Copper—Wetting Assessment. *Langmuir* **2022**, *38*, 15209–15219. [CrossRef]
38. Huo, Y.; Fu, S.-W.; Chen, Y.-L.; Lee, C.C. A Reaction Study of Sulfur Vapor with Silver and Silver–Indium Solid Solution as a Tarnishing Test Method. *J. Mater. Sci. Mater. Electron.* **2016**, *27*, 10382–10392. [CrossRef]
39. Reinert, L.; Zeiger, M.; Suárez, S.; Presser, V.; Mücklich, F. Dispersion Analysis of Carbon Nanotubes, Carbon Onions, and Nanodiamonds for Their Application as Reinforcement Phase in Nickel Metal Matrix Composites. *RSC Adv.* **2015**, *5*, 95149–95159. [CrossRef]
40. Philadelphia Museum of Art Finishing Techniques in Metalwork—Hands-Free Silver "Polishing". Available online: https://www.philamuseum.org/booklets/7_44_85_1.html?page=2 (accessed on 18 January 2021).
41. Alderete, B.; Mücklich, F.; Suarez, S. Tarnishing (Ag2S) Layer on Silver-Plated Electrical Contacts: Its Influence on Electrical Contact Resistance. *IEEE Trans. Compon. Packag. Manuf. Technol.* **2023**, *13*, 45–58. [CrossRef]
42. Alderete, B.; Mücklich, F.; Suarez, S. Wear Reduction via CNT Coatings in Electrical Contacts Subjected to Fretting. *Tribol. Lett.* **2023**, *71*, 54. [CrossRef]
43. Alderete, B.; Suarez, S.; Tejeda, D.B.; Mücklich, F. Fretting and Electrical Contact Resistance Characteristics of Carbon Nanoparticle-Coated Cu Electrical Contacts. In Proceedings of the 2022 IEEE 67th Holm Conference on Electrical Contacts (HLM), Tampa, FL, USA, 23–26 October 2022; IEEE: Piscataway, NJ, USA, 2022; pp. 1–8.
44. Thomas, B.J.C.; Boccaccini, A.R.; Shaffer, M.S.P. Multi-Walled Carbon Nanotube Coatings Using Electrophoretic Deposition (EPD). *J. Am. Ceram. Soc.* **2005**, *88*, 980–982. [CrossRef]
45. Boccaccini, A.R.; Cho, J.; Roether, J.A.; Thomas, B.J.C.; Jane Minay, E.; Shaffer, M.S.P. Electrophoretic Deposition of Carbon Nanotubes. *Carbon* **2006**, *44*, 3149–3160. [CrossRef]
46. Alderete, B.; Nayak, U.P.; Mücklich, F.; Suarez, S. Influence of Topography on Electrical Contact Resistance of Copper-Based Materials. *Surf. Topogr.* **2023**, *11*, 025027. [CrossRef]
47. Vafaei, S.; Podowski, M.Z. Theoretical Analysis on the Effect of Liquid Droplet Geometry on Contact Angle. *Nucl. Eng. Des.* **2005**, *235*, 1293–1301. [CrossRef]
48. Krainer, S.; Hirn, U. Contact Angle Measurement on Porous Substrates: Effect of Liquid Absorption and Drop Size. *Colloids Surf. A Physicochem. Eng. Asp.* **2021**, *619*, 126503. [CrossRef]
49. Alderete, B.; Puyol, R.; Slawik, S.; Espin, E.; Mücklich, F.; Suarez, S. Multipurpose Setup Used to Characterize Tribo-Electrical Properties of Electrical Contact Materials. *MethodsX* **2021**, *8*, 101498. [CrossRef] [PubMed]
50. Bock, E.M. Low-Level Contact Resistance Characterization. *AMP J. Technol.* **1993**, *3*, 64–68.
51. Johnson, K.L. *Contact Mechanics*; Cambridge University Press: Cambridge, UK, 1987; ISBN 0521347963.
52. Callister, W.D., Jr. *Materials Science and Engineering: An Introduction*, 7th ed.; John Wiley & Sons, Ltd.: Hoboken, NJ, USA, 2006; Volume 94, ISBN 9780470054888.

53. Shooshtari, M.; Salehi, A.; Vollebregt, S. Effect of Humidity on Gas Sensing Performance of Carbon Nanotube Gas Sensors Operated at Room Temperature. *IEEE Sens. J.* **2021**, *21*, 5763–5770. [CrossRef]
54. Tsai, J.T.H.; Lu, C.-C.; Li, J.G. Fabrication of Humidity Sensors by Multi-Walled Carbon Nanotubes. *J. Exp. Nanosci.* **2010**, *5*, 302–309. [CrossRef]
55. Lee, Y.; Yoon, J.; Kim, Y.; Kim, D.M.; Kim, D.H.; Choi, S.-J. Humidity Effects According to the Type of Carbon Nanotubes. *IEEE Access* **2021**, *9*, 6810–6816. [CrossRef]
56. Ling, Y.; Gu, G.; Liu, R.; Lu, X.; Kayastha, V.; Jones, C.S.; Shih, W.-S.; Janzen, D.C. Investigation of the Humidity-Dependent Conductance of Single-Walled Carbon Nanotube Networks. *J. Appl. Phys.* **2013**, *113*, 024312. [CrossRef]
57. Holm, R. *Electric Contacts*, 4th ed.; Springer: Berlin/Heidelberg, Germany, 1967; ISBN 978-3-642-05708-3.
58. Endres, H. *Praxishandbuch Steckverbinder*, 2nd ed.; Vogel COmmunications Group: Würzburg, Germany, 2021; ISBN 978-3-8343-3501-2.
59. Karousis, N.; Suarez-Martinez, I.; Ewels, C.P.; Tagmatarchis, N. Structure, Properties, Functionalization, and Applications of Carbon Nanohorns. *Chem. Rev.* **2016**, *116*, 4850–4883. [CrossRef] [PubMed]
60. Slade, P.G. *Electrical Contacts*, 2nd ed.; Slade, P.G., Ed.; CRC Press: Boca Raton, FL, USA, 2014; ISBN 9781315216829.
61. Merstallinger, A.; Sales, M.; Semerad, E.; Dunn, B.D. Assessment of Cold Welding between Separable Contact Surfaces Due to Impact and Fretting under Vacuum. *ESA Sci. Tech. Memo.* **2009**, *279*, 57.
62. Haddon, R.C. Chemistry of the Fullerenes: The Manifestation of Strain in a Class of Continuous Aromatic Molecules. *Science* **1993**, *261*, 1545–1550. [CrossRef]
63. Korczeniewski, E.; Zięba, M.; Zięba, W.; Kolanowska, A.; Bolibok, P.; Kowalczyk, P.; Wiertel-Pochopień, A.; Zawała, J.; Boncel, S.; Terzyk, A.P. Electrophoretic Deposition of Layer-by-Layer Unsheathed Carbon Nanotubes—A Step Towards Steerable Surface Roughness and Wettability. *Materials* **2020**, *13*, 595. [CrossRef]
64. Hilding, J.; Grulke, E.A.; George Zhang, Z.; Lockwood, F. Dispersion of Carbon Nanotubes in Liquids. *J. Dispers. Sci. Technol.* **2003**, *24*, 1–41. [CrossRef]

C Journal of Carbon Research

MDPI

Supplementary Material

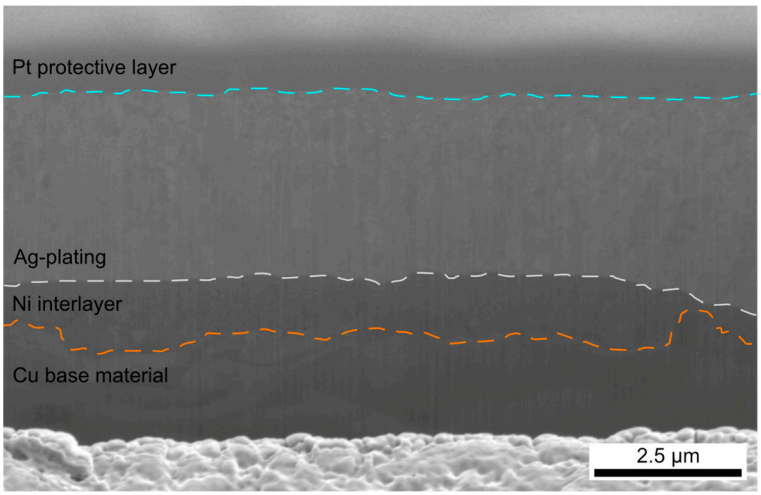

Figure S1. FIB cross section of silver-plated copper electrical contact. The platinum layer was deposited using the SEM with the purpose of protecting the sample and to minimize the curtaining effect during ion milling.

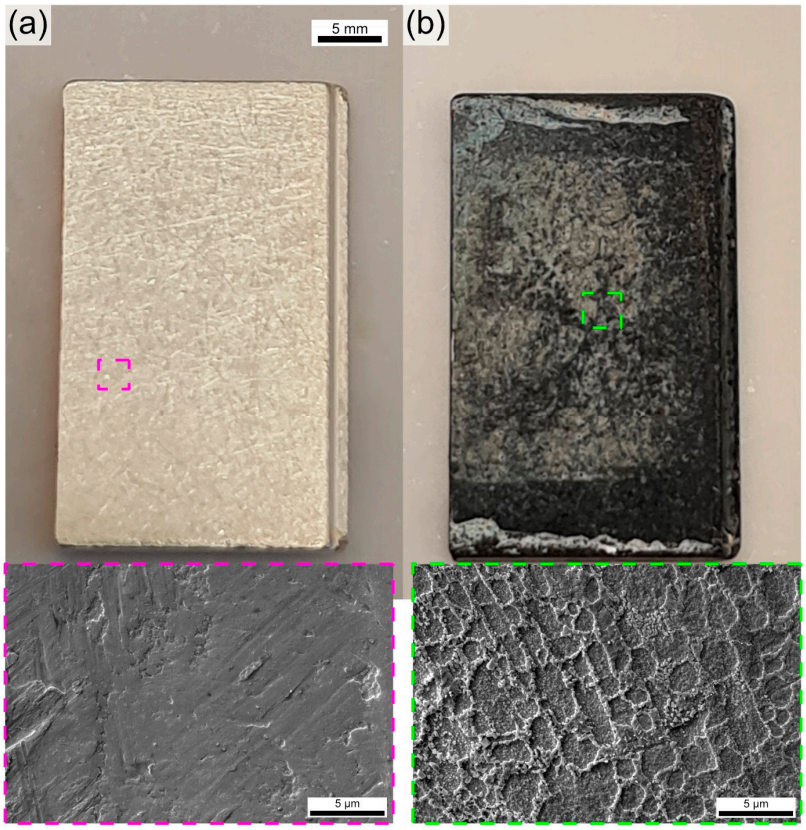

Figure S2. Silver sample **(a)** before and **(b)** after being subjected to sulfur-rich atmosphere. Highlighted regions show SEM micrographs of the surface before and after the accelerated tarnishing process.

Table S1. Colloid, dispersion, and EPD parameters.

	GF	CNT	CNH
Isopropyl alcohol volume /ml	0.2	0.2	0.05
CNP concentration /mg/ml	80	80	70
TEA volume /ml	10	5	5
Homogenization speed /rpm	7,000	7,000	12,000
Homogenization time /min	10	5	10
Ultrasound /min	10	10	015

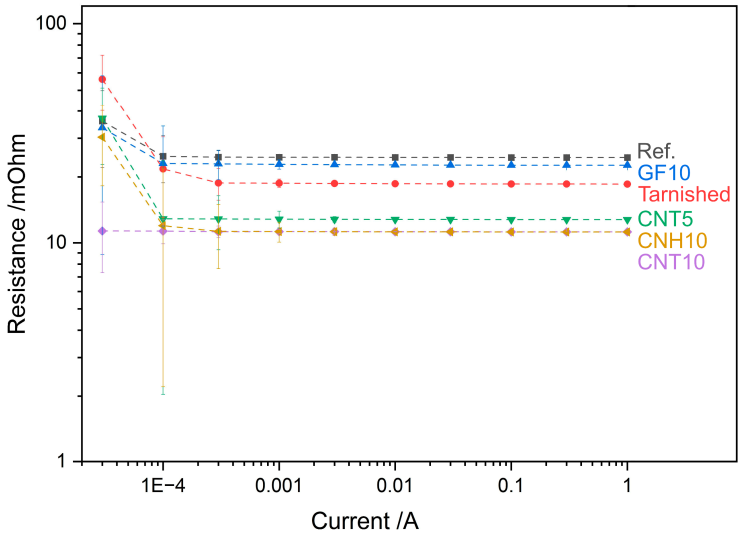

Figure S3. Current-dependent ECR of references, tarnished, and coated samples.

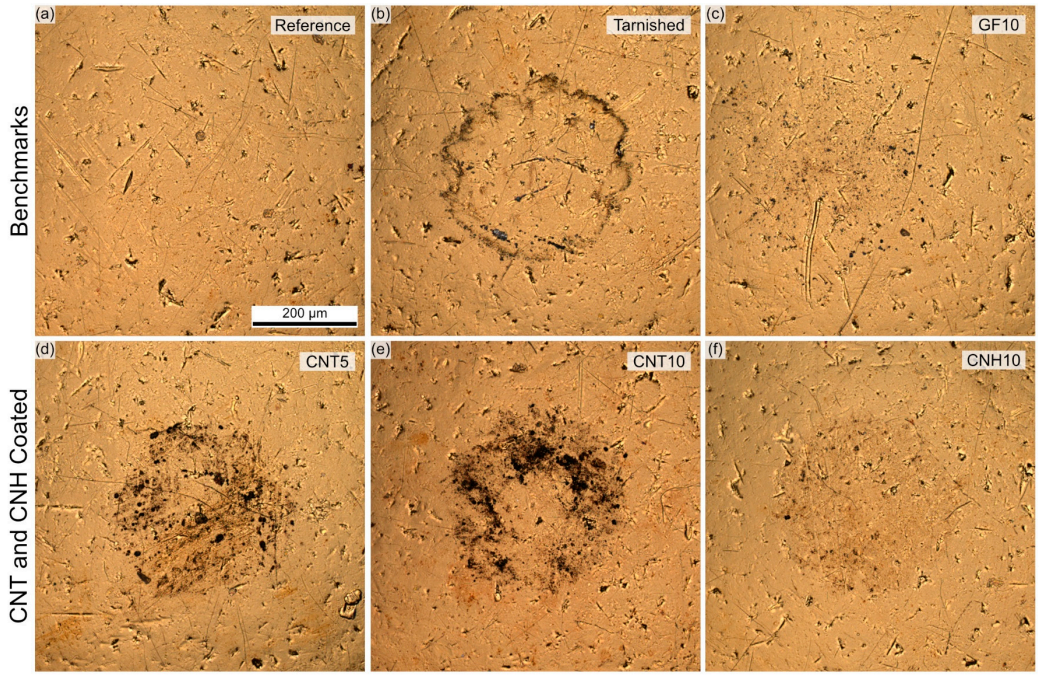

Figure S4. CLSM micrograph of counter electrodes after ECR measurements of **(a)** reference, **(b)** tarnished, **(c)** GF10, **(d)** CNT5, **(e)** CNT10, and **(f)** CNH10 sample.

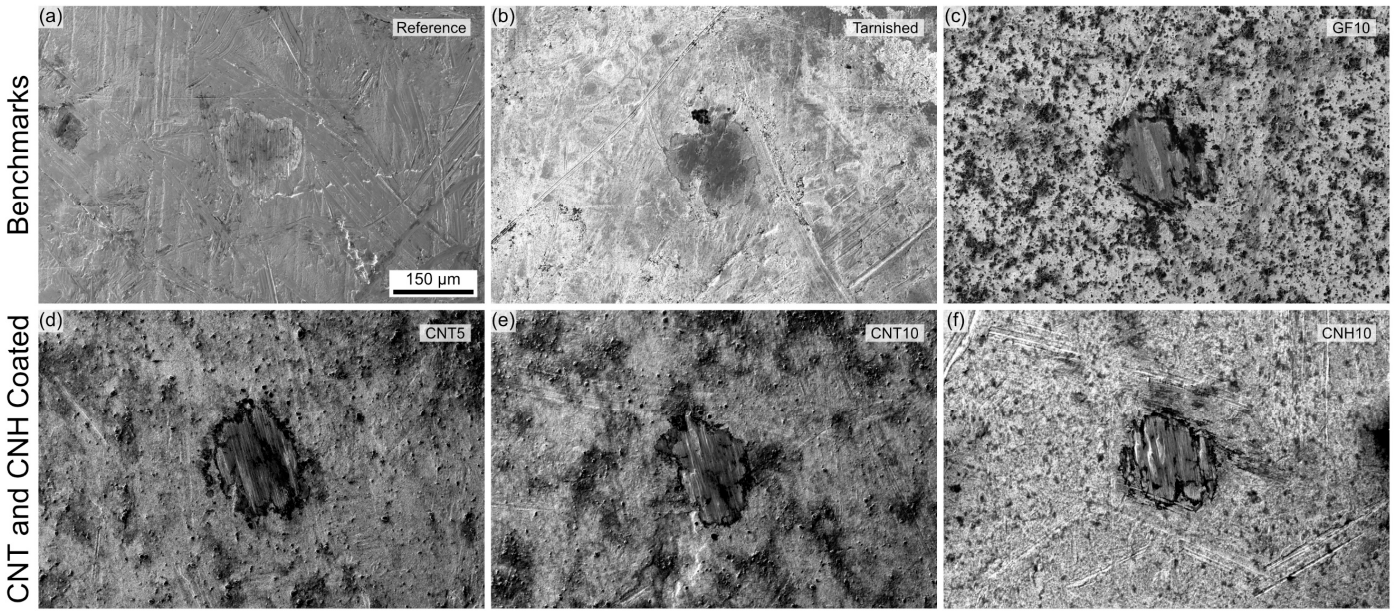

Figure S5. Secondary electron micrograph of fretting marks after 5,000 cycles of **(a)** reference sample, **(b)** tarnished sample, **(c)** GF10, **(d)** CNT5, **(e)** CNT10, and **(f)** CNH10. Micrographs **(a)** and **(b)** were acquired at 15 kV due to the presence of surface contaminants, whereas the rest were acquired at 5 kV acceleration voltage.

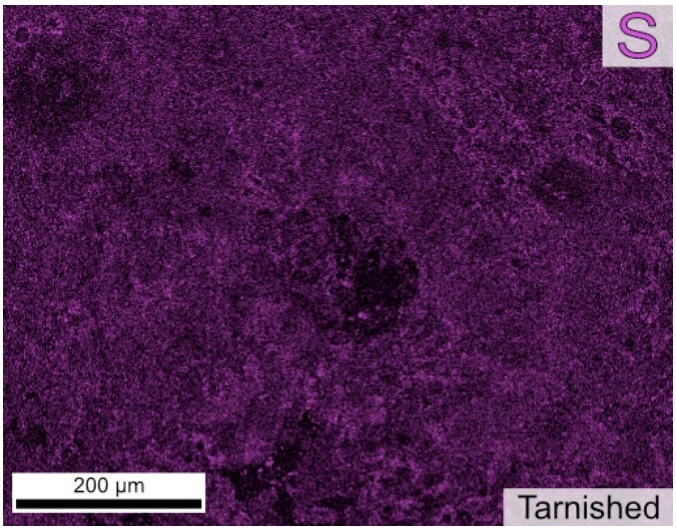

Figure S6. EDS map of the fretting mark after 5,000 cycles in the tarnished sample showing the signal for sulfur.

ARTICLE X
Load-Dependent Electrical Contact Resistance of Carbon Nanotube-Reinforced Metal matrix Composites

Sebastian Suarez[1,*], **Bruno Alderete**[1], Rafael Puyol[2], Frank Mücklich[1,3]

[1] Chair of Functional Materials, Saarland University, Campus D3.3, 66123 Saarbrücken, Germany
[2] ELEN, ICTEAM, UCLouvain, Place du Levant, 3 bte L5.03.02, 1348 Louvain-la-Neuve, Belgium
[3] Materials Engineering Center Saarland (MECS), Campus D3.3, 66123 Saarbrücken, Germany

Research article
Published in "*Proceedings of the 2022 IEEE 67th Holm Conference on Electrical Contacts (HLM)*" (2022)
Impact Factor: NA
Reproduced with permission from 'Institute of Electrical and Electronics Engineers - IEEE'
Accessible online at: doi.org/10.1109/HLM54538.2022.9969801

Own Contribution: Methodology; Validation; Data Curation; Writing – Original Draft.

Cite this article as: S. Suarez, B. Alderete, R. Puyol, F. Mücklich, Load-dependent electrical contact resistance of carbon nanotube-reinforced metal matrix composites, in: 2022 IEEE 67th Holm Conference on Electrical Contacts (HLM), IEEE, 2022: pp. 1–6. https://doi.org/10.1109/HLM54538.2022.9969801.

ARTICLE XI
On the Production & Tribo-Electrical Characterization of Carbon Nanotube-Reinforced Ag & Cu Metal Matrix Composites

Bruno Alderete*, Sebastian Suarez, Frank Mücklich

Chair of Functional Materials, Saarland University, Campus D3.3, 66123 Saarbrücken, Germany

Research article
Published in "*Proceedings of the 2023 IEEE 68th Holm Conference on Electrical Contacts (HOLM)"* (2023)
Impact Factor: NA
Reproduced with permission from 'Institute of Electrical and Electronics Engineers - IEEE'
Accessible online at: doi.org/10.1109/HOLM56075.2023.10352236

Own Contribution: Conceptualization; Methodology; Validation; Formal Analysis; Investigation; Data Curation; Writing – Original Draft; Visualization.

Cite this article as: B. Alderete, S. Suarez, F. Mücklich, On the Production & Tribo-Electrical Characterization of Carbon Nanotube-Reinforced Ag & Cu Metal Matrix Composites, in: 2023 IEEE 68th Holm Conference on Electrical Contacts (HOLM), IEEE, 2023: pp. 1–8. https://doi.org/10.1109/HOLM56075.2023.10352236.

On the Production & Tribo-Electrical Characterization of Carbon Nanotube-Reinforced Ag & Cu Metal Matrix Composites

Bruno Alderete*, Frank Mücklich, and Sebastian Suarez

Chair of Functional Materials, Saarland University, Campus D3.3, 66123 Saarbrücken Germany

* Corresponding author: bruno.alderete@uni-saarland.de

***Abstract*:**

Silver and copper are among the best metallic conductors, however, there are other aspects in which these contact materials could be improved on to enhance electrode performance; namely, thermal stability, mechanical properties, atmospheric protection, among others. In this work, carbon nanotube (CNT)-reinforced metal matrix composites (MMC) are sintered via powder metallurgy – seeking to achieve the highest MMC density possible – at two reinforcement phase concentrations, i.e., 0.5 and 1 wt.%. Through the reinforcement phase it is sought to improve wear performance of the electrode without affecting the bulk materials' conductivity. The densified MMC were characterized via load dependent and current dependent electrical contact resistance (ECR), as well as evolution of ECR during fretting tests. Further characterization focuses on fretting mark morphological and chemical analysis via electron microscopy and spectroscopy, as well as confocal laser microscopy. As the weight percentage of the reinforcement phase increases, an increase in load dependent ECR was observed; nonetheless, contact reproducibility increases. The addition of CNT into the metallic matrices also promoted a reduction in adhesive wear. Moreover, when observing the ECR evolution during fretting, the reinforced samples rapidly reached steady-state ECR, remaining constant throughout the entire duration of the fretting test.

Keywords: *carbon nanotubes, electrical contact resistance, metal matrix composites*

Introduction

Electrical contact resistance (ECR) is one of the most important characteristics of an electrode. However, for optimal performance, thermal and mechanical requirements must also be fulfilled by the contact materials. Furthermore, to guarantee electrode efficiency, reliability, and durability, the contact materials should not react under atmospheric conditions during transport and in operation, as well as limiting wear in moving components (e.g., sliding contacts) or due to external

factors (e.g., fretting wear). Different industrially accepted alternatives can be adopted to improve on these characteristics such as conductive coatings, metallic platings, and the addition of alloying elements, among others [1]. However, the main challenge when improving a specific characteristic is that the technique should not be detrimental to the conductive properties of the contact material. Since copper and silver are the two best metallic conductors [2], it is unlikely that the addition of foreign elements will improve their conductivity. Therefore, in this case a tradeoff must be determined, where one or more characteristics are improved at the cost of a certain tolerable amount of conductivity.

Carbon nanotubes (CNT) have been rigorously studied in the past decades due to their versatility, outstanding intrinsic physical properties, as well broad potential fields of applications. Not only do CNT present exceptional mechanical properties (high tensile strength and elastic modulus), but they also present high thermal conductivity and current carrying capacity, as well as behaving as solid lubricants and showing superhydrophobic wetting behavior [3]–[9]. Previous studies carried out by McBride et al. and Liu et al. have analyzed the wear and electrical performance of gold-coated CNT for electrical switching applications [10], [11]. The authors proved experimentally and theoretically that CNT improved wear performance in electrical switches. Furthermore, researchers have also decorated CNT with silver nanoparticles, thus improving the electrical conductivity of the CNT [12]. Furthermore, CNT-reinforced metal matrix composites (MMC) have been previously shown to improve the tribological behavior of nickel matrices [13]–[15]. In this case where the matrix is not as conductive, however, CNT have been shown to also improve the conductivity of the system [16]. Another potential benefits of using CNT as reinforcement phase is the reduction of contact melting due to localized heating (e.g., arcing) on account of their high reported thermal conductivity [4]–[7], [17]. Furthermore, to improve upon the chemical compatibility between copper and carbon, copper-nickel-MMC were electrically characterized by Garcia et al. [18]. The authors reported equal electrical behavior of the MMC to that of pure copper, even reporting improvements in some cases. Nonetheless, proper reinforcement phase distribution is crucial to obtain these benefits from the CNT [19]. Furthermore, it is important to not incur excessive damage onto the CNT structure; otherwise, the desired properties will be affected [20]. Therefore, the literature suggests that colloidal mixing and powder metallurgy are the best alternative to produce MMC with optimal conductive properties [21]–[27].

Therefore, this work aims at the production and characterization of silver and copper based, CNT reinforced MMC as potential electrical contacts for low-voltage applications (such as, for example, the automotive industry). The main objective is to improve on the bulk materials'

tribological behavior without having a substantial impact on their intrinsic conductive properties. Consequently, within the aim of this work four different MMC will be produced via powder metallurgy, namely: copper-based and silver-based MMC reinforced with two different CNT concentrations. Since the reinforcement phase presents electron scattering sites at the metal-CNT interface, small concentrations of the reinforcement phase will be evaluated, i.e., 0.5 wt.% and 1 wt.%. Furthermore, the production of dense MMC is crucial for optimal electron transport behavior, since porosities within the MMC will act as further scattering sites, consequently further impacting the conductivity of the system. Load dependent and current dependent ECR will be carried out on the produced MMC and on high purity copper and silver reference samples to evaluate the influence of the reinforcement phase on the electrical behavior of the metallic matrices, as well as the ohmic response to different direct current levels. Tribo-electrical characterization will be evaluated via fretting tests with periodic ECR measurements, thus evaluating the evolution of ECR while subjected to wear. Furthermore, the potential wear reduction achieved as a consequence of the reinforcement phase can be evaluated by confocal laser scanning microscopy (CLSM), along with scanning electron microscopy (SEM). Moreover, CNT distribution in the MMC and chemical analysis of fretting marks can be analyzed via energy dispersive x-ray spectroscopy (EDS).

Materials and Method

MMC Production

Copper and silver were reinforced with CNT at two different concentrations – 0.5 wt.% and 1 wt.% – via powder metallurgy. Dendritic copper powder with a 325 mesh and 99% purity (Alfa Aesar GmbH, Germany) and silver flakes with at least 80% of the flakes below 20 μm and a purity of 99.9% (Alfa Aesar GmbH, Germany) were used as metallic matrices. The reinforcement phase used were chemical vapor deposition (CVD)-grown multiwalled CNT (Graphene Supermarket, USA). The nanotubes have an outer diameter distribution between 50-85 nm, an as-received state length from 10-15 μm, and a carbon purity above 94%.

The metallic matrix powder and reinforcement phase need to be homogeneously mixed prior to sintering. This was done by a process known as colloidal mixing [18], [21]–[24], which consists in dispersion the CNT in a suitable solvent (in this case ethylene glycol, henceforth EG), followed by the addition of the metallic powder, and subsequently evaporating the solvent, thus achieving a uniform powder mixture. Initially, large CNT agglomerates must be broken down and dispersed in EG (0.2 mg/ml of CNT/EG). Large bundles are broken down by shear forces for 5 minutes in a homogenizer (Ultra-Turrax T-25, IKA) at 7500 rpm. After homogenization, smaller agglomerates are further disentangled by ultrasonication for 10 minutes (Sonorex Super RK 514

BH, 860 W, 35 kHz, Badelin). These steps are crucial to guarantee optimal CNT properties, however, the duration should not exceed these values to ensure that the structural integrity of the CNT is not compromised [20]. The metallic powder (0.2 g/ml of metallic powder/EG to prevent the powder from precipitating) is then added to the dispersion and homogenized for 5 minutes at 7500 rpm [18], [22], [24]. The colloid is then placed in a ventilated furnace at 150 °C for 12 hours. Once the solvent has completely evaporated, the powder mixture is removed from the furnace and crushed with an agate mortar and pestle to disassemble powder agglomerates. The broken-down powder is reintroduced into the furnace for at least 2 more hours to guarantee that the powder mixture is completely dry, otherwise the powder will be more prone to porosity during sintering.

Disk-shaped samples (known as green pellets) are made from the powder mixture (8 mm diameter and a height between 3 and 5 mm) by pressing the powder in a cylindrical steel die at 990 MPa. Hot uniaxial pressing (HUP) was carried out to densify the green pellets by eliminating internal and open porosities. HUP was carried out in a vacuum oven (working pressure of 2×10^{-6} mbar) at 264 MPa and an isothermal holding time of 2.5 hours at 750 °C (at a heating rate of 15 °C/min) between two Al_2O_3 pistons inside of a graphite die. After sintering, the sample cooling was performed within the oven and removed once the temperature fell below 150 °C. Prior to characterization, the MMC samples were ground and polished to achieve a mirror-polished surface, achieving a roughness between 30-60 nm.

MMC Characterization

The MMC produced and bulk material references – Ag and Cu samples obtained from silver rods with 99.95% purity (Alfa Aesar GmbH, Germany) and copper rods with 99.9% purity (Goodfellow Cambridge Limited, England), respectively – were tribo-electrically characterized in a self-developed multipurpose testing rig [28]. With the setup, load and current dependent ECR measurements can be carried out, as well as fretting tests. Load dependent ECR measurements were done by 4-terminal sensing with a constant current of 100 mA_{DC} (sourced by a Keithley 2400 SMU), so as to stay in dry-circuit conditions [29], following a loading sequence of 0.25, 0.5, 0.75, 1, 1.5, 2, 2.5, 3, 4, 5, 6, 7, 8, 9, and 10 N. The voltage drop was measured by a Keithley 2182a nanovoltmeter with a range of 1 V. Silver-nickel core ($AgNi_{0.15}$) hard-gold-coated rivets ($AuCo_{0.2}$) were used as counter electrodes (Adam Bornbaum GmbH, Germany). The counter electrodes have a curved head, with a mean diameter of curvature of 4 mm and a root mean square roughness of 0.26 µm. The hard-gold coating has an average thickness of 6.47 ± 0.18 µm, with a stiffness that is significantly higher than that of the MMC, and a hardness of 1.38 ± 0.01 GPa (measured via Vickers micro indentation), whereas the $AgNi_{0.15}$ core presents a hardness of 0.45-0.9 GPa [2]. Current dependent ECR was carried out with same setup and counter electrodes at a normal load

Table I – MMC microhardness and relative density

Metallic matrix	**Ag**			**Cu**		
wt.%	**0**	**0.5**	**1**	**0**	**0.5**	**1**
Hardness /MPa	847 ± 61	130 ± 26	227 ± 25	1335 ± 82	887 ± 44	760 ± 94
Relative density /%	100	66	86	100	99	99

of 1 N with the following direct currents: 30 μA, 100 μA, 300 μA, 1 mA, 10 mA, 30 mA, 100 mA, 300 mA, and 1 A. Furthermore, fretting tests were carried out at an oscillation amplitude and frequency of 35 μm and 8 Hz, respectively, using the same counter body. A total of 5000 fretting cycles were carried out at 1 N normal load, with periodic ECR measurements every 100 cycles (i.e., static ECR) [30], [31]. Ten ECR measurements were acquired per load/current/fretting interval, and then averaged, with a minimum of five tests per MMC and metallic reference. All measurements were conducted with ambient temperature and humidity values between 18-20 °C and 25-35% r.h., respectively.

MMC Vickers hardness was measured using a Dura Scan 50 microhardness tester (Struers Inc., USA) with a load of 0.098 N ($HV_{0.01}$), with a holding time of 15 seconds, and optically micrographed using 40× magnification. Nine indentations were carried out per sample and averaged. Furthermore, the density of the produced MMC (relative to the density of the reference samples) was determined by weighing the composites and measuring their volume with a pycnometer using distilled water. The resulting hardness and relative density of the MMC and reference samples are shown in **Table I**. As can be observed in **Table I**, the sintering process adequately densifies the Cu-based MMC. The Ag-based MMC, on the other hand, do not reach acceptable relative densities. Low density values not only promote the low hardness values measured and displayed in **Table I**, but also negatively impact the conductivity of the silver composites since extensive porous networks within the composite act as electron scattering sites. Furthermore, the low hardness values shown in **Table I** prove that the incorporation of CNT as secondary phase does not generate the reinforcement effect desired. This is due to the relatively high sintering temperature and prolonged isothermal holding time during HUP, which enables grain growth. Consequently, large grains reduce the hardness of the produced composites according to the Hall-Petch effect.

MMC and fretting marks were imaged with SEM (using ETD detector and 5 keV) and chemically analyzed via EDS (Thermo-Fisher Helios™ G4 PFIB CXe DualBeam™ Super). EDS

mappings were acquired to obtain a 2-dimensional view of MMC surfaces and wear tracks, acquired at an acceleration voltage of 15 keV. CLSM (LEXT OLS4100, Olympus) micrographs were acquired to measure roughness, dimensions of fretting marks, as well as worn volume.

Results and Discussions

Electrical Characterization

Load Dependent ECR

Load dependent ECR of the Ag-MMC is shown in **Fig. 1a**. This study shows a clear tendency where an increase in the reinforcement phase's concentration generates an increased contact resistance. Likewise, the mechanical hysteresis (i.e., the difference measured in ECR for the same load in the loading and unloading semi-cycle) is considerably smaller as the CNT concentration in the metallic matrix increases. By comparing the ECR values in the loading and unloading semi-cycles information on the repeatability of the contact can be obtained. Surfaces showing smaller mechanical hysteresis – i.e., marginal difference in ECR between semi-cycles – present higher contact reproducibility. Contrarily, surfaces which do not favor reproducible contacting situations (such as severely plastically deformed surfaces after loading) would present larger mechanical hysteresis by showing a larger difference in ECR between loading and unloading. Consequently, in the 1% sample, high contact reproducibility is achieved, as evidenced by the identical electrical behavior during loading and unloading. This ECR value is constant throughout the entire loading range at 42 mΩ. The sample with lower concentration, on the other hand, shows slight hysteresis below 9 N, with ECR values varying between 39 and 42 mΩ. The unreinforced reference sample oscillates between 12 and 20 mΩ, showing different values in loading and unloading throughout all the measured loads, thus showing the lowest contact reproducibility.

Observing the ECR *behavior* of the Cu MMC (shown in **Fig. 1b**), the same tendency as with Ag samples is observed – i.e., higher ECR as the reinforcement concentration increases, as well as lower hysteresis. Compared to Ag samples, the Cu samples show a significant reduction in ECR as the normal load increases. This is likely due to the presence of the native oxide layer. As the load increases this layer is punctured, thus producing the sharp decrease in ECR observed. This phenomenon is clearly visible in the reference sample, with it being less prominent as the CNT concentration increases. Increased CNT concentrations improve the Cu MMC-counter electrode contact at low normal loads (when contact pressures are not sufficient to puncture the native oxide layer) by enabling lower resistance pathways for the flow of current. Consequently, current flows through the reinforcement phase rather than through the non-conductive oxide film. Nonetheless, as the load increases and the oxide film is punctured, lower CNT concentrations promote lower ECR values due to the reduction in film resistance. In this case, the predominant

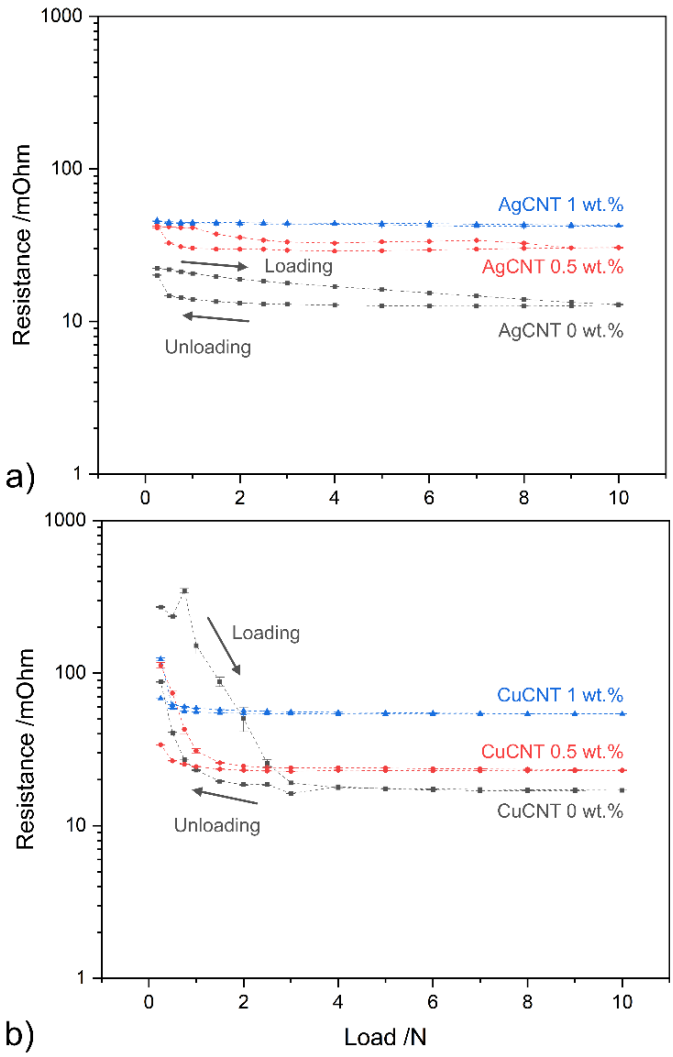

Fig. 1. Load dependent ECR of a) Ag and b) Cu CNT-reinforced metallic matrices. The arrows indicate the direction of the loading and unloading semi-cycles.

resistance type is the bulk resistance of each electrode and the constriction resistance as the current flow is concentrated in the a-spots. After puncturing the oxide film, the reinforcement phase presents higher resistance than the copper and gold contact interface, thus explaining the behavior observed in **Fig. 1b**. Since Ag does not form oxide layers this behavior was not observed in Ag-based MMC.

Although higher CNT concentrations produce higher ECR values, this analysis alludes to the fact that increased CNT-metal contacts tend to eliminate the reliance on load, thus promoting a constant load-independent ECR value. This was not only observed for Cu, but also for Ag samples. Rapidly reaching steady-state ECR is desirable since this equates to lower connection force requirements while maintaining optimal conductivity. In the unreinforced Cu sample, a normal load above 3 N is required to ensure optimal conduction. This load is reduced to below 1 N for both Cu MMC. Although it would be desirable to reach lower ECR values, the reinforced samples show highly reproducible electrical behavior, thus eliminating the requirement of

complex contact and housing designs to increase the load in the contact after insertion to ensure optimal conductivity.

The improved reproducibility in both CNT-reinforced metallic matrices is due to the high restitutional forces between CNT and CNT agglomerates. This phenomenon can be observed by the low mechanical hysteresis displayed by the reinforced samples during load dependent ECR (shown in **Fig. 1a** and **Fig. 1b**). As the load increases the voids within CNT bundles are compacted. However, when the load ceases, the internal voids are reestablished as the individual CNT return to their original position. Nonetheless, the ECR indicates that the normal load required to fill the voids is rather small since in all reinforced samples steady-state ECR is reached within the 1-2 N range. Although it could be argued that the lower mechanical hysteresis is due to the lack of proper sintering and thus the composites undergoing plastic deformation at relatively low loads, this would only be true for the Ag-based composites. However, observing the behavior of the Cu-based composites (**Fig. 1b**), the addition of CNT into the metallic matrix also reduces mechanical hysteresis, with a clear trend of lower hysteresis as CNT concentration increases.

Current Dependent ECR

Current dependent ECR of the Ag-MMC are shown in **Fig. 2a**. As the plot shows, from 100 μA up to 1 A both reinforced samples show ohmic behavior, with mean values of 35 and 39 mΩ for the 0.5% and 1% samples, respectively. Both reinforced samples show higher ECR at 30 μA, however, this low current level shows greater measurement uncertainty. The ohmic range of the unreinforced sample is smaller, starting at 1 mA. Considering the steady-state ECR values from **Fig. 2a** and comparing them with the those from **Fig. 1a** (also at 1 N), it can be observed that the values are similar. Nonetheless, in current dependent ECR, the 1% shows slightly lower ECR than the 0.5%. This could be caused by the heterogeneous distribution of CNT in the MMC surface; thus causing variations due to different CNT-metal contact throughout ECR measurements. The difference observed is, however, minor with the overall trend resembling the findings from load dependent ECR on Ag-based MMC.

The current dependent ECR results of the Cu-based MMC (shown in **Fig. 2b**) also follow the trend established in load dependent ECR (see **Fig. 1b** at 1 N). In current dependent ECR tests, the contact pressures achieved at 1 N are not sufficient to puncture the native oxide film. Therefore, as previously discussed, the CNT clusters found at the contact site offer lower resistance than the film resistance of the oxide layer. Consequently, the CNT reinforced Cu MMC show lower resistance than the unreinforced Cu samples irrespective of the current level. Furthermore, both Cu-based MMC show similar behavior, which also correlates to the results from load dependent

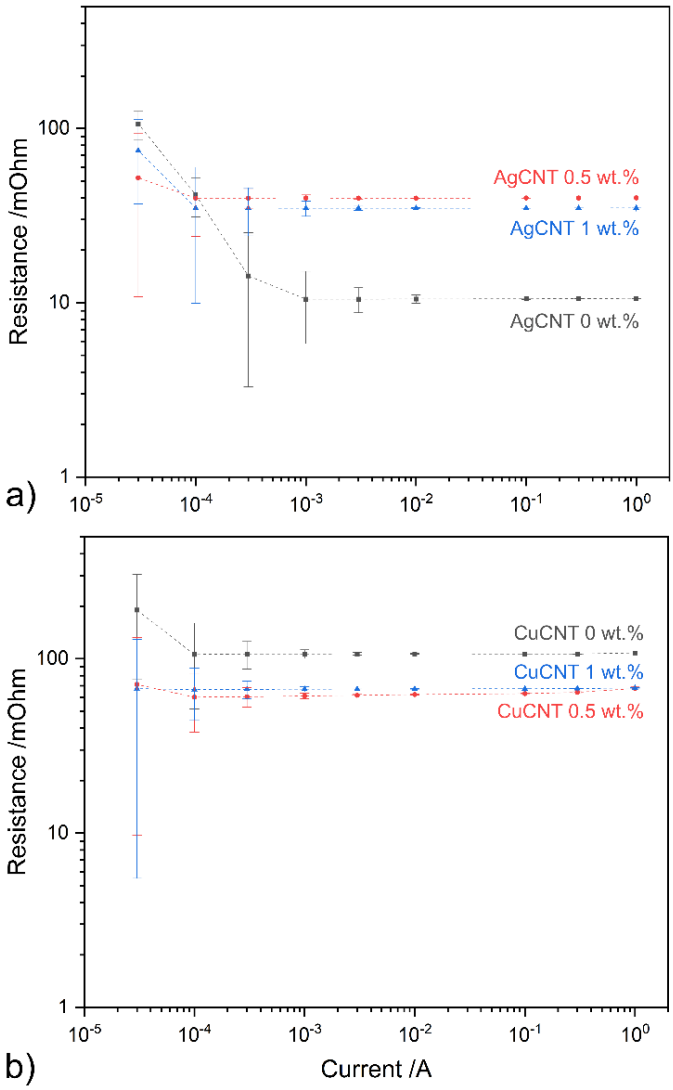

Fig. 2. Current dependent ECR of a) Ag and b) Cu CNT-reinforced metallic matrices.

ECR at 1 N. Although some discrepancies can be observed, these are minor and can be attributed to the heterogeneous CNT distribution. Moreover, as opposed to Ag, Cu composites show ohmic behavior in the entire current range measured, with the unreinforced sample showing ohmic behavior from 100 µA.

ECR Evolution During Fretting Tests

Static ECR was measured on the MMC and reference samples showing the evolution as a function of fretting cycle in **Fig. 3**. Observing the Ag samples (**Fig. 3a**), the same tendency as in load dependent ECR is observed. All samples show remarkably constant values throughout the 5 thousand fretting cycles, with the reference, 0.5%, and 1% stabilizing at approximately 12, 18, and 30 mΩ, respectively. In the initial cycles the 1% sample shows higher ECR than its steady-state value, stabilizing after approximately 500 cycles. This behavior was exclusive to the 1% sample. The 0.5% and unreinforced sample showed constant ECR throughout the fretting test.

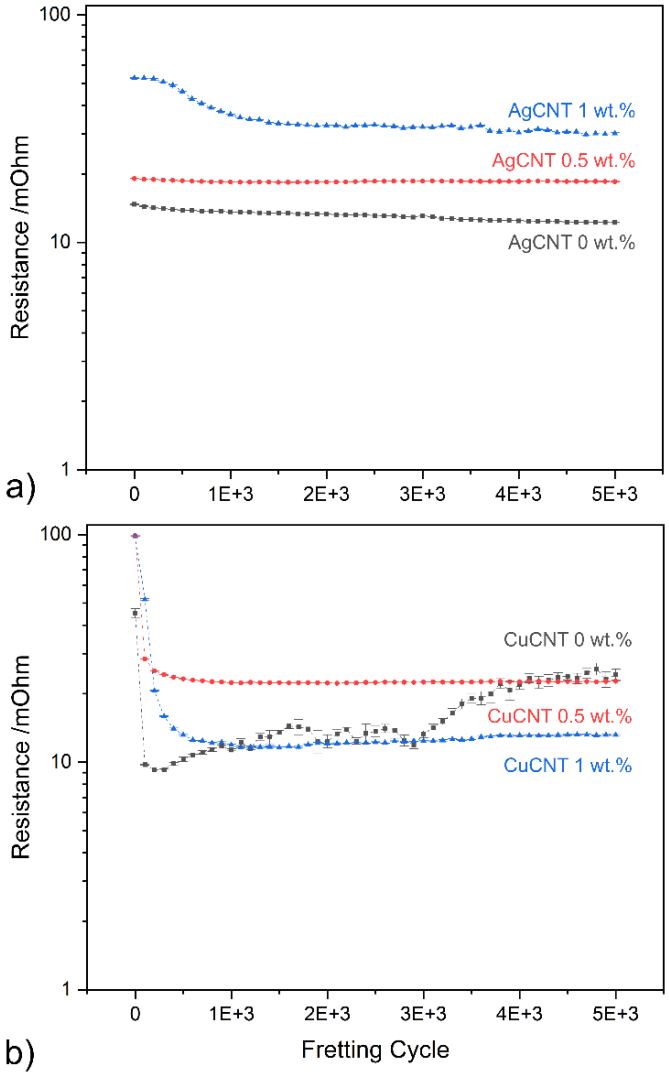

Fig. 3. Static ECR evolution during fretting tests of a) Ag and b) Cu CNT-reinforced metallic matrices.

The higher resistance observed in the first few hundred cycles of the 1% samples could be due to the heterogeneous distribution of CNT on the surface, as well as the presence of large CNT agglomerates. As fretting cycles progress, there is a reduction in ECR. The higher concentration of CNT increases the likelihood of their presence at the contacting site. Therefore, one hypothesis for this reduction in ECR is the breakdown of large CNT agglomerates during fretting wear. As CNT bundles are broken down, compacted, and adjusted due to fretting and the normal load applied, CNT-CNT interconnection improves, thus explaining the reduction observed in **Fig. 3a**.

The behavior of the Cu samples is considerably different than that of Ag samples. All Cu samples show higher initial ECR values, showing a sharp decrease after the first couple hundred cycles. This is due to the native oxide layer that is spontaneously formed when in contact with oxygen. Prior to fretting, the native oxide layer hinders the flow of current, thus producing the higher initial ECR values due to the dominance of film resistance. After fretting, however, the oscillatory motion of the counter electrode breaks down the oxide layer, minimizing film

resistance and thus causing a reduction in contact resistance, with constriction resistance dominating the system. This is more prominent in the unreinforced reference. However, the continuous regeneration and subsequent breakdown of the oxide layer generates debris in the contacting site. The debris trapped between the electrodes causes variations in static ECR in the Cu reference, in addition to the higher standard deviation. These fluctuations cause the shift from the Cu reference being the sample with the lowest initial ECR to it being on par – or even presenting higher ECR at certain points – than the 0.5% sample.

The reinforced Cu samples do not show fluctuation in static ECR evolution. These two samples show higher initial values – of approximately 100 mΩ – with the value falling to approximately 13 mΩ and 22 mΩ for the 1% and 0.5% sample, respectively. In this case, the 1% sample shows lower ECR values than the 0.5% sample. This could be a consequence of the lubricating capabilities of CNT. As the CNT concentration increases, the likelihood of contacting a larger area fraction of CNT increases; which decreases frictional forces during fretting wear. Wear reduction favors a more stable contacting area, which promotes lower ECR values. Although the ECR values of the 0.5% do not fluctuate, higher wear caused by fretting is detrimental to the real contact area between the electrodes; thus, causing inadequate contacting sites and increasing the overall resistance of the system. This phenomenon was not observed in the Ag sample since that material is much softer, in addition to the low densities of the Ag MMC. Therefore, the counter body can deform the Ag sample more easily, thus establishing a better contact area. Even after thousands of fretting cycles, the improved contact area promotes lower ECR values.

The lower resistance observed in the 1% Cu sample could also be caused by decreased reactivity between Cu and oxygen. As the CNT are degraded during fretting, the tubes become more reactive. The increased reactivity promotes the oxidation of the tubes themselves, rather than reacting with Cu. Consequently, higher CNT concentrations lead to lower ECR values by possibly slowing down the rate at which copper oxidizes.

Tribological and Chemical Characterization

Silver

SEM micrographs of the silver reference and MMC are shown in **Fig. 4**. The micrographs of the reinforced samples (**Fig. 4b** and **c**) show a considerably larger worn area compared to the unreinforced sample (**Fig. 4a**). The worn area was measured using CLSM, with both reinforced samples showing areas that are approximately three times larger than the unreinforced sample. Recalling the microhardness and density values of the Ag MMC, this is unsurprising. Porosities present within the MMC are detrimental to the mechanical stability of the composite, thus resulting in a more fragile solid. Upon being subjected to stress – be it from elevated normal

pressures or mechanical stress due to fretting – a considerable amount of plastic deformation takes place. Therefore, the poor sintering of Ag MMC – previously established by microhardness and relative density (see **Table I**) – is verified in tribological tests. This weak structural integrity of the Ag MMC could be problematic in terms of contact reproducibility, specifically in separable contacts. It is crucial that the sintering and densification steps in the production of Ag MMC is improved on, thus guaranteeing optimal structural integrity of the composites produces. This will not only favor better wear protection but would also favor lower resistance values. Consequently, the ECR values observed in **Fig. 1a**, **Fig. 2a**, and **Fig. 3a** could further approach those of the unreinforced reference sample, or even outperform the unreinforced sample [25].

Better Ag MMC sintering can be achieved by either augmenting the temperature in HUP or by increasing the isothermal holding time. These two changes in the sintering process – along with the elevated pressure used during HUP – would significantly reduce the trapped air within the MMC, thus reducing porosity and consequently increasing density and structural integrity – e.g., microhardness. The former could improve the quality by taking the green pellet's sintering temperature closer to silver's melting point, whereas the latter gives the air bubbles more time to exit the material and to densify more adequately. Another alternative would be increasing the applied pressure during HUP, however, since the pressure used in this study is already considerably high, it is believed that changes in temperature and sintering time would be a more straightforward alternative. Moreover, using a coarser Ag powder's morphology and particle size could improve densification.

The micrographs of the fretting marks do not reveal the generation of wear debris around the wear track. Therefore, we do not see detachment of material during fretting of either contacting bodies. CLSM measurements on the unreinforced sample reveal that there is a considerable volume of adhered material from the counter electrode, showing high volume (approximately 4000 μm^3) above the datum line and marginal values below it. Therefore, adhesive wear is the predominant wear mechanism active in this case [32]. Further confirmation is shown in the EDS maps in **Fig. 5b**, highlighting the pervasive presence of gold in the wear track which undoubtedly originates from the counter body's adhesion onto the silver surface.

The worn volume of the Ag MMC, on the other hand, show a higher volume below the datum line. This is due to the weak mechanical properties caused by internal porosities in the MMC and does not indicate abrasion. Material transfer also took place in the reinforced Ag samples (see **Fig. 5d** and **f**), however, to a lesser extent as in the unreinforced sample. In the reinforced samples, silver is still detected throughout the contacting site. One possible explanation is that the presence of CNT reduces the temperature at the fretting interface due to the high thermal conduction of the

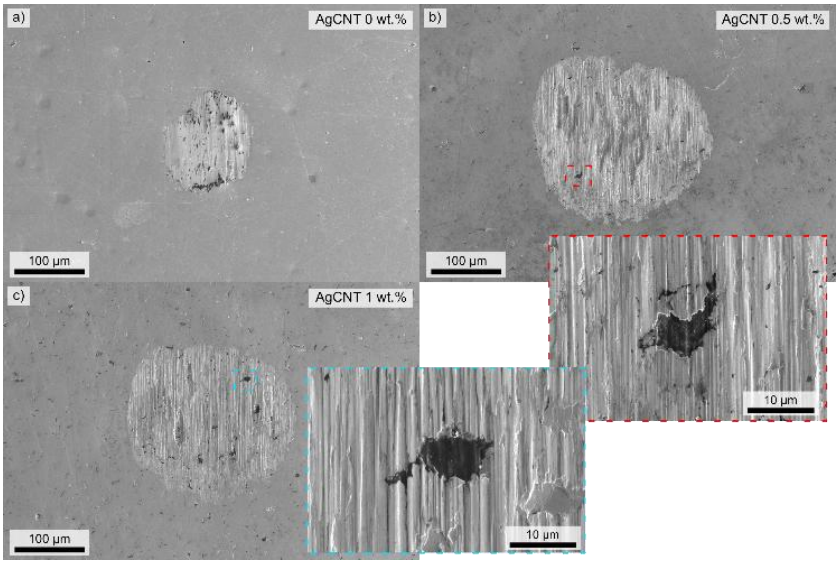

Fig. 4. SEM micrograph of Ag. a) 0 wt.%, b) 0.5 wt.%, and c) 1 wt.% CNT. The insets show a magnified view of open porosities in the wear track revealing the reinforcement phase.

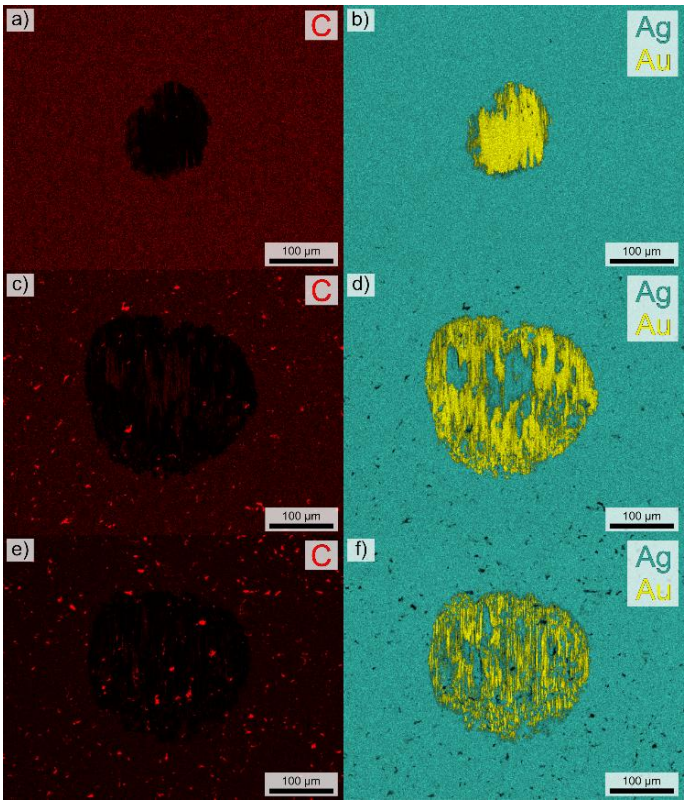

Fig. 5. EDS mappings of C, and Ag & Au overlay of a)-b) 0%, c)-d) 0.5%, and e)-f) 1%, respectively. Note that the carbon content in a) does not stem from the presence of CNT, but rather from organic contaminants that may be present on the surface of the reference sample (by adsorption).

CNT themselves. Furthermore, the presence of CNT in the composites also reduces friction-induced temperature increase on account of their previously reported solid lubricity [14]. The carbon EDS maps (**Fig. 5c** and **e**) show the presence of CNT clusters within the contacting site, therefore, providing a solid lubricant reservoir (see the insets of **Fig. 4b** and **c**), which validates this hypothesis.

Copper

The sintering process produced Cu MMC with high relative densities and good hardness values compared to high purity reference sample. Therefore, it was expected that these MMC would show worn areas that resemble that of the unreinforced sample, albeit the overall worn area is still higher in the reinforced samples (see **Fig. 6**). This could, however, be a consequence of the lubricity of the CNT. As the surface is damaged, and more CNT are exposed, friction should reduce. Therefore, lower frictional forces produce larger displacement of the counter body over the Cu surface.

As was observed in the Ag MMC, gold adhered in a considerable area fraction of the wear track (see EDS maps in **Fig. 7b**, **d**, and **f**). The gold transfer from the counter body is significant, with CLSM measurements showing in all cases that the volume above the datum line is higher than – or very similar to – the volume below it. Nonetheless, reinforced samples show a significant reduction in overall material transfer, with mean values above the datum line in the range of 45000 and 8000 μm^3 for the 0.5 and 1% sample, respectively. It was hypothesized that higher CNT concentrations would promote lower amounts of material transfer, however, the opposite was observed in the CLSM measurements of the Cu MMC. CLSM and SEM scans of the fretting marks also revealed that the main wear mechanism at play in the MMC (Ag and Cu) is adhesive wear. These techniques demonstrate that a considerable amount of gold is transferred from the counter electrode towards the MMC and reference samples – further verified with the EDS maps (see **Fig. 5** and **Fig. 7**). The fretting wear tests also revealed that material transfer occurs in a single direction. In other words, material transfer only took place from the gold counter electrode towards the Ag and Cu electrodes. Negligible damage was incurred onto the counter electrodes due to their

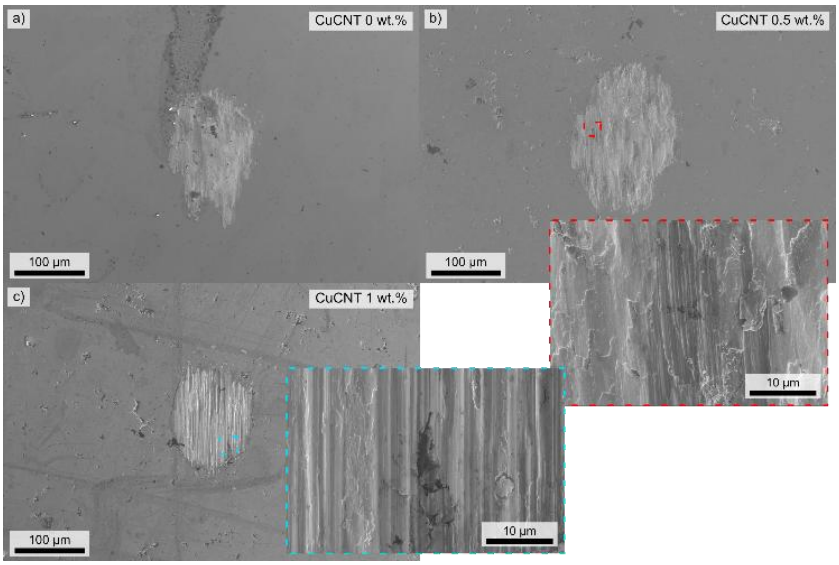

Fig. 6. SEM micrograph of Cu. a) 0 wt.%, b) 0.5 wt.%, and c) 1 wt.% CNT. The insets show a magnified view of open porosities in the wear track revealing the reinforcement phase.

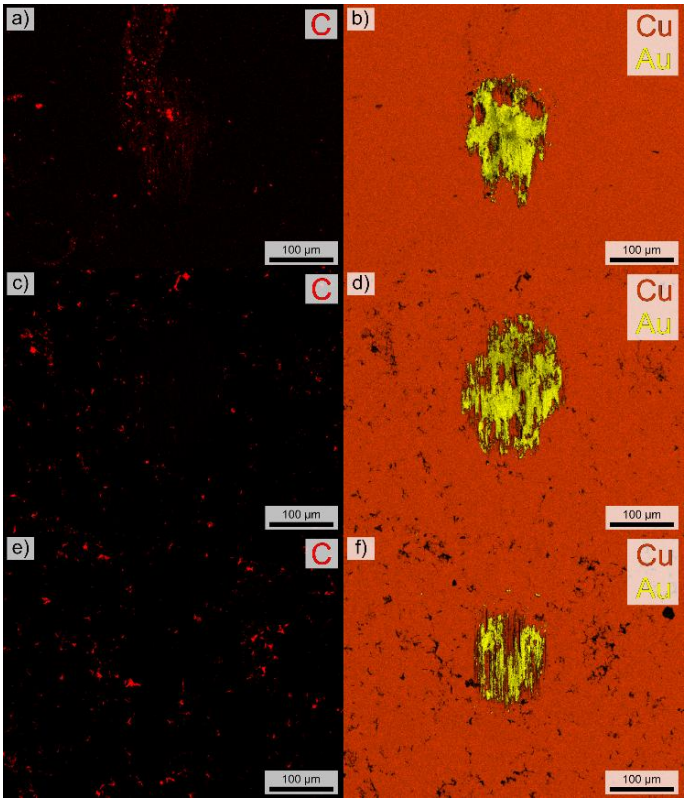

Fig. 7. EDS mappings of C, and Cu & Au overlay of a)-b) 0%, c)-d) 0.5%, and e)-f) 1%, respectively. Note that the carbon content in a) does not stem from the presence of CNT, but rather from organic contaminants that may be present on the surface of the reference sample, as well as from the breakdown of native oxide layers of the copper reference.

considerably higher hardness values compared to the Ag and Cu samples. Therefore, the CLSM and SEM micrographs are not presented in this work.

Observing the micrographs in **Fig. 6b** and **c** and the EDS carbon maps in **Fig. 7c** and **e**, larger CNT clusters can be identified compared to those from the Ag MMC. This heterogeneous distribution of larger CNT clusters generates higher deviations in tribological tests since the results will be highly dependent on the area fraction of CNT at the contacting site. Therefore, a better CNT dispersion is required to achieve higher contact homogeneity, thus ensuring the presence of CNT at the contacting site to reduce wear. However, two challenges arise when dispersing CNT.

1. When lengthening the dispersion process (i.e., homogenization and ultrasonication) higher mechanical stress is applied on the CNT and CNT agglomerates. To achieve a better dispersion, the agglomerates should be broken down as best possible. However, during this process the individual CNT also incur damage, which translates into a deterioration of the intrinsic physical properties of the CNT [33]. Therefore, when dispersing CNT great care should be taken to not produce significant damage in the tube's, thus causing disadvantageous results.

2. Chemical compatibility between carbon and copper is not as high as with other elements (e.g., nickel). Therefore, after dispersion the CNT tend to re-form agglomerates, thus reducing the reactivity with copper. This causes a more heterogeneous distribution of large CNT clusters in the Cu MMC.

Conclusions and Outlook

In this work, CNT-reinforced Ag and Cu MMC were sintered via powder metallurgy at two different concentrations, i.e., 0.5 and 1 wt.%. The Ag MMC were not adequately sintered, showing very low microhardness and relative density values caused by internal porosities. On account of the poor sintering quality of the Ag MMC, tribological performance of the unreinforced samples outperformed the reinforced samples. Furthermore, although the addition of CNT increased ECR, the reinforcement phase improved contact reproducibility and ohmic range. However, to properly assess the viability of CNT reinforced Ag composites for electrical and tribological applications the sintering process must be improved. This can be achieved by increasing the sintering temperature and/or by increasing the isothermal holding time during HUP. Improving MMC density would reduce internal and superficial porosities. This would not only improve tribological behavior by increasing mechanical stability, but could also improve electrical performance thus attaining ECR values that more closely resemble that of the reference material.

Cu MMC, on the other hand, showed high relative densities and adequate hardness values. Accordingly, Cu MMC showed promising electrical performance at low normal loads (when the native oxide film is not punctured) outperforming the reference material, as well as showing high contact reproducibility (i.e., small mechanical hysteresis) and reducing the dependence of normal load on ECR for sufficiently high contact pressures after the oxide film was punctured. In tribological tests, Cu MMC reached and sustained steady-state ECR after a few hundred fretting cycles, outperforming the unreinforced high purity reference. Furthermore, the addition of CNT into Cu metallic matrices reduces adhesive wear. Therefore, the Cu MMC produced show great potential as electrical contact materials.

Acknowledgment

B. Alderete wishes to acknowledge the support from the German Academic Exchange Service (DAAD) and the Roberto Rocca Education Program (RREP). The TÜV Saarland Stiftung is gratefully acknowledged for financially supporting the project. The authors gratefully acknowledge funding in the ZuMat project, supported by the State of Saarland from the European Regional Development Fund (Europäischen Fonds für Regionale Entwicklung, EFRE). Funding

for the PFIB/SEM instrument by German Research Foundation is greatly acknowledged (INST 256/510-1 FUGG).

References

[1] P. G. Slade, *Electrical Contacts Principles and Applications*, Second Ed. Boca Raton: Taylor & Francis, 2014.

[2] M. Braunovic, V. Konchits, and N. Myshkin, *Electrical Contacts - Fundamentals, Applications and Technology*, 1st ed. Boca Raton, FL, USA: CRC Press, 2007.

[3] B. Alderete, F. Mücklich, and S. Suarez, "Characterization and electrical analysis of carbon-based solid lubricant coatings," *Carbon Trends*, vol. 7, 2022, doi: 10.1016/j.cartre.2022.100156.

[4] M. S. Dresselhaus, G. Dresselhaus, and R. Saito, "Physics of carbon nanotubes," *Carbon N Y*, vol. 33, no. 7, pp. 883–891, 1995, doi: 10.1016/0008-6223(95)00017-8.

[5] R. Saito, G. Dresselhaus, and M. S. Dresselhaus, *Physical Properties of Carbon Nanotubes*. London: Imperial College Press, 1998. doi: 10.1142/p080.

[6] V. N. Popov, "Carbon nanotubes: Properties and application," *Materials Science and Engineering R: Reports*, vol. 43, no. 3, pp. 61–102, 2004, doi: 10.1016/j.mser.2003.10.001.

[7] T. W. Ebbesen, "Carbon nanotubes," *Chemical and Engineering News*, vol. 79, no. 41, p. 11, 2001.

[8] B. Alderete, S. M. Lößlein, D. Bucio Tejeda, F. Mücklich, and S. Suarez, "Feasibility of Carbon Nanoparticle Coatings as Protective Barriers for Copper─Wetting Assessment," *Langmuir*, Nov. 2022, doi: 10.1021/acs.langmuir.2c02295.

[9] B. Alderete, T. MacLucas, D. Espin, S. P. Brühl, F. Mücklich, and S. Suarez, "Near Superhydrophobic Carbon Nanotube Coatings Obtained via Electrophoretic Deposition on Low-Alloy Steels," *Adv Eng Mater*, vol. 23, no. 5, 2021, doi: 10.1002/adem.202001448.

[10] J. W. McBride, "The Wear Processes of Gold Coated Multi-Walled Carbon Nanotube Surfaces Used as Electrical Contacts for Micro-Electro-Mechanical Switching," *Nanoscience and Nanotechnology Letters*, vol. 2, no. 4, pp. 357–361, Dec. 2010, doi: 10.1166/nnl.2010.1109.

[11] H. Liu and J. W. McBride, "The influence of multiscale surface roughness on contact mechanics using finite element modeling: Applied to a Au-coated CNT composite electrical contact surface," in *2017 IEEE Holm Conference on Electrical Contacts*, IEEE, Sep. 2017, pp. 229–235. doi: 10.1109/HOLM.2017.8088092.

[12] P. C. Ma, B. Z. Tang, and J.-K. Kim, "Effect of CNT decoration with silver nanoparticles on electrical conductivity of CNT-polymer composites," *Carbon N Y*, vol. 46, no. 11, pp. 1497–1505, Sep. 2008, doi: 10.1016/j.carbon.2008.06.048.

[13] S. Suarez, A. Rosenkranz, C. Gachot, and F. Mücklich, "Enhanced tribological properties of MWCNT/Ni bulk composites - Influence of processing on friction and wear behaviour," *Carbon N Y*, vol. 66, pp. 164–171, 2014, doi: 10.1016/j.carbon.2013.08.054.

[14] L. Reinert, S. Suarez, and A. Rosenkranz, "Tribo-Mechanisms of Carbon Nanotubes: Friction and Wear Behavior of CNT-Reinforced Nickel Matrix Composites and CNT-Coated Bulk Nickel," *Lubricants*, vol. 4, no. 2, p. 11, 2016, doi: 10.3390/lubricants4020011.

[15] S. Suarez, N. Souza, F. Lasserre, and F. Mücklich, "Influence of the Reinforcement Distribution and Interface on the Electronic Transport Properties of MWCNT-Reinforced Metal Matrix Composites," *Adv Eng Mater*, vol. 18, no. 9, pp. 1626–1633, 2016, doi: 10.1002/adem.201600216.

[16] S. Suarez, B. Alderete, R. Puyol, and F. Mücklich, "Load-dependent electrical contact resistance of carbon nanotube-reinforced metal matrix composites," in *2022 IEEE 67th Holm Conference on Electrical Contacts (HLM)*, IEEE, Oct. 2022, pp. 1–6. doi: 10.1109/HLM54538.2022.9969801.

[17] S. Suarez, R. Puyol, C. Schäfer, and F. Mücklich, "Carbon Nanotube-reinforced Metal Matrix Composites as Novel Electrodes for Low-voltage Switching Applications: A Surface Degradation Analysis," in *2019 Proceedings of the 65th IEEE Holm Conference on Electrical Contacts*, 2019, pp. 135–141.

[18] D. García, S. Suárez, K. Aristizábal, and F. Mücklich, "Powder-Metallurgical Fabrication and Electrical Contact Resistance Characterization of Copper–Nickel Composites Reinforced by Multiwalled Carbon Nanotubes," *Adv Eng Mater*, vol. 24, no. 2, Feb. 2022, doi: 10.1002/adem.202100755.

[19] O. Hjortstam, P. Isberg, S. Söderholm, and H. Dai, "Can we achieve ultra-low resistivity in carbon nanotube-based metal composites?," *Appl Phys A Mater Sci Process*, vol. 78, no. 8, pp. 1175–1179, 2004, doi: 10.1007/s00339-003-2424-x.

[20] L. Reinert, M. Zeiger, S. Suárez, V. Presser, and F. Mücklich, "Dispersion analysis of carbon nanotubes, carbon onions, and nanodiamonds for their application as reinforcement phase in nickel metal matrix composites," *RSC Adv*, vol. 5, no. 115, pp. 95149–95159, 2015, doi: 10.1039/c5ra14310a.

[21] S. Suarez, F. Lasserre, O. Prat, and F. Mücklich, “Processing and interfacial reaction evaluation in MWCNT/Ni composites,” *Physica Status Solidi (a)*, vol. 211, no. 7, pp. 1555–1561, Jul. 2014, doi: 10.1002/pssa.201431018.

[22] S. Suarez, F. Lasserre, and F. Mücklich, “Mechanical properties of MWNT/Ni bulk composites: Influence of the microstructural refinement on the hardness,” *Materials Science and Engineering: A*, vol. 587, pp. 381–386, Sep. 2013, doi: 10.1016/j.msea.2013.08.058.

[23] S. Suarez, E. Ramos-Moore, B. Lechthaler, and F. Mücklich, “Grain growth analysis of multiwalled carbon nanotube-reinforced bulk Ni composites,” *Carbon N Y*, vol. 70, no. 681, pp. 173–178, 2014, doi: 10.1016/j.carbon.2013.12.089.

[24] S. Suarez, L. Reinert, and F. Mücklich, “Carbon Nanotube (CNT)-Reinforced Metal Matrix Bulk Composites: Manufacturing and Evaluation,” in *Diamond and Carbon Composites and Nanocomposites*, Mahmood. Aliofkhazraei, Ed., IntechOpen, 2016, p. 182.

[25] Y. Feng, H. L. Yuan, and M. Zhang, “Fabrication and properties of silver-matrix composites reinforced by carbon nanotubes,” *Mater Charact*, vol. 55, no. 3, pp. 211–218, Sep. 2005, doi: 10.1016/j.matchar.2005.05.003.

[26] A. Jamwal *et al.*, “Towards sustainable copper matrix composites: Manufacturing routes with structural, mechanical, electrical and corrosion behaviour,” *Journal of Composite Materials*, vol. 54, no. 19. SAGE Publications Ltd, pp. 2635–2649, Aug. 01, 2020. doi: 10.1177/0021998319900655.

[27] N. Silvestre, “State-of-the-art Review on Carbon Nanotube Reinforced Metal Matrix Composites,” *International Journal of Composite M aterials*, vol. 2013, no. 6A, pp. 28–44, 2013, doi: 10.5923/s.cmaterials.201309.04.

[28] B. Alderete, R. Puyol, S. Slawik, E. Espin, F. Mücklich, and S. Suarez, “Multipurpose setup used to characterize tribo-electrical properties of electrical contact materials,” *MethodsX*, vol. 8, 2021, doi: 10.1016/j.mex.2021.101498.

[29] E. M. Bock, “Low-Level Contact Resistance Characterization,” *AMP Journal of Technology*, vol. 3, pp. 64–68, 1993.

[30] B. Alderete, S. Suarez, D. B. Tejeda, and F. Mücklich, “Fretting and Electrical Contact Resistance Characteristics of Carbon Nanoparticle-Coated Cu Electrical Contacts,” in *2022 IEEE 67th Holm Conference on Electrical Contacts (HLM)*, IEEE, Oct. 2022, pp. 1–8. doi: 10.1109/HLM54538.2022.9969836.

[31] B. Alderete, F. Mücklich, and S. Suarez, “Wear Reduction via CNT Coatings in Electrical Contacts Subjected to Fretting,” *Tribol Lett*, vol. 71, no. 2, p. 54, Jun. 2023, doi: 10.1007/s11249-023-01724-5.

[32] K.-H. Zum Gahr, *Microstructure and Wear of Materials*, vol. 10. Amsterdam: Elsevier, 1987.

[33] J. Hilding, E. A. Grulke, Z. George Zhang, and F. Lockwood, “Dispersion of Carbon Nanotubes in Liquids,” *J Dispers Sci Technol*, vol. 24, no. 1, pp. 1–41, Jan. 2003, doi: 10.1081/DIS-120017941.

ARTICLE XII
Electrical Characterization of Carbon Nanotube Reinforced Silver and Copper Composites for Switching Contacts

Bruno Alderete*, Frank Mücklich, Sebastian Suarez*

Chair of Functional Materials, Saarland University, Campus D3.3, 66123 Saarbrücken, Germany

Research article
Published in "*Journal of Composites Science*" (2023)
Impact Factor: 3.0 (2023)

Accessible online at: doi.org/10.3390/jcs7070284

Own Contribution: Conceptualization; Methodology; Validation; Formal Analysis; Investigation; Data Curation; Writing – Original Draft; Visualization.

Cite this article as: B. Alderete, F. Mücklich, S. Suarez, Electrical Characterization of Carbon Nanotube Reinforced Silver and Copper Composites for Switching Contacts, Journal of Composites Science 7 (2023) 284. https://doi.org/10.3390/jcs7070284.

Journal of
Composites Science

MDPI

Article

Electrical Characterization of Carbon Nanotube Reinforced Silver and Copper Composites for Switching Contacts

Bruno Alderete *, Frank Mücklich and Sebastian Suarez *

Chair of Functional Materials, Saarland University, Campus D 3.3, 66123 Saarbrücken, Germany
* Correspondence: bruno.alderete@uni-saarland.de (B.A.); s.suarez@mx.uni-saarland.de (S.S.); Tel.: +49-681-30270544 (B.A.); +49-681-30270538 (S.S.)

Abstract: Carbon nanotube (CNT)-reinforced silver and copper metal matrix composites—at three different reinforcement phase concentrations (0.5 wt.%, 0.75 wt.%, and 1 wt.%)—were produced via powder metallurgy and sintered via hot uniaxial pressing. Optical and electron microscopy techniques were used to characterize the powder mixtures and sintered composites. The latter were also electrically characterized via load-dependent electrical contact resistance (ECR) and surface fatigue tests. Particle size and morphology play a crucial role in CNT deposition onto the metallic powder. CNT were deposited exceptionally well onto the dendritic copper powder regardless of its larger size (compared with the silver flakes) due to the higher surface area caused by the grooves and edges of the dendritic structures. The addition of CNT to the metallic matrices improved their electrical performance, in general outperforming the reference material. Higher CNT concentrations produced consistently low ECR values. In addition, high CNT concentrations (i.e., 1 wt.%) show exceptional contact repeatability due to the elastic restitutive properties of the CNT. The reproducibility of the contact surface was further evaluated by the fatigue tests, where the composites also showed lower ECR than the reference material, rapidly reaching steady-state ECR within the 20 fatigue cycles analyzed.

Keywords: carbon nanotubes; electrical switches; hot uniaxial pressing; metal matrix composites; powder metallurgy

Citation: Alderete, B.; Mücklich, F.; Suarez, S. Electrical Characterization of Carbon Nanotube Reinforced Silver and Copper Composites for Switching Contacts. *J. Compos. Sci.* **2023**, *7*, 284. https://doi.org/10.3390/jcs7070284

Academic Editors: Francesco Tornabene and Thanasis Triantafillou

Received: 7 June 2023
Revised: 20 June 2023
Accepted: 6 July 2023
Published: 11 July 2023

1. Introduction

Low-voltage, direct-current switches are crucial components in modern life. These small—yet important—devices can be ubiquitously found in many fields of application, e.g., consumer electronics, sensing devices, transport vehicles, etc. The task that these components must complete is simple: make and break the electrical circuit (i.e., close and open the circuit, respectively). Despite the simple nature of the switch's action, different mechanisms and circumstances at play during the making and breaking of the circuit—such as atmospheric conditions and other external factors, contact wear and corrosion, material transfer and degradation, as well as switch design and material selection—can considerably complicate the system.

In order to efficiently make and break the circuit, switches must fulfill several requirements. The main requirement is a low electrical contact resistance (ECR), since this will reduce energy loss at the contact interface, thus increasing the system's efficiency and reducing heat production. As a repercussion of lower contact temperatures, welding of the two surfaces is less likely to occur, improving the reliability of the system. This is a crucial requirement since contact welding could potentially prevent the breaking of the circuit when prompted. Therefore, low energy loss and high thermal dissipation capacity are essential in electrical switches. Other requirements include, but are not limited to, arc extinguishing capabilities, wear, erosion, and corrosion resistance, and minimizing contact bounce and chatter, among others.

The focus of this work is on material selection, describing a production method, and evaluating the low-current performance of carbon nanotube (CNT)-reinforced silver and copper-based metal matrix composites (MMC). The proposed composite materials could prove advantageous, presenting a multiscale approach to fulfilling the aforementioned requirements by tailoring the contact material employed in the electrical switch. Foremost, CNT presents the capability of conducting electricity exceptionally well, showing the interesting capability of behaving similar to a metallic conductor or semiconductor, depending on their chirality (structure-dependent electrical conductivity) [1–9]. Multi-walled carbon nanotubes (MWCNT), however, have the particular characteristic that they statistically always possess at least one metallic wall [10], where conduction takes place. Therefore, MWCNT ensures the metallic conduction of electrons, with metallic tubes having a longer electron mean free path than copper and quasi-ballistic electron transport properties [11–14]. Since MWCNT are easier to synthesize while having similar current carrying capacity as metallic single-walled CNT [15], MWCNT were implemented in the proposed composites.

In addition to CNT's electron transport properties, these sp^2-hybridzed one-dimensional nanostructures present exceptional thermal conductivity, albeit with anisotropy caused intrinsically by their structure. Although the conductance (thermal as well as electrical) is highly dependent on nanotubes' structural integrity, theoretical thermal conductivity values range from 3000 to 6000 W/m·K [16–18], higher than silver's and copper's (approximately 430 and 400 W/m·K, respectively) and even that of pure single-crystalline diamond (2400–2500 W/m·K) [19]. This high thermal conduction thus aids in heat dissipation at the contact interface generated by friction and/or constriction and film resistance [20]. Consequently, the likelihood of switch welding is considerably reduced when CNT are present in the system, even at elevated current levels. Moreover, multiple studies have reported that the addition of CNT as a reinforcement phase in nickel matrices has significantly reduced friction and wear [21–23], as well as CNT coatings providing wear protection while having a marginal impact on ECR [24–26]. Furthermore, the incorporation of CNT into the system could provide the electrical switch with secondary advantages due to the chemical inertness and hydrophobic wetting behavior of this carbon nanostructure [27–29], in addition to their exceptional mechanical properties [30–33].

Due to all the aforementioned properties and characteristics of CNT—in addition to the outstanding electrical properties of silver and copper—the objective of this study is to produce and characterize CNT-reinforced silver and copper metallic matrices. Production will follow conventional powder metallurgical methods since this is an industrially accepted technique. The powder mixtures will be prepared by colloidal mixing, and the green pellets will be densified by hot uniaxial pressing (HUP). These methods are simple, versatile, and allow a near-net-shaped manufacturing process. After sintering, the produced MMC will be characterized by optical and electron microscopy—using confocal laser scanning microscopy (CLSM) and scanning electron microscopy (SEM), respectively. Electrical characterization consisted of load-dependent ECR and surface fatigue tests on composite and reference samples. These methods provide insight into the impact of the reinforcement phase on the electrical behavior of the metallic matrix, on the repeatability of the contact when subjected to different normal loads, as well as the evolution of ECR after consecutive making and breaking cycle simulations.

2. Materials and Methods

2.1. MMC Production

Silver and Copper matrices were reinforced with MWCNT using three different concentrations through powder metallurgy—namely 0.5 wt.%, 0.75 wt.%, and 1 wt.%—and then sintered via HUP. Silver flakes having 99.9% purity, over 80% of which were below 20 µm in size, and 99.9% pure dendritic copper powder with a mesh size of 90%-325 (i.e., 90% of the particles are smaller than 44 µm) were used as metallic matrices (Alfa Aesar GmbH, Kandel, Germany). Pristine, chemical vapor deposition-grown MWCNT (Graphene Supermarket, New York, USA) with an outer diameter distribution between 50–85 nm,

an as-received state length from 10–15 µm, and a carbon purity above 94% were used as reinforcement phases.

The production of the MMC is comprised of three distinct processes:

1. CNT dispersion and metallic powder mixture (colloidal mixing process);
2. Cold pressing (consolidation of green pellet);
3. Sintering (densification via HUP).

The first process consists of dispersing the CNT in ethylene glycol (EG). Therefore, 0.2 mg_{CNT}/mL_{EG} are added in a beaker and then subjected to a homogenization (Ultra-Turrax T-25, IKA, Staufen, Germany) at 7500 rpm for 5 min. Large CNT agglomerates (formed by van der Waals interactions [34,35]) are thus broken down through shear forces. Subsequently, the colloid is placed in an ultrasound bath to further disentangle the smaller CNT bundles. After CNT dispersion, the metallic powder can be incorporated into the colloid, followed by homogenization for 5 additional minutes at 7500 rpm. The solvent must then be evaporated by placing the colloid in a ventilated furnace set at 150 °C for 24 h. The CNT-metallic powder mixture is then removed from the furnace and crushed using an agate mortar and pestle for 5 min to break apart powder agglomerates. The crushed powder is then returned to the furnace for 24 more hours to ensure proper drying since the presence of moisture during sintering negatively impacts MMC density. These steps are schematically represented and shown in Figure 1.

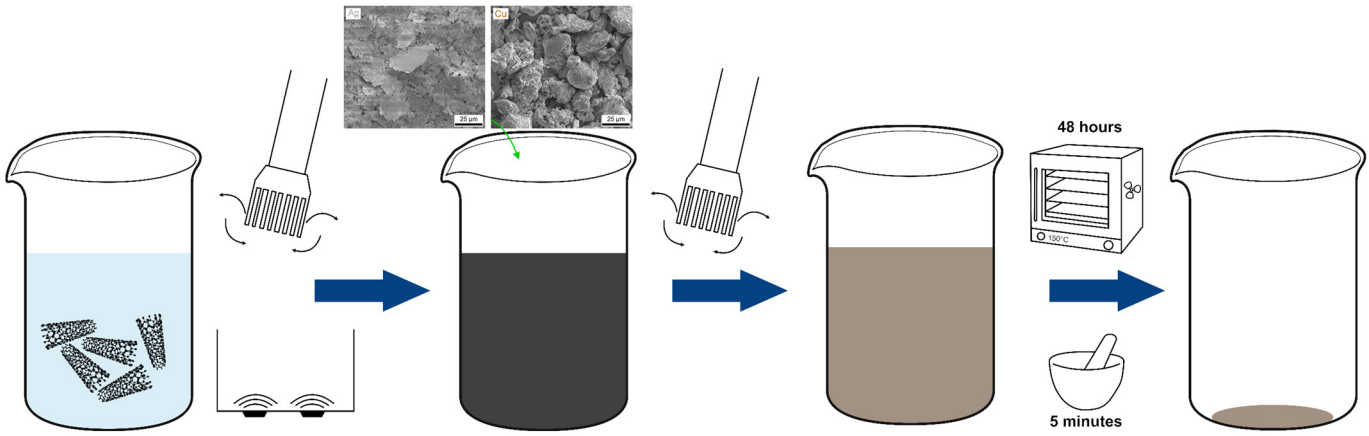

Figure 1. Powder mixture process, schematic representation.

The dry powder mixtures are then pressed with a hydraulic press (Matra-Werke GmbH, Hainburg, Germany) using a cylindrical steel die at 990 MPa, thus obtaining an 8 mm diameter disk-shaped sample (green pellet) with typical heights between 3 and 5 mm. To significantly increase sample density, the green pellet is then sintered via HUP in a vacuum chamber (working pressure of 2×10^{-6} mbar), a process that eliminates internal and open porosities. For HUP, the green pellet is placed between two alumina pistons inside a graphite die and pressed at 264 MPa. The sample, alumina pistons, and graphite die are then placed inside a cylindrical steel die and placed inside a water-cooled induction coil within the vacuum chamber (schematically represented in Figure 2). The sample is then heated to 750 °C with an approximate heating ramp of 15 °C/min, followed by an isothermal holding time of 2.5 h. The sample then cools inside the vacuum chamber until it reaches a temperature between 150 and 200 °C. The sintered sample can then be removed from the chamber.

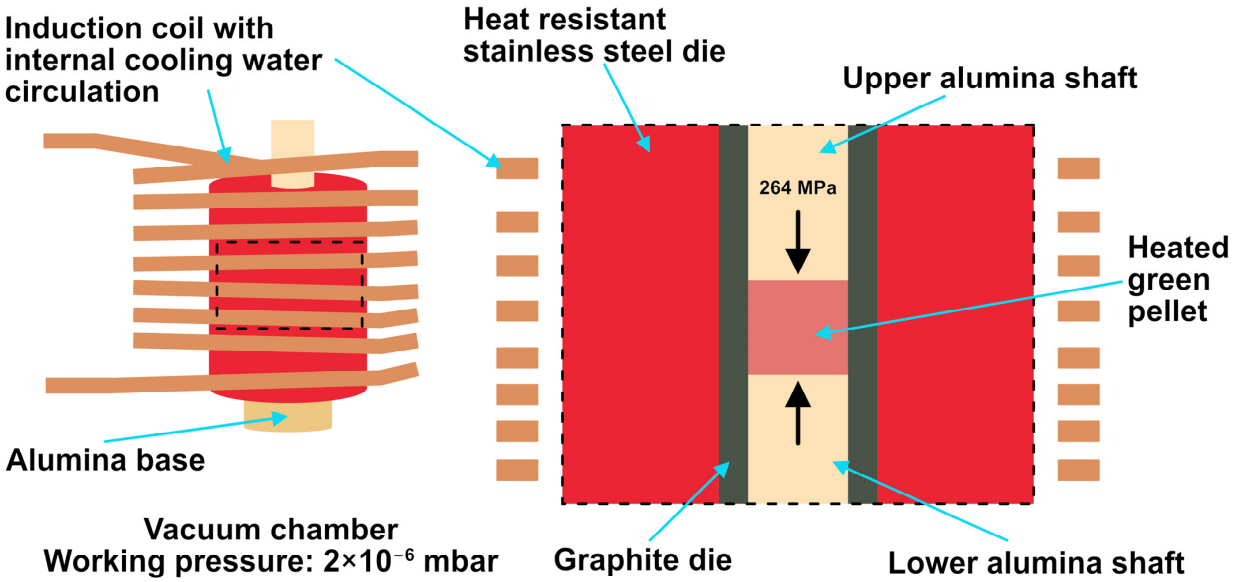

Figure 2. Schematic representation of HUP.

2.2. Characterization Techniques

The powder mixtures were characterized by SEM (Helios^{TM} G4 PFIB CXe DualBeam^{TM} Super, Thermo-Fisher Scientific, Eindhoven, The Netherlands) using Everhart-Thornley (ETD) and Through-the-Lens (TLD) detectors and a 5 keV acceleration voltage. With this technique, the deposition of the CNT on the metallic powders could be observed, and the homogeneity of the mixture could be qualitatively assessed.

After sintering the powder blends, relative density and microhardness measurements were carried out. Relative density was measured using distilled water and an adjusted 10 mL pycnometer, according to Gay-Lussac. Vickers hardness measurements were carried out using a microhardness tester (Dura Scan 50, Struers Inc., Cleveland, USA), a load of 0.098 N ($HV_{0.01}$), and a holding time of 15 s, the resulting imprints were optically micrographed using 40× magnification. A 3 × 3 indentation grid (separated from one another by 0.5 mm) was carried out per sample. The final hardness value considered is the average of the nine indentations.

Electrical characterization was conducted using a custom testing rig using four-terminal sensing with a constant current of 100 mA_{DC} (sourced by a Keithley 2400 SMU, Cleveland, USA) [36,37]. This current level was chosen to ensure dry circuit conditions [38]. Two different electrical tests were performed: (1) load-dependent ECR and (2) surface fatigue tests. The former consists of conducting two loading and unloading semi-cycles (following the sequence: 0.5, 1, 1.5, 2, 2.5, 3, 3.5, 4, 4.5, 5, 6, 7, 8, 9, and 10 N), whereas the latter consists of loading and unloading for 20 cycles at 1 N, 3 N, and 5 N to evaluate the performance of the MMC during monotonic loading. The results from surface fatigue tests are complex to graphically represent; therefore, 2D kernel density estimations were also plotted. These plots provide information on the overall trend of electrical performance during fatigue. ECR was measured ten times per load (using a Keithley 2182a nanovoltmeter with a range of 1 V, Cleveland, USA) and averaged. Silver-nickel core ($AgNi_{0.15}$), hard-gold-coated rivets ($AuCo_{0.2}$)—average coating thickness of 6.47 ± 0.18 µm—were used as counter electrodes (Adam Bornbaum GmbH, Neuhausen, Germany). These rivets have a curved head—a mean diameter of curvature of 4 mm—and a root mean squared roughness of 0.26 µm. A new counter electrode was used after every test. Both load-dependent ECR and surface fatigue tests were carried out at least three times per sample to ensure result reproducibility. The tests were conducted under laboratory conditions, with temperature and relative humidity ranging from 19–23 °C and 35–45% r.h., respectively. The electrical performance of the MMC was contrasted with high-purity reference materials,

namely: 99.95% and 99.9% purity silver (Alfa Aesar GmbH, Kandel, Germany) and copper (Goodfellow Cambridge Limited, Huntingdon, England) rods, respectively.

3. Results and Discussions

3.1. Powder Characterization

The metallic powders used in this study were micrographed by SEM (Figure 3a,b). The SEM micrographs in Figure 3c,d show the result of colloidal mixing after fully evaporating the solvent and drying the mixture, whereas Figure 3e,f show a magnified feature of the mixture. SEM micrographs of the pristine CNT used as reinforcement are shown in Figure S1.

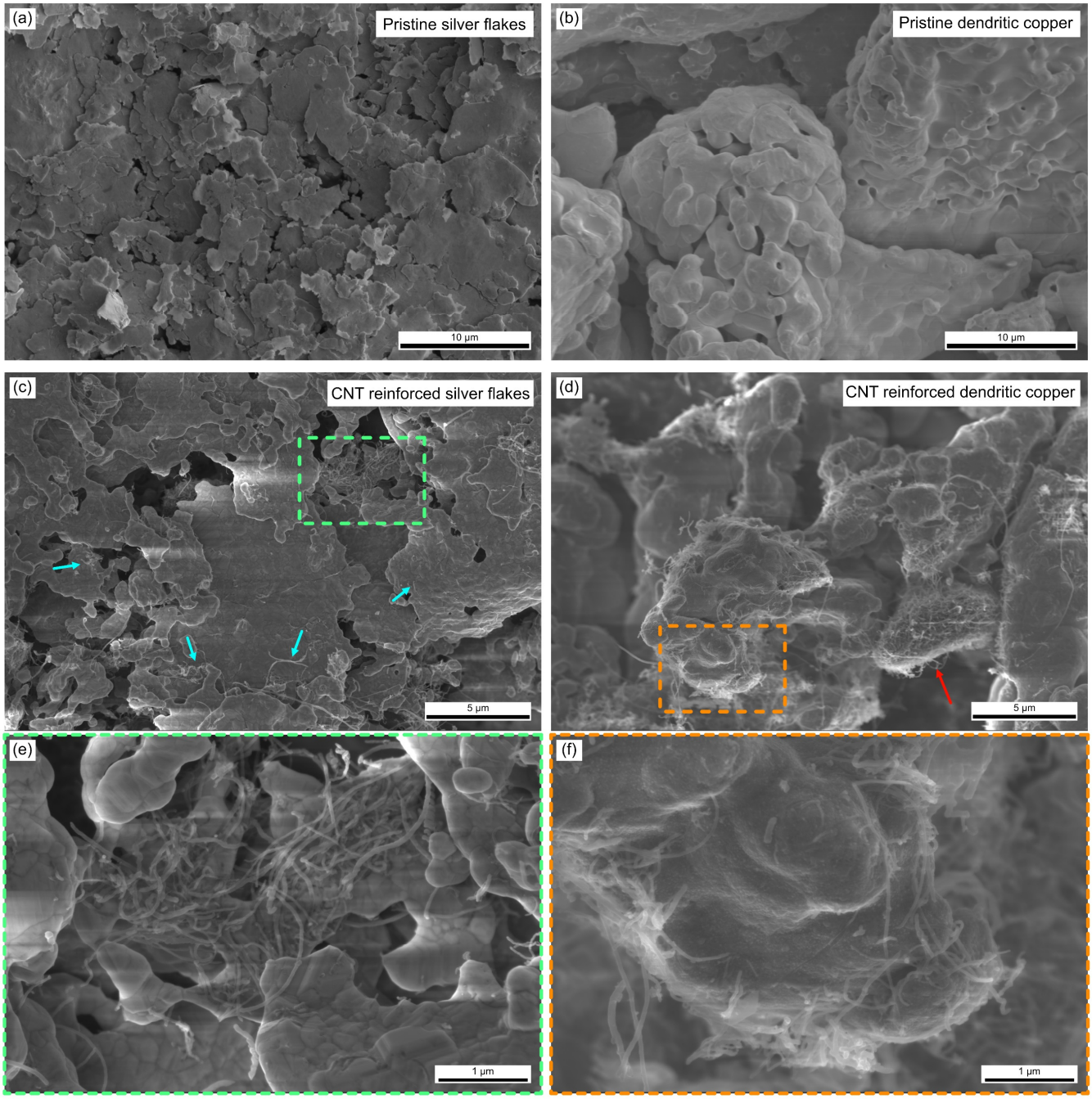

Figure 3. SEM micrograph of: (**a**) pristine silver flakes and (**b**) dendritic copper, CNT reinforced (**c**) silver flakes and (**d**) dendritic copper. (**e**,**f**) show a magnified micrograph of the CNT reinforced silver and copper powder, respectively.

Observing the silver-CNT mixture, regions with high CNT content can be observed, as highlighted by the green square in Figure 3e as well as at the bottom left of Figure 3c. Although the CNT dispersion is not as homogeneous as desired, regions with CNT depletion still present individual or small CNT bundles. These are found primarily at or near the edges of the silver flakes, as highlighted by the cyan arrows. The copper-CNT mixture, on the other hand, shows a much more homogeneous CNT distribution throughout the powder mixture. Small CNT bundles are deposited uniformly on the grooves and edges of the dendritic copper powder. This has also been observed and reported by Guiderdoni et al. for higher CNT concentrations [39]. They state that a proper distribution of the dispersed CNT leads to improved integration into Cu matrices after sintering. However, the final density of the high CNT content composites was strongly reduced (73%). Although the silver flakes are smaller than the dendritic copper (average particle sizes of 20 µm and 44 µm, respectively), the morphology of the copper powder increases surface area. This increased surface area in turn promotes CNT deposition onto the metallic powder. Nonetheless, this powder mixture presents the potential drawback of relatively large CNT agglomerates found within the mixture (highlighted by the red arrow). The presence of CNT agglomerates (similar to those observed in Figure S1a) could negatively impact the resulting CNT distribution in the sintered MMC. In this case, the silver-CNT mixture could prove more adequate since only small CNT bundles are found within the powder. A more uniform CNT distribution is desired not only to ensure consistency throughout the composite but also to maximize the sought-after properties of the reinforcement phase. A longer dispersion process could prove counterproductive since the shear forces and sonication shorten the tubes as well as damage the carbon lattice [40]. Consequently, a trade-off between agglomerate breakdown and tolerable incurred damage must be made [41], since structural damage and inter-tube interactions diminish the intrinsic physical properties of the CNT.

3.2. Characterization of Sintered MMC

The relative density of the composite samples is a crucial parameter to evaluate the effectiveness of the sintering process—results shown in Table 1. As observed, the copper MMC reached remarkable density levels. However, this was not the case with silver MMC (Ag-p), with values below 80%. The graphs in Figure S2 show the pressure variation in HUP during the heating stage. In both metallic matrices, pressure gradually decreases as the temperature increases, reaching final values of approximately 175 MPa.

Table 1. Sintered MMC relative density and hardness.

	Reinforcement Concentration/wt.%	**Ag-p ***	**Ag ****	**Cu**
Relative density/%	0.5	64	99	95
	0.75	74	92	99
	1	78	99	99
Hardness/MPa	0 ***	847 ± 61	-	1335 ± 82
	0.5	-	515 ± 21	582 ± 93
	0.75	-	351 ± 18	467 ± 96
	1	-	505 ± 37	619 ± 88

* Low density silver samples sintered for 2.5 h isothermal holding time. ** Re-pressed silver samples sintered for an additional 7.5 h isothermal holding time. *** Reference samples from high-purity rods.

Low densities in silver MMC will not only lower the mechanical properties of the resulting composite but also the electrical performance since internal porosities are potential electron scattering sites. Therefore, a re-pressing process was incorporated into the production process of silver MMC. Re-pressing consisted of an additional HUP process with the same conditions but with an isothermal holding time of 7.5 h. The longer holding time allows for improved diffusion of the metallic matrix, thus eliminating internal porosities and consequently improving density. Observing Table 1, the re-pressing process indeed

improved density, with silver MMC now reaching satisfactory values above 90%. Therefore, electrical characterization of silver MMC was carried out after the re-pressing process.

It is unclear as to why silver requires longer isothermal holding times compared with copper under identical HUP parameters. Considering the equation of diffusion, shown in Equation (1) [42], there are two parameters that could justify the prolonged thermal energy required by silver MMC, namely: the self-diffusion coefficient (D_0) and the activation energy (E_a)—i.e., thermal energy—which are both independent of temperature [42]. However, both the self-diffusion coefficient and activation energy are lower for silver [43–45], thus resulting in an approximate diffusion coefficient at 750 °C of 1.09 × 10^{-9} cm^2/s and 3.98 × 10^{-11} cm^2/s for silver and copper (determined via Equation (1), respectively).

$$D_{(T)} = D_0 \cdot e^{\frac{-E_a}{R \cdot T}} \quad (1)$$

Moreover, since the melting point of silver is lower than that of copper (961 °C and 1083 °C, respectively [46]), the sintering temperature of both these metallic matrices is closer to the melting point of silver than copper. Therefore, the different isothermal holding times could be caused by different degrees of porosity prior to the sintering process. Accordingly, CLSM measurements of the pre-sintered surfaces were micrographed to further understand the state of the green pellets (see Figure S3). This analysis shows that copper MMC has larger open porosities and a more heterogeneous surface prior to sintering. The silver MMC, on the other hand, shows a considerably more homogeneous surface with few open porosities. This could explain the better densification of copper, since open porosities are more easily eliminated compared with internal porosities due to the bloating of internal pores during sintering [47,48]. At the consolidated state (i.e., only cold pressed), superficial oxidation of the powder plays a fundamental role in the green pellet density since there is significantly less diffusion driving force than when the samples are sintered. Silver is chemically very stable and mechanically softer, therefore rendering a more 'homogeneous' and finer porosity structure than the copper samples.

To gain further insight into the porosity levels of the green pellets, two reference pellets were produced using silver flakes and dendritic copper powder. Focused ion beam (FIB) cross sections were performed on each green pellet to observe the sub-surface porosity state of each green pellet, as shown in Figure 4. Furthermore, Figure S4 shows a micrograph of the consolidated pellets' surface. It is clear that dendritic copper generates green pellets with large pores, both internally and superficially. Silver flakes, on the other hand, produce a surface with fewer open porosities, as demonstrated by Figures S3 and S4. The cross section shown in Figure 4 highlights the considerable number of pores within the consolidated silver pellets. Although the pores observed in silver are smaller than the ones in copper, the magnified micrograph (Figure 4c) shows that these are pervasively found throughout the entirety of the green pellet. The abundance of internal micro-pores within the silver pellet is the main cause of the extended sintering requirements [47,48]. The larger pores observed in the copper pellets, on the other hand, are less abundant. Therefore, 2.5 h of isothermal holding time is sufficient to achieve sintered relative densities above 90%.

CLSM light scans of the sintered composite samples are shown in Figure 5. From these micrographs, insight into CNT distribution and homogeneity can be obtained. The micrographs show that CNT are better distributed in silver MMC, with smaller, more evenly spaced clusters. For copper, on the other hand, larger CNT bundles are observed, especially at higher concentrations (e.g., Figure 5f). These larger clusters in copper composites are caused by the greater affinity between CNT and CNT agglomerates rather than with copper. Consequently, higher reinforcement phase uniformity is observed in silver composites. A uniform distribution promotes homogeneous behavior regardless of the site contacted. This plays a crucial role not only in the repeatability of ECR but also in the elastic restitution of the contacting surfaces.

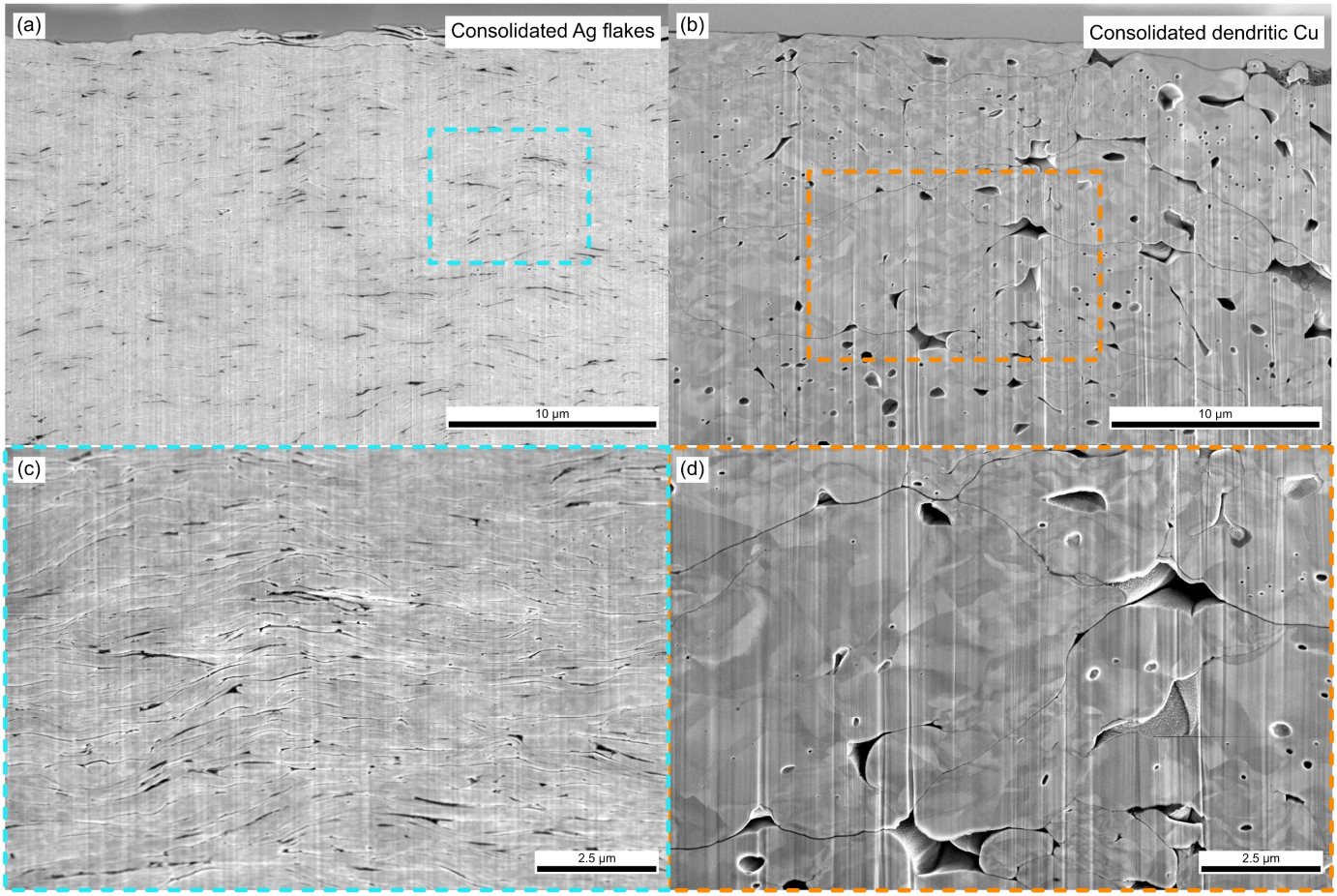

Figure 4. FIB cross section of consolidated (**a**) silver flakes and (**b**) dendritic copper powder. Magnified view of the consolidated (**c**) silver and (**d**) copper pellets.

The Vickers hardness ($HV_{0.01}$) of the composites and reference samples is also shown in Table 1. These results show that no mechanical reinforcement during the second phase took place in the composite samples. However, it should be noted that these hardness values are compared with high-purity reference materials. Softer composites were to be expected on account of the sintering process at relatively high temperatures and prolonged holding times—particularly in the silver MMC due to the re-pressing process. As reported by Garcia et al. [49], a reduction in the sintering temperature of 200 °C yields much harder composites as a consequence of shorter coarsening times for microstructural processes to occur (i.e., recovery and grain growth). Consequently, a trade-off must be made between better mechanical performance and proper densification of our composite samples. Since the intended application for the MMC produced is electrical switches, higher composite densities take precedence over mechanical properties. Moreover, proper densification also plays an important role in the composite's mechanical behavior, as exemplified by the re-pressed Ag 0.75% MMC. This sample shows the lowest relative density (92%) even after re-pressing, which negatively impacts the hardness of the composite, showing a hardness value that is approximately 30% lower than the denser silver MMC. Therefore, even though the CNT reinforcement phase weakens—to a certain extent—the mechanical performance of the MMC, adequate densification also plays an important role.

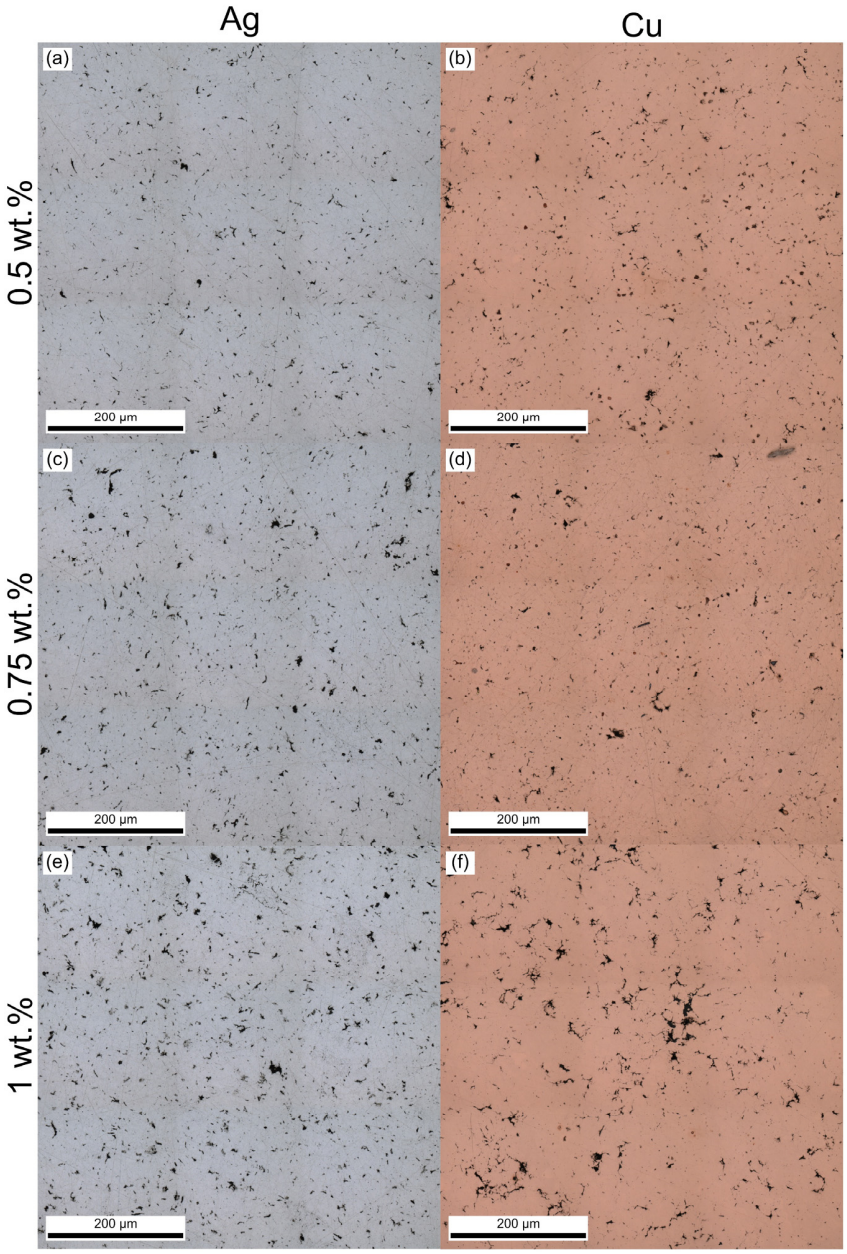

Figure 5. 3 × 3 stitching at 50× CLSM scan of CNT reinforced samples' surface. (**a**) Ag 0.5%, (**b**) Cu 0.5%, (**c**) Ag 0.75%, (**d**) Cu 0.75%, (**e**) Ag 1%, and (**f**) Cu 1%.

3.3. Electrical Tests

3.3.1. Load-Dependent ECR

The load-dependent ECR of the reference and CNT-reinforced silver matrices is shown in Figure 6. Comparing the ECR values of the reference sample with the reinforced samples, it is clear that the addition of CNT promotes lower resistances. At all loads in both cycles, the reference sample shows an ECR that ranges from 5 to 7 mΩ. Ag 0.5%, on the other hand, shows ECR values that range from 2 to 6 mΩ, whereas Ag 0.75% and Ag 1% achieved ECR values of approximately 1 mΩ, even falling below that value for higher normal loads.

Although all MMC show exceptional densities post-sintering, it was not expected that they would outperform the reference sample since the interface between CNT clusters and the metallic matrix can act as electron scattering sites, thus increasing the electrical resistance of the system. It is hypothesized that the reduction in ECR observed is both a direct result of the reinforcement phase and also due to the relative softness of the contact material. Although silver is considered a soft metal, the resulting silver MMC are, on

average, about 40% softer than the reference (see Table 1)—with Ag 0.75% resulting in even lower hardness values. Therefore, the combination of the considerably harder counter electrode and the softer silver MMC favors lower ECR values due to an enlarged contact area. As the hard counter electrode (Vickers microhardness: 1.38 ± 0.01 GPa) is pressed against the soft composites, topographic features on the surface of the composites are flattened while the topographic features of the counter electrode are imprinted onto the MMC's surface. As a consequence of the permanent deformation of the MMC's surface, the real contacting area of the two surfaces approaches the apparent contact area, thus improving the electrical performance of the system. This hypothesis is further supported by the fact that Ag 0.75% (sample with the lowest hardness) shows the lowest ECR values.

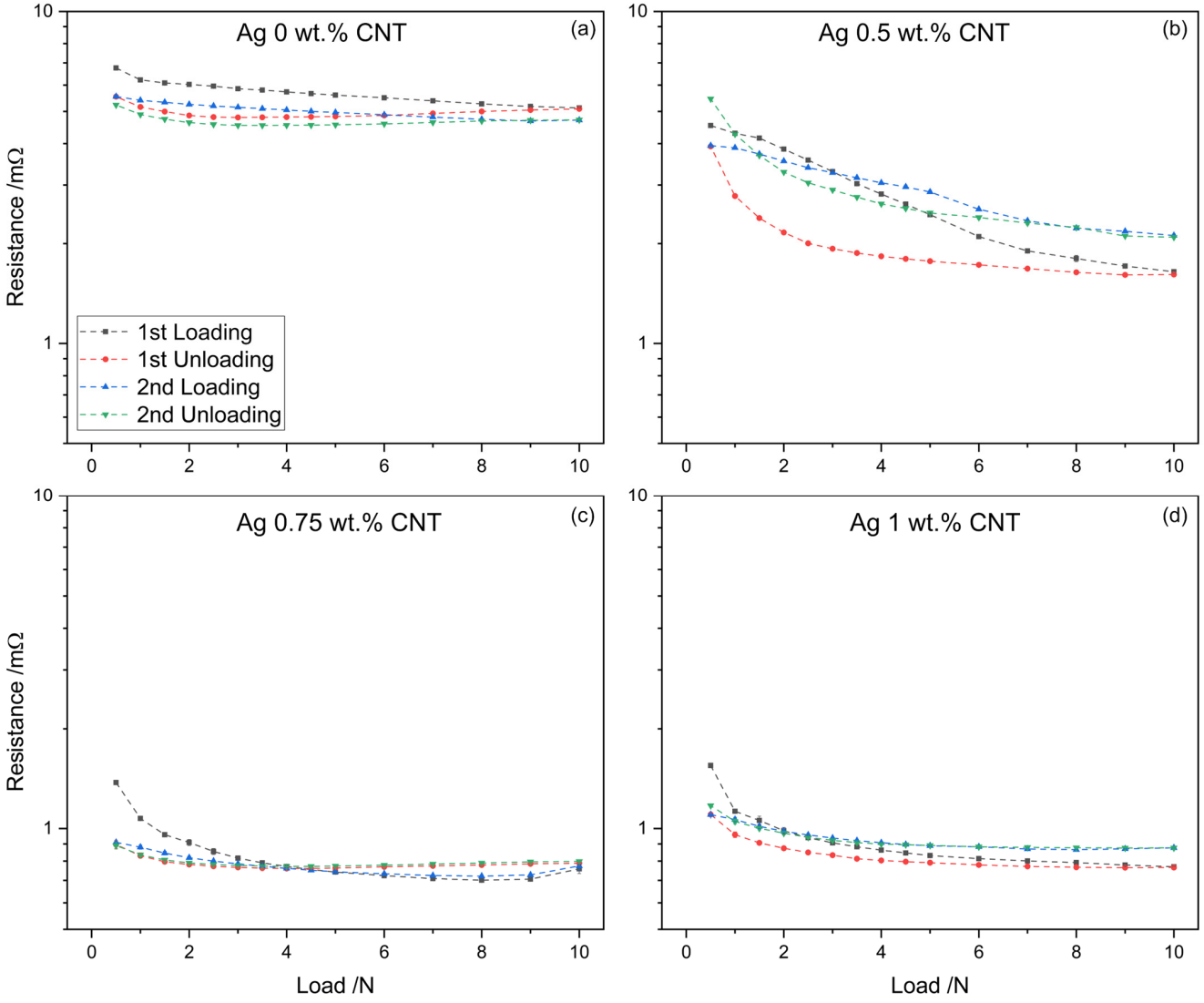

Figure 6. Two cycles of load dependent ECR of CNT reinforced Ag matrices. (**a**) Ag 0%, (**b**) Ag 0.5%, (**c**) Ag 0.75%, and (**d**) Ag 1%.

To validate the proposed hypothesis, post-ECR CLSM measurements were carried out on the reference and composite samples. The root mean squared roughness of the polished surface prior to ECR and the imprint left by the counter electrode after ECR, as well as the diameter of the imprint left by the counter electrode, are shown in Table 2. As the table demonstrates, the roughness of the composites' surfaces increases after ECR measurements. The degree to which the roughness increases appears to depend on the hardness of the sample since the increase is negligible in the reference sample, with Ag 0.75% showing the highest increase. The increment in roughness is due to the roughness present in the counter

electrode (which has a root mean square roughness of 260 nm). Similarly, contacting softer surfaces generates a larger imprint. Therefore, the CLSM results validate the hypothesis, thus explaining the behavior of Ag 0.75%.

Table 2. Roughness values prior to and post-ECR of silver and copper MMC, as well as approximate imprint diameter left by counter electrode.

	Roughness Prior to ECR/nm	Roughness Post-ECR/nm	Imprint Diameter/µm
Ag 0%	10 ± 10	40 ± 10	47.7 ± 4.4
Ag 0.5%	20 ± 10	100 ± 10	87.2 ± 1.5
Ag 0.75%	40 ± 10	130 ± 20	119.9 ± 5.1
Ag 1%	60 ± 10	110 ± 10	98.2 ± 2.1
Cu 0.5%	10 ± 10	110 ± 20	95.2 ± 5.9
Cu 0.75%	10 ± 10	120 ± 20	101.5 ± 3.6
Cu 1%	10 ± 10	110 ± 20	94.2 ± 2.8

These tests were conducted for two loading and unloading cycles; therefore, the repeatability of the contacting surfaces can be evaluated by the difference in ECR values in the second measurement cycle compared with the first. As shown in Figure 6, higher CNT concentrations promote more repeatable contacting surfaces. Comparing the reference sample with Ag 0.75% and Ag 1%, the former shows a higher mechanical hysteresis than the reinforced samples. The improved contact repeatability is likely a consequence of the high elastic restitution provided by the addition of CNT, coupled with the relative softness of the composite samples. Ag 0.5% on the other hand, shows the largest mechanical hysteresis. This could be caused by contact heterogeneity. Since this sample contains the lowest concentration of CNT, the presence of larger CNT clusters instead of a homogeneous CNT distribution could cause differences in the contacting situation throughout the contact material. Therefore, regions with more CNT clusters could prove more repeatable, whereas regions with fewer CNT clusters would show higher mechanical hysteresis (see Figure 5). Consequently, composites with higher concentrations—and therefore higher likelihood of larger CNT clusters—show improved elastic restitutive behavior. Furthermore, the lack of restitution coupled with a softer—and thus a more easily deformed surface—negatively impacts the contact area. Consequently, the ECR during unloading will tend to be higher than while loading.

The load-dependent ECR results for the copper-based composites are shown in Figure 7. As for silver, the average roughness prior to and post-ECR was measured—shown in Table 2. These values correlate with the microhardness values measured (see Table 1). The imprint on the reference sample could not be observed using CLSM due to the higher hardness value.

Since the hardness and, correspondingly, the imprint size for the reinforced copper samples are—to a certain extent—similar, the influence of reinforcement phase concentration on the electrical performance of the composite can be better evaluated. Observing Figure 7, higher CNT concentrations promote lower ECR values throughout the measurement cycles, the same tendency that was observed in silver-based composites. All reinforced samples outperformed the reference, with values below 100 mΩ at 10 N after both cycles. The reference sample, on the other hand, showed three-fold and two-fold resistance after the first and second cycles, respectively. Therefore, load-dependent ECR on copper-based composites proves that the addition of CNT within the metallic matrix improves electrical performance.

Interestingly, the second measurement cycle showed higher resistance in the reinforced samples, whereas in the reference sample the opposite was true. This behavior, in combination with the mechanical hysteresis observed in the reinforced samples, demonstrates the elastic restitution of the resulting contact material as a consequence of the CNT. Although all copper composites show some degree of elastic restitution, Cu 1% displays the highest contact repeatability, as demonstrated by the low mechanical hysteresis exhibited.

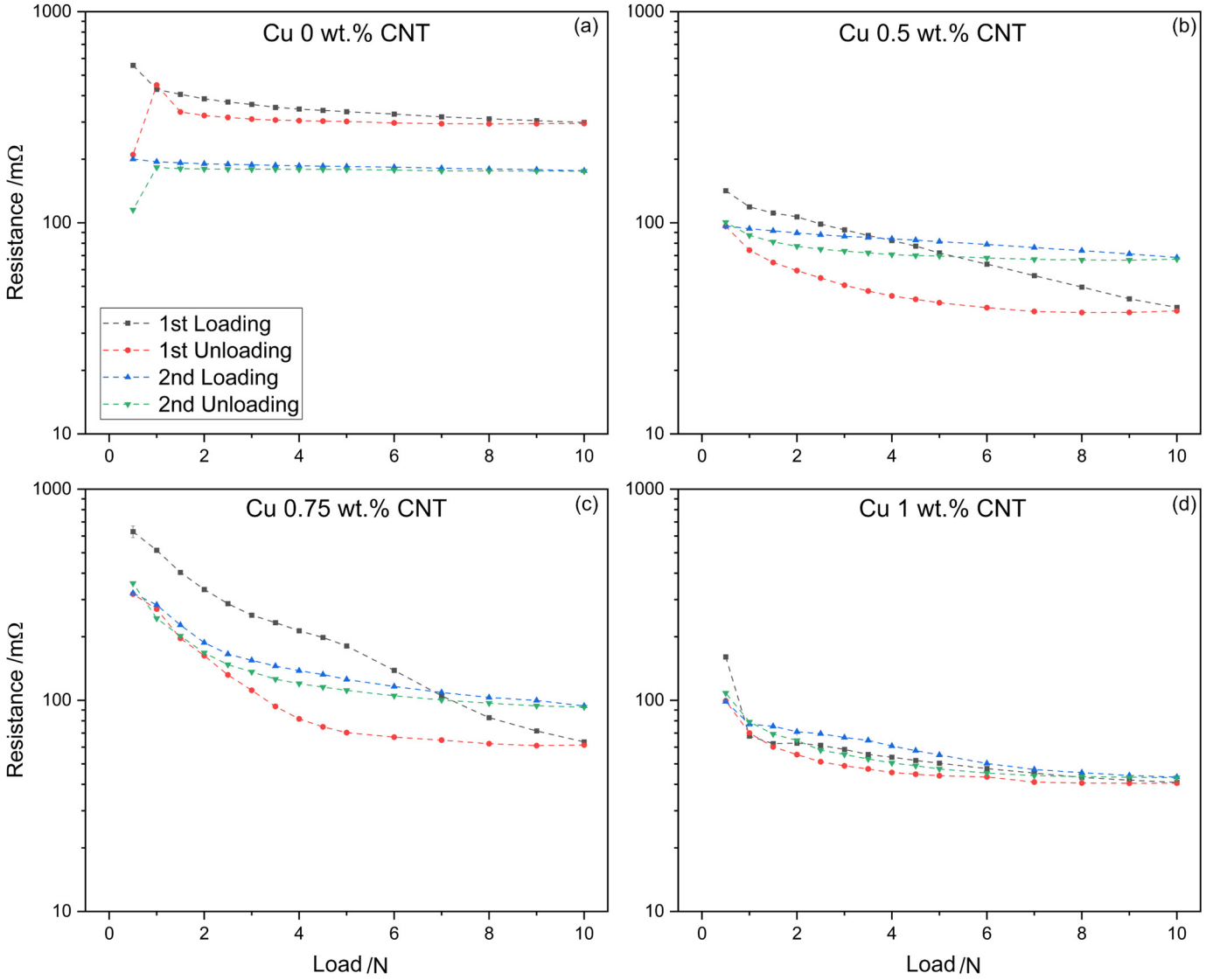

Figure 7. Two cycles of load dependent ECR of CNT reinforced Cu matrices. (**a**) Cu 0%, (**b**) Cu 0.5%, (**c**) Cu 0.75%, and (**d**) Cu 1%.

3.3.2. Fatigue Cycles

Fatigue tests aim to evaluate the ECR evolution during monotonic loading. Therefore, 20 loading and unloading cycles were performed, tracking the ECR of the composites and reference samples at 1 N, 3 N, and 5 N. The results for silver MMC are shown in Figure 8. The reference sample performed consistently throughout the fatigue tests, with ECR values ranging from 20 to 48 mΩ. Ag 0.5% and Ag 0.75%, on the other hand, performed well initially—9–20 mΩ and 2.5–6.5 mΩ, respectively. However, as the fatigue test progressed, ECR steadily increased, stabilizing at 50–70 mΩ and 17–21.6 mΩ, respectively. Although the resistance increased during fatigue cycles, the steady-state values resemble or even outperform those measured for the reference sample. Ag 1% behaves akin to the reference sample, however, with significantly lower resistance values—between 4 and 6 mΩ throughout the fatigue test. It is unclear as to why the ECR of Ag 0.5% and Ag 0.75% increases. One possible explanation is that higher CNT concentrations favor a more homogeneous contact, thus improving contacting surface uniformity and consequently showing an electrical performance that resembles that of the unreinforced sample. As was the case with load-dependent ECR, the lower ECR values observed during fatigue tests are attributed to the larger contact area achieved due to the softer composites.

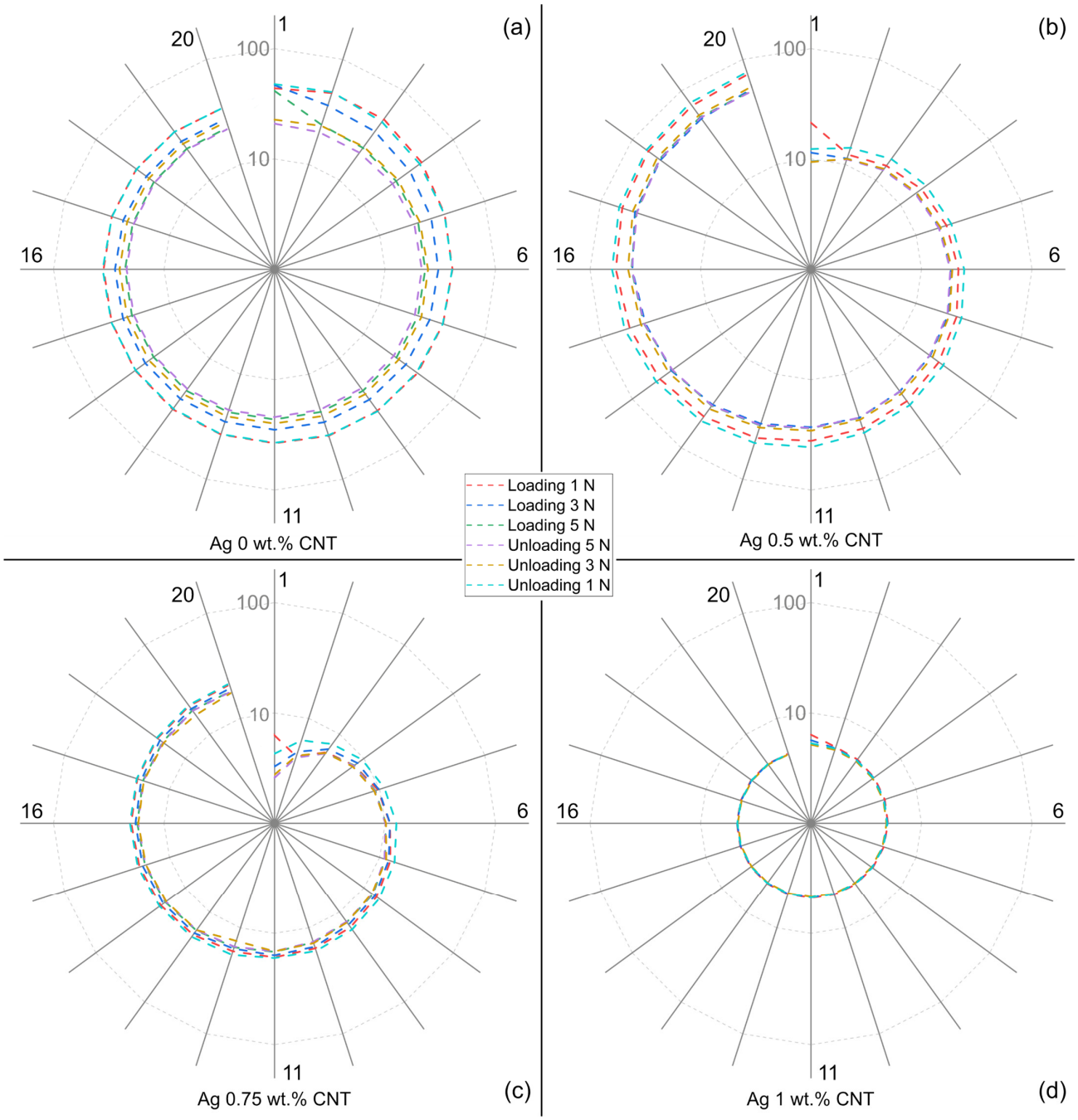

Figure 8. Fatigue cycle tests of CNT reinforced Ag matrices. (**a**) Ag 0%, (**b**) Ag 0.5%, (**c**) Ag 0.75%, and (**d**) Ag 1%. The radial lines indicate the progression of fatigue cycles (clockwise). Error in measurements below 5%.

The electrical behavior during fatigue tests of the silver MMC can be better visualized in a 2D kernel density estimation plot, shown in Figure S5. Here, the tendencies of the MMC can be more easily observed. The plot shows that for CNT concentrations greater than 0.75 wt.% the steady-state ECR values outperform the unreinforced reference. Furthermore, CLSM analysis prior to and post-fatigue tests was carried out, with the results shown in Table S1. The results obtained correlate with the results from load-dependent ECR.

The evolution of ECR during fatigue tests in copper MMC is shown in Figure 9, with the 2D kernel density estimation plot shown in Figure S6. The behavior of the reference sample oscillates considerably throughout the test, with ECR values ranging from 45 to 950 mΩ (between 200 and 300 mΩ at 5 N). This constant fluctuation in ECR could

jeopardize the reliability of the electrical contacts. The reinforced samples, on the other hand, show uniform electrical behavior. In all cases, the ECR values fluctuate from 50 to 190 mΩ. Not only does the reinforcement phase improve the repeatability of the contact, but it also stabilizes and reduces the overall resistance of the system. Cu 0.5% showed the most constant results, with Cu 0.75% showing a slight increase in ECR and Cu 1% a slight decrease. Nonetheless, the steady-state values outperform the reference sample for all CNT concentrations. Results from CLSM analysis prior to and post-fatigue tests are shown in Table S2.

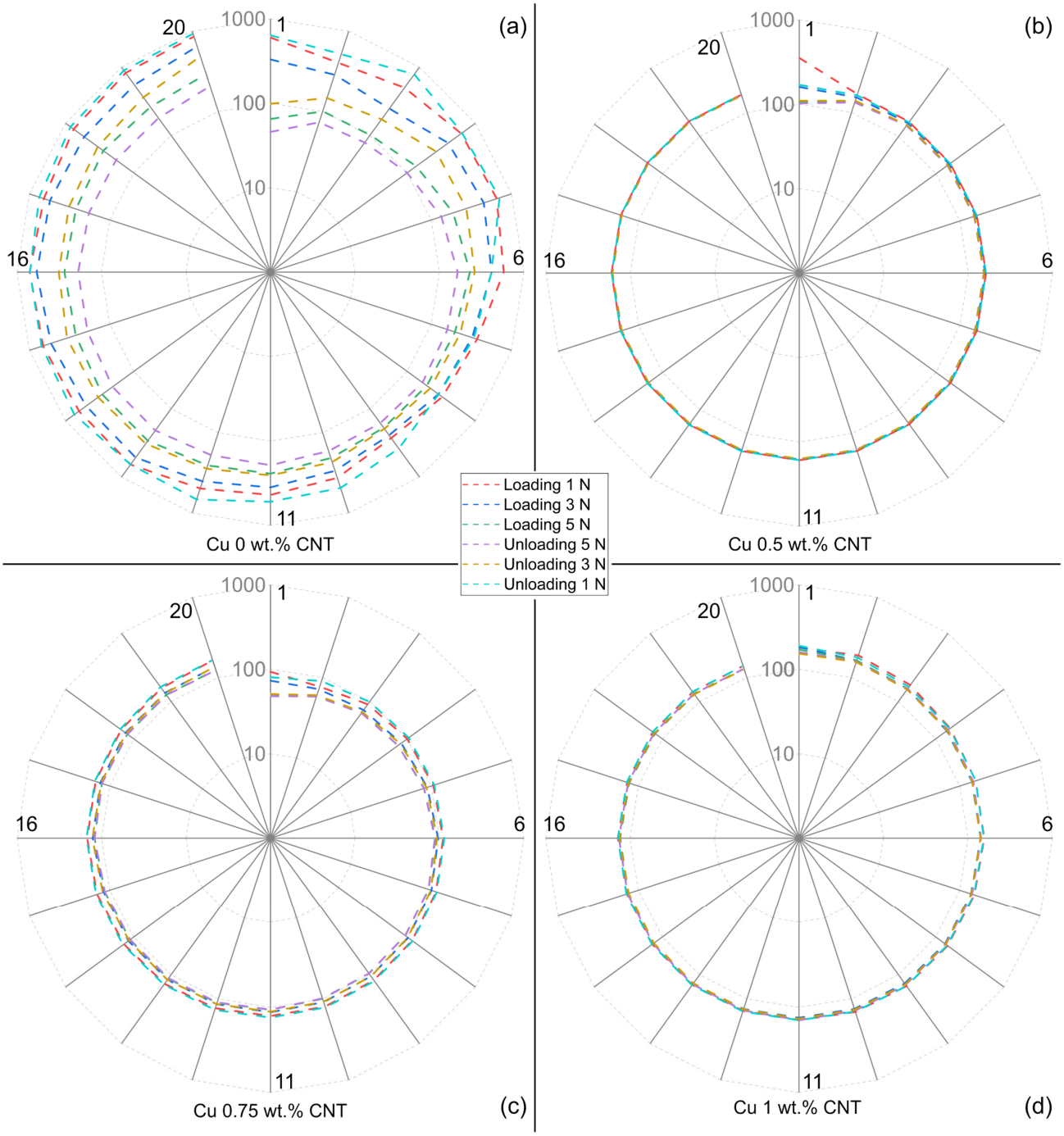

Figure 9. Fatigue cycle tests of CNT reinforced Cu matrices. (**a**) Cu 0%, (**b**) Cu 0.5%, (**c**) Cu 0.75%, and (**d**) Cu 1%. The radial lines indicate the progression of fatigue cycles (clockwise). Error in measurements below 5%.

4. Conclusions

Carbon nanotube-reinforced silver and copper metal matrix composites at three different reinforcement concentrations (0.5 wt.%, 0.75 wt.%, and 1 wt.%) were produced via powder metallurgy. The powder blends and sintered samples were characterized using light and electron microscopy techniques, followed by in-depth electrical characterization—namely, load-dependent ECR and surface fatigue tests. From this study, the following conclusions can be drawn:

- Not only does particle size play an important role in CNT integration but also particle morphology, with the larger-sized copper powder showing better CNT deposition than the smaller-sized silver powder;
- Green pellets formed with silver flakes present an abundance of internal micro-pores. Consequently, a re-pressing post process with prolonged isothermal holding times was required to achieve acceptable silver composite densities;
- The MMC produced did not show the reinforcement effect due to the prolonged sintering process at relatively elevated temperatures. As a consequence, the composites showed low hardness values, which in turn allowed the hard counter electrode to imprint onto the composites' surfaces—an effect that was more noticeable in the softer silver composites. Nonetheless, the addition of CNT reduced the contact resistance throughout all normal loads measured, with higher concentrations producing the lowest resistance values. Higher CNT concentrations also produced highly reproducible contact surfaces;
- All MMC outperformed the reference material in fatigue tests, rapidly reaching steady-state ECR values and maintaining low resistance throughout the 20 fatigue cycles measured.

In future work, it would be of interest to evaluate the viability of different metallic powder morphology. Furthermore, studies on the influence of CNT size and chemical state (i.e., pristine or functionalized/oxidized state) could provide insight into the mechanisms behind the integration of the reinforcement phase onto the metallic powder, as well as on the homogeneity/uniformity of the reinforcement phase distribution. Moreover, microstructural analysis of the sintered samples would grant deeper insight into the lack of reinforcement effect with the addition of CNT.

Supplementary Materials: The following supporting information can be downloaded at: https://www.mdpi.com/article/10.3390/jcs7070284/s1. Figure S1: SEM micrographs of pristine CNT at different magnifications; Figure S2: Pressure variation during heating stage of HUP for (a) Ag-MMC and (b) Cu-MMC; Figure S3: 50× surface CLSM scan of green pellets (pre-sintered samples) showing three linear roughness scans in regions with open porosities; Figure S4: Surface SEM micrograph of consolidated a) silver flakes and b) dendritic copper powder; Figure S5: Kernel density estimation plot of ECR during multiple fatigue cycles of CNT reinforced Ag matrices. (a) Ag 0%, (b) Ag 0.5%, (c) Ag 0.75%, and (d) Ag 1%. Note the different y-axis ranges; Table S1: Roughness values prior to and post-fatigue tests of silver MMC, as well as approximate imprint diameter left by counter electrode; Figure S6: Kernel density estimation plot of ECR during multiple fatigue cycles of CNT reinforced Cu matrices. (a) Cu 0%, (b) Cu 0.5%, (c) Cu 0.75%, and (d) Cu 1%. Note the different y-axis ranges; Table S2: Roughness values prior to and post-fatigue tests of copper MMC, as well as approximate imprint diameter left by counter electrode.

Author Contributions: Conceptualization, B.A. and S.S.; methodology, B.A. and S.S.; validation, B.A.; formal analysis, B.A.; investigation, B.A.; resources, F.M.; data curation, B.A.; writing—original draft preparation, B.A.; writing—review and editing, S.S.; visualization, B.A.; supervision, S.S.; project administration, F.M. and S.S.; funding acquisition, F.M. and S.S. All authors have read and agreed to the published version of the manuscript.

Funding: This research received no external funding.

Data Availability Statement: Data available upon reasonable request from the corresponding author.

Acknowledgments: B. Alderete wishes to acknowledge the support from the German Academic Exchange Service (DAAD) and the Roberto Rocca Education Program (RREP). The authors gratefully acknowledge funding in the ZuMat project, supported by the State of Saarland from the European Regional Development Fund (Europäischen Fonds für Regionale Entwicklung, EFRE). Funding for the PFIB/SEM instrument by German Research Foundation is greatly acknowledged (INST 256/510-1 FUGG). The authors wish to thank Christoph Pauly for his assistance in the acquisition of SEM micrographs.

Conflicts of Interest: The authors declare no conflict of interest.

References

1. Saito, R.; Dresselhaus, G.; Dresselhaus, M.S. *Physical Properties of Carbon Nanotubes*; Imperial College Press: London, UK, 1998; ISBN 978-1-86094-223-5.
2. Dresselhaus, M.S.; Dresselhaus, G.; Saito, R. Physics of Carbon Nanotubes. *Carbon* **1995**, *33*, 883–891. [CrossRef]
3. Popov, V.N. Carbon Nanotubes: Properties and Application. *Mater. Sci. Eng. R Rep.* **2004**, *43*, 61–102. [CrossRef]
4. Saifuddin, N.; Raziah, A.Z.; Junizah, A.R. Carbon Nanotubes: A Review on Structure and Their Interaction with Proteins. *J. Chem.* **2013**, *2013*, 18. [CrossRef]
5. Nasir, S.; Hussein, M.Z.; Zainal, Z.; Yusof, N.A. Carbon-Based Nanomaterials/Allotropes: A Glimpse of Their Synthesis, Properties and Some Applications. *Materials* **2018**, *11*, 295. [CrossRef]
6. Ebbesen, T.W. Carbon Nanotubes. *Chem. Eng. News* **2001**, *79*, 11.
7. Maiti, A.; Svizhenko, A.; Anantram, M.P. Electronic Transport through Carbon Nanotubes: Effects of Structural Deformation and Tube Chirality. *Phys. Rev. Lett.* **2002**, *88*, 4. [CrossRef]
8. Yanagi, K.; Udoguchi, H.; Sagitani, S.; Oshima, Y.; Takenobu, T.; Kataura, H.; Ishida, T.; Matsuda, K.; Maniwa, Y. Transport Mechanisms in Metallic and Semiconducting Single-Wall Carbon Nanotube Networks. *ACS Nano* **2010**, *4*, 4027–4032. [CrossRef]
9. Krupke, R.; Hennrich, F.; Löhneysen, H.V.; Kappes, M.M. Separation of Metallic from Semiconducting Single-Walled Carbon Nanotubes. *Science* **2003**, *301*, 344–347. [CrossRef]
10. Robertson, J.; Zhong, G.; Hofmann, S.; Bayer, B.C.; Esconjauregui, C.S.; Telg, H.; Thomsen, C. Use of Carbon Nanotubes for VLSI Interconnects. *Diam. Relat. Mater.* **2009**, *18*, 957–962. [CrossRef]
11. Ando, T.; Matsumura, H.; Nakanishi, T. Theory of Ballistic Transport in Carbon Nanotubes. *Physica B* **2002**, *323*, 44–50. [CrossRef]
12. Svizhenko, A.; Anantram, M.P.; Govindan, T.R. Ballistic Transport and Electrostatics in Metallic Carbon Nanotubes. *IEEE Trans. Nanotechnol.* **2005**, *4*, 557–562. [CrossRef]
13. Li, H.J.; Lu, W.G.; Li, J.J.; Bai, X.D.; Gu, C.Z. Multichannel Ballistic Transport in Multiwall Carbon Nanotubes. *Phys. Rev. Lett.* **2005**, *95*, 086601. [CrossRef] [PubMed]
14. Van Der Veen, M.H.; Barbarin, Y.; Kashiwagi, Y.; Tokei, Z. Electron Mean-Free Path for CNT in Vertical Interconnects Approaches Cu. In Proceedings of the 2014 IEEE International Interconnect Technology Conference/Advanced Metallization Conference, San Jose, CA, USA, 20–23 May 2014; pp. 181–184.
15. Li, H.; Yin, W.Y.; Banerjee, K.; Mao, J.F. Circuit Modeling and Performance Analysis of Multi-Walled Carbon Nanotube Interconnects. *IEEE Trans. Electron. Devices* **2008**, *55*, 1328–1337. [CrossRef]
16. Che, J.; Tahir, T.; Gın, Ť.; Iii, W.A.G. Thermal Conductivity of Carbon Nanotubes. *Nanotechnology* **2000**, *11*, 65–69. [CrossRef]
17. Osman, M.A.; Srivastava, D. Temperature Dependence of the Thermal Conductivity of Single-Wall Carbon Nanotubes. *Nanotechnology* **2001**, *12*, 21–24. [CrossRef]
18. Kim, P.; Shi, L.; Majumdar, A.; McEuen, P.L. Thermal Transport Measurements of Individual Multiwalled Nanotubes. *Phys. Rev. Lett.* **2001**, *87*, 215502. [CrossRef]
19. Graebner, J.E. Thermal Conductivity of Diamond. In *Diamond: Electronic Properties and Applications*; Springer: Boston, MA, USA, 1995; pp. 285–318.
20. Braunovic, M. Effect of Connection Design on the Contact Resistance of High Power Overlapping Bolted Joints. *IEEE Trans. Compon. Packag. Technol.* **2002**, *25*, 642–650. [CrossRef]
21. Suarez, S.; Rosenkranz, A.; Gachot, C.; Mücklich, F. Enhanced Tribological Properties of MWCNT/Ni Bulk Composites—Influence of Processing on Friction and Wear Behaviour. *Carbon* **2014**, *66*, 164–171. [CrossRef]
22. Reinert, L.; Suarez, S.; Rosenkranz, A. Tribo-Mechanisms of Carbon Nanotubes: Friction and Wear Behavior of CNT-Reinforced Nickel Matrix Composites and CNT-Coated Bulk Nickel. *Lubricants* **2016**, *4*, 11. [CrossRef]
23. Suarez, S.; Souza, N.; Lasserre, F.; Mücklich, F. Influence of the Reinforcement Distribution and Interface on the Electronic Transport Properties of MWCNT-Reinforced Metal Matrix Composites. *Adv. Eng. Mater.* **2016**, *18*, 1626–1633. [CrossRef]
24. Alderete, B.; Mücklich, F.; Suarez, S. Characterization and Electrical Analysis of Carbon-Based Solid Lubricant Coatings. *Carbon Trends* **2022**, *7*, 100156. [CrossRef]
25. Alderete, B.; Suarez, S.; Tejeda, D.B.; Mücklich, F. Fretting and Electrical Contact Resistance Characteristics of Carbon Nanoparticle-Coated Cu Electrical Contacts. In Proceedings of the 2022 IEEE 67th Holm Conference on Electrical Contacts (HLM), Tampa, FL, USA, 23–26 October 2022; pp. 1–8.

26. Alderete, B.; Mücklich, F.; Suarez, S. Wear Reduction via CNT Coatings in Electrical Contacts Subjected to Fretting. *Tribol. Lett.* **2023**, *71*, 54. [CrossRef]
27. Kozbial, A.; Zhou, F.; Li, Z.; Liu, H.; Li, L. Are Graphitic Surfaces Hydrophobic? *Acc. Chem. Res.* **2016**, *49*, 2765–2773. [CrossRef] [PubMed]
28. Alderete, B.; Lößlein, S.M.; Bucio Tejeda, D.; Mücklich, F.; Suarez, S. Feasibility of Carbon Nanoparticle Coatings as Protective Barriers for Copper–Wetting Assessment. *Langmuir* **2022**, *38*, 15209–15219. [CrossRef]
29. Alderete, B.; MacLucas, T.; Espin, D.; Brühl, S.P.; Mücklich, F.; Suarez, S. Near Superhydrophobic Carbon Nanotube Coatings Obtained via Electrophoretic Deposition on Low-Alloy Steels. *Adv. Eng. Mater.* **2021**, *23*, 2001448. [CrossRef]
30. Feng, Y.; Yuan, H.L.; Zhang, M. Fabrication and Properties of Silver-Matrix Composites Reinforced by Carbon Nanotubes. *Mater. Charact.* **2005**, *55*, 211–218. [CrossRef]
31. Silvestre, N. State-of-the-Art Review on Carbon Nanotube Reinforced Metal Matrix Composites. *Int. J. Compos. Mater.* **2013**, *2013*, 28–44. [CrossRef]
32. Jamwal, A.; Mittal, P.; Agrawal, R.; Gupta, S.; Kumar, D.; Sadasivuni, K.K.; Gupta, P. Towards Sustainable Copper Matrix Composites: Manufacturing Routes with Structural, Mechanical, Electrical and Corrosion Behaviour. *J. Compos. Mater.* **2020**, *54*, 2635–2649. [CrossRef]
33. Suarez, S.; Lasserre, F.; Mücklich, F. Mechanical Properties of MWNT/Ni Bulk Composites: Influence of the Microstructural Refinement on the Hardness. *Mater. Sci. Eng. A* **2013**, *587*, 381–386. [CrossRef]
34. Pérez, E.M.; Martín, N. π-π Interactions in Carbon Nanostructures. *Chem. Soc. Rev.* **2015**, *44*, 6425–6433. [CrossRef]
35. Klinovaja, J.; Schmidt, M.J.; Braunecker, B.; Loss, D. Carbon Nanotubes in Electric and Magnetic Fields. *Phys. Rev. B* **2011**, *84*, 085452. [CrossRef]
36. Puyol, R.; Suarez, S. A Contact Resistance Measurement Setup for the Study of Novel Contacts. In Proceedings of the IEEE URUCON, Montevideo, Uruguay, 23–25 October 2017; pp. 3–6.
37. Suarez, S.; Alderete, B.; Puyol, R.; Mücklich, F. Load-Dependent Electrical Contact Resistance of Carbon Nanotube-Reinforced Metal Matrix Composites. In Proceedings of the 2022 IEEE 67th Holm Conference on Electrical Contacts (HLM), Tampa, FL, USA, 23–26 October 2022; pp. 1–6.
38. Bock, E.M. Low-Level Contact Resistance Characterization. *AMP J. Technol.* **1993**, *3*, 64–68.
39. Guiderdoni, C.; Pavlenko, E.; Turq, V.; Weibel, A.; Puech, P.; Estournes, C.; Peigney, A.; Bacsa, W.; Laurent, C. The preparation of carbon nanotube (CNT)/copper composites and the effect of the number of CNT walls on their hardness, friction and wear properties. *Carbon* **2013**, *58*, 185–197. [CrossRef]
40. Hilding, J.; Grulke, E.A.; George Zhang, Z.; Lockwood, F. Dispersion of Carbon Nanotubes in Liquids. *J. Dispers. Sci. Technol.* **2003**, *24*, 1–41. [CrossRef]
41. Reinert, L.; Zeiger, M.; Suárez, S.; Presser, V.; Mücklich, F. Dispersion Analysis of Carbon Nanotubes, Carbon Onions, and Nanodiamonds for Their Application as Reinforcement Phase in Nickel Metal Matrix Composites. *RSC Adv.* **2015**, *5*, 95149–95159. [CrossRef]
42. Zener, C. Theory of D0 for Atomic Diffusion in Metals. *J. Appl. Phys.* **1951**, *22*, 372–375. [CrossRef]
43. Tomizuka, C.T.; Sonder, E. Self-Diffusion in Silver. *Phys. Rev.* **1956**, *103*, 1182–1184. [CrossRef]
44. Kuper, A.; Letaw, H.; Slifkin, L.; Sonder, E.; Tomizuka, C.T. Self-Diffusion in Copper. *Phys. Rev.* **1954**, *96*, 1224–1225. [CrossRef]
45. Burton, J.J. Analysis of Silver Self-Diffusion Data. *Philos. Mag. A J. Theor. Exp. Appl. Phys.* **1974**, *29*, 121–133. [CrossRef]
46. Slade, P.G. *Electrical Contacts Principles and Applications*, 2nd ed.; Slade, P.G., Ed.; Taylor & Francis: Boca Raton, FL, USA, 2014; ISBN 13:978-1138077102.
47. Kang, S.-J. *Sintering: Densification, Grain Growth and Microstructure*, 1st ed.; Butterworth-Heinemann: Oxford, UK, 2005; ISBN 9780750663854.
48. Suarez, S. Development of Carbon Nanotube-Reinforced Nickel Matrix Composites: Processing, Microstructure and Physical Properties. Ph.D. Thesis, Universität des Saarlandes, Saarbrücken, Germany, 2014.
49. García, D.; Suárez, S.; Aristizábal, K.; Mücklich, F. Powder-Metallurgical Fabrication and Electrical Contact Resistance Characterization of Copper–Nickel Composites Reinforced by Multiwalled Carbon Nanotubes. *Adv. Eng. Mater.* **2022**, *24*, 2100755. [CrossRef]

Supplementary Material

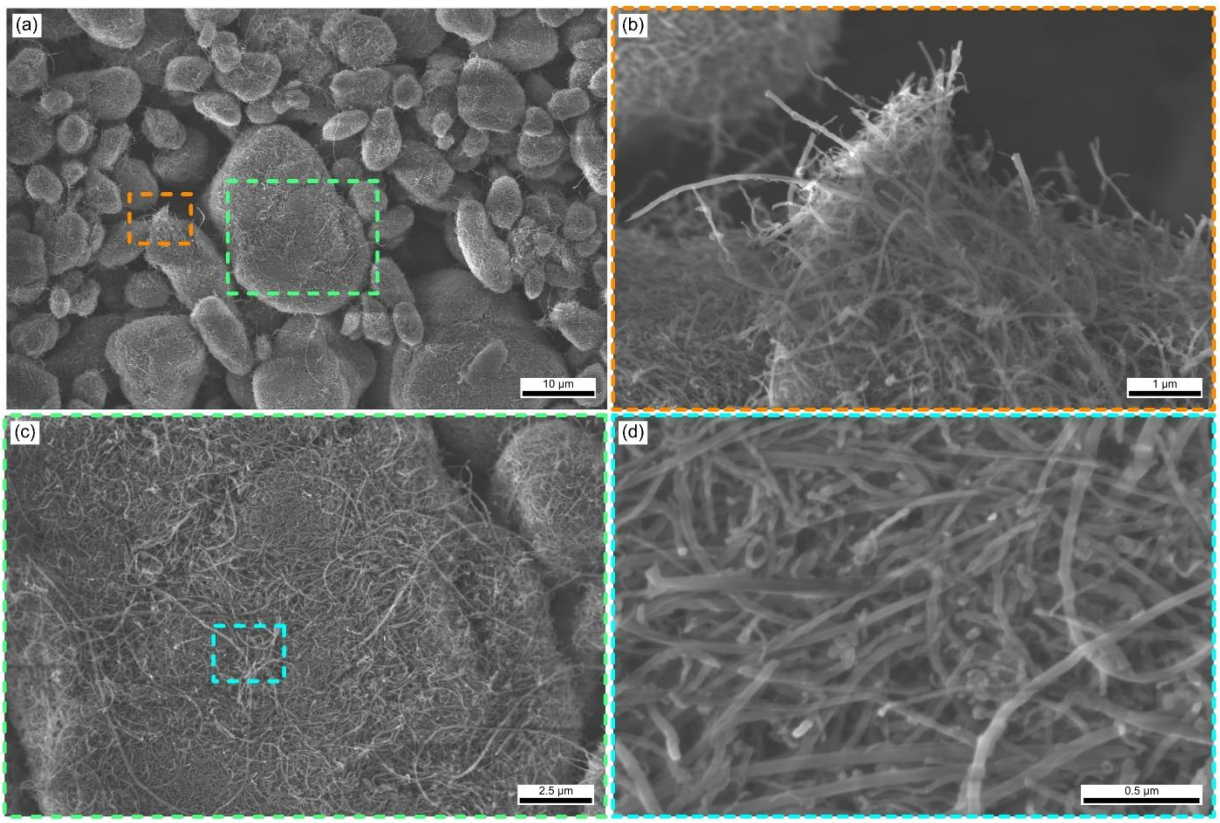

Figure S1. SEM micrographs of pristine CNT at different magnifications.

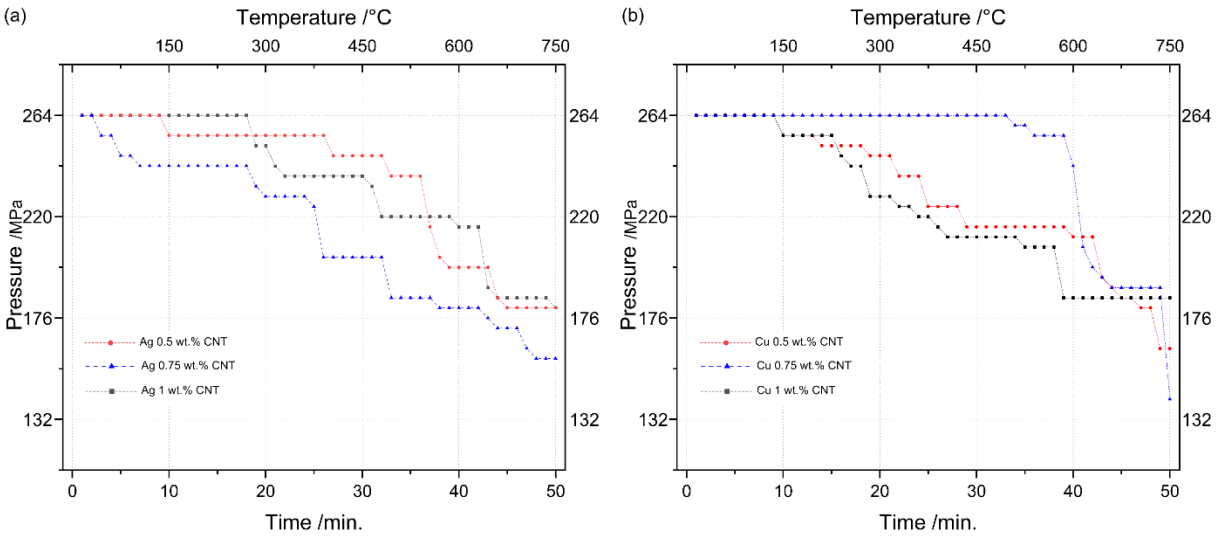

Figure S2. Pressure variation during heating stage of HUP for (a) Ag-MMC and (b) Cu-MMC.

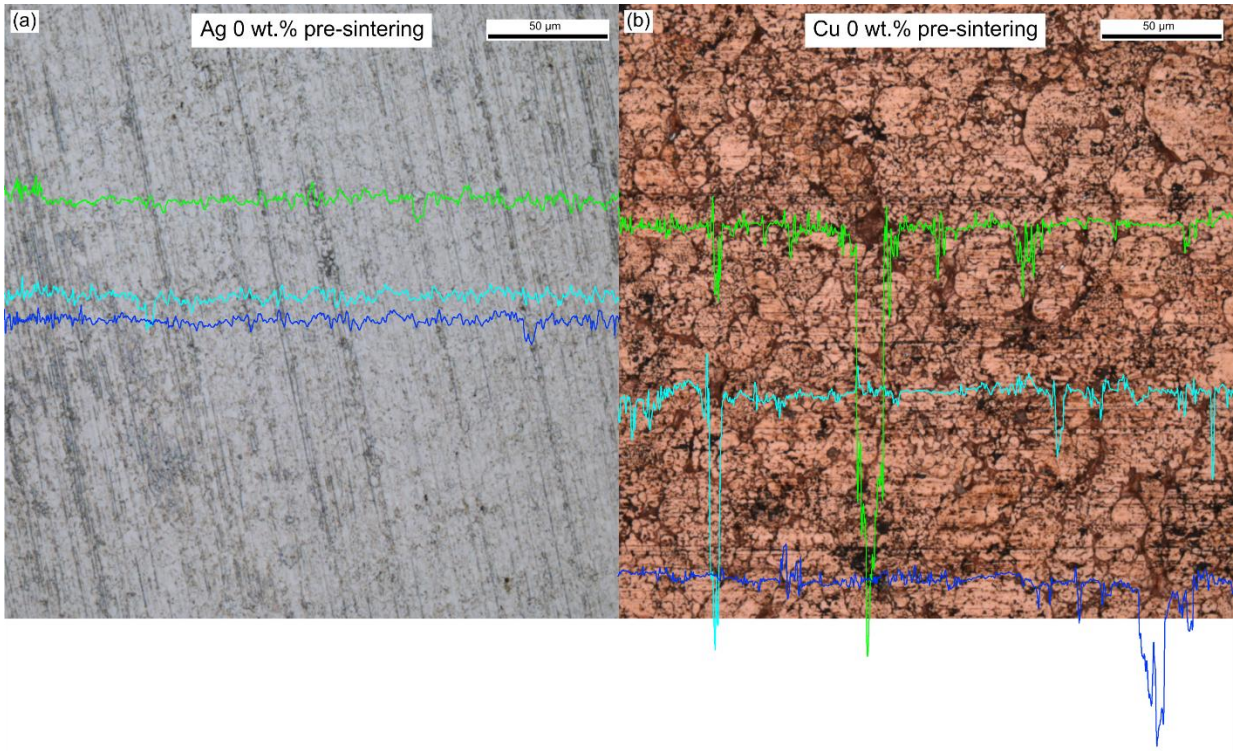

Figure S3. 50× surface CLSM scan of green pellets (pre-sintered samples) showing three linear roughness scans in regions with open porosities.

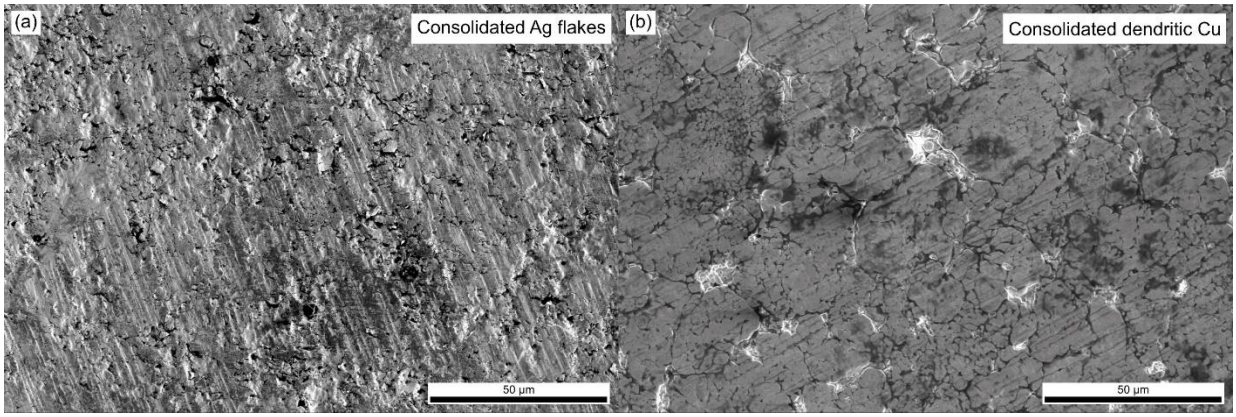

Figure S4. Surface SEM micrograph of consolidated a) silver flakes and b) dendritic copper powder.

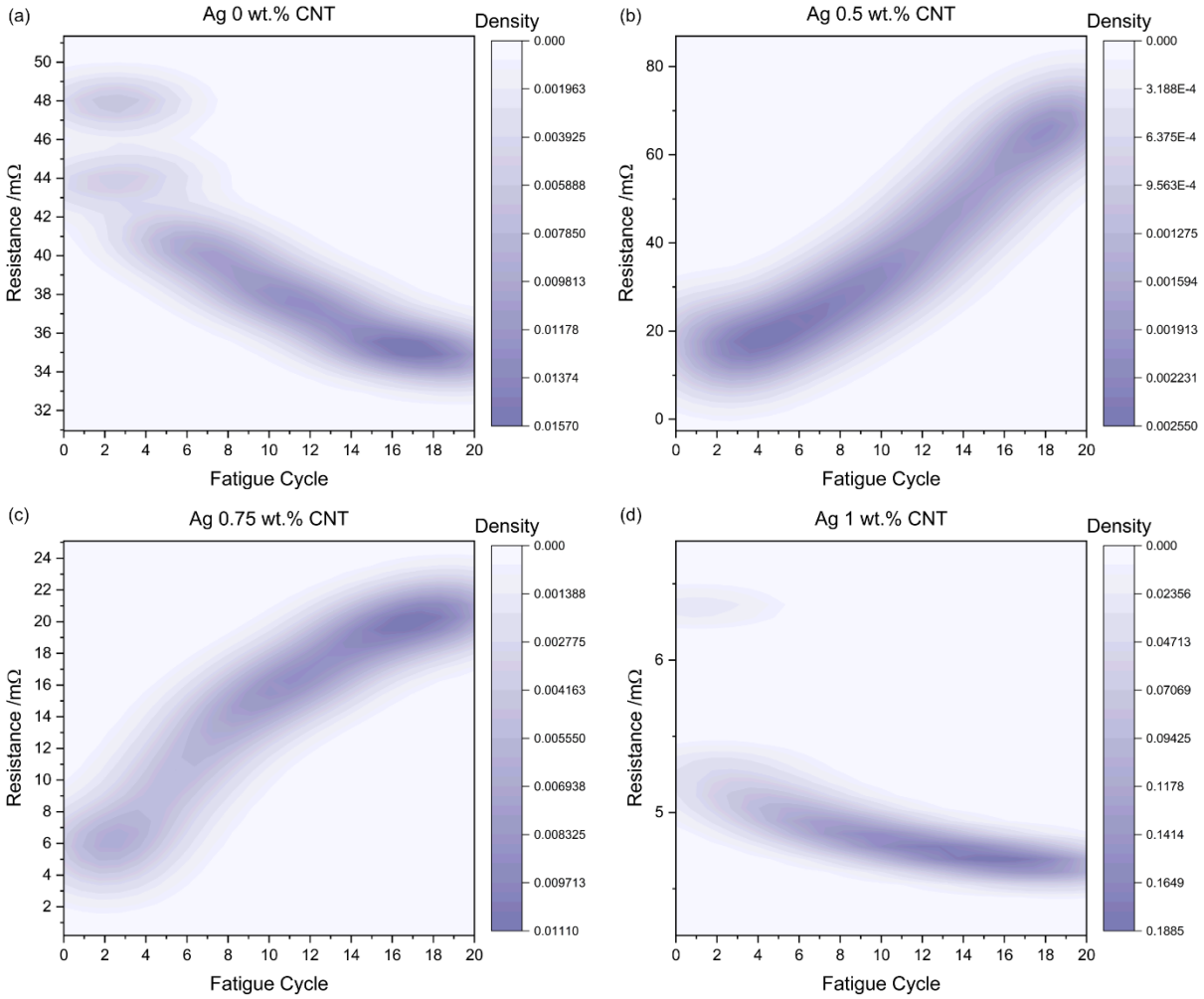

Figure S5. Kernel density estimation plot of ECR during multiple fatigue cycles of CNT reinforced Ag matrices. (a) Ag 0%, (b) Ag 0.5%, (c) Ag 0.75%, and (d) Ag 1%. Note the different y-axis ranges.

Table S1. Roughness values prior to and post-fatigue tests of silver MMC, as well as approximate imprint diameter left by counter electrode.

	Roughness prior to fatigue tests/nm	**Roughness post-fatigue tests/nm**	**Imprint diameter/μm**
Ag 0%	10 ± 10	30 ± 10	58.4 ± 5.2
Ag 0.5%	20 ± 10	80 ± 10	74.8 ± 8.7
Ag 0.75%	40 ± 10	120 ± 30	87.5 ± 2.5
Ag 1%	60 ± 10	100 ± 10	76.3 ± 2.7

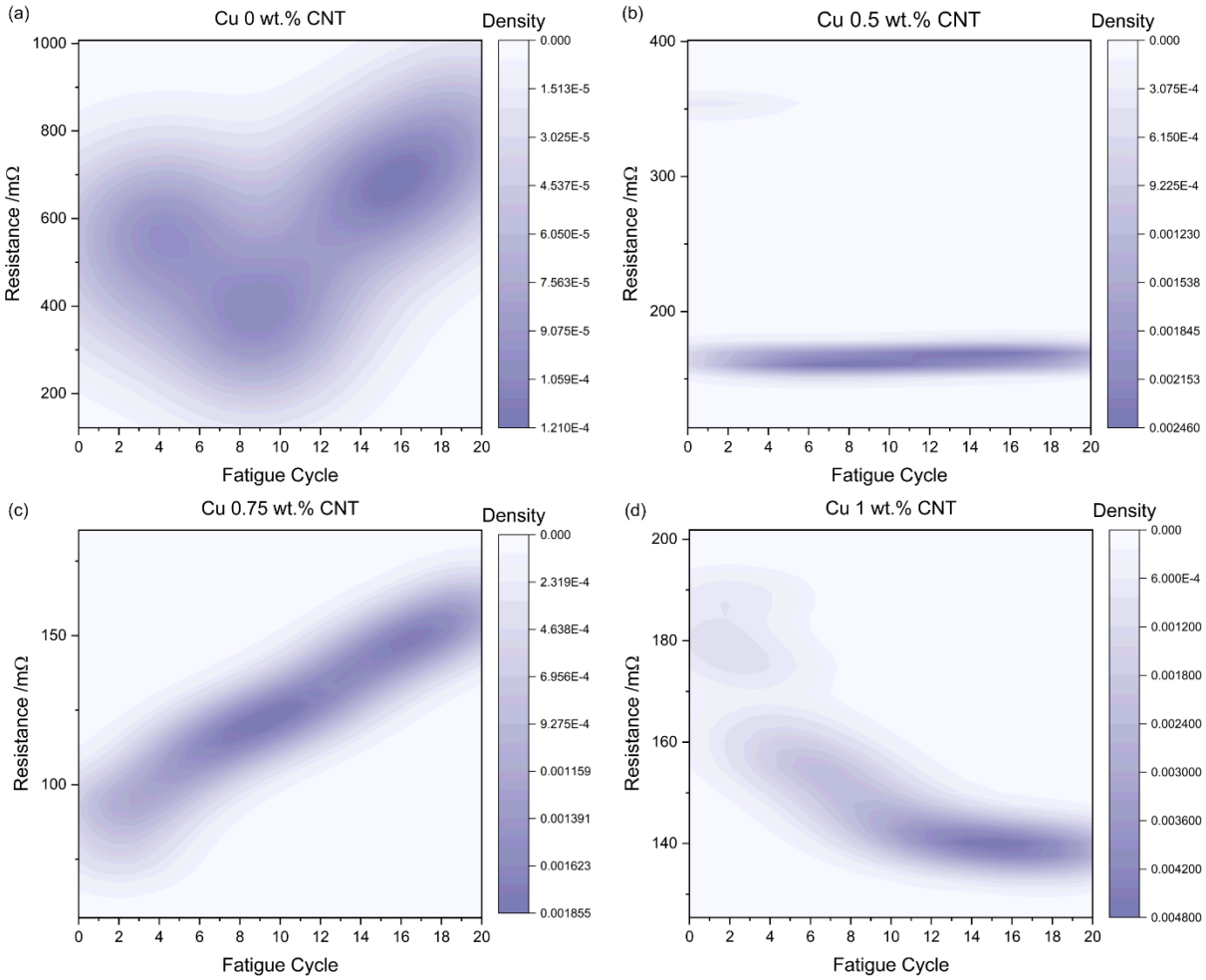

Figure S6. Kernel density estimation plot of ECR during multiple fatigue cycles of CNT reinforced Cu matrices. (a) Cu 0%, (b) Cu 0.5%, (c) Cu 0.75%, and (d) Cu 1%. Note the different y-axis ranges.

Table S2. Roughness values prior to and post-fatigue tests of copper MMC, as well as approximate imprint diameter left by counter electrode.

	Roughness prior to fatigue tests/nm	**Roughness post-fatigue tests/nm**	**Imprint diameter/μm**
Cu 0.5%	70 ± 10	220 ± 90	58.5 ± 3.5
Cu 0.75%	90 ± 10	150 ± 20	76.0 ± 1.6
Cu 1%	80 ± 10	130 ± 30	60.1 ± 3.2

* Cu 0% could not be measured. The imprint of the counter electrode could not be observed due to the higher hardness of the reference sample.

ANNEX I
Electrical Contact Resistance and Fretting Performance of Re-Pressed Silver MMC

The prolonged sintering process described in ARTICLE XII was successful in densifying the silver based MMC. This section will further discuss the improved density of the silver MMC, with particular emphasis on the enhanced tribo-electrical performance in contrast to the low-density samples (samples denominated by *'_p'*) from ARTICLE XI.

The increased density of the silver MMC has a significant impact on the ECR – as previously discussed in ARTICLE XII. To illustrate the enhanced electrical performance more clearly, normalized ECR curves were plotted and presented in **Figure A.I.1**. The normalized curves utilize the ECR of the unreinforced silver sample at 0.25 N in the loading semi-cycle as the reference point. Both low-density samples exhibited ECR values that were between 125% and 230% higher than the reference value, with the 1 wt.% sample presenting the highest values. Conversely, the high-density samples exhibited ECR values that range from 70% to 10% that of the reference value.

The low-density 0.5% sample (**Figure A.I.1a**) exhibits approximately 180% higher ECR than the reference sample in the loading semi-cycle, despite its significantly lower hardness – as evidenced by the hardness values presented in ARTICLE XI. Following the appropriate densification process, however, the ECR of the sample in question is approximately one-third that of the reference sample. The lower resistance was anticipated, since the dense reinforced sample is softer than the high-purity reference. Consequently, upon indentation, the real contact area between the MMC and the counter electrode is greater, which in turn reduces constriction resistance. Comparative analysis of the 0.5% samples reveals that the ECR of the high-density sample is initially 37% that of the low-density sample, decreasing to 17% at 10 N. The differences are more pronounced in the 1% MMC (**Figure A.I.1b**). The low-density sample exhibits ECR values that range from 200% to 230% at 0.25 N and 10 N, respectively. In contrast, the high-density samples exhibited a resistance of 23% and 19% in the same loading range, respectively, when compared to the reference. Furthermore, a comparison of the ECR of the 1% MMC at 0.25 N and 10 N reveals that the high-density sample exhibits 10% and 5% the resistance of the low-density sample. Nevertheless, both the low- and high-density samples exhibited considerably more reproducible ECR values, thereby highlighting their increased contact elasticity in comparison to the reference sample.

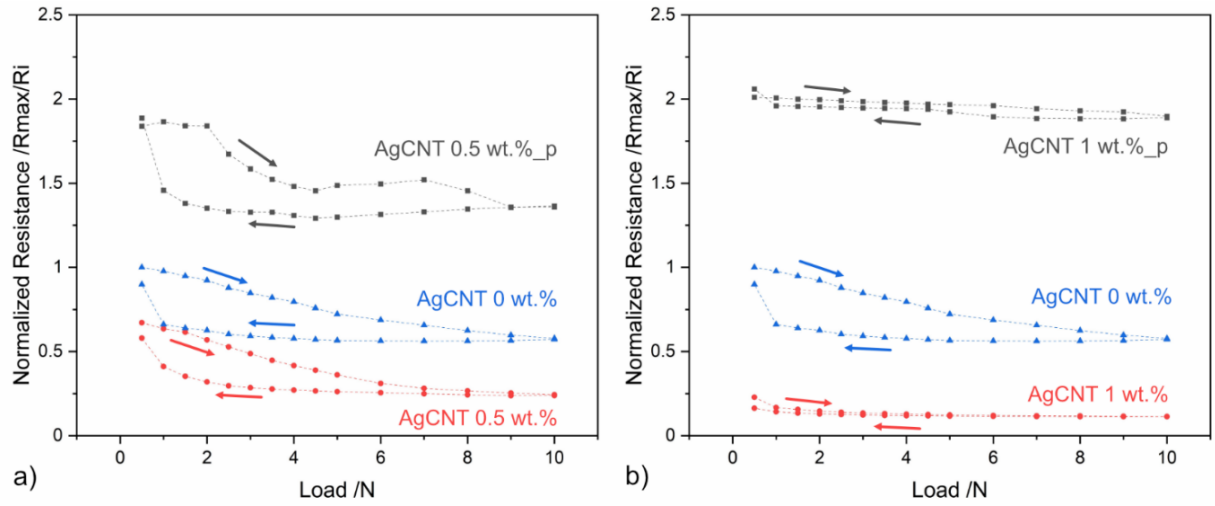

Figure A.I.1: Normalized ECR comparing the low-density MMC from ARTICLE XI with the high-density MMC from ARTICLE XII. CNT content: **a)** 0.5 wt.% and **b)** 1 wt.%.

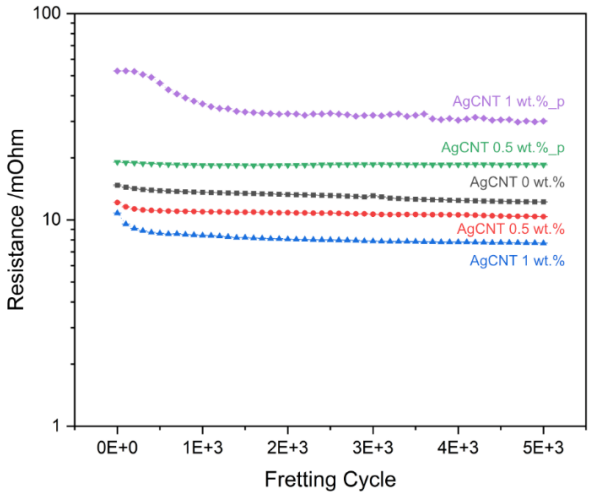

Figure A.I.2: ECR evolution during fretting wear of low-density silver MMC from ARTICLE XI and high-density MMC from ARTICLE XII.

The evolution of ECR during fretting wear following enhanced densification was evaluated and compared to the low-density samples (**Figure A.I.2**). The low-density samples exhibited a higher ECR throughout the duration of the fretting tests, as reported in ARTICLE XI. The higher CNT content resulted in an increase in ECR in these samples. Following the prolonged sintering time, the high-density samples exhibited enhanced ECR relative to the low-density and high-purity reference sample. Prior to fretting wear, the reference sample exhibited an ECR of 14.7 mΩ. This value gradually decreased as the fretting intervals progressed. After 5,000 cycles, the final value reached was 12.2 mΩ, representing a 17% reduction in ECR due to fretting. The high-density samples exhibited a lower ECR prior to fretting (12.1 mΩ and 10.8 mΩ for the 0.5% and 1% samples, respectively). The same trend is observed in these samples, with a final ECR of 10.4 mΩ and 7.7 mΩ reached after 5,000 cycles. Consequently, it can be concluded that

proper sintering is of paramount importance for the performance of the MMC during both static loading and when motion is present in the system.

Figure A.I.3 illustrates the fretting marks after observed 5,000 fretting cycles on the high-density silver MMC. The SEM micrographs demonstrate the presence of larger fretting marks, particularly for the high-density 1% sample, despite the higher hardness relative to the low-density sample. This is evident from the approximate dimensions of the wear track, as shown in **Table A.I.1**. Nonetheless, the high-density samples exhibited less severe wear than the low-density samples. This is further corroborated by the EDS maps in **Figure A.I.3**, which demonstrate that minimal gold was transferred from the counter electrode (i.e., lower adhesive wear). Moreover, as observed in the low-density samples (ARTICLE XI), carbon is still present in the fretting mark after wear tests – as highlighted by the magnified micrographs.

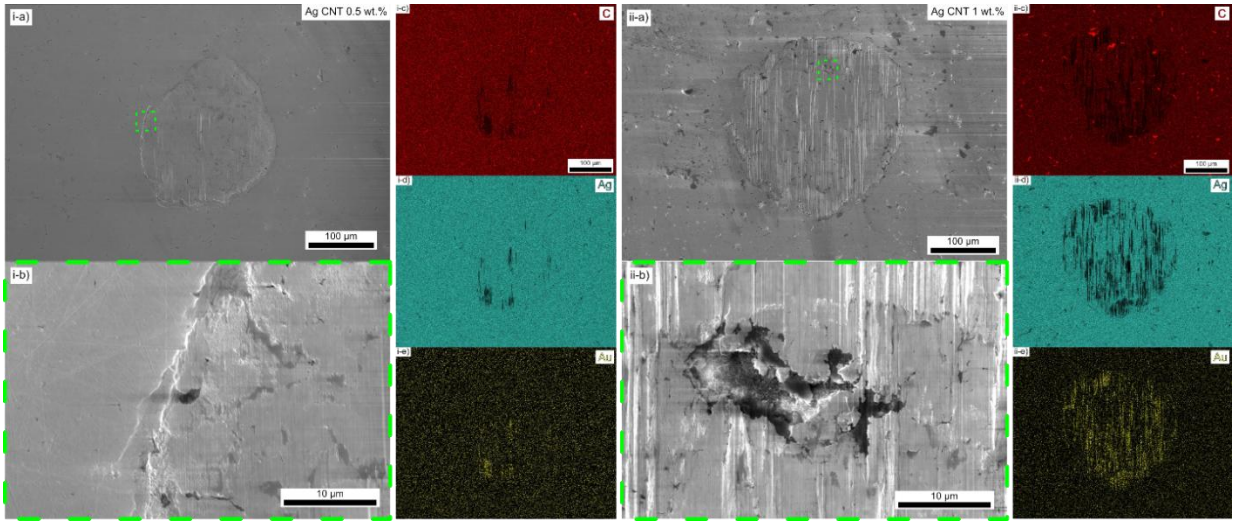

Figure A.I.3: a) SEM **and b)** magnified macrograph of fretting track **i)** AgCNT0.5 wt.% and **ii)** AgCNT1 wt.%. EDS **c)** carbon, **d)** silver, and **e)** gold maps.

Table A.I.1 – Approximate fretting mark dimensions.

Sample	Fretting mark width /µm	Fretting mark height /µm
Ag reference *	125	145
AgCNT 0.5 wt.%_p *	250	230
AgCNT 1 wt.%_p *	240	220
AgCNT 0.5 wt.%	205	230
AgCNT 1 wt.%	260	275

* Dimensions measured from SEM micrographs in ARTICLE XI.

ARTICLE XIII

Modifying the Characteristics of the Electrical Arc Generated during Hot Switching by Reinforcing Silver and Copper Matrices with Carbon Nanotubes

Bruno Alderete*, Christian Schäfer, U. Pranav Nayak, Frank Mücklich, Sebastian Suarez*

Department of Materials Science and Engineering, Saarland University, Campus D3.3, 66123 Saarbrücken, Germany

Research article
Published in "*Journal of Composites Science*" (2024)
Impact Factor: 3.0 (2023)

Accessible online at: doi.org/10.3390/jcs8070285

Own Contribution: Conceptualization; Methodology; Validation; Formal Analysis; Investigation; Data Curation; Writing – Original Draft; Visualization.

Cite this article as: B. Alderete, C. Schäfer, U.P. Nayak, F. Mücklich, S. Suarez, Modifying the Characteristics of the Electrical Arc Generated during Hot Switching by Reinforcing Silver and Copper Matrices with Carbon Nanotubes, Journal of Composites Science 8 (2024) 285. https://doi.org/10.3390/jcs8070285.

Journal of
Composites Science

MDPI

Article

Modifying the Characteristics of the Electrical Arc Generated during Hot Switching by Reinforcing Silver and Copper Matrices with Carbon Nanotubes

Bruno Alderete *, Christian Schäfer, U. Pranav Nayak, Frank Mücklich and Sebastian Suarez *

Department of Materials Science and Engineering, Saarland University, Campus D3.3, 66123 Saarbrücken, Germany; christian.schaefer@uni-saarland.de (C.S.); pranav.nayak@uni-saarland.de (U.P.N.); frank.muecklich@uni-saarland.de (F.M.)

* Correspondence: bruno.alderete@uni-saarland.de (B.A.); s.suarez@mx.uni-saarland.de (S.S.)

Abstract: Switching elements are crucial components in electrical and electronic systems that undergo severe degradation due to the electrical arc that is generated during breaking. Understanding the behavior of the electrical arc and modifying its characteristics via proper electrode design can significantly improve durability while also promoting optimal performance, reliability, and safety in circuit breakers. This work evaluates the feasibility of carbon nanotube (CNT)-reinforced silver and copper metal matrix composites (MMCs) as switching electrodes and the influence of CNT concentration on the characteristics of the arcs generated. Accordingly, three different concentrations per MMC were manufactured via powder metallurgy. The MMCs and reference materials were subjected to a single break operation and the electrical arcs generated using 100 W and 200 W resistive loads were analyzed. The proposed MMCs displayed promising results for application in low-voltage switches. The addition of CNTs improved performance by maintaining the arc's energy in the silver MMCs and reducing the arc's energy in the copper MMCs. Moreover, a CNT concentration of at least 2 wt.% is required to prevent unstable arcs in both metallic matrices. Increased CNT content further promotes the splitting of the electrical arc due to a more complex phase distribution, thereby reducing the arc's spatial energy density.

Keywords: carbon nanotubes; electrical arc; hot switching; metal matrix composites; powder metallurgy

Citation: Alderete, B.; Schäfer, C.; Nayak, U.P.; Mücklich, F.; Suarez, S. Modifying the Characteristics of the Electrical Arc Generated during Hot Switching by Reinforcing Silver and Copper Matrices with Carbon Nanotubes. *J. Compos. Sci.* **2024**, *8*, 285. https://doi.org/10.3390/jcs8070285

Academic Editors: Jinyang Xu and Prashanth Konda Gokuldoss

Received: 12 June 2024
Revised: 18 July 2024
Accepted: 19 July 2024
Published: 22 July 2024

1. Introduction

Silver is widely used in circuit breakers and in low-voltage switches in air due to its outstanding electrical conductivity, as well as its low tendency towards welding. It is common practice to alloy or improve the performance of silver to further enhance its erosion resistance during arcing and to minimize its weldability in high-current applications, thus guaranteeing proper operation of the circuit breaker. However, the lifetime of silver switches is significantly reduced by electro-erosion, caused by ion and electron bombardment during arcing. Zinc, copper, nickel, and palladium are frequently utilized as an alloying element in switching applications in order to decrease electrode erosion. Other options involve creating silver composites with metal oxide materials, such as cadmium, zinc, tungsten, and tin oxide. These materials vary in their applicability, but are generally utilized in low-voltage direct current (LVDC) applications such as relays, switches, and protective components [1–3]. Due to its toxicity and associated health risks [4], silver-cadmium oxide is no longer utilized, with it predominantly being replaced by Ag/SnO_2. However, while the addition of tin oxide increases the resistivity of the material, in-operando heat increments due to long-term use negatively impact the service life of this contact material [5]. As previously reported by Selzner et al. [6], the transport properties of Ag/SnO_2

differ significantly between the affected area (after the first break operation) and the surrounding, unaffected area. This is attributed to a heterogenous distribution of silver, pores, and oxides within the area affected by the electrical arc. Moreover, the energy from the arc promotes the formation of layered tin oxide structures, which negatively impact the material's conductivity. Furthermore, metal oxide content, particle size, and production processes influence the performance of the silver–tin oxide contact materials [7].

Pure copper also finds applicability in switching components due to its cost-effectiveness and good conductivity. However, copper electrodes are generally paired with silver-based materials to reduce the likelihood of welding. The performance of copper contacts is improved by coating them with tin, silver, etc., or by alloying them with other materials, such as cadmium, tin, chromium, tellurium, etc. [2]. In this manner, lower amounts of silver are required while still maintaining their switching characteristics [3].

Previous reports have studied the performance of graphite-containing silver switches [8–12]. These studies reported improved switching performance; however, due to the anisotropic properties of graphite, their performance is highly dependent on the relative orientation of the graphite reinforcement phase. The advantage of graphite-containing silver-based materials is not only that graphite reduces weldability, but also that it prevents the formation of non-conductive oxides on the metal's surface [13]. However, the addition of graphite increases erosion in silver materials and the likelihood of arc reignition [13]. Likewise, graphite-containing copper contact materials have shown weld resistance due to arcing and have been found to have applications even for elevated switching currents [3,14]. However, copper-graphite contacts are primarily designed to operate in moving (i.e., rotating) contacts, such as brushes [15]. These composite materials show exceptional self-lubricating capabilities, with the carbonaceous tribofilm slowing down wear and corrosion. Furthermore, copper composites reinforced with graphene nanoplatelets have demonstrated enhanced arc erosion resistance, as reported by Shao et al. [16].

Moreover, carbon nanotube-containing metal matrix composites (MMCs) are not only a viable option for electrical contact materials in general [17,18], but also for use in switching applications [5,19]. Individual carbon nanotubes (CNTs) possess exceptional mechanical and transport properties [20–25], albeit the latter present high anisotropy. However, single CNTs are seldom found, but rather CNT agglomerates [26,27]. Therefore, CNT composite materials have the potential to incorporate the advantages of graphite-containing composites without this disadvantage and without incurring significant additional costs. Therefore, the main objective of this study is to evaluate both the feasibility of CNT-containing MMCs for switching applications and the influence that the reinforcement phase's concentration has on the behavior of the electrical arc generated during hot switching. Accordingly, the characteristics of the arc generated during a single break operation will be analyzed and discussed.

It is important to understand the characteristics of the electrical arcs produced during hot switching, since this can provide abundant information on the circuit and on system efficiency, as well as provide insight into the breaker's durability. It is well-established that LVDC switches (e.g., automotive contacts) operating under resistive loads produce arcs with durations that do not exceed 500 µs and arc lengths below 100 µm [28,29], whereas high inductances extend the duration (between 500 µs and 5 ms) and length (up to a few mm) of the arc [28]. Furthermore, arc duration (i.e., type of load) and the contact material used affect the erosion mechanism that takes place during arcing. Short arcs (i.e., resistive load) show an anode mass loss and cathode mass gain, whereas the opposite is true for long arcs (i.e., inductive loads) [28,30].

The mechanism behind arcing is schematically shown in Figure 1. As a load (F) is applied between the two electrodes, the topographic features of the surfaces meet, generating the a-spots whereby conduction takes place (Figure 1a). Upon reaching the contact interface, the current (I) constricts and flows through the asperities in contact, which locally heats up the asperities to reach a temperature (T) above the melting temperature (T_m) of the metal (Figure 1b). As the electrodes separate (at a certain velocity v), the molten

metal is drawn by the moving electrode (Figure 1c), thus forming a bridge between them. As the electrodes continue to move apart from one another, the molten bridge is drawn out, becomes unstable, and ruptures due to a significant local increase in the current density (J), as shown in Figure 1d. The instability within the molten bridge is caused by the flow of colder material from the root of the bridge towards the hotter regions and the ejection of the bridge's material due to temperatures exceeding the boiling temperature (T_b) of the metal [2]. The bridges' explosion establishes the arc, releasing metallic vapor into the contact gap and considerably increasing the pressure (Figure 1e,f) [2]. As the metallic vapor expands into lower pressure regions, the pressure between the electrodes decreases and what is known as a pseudo arc is established, where ions conduct current. Since the opening operation does not occur under vacuum, the continued reduction in pressure causes the arc's transition from a metallic phase to a gaseous phase due to the flow of atmospheric gases into the gap. In the gaseous phase, the current is conducted by electrons rather than by the ions.

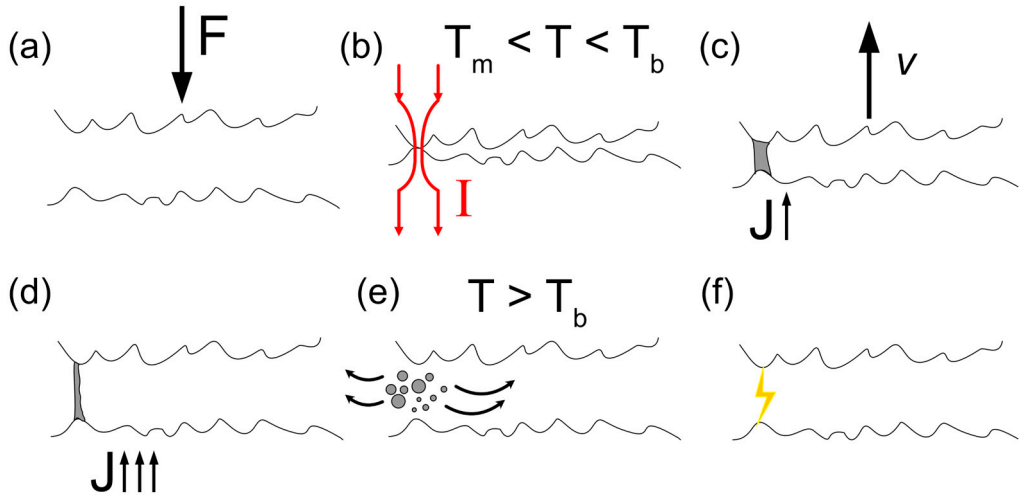

Figure 1. Schematic representation of arcing mechanism. The schematic illustrates when (**a**) contacting surfaces approach each other and (**b**) two asperities come into contact, allowing current to constrict and flow between the electrodes. Here, the temperature at the contact spot T exceeds the melting temperature T_m of the metals. (**c**,**d**) As the moving electrode begins to retreat at velocity v, the molten bridge is pulled by the moving electrode, increasing the current density J. (**e**) The metallic bridge ruptures due to instability, significantly increasing the pressure and forming metallic vapor between the electrodes. The increased current density increases the temperature at the contact sites above the boiling temperature T_b of the metal. (**f**) After the metallic vapor expands and the pressure decreases, the electrical arc is generated.

The metallic vapor generated in the arc's explosion is the cause for material transfer. In the initial stages of the arc's ignition, anodic erosion occurs due to electron bombardment, while the cathode gains mass due to particle recombination and condensation on the cathode's surface [30]. If the arc's duration is sufficiently long, there is a transition period wherein the cathode undergoes mass loss due to ion bombardment [1]. This transition only depends on the duration and length of the arc, where the latter is the predominant parameter governing the direction of mass transfer [28]. During the anodic to cathodic arc transition, there is an instance where the material deposited on the cathode during the anodic loss stage is removed, thereby leading to net zero erosion [31]. The anodic to cathodic transition is arc length dependent, and does not depend on electrode material or arc duration. On the other hand, the point at which net zero erosion occurs depends on the amount of material transferred during the anode loss stage. Therefore, it is dependent on arc duration (i.e., circuit type) and electrode material [28]. Although the current flowing

through the electrodes does not influence the arc type, it does increase the arc's energy, which in turn delays net zero erosion.

Therefore, it is established that, irrespective of the current level that circulates through the joint, for an electrical arc to generate, material melting takes place within the contact spot [2,32]. This is because as the electrodes separate and F tends to zero, the real contact area between the electrodes also tends to zero. The reduction in the contact area results in a rise in the constriction resistance (R_c), as stated in Equation (1) [1,2]. H and ρ in Equation (1) are the contact material's hardness and resistivity, respectively, whereas α is the radius of the real contact area, under the assumption that it is circular (known as the Holm radius), and η is a coefficient that describes the cleanliness of the contacts. The increased constriction resistance produces an increased voltage drop between the contacts (V_c), which in turn significantly increases the temperature at the contact spot (T_c)—this relationship is shown in Equation (2), where T_0 is the ambient temperature. Therefore, the increased constriction resistance due to the breaking of the circuit will cause the melting temperature of the metals to be reached, thus generating molten bridges.

$$R_c = \frac{\rho}{2\alpha} = \rho\sqrt{\frac{\eta\pi H}{4F}} \quad (1)$$

$$T_c = \sqrt{{T_0}^2 + {V_c}^2 \times 10^7} \quad (2)$$

The objective of this study is to gain a deeper understanding of the arc characteristics of established switching materials and compare them to the arc characteristics of CNT-reinforced, silver- and copper-based metal matrix composites produced via powder metallurgy, and to evaluate the influence of the reinforcement phase's concentration on the behavior of the resulting arc [33,34]. This understanding will enable the appraisal of the proposed materials in terms of feasibility, applicability, and efficiency for LVDC circuits. Therefore, break operations (hot switching) were conducted on different reference samples and on the proposed MMCs. The arcs in question were generated using a purely resistive load (standard automotive halogen lamps) while performing a single break operation. Two different ohmic loads were evaluated—i.e., 100 and 200 W. Voltage, current, and power curves during arcing were measured and evaluated to obtain arc duration and energy. Furthermore, the electrical contact resistance (ECR) of the different material systems was determined directly prior to the arc's ignition. Moreover, high-speed videos were captured during arcing in 200 W tests to observe the arcs' ignition, the existence of unstable arcs, and to qualitatively assess arc mobility. In addition, quantitative image analysis was carried out to provide insight into the mechanisms that modify the behavior of the arc produced as a consequence of the reinforcement phase: namely, the heterogeneity of the reinforcement phase in the MMCs.

2. Materials and Methods

2.1. Composite Production & Materials Characterization

Silver and copper MMCs reinforced with multiwalled CNTs were produced via powder metallurgy at three different concentrations, namely, 1 wt.%, 2 wt.%, and 3 wt.%. The composition of the samples and the nomenclature used in this work are shown in Table 1. Since the metallic matrices have relatively similar densities (10.49 and 8.95 g/cm^3 for silver and copper, respectively [2]), the difference in CNT content in vol.% and wt.% is marginal. Dendritic copper powder with a 325 mesh and 99% purity (Alfa Aesar GmbH, Berlin, Germany) and silver flakes with at least 80% of the flakes below 20 µm and a purity of 99.9% (Alfa Aesar GmbH, Berlin, Germany) were used as metallic matrices. The reinforcement phase used was chemical vapor deposition (CVD)-grown, multiwalled CNT (Graphene Supermarket, New York, NY, USA). The nanotubes have an outer diameter distribution between 50 and 85 nm, an as-received state length from 10 to 15 µm, and a carbon purity above 94%. To fully assess the performance of the proposed composite materials, different reference samples were also characterized—i.e., 0 wt.% sintered silver and copper samples,

and high-purity samples (silver rod: 99.95% purity, Alfa Aesar GmbH, Berlin, Germany and copper rod: 99.9% purity, Goodfellow Cambridge Limited, Huntingdon, UK). The unreinforced, sintered samples (i.e., Ag 0% and Cu 0%) were included in the analysis in order to evaluate samples with similar hardness and mechanical properties while excluding the influence of the reinforcement phase. Furthermore, materials commonly used in hot switching applications were also characterized, namely: Ag/Ni 90/10, Ag/SnO_2 88/12, Ag/SnO_2 90/10, and Ag/SnO_2 92/8 (Umicore N.V., Brussels, Belgium).

Table 1. Sample composition and nomenclature.

Matrix/vol.%	Reinforcement/vol.%	Reinforcement/wt.%	Nomenclature
100	0.00	0	Ag 0%
94.77	5.23	1	Ag 1%
89.97	10.03	2	Ag 2%
85.54	14.46	3	Ag 3%
100	0.00	0	Cu 0%
95.50	4.50	1	Cu 1%
91.30	8.70	2	Cu 2%
87.39	12.61	3	Cu 3%

The metallic powder and the CNT were blended through colloidal mixing in ethylene glycol. After evaporating the solvent, disk-shaped (8 mm diameter) green pellets were produced by placing the mixed powders in a steel die and pressing at 990 MPa for 20–30 s. The green pellets were densified (achieving relative densities higher than 95%) via hot uniaxial pressing (HUP). The sintering temperature is crucial for achieving sufficient sample density [18], particularly for electrical applications. Suarez et al. have previously reported that the structural integrity of multiwalled CNTs is not compromised during high temperature sintering [35]. The authors showed that, for CNT content of up to 3 wt.%, sintering at 850 °C in vacuum improved the crystallinity of the CNT compared to their state after dispersion, due to thermal annealing processes which alleviated defects. Moreover, thermogravimetric analyses have demonstrated that multiwalled CNTs are more stable to oxidation during vacuum annealing than single-walled CNTs [36], while also improving graphitization due to the removal of metallic and metal oxide content stemming from the manufacturing process [37]. Accordingly, HUP was carried out at a temperature of 750 °C and a pressure of 264 MPa at high vacuum (2×10^{-6} mbar) to minimize oxidation of the samples. The copper MMCs were sintered for 2.5 h. The silver MMCs, on the other hand, required longer isothermal holding times to achieve sufficient densities. Silver samples sintered for 2.5 h did not surpass 90% relative density [38]. As a result of the higher degree of internal porosity in the green pellet prior to sintering, silver samples required an isothermal holding time of 7.5 h [39]. Further details on the preparation of the colloid and sample production can be found in [38,39].

The hardness of the sintered MMCs and reference materials was evaluated via microhardness measurements (Dura Scan 50 Micro-Hardness Tester, Struers Inc., Cleveland, OH, USA). A load of 0.098 N ($HV_{0.01}$) was used to generate the imprint, holding the load for 15 s and optically micrographing the imprint using 40× magnification. At least 20 indentations were carried out per sample and averaged—results are shown in Table 2.

2.2. Hot Switching Tests

The electrical arc was generated by a breaking operation (hot switching) between the sample in question and a hard-gold-coated ($AuCo_{0.2}$), silver–nickel core ($AgNi_{0.15}$) rivet (Adam Bornbaum GmbH, Neuhausen, Germany). The counter electrode (rivet) has a hemispherical geometry, with a radius of curvature at its tip of 4 mm and a hardness value of 1.38 ± 0.01 GPa. Both electrodes were mounted on a custom testing rig and connected to a 3000 W direct current power source (Gossen Metrawatt SSP 3000-52, Nürnberg, Germany) [40]. An oscilloscope (LeCroy WaveRunner 6100A, New York, NY, USA) was used

to acquire the voltage drop between the electrodes during breaking. The current before, during, and after breaking was measured using the same device via a LeCroy CP031 current probe [19]. Two ohmic loads were evaluated: 100 W and 200 W. The loads were changed by adding or subtracting automotive 50 W halogen lamps. At least three hot switching tests were carried out per ohmic load and sample under atmospheric conditions (i.e., 23 ± 1 °C and 23 ± 2% temperature and relative humidity, respectively). A new counter electrode was used for each test. Prior to hot switching, the rivets were cleaned using isopropanol-based contact cleaner and dried with compressed air. Furthermore, the current probe was degaussed between measurements. Prior to electrical characterization, the MMCs and reference samples were ground and polished, achieving a mirror-polished surface. The polished samples were micrographed via confocal laser scanning microscopy (CLSM—LEXT OLS4100, Olympus, Tokyo, Japan), acquiring a 3 × 3 stitching at 50× with an overlap of 20% to obtain a larger field of view with high resolution. The root mean square roughness S_q of the stitching was measured. The reference samples and MMCs achieved an S_q value between 0.3–0.6 µm, whereas the counter electrode presented a roughness value of 0.3 µm.

The composite and reference samples were mounted on a moving platform and connected to the positive terminals of the source and oscilloscope (anode), whereas the rivet remained static and was connected to the negative terminals of the source and oscilloscope (cathode). A normal load of 4 N was established between both electrodes, and a current stabilization time of 10 s passed prior to breaking the circuit. Subsequently, the circuit was opened by retreating the linear stage at a constant acceleration of 8000 mm/s^2 and a top speed of 58 mm/s. Further information on the accuracy of this setup, as well as schematic representations thereof, was previously reported by Puyol et al. and Suarez et al. [19,40]. Video footage of the arc during the break operation was recorded with a high-speed camera (Photron, FASTCAM SA-Z, Tokyo, Japan) using a macro-lens (LAOWA, 100 mm f2.8 2:1 Ultra Macro APO, Hefei, China), a 2:1 magnification ratio, and a frame rate of 210,000 frames per second. The field of vision was 2.5 mm × 1.0 mm with a resolution of 284 × 160 pixels, resulting in a pixel size of 6.5 µm.

2.3. Heterogeneity Analysis

To assess the heterogeneity of the silver and copper MMCs, a detailed analysis of the near neighbor distance (nnd) for each sample was conducted. The micrographs acquired with the CLSM of each sample were first binarized using Gaussian blur filtering and thresholding operation in ImageJ, and later subjected to particle analysis. This process allowed for the identification and measurement of the centroids of each particle in each image [41]. Using the centroid coordinates, the pairwise Euclidean distances between all particles were then calculated. For each particle, the smallest distance from one particle to another was recorded as its nnd. Considering the magnification and resolution of the image acquisition, all pixelated particles having an area below 0.8 µm^2 (corresponding to 2 pixels) were excluded from the analysis.

Based on the skewness present in the raw data, it was assumed that the particle sizes and near neighbor distances were log-normally distributed [42]. Moreover, the coefficient of variation (COV) was introduced to quantify the heterogeneity of the CNT distribution based on the log-normal distribution of the nnd [43,44]. The standard deviation (σ_{In}) of the log-normal distribution of the nnd was calculated and used to determine the COV using Equation (3). It is worth noting that a higher COV value corresponds to more heterogeneous particle distributions. Furthermore, the average size and area fraction of the particles in each sample were determined to further characterize the dispersion and distribution of the reinforcement phase.

$$\mathrm{COV} = \sqrt{e^{\sigma_{In}^2} - 1} \tag{3}$$

3. Results and Discussions

Assessment of the proposed reinforced materials is crucial in order to fully understand their viability as contact materials for LVDC relays, contactors, and other switching

applications. Accordingly, the focus of this study is to carry out an in-depth analysis of the arc's characteristics for arcs generated by a single break operation with a resistive load of 200 W, as well as the influence that CNT concentration has on the characteristics of the arc generated. Resistive loads of 100 W generated arcs with similar behavior and tendencies to those generated with 200 W—further information on 100 W tests can be found in the Supplementary Information (Figures S1 and S2 and Table S1).

3.1. ECR Prior to Arcing

The ECR before electrode separation (i.e., prior to arcing) can be directly obtained from the current and voltage curves (using Ohm's law). The average ECR value for each material prior to arcing at 200 W is shown in Table 2. The reference materials exhibit varying ECR values, ranging from approximately 2.5 mΩ to 6 mΩ, with the latter corresponding to Ag/Ni. As expected, the resistance of Ag/SnO_2 increases alongside the tin oxide content. Among the materials tested, the silver MMC exhibited the lowest ECR value despite the addition of CNT. Similar to Ag/SnO_2, the ECR tends to slightly increase with increasing CNT content. The resistance values of copper MMCs vary considerably depending on the content of CNT. This is because of the heterogeneous distribution of CNTs within the copper composite (further discussed in Section 3.4) [18,38,39]. The chemical incompatibility between copper and carbon causes CNTs to re-agglomerate during the production process. As a result, larger CNT clusters are found on the surface of copper MMCs compared to silver MMCs; this phenomenon is more prevalent in copper MMCs with lower CNT concentrations. Furthermore, it is important to consider the potential heterogeneity in material hardness caused by inhomogeneous CNT distribution, which could result in variations in ECR values depending on the area where the measurements were taken. However, in general, the resistance values fall within the range of the reference materials. Therefore, based solely on the ECR, copper MMCs are a viable material that should perform similarly to silver–nickel alloys and silver–tin oxide composites.

Table 2. ECR and hardness values of the reference and composite materials. ECR values were calculated prior to electrode separation for 200 W tests.

Sample	ECR/mΩ	Hardness/MPa
Ag Rod	1.36 ± 0.32	847 ± 61
Ag 0%	1.65 ± 0.36	470 ± 49
Ag 1%	1.79 ± 0.53	505 ± 37
Ag 2%	1.94 ± 0.27	369 ± 54
Ag 3%	2.13 ± 0.73	408 ± 61
Cu Rod	6.86 ± 2.79	1335 ± 82
Cu 0%	3.59 ± 0.86	650 ± 70
Cu 1%	2.66 ± 0.06	619 ± 88
Cu 2%	2.73 ± 0.55	555 ± 81
Cu 3%	6.80 ± 0.28	512 ± 87
Ag/Ni 90/10	5.75 ± 1.14	615 ± 89
Ag/SnO_2 92/8	2.93 ± 0.47	728 ± 42
Ag/SnO_2 90/10	2.63 ± 0.66	757 ± 58
Ag/SnO_2 88/12	4.57 ± 0.92	820 ± 46

According to Holm, the spreading resistance of an isotropic material—i.e., the ideal resistance directly under the contact interface due to the spreading of the current within the conductor—is half that of the constriction resistance [1,45], as shown in Equation (4). Using the ECR values measured prior to arcing and the hardness values from Table 2 and Equation (1), the resistivity and the Holm radius of the contacting electrodes can be determined. These two parameters can then be used to determine the spreading resistance

of the materials in question via Equation (4). The Holm radius of the contact as well as the resistivity and spreading resistance of the samples are shown in Table 3.

$$R_s = \frac{\rho}{4\alpha} \tag{4}$$

Table 3. Resistivity, Holm radius and spreading resistance of the reference and MMC samples calculated using Equations (1) and (4). Hardness and resistance values were obtained from Table 2. The hardness of the samples was used for the calculations since the rivet is considerably harder than the samples.

Sample	Resistivity/Ωm	Holm Radius/µm	Spreading Resistance/mΩ
Ag Rod	2.6×10^{-8}	9.70	0.68
Ag 0%	4.3×10^{-8}	13.02	0.83
Ag 1%	4.5×10^{-8}	12.56	0.90
Ag 2%	5.7×10^{-8}	14.69	0.97
Ag 3%	6.0×10^{-8}	13.97	1.07
Cu Rod	1.1×10^{-7}	7.72	3.43
Cu 0%	7.9×10^{-8}	11.07	1.80
Cu 1%	6.0×10^{-8}	11.34	1.33
Cu 2%	6.5×10^{-8}	11.98	1.37
Cu 3%	1.7×10^{-7}	12.47	3.40
Ag/Ni 90/10	1.3×10^{-7}	11.38	2.88
Ag/SnO_2 92/8	6.1×10^{-8}	10.46	1.47
Ag/SnO_2 90/10	5.4×10^{-8}	10.26	1.32
Ag/SnO_2 88/12	9.0×10^{-8}	9.85	2.29

Resistivity of AuCo (rivet) between 6.2×10^{-8} and 55.5×10^{-8} [3,46].

The results from these numerical calculations correlate with the expectations generated from the MMC samples and reference samples. Since the hardness of the rod samples is higher than that of the sintered samples, the resulting Holm radius is smaller, thereby resulting in higher resistivity and resistances, whereas in the MMCs the rise in CNT concentration leads to a marginal rise in resistivity and spreading resistance. However, apart from Cu 3%, the increment in spreading resistance is negligible, representing a 0.17 mΩ increment between Ag 1% and Ag 3% for similar Holm radii. Likewise, the addition of tin oxide increases the samples' hardness, which in turn reduces the Holm radii, thereby leading to higher resistances.

3.2. Arc Characterization

The current and voltage curves prior to, during, and after the arc's extinction for all the materials tested are shown in Figure 2. Since the tests were conducted using direct current, the power curves can be directly obtained by multiplying the contact voltage and current, as shown in Figure 3. As the figures depict, the high purity samples, unreinforced sintered samples, and most reference materials show reduction peaks in the current flow and spikes in the voltage and the power curves (as indicated by the arrows in Figure 3). However, this was not observed in the 2% and 3% reinforced samples, nor in the Ag/SnO_2 88/12 sample. To determine the duration and energy of the arcs accurately and systematically, the arc's initiation was defined as the point when the current flow dropped by at least 20% of the nominal value. For the 200 W tests, the nominal current was approximately 17 A, whereas for the 100 W tests the nominal current was approximately 9 A. The durations and energy values over which the arc was considered are highlighted by the shaded areas in Figures 2 and 3. Table 4 shows the values for the 200 W tests, whereas the results for 100 W are shown in Table S1.

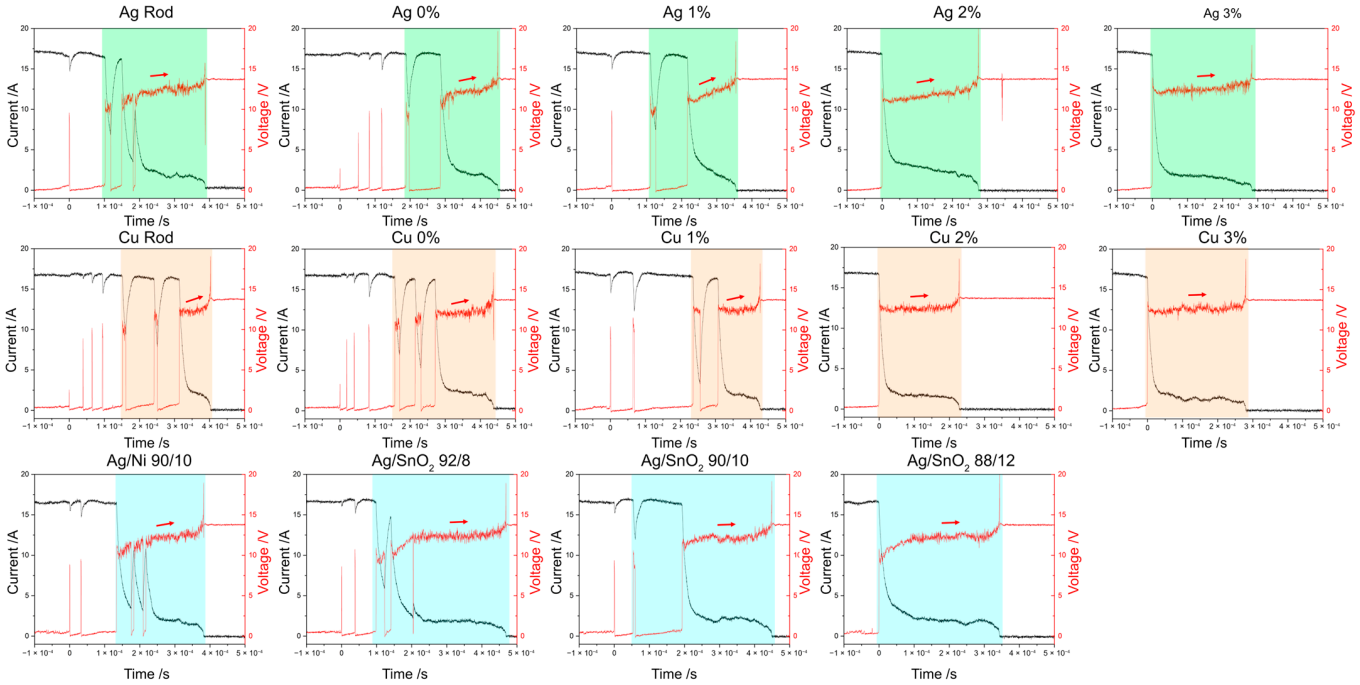

Figure 2. Current and voltage curves for reference and reinforced samples during 200 W hot switching tests. The shaded region highlights the time considered for the arc's characteristics. The arrows highlight the tendency of the voltage curve during the arc's duration. These plots show the most representative curves based on the average arc duration and energy.

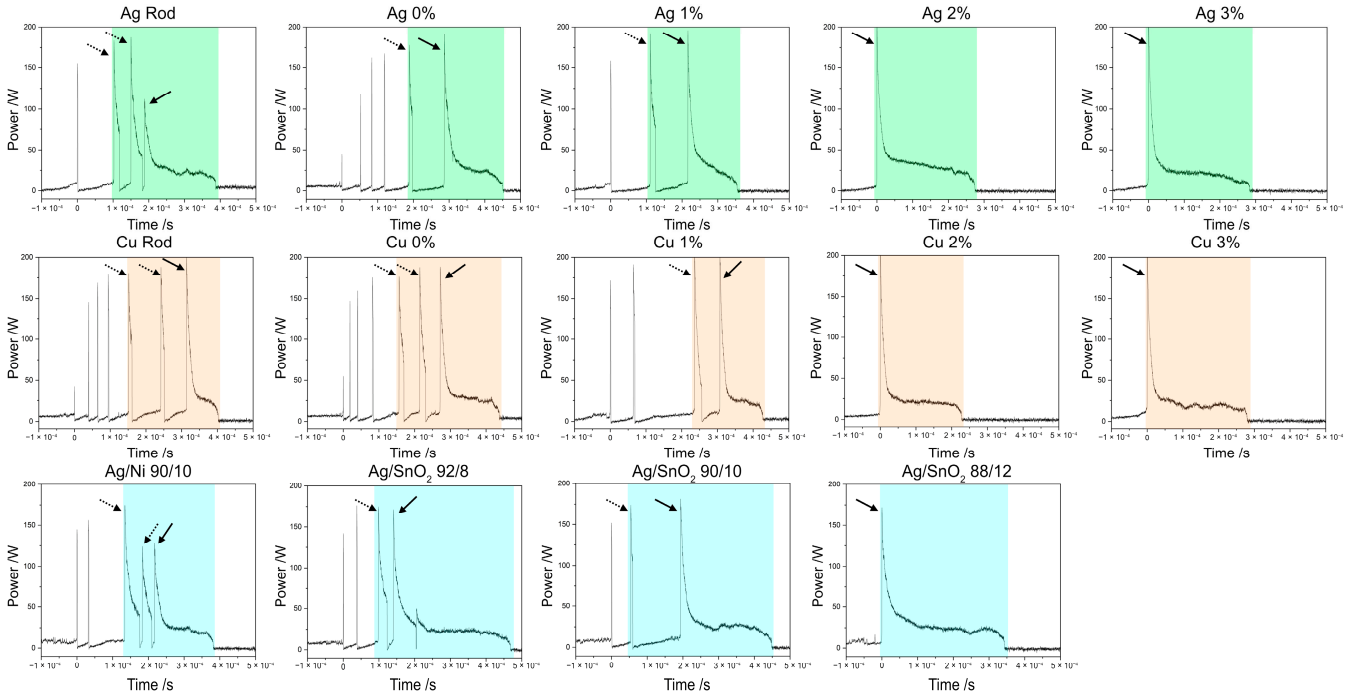

Figure 3. Power curves for reference and reinforced samples during 200 W hot switching tests. The shaded region highlights the time considered for the arc's characteristics. The arrows point out the power spikes that were considered within the arc duration calculations. Dashed arrows point out the unstable arcs, whereas solid arrows highlight the main arc. These plots show the most representative curves based on the average arc duration and energy.

Table 4. Arc characteristics of reference and reinforced samples for tests carried out at 200 W.

Sample	Arc Duration/ms	Arc Energy/mJ
Ag Rod	0.29 ± 0.01	10.25 ± 0.36
Ag 0%	0.30 ± 0.02	9.86 ± 2.11
Ag 1%	0.29 ± 0.04	8.79 ± 1.64
Ag 2%	0.37 ± 0.08	12.62 ± 2.45
Ag 3%	0.36 ± 0.05	10.71 ± 2.52
Cu Rod	0.30 ± 0.01	8.28 ± 1.30
Cu 0%	0.34 ± 0.04	10.87 ± 0.82
Cu 1%	0.20 ± 0.01	6.38 ± 0.25
Cu 2%	0.23 ± 0.06	6.30 ± 0.76
Cu 3%	0.23 ± 0.05	6.19 ± 0.95
Ag/Ni 90/10	0.27 ± 0.09	8.34 ± 1.68
Ag/SnO_2 92/8	0.40 ± 0.02	11.49 ± 0.78
Ag/SnO_2 90/10	0.36 ± 0.03	9.56 ± 1.11
Ag/SnO_2 88/12	0.37 ± 0.03	11.71 ± 1.13

During the ignition of the arc, the voltage curves show fluctuations that could be attributed to the variable contact of the inter-electrode molten bridges. The heat generated at these sites causes localized melting of the materials due to increased current constriction, which produces inconsistent voltage values. As the voltage and current curves in Figure 2 highlight, the MMCs with higher CNT concentrations produce more stable voltage curves. On the other hand, samples with lower CNT content possess variable voltage curves. In this case, the voltage curve while the arc is ignited tends to increase until the nominal voltage of 13.5 V is reached and the arc is extinguished (highlighted by the arrows in Figure 2). The more stable voltage curves during arcing in the MMCs could therefore be associated with fewer melting points in the contact due to the improved thermal conductivity of the contact material. As shown in Figure 2, the voltage curve for Ag 2% still shows an increasing trend during the arc; however, this is not the case with Cu 2%. This behavior could be attributed to the lower melting voltage of silver (0.37 V) compared to that of copper and gold, both of which have a melting voltage of 0.43 V [1,2]. These fluctuations could also be linked to the sublimation of the CNTs, which in turn causes the release of adsorbed gases and a non-conductive metal vapor (stemming from the explosion of the metallic bridge) in the vicinity of the electrodes, thereby locally increasing the pressure between the two surfaces [2,19]. Furthermore, the slope of the voltage curves while the main arc is ignited can provide information on the arc's phase. The curve's slope transitioning from a shallower slope to a steeper slope suggests the transition from a metallic ion phase to a gaseous ion phase [31]. Observing Figure 2, it is clear that lower CNT content promotes a longer gaseous arc phase. Therefore, the CNTs show the potential to minimize the ingress of gaseous ions within the electrode gap, which can consequently reduce gaseous ion erosion. The same behavior was observed for the 100 W tests (see Figure S1).

By observing the arc characteristics of the reference materials in Table 4, a clear distinction can be made between silver–tin oxide and silver–nickel contact materials. However, all values fall within the range reported by Ben Jemaa et al. for resistive loads [28,29]. The arc duration and energy levels of silver–tin oxide reference materials remain relatively constant regardless of the tin oxide content. In all three cases, the arc is extinguished within 400 µs, and the arc's energy does not exceed 13 mJ. However, the silver–nickel alloy, on the other hand, presents a shorter arc duration (below 300 µs) and a lower energy input (below 10 mJ).

The results in Table 4 for silver samples do not exceed those observed for the references. In other words, the mean duration of the arc is not greater than that of the silver–tin oxide and silver–nickel samples. However, the arc duration tends to increase as the concentration of the reinforcement phase increases. Nevertheless, the increase in arc duration is marginal, typically in the range of 60 µs in the 2% and 3% reinforced silver samples. In contrast, the

copper samples exhibit the opposite behavior. As the CNT concentration increases, the duration of the arc shortens, with a reduction of approximately 70 µs.

Regarding the energy input, the copper samples had the lowest amount of energy. The unreinforced copper samples performed similarly to the silver and reference samples. However, when CNTs were incorporated into the copper samples, a significant reduction in arc energy was observed (as well as in arc duration), resulting in the lowest arc energy among all evaluated samples. In contrast, the reinforced silver samples did not show a reduction in arc energy and had values that matched those of the reference materials. Therefore, the reinforcement phase has a stronger impact on the characteristics of the arc in copper electrodes.

The hot switching tests at 100 W (Table S1) showed similar performance. The arc duration in the reference materials did not exceed 350 µs, with a maximum mean energy of approximately 4 mJ. The silver samples exhibited slightly shorter arc durations, with a maximum duration of approximately 230 µs, corresponding to the high-purity (rod) silver sample and the 3% sample. As with the 200 W tests, higher CNT concentrations tended to increase arc duration in silver MMCs. The energy of the arc in the silver samples did not exceed the values of the reference materials, which ranged from 2.3 to 3.5 mJ. Copper samples in the 100 W tests showed moderately consistent results. The mean duration of the arc was approximately 240 µs for all samples. However, as with the 200 W tests, the lowest arc energy was observed in the copper samples with higher CNT content. Both the 2% and 3% reinforced copper MMCs showed arc energy values below 3 mJ. In both hot switching tests (i.e., 100 W and 200 W), the samples with the highest content of CNT also presented the highest standard deviation. However, this is due to the heterogeneous distribution of CNTs within the metallic matrix [17,39].

The spikes in current, voltage, and power observed prior to the proper ignition of the arc considered in this study (highlighted by the arrows in Figure 3) are not characteristic of a break operation. Instead, they resemble the bouncing phenomenon commonly seen in make operations. These spikes are short-lived and do not tend to decrease over time, as is the case with bouncing. On the contrary, these signal perturbations tend to exhibit a greater reduction in current flow (resulting in an increase in voltage and power signals) as the tests progress. It is hypothesized that the voltage and current spikes are caused by the extinction of smaller unstable arcs that occur during the initial stages of the breaking operation before the main arc is established. As these signal disruptions were not observed for all materials, it was of interest to observe the evolution of the electrical arc during break operations using a high-speed camera to better understand these perturbations.

3.3. High-Speed Footage

The high-speed video footage correlates with the voltage and current curves recorded during arcing (example for Cu 1% shown in Figure 4). High-speed camera videos for all samples can be found at https://doi.org/10.5281/zenodo.10838984 (accessed on 19 March 2024). As initially observed in Figures 2 and 3, the videos highlight that most reference samples and unreinforced silver and copper samples show a larger tendency towards the establishment of unstable arcs. Unstable arcs are defined as small, short-lived electrical arcs that are established prior to the ignition of the main arc. These arcs can be identified as the small spikes in the current, the voltage, and the power curves (see Figures 2 and 3). Unstable arcs ignite and are extinguished in a matter of tens of µs, whereas the main arcs last for several hundred µs (see Table 4). The dashed arrows in the power curves (Figure 3) point out the presence of unstable arcs, which were considered in the arc characteristics, whereas the solid arrows highlight the ignition of the main arc.

Unstable arcs ignite earlier in samples with low or no CNT content. In other words, as the CNT content increases in the MMCs, the ignition of unstable arcs takes place closer to the ignition of the main arc. For sufficiently high CNT content (namely 3%), the ignition of unstable arcs is avoided altogether, similar to the Ag/SnO_2 88/12 sample. It is important to report that 2% samples in particular show variable results. In other words, unstable

arcs were observed in one out of the three tests carried out at 100 W and 200 W. Therefore, it seems that 2% CNT content is the lower limit required to eliminate unstable arcs from taking place, with higher concentrations not showing unstable arcs throughout all tests. However, the 2% curves presented in Figures 2 and 3 do not include curves where unstable arcing took place, as they were not fully representative of the general results.

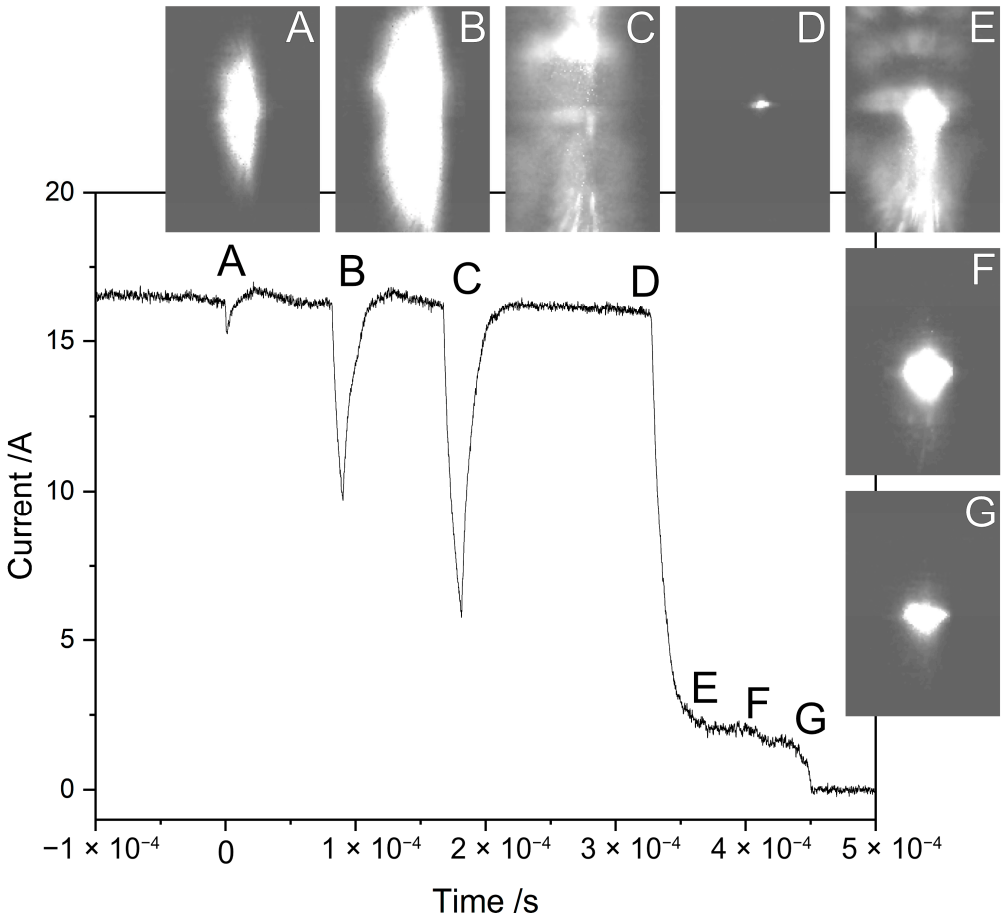

Figure 4. Current curve and snapshots of high-speed video at different times during breaking for Cu 1% sample.

The Cu 1% sample (exhibited in Figure 4) is a prime example of unstable arcing in MMCs with low CNT content. These unstable arcs initially marginally reduce the nominal current (as is the case in snapshot A). As the breaking operation progresses, the nominal current briefly decreases more markedly (B and C) until the main arc is ignited (D). These current reductions prior to the ignition of the main arc last a few tens of μs, followed by the extinction of the unstable arcs and the current approaching the nominal value. In this example, the unstable arcs shown in A, B, and C last for approximately 25, 45, and 50 μs. Snapshot C depicts the extinction of this unstable arc and the corresponding plume generated. Snapshot D exhibits the ignition of the main arc, with E, F, and G showing snapshots at different moments in the main arc's duration.

The reference and unreinforced samples exhibit significant arc motion and small plumes. In particular, the Ag/Ni samples display multiple short, unstable arcs that gradually become longer until the main arc is established. On the other hand, the Ag/SnO_2 samples exhibit significantly steadier arcs compared to Ag/Ni. The higher mobility in Ag/Ni samples is attributed to the higher work function of nickel (4.7–5.2 eV) compared to that of tin (3.6–4.1 eV) [2]. The addition of CNTs to the MMCs results in a confinement-effect of the electrical arc, reducing its mobility. It is important to note that this is a qualitative analysis and the degree to which CNT concentrations affect arc mobility cannot be dis-

cussed based solely on the high-speed video footage. However, the video footage confirms that the CNT clusters on the MMCs' surfaces hinder the arc's mobility. This is supported by the observation that electrical arcs on copper MMCs tend to show more mobility than those on silver MMCs. The effectiveness of CNTs in copper MMCs for confining the arc is not as high as in silver MMCs due to its less homogeneous CNT distribution (further discussed in Section 3.4).

Moreover, the work function of the materials in question can impact the behavior of the arcs. In other words, low work function will favor a steady and localized arc since it is easier to extract an electron from said material—as is the case with Ag/SnO_2. The higher work function of copper (4.5 eV) compared to that of silver (4.2 eV to 4.5 eV) [2], coupled with its more heterogeneous phase distribution, explains the higher mobility of the arc in copper MMCs, with previous studies from Guo et al. reporting that CNT content increases the work function of copper MMCs [47], thereby further increasing arc mobility. In the proposed MMCs, the arc is more easily established between the metallic matrices and the counter electrode rather than between the reinforcement phase and the counter electrode. This is due to their higher electrical conductivity and to the higher work function of the multiwalled CNTs (4.95 eV and 5.05 eV for multiwalled and single-walled CNTs [48], respectively) used to produce the MMCs. The CNT-reinforced samples exhibit large plumes being expelled as arcing takes place. This behavior could be caused by two mechanisms, which are not mutually exclusive. The first mechanism is the increased material removal rate when adding CNTs, similarly to when adding graphite into these metallic matrices [8]. Furthermore, the large plumes observed are due to CNT sublimation, which increases local pressure. As the high-pressure regions expand to lower-pressure regions (i.e., the plume observed) it leads to material ejection, and it aids in arc extinction. It is worth noting that the plumes and metallic bridge explosions appear to be more severe in copper samples, both in the main arc and in unstable arcs. Compared to silver-based materials, unstable arcs occur more frequently and last longer in copper samples, resulting in more severe explosions. This is due to copper's poorer resistance to welding and lower thermal conductivity compared to silver.

3.4. Reinforcement Phase Distribution

Due to the complexity of the systems herein analyzed, multiple mechanisms can explain the observed behavior of the aforementioned materials. These mechanisms are not mutually exclusive; therefore, a combination of these mechanisms can justify the performance of Ag 2%, Ag 3%, Cu 2%, and Cu 3%. One possible explanation for the absence of unstable arcing in the high concentration samples is their relative softness compared to purer samples. In softer materials, the contact area at 4 N is larger, which increases the potential area in which an arc can be established between the electrodes due to a larger number of asperities establishing electrical contact—this is corroborated by the larger Holm radius presented in Table 3. However, the difference in hardness between material types is minor, therefore it is unlikely that this is the sole cause of the lack of unstable arcing in MMCs containing higher amounts of CNTs. Additionally, the Ag/SnO_2 88/12 sample is harder than the other silver–tin oxide samples and does not exhibit unstable arcing. It is probable that the unstable arcing occurs due to the explosion of smaller contact bridges as the electrodes separate. The contacts experience significant localized heating due to high currents flowing through the electrodes and the increased current density flowing through certain metallic bridges. This causes melting and the subsequent explosion of the bridges. This phenomenon is hindered in the reinforced sample due to the CNT content, which increases the thermal diffusivity of the material. Improved thermal characteristics have two benefits. Firstly, they eliminate or minimize unstable arcing in favor of a main arc with longer duration, and, secondly, they reduce the likelihood of welding, thereby ensuring optimal switching.

The incorporation of CNTs into silver and copper matrices results in a varied phase distribution, depending on the concentration of the reinforcement phase. An example of

the CNT distribution produced is shown in Figure 5, which illustrates the heterogeneity of the CNT in the Ag 3% and Cu 3% samples. Micrographs of Ag 1%, Ag 2%, Cu 1%, and Cu 2% can be found in the Supplementary Information (Figure S3). A quantitative analysis of the micrographs was conducted to describe the distribution of the reinforcement phase and its heterogeneity as a function of CNT concentration, shown in Table 5. Initial calculations revealed that the COV for the nnd was above 100%, indicating significant variability, likely due to the presence of outliers. These outliers were eliminated from the dataset as described in Appendix A.

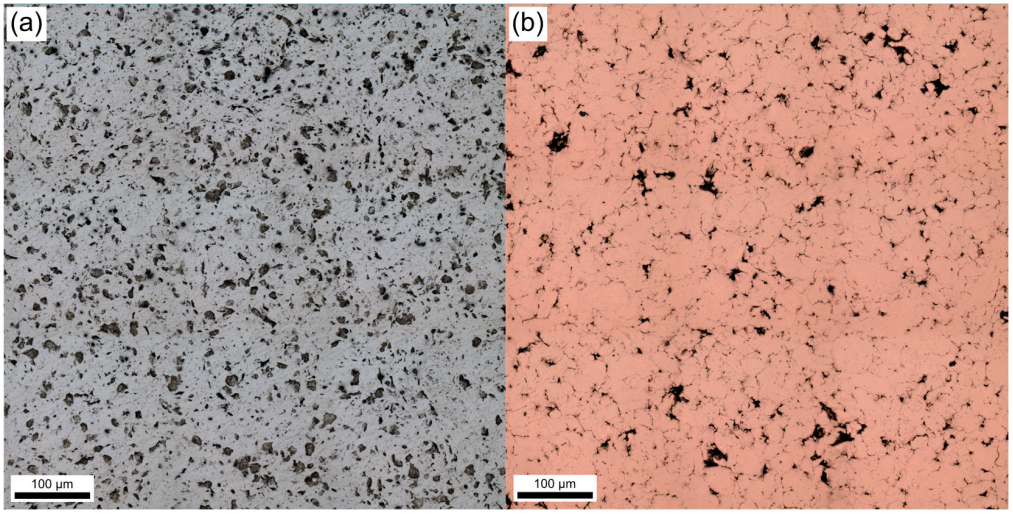

Figure 5. 3 × 3 stitching at 50× optical micrographs of (**a**) Ag 3% and (**b**) Cu 3% via CLSM.

Table 5. Particle count, average size, and area fraction for silver and copper MMC.

Sample	Count	Size/µm^2	Area/%	COV
Ag 1%	1374	16.48	5.05	0.49
Ag 2%	1977	20.64	9.10	0.44
Ag 3%	3018	24.32	16.36	0.41
Cu 1%	1106	9.86	2.43	0.53
Cu 2%	1124	14.72	3.69	0.50
Cu 3%	1367	18.05	5.51	0.47

The characteristics of the arc generated will depend heavily on the distribution, agglomerate size, and area fraction of CNTs that the electrode encounters on the MMCs' surfaces. Therefore, these parameters were determined using micrographs of the polished MMCs' surfaces. The 3 × 3 stitching corresponds to a square area of approximately 0.45 mm^2, which is a considerably larger area than the contact area and crater area. The largest crater generated due to the arc during the break operation among the samples herein analyzed had an approximate diameter of 240 µm. Overestimating the diameter to 300 µm, this corresponds to an affected area of approximately 0.07 mm^2. This estimation is over 6 times smaller than the area used to analyze phase distribution and heterogeneity. Furthermore, it must be considered that this estimation is the affected area, which is expected to be considerably larger than the apparent contact area between the rivet and the MMC samples.

The parameters determined are summarized in Table 5. Logically, size and area fraction of CNT increases as the concentration increases. This indicates that higher CNT concentrations lead to larger and more widespread particle distribution within the matrices. It is of particular interest to note that both the particle size and area fraction increase at a lower rate in the copper MMCs compared to the silver MMCs. The difference between the area fraction in the 1% samples is approximately 1/2, whereas 2% and 3% copper MMCs

show approximately 1/3 the area fraction of the silver MMCs. This is due to the clustering of the CNTs in the copper MMCs. As evidenced in Figures 5 and S3, the surfaces of the copper MMCs present large CNT bundles and regions with minimal amounts of CNTs. The micrographs of the silver samples, on the other hand, show a more homogeneous distribution without the presence of large clusters. The increasing average size and area fraction with higher CNT concentrations indicates a more extensive and uniform coverage of the reinforcement phase within the silver matrix, contributing to the observed improvements in homogeneity. Therefore, the descriptive statistics correlate with the micrographs acquired (see Figures 5 and S3). The comparison between the silver and copper MMCs at equivalent CNT concentrations suggests that silver facilitates better dispersion and distribution of the CNTs, although the dispersion process during manufacturing is identical [18,38,39,49].

The COV values for both copper and silver MMC samples show a decreasing trend with increasing reinforcement phase concentrations. Specifically, the COV for the silver and copper samples decreases from 0.49 to 0.41 and from 0.53 to 0.47 for 1% and 3% silver and copper MMCs, respectively. This indicates that the particle distribution becomes more homogeneous as the CNT concentration increases. Nonetheless, for equivalent concentrations, the silver MMCs exhibit slightly lower COV values compared to the copper MMCs. Therefore, a more uniform particle distribution within the silver matrix is achieved. The behavior suggests that the reinforcement phase exhibits greater affinity towards silver matrices as opposed to copper matrices. CNTs have a high affinity towards agglomeration as a result of Van der Waals interactions (primarily π-π interactions) [26,27]. Prior to mixing the metallic powders, large CNT agglomerates are broken down via shear mixing and ultrasonication [38,39]; however, the mechanical stress during ultrasonication can severely damage the structural integrity of the CNTs [49,50]. Consequently, prolonging the dispersion process for copper MMCs could prove counterproductive, since this would increase the reinforcement phase's structural damage. After dispersion, and during the manufacturing process, CNTs tend to re-agglomerate to a higher extent when using copper metallic powder as opposed to silver, favoring re-agglomeration rather than copper-CNT entanglement, thereby leading to larger CNT clusters in the former.

The relative nnd frequency distribution and rug plots for both the silver- and copper-based MMCs exhibit a clear trend of increasing homogeneity with higher CNT concentrations (Figure 6a,b). For both matrices, the nnd distribution becomes narrower and more peaked as the CNT concentration increases, indicating a more uniform particle distribution. The cumulative distribution plot, shown in Figure 6c, further supports these observations. The 3% samples exhibit the steepest rise, indicating the highest homogeneity, followed by the 2% and then the 1% samples. This trend was observed irrespective of the metallic matrix. Nonetheless, the silver MMCs exhibit slightly lower standard deviation values compared to the copper MMCs for identical CNT concentrations. These findings demonstrate that higher CNT concentrations enhance the homogeneity of the composites, with silver matrices achieving better dispersion and uniformity compared to the copper matrices under similar conditions.

The complex phase distribution of the CNTs in the MMCs promotes the splitting of the main arc, which reduces the arc's spatial energy density. This is favorable since a reduction in the arc's energy density could reduce the area affected by it, thus potentially reducing erosion severity during switching. Furthermore, splitting the electrical arc could prevent the formation of unstable arcs by igniting the main arc over a larger area from the initial stages of the break operation. The CNTs dispersed throughout the surface act as bifurcating elements, causing the electrical arc to split onto different spots on the MMCs' surfaces. As the electrodes separate, some smaller arcs (belonging to the main arc) may be extinguished while others remain. Therefore, the CNT-reinforced samples exhibited longer, continuous main arcs. Additionally, the CNT clusters on the surface minimize arc wandering, confining the motion of the arc to a specific region on the MMC's surface where smaller clusters are located.

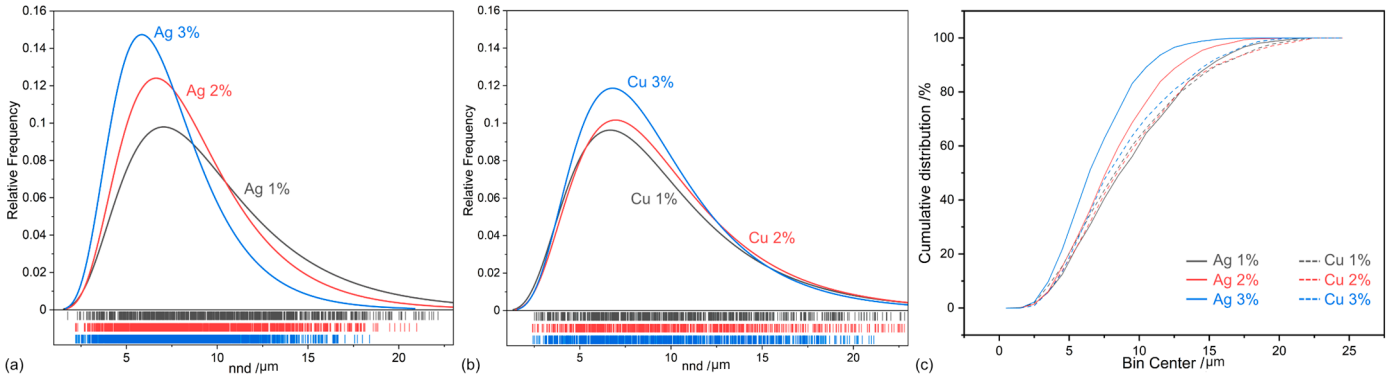

Figure 6. Relative frequency for the nnd of (**a**) silver MMCs, (**b**) copper MMCs, and (**c**) comparison of the cumulative distribution.

The lack of unstable arcing in the MMCs with higher CNT concentrations may also be explained by the elastic characteristics of the reinforcement phase. The CNTs exhibit outstanding elastic restitutive behavior [51–53], which could result in a conductive bridge between the electrodes remaining during the initial stages of the breaking operation, specifically between the counter electrode and the elastic CNTs. Thus, the current is constricted and continues to flow through the clusters of CNTs instead of producing the electrical arc. Once the separation between the electrodes is sufficiently high, the main arc is generated without the ignition of unstable arcs (as observed in samples with low or no CNT concentrations).

4. Conclusions

CNT-reinforced silver and copper MMCs were produced via powder metallurgy. These samples and reference silver and copper were subjected, along with well-established reference materials, to DC hot switching tests, and the characteristics of the arcs are herein reported. From this work, the main conclusions are the following:

1. All composite materials proposed performed similarly to the reference materials. The copper MMCs have the shortest arc duration and lowest arc energy among the materials herein evaluated.
2. 2 wt.% CNT content is the lower limit to avoid unstable arcing. These MMCs showed unstable arcing one-third of the time, whereas unstable arcing was not observed for samples with 3 wt.% CNT.
3. Increased CNT content confines the arcs, thus reducing its mobility. This effect is more significant in silver MMCs due to a more homogeneous distribution of the CNTs. Heterogeneity on the copper MMCs' surfaces—produced by large CNT clusters—favors arc wandering.
4. The results shown highlight that although copper MMCs present higher resistance values, their arcing performance is comparable to silver-based materials. Therefore, in applications where low ECR is not crucial and atmospheric conditions allow it, copper MMCs are a low-cost option for switching contact materials, thereby reducing the demand for precious metals.

These results demonstrate the feasibility of CNT-based silver and copper MMCs for LVDC switching applications based on the characteristics of the electrical arcs produced. Future work should be carried out to evaluate the rate of material transfer and removal during arcing, as well as crater morphology and the degree to which the CNTs endured the electrical arc. Further evaluations of the heat generated and of dissipation are of significant importance for an in-depth understanding of the influence of CNTs on the MMCs' molten pools and on the weld resistance provided.

Supplementary Materials: The following supporting information can be downloaded at: https://www.mdpi.com/article/10.3390/jcs8070285/s1. Figure S1: Current and voltage curves for reference and reinforced samples during 100 W hot switching tests. The shaded region highlights the time considered for the arc's characteristics. The arrows highlight the tendency of the voltage curve during the arc's duration. These plots show the most representative curves based on the average arc duration and energy; Figure S2: Power curves for reference and reinforced samples during 100 W hot switching tests. The shaded region highlights the time considered for the arc's characteristics. The arrows point out the power spikes that were considered within the arc duration calculations. Dashed arrows point out the unstable arcs, whereas solid arrows highlight the main arc. These plots show the most representative curves based on the average arc duration and energy; Table S1: Arc characteristics of reference and reinforced samples for tests carried out at 100 W; Figure S3: 3 × 3 stitching at 50× optical micrographs of (a) Ag 1%, (b) Cu 1%, (c) Ag 2%, and (d) Cu 2% obtained via CLSM.

Author Contributions: Conceptualization, B.A. and S.S.; Methodology, B.A., C.S., U.P.N. and S.S.; Validation, B.A.; Formal Analysis, B.A.; Investigation, B.A.; Resources, F.M.; Data Curation, B.A. and U.P.N.; Writing—Original Draft, B.A.; Writing—Review and Edition, C.S., U.P.N. and S.S.; Visualization, B.A.; Supervision, S.S.; Project Administration, F.M. and S.S.; Funding Acquisition, F.M. and S.S. All authors have read and agreed to the published version of the manuscript.

Funding: This research received funding from Deutsche Forschungsgemeinschaft (DFG), project number 426339194 and the State of Saarland from the European Regional Development Fund in the Mat-Innovat ("Kreislauffähige Materialsysteme für innovatives Hochleistungswerkstoffe") project.

Data Availability Statement: Data available upon reasonable request from the corresponding authors. High-speed camera footage can be found at https://doi.org/10.5281/zenodo.10838984 (accessed on 19 March 2024).

Acknowledgments: B. Alderete wishes to acknowledge the support from the German Academic Exchange Service (DAAD) and the Roberto Rocca Education Program (RREP). The authors wish to acknowledge funding from Deutsche Forschungsgemeinschaft (DFG), project number 426339194. The authors gratefully acknowledge funding in the Mat-Innovat ("Kreislauffähige Materialsysteme für innovatives Hochleistungswerkstoffe") project, supported by the State of Saarland from the European Regional Development Fund (Europäischen Fonds für Regionale Entwicklung, EFRE).

Conflicts of Interest: The authors declare no conflicts of interest.

Appendix A

The interquartile range (*IQR*) method was applied to identify and remove outliers. This involved calculating the first quartile (Q_1) and third quartile (Q_3) of the nnd. Outliers were defined and removed following Equations (A1) and (A2), obtaining the lower (*OLL*) and upper limit (*OUL*) for outliers, respectively. The removal of these outliers refined the nnd values obtained.

$$OLL = Q_1 - 1.5IQR \quad \text{(A1)}$$

$$OUL = Q_3 + 1.5IQR \quad \text{(A2)}$$

References

1. Holm, R. *Electric Contacts*; Springer: Berlin/Heidelberg, Germany, 1967.
2. Slade, P.G. *Electrical Contacts: Principles and Applications*; CRC Press: Boca Raton, FL, USA, 2014.
3. Braunovic, M.; Konchits, V.V.; Myshkin, N.K. *Electrical Contacts: Fundamentals, Applications and Technology*; CRC Press: Boca Raton, FL, USA, 2017.
4. Genchi, G.; Sinicropi, M.S.; Lauria, G.; Carocci, A.; Catalano, A. The Effects of Cadmium Toxicity. *Int. J. Environ. Res. Public Health* **2020**, *17*, 3782. [CrossRef] [PubMed]
5. Li, A.; Xie, M.; Yang, Y.; Zhang, J.; Wang, S.; Chen, Y.; Zhou, W. Effect of CNTs content on the mechanical and arc-erosion performance of Ag-CNTs composites. *Diam. Relat. Mater.* **2022**, *128*, 109211. [CrossRef]
6. Selzner, C.; Mücklich, F. New microstructure investigations of arc damaged silver/tinoxide electrodes by means of FIB-technique. In Proceedings of the 27th International Conference on Electrical Contacts, Dresden, Germany, 22–26 June 2014; pp. 1–5.
7. Rohberg, J.; Honig, T.; Witulski, N.; Finkbeiner, M.; Behrens, V. Performance of Different Silver/Tin Oxide Contact Materials for Applications in Low Voltage Circuit Breakers. In Proceedings of the 2009 55th IEEE Holm Conference on Electrical Contacts, Vancouver, BC, Canada, 14–16 September 2009; pp. 189–196. [CrossRef]

8. Behrens, V.; Honig, T.; Kraus, A.; Mahle, E.; Michal, R.; Saeger, K.E. Test results of different silver/graphite contact materials in regard to applications in circuit breakers. In *Electrical Contacts—1995, Proceedings of the Forty-First IEEE Holm Conference on Electrical Contacts, Montreal, QC, Canada, 2–4 October 1995*; IEEE: Piscataway, NJ, USA, 1995; pp. 393–397. [CrossRef]
9. Michal, R.; Saegar, K.E. Metallurgical aspects of silver-based contact materials for air-break switching devices for power engineering. *IEEE Trans. Compon. Hybrids Manuf. Technol.* **1989**, *12*, 71–81. [CrossRef]
10. Wingert, P.; Bevington, R.; Horn, G. The effect of graphite additions on the performance of silver-nickel contacts. In Proceedings of the Thirty-Sixth IEEE Conference on Electrical Contacts, and the Fifteenth International Conference on Electrical Contacts, Montreal, QC, Canada, 20–24 August 1990; pp. 524–529. [CrossRef]
11. Shobert, E. Carbon, Graphite, and Contacts. *IEEE Trans. Parts Hybrids Packaging* **1976**, *12*, 62–74. [CrossRef]
12. Jiang, P.; Li, F.; Wang, Y. Effect of different types of carbon on microstructure and arcing behavior of Ag/C contact materials. *IEEE Trans. Compon. Packag. Technol.* **2006**, *29*, 420–423. [CrossRef]
13. Wingert, P.C. The effects of interrupting elevated currents on the erosion and structure of silver-graphite. In *Electrical Contacts—1996, Proceedings of the Forty-Second IEEE Holm Conference on Electrical Contacts, Joint with the 18th International Conference on Electrical Contacts, Chicago, IL, USA, 16–20 September 1996*; IEEE: Piscataway, NJ, USA, 1996; pp. 60–69. [CrossRef]
14. Xie, W.; Wu, G.; Yang, Z.; She, P.; Wang, H.; Zuo, H.; Wei, W.; Gao, G.; Tu, C. Study on the erosion characteristics of copper-carbon electrode pairs by DC air arc. *High Volt.* **2021**, *6*, 674–683. [CrossRef]
15. Sawa, K.; Ueno, T.; Nakano, K. Evaluation of Arc Erosion of Cu-graphite Brush Used in Small DC Motors with and without Quenching Device. In Proceedings of the 2020 IEEE 66th Holm Conference on Electrical Contacts and Intensive Course (HLM), San Antonio, TX, USA, 30 September–7 October 2020; pp. 170–175. [CrossRef]
16. Shao, G.; Liu, P.; Li, W.; Chen, X.; Ma, F.; Liu, X.; Zhou, H.; Zhang, K. Effects of graphene nanoplates on arc erosion resistance and wear behavior under electric current of copper matrix composites. *J. Alloys Compd.* **2020**, *829*, 154356. [CrossRef]
17. Suarez, S.; Alderete, B.; Puyol, R.; Mücklich, F. Load-dependent electrical contact resistance of carbon nanotube-reinforced metal matrix composites. In Proceedings of the 2022 IEEE 67th Holm Conference on Electrical Contacts (HLM), Tampa, FL, USA, 23–26 October 2022; pp. 1–6. [CrossRef]
18. García, D.; Suárez, S.; Aristizábal, K.; Mücklich, F. Powder-Metallurgical Fabrication and Electrical Contact Resistance Characterization of Copper–Nickel Composites Reinforced by Multiwalled Carbon Nanotubes. *Adv. Eng. Mater.* **2022**, *24*, 2100755. [CrossRef]
19. Suarez, S.; Puyol, R.; Schafer, C.; Mucklich, F. Carbon Nanotube-reinforced Metal Matrix Composites as Novel Electrodes for Low-voltage Switching Applications: A Surface Degradation Analysis. In Proceedings of the 2019 IEEE Holm Conference on Electrical Contacts, Milwaukee, WI, USA, 14–18 September 2019; pp. 135–141. [CrossRef]
20. Dresselhaus, M.S.; Dresselhaus, G.; Saito, R. Physics of carbon nanotubes. *Carbon* **1995**, *33*, 883–891. [CrossRef]
21. Saito, R.; Dresselhaus, G.; Dresselhaus, M.S. *Physical Properties of Carbon Nanotubes*; Imperial College Press: London, UK, 1998.
22. Saifuddin, N.; Raziah, A.Z.; Junizah, A.R. Carbon Nanotubes: A Review on Structure and Their Interaction with Proteins. *J. Chem.* **2013**, *2013*, 676815. [CrossRef]
23. Popov, V.N. Carbon nanotubes: Properties and application. *Mater. Sci. Eng. R Rep.* **2004**, *43*, 61–102. [CrossRef]
24. Ebbesen, T.W. Carbon Nanotubes. *Annu. Rev. Mater. Sci.* **1994**, *24*, 235–264. [CrossRef]
25. Maiti, A.; Svizhenko, A.; Anantram, M.P. Electronic Transport through Carbon Nanotubes: Effects of Structural Deformation and Tube Chirality. *Phys. Rev. Lett.* **2002**, *88*, 126805. [CrossRef] [PubMed]
26. Pérez, E.M.; Martín, N. π–π interactions in carbon nanostructures. *Chem. Soc. Rev.* **2015**, *44*, 6425–6433. [CrossRef] [PubMed]
27. Klinovaja, J.; Schmidt, M.J.; Braunecker, B.; Loss, D. Carbon nanotubes in electric and magnetic fields. *Phys. Rev. B* **2011**, *84*, 085452. [CrossRef]
28. Ben Jemaa, N.; Morin, L.; Benhenda, S.; Nedelec, L. Anodic to cathodic arc transition according to break arc lengthening. *IEEE Trans. Compon. Packag. Manuf. Technol. Part A* **2005**, *21*, 599–603. [CrossRef]
29. Ben Jemaa, N.; Nedelec, L.; Benhenda, S. Break arc duration and contact erosion in automotive application. *IEEE Trans. Compon. Packag. Manuf. Technol. Part A* **1996**, *19*, 82–86. [CrossRef]
30. Jemaa, N.; Nedelec, L.; Benhenda, S.; Neveu, J. Anodic and cathodic erosion of Ag, Ag alloys and Ag-MeO contact materials in energy range below 10 joules. In *Electrical Contacts—1996, Forty-Second IEEE Holm Conference on Electrical Contacts, Joint with the 18th International Conference on Electrical Contacts, Chicago, IL, USA, 16–20 September 1996*; IEEE: Piscataway, NJ, USA, 1996; pp. 70–74.
31. Swingler, J.; McBride, J. The net zero erosion phenomena on opening switching contacts with AC loading. In *Electrical Contacts—1997, Forty-Third IEEE Holm Conference on Electrical Contacts, Philadelphia, PA, USA, 20–22 October 1997*; IEEE: Piscataway, NJ, USA, 1997; pp. 238–245. [CrossRef]
32. Braunovic, M. Effect of connection design on the contact resistance of high power overlapping bolted joints. *IEEE Trans. Compon. Packag. Technol.* **2002**, *25*, 642–650. [CrossRef]
33. Feng, Y.; Yuan, H.L.; Zhang, M. Fabrication and properties of silver-matrix composites reinforced by carbon nanotubes. *Mater. Charact.* **2005**, *55*, 211–218. [CrossRef]
34. Silvestre, N. State-of-the-art Review on Carbon Nanotube Reinforced Metal Matrix Composites. *Int. J. Compos. Mater.* **2013**, *3*, 28–44. [CrossRef]

35. Suarez, S.; Lasserre, F.; Prat, O.; Mücklich, F. Processing and interfacial reaction evaluation in MWCNT/Ni composites. *Phys. Status Solidi (a)* **2014**, *211*, 1555–1561. [CrossRef]
36. Singh, D.K.; Iyer, P.K.; Giri, P.K. Diameter dependence of oxidative stability in multiwalled carbon nanotubes: Role of defects and effect of vacuum annealing. *J. Appl. Phys.* **2010**, *108*, 084313. [CrossRef]
37. Huang, W.; Wang, Y.; Luo, G.; Wei, F. 99.9% purity multi-walled carbon nanotubes by vacuum high-temperature annealing. *Carbon* **2003**, *41*, 2585–2590. [CrossRef]
38. Alderete, B.; Suarez, S.; Mücklich, F. On the Production & Tribo-Electrical Characterization of Carbon Nanotube-Reinforced Ag & Cu Metal Matrix Composites. In Proceedings of the 2023 IEEE 68th Holm Conference on Electrical Contacts (HOLM), Seattle, WA, USA, 4–11 October 2023; pp. 1–8. [CrossRef]
39. Alderete, B.; Mücklich, F.; Suarez, S. Electrical Characterization of Carbon Nanotube Reinforced Silver and Copper Composites for Switching Contacts. *J. Compos. Sci.* **2023**, *7*, 284. [CrossRef]
40. Puyol, R.; Suarez, S. A contact resistance measurement setup for the study of novel contacts. In Proceedings of the 2017 IEEE URUCON, Montevideo, Uruguay, 23–25 October 2017; pp. 1–4. [CrossRef]
41. Nayak, U.P.; Müller, M.; Britz, D.; Guitar, M.A.; Mücklich, F. Image Processing using Open Source Tools and their Implementation in the Analysis of Complex Microstructures. *Pract. Metallogr.* **2021**, *58*, 484–506. [CrossRef]
42. Limpert, E.; Stahel, W.A.; Abbt, M. Log-normal Distributions across the Sciences: Keys and Clues: On the charms of statistics, and how mechanical models resembling gambling machines offer a link to a handy way to characterize log-normal distributions, which can provide deeper insight into variability and probability—Normal or log-normal: That is the question. *BioScience* **2001**, *51*, 341–352. [CrossRef]
43. Yang, N.; Boselli, J.; Sinclair, I. Simulation and quantitative assessment of homogeneous and inhomogeneous particle distributions in particulate metal matrix composites. *J. Microsc.* **2001**, *201*, 189–200. [CrossRef]
44. Nayak, U.P.; Mücklich, F.; Guitar, M.A. Time-Dependant Microstructural Evolution and Tribological Behaviour of a 26 wt% Cr White Cast Iron Subjected to a Destabilization Heat Treatment. *Met. Mater. Int.* **2023**, *29*, 934–947. [CrossRef]
45. Seki, K.; Kubo, T.; Ye, N.; Shimizu, T. Quantifying the spreading resistance of an anisotropic thin film conductor. *Sci. Rep.* **2020**, *10*, 10633. [CrossRef]
46. Henger, U.; Korn, D. Electrical resistivity of thin films of AuCo solid solutions. *J. Phys. F Met. Phys.* **1981**, *11*, 2575–2584. [CrossRef]
47. Guo, X.; Yang, Y.; Song, K.; Shaolin, L.; Jiang, F.; Wang, X. Arc erosion resistance of hybrid copper matrix composites reinforced with CNTs and micro-TiB_2 particles. *J. Mater. Res. Technol.* **2021**, *11*, 1469–1479. [CrossRef]
48. Shiraishi, M.; Ata, M. Work function of carbon nanotubes. *Carbon* **2001**, *39*, 1913–1917. [CrossRef]
49. Reinert, L.; Zeiger, M.; Suárez, S.; Presser, V.; Mücklich, F. Dispersion analysis of carbon nanotubes, carbon onions, and nanodiamonds for their application as reinforcement phase in nickel metal matrix composites. *RSC Adv.* **2015**, *5*, 95149–95159. [CrossRef]
50. Hilding, J.; Grulke, E.A.; Zhang, Z.G.; Lockwood, F. Dispersion of Carbon Nanotubes in Liquids. *J. Dispers. Sci. Technol.* **2003**, *24*, 1–41. [CrossRef]
51. Alderete, B.; Nayak, U.P.; Mücklich, F.; Suarez, S. Influence of topography on electrical contact resistance of copper-based materials. *Surf. Topogr. Metrol. Prop.* **2023**, *11*, 025027. [CrossRef]
52. Alderete, B.; Mücklich, F.; Suarez, S. Characterization and electrical analysis of carbon-based solid lubricant coatings. *Carbon Trends* **2022**, *7*, 100156. [CrossRef]
53. Alderete, B.; Mücklich, F.; Suarez, S. Evaluating the effect of unidirectional loading on the piezoresistive characteristics of carbon nanoparticles. *Sci. Rep.* **2024**, *14*, 9247. [CrossRef]

Supplementary Materials

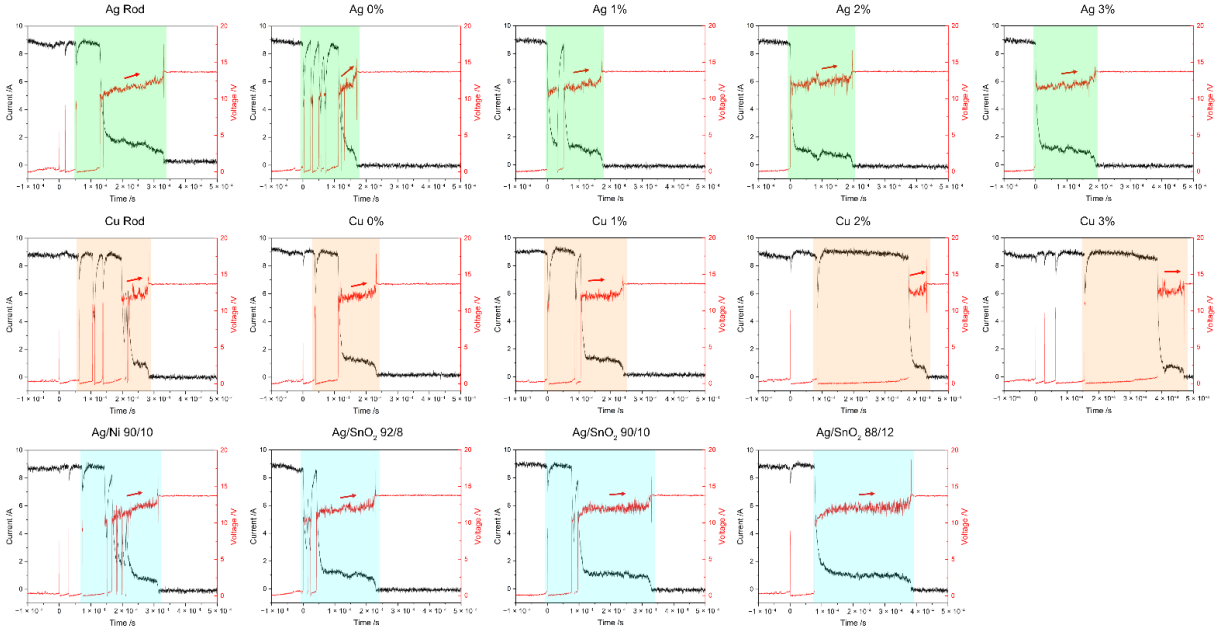

Figure S1. Current and voltage curves for reference and reinforced samples during 100 W hot switching tests. The shaded region highlights the time considered for the arc's characteristics. The arrows highlight the tendency of the voltage curve during the arc's duration. These plots show the most representative curves based on the average arc duration and energy.

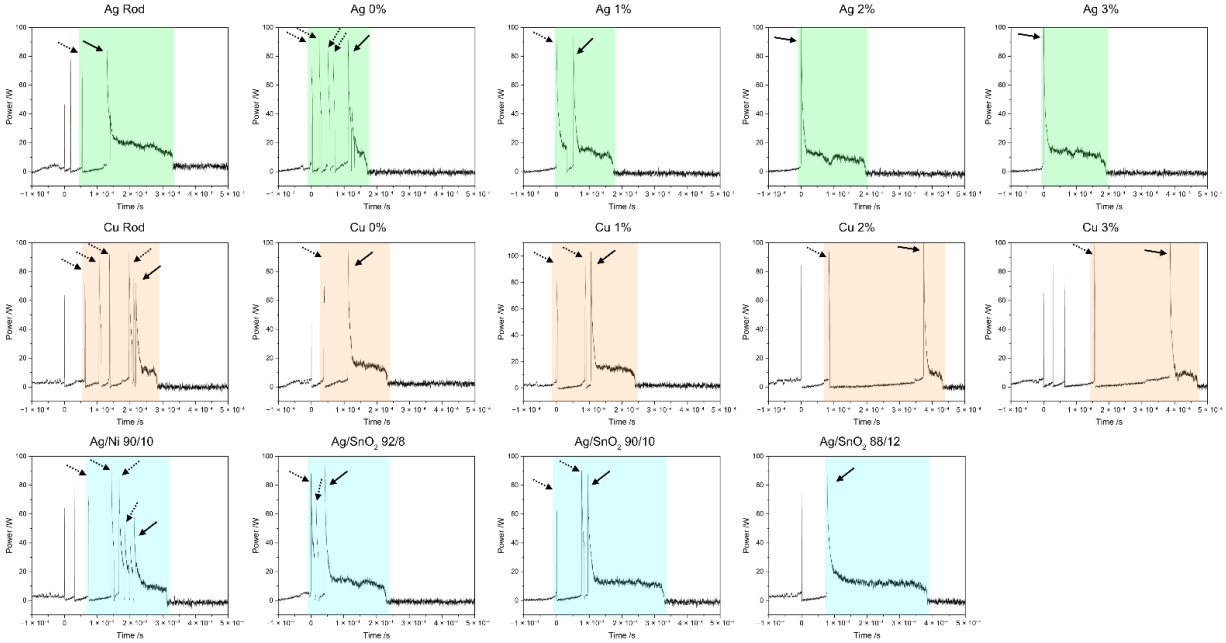

Figure S2. Power curves for reference and reinforced samples during 100 W hot switching tests. The shaded region highlights the time considered for the arc's characteristics. The arrows point out the power spikes that were considered within the arc duration calculations. Dashed arrows point out the unstable arcs, whereas solid arrows highlight the main arc. These plots show the most representative curves based on the average arc duration and energy.

Table S1. Arc characteristics of reference and reinforced samples for electro-erosion tests carried out at 100 W.

Sample	Arc duration /ms	Arc energy /mJ
Ag Rod	0.23 ± 0.04	3.39 ± 0.60
Ag 0%	0.15 ± 0.04	2.32 ± 0.06
Ag 1%	0.19 ± 0.05	2.46 ± 0.82
Ag 2%	0.20 ± 0.05	2.37 ± 1.32
Ag 3%	0.23 ± 0.14	3.50 ± 2.10
Cu Rod	0.24 ± 0.02	2.73 ± 0.11
Cu 0%	0.24 ± 0.03	3.50 ± 0.73
Cu 1%	0.27 ± 0.02	3.28 ± 0.22
Cu 2%	0.22 ± 0.12	1.50 ± 0.47
Cu 3%	0.24 ± 0.15	1.94 ± 1.05
Ag/Ni 90/10	0.25 ± 0.05	3.07 ± 0.22
Ag/SnO_2 92/8	0.26 ± 0.02	3.33 ± 0.04
Ag/SnO_2 90/10	0.32 ± 0.02	4.22 ± 0.24
Ag/SnO_2 88/12	0.28 ± 0.04	3.96 ± 0.61

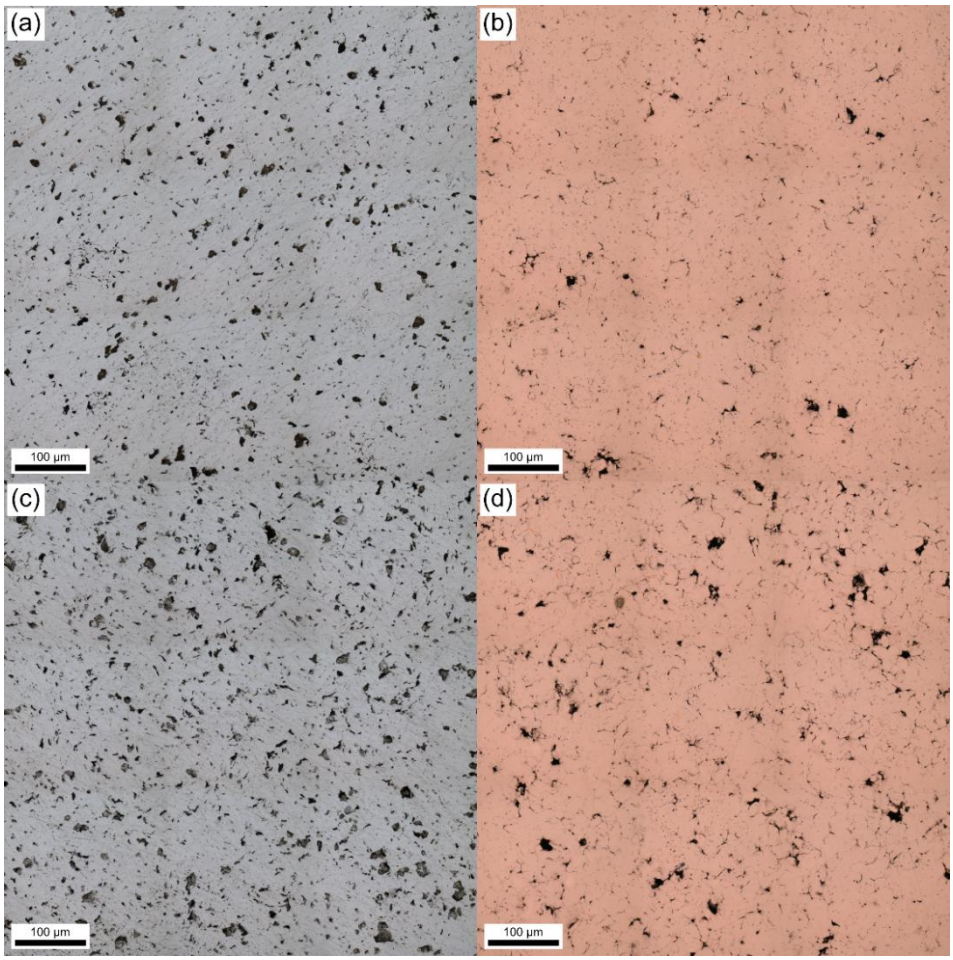

Figure S3. 3 ×3 stitching at 50× optical micrographs of **(a)** Ag 1%, **(b)** Cu 1%, **(c)** Ag 2%, and **(d)** Cu 2% obtained via CLSM.

ARTICLE XIV
Performance and Degradation of Carbon Nanotube-Reinforced Silver and Copper Composites for DC Switches

Bruno Alderete[1,*], Francisco A. Delfin[2,3], Frank Mücklich[1], Sebastian Suarez[1]

[1] Chair of Functional Materials, Saarland University, Campus D3.3, 66123 Saarbrücken, Germany
[2] Department of Materials Science, University of Applied Sciences Upper Austria, Stelzhamerstraße 23, 4600 Wels, Austria
[3] Faculty of Concepción del Uruguay, National University of Technology (UTN-FRCU), Ing. Pereyra 676, E3264 Concepción del Uruguay, Argentina

Research article
Submitted to "*Tribology International*" (2024)
Impact Factor: 6.1 (2023)
Article currently under review.

Own Contribution: Conceptualization; Methodology; Validation; Formal Analysis; Investigation; Data Curation; Writing – Original Draft; Visualization.

Performance and Degradation of Carbon Nanotube-Reinforced Silver and Copper Composites for DC Switches

Bruno Alderete[1,*], Francisco A. Delfin[2,3], Frank Mücklich[1], Sebastian Suarez[1]

[1] Chair of Functional Materials, Department of Materials Science and Engineering, Saarland University, Campus D3.3, 66123 Saarbrücken, Germany.

[2] Department of Materials Science, University of Applied Sciences Upper Austria, Stelzhamerstraße 23, 4600 Wels, Austria.

[3] Faculty of Concepción del Uruguay, National University of Technology (UTN-FRCU), Ing. Pereyra 676, E3264 Concepción del Uruguay, Argentina.

* Corresponding author: bruno.alderete@uni-saarland.de

Abstract: Hot switching creates an electrical arc that causes electro-erosion on electrodes due to ion and electron bombardment. This study characterizes electro-erosion craters from single-break operations of CNT-reinforced metal matrix composites and reference materials. Crater morphology was analyzed via confocal laser and electron microscopy, in addition to energy-dispersive X-ray and Raman spectroscopy. Adding up to 2 wt.% CNT resulted in crater roughness, displaced volume, and dimensions similar to references, while 3 wt.% led to increased roughness and volume. Although CNT did not affect the molten front dimensions, it reduced molten pool duration. Raman spectroscopy confirmed CNT structural integrity post-manufacturing, despite minor degradation from the arc. CNT-reinforced silver and copper MMCs (up to 2 wt.%) demonstrate potential for cost-effective, durable switching electrodes.

Keywords: carbon nanotubes, electro-erosion, metal matrix composites, switching electrical contacts

INTRODUCTION

A switching device is an electrical component that is responsible for interrupting the flow of current in a circuit. The necessity for current interruption may be attributed to the specific characteristics of the application in question, such as the use of electromechanical relays and contactors. Alternatively, it may be a consequence of safety considerations, as exemplified by the deployment of magnetic circuit breakers and ground fault interrupters. During a break operation (hot switching), the separation

of the electrodes results in an increase in the current density flowing through the contacting asperities (also known as a-spots) [1]. The elevated current density results in the generation of localized heat at the a-spots, reaching temperatures above the melting point of the metals as the real contact area tends to zero and the constriction resistance increases. The molten material is drawn by the receding electrode, thereby generating a molten bridge between the two electrodes. As the gap between the electrodes increases, the bridge is further extended, thereby further increasing the current density. The molten bridge is extended until it becomes unstable and ruptures. The instability of the molten bridge can be attributed to the influx of cold material from the base of the bridge or to particle ejection due to temperatures exceeding the boiling temperature of the metal. Upon the rupture of the bridge, the arc is extinguished, resulting in the release of metallic vapor into the gap between the electrodes. The release of metallic vapor into the gap significantly increases the pressure. However, as the vapor expands into the surrounding low-pressure regions, a pseudo-arc is ignited in which the current is conducted by the ions. In atmospheric conditions, the flow of atmospheric gases into the electrode gap is driven by the reduction in pressure. Subsequently, the arc undergoes a transition from a metallic phase to a gaseous phase, wherein electrons assume the role of current conductors, rather than ions.

In the initial stages of the spark, anodic erosion occurs as a result of electron bombardment, while the cathode gains mass from particle recombination and condensation on its surface. The recombination and condensation that occur on the colder electrodes are the primary cause of material transfer during hot switching [2]. An extension of the arc's duration results in a transition period during which the cathode experiences mass loss due to ion bombardment [3]. The transition is governed by the length and duration of the arc generated between the electrodes, with the latter being the predominant factor influencing the direction of mass transfer [4]. During the transition from anodic to cathodic arc, the material deposited on the cathode during the initial phase is removed, resulting in net zero erosion [5]. This transition is dependent on arc length and is independent of the electrode material or arc duration. Conversely, the point of net zero erosion is determined by the amount of material transferred during the anodic erosion phase, which is influenced by both arc duration – which is related to the circuit type – and electrode material [4]. While the current passing through the electrodes does not alter the type of arc generated, it does increase the energy of the arc, thereby delaying the onset of net zero erosion [5].

The service life of a circuit breaker depends upon its capacity to withstand erosion due to arcing. In order to ensure optimal performance and safety, electrode materials should exhibit a low electrical resistance, be resistant to excessive heating, be erosion-resistant, demonstrate good interruption capabilities, not be toxic, be cost-effective, and

exhibit low welding tendencies and low weld force to ensure that the circuit opens when required [1,6]. Silver is a material that is extensively utilized in switching applications, presenting exceptional conductivity and low welding tendencies. The performance and durability of silver electrodes can be further enhanced by alloying it with zinc, nickel, copper, palladium, among other metals, or by using silver-metal oxide composite materials, including silver-cadmium oxide, silver-zinc oxide, silver-tungsten oxide, silver-tin oxide, and others. Additionally, copper is utilized in select switching applications due to its exceptional conductivity and cost-effectiveness. However, it exhibits higher welding potential in comparison to silver. Consequently, copper electrodes are typically plated with silver-based materials to enhance the weld resistance of the electrode. Additional techniques employed to enhance the switching performance of copper include the deposition of tin or silver coatings and the alloying of copper with elements such as zinc, tin, cadmium, chromium, or tellurium [1,6].

Previous researchers have evaluated the performance of graphite-containing silver and copper switches [7–12]. The studies underscore the enhanced switching performance, reducing weldability of the electrodes even when subjected to elevated switching currents [6,13]. Additionally, the studies illustrate how the formation of non-conductive oxide layers on the electrode's surface is prevented, thereby maintaining low resistances [12]. However, the behavior exhibited by these graphite-MMC electrodes depends on the relative orientation of the reinforcement phase due to the anisotropic properties of graphite. Nonetheless, the addition of graphite into these metals has been observed to result in increased erosion rates and arc reignition. Therefore, the aim of this study is to assess the potential and understand the degradation of CNT-reinforced silver and copper MMC as switching electrodes in low-voltage direct current circuits. The characteristics of the arc generated, electrical performance, distribution of the reinforcement phase, and the influence of ohmic load, as well as the influence of CNT and their concentration on the characteristics of the arc generated, have been previously studied and reported [14]. Accordingly, the objective of this study was to characterize the crater resulting from a single break operation under an ohmic load of 200 W. The crater was micrographed via confocal laser scanning microscopy (CLSM) and scanning electron microscopy (SEM), whereas chemical analysis was carried out via energy dispersive X-ray spectroscopy (EDS). The area affected beneath the electro-erosion crater was visualized by conducting focused ion beam (FIB) cross sections at the center of the craters. The CLSM measurements were also employed to determine the most relevant crater attributes – i.e., dimensions, topographic parameters, mass gained/loss, and load-bearing capacity following the initial opening cycle. Finite element method thermal simulations were conducted on the pure metals and CNT-reinforced MMC based on the real power input of the electrical arcs to determine the maximum

temperature, dimensions of the melting and boiling fronts, and the duration of the molten pool as well as the time that the material is evaporated. Furthermore, Raman spectroscopy was carried out to assess the structural integrity of the CNT clusters within and outside the crater, with a view to determine the extent of damage that the reinforcement phase may have sustained during arcing.

MATERIALS AND METHODS

Materials

Silver and copper MMC reinforced with multi-walled CNT were produced via powder metallurgy (1, 2, and 3 wt.%). Silver flakes with at least 80% of the flakes being below 20 μm in size and a purity of 99.9% (Alfa Aesar GmbH) and dendritic copper powder with a mesh size of 325 and 99% purity (Alfa Aesar GmbH) were used as metallic matrices. Chemical vapor deposition grown multi-walled CNT (Graphene Supermarket, USA) were used as reinforcement phase. The CNT possess an outer diameter distribution between 50-85 nm, an as-received state length from 10-15 μm, and a carbon purity above 94%.

The performance of the proposed MMC were compared to pure metals and commonly used switching material to fully assess their feasibility. High-purity samples (silver rod 99.95% purity, Alfa Aesar GmbH, and copper rod 99.9% purity, Goodfellows Cambridge Limited) and sintered silver and copper reference samples (i.e., 0 wt.% CNT) were employed as pure metal references. Two different silver-based switching materials were evaluated due to their pervasive commercial applications, namely Ag/Ni 90/10, Ag/SnO_2 88/12, Ag/SnO_2 90/10, and Ag/SnO_2 92/8 (Umicore N.V.).

Hard gold-coated ($AuCo_{0.2}$) silver-nickel core ($AgNi_{0.15}$) rivets (Adam Bornbaum GmbH) were used as counter electrodes in all electro-erosion tests. The rivets have a hemispherical geometry, with a radius of curvature at its tip of 4 mm, a hardness value of 1.38 ± 0.01 GPa (measured via Vickers hardness), and an S_q of 0.3 μm.

MMC manufacturing

The CNT were dispersed in ethylene glycol via homogenization (Ultra-Turrax T25, IKA) and ultrasonication. The metallic powder was added into the colloid, followed by a subsequent homogenization step, and evaporation of the solvent in a ventilated furnace at 150 °C. After evaporation, 8 mm in diameter disk-shaped green pellets were produced by placing the CNT-metallic powder mixture in a steel die and pressed at 990 MPa for approximately 30 s. Further densification (reaching relative density values of at least 95%) was achieved by subjecting the green pellets to hot uniaxial pressing (HUP) under vacuum (2×10^{-6} mbar) to minimize sample oxidation. Both samples were sintered at 264 MPa and a temperature of 750 °C. The isothermal holding time for the

silver samples was 7.5 hours, whereas the copper samples required 2.5 hours. Further details on the preparation of the colloid and the manufacturing of the MMC samples can be found in [15,16].

Electro-erosion tests

The electrical arc was generated by simulating a break operation between the sample and the counter electrode. Both electrodes were mounted on a custom testing rig [17]. The samples were mounted on a moving stage and connected to the positive terminal of a 300 W direct current power source (Gossen Metrawatt SSP 3000-52), whereas the rivet was mounted on the negative, static terminal. An oscilloscope (LeCroy WaveRunner 6100A) was used to record the voltage drop prior, during, and after the break operation. The current was measured with the same device with the use of a LeCroy CP031 current probe [18]. Four 50 W automotive halogen lamps were used as load – ohmic load, 200 W. A normal load of 4 N was applied between the electrodes and a current stabilization time of 10 s passed prior to opening the circuit. After the current stabilization time, the linear stage retreated at a constant acceleration of 8000 mm/s^2, reaching a top speed of 58 mm/s – further details on the accuracy of the setup and schematic representations were previously reported by Puyol et al. and Suarez et al. [17,18]. At least three switching operations were carried out per sample (in different spots). The current probe was degaussed between measurements, with a new counter electrode being used for each test. The rivets were cleaned using an isopropanol-based contact cleaner and dried with compressed air prior to each test. All tests were carried out under atmospheric conditions – 23 ± 1 °C and 23 ± 2 % relative humidity. All samples underwent grinding and polishing prior to electro-erosion tests, achieving a mirror-polished surface with an S_q value between 0.3 and 0.6 μm.

Confocal laser and scanning electron microscopy

The samples and rivets were micrographed via confocal laser scanning microscopy (LEXT OLS4100, Olympus) using a laser with a wavelength of 532 nm. Micrographs of the craters on the samples' surface were acquired with a magnification of 50×, whereas 20× magnification was used for the counter electrodes due to their curvature.

SEM micrographs of the electro-erosion craters on the samples were acquired using an ICE detector and an acceleration voltage and beam current of 10 kV and 1.6 nA, respectively (Thermo-Fisher Helios™ G4 PFIB CXe DualBeam™ FIB/SEM equipped with an EDS detector EDAX Octane Elite Super). Furthermore, for a two-dimensional chemical distribution analysis, EDS mappings were acquired using 10 kV. FIB milling was carried out using Xe ions with an acceleration voltage of 30 kV and a beam current of 1 μA. Subsequent ion polishing of the cross section was conducted using a beam current of 0.2 μA, 60 nA, and 15 nA to minimize curtaining. An approximate volume of

0.5 mm^3 was removed. The cross section was micrographed using an ICE and TLD detector, with an acceleration voltage and beam current of 5 kV and 1.6 nA, respectively.

Thermal simulations

Finite element method thermal simulations based on Fourier's law of heat conduction were carried out for each MMC and pure metal references using Flex-PDE software [19]. The heat input was obtained by linearly fitting the power curves of each electro-erosion test reported in [14]. The energy from the electrical arc was assumed to be cylindrical, with a radius of 50 μm, encountering a 1 mm in radius and height cylindrical electrode from the z-axis. All phase transitions were considered in the simulations by incorporating the power per unit of volume involved solid-liquid and liquid-vapor phase transitions, as described by Soldera et al. [20]. From the thermal simulations, the dimensions of the molten and boiling fronts were determined, as well as the duration of material melting and evaporation. The simulations were conducted under the assumption that evaporated material left the system – i.e., there is no re-deposition through condensation. Material properties (i.e., melting and boiling temperatures, specific heat capacity, thermal conductivity, and density) were obtained from [1,21–26]. Due to the aleatory nature of the reinforcement phase's distribution within the MMC, the specific heat capacity and thermal conductivity for the MMC were determined using the effective medium theory [27].

Raman spectroscopy

A Raman spectrometer (Horiba XploRA Plus) was used to evaluate the structural integrity of the reinforcement phase prior to and after electro-erosion tests. The Raman spectrometer was equipped with a 532 nm laser. The data was acquired using a grating of 2400 lines mm^{-1}, a 100× objective, and a laser power of 2 mW, with a spectral resolution of approximately 5.9 cm^{-1}. The acquisition time was determined for every measurement using the auto-exposure tool, thus obtaining a better signal-to-noise ratio. Within the same measurement, at least three repetitions were performed to reduce sporadic external influences and to improve smoothness. Measurements were conducted on at least three different CNT clusters within the crater and outside of the crater, thereby obtaining statistically significant results. Prior to analyzing the data, the spectra's cosmic ray and background were removed using CrystalSleuth [28], and the spectra intensities were normalized. The Raman peaks were subsequently fitted. The D- and G'-bands were fitted using a Lorentz fitting. The (G+D')-band was fitted using a combined Lorentz-Voigt fitting, where the G-band was fitted using a Lorentzian curve and the D'-band a Voigtian curve [29]. Due to the convolution of these two peaks, the theoretical peak center values for graphite according to Ferrari and Robertson were fixed [30] – i.e., 1582 cm^{-1} and 1620 cm^{-1} for the G- and D'-band, respectively.

Subsequently, the fitted Raman spectra were analyzed by determining the G-band's Raman shift (position of the peak's center), intensity and integral intensity ratios (i.e., the crystallinity and purity ratios: I_D/I_G, A_D/A_G, $I_{G'}/I_D$, and $A_{G'}/A_D$, respectively), and the FWHM of the G-band.

RESULTS AND DISCUSSIONS

Electro-erosion crater morphology and topography

CLSM analysis of the craters after electro-erosion tests can provide insight into the degree to which the electrodes have eroded and/or material was transferred, as well as the modification of the electrodes' topography due to the electrical arc. The crater average attributes determined via CLSM after a single break operation under a 200 W ohmic load for the reference and MMC samples are shown in **Table 1**.

On average, the resulting crater area for the Ag/SnO_2 samples does not appear significantly affected by tin-oxide concentration. Irrespective of the reinforcement's concentrations, silver tin-oxide samples exhibit a crater area of approximately 2×10^4 μm^2, whereas the silver-nickel sample presents a crater area of approximately 3×10^4 μm^2. The same trend is observed in the crater's surface area, and the corresponding S-ratio – i.e., the relationship between the crater's surface area (caused by topographic features) and the projected area of the crater.

For the silver MMC, on the other hand, the crater's attributes vary considerably depending on the sample type. The pure silver and copper samples (i.e., Ag rod and Ag 0%) and the Ag 3% sample exhibit the largest crater area, whereas the addition of 1 wt.% and 2 wt.% CNT reduces the projected area of the crater. Nonetheless, the

Table 1. Average crater attributes after a single break operation.

Sample	*Crater area (×10⁴) /μm²*	*Crater surface area (×10⁴) /μm²*	*S-ratio*
Ag/Ni 90/10	3.03 ± 0.48	4.48 ± 0.77	1.48 ± 0.03
Ag/SnO_2 92/8	2.30 ± 0.16	3.21 ± 0.32	1.39 ± 0.05
Ag/SnO_2 90/10	2.54 ± 0.29	3.47 ± 0.50	1.36 ± 0.05
Ag/SnO_2 88/12	2.30 ± 0.33	3.14 ± 0.38	1.37 ± 0.03
Ag rod	3.24 ± 0.25	4.81 ± 0.44	1.43 ± 0.04
Ag 0%	3.21 ± 0.31	4.73 ± 0.42	1.47 ± 0.02
Ag 1%	2.97 ± 0.44	5.18 ± 0.72	1.75 ± 0.02
Ag 2%	2.85 ± 0.42	5.22 ± 0.80	1.83 ± 0.04
Ag 3%	3.57 ± 0.73	7.64 ± 2.77	2.07 ± 0.34
Cu rod	2.08 ± 0.32	2.61 ± 0.35	1.26 ± 0.04
Cu 0%	2.72 ± 0.25	3.51 ± 0.30	1.29 ± 0.01
Cu 1%	2.41 ± 0.08	3.95 ± 0.13	1.64 ± 0.01
Cu 2%	2.33 ± 0.39	4.06 ± 0.66	1.74 ± 0.02
Cu 3%	2.77 ± 0.45	5.27 ± 0.76	1.91 ± 0.03

surface area of the craters (and consequently the S-ratio) in the reinforced samples does not follow this same trend. The craters on the pure silver samples have the smallest surface area. Contrarily, the craters on the reinforced silver samples exhibit an increasing surface area as the CNT concentrations increases. The same behavior can be observed for the pure copper sample and CNT-reinforced copper MMC. Although the craters on the copper MMC are smaller than those on the silver MMC, the S-ratio values are similar.

Zum Gahr developed a model to determine the materials' interaction during abrasive wear [31–33]. The f_{ab} parameter (shown in **Equation 1**) is the ratio of volume removed due to micro-cutting to the volume of the resulting groove. f_{ab} ranges from zero to one, with the former indicating pure micro-plowing, whereas the latter indicates pure micro-cutting. To further expand on the craters' dimensionality, this model is analogously used in this study. Accordingly, the volume above and below the datum line were determined using CLSM and the analogous material removal factor was calculated using **Equation 1** – results shown in **Table 2**. It is important to note that this analogy is not ideal, but rather an approximation to qualitatively appraise the crater resulting from electro-erosion. Therefore, this methodology is subject to limitations, the primary being that the values may fall outside of the theoretical bounds set by Zum Gahr. Since in this case there is material that evaporates, melts, solidifies, and condensates, it is possible to obtain negative f_{ab} values. Such cases imply one of two scenarios: 1) a considerable amount of material was transferred from the counter electrode towards the electrode,

Table 2. Volume above and below the datum line and the analogous material removal factor (f_{ab}) for an electro-erosion crater in the reference and MMC samples.

Sample	*Volume up (×10⁴) /µm³*	*Volume down (×10⁴) /µm³*	f_{ab}
Ag/Ni 90/10	1.89	1.53	-0.23
Ag/SnO_2 92/8	0.70	1.68	0.59
Ag/SnO_2 90/10	1.30	1.44	0.10
Ag/SnO_2 88/12	1.00	1.73	0.42
Ag rod	3.20	1.80	-0.78
Ag 0%	2.09	1.57	-0.33
Ag 1%	1.78	1.97	0.10
Ag 2%	1.46	2.21	0.34
Ag 3% *	3.81	3.17	-0.20
Cu rod	1.11	1.19	0.06
Cu 0%	1.16	1.42	0.18
Cu 1%	1.31	2.73	0.52
Cu 2%	1.37	1.52	0.10
Cu 3% *	3.60	1.28	-1.81

* The values reported in this table are representative of three measured craters per sample. The variation between individual volume measurements does not exceed 20%, except for the samples marked with an asterisk.

$$f_{ab} = \frac{V_{down} - V_{up}}{V_{down}} \qquad \textbf{Equation 1}$$

thus increasing the volume above the datum line in relation to the volume below it, or 2) that the molten pool upon the rupturing of the molten bridge or after the arc is extinguished rapidly solidifies, thereby significantly increasing the volume above the datum line. Furthermore, a f_{ab} value of zero in this analogy implies pure fusion with no or minimal material transfer, whereby the material below the datum line melted and was displaced above the datum line. A value that approaches one, however, implies that primarily evaporation took place, since the volume below is not present above the datum line.

The material volumes measured above and below the datum line, shown in **Table 2**, highlight the exceptional performance of the proposed materials. Apart from the 3 wt.% samples, the proposed MMC perform similarly to the reference materials. Certain samples exhibit deviations in the amount of displaced volume, however this due to the heterogeneous CNT distribution [14–16]. Therefore, the degree to which volume is displaced after electro-erosion will depend on the characteristics of the contact spot, i.e., amount and size of CNT clusters at the contacting site. The 3 wt.% samples not only show the largest craters in terms of area (see **Table 1**), but these samples also exhibit the largest volume displacement, with the Ag 3% sample presenting the highest volume above and below the datum line. Although the Cu 3% sample also exhibits large volumes above the datum line, the volume below falls within the range of the other copper and reference samples, thereby producing a considerably negative f_{ab}. The higher displaced volume of the samples containing higher CNT concentrations is likely due to the improved thermal diffusivity of the composite, thereby rapidly re-solidifying and preventing the molten material from flowing and forming a flat surface. Silver MMC tend to present higher displaced volumes than the silver-based references and the copper materials. This is a consequence of the lower viscosity of molten silver, compared to that of copper and nickel [34]. Nonetheless, Ag 1% and Ag 2% samples exhibit relatively good results compared to the other materials evaluated.

Different roughness parameters of the craters were determined via CLSM, namely: the root mean square roughness S_q, the maximum valley depth S_v and peak height S_p, the maximum height S_z, and the skewness S_{sk} – shown in **Table 3** [35]. S_v, S_p, S_z, and S_{sk} are particularly interesting since they provide further insight into the geometry of the resulting crater after the electrical arc. The first three parameters express the overall height modification of the surface, whereas the latter represents the degree to which the asperities skew in reference to the datum line [35]. A positive S_{sk} value indicates that the surface presents few very high peaks with many shallow valleys, whereas a negative value indicates the inverse scenario. An S_{sk} value that approaches zero implies a symmetrical distribution of peak heights and valley depths.

Table 3. Average topographic parameters of a crater after a single break operation.

Sample	S_q /µm	S_v /µm	S_p /µm	S_z /µm	S_{sk}
Ag/Ni 90/10	1.12 ± 0.12	12.21 ± 4.51	10.64 ± 2.31	22.85 ± 6.78	0.27 ± 0.27
Ag/SnO_2 92/8	0.68 ± 0.08	8.11 ± 1.38	9.75 ± 2.39	17.86 ± 3.00	1.27 ± 1.04
Ag/SnO_2 90/10	0.65 ± 0.08	5.44 ± 0.62	7.36 ± 1.28	12.80 ± 1.80	0.72 ± 0.44
Ag/SnO_2 88/12	0.62 ± 0.04	6.25 ± 1.31	7.73 ± 1.89	13.97 ± 3.05	0.66 ± 0.46
Ag rod	0.99 ± 0.04	6.56 ± 0.26	7.31 ± 1.70	13.87 ± 1.55	0.13 ± 0.03
Ag 0%	0.96 ± 0.07	7.99 ± 1.43	6.26 ± 0.15	14.24 ± 1.44	-0.10 ± 0.26
Ag 1%	0.98 ± 0.09	8.59 ± 0.37	8.52 ± 0.35	17.11 ± 0.61	0.62 ± 0.12
Ag 2%	0.99 ± 0.09	8.14 ± 0.91	9.50 ± 0.43	17.64 ± 0.51	1.21 ± 0.34
Ag 3%	1.32 ± 0.29	9.17 ± 1.10	11.95 ± 3.76	21.12 ± 4.58	0.64 ± 0.57
Cu rod	0.65 ± 0.05	6.56 ± 1.13	5.96 ± 1.25	12.51 ± 1.91	0.39 ± 0.09
Cu 0%	0.75 ± 0.03	8.76 ± 1.84	5.29 ± 0.33	14.05 ± 1.91	0.08 ± 0.20
Cu 1%	1.05 ± 0.04	8.39 ± 1.01	8.83 ± 0.99	17.22 ± 0.85	0.73 ± 0.20
Cu 2%	0.97 ± 0.06	7.96 ± 0.53	8.39 ± 0.94	16.35 ± 1.46	0.35 ± 0.44
Cu 3%	1.27 ± 0.02	9.27 ± 0.98	10.77 ± 1.31	20.05 ± 1.72	0.59 ± 0.35

The topographic parameters presented in **Table 3** showcase the surface modification endured by the electrodes after a single break operation. The root mean square roughness show that the arc on the silver samples results in the highest roughness. Although the S_q in the copper samples are also higher than the reference samples, these parameters do not increase as significantly as in the silver samples. However, comparing the pure metal samples with their reinforced counterparts, the increased roughness is not as significant for samples reinforced with up to 2 wt.% CNT. Higher CNT concentrations (i.e., 3 wt.%) bring about a significantly higher roughness. This increased roughness is due to the higher degree to which molten material is displaced and re-solidifies – see **Table 2**. The S_v, S_p and S_z roughness parameters show a similar trend, with reinforcement concentrations of 3 wt.% showing the highest peaks and deepest valleys – excluding the Ag/Ni 90/10 sample which shows the largest values among the samples herein considered. Moreover, the S_{sk} parameter indicates that all samples exhibit skewed topographic features. In other words, the craters present numerous shallow peaks, with few high peaks. Nevertheless, as previously shown in **Table 2**, the volume displaced above is generally lower than the volume displaced below the datum line. The pure sintered samples are the exception, exhibiting a relatively symmetrical crater. Although most of the samples tend towards a positive topographic skew, the copper-based electrodes exhibit the lowest values, implying a relatively symmetrical crater. This observation for the copper-based electrodes correlates with the values presented in **Table 2**.

Relays, contactors, and other switching components are subjected to numerous make and break operations. As a result, the contacting surfaces are constantly being modified due to the topographic changes generated by the electrical arc. Therefore, the

morphology of the resulting crater after the break operation is of particular interest since this enables the prediction of the contact physics for the subsequent make operation. Accordingly, the Abbott-Firestone curves and the corresponding parameters were determined to gather information on the peak and valley distribution to complement the topographic parameters shown in **Table 3** [36–38]. Exemplary Abbott-Firestone curves for all the materials herein evaluated are shown in **Supplementary Figure 1**. Topographic information of the samples' surface after electro-erosion is further presented in **Supplementary Figure 2**, **Supplementary Figure 3**, and **Supplementary Figure 4**. These figures depict a three-dimensional view of the crater's morphology of all samples and counter electrodes, as well as the height distribution of each sample's crater.

The Abbott-Firestone parameters corresponding to the curves from **Supplementary Figure 1** are shown in **Table 4**. As can be seen, the core roughness depth – i.e., load bearing volume, R_k – of the MMC tends to be higher than that of the reference materials, with certain exceptions. For example, the core roughness depth of the copper rod is the lowest among the evaluated craters. Observing the reduced peak height (R_{pk}) and reduced valley depth (R_{vk}) for the crater and recalling the roughness parameters from **Table 3**, it is clear that the energy input did not produce significant topographic changes in this reference material. This sample also presents the lowest higher material ratio (M_{r1}) and lower material ratio (M_{r2}). These parameters represent the amount of material above (asperities) the core material and the amount of material below (valleys) the core material, respectively [37,39,40]. For the example of the high-purity copper, after the electro-erosion test, this sample exhibits only 15.1% material above the load bearing

Table 4. Exemplary Abbott-Firestone parameters for reference, silver, and copper samples after a single break operation. Note that R_k, R_{pk}, and R_{vk} do not have a unit since these values were normalized in order to compare the values between different materials.

Sample	R_k	R_{pk}	R_{vk}	M_{r1} /%	M_{r2} /%
Ag/Ni 90/10	1.6	67.9	5.7	20.2	80.3
Ag/SnO_2 92/8	1.6	12.4	9.1	18.9	79.4
Ag/SnO_2 90/10	2.5	14.0	12.2	23.2	78.3
Ag/SnO_2 88/12	1.9	14.4	10.1	19.7	77.2
Ag rod	3.8	15.0	11.4	23.3	76.9
Ag 0%	2.1	11.9	9.4	23.4	76.4
Ag 1%	2.3	13.4	7.9	18.8	74.1
Ag 2%	2.7	12.5	7.0	18.5	73.5
Ag 3%	6.5	11.3	9.3	24.1	82.5
Cu rod	0.9	12.4	8.0	15.1	79.3
Cu 0%	2.0	10.4	11.4	24.6	81.9
Cu 1%	2.2	14.5	10.3	20.5	76.6
Cu 2%	1.5	13.0	10.4	19.8	80.2
Cu 3%	6.9	15.8	10.6	19.8	80.0

volume, the lowest amount among all the samples herein analyzed. The M_{r2}, on the other hand, is similar to that of the other samples. The Abbott-Firestone parameters validate the roughness parameters presented in **Table 3**. The resulting surfaces after a single break operation of the proposed MMC are similar to that of the reference silver-based materials. Therefore, the incorporation of CNT into the silver and copper matrices does not significantly change the resulting surface in comparison to the reference materials. Therefore, the load-bearing capacity of the proposed electrodes should perform similarly to the reference materials in subsequent make and break operations.

SEM micrographs and the corresponding EDS mappings of the craters after a break operation were acquired. An SEM micrograph and EDS map of an electro-erosion crater for the reference samples, Ag rod, Ag 0%, Ag 3%, Cu rod, Cu 0%, and Cu 3% are shown in **Figure 1**, whereas a crater for the remaining samples are shown in **Supplementary Figure 5**. Magnified micrographs of the electro-erosion craters as well as carbon-gold EDS map overlays are shown in **Supplementary Figure 6**, **Supplementary Figure 7**, and **Supplementary Figure 8**.

The shape, size, amount of material transfer, and morphology of the resolidified metal on the reference materials (**Figure 1a**, **b**, **c**, and **d**) are similar. In general, the craters have a noncircular shape, suggesting arc motion. All reference samples show a considerable amount of material transferred from the counter electrode towards the sample electrodes, as indicated by the large surfaces where gold signal was detected in the EDS maps. Particularly in the Ag/SnO_2 samples, lower tin oxide content presented larger areas with deposited gold. Interestingly, the gold signals are not centered within the crater, but rather surrounding the severely eroded regions. Based on the SEM micrographs and EDS maps, it can be hypothesized that the areas with stronger gold signals are the regions where the arc was ignited. As the arc ignites, the temperature quickly rises, leading to the melting of the metals. The silver-based samples melt before the hard-gold coated counter electrode, whereas in copper-based samples the gold counter electrode melts before the matrix. Therefore, it can be hypothesized that after the ignition of the arc, gold is no longer deposited, and the samples are eroded by ion and electron bombardment. This would explain why the gold signals in the EDS mappings are found primarily surrounding the crater rather than within the crater. This hypothesis can, in part, be validated by observing the protruding gold signals (relative to the center of the craters) highlighted by the black arrows in the Ag/Ni 90/10 and Ag/SnO_2 92/8 samples (**Figure 1a** and **b**). In these samples, high-speed camera footage and the I-V and power curves prove the presence of unstable arcing [14]. Consequently, multiple small electrical arcs ignited on the surface, thereby producing multiple rather than a single protrusion.

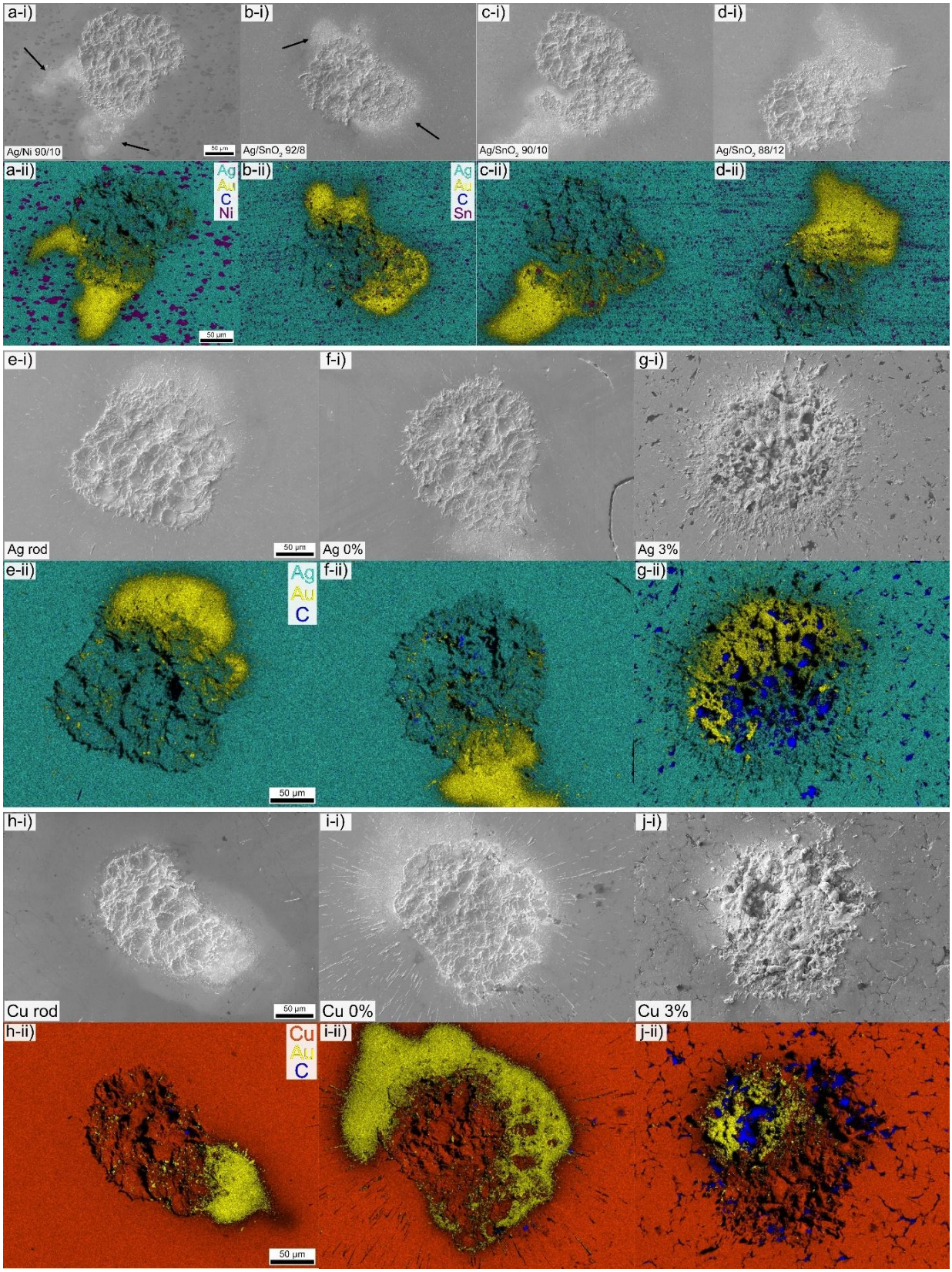

Figure 1. i) SEM micrograph and **ii)** EDS map of **a)** Ag/Ni 90/10, **b)** Ag/SnO_2 92/8, **c)** Ag/SnO_2 90/10, **d)** Ag/SnO_2 88/12, **e)** Ag rod, **f)** Ag 0%, **g)** Ag 3%, **h)** Cu rod, **i)** Cu 0%, and **j)** Cu 3%. The black arrows highlight potential multiple arc ignition sites. Black regions within the crater in the EDS maps are areas where no signal was detected due to shadowing effects as a result of the crater's topography.

As is the case with the reference materials, the high-purity silver (rod) sample and the unreinforced, sintered silver sample (Ag 0%) show considerable gold transfer

(**Figure 1e** and **f**). The transferred material is primarily located on one side of the crater, with minimal gold intensity scattered within the crater. The reinforced sample (**Figure 1g**), on the other hand, presents a more uniform gold deposition within the crater. Since the Ag 0% and Ag 3% sample present similar hardness values, it can be assumed that both have similar contact areas once the normal load was established. Therefore, the more uniform transfer of material may be caused by the ignition of a wider arc in the initial instances of the break operation. It is reasonable to assume that a wider arc ignites in the reinforced sample due to the elasticity of the reinforcement phase, which remain in electrical contact with the counter electrode as the rivet recedes and the CNT restitute to their original position. Moreover, the EDS map in **Figure 1g-ii** showcases the presence of large CNT clusters throughout the crater, whereas the surrounding regions present significantly smaller CNT agglomeration. As the electrode's material melts during arcing, the CNT on the surface of the electrode re-agglomerate and tend to move towards the surface of the electrode on account of the density difference between the molten metal and the reinforcement phase (10.49 and 1.92 g/cm^3 for silver and pristine multiwalled CNT herein utilized, respectively [1,41]), analogous to flocculation in colloids.

The high mobility of the arc is easily verified by observing the electro-erosion crater of the high-purity (rod) copper sample (**Figure 1h**). On this sample, the arc was ignited on the bottom right of the micrograph, where high intensities of gold were detected, and as the gap grew the arc moved upwards and towards the left side of the micrograph. Furthermore, the varying size of the crater indicates that as the arc moved it also widened. The unreinforced sintered copper sample (**Figure 1i**) experienced more material transfer compared to the high-purity copper sample. Considerable amounts of gold were detected surrounding the electro-erosion crater. However, the size and shape of the crater suggests that the arc did not move as much as in the Cu rod sample. The crater of the Cu 3% (**Figure 1j**) sample presents the lowest gold intensities among the copper samples. As was observed in the Ag 3%, larger CNT clusters are observed within the crater. However, in this case the degree to which CNT re-agglomerate is not as significant since the reinforcement phase distribution prior to arc is more heterogeneous [14,16]. Moreover, the SEM micrographs of both reinforced samples (**Figure 1g** and **j**) illustrate the increased topographic features generated due to arcing – as previously described in **Table 3** and **Table 4**.

A FIB cross section was conducted on the electro-erosion crater of a silver and a copper MMC to observe the buckling of the surface beneath the re-solidified and re-deposited material following the break operation. In addition, the cross sections facilitate a depth-resolved visualization of the state of the reinforcement phase beneath the crater. The micrographs corresponding to the cross sections conducted on the Ag

2% and Cu 2% samples are shown in **Figure 2**. As illustrated in the micrograph and inset (**Figure 2a**), the silver MMC sample exhibit minimal buckling beneath the electro-erosion crater. A slight depression in the surface's datum line was discerned in the vicinity of the crater's center, yet the surrounding regions of the cross section exhibited no indications of alterations – as previously described by the S_{sk} parameters (**Table 3**). Upon examination of the magnified micrograph of the Ag 2% sample (**Figure 2b**), it can be observed through the presence of CNT on the crater surface – highlighted by the violet arrows – that the reinforcement phase endured the electrical arc. It can thus be inferred that subsequent make and break operations will yield comparable electrical performance and arc behavior as in the first break operation given the presence of CNT on the contacting site [14]. Unaffected clusters of CNT are observed beneath the crater, as indicated by the orange arrows in **Figure 2b**. In comparison to the CNT situated on the surface, the clusters beneath the crater exhibit a higher contrast with the matrix, whereas the superficial CNT are a light shade of gray. The alteration in contrast may suggest a degree of amorphization resulting from the electrical arc, which reduces the conductivity of the CNT, thereby changing the contrast in the SEM micrograph. Furthermore, the deposition of small-scale metallic droplets originating from the formation of metallic vapor upon the explosion of the molten bridges could also favor a lighter shade of gray for the CNT situated on the surface of the MMC. The cross section

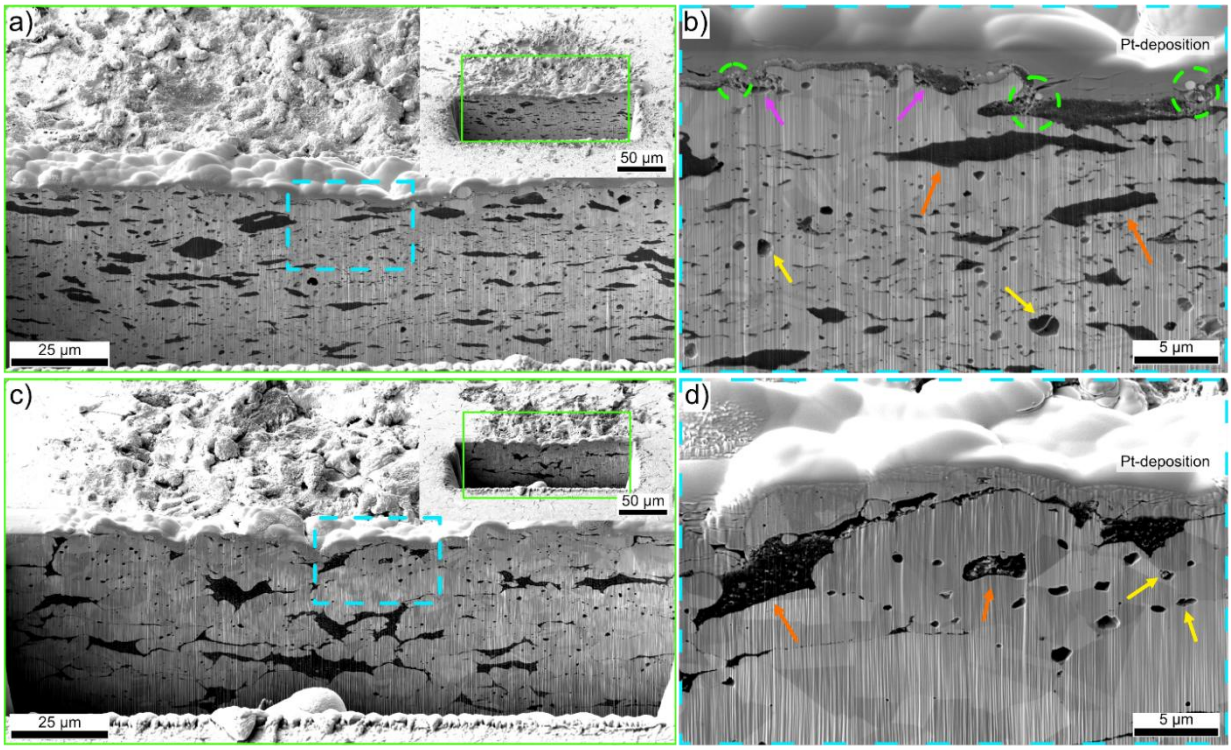

Figure 2. a) FIB cross section and **b)** magnified micrograph of the cross section near the surface of the Ag 2% sample. **c)** FIB cross section and **d)** magnified micrograph of the cross section near the surface of the Cu 2% sample. The green squares show the region of interest in the cross section, whereas the cyan dashed squares highlight a magnified region near the surface beneath the crater. The violet arrows indicate carbon content on the surface of the crater, the orange arrows show unaffected CNT beneath the crater, and the yellow arrows point out voids within the MMC. The green dashed circles highlight metallic vapor re-deposition on the reinforcement phase.

not only exhibits small-scale droplets, but also demonstrates that larger metallic droplets were deposited on the reinforcement phase, as indicated by the dashed green circles and shown in **Supplementary Figure 9a**. These droplets are pervasively found re-deposited throughout the surface of the crater, coating the re-solidified metal and the CNT on the surface – as indicated by the red arrows in **Supplementary Figure 9a**. Moreover, the yellow arrows in **Figure 2b** highlight the presence of pores within the silver MMC. Nonetheless, these pores are not devoid of material. The perimeter of the highlighted voids has adhered CNT, whereas the void on the right has a CNT extending radially from one end of the void to another.

Contrarily to what was observed in the silver MMC, the copper MMC (**Figure 2c**) does not present significant amounts of CNT on the surface of the crater. The silver MMC exhibits a thin, yet pervasive layer of CNT uniformly distributed across its surface, creating an even and consistent coverage. In contrast, the copper MMC demonstrates minimal presence of CNT, with the nanotubes appearing in clustered formations due to their agglomeration. The stark difference in distribution highlights the superior dispersal of CNT on the silver matrix compared to the copper [14], where the tendency of CNT to agglomerate has led to uneven and sparse coverage. The cross section of the copper MMC also demonstrates the increased buckling present in this metallic matrix. The depression of the surface below the datum is higher than in silver, showing a particularly higher depression at the center of the crater. Nonetheless, the region with the highest depression coincides with a CNT cluster which could further promote buckling of the surface – although there is a thin layer of copper between the surface of the crater and the CNT cluster. Recalling S_{sk} the values for copper samples from **Table 3**, these samples presented, on average, the most symmetrical craters' topographies. Therefore, a further explanation for the depression in the FIB cross section may be that material transfer – i.e., re-deposition of metallic vapor – is more significant in topographic maxima on the copper electrodes. Nonetheless, since FIB is a highly localized technique, the more significant depression at the center of this crater may not be fully representative of all copper-based samples due to the presence of the aforementioned CNT cluster close to the surface of the crater.

The magnified micrograph of the Cu 2% sample's cross section (**Figure 2d**) highlights the presence of voids, voids encompassing CNT (yellow arrows), and the presence of large CNT bundles beneath the electro-erosion crater (orange arrows). The magnified micrographs in **Figure 2d** and **Supplementary Figure 9b** highlight the absence of condensation droplets at the interface originating from the metallic vapor after the explosion of the molten bridge. Nonetheless, as the red arrows in **Supplementary Figure 9b** demonstrate, the surface of the crater shows an undulating surface, likely caused by re-deposition; however, droplets were not discernible on the cross section as

was the case with the silver sample. Moreover, the violet arrows in **Supplementary Figure 9b** highlight the presence of CNT within open porosities on the crater's surface.

Moreover, FIB cross sections of the electro-erosion craters for the sintered reference samples (i.e., Ag 0% and Cu 0%), as well as the 1 wt.% and 3 wt.% silver and copper MMC are shown in **Supplementary Figure 10**.

Thermal simulations

The results emphasize the exceptional performance of the proposed MMC. The radius of the melting front (**Figure 3a** and **b**) highlights the fact that the addition of the reinforcement phase, as well as the increment in its concentration, does not imply a wider melting front. Irrespective of CNT content, the melting front has a radius of approximately 49 µm and 46 µm for silver and copper matrices, respectively. Likewise, the depth of the melting front does not appear to be significantly affected, with silver and copper matrices showing average melting front depths of approximately 20 µm and 14 µm, respectively. The heat affected zone obtained in the thermal simulations is in agreement with those observed in the FIB cross sections presented in **Figure 2**. Furthermore, the results from the thermal simulations validate the hypothesis that the higher degree of buckling observed in the cross section of the copper MMC is due to the

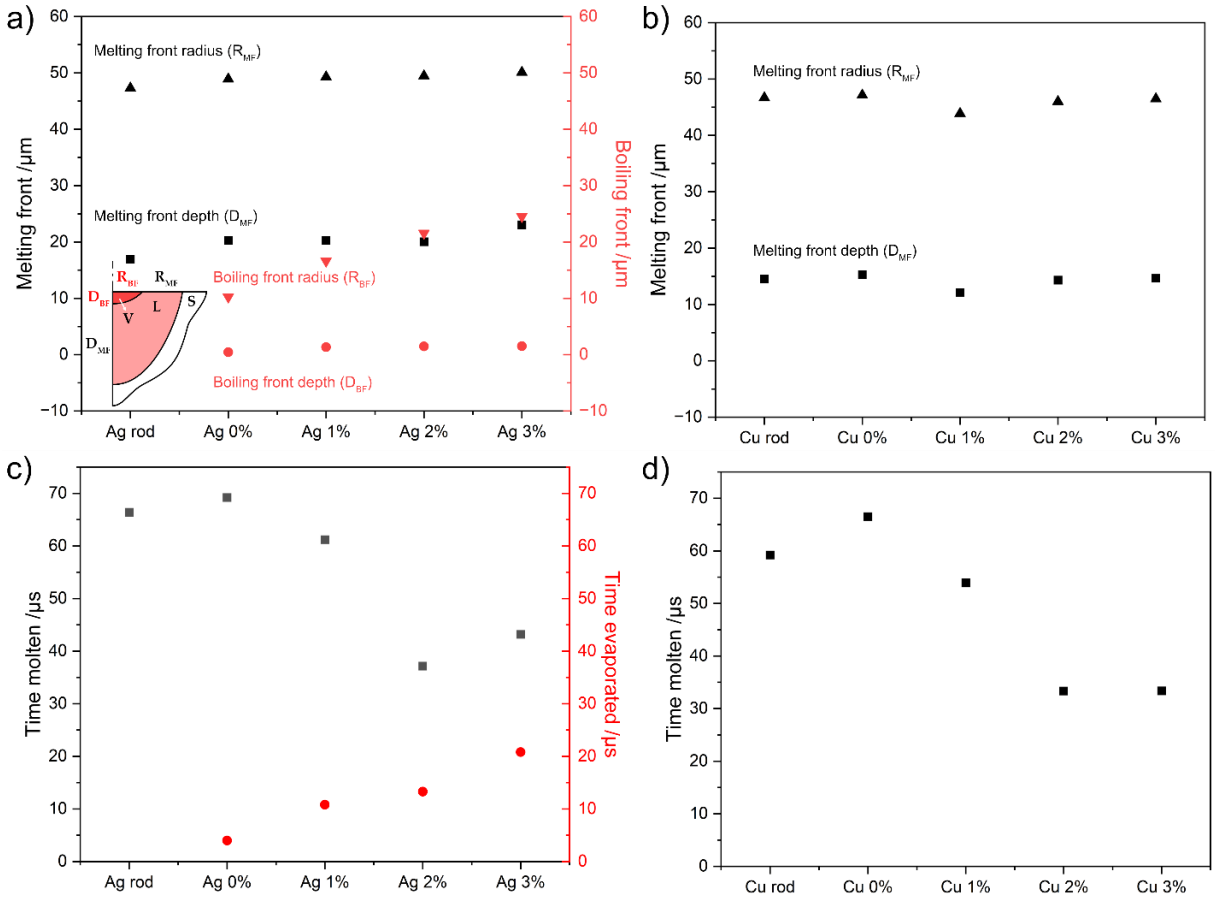

Figure 3. Dimensions of the melting and boiling from of **a)** silver and **b)** copper samples; and duration of the molten pool and duration of material evaporation of **c)** silver and **d)** copper samples. The inset in **a)** schematically represents the dimensions of both fronts. Each front can be portrayed as a quarter ellipsis, forming the volume as a solid of revolution along the y-axis.

presence of the CNT cluster, as opposed to increased re-deposition and/or material transfer at the topographic maxima.

Interestingly, the copper-based materials did not experience material evaporation since the temperature did not exceed its boiling temperature. Based on the results from the thermal simulations, the copper electrodes did not exceed 2600 K. This result from the simulation justifies why the copper samples exhibit the most symmetrical topographic features, presenting S_{sk} values that approach zero (**Table 3**). Furthermore, the lack of small-scale metallic droplets observed in the FIB cross section (**Figure 2c** and **d**) is validated by the thermal simulations, which highlight the fact that the electrical arc did not exceed the boiling temperature of copper. The silver electrodes, on the other hand, reached maximum temperatures of 2550 K, exceeding the boiling temperature of silver by over 100 K. A notable outlier is the high-purity silver sample (i.e., Ag rod), which did not reach the boiling temperature and therefore did not exhibit a melting front. The lower temperature of the Ag rod electrode is due to the instability of the electrical arc (refer to the power curves in [14]). Moreover, the maximum temperatures reached during arcing are insufficient to sublimate the reinforcement phase, falling well below the boiling temperature of CNT.

As observed for the melting front, the depth of the boiling front does not show discernible changes irrespective of CNT content, exhibiting an average depth of 1 μm. Conversely, the width of the boiling front does change, increasing in radius as the CNT concentration increases. The sintered, unreinforced silver sample (i.e., Ag 0%) exhibits an approximate boiling front radius of 10 μm, whereas the Ag 3% samples 24 μm. The higher amounts of material evaporation justify the higher volumes below the datum line of the craters shown in **Table 2**.

The duration of the metallic molten pools and the duration of silver evaporation are shown in **Figure 3c** and **d**. Both metallic matrices show the same trend, a slight increase in molten pool duration between the high purity reference and the sintered reference. As the concentration of the reinforcement phase increases, a noticeable reduction in molten pool duration is observed. Incorporating 1 wt.% of CNT does not produce significant reductions, however 2 wt.% and 3 wt.% CNT content incurs faster re-solidification of the molten pool due to the increased thermal diffusivity of the electrode. The faster re-solidification process observed in the thermal simulations can be verified with the CLSM measurements (**Table 2** and **Table 3**). The samples that re-solidify faster are the samples that present the highest S_p and highest volume displaced above the datum line. As the width of the boiling front increases for higher CNT concentrations, there is a clear trend towards longer evaporations times. This is due to the fact that the electrical arcs generated are more stable, which does not allow the temperature of the

electrode to reduce below its boiling temperature between unstable arcs – refer to I-V and power curves in [14].

CNT structural characterization

Raman spectroscopy was carried out after electro-erosion tests on the CNT within the crater to evaluate the structural damage that the reinforcement phase might have sustained due to arcing. The Raman spectrum of CNT in unaffected areas were also obtained, as well as the spectrum of pristine CNT as reference – shown in **Supplementary Figure 11** and **Supplementary Figure 12**.

The Raman spectrum of pristine CNT features their characteristic D-, G-, D′, and G′-bands. The D-band, usually observed at a Raman shift of 1350 cm^{-1}, corresponds to the A_{1g} symmetry breathing mode [30,42]. This mode only becomes active in the presence of defects in the carbon structure. The (G+D′)-band is the result of the convolution of the G- and D′-bands. This convoluted peak is a prominent feature in the Raman spectrum of CNT [43]. The G-band, observed at a Raman shift of 1581 cm^{-1}, is associated with the E_{2g} phonon mode [30]. In pristine CNT, the (G+D′)-band shows a distinct shoulder at higher wavenumbers due to the defect-induced double resonance, leading to the D′-band appearing between 1617 cm^{-1} and 1625 cm^{-1}. Like the D-band, the D′-band is activated by crystalline defects and its increment represents the transition from a monocrystalline to a polycrystalline state. The dispersive G′-band appears around 2700 cm^{-1} and arises from a second-order scattering process. As an overtone of the D-band, the G′-band indicates long-range order and fades with increasing degradation or amorphization [44].

The G-band is a non-dispersive peak [30]; consequently, its position does not depend on the excitation energy of the laser used for Raman spectroscopy. Accordingly, Ferrari and Robertson proposed a way of identifying the level of degradation in carbon by tracing the defect ratio (I_D/I_G) and the position of the G-band [30]. A three-stage phenomenological model for the amorphization of graphitic carbon was developed, where the first stage comprises the transition from graphite to nanocrystalline graphite. Within this stage, the G-band's position moves between 1581 cm^{-1} to 1600 cm^{-1}. The G-band position of the pristine CNT and of CNT clusters outside and inside the electro-erosion craters are shown in **Figure 4a**. As the plots present, there is a slight upshift in wavenumber comparing the state of the CNT clusters outside and inside the craters. The upshift is related to the appearance and development of the D′-band at approximately 1620 cm^{-1}. Nonetheless, the upshift is marginal, with the Raman shift values remaining within the theoretical range, highlighted by the shaded area. Therefore, the position of the G-band indicates that the sp^2 graphitic carbon structure remains without reaching the amorphization state (stage 3). However, the upshift suggests a slight tendency towards a nanocrystalline graphitic carbon structure – which corresponds to stage 2 in

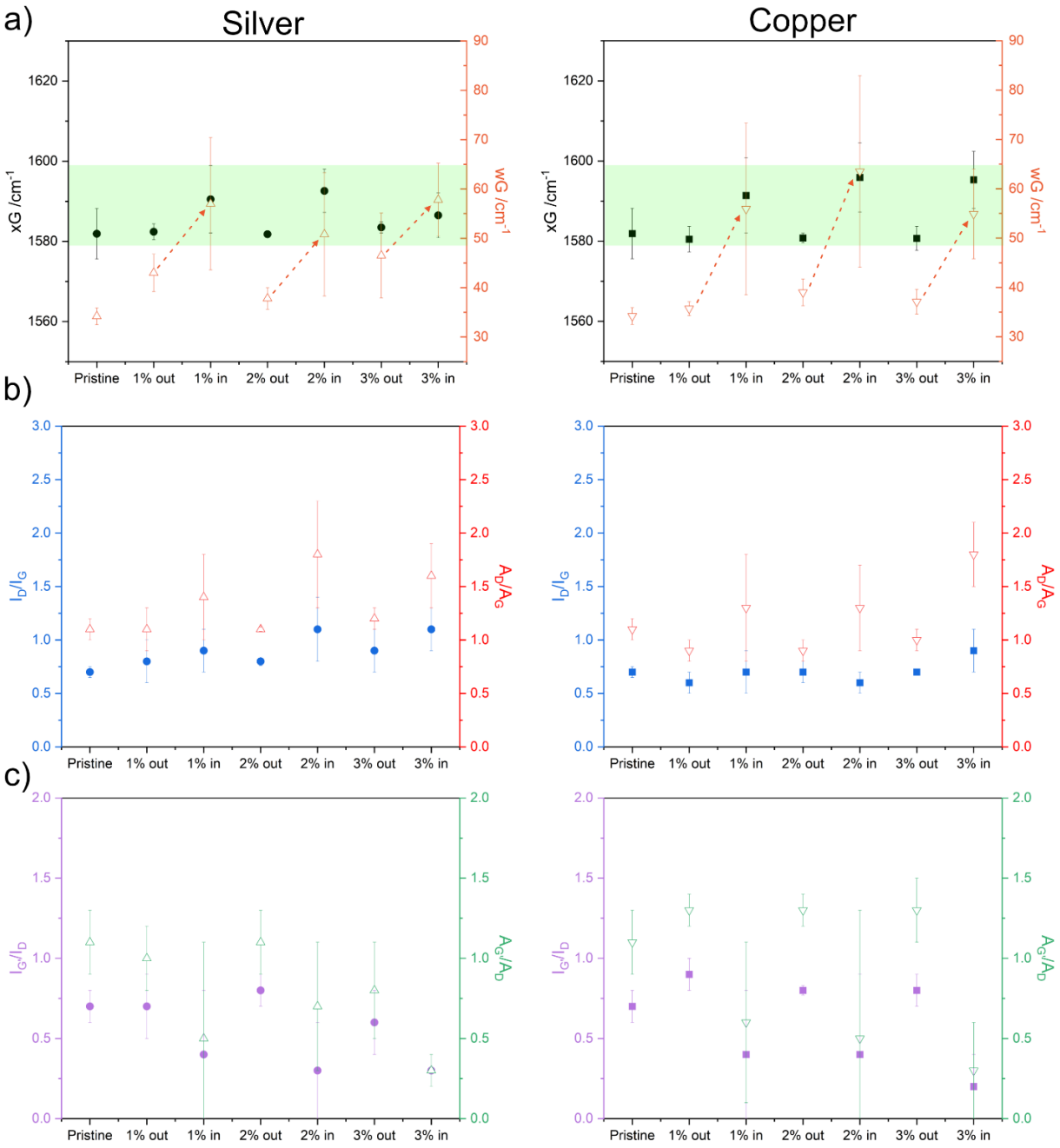

Figure 4. a) Raman shift and FWHM of the G-band (xG and wG), **b)** defect and **c)** purity indeces of pristine CNT, CNT outside, and CNT inside the electro-erosion crater of silver (left) and copper (right) MMC. The shaded region in **a)** highlights the theoretical position of the G-band of disordeded graphite, as reported by Ferrari and Robertson [30], whereas the dashed arrow emphasized the widening of the G-band after electro-erosion tests. Note: the intensity and integral intensity defect ratio inside the crater in Ag 3% are identical (i.e., 0.3 ± 0.1).

the amorphization trajectory. Moreover, comparing the Raman shift of the G-band (xG) measured outside of the electro-erosion craters with those of the pristine CNT demonstrates that the manufacturing process of the MMC does not affect the sp^2 graphitic structure of the CNT.

The full width at half maximum (FWHM) of the G-band is of interest since the width of this band provides insight into the structural integrity of the CNT. Raman spectroscopy is a harmonic oscillator system based on the inelastic scattering of photons (anti-Stokes scattering), thus considering the graphitic structure of the CNT as a

harmonic resonator, structural defects (such as a missing carbon atom) will affect the oscillation half-time of the graphitic structure. Therefore, a narrower G-band (low energy and longer oscillation times according to the uncertainty principle) indicates higher crystallinity of the CNT [45]. Conversely, a wider G-band (higher energy and shorter oscillation times) suggests that increased crystallographic defects are present in the CNT's structure. The FWHM of the G-band (shown in **Figure 4a**) suggests increased defects in the CNT after electro-erosion tests, evidenced by the broadening of the peak, which could be caused by the adsorption of oxygen atoms during electro-erosion tests.

Both defect ratios (i.e., intensity and integral intensity) for the pristine CNT and all MMC are shown in **Figure 4b**. As previously suggested by the position of the G-band, the defect ratios confirm that the sintering process did not significantly affect the structural integrity of the CNT, since all values are very close to that of the pristine state. Interestingly, the CNT that were exposed to the electrical spark (inside the crater) show marginal increase in their I_D/I_G indices, being the highest values observed for the silver-based MMC. The most likely degradation processes undergone by the CNT are amorphization and oxidation, since the energy input is meaningful [46]. Since the experiments were carried out under uncontrolled environment (i.e., atmospheric conditions), oxygen is readily available in the vicinity of the molten pool. This adsorption of oxygen by the CNT in the silver-based MMC is likely the cause of the lighter contrast of superficial CNT in the SEM micrographs from **Figure 2a** and **b**. As opposed to silver, copper is able to intake the available oxygen, which might explain why the I_D/I_G ratio does not significantly increase for the copper MMC, whereas for the silver, it is higher than the pristine state. This hypothesis is further verified by the appearance of a peak in the Raman spectra acquired inside the crater for the copper MMC (highlighted by the orange arrow in **Supplementary Figure 12**). Based on the Raman shift of this peak (approximately 620-630 cm^{-1}), it is likely that CuO and/or Cu_2O is formed inside the crater [47,48]. EDS maps focusing on large CNT clusters both inside and outside of the crater were acquired for both metallic matrices, however, no discernible difference was observed in the oxidative state of the CNT or surrounding matrix – SEM micrograph and EDS map of CNT clusters inside and outside of the electro-erosion crater in the Ag 3% and Cu 3% samples are shown in **Supplementary Figure 13** and **Supplementary Figure 14**, respectively.

The integral intensity defect ratio encompasses all types of defects, whereas the intensity defect ratio does not. Consequently, the A_D/A_G in each measurement spot are higher than the I_D/I_G. Comparing the integral intensity defect ratio of the pristine CNT with those of the CNT clusters outside of the electro-erosion crater shows that the sintering process does not cause any previously unaccounted type of damage onto the structure of the CNT, since the same trend as with the intensity defect ratio is observed.

Focusing on the defect state of the CNT outside and inside the craters, the A_D/A_G shows similar damage after arcing irrespective of the metallic matrix. However, this is not the case for the I_D/I_G, where the ratio increases in silver matrices and remains constant in copper matrices. As previously discussed, the constant intensity defect ratio observed for copper matrices is due to the oxidation of the matrix rather than the reinforcement phase. Therefore, I_D/I_G is more sensitive to oxidation than A_D/A_G.

The purity of the multi-walled CNT can be assessed by determining the intensity and integral intensity of the G'- and D-bands ($I_{G'}/I_D$ and $A_{G'}/A_D$), as proposed by DiLeo et al. [44,49,50]. The purity indices for pristine CNT and CNT clusters outside and inside the electro-erosion crater are shown in **Figure 4c**. The purity indices in the silver-based MMC do not show any noteworthy difference between the pristine state and the state outside the crater. In the copper-based MMC, on the other hand, a marginal improvement in the purity indices is observed. Therefore, the purity indices demonstrate that the manufacturing process does not affect the purity of the reinforcement phase. On the other hand, the purity drops markedly within the craters for all the studied composites due to the arc's energy input.

Conclusions

The electro-erosion crater resulting from a single break operation under 200 W ohmic load was thoroughly characterized, comparing the resulting crater of standard switching materials and pure metals with those of CNT-reinforced silver and copper MMC. The area and displaced volume of the proposed MMC does not significantly differ from the values observed for the reference material. Silver and copper MMC with up to 2 wt.% CNT exhibit craters with similar dimensions and displaced material volumes, whereas MMC containing 3 wt.% CNT resulted in larger electro-erosion craters and higher amounts of displaced material volumes. This, in turn, affected the roughness and load-bearing capacity of the MMC. CNT content below 3 wt.% resulted in roughness values similar to that of the reference materials, whereas the samples with 3 wt.% CNT exhibited higher roughness and a higher proportion of material above the core load-bearing volume – particularly in the Ag 3% sample.

The dimensionality of the crater in the reinforced samples tends to be more circular, highlighting the lower mobility of the arc. The CNT content also promotes a more uniform transfer of gold from the counter electrode, likely as a result of a wider arc on account of the heterogeneous distribution of the reinforcement phase. After the arc was extinguished, CNT agglomerates within the craters are larger than those outside – particularly in copper matrices. This is due to the tendency towards CNT re-agglomerations upon melting the matrix, as well as due to the difference in matrix and reinforcement phase density.

Finite element method thermal simulations proved that the temperatures reached for the copper electrode were not sufficient to evaporate the metallic matrix, as well as being far below the sublimation temperature of CNT. The sintered silver samples, on the other hand, did surpass the boiling temperature of the matrix, thus leading to material evaporation. Irrespective of CNT content, the dimensions of the melting front remained relatively constant throughout all samples. Moreover, CNT contents above 1 wt.% significantly reduced the duration of the molten pool to approximately 50% the duration of the unreinforced samples.

Raman spectroscopy revealed that the MMC manufacturing process did not affect the structural integrity nor the purity of the reinforcement phase. Although the arc's energy input did affect crystallinity and purity of the CNT, the damage sustained by the CNT was not enough to degrade the CNT into amorphous carbon.

Therefore, the use of CNT as reinforcement phase in silver- and copper-based MMC shows promising results for switching applications. The incorporation of the reinforcement phase results in a material that performs similarly to reference and standard switching materials. Nonetheless, the proposed MMC require fewer amounts of metallic powders, thereby reducing material demand, weight, and costs. These MMC can be manufactured in a straightforward, easily scalable, cost-effective, and standard method, with the capability of producing near-net-shape electrodes.

Based on the findings from this work, CNT concentrations of up to 2 wt.% result in optimal switching performance in silver- and copper-based MMC. Increasing the concentration of the reinforcement phase impacts the roughness of the crater and the displaced material volume after a single break operation; thus, potentially accelerating the electrode's erosion – as previous studies have reported for graphite-containing electrodes. This was further ratified by the thermal simulations, where silver-based MMC exhibited a larger boiling front despite the constant melting front and shorter duration of the molten pool.

ACKNOWLEDGEMENTS

B. A. wishes to acknowledge the support from the German Academic Exchange Service (DAAD) and the Roberto Rocca Education Program (RREP). F. A. D. acknowledges the financial support provided by the government of Upper Austria (Wi-2021-305611/21-Au / NaKuRe). The authors gratefully acknowledge funding in the Mat-Innovat ("Kreislauffähige Materialsysteme für in-novatives Hochleistungswerkstoffe") project, supported by the State of Saarland from the Euro-pean Regional Development Fund (Europäischen Fonds für Regionale Entwicklung, EFRE). Funding for the PFIB/SEM instrument by German Research Foundation is greatly acknowledged (INST 256/510-1 FUGG).

AUTHOR CONTRIBUTIONS

B.A.: conceptualization, methodology, validation, formal analysis, investigations, data curation, writing – original draft, visualization; F.D.: investigation, writing – review & editing; F.M.: resources, project administration, funding acquisition; S.S.: conceptualization, methodology, formal analysis, writing – review & editing, supervision, project administration, funding acquisition.

COMPETING INTERESTS

The authors declare no competing interests.

DATA AVAILABILITY

The data that supports the findings in this study are available from the corresponding author upon reasonable request.

REFERENCES

[1] P.G. Slade, Electrical Contacts, Second Ed., CRC Press, Boca Raton, 2014. https://doi.org/10.1201/b15640.

[2] N. Ben Jemaa, L. Nedelec, S. Benhenda, J. Neveu, Anodic and cathodic erosion of Ag, Ag alloys and Ag-MeO contact materials in energy range below 10 joules, in: Electrical Contacts - 1996. Proceedings of the Forty-Second IEEE Holm Conference on Electrical Contacts. Joint with the 18th International Conference on Electrical Contacts, IEEE, 1996: pp. 70–74. https://doi.org/10.1109/HOLM.1996.557181.

[3] R. Holm, Electric Contacts, 4th Ed., Springer Berlin Heidelberg, Berlin, Heidelberg, Heidelberg, 1967. https://doi.org/10.1007/978-3-662-06688-1.

[4] N. Ben Jemaa, L. Morin, S. Benhenda, L. Nedelec, Anodic to cathodic arc transition according to break arc lengthening, IEEE Transactions on Components, Packaging, and Manufacturing Technology: Part A 21 (2005) 599–603. https://doi.org/10.1109/tcpma.1998.740053.

[5] J. Swingler, J.W. McBride, The net zero erosion phenomena on opening switching contacts with AC loading, in: Electrical Contacts - 1997 Proceedings of the Forty-Third IEEE Holm Conference on Electrical Contacts, IEEE, 1997: pp. 238–245. https://doi.org/10.1109/HOLM.1997.638048.

[6] M. Braunovic, V. V. Konchits, N.K. Myshkin, Electrical Contacts, 1st ed., CRC Press, Boca Raton, FL, USA, 2017. https://doi.org/10.1201/9780849391088.

[7] V. Behrens, Th. Honig, A. Kraus, E. Mahle, R. Michal, K.E. Saeger, Test results of different silver/graphite contact materials in regard to applications in circuit breakers, in: Electrical Contacts - 1995. Proceedings of the Forty-First IEEE Holm Conference on Electrical Contacts, IEEE, 1995: pp. 393–397. https://doi.org/10.1109/HOLM.1995.482896.

[8] R. Michal, K.E. Saegar, Metallurgical aspects of silver-based contact materials for air-break switching devices for power engineering, IEEE Transactions on Components, Hybrids, and Manufacturing Technology 12 (1989) 71–81. https://doi.org/10.1109/33.19015.

[9] P. Wingert, R. Bevington, G. Horn, The effect of graphite additions on the performance of silver-nickel contacts, in: Thirty-Sixth IEEE Conference on Electrical Contacts, and the Fifteenth International Conference on Electrical Contacts, IEEE, 1990: pp. 524–529. https://doi.org/10.1109/HOLM.1990.113053.

[10] E. Shobert, Carbon, Graphite, and Contacts, IEEE Transactions on Parts, Hybrids, and Packaging 12 (1976) 62–74. https://doi.org/10.1109/TPHP.1976.1135101.

[11] P. Jiang, F. Li, Y. Wang, Effect of different types of carbon on microstructure and arcing behavior of Ag/C contact materials, IEEE Transactions on Components and Packaging Technologies 29 (2006) 420–423. https://doi.org/10.1109/TCAPT.2006.875873.

[12] P.C. Wingert, The effects of interrupting elevated currents on the erosion and structure of silver-graphite, in: Electrical Contacts - 1996. Proceedings of the Forty-Second IEEE Holm Conference on Electrical Contacts. Joint with the 18th International Conference on Electrical Contacts, IEEE, 1996: pp. 60–69. https://doi.org/10.1109/HOLM.1996.557180.

[13] W. Xie, G. Wu, Z. Yang, P. She, H. Wang, H. Zuo, W. Wei, G. Gao, C. Tu, Study on the erosion characteristics of copper-carbon electrode pairs by DC air arc, High Voltage 6 (2021) 674–683. https://doi.org/10.1049/hve2.12124.

[14] B. Alderete, C. Schäfer, U.P. Nayak, F. Mücklich, S. Suarez, Modifying the Characteristics of the Electrical Arc Generated during Hot Switching by Reinforcing Silver and Copper Matrices with Carbon Nanotubes, Journal of Composites Science 8 (2024). https://doi.org/10.3390/jcs8070285.

[15] B. Alderete, S. Suarez, F. Mücklich, On the Production & Tribo-Electrical Characterization of Carbon Nanotube-Reinforced Ag & Cu Metal Matrix Composites, in: 2023 IEEE 68th Holm Conference on Electrical Contacts (HOLM), IEEE, 2023: pp. 1–8. https://doi.org/10.1109/HOLM56075.2023.10352236.

[16] B. Alderete, F. Mücklich, S. Suarez, Electrical Characterization of Carbon Nanotube Reinforced Silver and Copper Composites for Switching Contacts, Journal of Composites Science 7 (2023) 284. https://doi.org/10.3390/jcs7070284.

[17] R. Puyol, S. Suarez, A contact resistance measurement setup for the study of novel contacts, in: 2017 IEEE URUCON, IEEE, 2017: pp. 1–4. https://doi.org/10.1109/URUCON.2017.8171881.

[18] S. Suarez, R. Puyol, C. Schafer, F. Mucklich, Carbon Nanotube-reinforced Metal Matrix Composites as Novel Electrodes for Low-voltage Switching Applications: A Surface Degradation Analysis, in: 2019 IEEE Holm Conference on Electrical Contacts, IEEE, 2019: pp. 135–141. https://doi.org/10.1109/HOLM.2019.8923921.

[19] PDE Solutions Inc., FlexPDE, (2023). https://www.pdesolutions.com/flexpde-7-support/ (accessed June 27, 2024).

[20] F. Soldera, A. Lasagni, F. Mücklich, T. Kaiser, K. Hrastnik, Determination of the cathode erosion and temperature for the phases of high voltage discharges using FEM simulations, Comput Mater Sci 32 (2005) 123–139. https://doi.org/10.1016/j.commatsci.2004.06.004.

[21] K.C. Mills, B.J. Monaghan, B.J. Keene, Thermal conductivities of molten metals: Part 1 Pure metals, International Materials Reviews 41 (1996) 209–242. https://doi.org/10.1179/imr.1996.41.6.209.

[22] M.J. Laubitz, Transport Properties of Pure Metals at High Temperatures: I. Copper, Can J Phys 45 (1967) 3677–3696. https://doi.org/10.1139/p67-309.

[23] M.J. Laubitz, Transport properties of pure metals at high temperatures. II. Silver and gold, Can J Phys 47 (1969) 2633–2644. https://doi.org/10.1139/p69-322.

[24] A.D. Kirshenbaum, J.A. Cahill, A.V. Grosse, The density of liquid silver from its melting point to its normal boiling point 2450°K, Journal of Inorganic and Nuclear Chemistry 24 (1962) 333–336. https://doi.org/10.1016/0022-1902(62)80188-2.

[25] J.A. Cahill, A.D. Kirshenbaum, The Density of Liquid Copper from its Melting Point (1356°K) to 2500°K and an Estimate of its Critical Constants, J Phys Chem 66 (1962) 1080–1082. https://doi.org/10.1021/j100812a027.

[26] T.W. Chapman, The heat capacity of liquid metals, Materials Science and Engineering 1 (1966) 65–69. https://doi.org/10.1016/0025-5416(66)90012-7.

[27] M. Wang, N. Pan, Predictions of effective physical properties of complex multiphase materials, Materials Science and Engineering: R: Reports 63 (2008) 1–30. https://doi.org/10.1016/j.mser.2008.07.001.

[28] T. Laetsch, R. Downs, Software for Identification and Refinement of Cell Parameters from Powder Diffraction Data of Minerals Using the RRUFF Project and American Mineralogist Crystal Structure Databases, in: Abstracts from the 19th General Meeting of the International Mineralogical Association, Kobe, Japan, 2006. https://rruff.info/about/about_download.php (accessed August 6, 2024).

[29] T. MacLucas, P. Grützmacher, S. Husmann, J. Schmauch, S. Keskin, S. Suarez, V. Presser, C. Gachot, F. Mücklich, Degradation analysis of tribologically loaded carbon nanotubes and carbon onions, Npj Mater Degrad 7 (2023). https://doi.org/10.1038/s41529-023-00346-5.

[30] A.C. Ferrari, J. Robertson, Interpretation of Raman spectra of disordered and amorphous carbon, Phys Rev B Condens Matter Mater Phys 61 (1999) 14095–14107. https://doi.org/10.1103/PhysRevB.61.14095.

[31] K.H. Zum Gahr, Modelling of two-body abrasive wear, Wear 124 (1988) 87–103. https://doi.org/10.1016/0043-1648(88)90236-0.

[32] K.H. Zum Gahr, Formation of wear debris by the abrasion of ductile metals, Wear 74 (1981) 353–373. https://doi.org/10.1016/0043-1648(81)90173-3.

[33] L.A. Franco, A. Sinatora, Material removal factor (fab): A critical assessment of its role in theoretical and practical approaches to abrasive wear of ductile materials, Wear 382–383 (2017) 51–61. https://doi.org/10.1016/j.wear.2017.04.006.

[34] T.W. Chapman, The viscosity of liquid metals, AIChE Journal 12 (1966) 395–400. https://doi.org/10.1002/aic.690120233.

[35] E.S. Gadelmawla, M.M. Koura, T.M.A. Maksoud, I.M. Elewa, H.H. Soliman, Roughness parameters, J Mater Process Technol 123 (2002) 133–145. https://doi.org/10.1016/S0924-0136(02)00060-2.

[36] E.J. Abbott, F.A. Firestone, Specifying Surface Quality - A Method Based on Accurate Measurement and Comparison, Journal of Mechanical Engineering 55 (1933) 569–572.

[37] International Organization for Standardization (ISO), 13565 Geometrical Product Specifications (GPS) - Surface texture: Profile method; Surfaces having stratified functional properties, (1996).

[38] M.C. Salcedo, I.B. Coral, G.V. Ochoa, Characterization of surface topography with Abbott Firestone curve, Contemporary Engineering Sciences 11 (2018) 3397–3407. https://doi.org/10.12988/ces.2018.87319.

[39] M. Bigerelle, A. Iost, A numerical method to calculate the Abbott parameters: A wear application, Tribol Int 40 (2007) 1319–1334. https://doi.org/10.1016/j.triboint.2006.12.007.

[40] R. Laheurte, P. Darnis, N. Darbois, O. Cahuc, J. Neauport, Subsurface damage distribution characterization of ground surfaces using Abbott–Firestone curves, Opt Express 20 (2012) 13551. https://doi.org/10.1364/OE.20.013551.

[41] L. Reinert, M. Zeiger, S. Suárez, V. Presser, F. Mücklich, Dispersion analysis of carbon nanotubes, carbon onions, and nanodiamonds for their application as reinforcement phase in nickel metal matrix composites, RSC Adv 5 (2015) 95149–95159. https://doi.org/10.1039/C5RA14310A.

[42] X. Zhao, Y. Ando, L.-C. Qin, H. Kataura, Y. Maniwa, R. Saito, Characteristic Raman spectra of multiwalled carbon nanotubes, Physica B Condens Matter 323 (2002) 265–266. https://doi.org/10.1016/S0921-4526(02)00986-9.

[43] X. Zhao, Y. Ando, L.-C. Qin, H. Kataura, Y. Maniwa, R. Saito, Multiple splitting of G-band modes from individual multiwalled carbon nanotubes, Appl Phys Lett 81 (2002) 2550–2552. https://doi.org/10.1063/1.1502196.

[44] R.A. DiLeo, B.J. Landi, R.P. Raffaelle, Purity assessment of multiwalled carbon nanotubes by Raman spectroscopy, J Appl Phys 101 (2007) 064307/1–5. https://doi.org/10.1063/1.2712152.

[45] S. Suarez, F. Lasserre, O. Prat, F. Mücklich, Processing and interfacial reaction evaluation in MWCNT/Ni composites, Physica Status Solidi (a) 211 (2014) 1555–1561. https://doi.org/10.1002/pssa.201431018.

[46] B.M. Maciejewska, M. Jasiurkowska-Delaporte, A.I. Vasylenko, K.K. Kozioł, S. Jurga, Experimental and theoretical studies on the mechanism for chemical oxidation of multiwalled carbon nanotubes, RSC Adv. 4 (2014) 28826–28831. https://doi.org/10.1039/C4RA03881A.

[47] RRUFF Project, Tenorite R120076 - Raman Spectrum, (n.d.). https://rruff.info/tenorite/names/asc/R120076 (accessed May 30, 2024).

[48] RRUFF Project, Cuprite R140763 - Raman Spectrum, (n.d.). https://rruff.info/chem=Cu/chemistry/asc/display=default/R140763 (accessed May 30, 2024).

[49] R.A. DiLeo, B.J. Landi, R.P. Raffaelle, Application of the G'/D Raman Ratio for Purity Assessment of Multi-Walled Carbon Nanotubes, MRS Proceedings 1018 (2011) 1018-EE05-11. https://doi.org/10.1557/PROC-1018-EE05-11.

[50] J.H. Lehman, M. Terrones, E. Mansfield, K.E. Hurst, V. Meunier, Evaluating the characteristics of multiwall carbon nanotubes, Carbon N Y 49 (2011) 2581–2602. https://doi.org/10.1016/j.carbon.2011.03.028.

Supplementary Materials

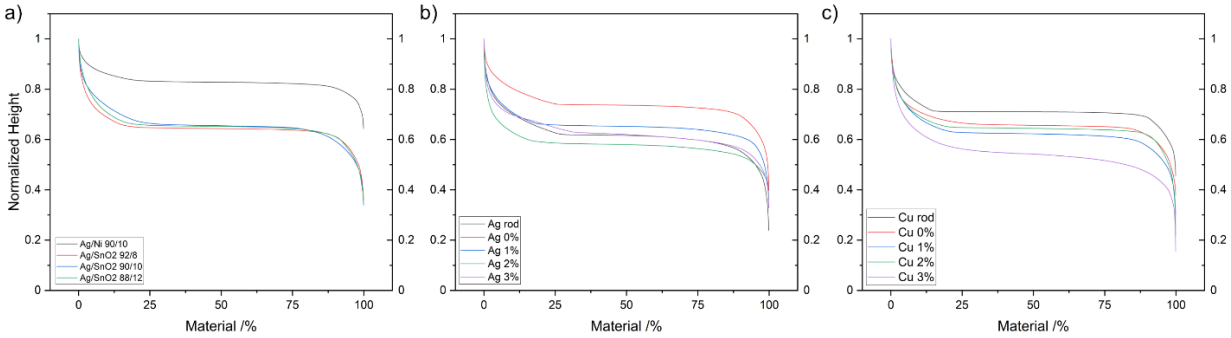

Supplementary Figure 1. Exemplary bearing area curves after arcing for **a)** the reference, **b)** the silver, and **c)** the copper samples.

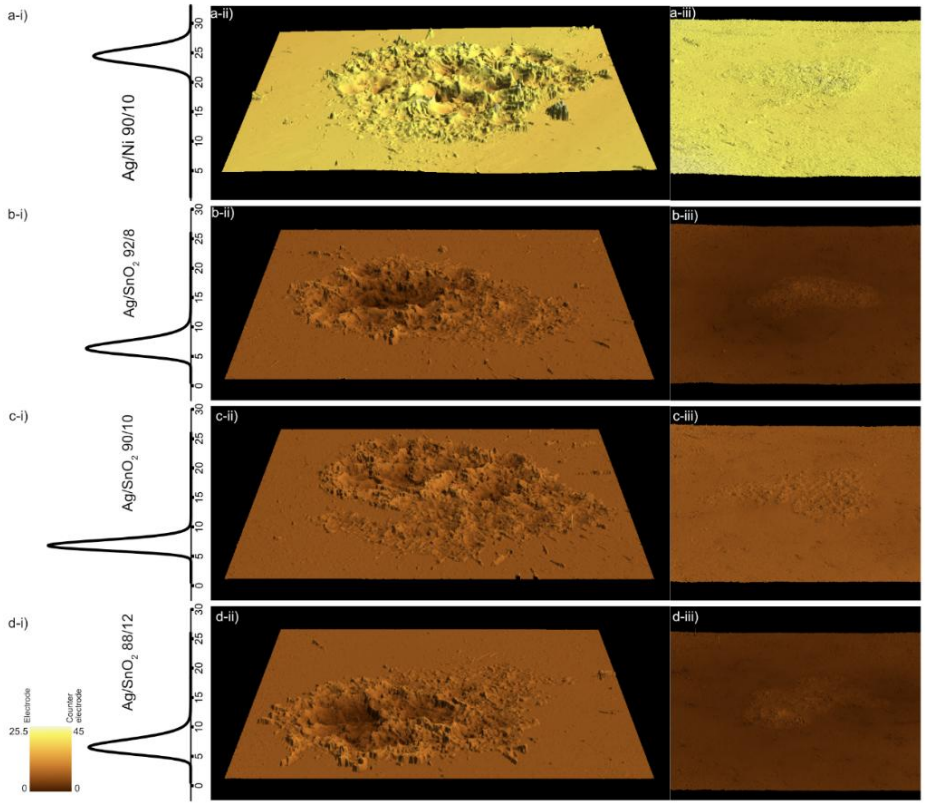

Supplementary Figure 2. i) Height distribution, **ii)** 3D scan of the sample, and **iii)** of the counter electrode for **a)** Ag/Ni 90/10, **b)** Ag/SnO_2 92/8, **c)** Ag/SnO_2 90/10, and **d)** Ag/SnO_2 88/12.

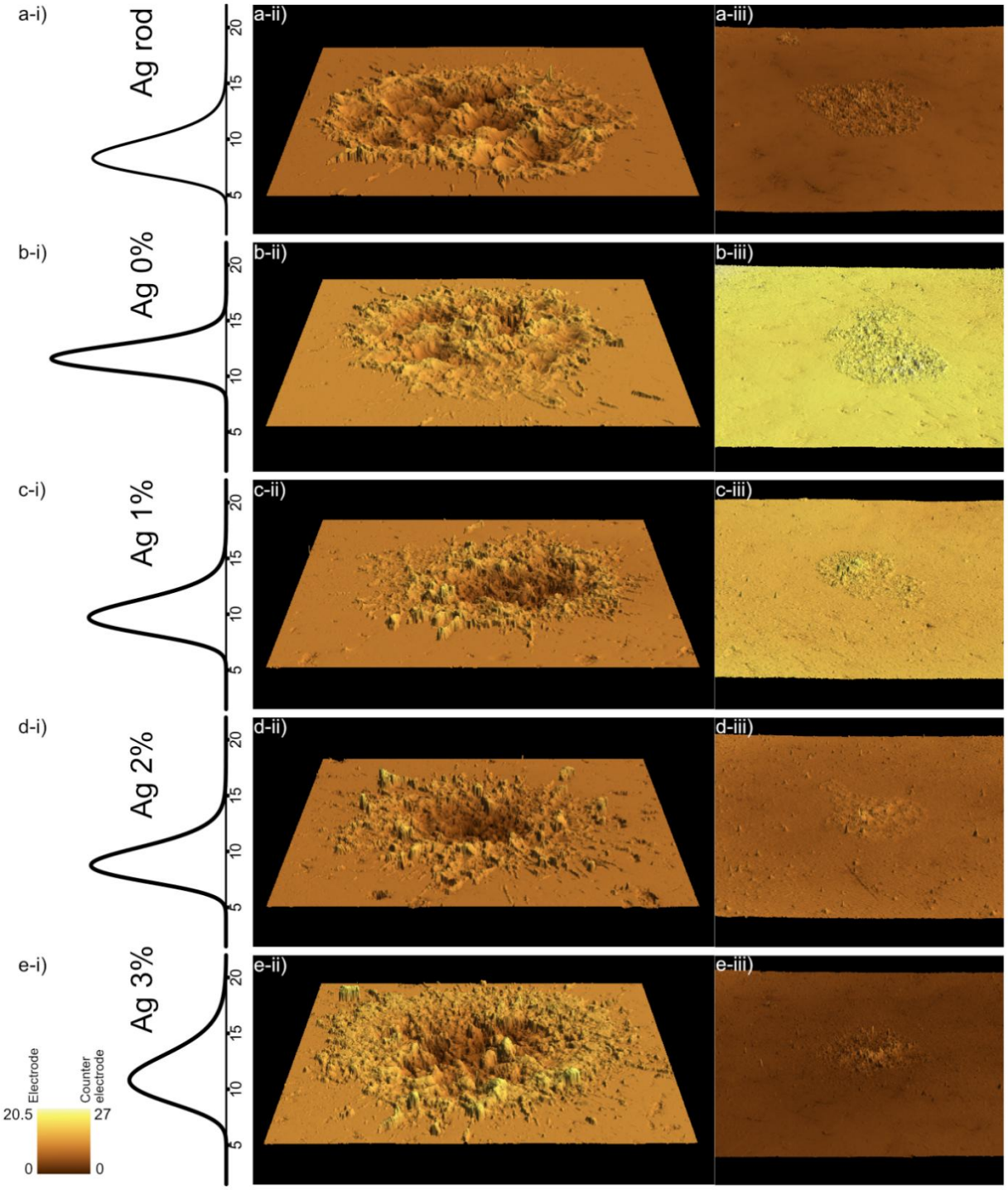

Supplementary Figure 3. i) Height distribution, **ii)** 3D scan of the sample, and **iii)** of the counter electrode for **a)** Ag rod, **b)** Ag 0%, **c)** Ag 1%, **d)** Ag 2%, and **e)** Ag 3%.

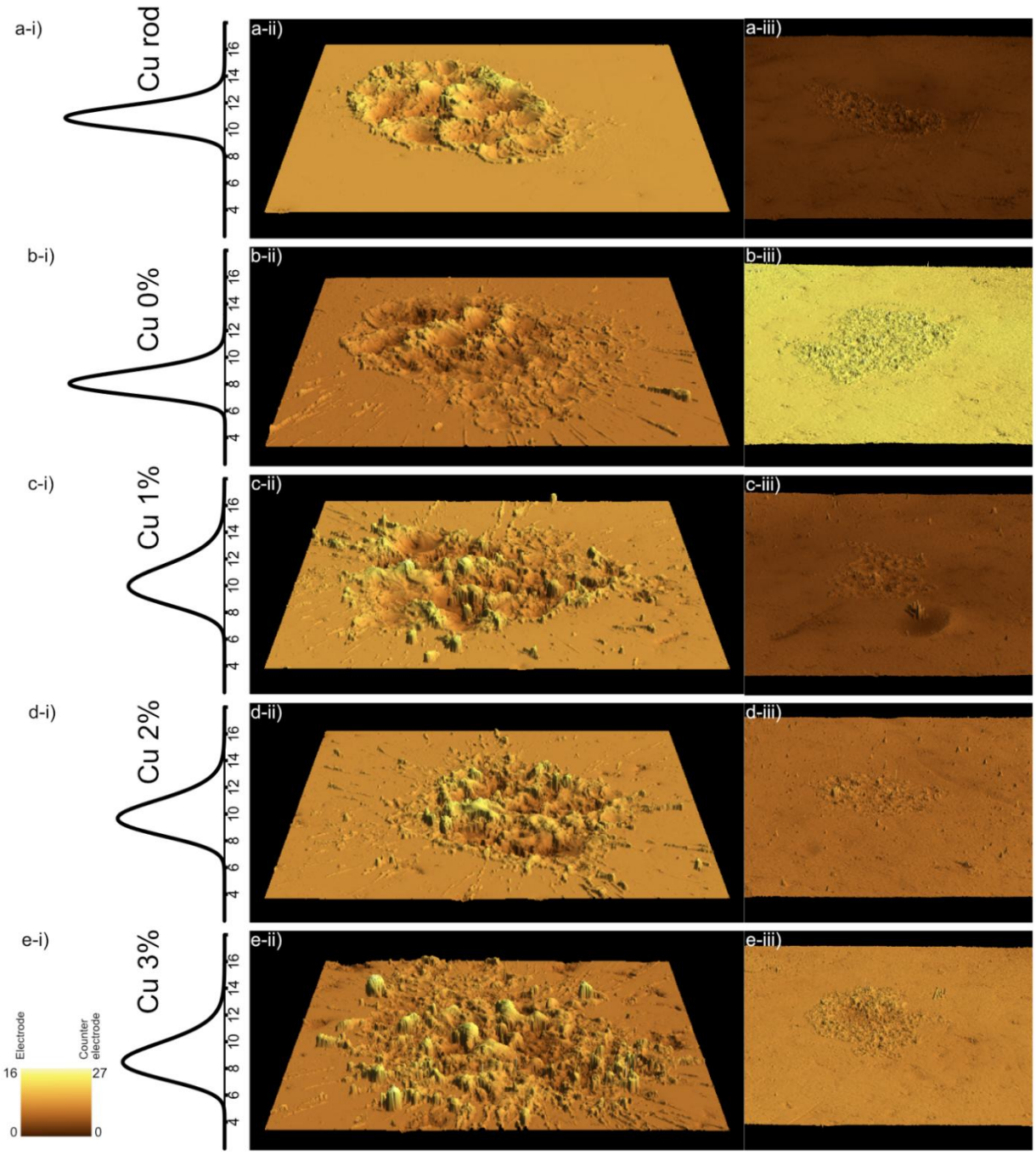

Supplementary Figure 4. i) Height distribution, **ii)** 3D scan of the sample, and **iii)** of the counter electrode for **a)** Cu rod, **b)** Cu 0%, **c)** Cu 1%, **d)** Cu 2%, and **e)** Cu 3%.

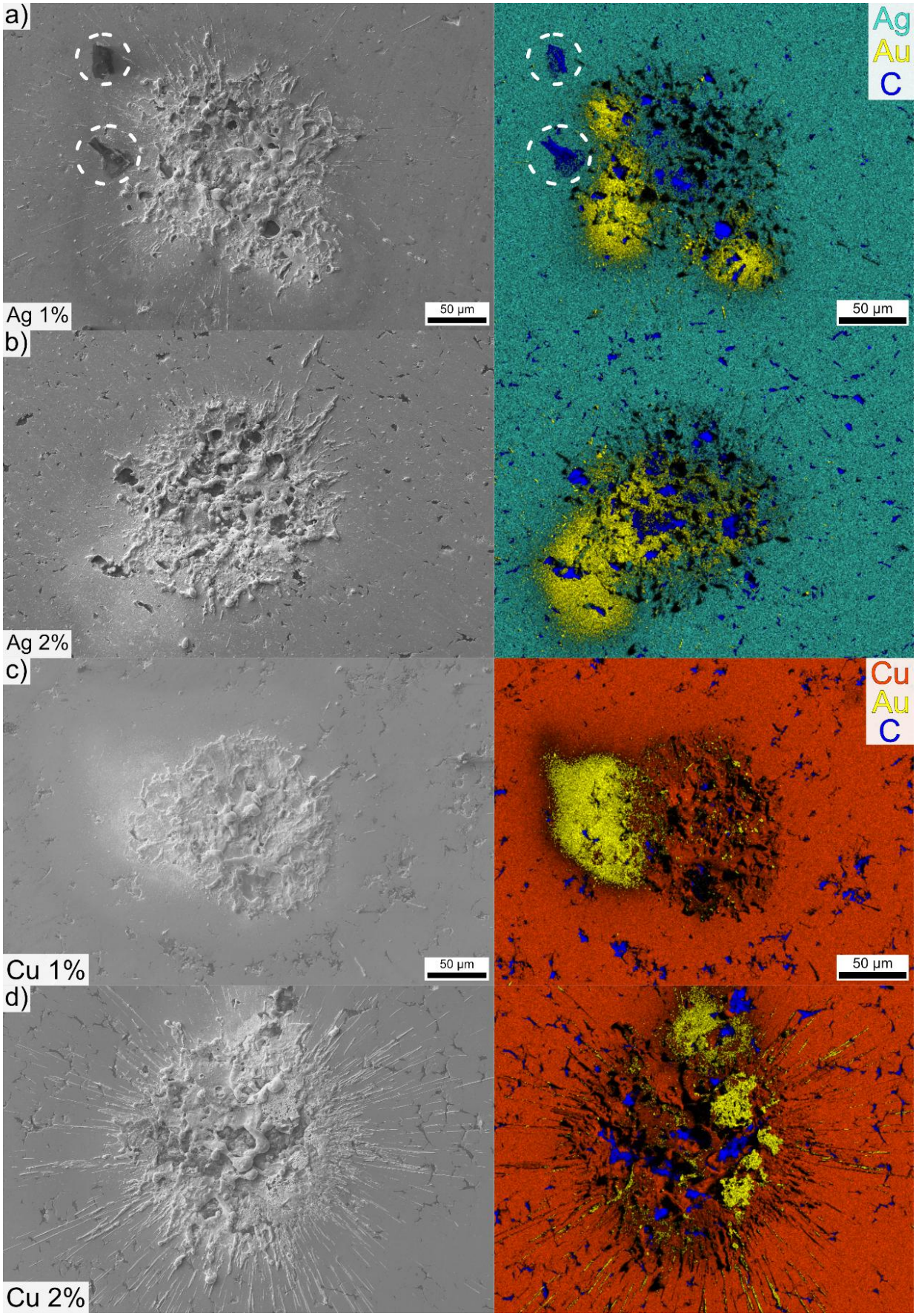

Supplementary Figure 5. SEM micrograph (left) and EDS map (right) of **a)** Ag 1%, **b)** Ag 2%, **c)** Cu 1%, and **d)** Cu 2%. The encircled carbon in the EDS map and corresponding region in the SEM micrograph in subfigure **a)** originates from external contaminants rather than from the reinforcement phase. Black regions within the crater in the EDS maps are areas where no signal was detected due to shadowing effects as a result of the crater's topography.

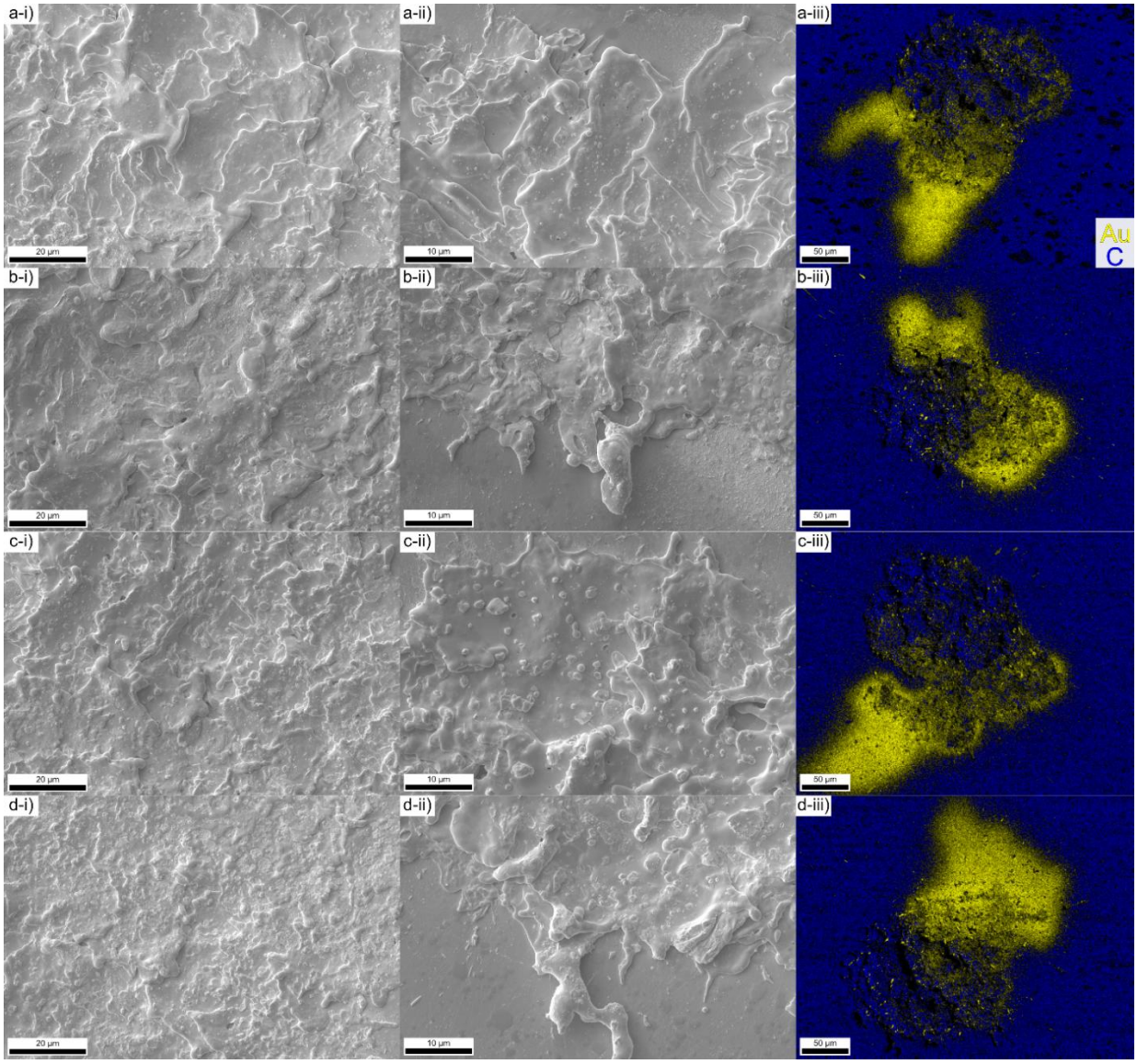

Supplementary Figure 6. i) Magnified SEM micrograph at the center and **ii)** on a feature of the crater. **iii)** EDS map overlay of gold (yellow) and carbon (blue) signals of **a)** Ag/Ni 90/10, **b)** Ag/SnO_2 92/8, **c)** Ag/SnO_2 90/10, and **d)** Ag/SnO_2 88/12.

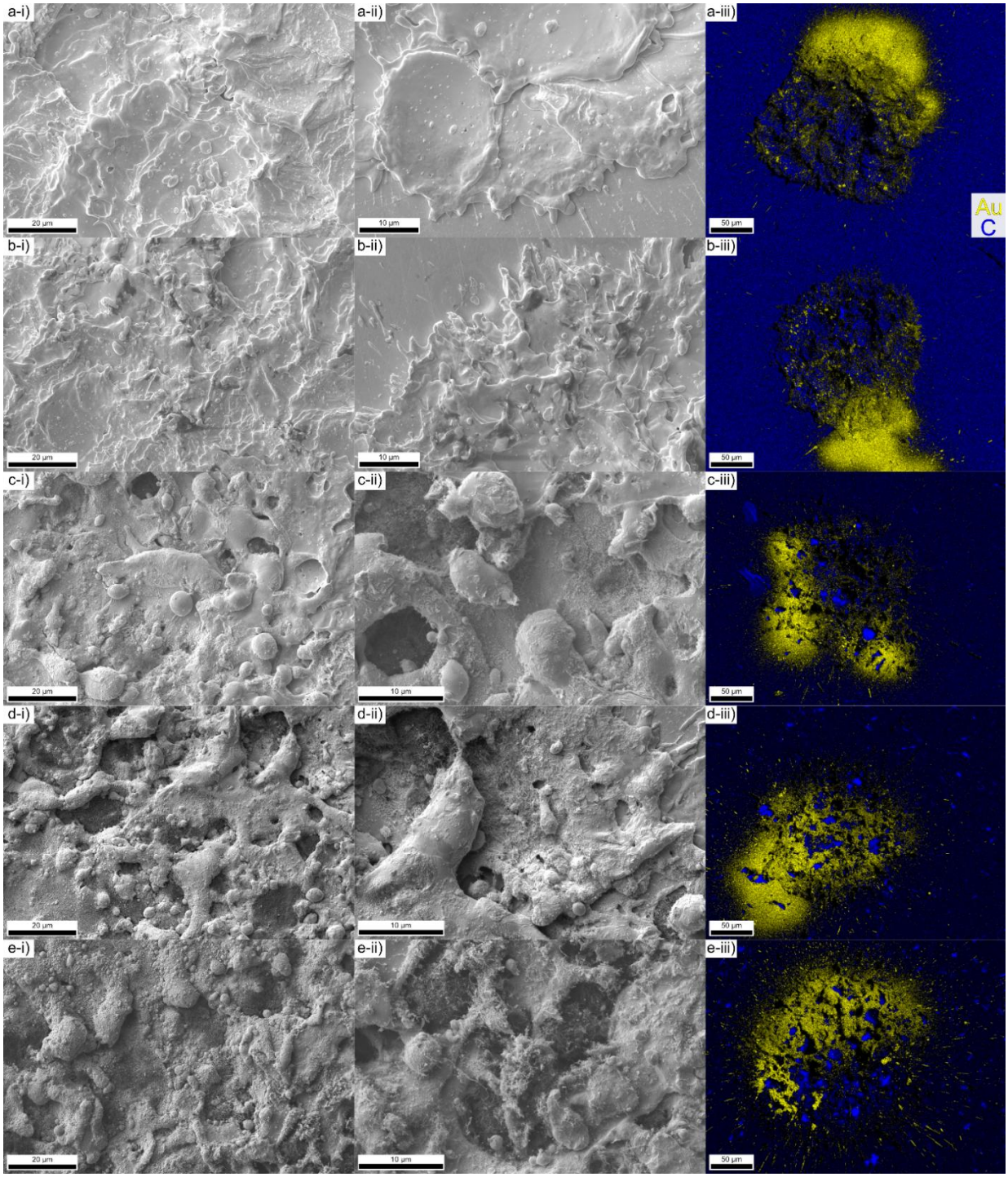

Supplementary Figure 7. i) Magnified SEM micrograph at the center and **ii)** on a feature of the crater. **iii)** EDS map overlay of gold (yellow) and carbon (blue) signals of **a)** Ag rod, **b)** Ag 0%, **c)** Ag 1%, **d)** Ag 2%, and **e)** Ag 3%.

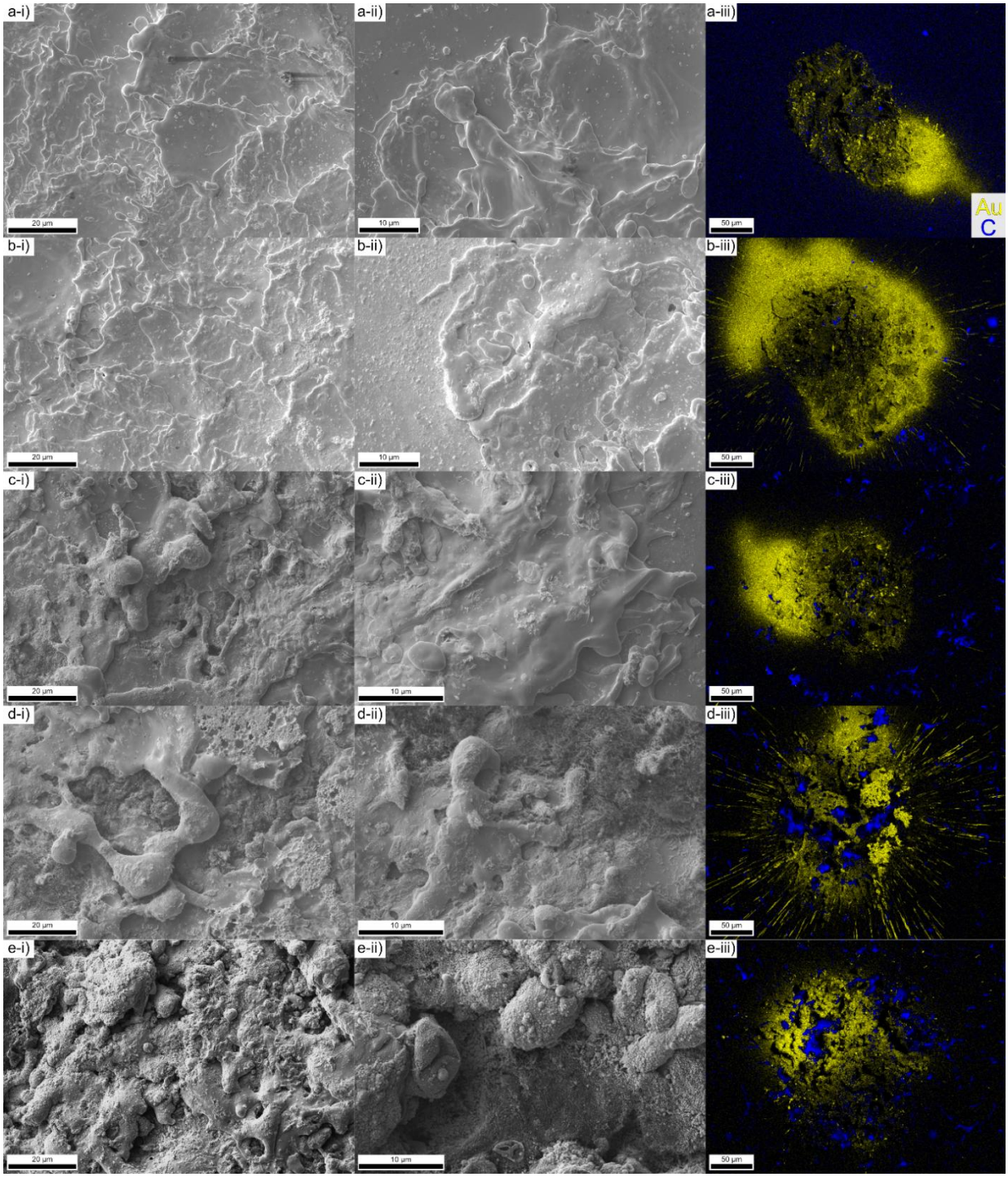

Supplementary Figure 8. i) Magnified SEM micrograph at the center and **ii)** on a feature of the crater. **iii)** EDS map overlay of gold (yellow) and carbon (blue) signals of **a)** Cu rod, **b)** Cu 0%, **c)** Cu 1%, **d)** Cu 2%, and **e)** Cu 3%.

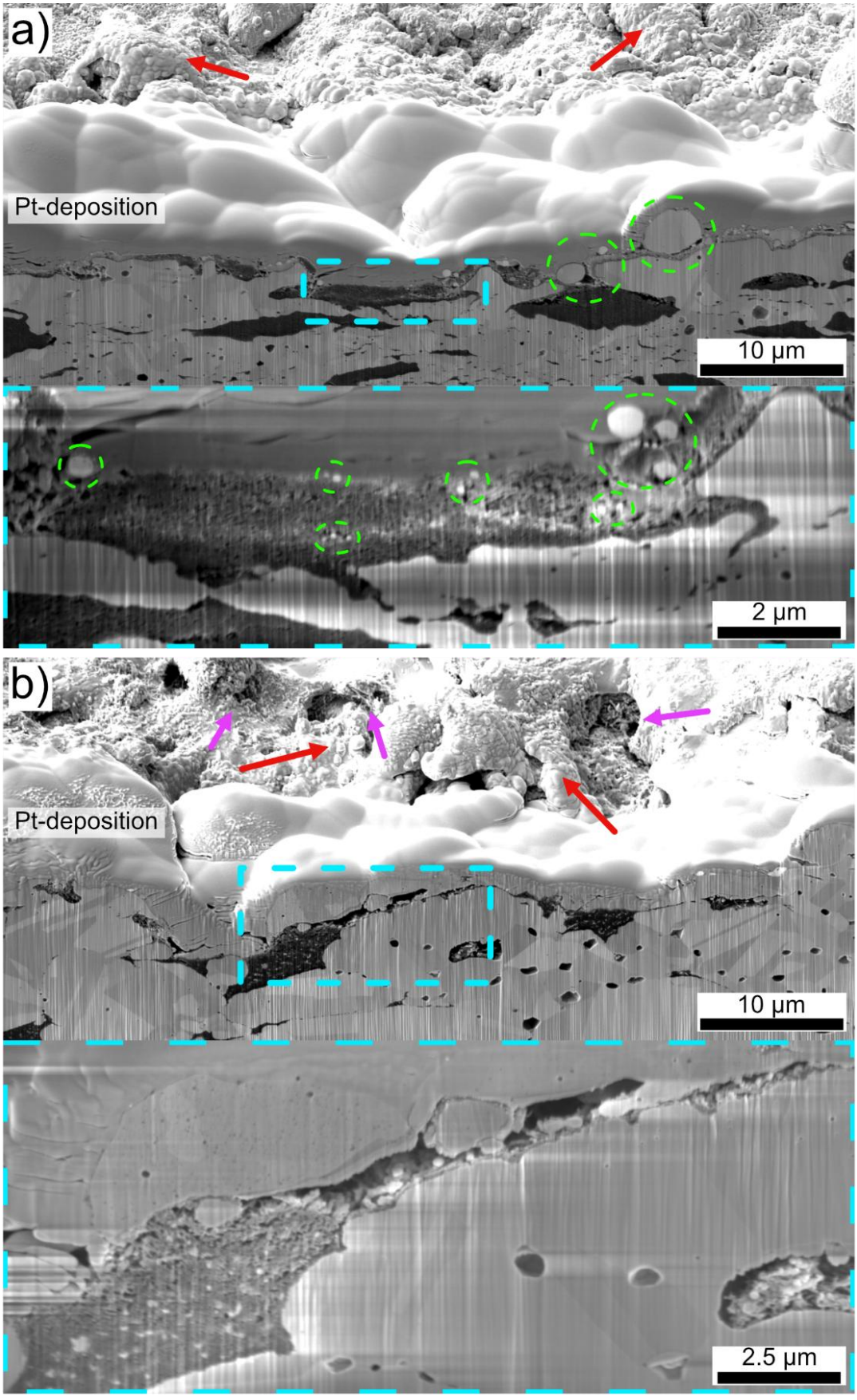

Supplementary Figure 9. Magnified view of the FIB cross section highlighting the condensation of metallic droplets on the reinforcement phase of **a)** Ag 2% and **b)** Cu 2%. The dashed cyan square indicates the magnified region of interest. The dashed green circles highlight the deposited metallic droplets on the CNT, whereas the red arrows emphasize the condensation of the droplets on the surface of the crater and the violet arrows indicate CNT on the surface of the crater.

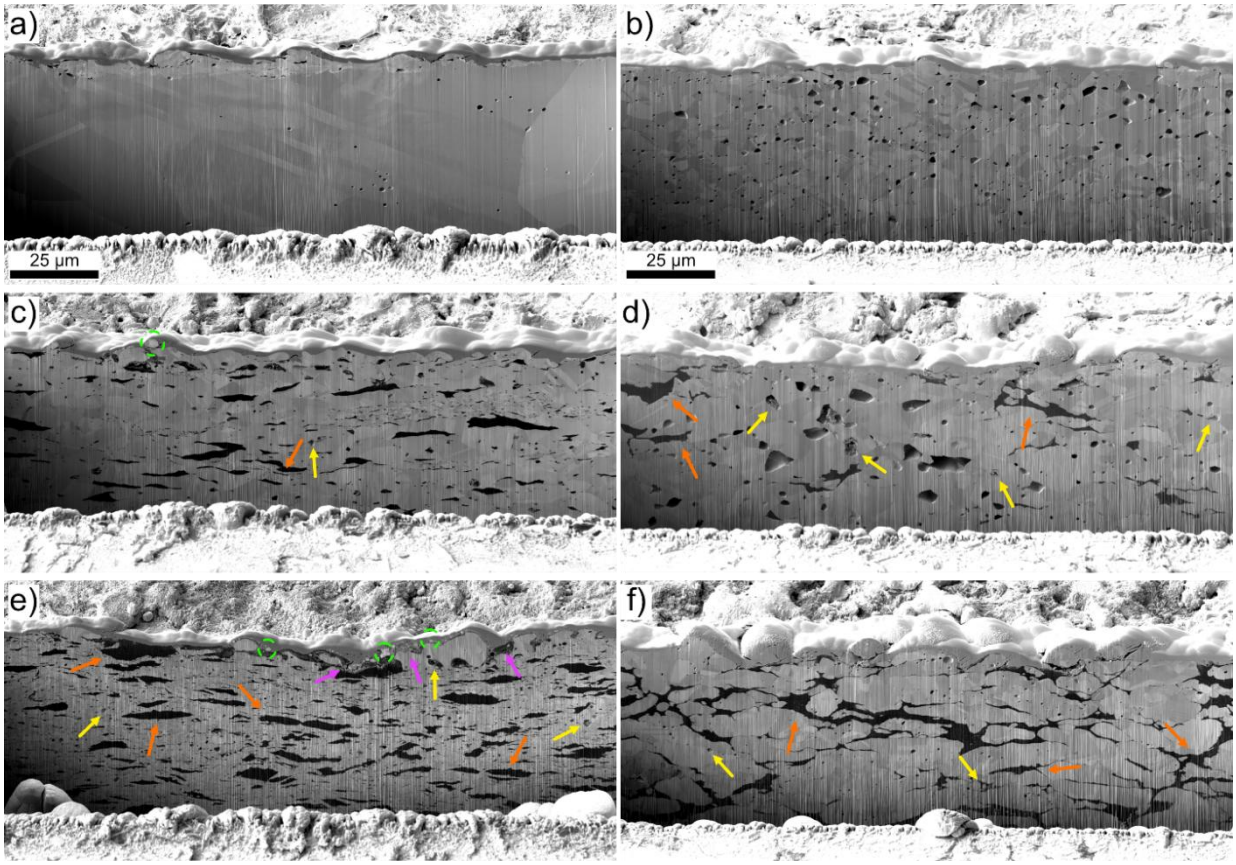

Supplementary Figure 10. Micrographs of FIB cross sections of **a)** Ag 0%, **b)** Cu 0%, **c)** Ag 1%, **d)** Cu 1%, **e)** Ag 3%, and **f)** Cu 3%. The violet arrows indicate carbon content on the surface of the crater, the orange arrows show unaffected CNT beneath the crater, and the yellow arrows point out voids within the MMC. The green dashed circles highlight metallic vapor re-deposition on the reinforcement phase.

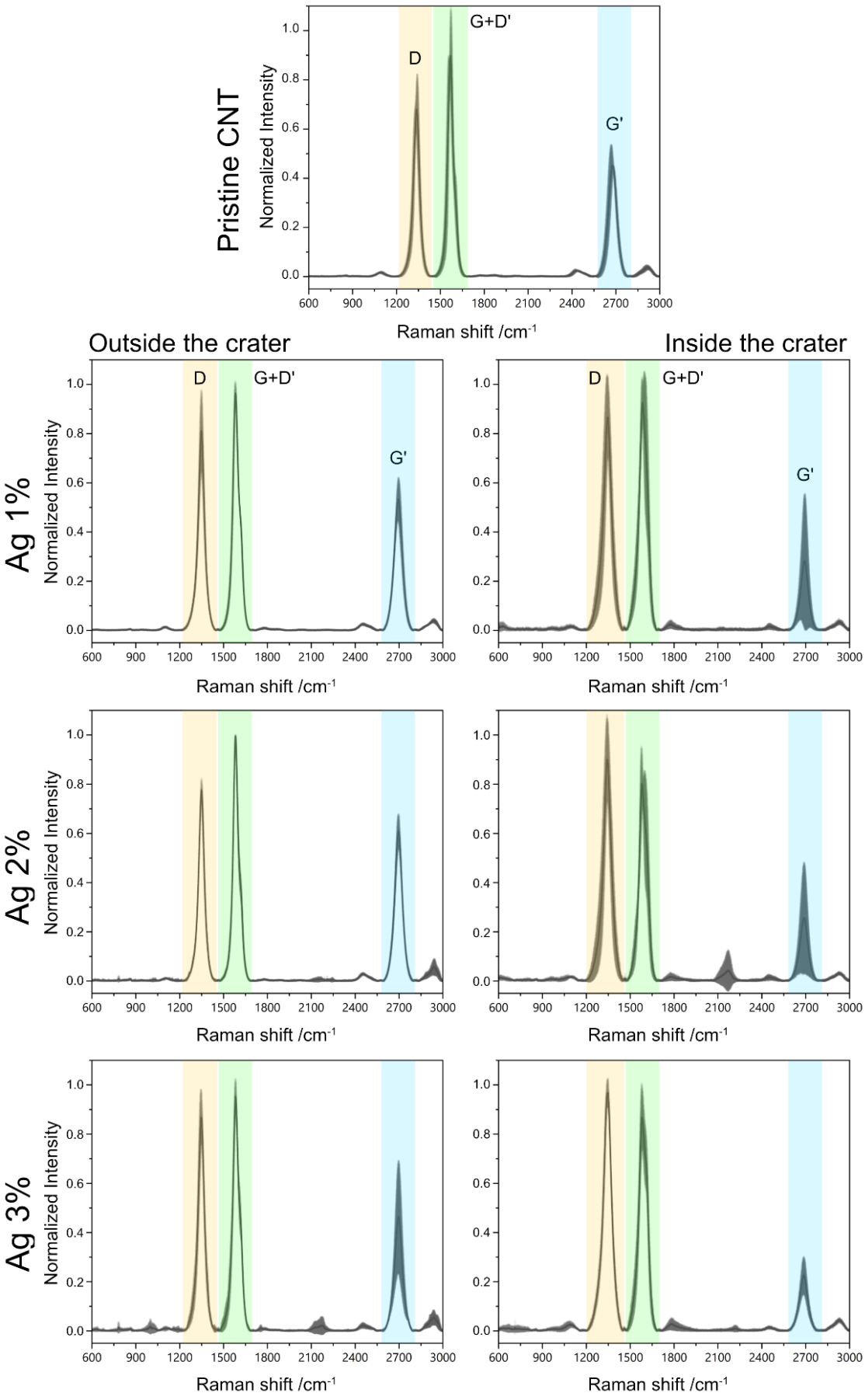

Supplementary Figure 11. Raman spectra of pristine CNT and silver-based MMC. The spectra on the left correspond to CNT clusters outside of the electro-erosion crater (i.e., unaffected by the electrical arc), whereas the spectra on the right correspond to CNT clusters inside of the electro-erosion crater.

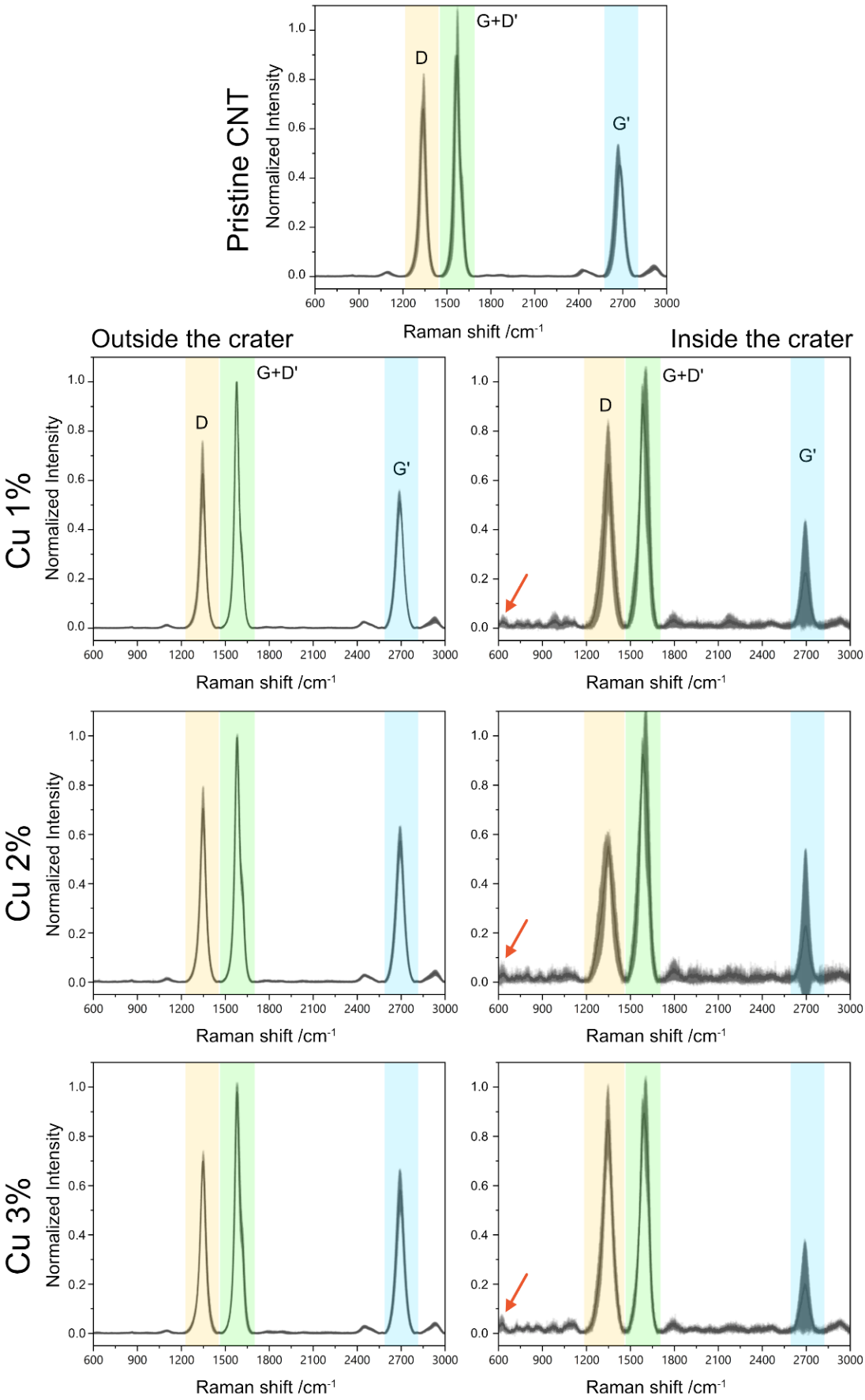

Supplementary Figure 12. Raman spectra of pristine CNT and copper-based MMC. The spectra on the left correspond to CNT clusters outside of the electro-erosion crater (i.e., unaffected by the electrical arc), whereas the spectra on the right correspond to CNT clusters inside of the electro-erosion crater. The arrow indicates the peak corresponding to possible copper oxides formed due to the electrical arc.

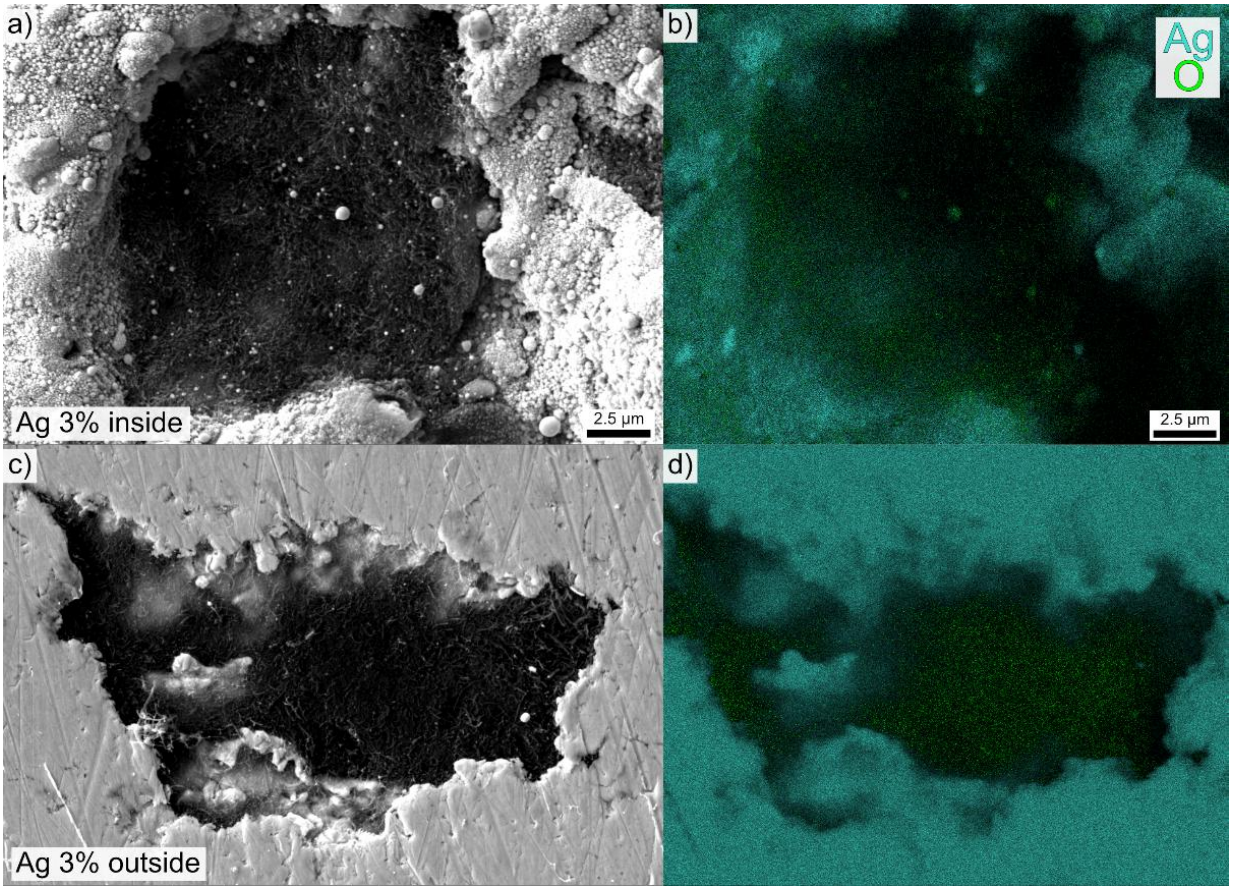

Supplementary Figure 13. a) SEM micrograph and **b)** EDS map of CNT clusters inside and **c)** and **d)** outside of the electro-erosion crater in the Ag 3% sample.

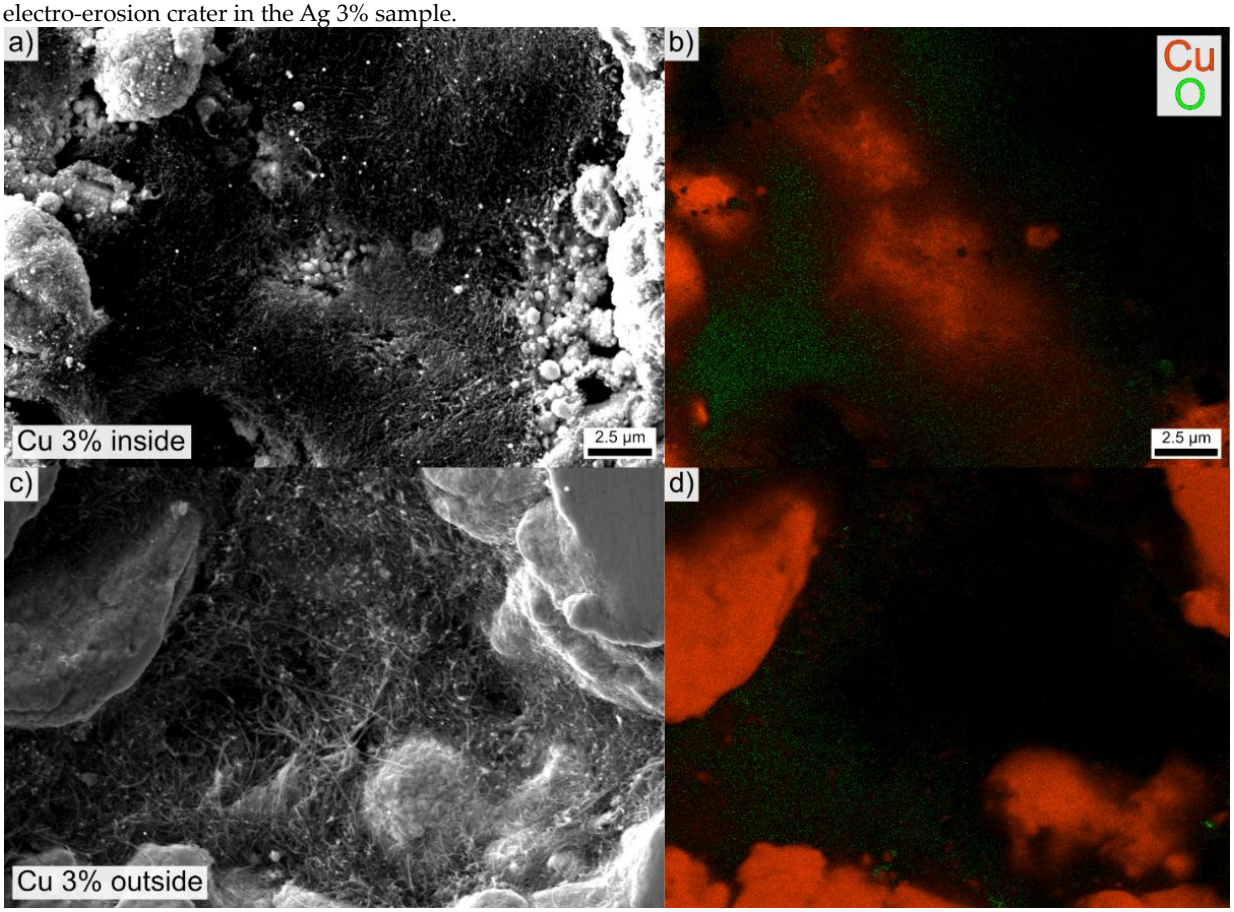

Supplementary Figure 14. a) SEM micrograph and **b)** EDS map of CNT clusters inside and **c)** and **d)** outside of the electro-erosion crater in the Cu 3% sample.

ARTICLE XV
Carbon Nanotube Reinforced Silver-Copper Hybrid Metal Matrix Composites as Bimetallic Electrodes

Bruno Alderete[1,*], Léane Chastagner[1], Frank Mücklich[1,2], Sebastian Suarez[1,3]

[1] Chair of Functional Materials, Saarland University, Campus D3.3, 66123 Saarbrücken, Germany
[2] SurFunction GmbH, Campus A1.1, 66123 Saarbrücken, Germany
[3] Materials Engineering Center Saarland (MECS), Campus D3.3, 66123 Saarbrücken, Germany

Research article
Published in "*Proceedings of the 2024 IEEE 69th Holm Conference on Electrical Contacts (HOLM)"* (2024)
Impact Factor: NA
Reproduced with permission from 'Institute of Electrical and Electronics Engineers - IEEE'
Accessible online at: doi.org/10.1109/HOLM56222.2024.10768450

Own Contribution: Conceptualization; Methodology; Validation; Formal Analysis; Investigation; Data Curation; Writing – Original Draft; Visualization.

Cite this article as: B. Alderete, L. Chastagner, F. Mücklich, S. Suarez, Carbon Nanotube Reinforced Silver-Copper Hybrid metal Matrix Composites as Bimetallic Electrodes, in: 2024 IEEE 69th Holm Conference on Electrical Contacts (HOLM), IEEE, 2024: pp. 1–8. https://doi.org10.1109/HOLM56222.2024.10768450.

Carbon Nanotube Reinforced Silver-Copper Hybrid Metal Matrix Composites as Bimetallic Electrodes

Bruno Alderete *[,a], Léane Chastagner [a], Frank Mücklich [a,b], Sebastian Suarez [a,c]

[a] Chair of Functional Materials, Saarland University, Saarbrücken, Germany

[b] SurFunction GmbH, Saarbrücken, Germany

[c] Materials Engineering Center Saarland (MECS), Saarbrücken, Germany

* Corresponding author: bruno.alderete@uni-saarland.de

Abstract:

This work proposes and optimizes the sintering process to produce hybrid metal matrix composites (HMMC) electrodes with optimal performance while minimizing the required energy input and production times. Four sets of carbon nanotube (CNT)-reinforced HMMC were manufactured via powder metallurgy and sintered via hot uniaxial pressing, techniques which are easily scalable and produce near-net shape components. The sintering temperature and time were optimized using relative density to determine if the parameters were satisfactory. Following sintering, metallographic cross sections of the HMMC (i.e., Ag/Cu, Ag/Cu+CNT, Ag+CNT/Cu, and Ag+CNT/Cu+CNT) were prepared and characterized via confocal laser and scanning electron microscopy. A qualitative assessment of the elemental distribution near the interface was conducted via energy dispersive X-ray spectroscopy linear and map scans. Moreover, load- and current-dependent electrical contact resistance was evaluated. The sintering times and temperatures required for the HMMC are lower than those required for pure metals due to the decreased eutectic temperature of the silver-copper mixture. Sintering at 550 °C for 2.5 hours is sufficient to achieve densities above 90%. The CNT act as diffusion barriers, slowing down the formation of Kirkendall voids. The Ag/Cu+CNT and Ag+CNT/Cu+CNT samples exhibited the most promising results, based on their low resistance and exceptional contact elasticity.

Keywords: *carbon nanotubes, electrical contact resistance, hybrid metal matrix composites (HMMC)*

Introduction

Copper is employed extensively due to its exceptional transport properties and its good mechanical properties. Nevertheless, in certain high-performance applications, silver is preferred not only for its enhanced conductivity, but also for its superior corrosion resistance. In numerous

industrial applications, silver plating over a copper base is a common practice. These platings are in the micrometer range, with the thickness varying depending on tribological and atmospheric conditions [1].

As society becomes increasingly electrified, the requirements of electrical contacts become more demanding. In order to meet these demands, electrical contacts must present the best electrical performance possible, in addition to being durable, efficient, and sustainable. Nevertheless, the availability and associated costs of silver must be taken into consideration [2], [3]. Consequently, silver-copper bimetallic joints may be a viable alternative to pure silver electrodes.

A multitude of metal joining methods can be employed to produce bimetallic joints, including solid-state joining, liquid-phase joining, fusion joining, etc. [4]. Liquid-phase joining encompasses welding, soldering, and brazing. Among these, brazing is particularly suited to the production of bimetallic joints, as it can join metals with varying thicknesses, it is a simple method which can join large components, the joints present outstanding stress distribution, and requires relatively low temperatures (compared to welding for example), among others [1], [5]. However, brazing (and for example, ultrasonic welding) requires clean, oxide-free surfaces to ensure the quality and integrity of the brazed joint. Furthermore, the necessity for filler material and the difficulty in controlling the temperature may result in the eutectic temperature being exceeded during brazing. This can lead to heterogeneities in the brazed joint due to differing chemical compositions, which in turn can alter the physical and chemical properties [5].

Sintering of bimetallic joints may be a suitable alternative to other bimetallic electrode production techniques. Sintering is a relatively simple process that is widely adopted in a plethora of industrial sectors. It is reproducible and reliable, facilitating quality control. Furthermore, with the appropriate mold, the outcome from sintering is a near-net-shape electrode with the possibility of producing large and complex shapes, making it fast and less labor intensive than other joining methods. Nevertheless, the most significant advantage of this method is that it allows for precise control over the temperature. Notwithstanding, a disadvantage that sintering presents is that prolonged sintering times are required.

The production of bimetallic electrodes via powder metallurgy and sintering, however, allows for the implementation of preliminary manufacturing steps. The reinforcement of metallic powders with carbon nanotubes (CNT) has yielded promising tribological, thermal, electrical, and mechanical outcomes [6]–[13], presenting long-lasting lubricity and durability during tribological tests [14], as well as stability under surface fatigue tests and fretting wear [15], [16]. Moreover, CNT coatings have the potential to protect the surface from atmospheric conditions due to their

hydrophobic nature [17], [18]. Furthermore, they maintain tribological wear protection during prolonged fretting wear even at low relative humidities [19]. It is therefore of interest to evaluate the feasibility of hybrid metal matrix composites (HMMC) as potential bimetallic electrodes. In addition to the previously reported advantages that the reinforcement phase provides, the incorporation of CNT into the metallic matrices reduces the required amount of metallic powder, thus potentially reducing weight and costs while improving material efficiency and maintaining the desired performance. Previously, Afonin et al. [20] have successfully manufactured silver-copper bimetallic joints via powder metallurgy, sintering at 730 °C and 830 °C. However, the authors reported that sintering above the eutectic temperature rendered unsatisfactory bimetallic electrodes. Therefore, for the purposes of this study, we will remain below this temperature – i.e., 779 °C [21].

This work aims to optimize the production parameters to obtain high-density HMMC and evaluate their electrical performance for potential applications as bimetallic electrodes. Accordingly, metallographic cross sections of the proposed electrodes, as well as reference material, were carried out and observed via scanning electron microscopy (SEM) and their chemical composition was analyzed via energy dispersive X-ray spectroscopy (EDS), focusing on the silver-copper interface. In addition, load-dependent and current-dependent electrical contact resistance (ECR) measurements were conducted to understand the influence of the reinforcement phase on the electrical performance of the HMMC.

Materials and Method

Four different bimetallic material systems were produced via powder metallurgy, namely: Ag/Cu, Ag/Cu+CNT, Ag+CNT/Cu, and Ag+CNT/Cu+CNT. The reinforced section of the HMMC contain 1% CNT by weight. These metallic powder-reinforcement mixtures were obtained by colloidal mixing. The HMMC were then consolidated into green pellets in an approximate ratio of 50/50 by volume, followed by sintering via hot uniaxial pressing (HUP). Detailed information on the CNT dispersion, colloidal mixing, consolidation of the powders, and sintering was previously reported in [15], [16]. Two disk-shaped samples were produced for each HMMC type. Subsequently, two small sections of each sample were cut and prepared for metallographic examination. The two smaller sections were utilized for observations of the cross section, whereas the larger central section was employed for hardness, current- and load-dependent ECR measurements.

Dendritic copper powder with a 325 mesh and 99% purity (Alfa Aesar GmbH, Germany) and silver flakes with at least 80% of the flakes below 20 µm and a purity of 99.9% (Alfa Aesar GmbH,

Germany) were used as metallic matrices. Chemical vapor deposition-grown multiwalled CNT (Graphene Supermarket, USA) were used as reinforcement phase. The nanotubes have an outer diameter distribution ranging from 50 to 85 nm, an as-received length between 10 and 15 μm, and a carbon purity above 94%.

The interface of the bimetallic junction is crucial for its electrical performance. Accordingly, SEM micrographs (Thermo-Fisher Helios^{TM} G4 PFIB CXe DualBeam^{TM} Super, equipped with an EDS detector EDAX Octane Elite Super) of the silver-copper interface were acquired at 5 kV using a primary electron detector, thus providing elemental contrast. Two-dimensional EDS mappings and linear scans were acquired at 10 kV to observe the elemental distribution in the vicinity of the interface.

Electrical characterization was carried out via 4-terminal sensing using a direct current source (Keithley 2400 SMU) and a nanovoltmeter (Keithley 2182a) to measure the voltage drop between the samples and the counter electrode, details on the testing rig reported by Puyol et al. and Suarez et al. [12], [22]. The counter electrode used was a silver-nickel core ($AgNi_{0.15}$) hard-gold-coated ($AuCo_{0.2}$) rivet with a curved head, a mean radius of curvature at its tip of 4 mm and a root mean square roughness S_q of 0.26 μm (Adam Bornbaum GmbH, Germany). The rivet's coating has an average thickness of 6.47 ± 0.18 μm, a coating and core hardness of 1.38 ± 0.01 GPa and 0.45-0.9 GPa [23], respectively, and a stiffness that is significantly higher than that of the samples.

The four configurations of HMMC and a standard bimetallic contact were characterized. Prior to electrical characterization, all samples were ground and polished to obtain a mirror-polished silver surface. The resulting roughness was measured via confocal laser scanning microscopy (CLSM). The root mean square roughness for all samples was between S_q = 30-60 nm. Furthermore, Vickers hardness was measured using a Dura Scan 50 microhardness tester (Struers Inc., USA) with a load of 0.098 N ($HV_{0.01}$), a holding time of 15 seconds, and optically micrographed using 40× magnification. At least 24 indentations were performed (on the silver side of the HMMC and reference material) and averaged – results shown in **Table I**. Moreover, the density of all HMMC characterized was at least 90%.

Table I – HMMC microhardness (measured on the silver side of the bimetallic material).

Sample	**Ref. rivet**	**Ag/Cu**	**Ag/Cu+CNT**	**Ag+CNT/Cu**	**Ag+CNT/Cu+CNT**
Hardness /MPa	839 ± 68	407 ± 38	452 ± 44	377 ± 96	427 ± 76

Current-dependent ECR was carried out at a constant normal load of 1 N on the silver side while sourcing the following direct currents: 30 µA, 100 µA, 300 µA, 1 mA, 3 mA, 10 mA, 30 mA, 100 mA, 300 mA, and 1 A. Load-dependent ECR, on the other hand, was carried out at a constant current of 100 mA_{DC}, so as to stay in dry-circuit conditions [24], also on the silver side of the samples. One loading and one unloading cycle were evaluated following a loading sequence of 1, 2.5, 5, 7.5, and 10 N. Ten ECR measurements were acquired per current or load and averaged. At least three current- and load-dependent ECR tests were conducted per sample and averaged. A new counter electrode was used for each test. The nanovoltmeter range was set to 0.1 V, to ensure the lowest uncertainty in the measurements without overflowing the measurement instrument [22], [25]. All tests were conducted under atmospheric conditions, i.e., 20.5 ± 0.5 °C and 33 ± 3% relative humidity.

Results and Discussions

HMMC Production & Characterization

To ensure optimal electrical performance, it is of utmost importance to achieve proper composite densities since internal porosities not only compromise its mechanical properties, but also its transport properties. Previous studies have demonstrated that silver composites require a holding time of 7.5 hours at a constant temperature during HUP to achieve relative densities above 90% [15], [16], whereas copper composites reach satisfactory relative densities with an isothermal holding time of only 2.5 hours. In both cases, the sintering temperature was 750 °C. However, in those studies, the sintering parameters were for pure silver or copper reinforced with CNT. Therefore, the HUP parameters needed to be evaluated and optimized. Initial HMMC sintering attempts were carried out for 7.5 hours at 750 °C, since these were the conditions that produced the high-density silver composites. After sintering, the samples reached densities above 90%. However, as illustrated in the optical micrographs in **Figure 1a-c**, there is no discernible distinction between the silver and copper section of the HMMC. Consequently, following the sintering process, the sample is a two-phase material with no distinct interface between the two metals. During the sintering process, silver and copper diffused through the initial interface region, resulting in the formation of a complex two-phase system, which is clearly visible in the EDS maps in **Figure 1d-e**. Copper atoms are smaller than silver atoms and exhibit greater mobility. At elevated temperatures this mobility is favored, which explains why more copper diffuses into silver rather than silver into copper. In addition, the external pressure applied during HUP (264 MPa) and the sintering temperature results in the densification of the HMMC through plastic flow, which also promotes the diffusion of the metals into one another. Furthermore, the micrographs in **Figure 1** demonstrate the re-agglomeration of the CNT, resulting in the formation

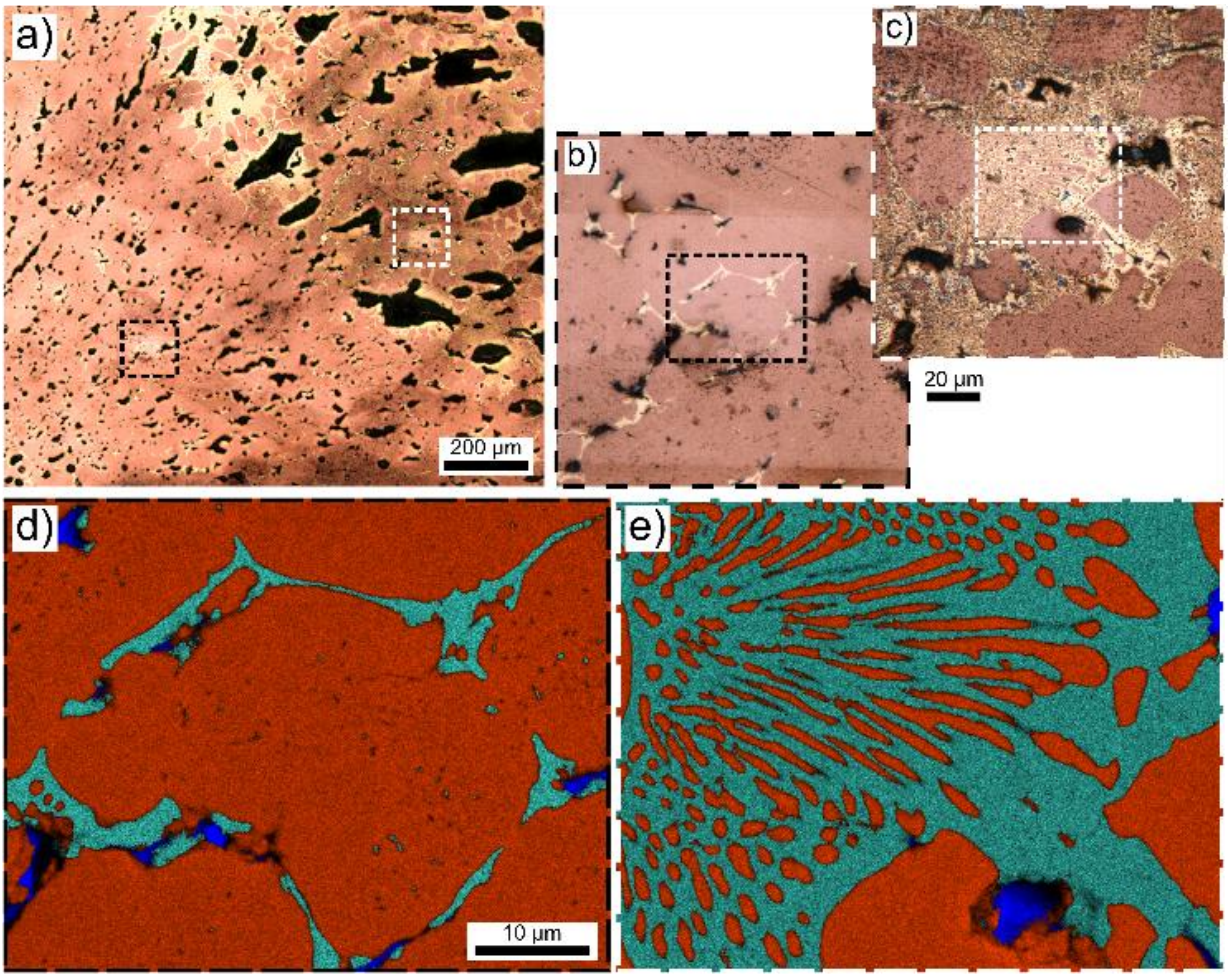

Figure 1. a) Optical micrograph acquired with CLSM of the cross section of the Ag+CNT/Cu+CNT sample sintered at 750 °C for 7.5 hours. **b)** and **c)** magnified micrographs at different regions. **d)** and **e)** EDS maps of the highlighted regions from **b)** and **c)**, respectively. The orange areas in the EDS maps correspond to copper, turquoise to silver, and blue to carbon.

of large carbon clusters. This re-agglomeration indicates that the metals have undergone a degree of melting, thereby enabling the CNT to flow and re-agglomerate [26], [27]. Observing the silver-copper phase diagram reveals that these two metals exhibit limited solid solubility [21], [28], forming a binary eutectic system. The eutectic temperature of the system is 779 °C under equilibrium conditions, which is slightly higher than the sintering temperature. Consequently, at the silver-copper interface, the eutectic concentration (71.9 wt.% Ag and 28.1 wt.% Cu) is locally met, which may enable the melting of both metals in an undercooling regime. In this case, the melting of both metals results in the extensive diffusion of each metal towards the opposing section of the bimetallic junction – as evidenced by the resulting microstructure shown in **Figure 1**. Additionally, the regrouping of the CNT is observed due to the significant difference in density between the CNT and the metals. Consequently, the sintering temperature must be reduced further below the eutectic temperature and undercooling regime in order to prevent the two metals from reaching the liquid state. This process minimizes the mixing of the metals through the

interface and restricts CNT re-agglomeration, while still densifying the composites. **Figure 2a** depict an optical micrograph and an EDS map of a HMMC sintered at 550 °C for 7.5 hours. At this lower temperature, copper still diffused towards the silver section, exhibiting small coral-like copper clusters – shown in **Figure 2b**. Despite copper's diffusion, the silver-copper interface remains intact. This is desired since maintaining the silver-copper interface reduces the effective phase boundary between the metals. In the samples sintered at 750 °C, the phase boundary between silver and the coral-shaped copper clusters significantly increases the effective phase boundary. Having a larger interfacial region can be detrimental towards the conductivity of the material, since the likelihood of electron scattering is higher at the boundaries.

Three distinct isothermal holding times were evaluated at 550 °C, all of which yielded HMMC with relative densities above 90%. The shortest holding time of 2.5 hours was selected as the definitive sintering time since this minimizes production times and the energy input required. SEM micrographs, EDS line scans and EDS mappings of the HMMC sintered at 550 °C for 2.5 hours and of a reference rivet are shown in **Figure 3**. Due to the nature of the manufacturing process, it is inevitable that a heterogeneous CNT distribution will be present within the HMMC and at the interface. The micrographs and EDS scans presented in **Figure 3** highlight specific features of the interfacial region. Although the micrographs provide a highly localized view of the interface (approximately 29,000 μm^2), they are representative of the most unfavorable spot at the silver-copper interface in terms of the system's transport properties.

The SEM micrograph and EDS scans of the reference rivet (**Figure 3a**) demonstrate the diffusion of copper towards the top silver layer. Coral-like copper regions are pervasively present

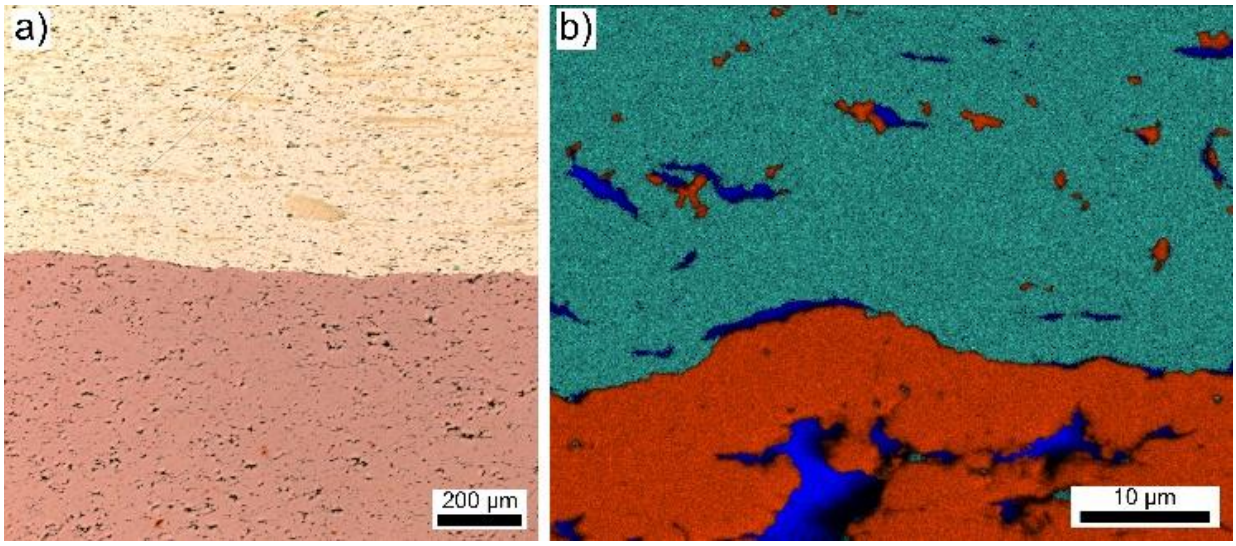

Figure 2. a) Optimal micrograph acquired with CLSM of the cross section of the Ag+CNT/Cu+CNT sample sintered at 550 °C for 7.5 hours. **b)** EDS map at the HMMC interface. The orange areas in the EDS maps correspond to copper, turquoise to silver, and blue to carbon.

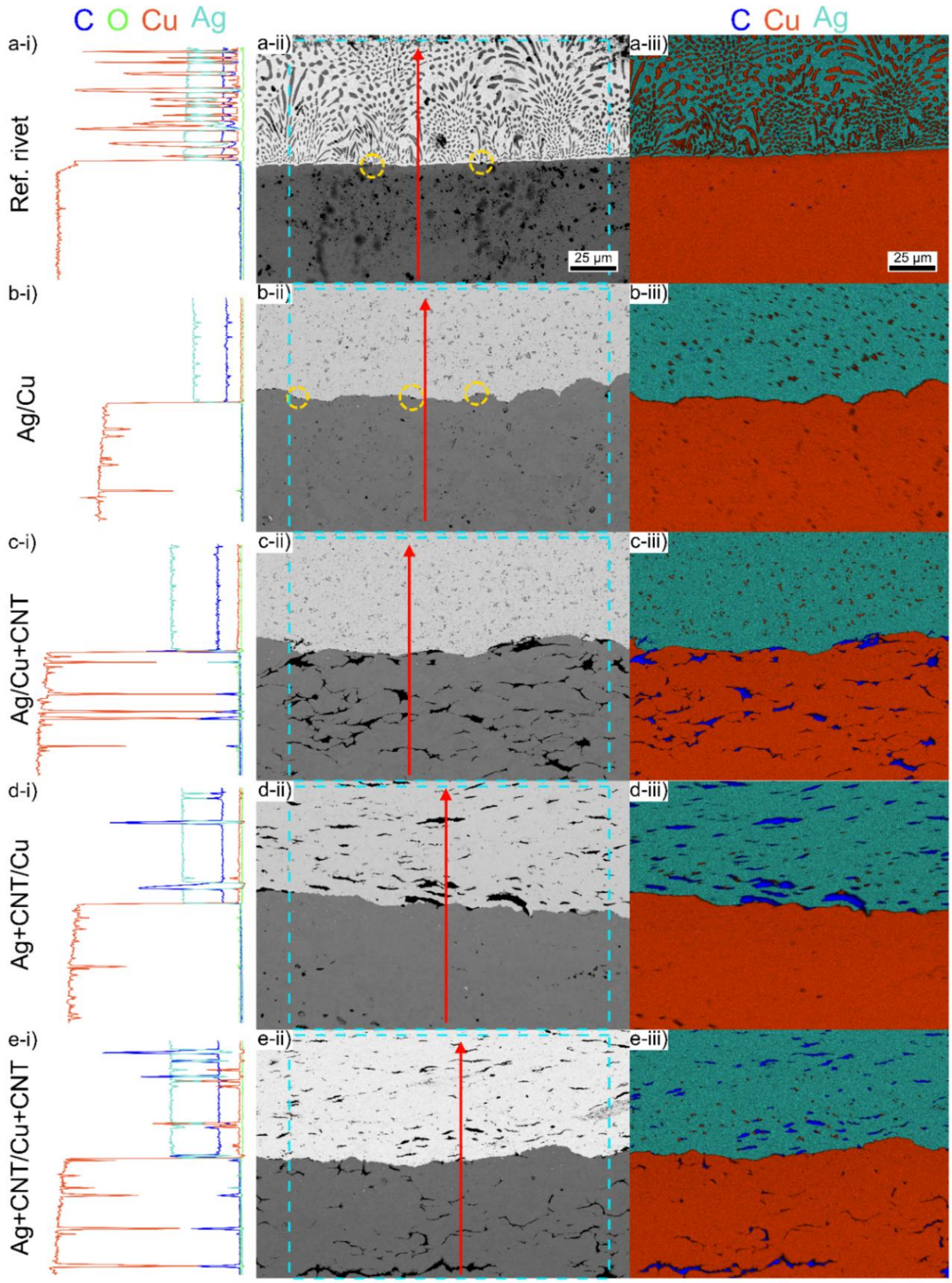

Figure 3. i) Linear EDS scans, **ii)** SEM micrograph, and **iii)** EDS mapping of the cross section of **a)** the reference rivet, **b)** Ag/Cu, **c)** Ag/Cu+CNT, **d)** Ag+CNT/Cu, and **e)** Ag+CNT/Cu+CNT. The red arrows in **ii)** indicate the scan location and direction of the linear EDS scan, whereas the dashed square highlights the area where the EDS maps were acquired. The orange areas in the EDS maps correspond to copper, turquoise to silver, and blue to carbon. The dashed circles in **a-ii)** and **b-ii)** highlight the Kirkendall voids at the silver-copper interface in the reference rivet and Ag/Cu sample.

within the silver region, exhibiting a resemblance to the structures observed in the HMMC sintered at 750 °C (**Figure 1e**). Upon examination of the copper section, no evidence of silver diffusion was observed. This is further corroborated by the EDS line scan, which reveals minimal presence of silver until the interface region. The Ag/Cu sample (**Figure 3b**) also demonstrates unidirectional diffusion of copper towards the silver section, although to a significantly lower extent than observed in the reference rivet. In the Ag/Cu sample, small but ubiquitous copper regions are observed in the silver section. However, the EDS scans do not demonstrate a significant copper signal in the silver section. The Ag/Cu+CNT sample (**Figure 3c**) also exhibits copper diffusing into the silver section. However, in this sample, the diffusion appears to be lower than in the Ag/Cu sample, as the copper clusters are smaller. Nevertheless, the small copper clusters are distributed ubiquitously in the silver section, as was observed in Ag/Cu. In contrast, the Ag+CNT/Cu sample (**Figure 3d**) exhibits minimal diffusion of copper towards the silver section. It seems that the CNT content in the silver section may act as a barrier to copper diffusion, particularly given the presence of large CNT clusters at the interface, as observed in the micrograph of the cross section.

Comparing the diffusion of copper between Ag/Cu+CNT and Ag+CNT/Cu samples indicates that the larger CNT clusters situated at the interface in the Ag+CNT/Cu sample are more effective at mitigating diffusion than the smaller clusters in the Ag/Cu+CNT sample (see the micrographs in **Figure 3c** and **d**). The number of copper clusters observed on the silver side of the Ag+CNT/Cu sample is notably lower than that observed on the silver side of the Ag/Cu+CNT sample. The diffusion of copper into the silver section was observed to be more pronounced in the Ag/Cu+CNT sample than in the Ag+CNT/Cu sample due to the presence of the reinforcement phase on the silver side, which impedes the mobility of copper atoms. This indicates that in order to minimize the diffusion of copper in silver-copper pairs, the reinforcement phase should be located on the silver section. The Ag+CNT/Cu+CNT sample (**Figure 3e**) exhibits distinctive characteristics when compared to the other reinforced HMMC. These include a reduction in the size of the CNT clusters and a more uniform distribution within each metallic matrix. In contrast, the Ag/Cu+CNT and Ag+CNT/Cu samples exhibit the presence of larger CNT clusters. As was the case for Ag+CNT/Cu, minimal copper diffusion was observed in the silver section of the Ag+CNT/Cu+CNT sample. The copper traces identified in the EDS map are scarce and situated in close proximity to the interface, which substantiates the efficacy of the CNT in impeding copper diffusion, despite the absence of CNT clusters at the interface in the Ag+CNT/Cu+CNT sample.

Since all HMMC were sintered at the same temperature, the thermal diffusion driving force is identical. Therefore, the different diffusion rates observed in the HMMC is solely due to the concentration gradient (according to Fick's law [29]). The CNT in HMMC reduce the concentration gradient at the interface, thus hindering the diffusion of copper atoms into silver. However, atomic diffusion still takes place due to the thermal driving force as well as the interfacial concentration gradient in regions without CNT.

The incorporation of CNT into the metallic matrices not only affects the diffusion rate of copper, but it also slows the formation of Kirkendall voids. The reference rivet and Ag/Cu sample both exhibit Kirkendall voids at the silver-copper interface – as highlighted by the dashed circle in **Figure 3a** and **Figure 3b**. These voids form due to the differing diffusivity between silver and copper [30]. The concentration gradient at the interface generates a higher atomic diffusion of copper towards silver rather than vice versa. The slower – or lack thereof – diffusion of silver towards copper produces the voids on the copper section. The formation of such voids will inevitably impact the conductivity of the bimetallic electrode. Therefore, it is highly sought after to minimize diffusion through, for example, the use of diffusion barriers. When CNT are incorporated into the metallic matrices, high concentrations of the nanostructures are situated at or near the interface. As previously discussed, diffusion primarily occurs from the copper section towards the silver section. Due to the chemical incompatibility between carbon and copper, the CNT content in the vicinity of the interface acts as a diffusion barrier, thus slowing the atomic diffusion of copper onto the silver section. The aforementioned behavior of the reinforcement phase in mitigating diffusion is analogous to that observed in solder joints, where CNT hinder the formation of interfacial intermetallic compounds [31], [32].

Electrical Performance

The electrical characterization of the sintered HMMC and reference rivet is presented in **Figure 4**. Current-dependent ECR (current sweep) provides information on the ohmic response of the materials in question. As shown in **Figure 4a**, all samples analyzed exhibit an ohmic range from 1 mA to 1 A, with the shaded region serving to emphasize this behavior. The Ag/Cu, Ag/Cu+CNT and Ag+CNT/Cu+CNT samples exhibited the lowest ECR during the current sweep, with resistance values between 2 and 3 mΩ. The reference rivet demonstrated a resistance value similar to that of the Ag+CNT/Cu+CNT sample (approximately 3 mΩ). In contrast, the Ag+CNT/Cu sample exhibited the highest ECR, with a value of approximately 5 mΩ.

The load-dependent ECR (**Figure 4b**) demonstrates the low ECR of the HMMC. The ECR results fall within the ohmic range of the materials given that the measurements were carried out

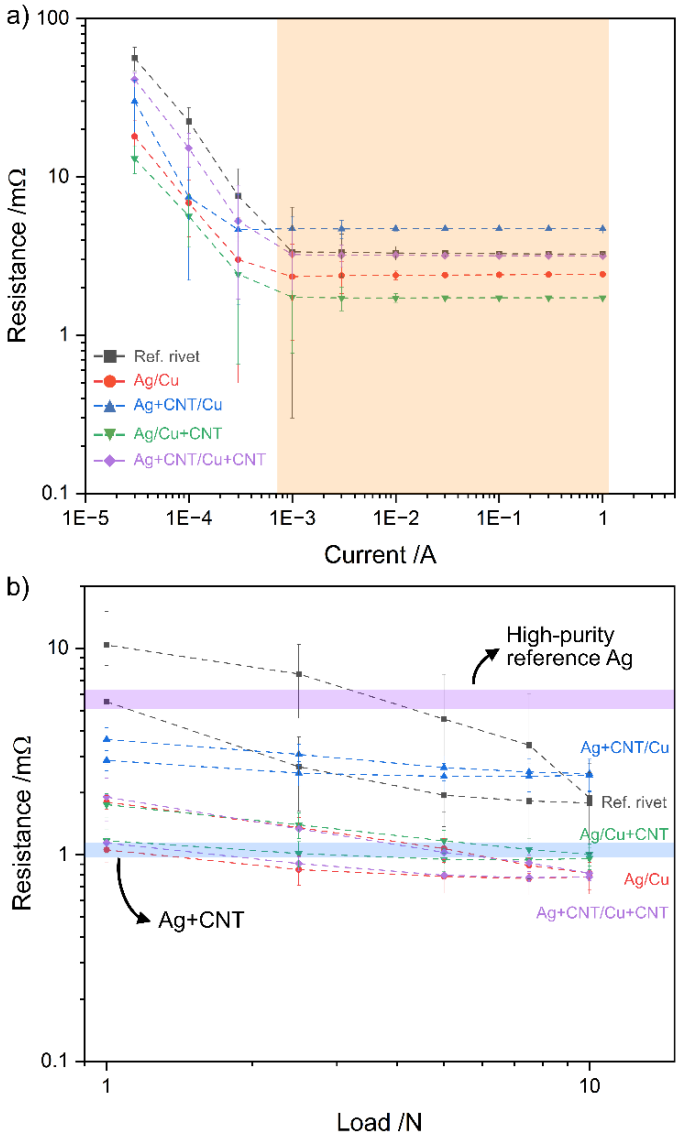

Figure 4. a) Current-dependent and **b)** load-dependent ECR of HMMC and the reference rivet. The highlighted region in **a)** emphasizes the ohmic range of the HMMC. The highlighted regions in **b)** show the ECR in the same loading ranges of high purity reference silver (upper) and sintered 1 wt.% CNT-reinforced silver composite (lower). ECR values of high-purity reference and silver composite from [16].

at 100 mA (dry circuit conditions [24]). With the exception of Ag+CNT/Cu, all HMMC exhibit an ECR below 2 mΩ. At 1 N, the ECR values for Ag/Cu, Ag/Cu+CNT and Ag+CNT/Cu+CNT are 2 mΩ, which correlates with the values obtained in the current sweep – which was also carried out at 1 N. At 10 N, the ECR values reached approximately 1 mΩ or lower. In contrast, the reference rivet exhibited an ECR of approximately 10 mΩ and 2 mΩ at 1 and 10 N, respectively. Among the HMMC, Ag+CNT/Cu is a notable outlier, exhibiting an ECR between 3 and 4 mΩ within the loading range studied. These results are comparable to those observed in the current sweep. This behavior was not anticipated, given that Ag+CNT/Cu exhibits similar hardness values to the other HMMC. Consequently, the real contact area between the counter electrode and Ag+CNT/Cu should be similar to that of Ag+CNT/Cu+CNT. The elevated ECR may be attributed

to the conspicuous CNT clusters discernible in the SEM micrograph depicted in **Figure 3d**, which are significantly larger than those observed for Ag+CNT/Cu+CNT (**Figure 3e**). Additionally, large CNT clusters are observed in the Ag/Cu+CNT sample. However, since the silver surface is being considered as the contacting surface, the resistance is not as significantly affected as it is in the Ag+CNT/Cu sample. Moreover, the Ag+CNT/Cu+CNT sample does not exhibit the same degree of CNT clustering as the other samples. Instead, it contains smaller CNT agglomerates that are relatively homogeneously distributed throughout the material's cross section – see micrograph of the cross section in **Figure 3**.

It is noteworthy that the reinforced composites all show exceptional elasticity, as evidenced by the low electrical hysteresis observed in load-dependent ECR. The maximum discrepancy in ECR at 1 N between the loading and unloading cycles is approximately 1 mΩ. In contrast, the reference rivet exhibits a difference of approximately 4 mΩ in the same loading conditions. The enhanced elasticity observed in the contact is not solely a consequence of the reduced hardness of the contacting surfaces; it is also a result of the incorporation of the highly elastic reinforcement phase. With regards to this matter, the existence of substantial CNT clusters in the Ag+CNT/Cu could yield promising outcomes, as these clusters could further promote contact elasticity, particularly for high load applications. This, in turn, could lead to a further reduction in the ECR past the loading range herein evaluated.

The highlighted regions in **Figure 4b** show the ECR performance of a high-purity reference silver sample and CNT-reinforced silver MMC (also 1 wt.% CNT) within the same loading ranges. The high-purity reference sample has a similar hardness as the reference rivet (847 ± 61 MPa) and the sintered silver MMC similar to that of the HMMC (505 ± 37 MPa) [16]. The ECR of high-purity copper and 1 wt.% copper MMC are not shown in **Figure 4b** due to their significantly higher resistance. In the same loading range, the high-purity copper reference (with a hardness of approximately 1300 MPa) presents resistances between 295 and 450 mΩ, whereas the copper MMC (with an approximate hardness of 620 MPa) presents resistances between 40 and 70 mΩ. In comparison to the silver MMC, the HMMC exhibit a greater degree of variability in the ECR values within the same loading range. At low loads, all HMMC have a larger ECR. However, from 5 N the ECR values fall within the range of the silver MMC. For Ag/Cu and Ag+CNT/Cu+CNT, in particular, from 7.5 N the ECR values fall below that of the silver MMC. Therefore, the performance of the bimetallic joint is comparable to that of silver composites produced via the same method. This performance features the viability of the CNT-reinforced HMMC over the silver MMC for two crucial reasons: 1) the HMMC considerably reduce the amount of silver required for the same or improved electrical performance, and 2) the sintering

process of the HMMC require significantly shorter sintering times as well as lower temperatures – 2.5 hours against 7.5 hours and 550 °C against 750 °C, respectively.

Conclusions

Dense carbon nanotube-reinforced silver-copper hybrid metal matrix composites were produced via powder metallurgy. Due to the relatively low eutectic temperature of silver-copper mixtures, the sintering process was optimized in order to prevent the melting of the metals and thus maintaining the integrity of the silver-copper interface. Consequently, the sintering temperatures were reduced from 750 °C to 550 °C. Furthermore, shorter sintering times (2.5 hours as opposed to 7.5 hours) are required to achieve relative densities above 90%, thus reducing the duration of the process and reducing the energy required to produce the bimetallic electrodes. This sintering method allows for the controlled production of reinforced bimetallic electrodes, in addition to reducing the amounts of metals required. This is achieved by replacing certain content of silver and copper with carbon, which increases material efficiency and reduces costs (i.e., dematerialization).

Upon incorporation of CNT into the metallic matrices, these tend to situate themselves at or near the silver-copper interface, thus acting as a diffusion barrier that reduces the likelihood of the formation of Kirkendall voids due to the faster diffusion rate of copper towards silver. Although Kirkendall voids were observed in the Ag/Cu (as well as the reference rivet), these do not seem to have a significant impact on the ECR at the time of the measurements. However, following sample aging, the size of the pores is likely to increase, potentially exerting a more significant influence on electrical performance. Diffusion still occurred in the HMMC samples, albeit, to a lesser extent. Consequently, if Kirkendall voids do form, it is anticipated that longer aging times will be required.

The Ag+CNT/Cu sample herein evaluated exhibited suboptimal performance, likely due to the substantial agglomeration of CNT within the silver section. The presence of large CNT clusters in the silver section has a detrimental impact on the transport properties of the material, resulting in the highest ECR among the measured samples. The HMMC that demonstrated the most promising results were the Ag/Cu+CNT and Ag+CNT/Cu+CNT samples, despite the former also exhibiting larger CNT agglomerates. In both cases, the diffusion process was found to be impeded by the presence of CNT. Moreover, both samples exhibited a considerable ohmic range and low load-dependent ECR with high contact elasticity, performing on par or even outperforming CNT-reinforced silver composites produced via the same method. This reduces the amount of silver required while also reducing production times and energy consumption.

Further studies are required on the long-term performance of the HMMC – particularly in regard to the effect of aging. Additionally, tribological evaluations are necessary. Moreover, the performance of this type of hybrid material under switching applications is of particular interest. Furthermore, the manufacturing and subsequent characterization of HMMC with higher CNT concentrations should be conducted in order to further enhance material efficiency.

Acknowledgment

B. Alderete wishes to acknowledge the support from the German Academic Exchange Service (DAAD) and the Roberto Rocca Education Program (RREP). The TÜV Saarland Stiftung is gratefully acknowledged for financially supporting the project. The authors gratefully acknowledge funding in the Mat-Innovat ("Kreislauffähige Materialsysteme für innovatives Hochleistungswerkstoffe") project, supported by the State of Saarland from the European Regional Development Fund (Europäischen Fonds für Regionale Entwicklung, EFRE). Funding for the PFIB/SEM instrument by German Research Foundation is greatly acknowledged (INST 256/510-1 FUGG).

References

[1] P. G. Slade, *Electrical Contacts*, Second Ed. Boca Raton: CRC Press, 2014. doi: 10.1201/b15640.

[2] A. Cremona and G. Mestl, "Silver Perspectives," Novara, Jul. 2023. Accessed: Apr. 29, 2024. [Online]. Available: https://www.soc.chim.it/sites/default/files/chimind/pdf/2023_4_46_ca.pdf

[3] N. Malina and R. Bebiano, "The Green Energy Transition as a Driver of Demand for Silver, Platinum, and Cobalt," Denver, May 2022. Accessed: Apr. 29, 2024. [Online]. Available: https://www.jpmcc-gcard.com/digest-uploads/newsletters/2022-05/GCARD%20TM2%20May%202022%20051122.pdf

[4] C. L. Bauer and G. G. Lessmann, "Metal-Joining Methods," *Annual Review of Materials Science*, vol. 6, no. 1, pp. 361–387, Aug. 1976, doi: 10.1146/annurev.ms.06.080176.002045.

[5] ASM International, *Welding, Brazing, and Soldering*, vol. 6. ASM International, 1993. doi: 10.31399/asm.hb.v06.9781627081733.

[6] L. Reinert, I. Green, S. Gimmler, B. Lechthaler, F. Mücklich, and S. Suárez, "Tribological behavior of self-lubricating carbon nanoparticle reinforced metal matrix composites," *Wear*, vol. 408–409, pp. 72–85, Aug. 2018, doi: 10.1016/j.wear.2018.05.003.

[7] S. Suarez, R. Puyol, C. Schafer, and F. Mucklich, "Carbon Nanotube-reinforced Metal Matrix Composites as Novel Electrodes for Low-voltage Switching Applications: A Surface Degradation Analysis," in *2019 IEEE Holm Conference on Electrical Contacts*, IEEE, Sep. 2019, pp. 135–141. doi: 10.1109/HOLM.2019.8923921.

[8] S. Suarez, N. Souza, F. Lasserre, and F. Mücklich, "Influence of the Reinforcement Distribution and Interface on the Electronic Transport Properties of MWCNT-Reinforced Metal Matrix Composites ," *Adv Eng Mater*, vol. 18, no. 9, pp. 1626–1633, Sep. 2016, doi: 10.1002/adem.201600216.

[9] D. García, S. Suárez, K. Aristizábal, and F. Mücklich, "Powder-Metallurgical Fabrication and Electrical Contact Resistance Characterization of Copper–Nickel Composites Reinforced by Multiwalled Carbon Nanotubes," *Adv Eng Mater*, vol. 24, no. 2, p. 2100755, Feb. 2022, doi: 10.1002/adem.202100755.

[10] L. Reinert, S. Suárez, and A. Rosenkranz, "Tribo-Mechanisms of Carbon Nanotubes: Friction and Wear Behavior of CNT-Reinforced Nickel Matrix Composites and CNT-Coated Bulk Nickel," *Lubricants*, vol. 4, no. 2, p. 11, Apr. 2016, doi: 10.3390/lubricants4020011.

[11] S. Suarez, F. Lasserre, and F. Mücklich, "Mechanical properties of MWNT/Ni bulk composites: Influence of the microstructural refinement on the hardness," *Materials Science and Engineering: A*, vol. 587, pp. 381–386, Dec. 2013, doi: 10.1016/j.msea.2013.08.058.

[12] S. Suarez, B. Alderete, R. Puyol, and F. Mücklich, “Load-dependent electrical contact resistance of carbon nanotube-reinforced metal matrix composites,” in *2022 IEEE 67th Holm Conference on Electrical Contacts (HLM)*, IEEE, Oct. 2022, pp. 1–6. doi: 10.1109/HLM54538.2022.9969801.

[13] S. Suarez, F. Lasserre, F. Soldera, R. Pippan, and F. Mücklich, “Microstructural thermal stability of CNT-reinforced composites processed by severe plastic deformation,” *Materials Science and Engineering A*, vol. 626, pp. 122–127, 2015, doi: 10.1016/j.msea.2014.12.065.

[14] L. Reinert *et al.*, “Long-lasting solid lubrication by CNT-coated patterned surfaces,” *Sci Rep*, vol. 7, no. 1, p. 42873, Feb. 2017, doi: 10.1038/srep42873.

[15] B. Alderete, S. Suarez, and F. Mücklich, “On the Production & Tribo-Electrical Characterization of Carbon Nanotube-Reinforced Ag & Cu Metal Matrix Composites,” in *2023 IEEE 68th Holm Conference on Electrical Contacts (HOLM)*, IEEE, Oct. 2023, pp. 1–8. doi: 10.1109/HOLM56075.2023.10352236.

[16] B. Alderete, F. Mücklich, and S. Suarez, “Electrical Characterization of Carbon Nanotube Reinforced Silver and Copper Composites for Switching Contacts,” *Journal of Composites Science*, vol. 7, no. 7, p. 284, Jul. 2023, doi: 10.3390/jcs7070284.

[17] B. Alderete, S. M. Lößlein, D. Bucio Tejeda, F. Mücklich, and S. Suarez, “Feasibility of Carbon Nanoparticle Coatings as Protective Barriers for Copper─Wetting Assessment,” *Langmuir*, vol. 38, no. 49, pp. 15209–15219, Dec. 2022, doi: 10.1021/acs.langmuir.2c02295.

[18] B. Alderete, F. Mücklich, and S. Suarez, “Comprehensive Study on Carbon-Coated Silver for Improved Tribo-Electrical and Wetting Performance,” *C (Basel)*, vol. 10, no. 1, p. 16, Feb. 2024, doi: 10.3390/c10010016.

[19] B. Alderete, F. Mücklich, and S. Suarez, “Wear Reduction via CNT Coatings in Electrical Contacts Subjected to Fretting,” *Tribol Lett*, vol. 71, no. 2, p. 54, Jun. 2023, doi: 10.1007/s11249-023-01724-5.

[20] M. P. Afonin, N. L. Pravoverov, and A. K. Dorozhkin, “Properties and structure of sintered bimetallic contacts with copper undercoats,” *Soviet Powder Metallurgy and Metal Ceramics*, vol. 20, no. 11, pp. 790–794, Nov. 1981, doi: 10.1007/BF00796479.

[21] ASM International, *Alloy Phase Diagrams*, vol. 3. ASM International, 1992. doi: 10.31399/asm.hb.v03.9781627081634.

[22] R. Puyol and S. Suarez, “A contact resistance measurement setup for the study of novel contacts,” in *2017 IEEE URUCON*, IEEE, Oct. 2017, pp. 1–4. doi: 10.1109/URUCON.2017.8171881.

[23] M. Braunovic, V. V. Konchits, and N. K. Myshkin, *Electrical Contacts*, 1st ed., vol. 1st Ed. Boca Raton, FL, USA: CRC Press, 2017. doi: 10.1201/9780849391088.

[24] E. M. Bock, “Low-Level Contact Resistance Characterization,” *AMP Journal of Technology*, vol. 3, pp. 64–68, 1993.

[25] B. Alderete, R. Puyol, S. Slawik, E. Espin, F. Mücklich, and S. Suarez, “Multipurpose setup used to characterize tribo-electrical properties of electrical contact materials,” *MethodsX*, vol. 8, p. 101498, 2021, doi: 10.1016/j.mex.2021.101498.

[26] P. C. Ma, S. Y. Mo, B. Z. Tang, and J. K. Kim, “Dispersion, interfacial interaction and re-agglomeration of functionalized carbon nanotubes in epoxy composites,” *Carbon N Y*, vol. 48, no. 6, pp. 1824–1834, May 2010, doi: 10.1016/j.carbon.2010.01.028.

[27] S. Jamali, M. C. Paiva, and J. A. Covas, “Dispersion and re-agglomeration phenomena during melt mixing of polypropylene with multi-wall carbon nanotubes,” *Polym Test*, vol. 32, no. 4, pp. 701–707, 2013, doi: 10.1016/j.polymertesting.2013.03.005.

[28] C. P. Wang, L. N. Yan, J. J. Han, and X. J. Liu, “Diffusion mobilities in the fcc Ag-Cu and Ag-Pd alloys,” *CALPHAD*, vol. 37, pp. 57–64, Jun. 2012, doi: 10.1016/j.calphad.2012.01.001.

[29] W. D. Jr. Callister, *Materials Science and Engineering: An Introduction*, 7 Ed., vol. 94. John Wiley & Sons, Ltd, 2006.

[30] R. Abbaschian, L. Abbaschian, and R. E. Reed-Hill, *Physical Metallurgy Principles*, 4th ed. Stamford: Cengage Learning, 2008.

[31] K. kai Xu, L. Zhang, and N. Jiang, “Effect of CNTs on the intermetallic compound growth between Sn solder and Cu substrate during aging and reflowing,” *Journal of Materials Science: Materials in Electronics*, vol. 32, no. 3, pp. 2655–2666, Feb. 2021, doi: 10.1007/s10854-020-04755-z.

[32] S. Xu, Y. C. Chan, K. Zhang, and K. C. Yung, “Interfacial intermetallic growth and mechanical properties of carbon nanotubes reinforced Sn3.5Ag0.5Cu solder joint under current stressing,” *J Alloys Compd*, vol. 595, pp. 92–102, May 2014, doi: 10.1016/j.jallcom.2014.01.083.

6. SUMMARY & CONCLUSIONS

The work herein presented focused on designing, manufacturing, and extensively characterizing carbon nanostructure-based coatings and metal matrix composites with the intended application of static electrical connectors and switching electrodes. Due to the prominence of silver- and copper-based materials in this field, the project concentrated on these two materials. On account of the exceptional transport properties of silver and copper, the primary objective was to enhance the performance of the materials in question without adversely impacting their conductivity. It is reasonable to conclude that the introduction of a less conductive material will inevitably affect the conductivity of these inherently excellent conductors. However, the CNP coatings and CNT reinforcements incorporate additional factors into the system, resulting in an overall improvement in the performance, durability, and reliability of the contact material. These three attributes were identified as the primary focus of this work. Nevertheless, technical requirements – such as industrial viability and scalability, operational safety, sustainable practices, material and energy efficiency – were also considered throughout the process. Moreover, the contact material systems herein developed and described were benchmarked and compared to reference materials to provide a holistic assessment of the feasibility of the proposed systems.

The findings from this work can be grouped into four categories, namely: *setup*, *materials*, *coatings*, and *composites*. The first category involved assembling, commissioning, and appraising a novel tribo-electrical testing rig, on which the subsequent characterization of the developed materials would be based off. This was the subject of study of ARTICLE I, where the components, programming, capabilities, and validation of the novel testing rig were described. The *materials* category was dedicated to identifying and characterizing silver- and copper-based connectors, in addition to the carbon nanostructures, and a preliminary characterization of CNP-containing systems. Moreover, the *coatings* category focused on the wear and atmospheric protection that CNP-based coatings could provide both silver and copper substrates. Lastly, the *composites* classification dealt with optimizing the manufacturing process of CNT-reinforced silver and copper MMC, their tribo-electrical characterization, and the manufacturing of sintered HMMC.

Apart from the costs associated with silver, one of its major challenges in the electrical industry is the formation of its characteristic silver sulfide tarnishing film. Although there are different techniques commonly used to slow down or prevent silver from tarnishing, the objective of ARTICLE II was to evaluate different methods to circumvent its influence on silver connectors' conductivity. It was found that mechanically

puncturing the tarnishing film managed to reduce the ECR to values similar to that of chemically cleaned samples, whereas resistive heating and mechanically scratching the film did not lower ECR. Nevertheless, scratch tests revealed that the tarnishing film reduces friction – however, it does not reduce wear – and the piling-up of silver sulfide at the end of the scratch track does not significantly affect conductivity.

When depositing different CNP onto copper substrates via EPD, 1D and 0D nanostructures (namely CNT and CNH) outperformed GF and GO (2D nanostructures) coatings in terms of ECR, contact reproducibility, coating compactness, homogeneity, adhesion and interface quality (ARTICLE III). To better understand the electrical resistance associated with bulk CNP agglomerates, load-dependent ECR during compressive loading was conducted (ARTICLE IV). It was found that 2D and 1D CNP (namely GF, GNP, and CNT) tended to exhibit the lowest overall electrical resistance, whereas (quasi)-0D CNP (i.e., CB, OLC, and CNH) presented the highest resistance. Normalizing the resistance values revealed that 0D nanostructures exhibited the greatest resistance drop within the loading range evaluated.

Copper-based connectors exhibit a strong correlation between topographic features, material hardness, and their electrical performance, with increased roughness typically leading to significantly lower ECR in harder (e.g., brass and bronze) connectors compared to softer (e.g., tin plated copper) connectors (ARTICLE V). This is due to the plastic deformation of the asperities, consequently increasing the conduction area (a-spots). Furthermore, CNT coatings produced via EPD on rough copper contacts highlighted the ability of CNT clusters to mitigate the influence of electrode topography due to their elastic properties.

The capability of CNP coatings to protect copper substrates from wear and the evolution of ECR during fretting wear was evaluated in ARTICLE VI. Different CNP and coating thicknesses were evaluated, and compared to uncoated copper, for 5,000 and 50,000 fretting cycles. The coated samples initially exhibit higher ECR than uncoated copper. However, within the first 10% of the total fretting cycles, the ECR fell below that of the copper reference and remained stable throughout the entirety of the test. In addition to low and stable ECR values, CB and CNT showed the best wear protection due to the low amount of coating displacement during fretting. Not only did the CNT-coated samples exhibited the least amount of material transfer from the counter electrode, but these coatings also protected the substrate from oxidation. Consequently, ARTICLE VII focused on evaluating the influence of CNT coating thickness and atmospheric humidity during fretting. Moreover, fretting conditions (i.e., normal load and duration) were evaluated. Thicker CNT coatings offered the most wear

protection – up to 96% in worn area reduction compared to uncoated copper. Nonetheless, fretting normal loads of at least 1 N are required in order to reach low and stable ECR values. Prolonged fretting tests (500,000 cycles) revealed that coating displacement negatively impacts wear protection provided, with worn area reductions below 20%. Nevertheless, the coating stabilized the ECR values below that of the copper reference. In low humidity fretting tests, the coated systems exhibited higher ECR than the uncoated reference. This is not due to tribologically-induced gains in resistance, but rather likely due to the absence of moisture within the porous network of the coatings.

As a result of the hydrophobic nature of the CNP herein discussed, the potential atmospheric protection that CNP-based coatings could provide to copper substrates were evaluated in ARTICLE VIII. All CNP coatings exhibited hydrophobic wetting behavior during static sessile drop tests (with purified water and saline water solution), although only GF, GO, and CNT exhibited superhydrophobicity. The latter, however, only exhibited superhydrophobicity for thicker coatings, highlighting the importance of completely coating the substrate.

Similarly, silver substrates were coated with CNP via EPD and subjected to tribo-electrical and wetting characterization (ARTICLE IX). In this case, clean and tarnished silver connectors were used as reference. Although the CNP coatings increased the ECR of the connector, the values remained below those of the tarnished samples both in load-dependent ECR and fretting tests. Nevertheless, the tarnishing film prevented adhesive wear during fretting to a higher extent than the CNP coatings. Moreover, GF and CNT coatings exhibited near-superhydrophobic wetting behavior even after prolonged droplet exposure times (300 s), whereas the silver sulfide tarnishing film did not affect wettability. When measuring contact angle with a more aggressive medium (i.e., potassium sulfide – K_2S), all surfaces showed hydrophilic wetting behavior. In this case, the tarnished and GF-coated surfaces showed the highest resistance towards wetting.

CNT-reinforced nickel MMC were manufactured via PM. The reinforcement phase's distribution and electrical performance of the MMC were characterized (ARTICLE X). These composites exhibited inferior resistances compared to unreinforced nickel, however, proper CNT distribution is crucial to maximize the advantages of the reinforcement phase. Subsequently, CNT-reinforced silver- and copper-based MMC were manufactured via the same methodology (ARTICLE XI). Tribo-electrical characterization of the copper MMC revealed that CNT concentrations of 0.5 and 1 wt.% were sufficient to improve contact reproducibility during load-dependent ECR and steady state ECR during fretting. Although the ECR increased compared to unreinforced copper, the addition of the reinforcement phase reduced adhesive wear

during fretting. Silver MMC, on the other hand, did not show promising results due to the lack of proper densification (relative density below 90%). Therefore, the manufacturing process required improvements (ARTICLE XII). Longer isothermal holding times during densification is required to increase the density (and tribo-electrical performance) of silver MMC due to complex and abundant micro-pores present in the consolidated green pellet caused by metallic powder morphology (silver flakes). ECR during fatigue cycle tests revealed that CNT-reinforced silver and copper MMC rapidly reach low and steady state ECR compared to their unreinforced counterparts.

The addition of CNT into silver and copper metallic matrices improves these metals' switching performance, with the proposed composites performing on par with standard switching materials – i.e., silver-nickel alloys and silver-tin oxide composites (ARTICLE XIII). Single break operation tests proved that CNT concentrations of at least 2 wt.% are required to prevent unstable arcing from taking place. Furthermore, the complex microstructure obtained due to the reinforcement phase reduces the electrical arc's mobility – confirmed with high-speed video footage. This effectively confines the arc to a specific area in the electrode, thereby minimizing the electrode's electro-erosion (ARTICLE XIV). The energy input from the arc favors CNT re-agglomeration (particularly in copper matrices due to the low chemical compatibility between copper and carbon), however, Raman spectroscopy indicates that the CNT do not undergo significant amorphization. Moreover, finite element method thermal simulations demonstrated that copper MMC do not reach sufficiently high temperatures to cause material evaporation, whereas sintered silver electrodes did surpass their boiling temperature. Although no considerable changes in molten pool dimensions were observed, the simulations did reveal that CNT contents above 1 wt.% reduce the duration of the molten pool by approximately 50% compared to the unreinforced samples – likely due to improved thermal properties (i.e., quicker re-solidification).

Lastly, CNT-reinforced silver-copper HMMC were produced via PM (ARTICLE XV). The process was optimized so as to remain far below the eutectic temperature of the system, thus obtaining a bimetallic joint with a clear interface. Bimetallic electrodes manufactured via PM and sintering require lower temperature and shorter sintering times than CNT-reinforced pure metal MMC. Metallographic cross sections of the bimetallic electrodes revealed that the addition of the reinforcement phase acts as a diffusion barrier, effectively slowing down or preventing the formation of Kirkendall voids at the silver-copper interface. Moreover, with proper CNT distribution within the HMMC, the electrical performance of the bimetallic electrode is similar to that of unreinforced bimetallic joints.

The results from this work highlight the benefits and drawbacks of CNP-containing electrical contact materials, both for static connectors and switching electrodes. These versatile nanostructures show great potential to tailor the characteristics and performance of electrical contact materials depending on the requirements of the intended application, with marginal impact on the conductive properties of silver and copper. This work provides the insight required to carry out material design choices to improve contact materials' reliability and prolong their durability.

7. OUTLOOK

Based on the work herein presented, it is evident that further research is required to better exploit the advantages that nanocarbon-containing systems could provide to electrical systems. The following points serve to outline potential lines of research that may provide further insight into these systems.

- Depositing CNP via EPD on CNT-reinforced MMC, thereby obtaining a tailored electrical contact which harnesses the benefits from the reinforcement phase as well as from the coatings.

- Tribo-electrical characterization of CNP-based coatings under extreme conditions, such as under vacuum, low (below 10%) and high (above 80%) relative humidity, influence of thermal cycling, etc.

- In-depth corrosion tests to fully assess the viability of the CNP coatings. Although all CNP exhibit hydrophobic wetting behavior, salt fog tests for example, would provide invaluable information on the atmospheric protection offered. These tests are of particular interest for offshore applications.

- Manufacturing MMC using different metallic powder morphology and different CNT sizes and chemical state, since these factors play a role in reinforcement phase distribution and sintering requirements (as discussed in ARTICLE XII).

- Due to the exceptional tribo-electrical performance demonstrated by CB coatings, it would be of interest to manufacture CB-reinforced silver and copper MMC since these particles are considerably cheaper to synthesize than CNT.

- Regarding electro-erosion tests:

    - Investigations on the performance of the proposed MMC when subjected to multiple make and break operations is required. Moreover, the erosion rate after x number of switching cycles should be determined.

    - Electro-erosion tests using different types of loads (i.e., resistive, inductive, capacitive, and combinations thereof) should be investigated.

    - Performance of the proposed MMC during hot switching with alternating currents is of interest to study.

- Depth-resolved characterization of the electro-erosion craters from ARTICLE XIII and ARTICLE XIV through techniques such as serial cutting tomography. This

would provide insight into the influence that the electrical arc has on the matrix and reinforcement phase in the subsurface – e.g., grain refinement, recrystallization, CNT re-agglomeration or amorphization, etc.

- Long term performance (aging) of HMMC (from ARTICLE XV) to evaluate the efficacy of the reinforcement phase at preventing or slowing down the formation of Kirkendall voids. Manufacturing HMMC with higher reinforcement phase concentrations to further reduce material requirements and weight.

- Manufacturing MMC with varying reinforcement phase concentrations (gradient composites) to fully tailor the electrode. For example, generating a superficial region with low reinforcement phase content can be achieved to maximize metal-metal contact, whereas the core region of the electrode could contain higher reinforcement phase concentrations to maximize thermal diffusivity while minimize weight and material requirements.

- Linked to the 5th point, manufacturing hybrid-reinforced MMC where the superficial region and the core could be reinforced with different CNP – CB and CNT for example. In this regard, CNT reinforcements at the core could be replaced with CB, whereas high-performing CNT reinforcements could be found at the superficial contacting regions.

REFERENCES

[1] P. Moller, Electric Fish, Bioscience 41 (1991) 794–796. https://doi.org/10.2307/1311732.

[2] A.K. Erenoğlu, O. Erdinç, A. Taşcıkaraoğlu, History of Electricity, in: Pathways to a Smarter Power System, Elsevier, 2019: pp. 1–27. https://doi.org/10.1016/B978-0-08-102592-5.00001-6.

[3] B. Spear, James Watt: The steam engine and the commercialization of patents, World Patent Information 30 (2008) 53–58. https://doi.org/10.1016/j.wpi.2007.05.009.

[4] R. Cecchini, G. Pelosi, Alessandro Volta and his battery, IEEE Antennas Propag Mag 34 (1992) 30–37. https://doi.org/10.1109/74.134307.

[5] G.S. Smith, Faraday's first dynamo: A retrospective, Am J Phys 81 (2013) 907–917. https://doi.org/10.1119/1.4825232.

[6] R.M. Black, The History of Electric Wires and Cables, Institution of Engineering and Technology, 1983.

[7] A. Mazur, Does increasing energy or electricity consumption improve quality of life in industrial nations?, Energy Policy 39 (2011) 2568–2572. https://doi.org/10.1016/j.enpol.2011.02.024.

[8] International Energy Agency, Electricity 2024: Analysis and forecast to 2026, Paris, 2024. https://iea.blob.core.windows.net/assets/18f3ed24-4b26-4c83-a3d2-8a1be51c8cc8/Electricity2024-Analysisandforecastto2026.pdf (accessed November 30, 2024).

[9] B.A. Bridge, D. Adhikari, M. Fontenla, Electricity, income, and quality of life, Soc Sci J 53 (2016) 33–39. https://doi.org/10.1016/j.soscij.2014.12.009.

[10] A.X. Andresen, L.C. Kurtz, D.M. Hondula, S. Meerow, M. Gall, Understanding the social impacts of power outages in North America: a systematic review, Environmental Research Letters 18 (2023). https://doi.org/10.1088/1748-9326/acc7b9.

[11] United Nations, The United Nations Sustainable Development Goals for 2030, (2015). https://sdgs.un.org/goals (accessed May 16, 2024).

[12] International Energy Agency, The Role of Critical Minerals in Clean Energy Transitions, Paris, 2021. https://www.iea.org/reports/the-role-of-critical-minerals-in-clean-energy-transitions (accessed May 16, 2024).

[13] International Copper Association, Regional trends and the green energy transition are expected to increase global copper demand by 12.6Mt from 2020 to 2040, (2024). https://internationalcopper.org/resource/regional-trends-and-the-green-energy-transition-are-expected-to-increase-global-copper-demand-by-12-6mt-from-2020-to-2040/ (accessed November 30, 2024).

[14] International Energy Agency, Global EV Outlook 2022: Securing supplies for an electric future, 2022. www.iea.org/t&c/.

[15] International Energy Agency, Global EV Outlook 2024: Moving towards increased affordability, Paris, 2024. https://www.iea.org/reports/global-ev-outlook-2024 (accessed May 16, 2024).

[16] CRU International Ltd, Silver and Global Connectivity, 2021. https://www.silverinstitute.org/wp-content/uploads/2021/09/SilverGlobalConnectivity_MmktTR2021.pdf (accessed May 17, 2024).

[17] Metals Focus, Silver's Growing Role in the Automotive Industry, 2021. https://www.silverinstitute.org/wp-content/uploads/2021/01/SilverAutomotive_MmktTR2021.pdf (accessed May 17, 2024).

[18] IDTechEx, The Electric Vehicle Market and Copper Demand, 2017. https://internationalcopper.org/wp-content/uploads/2017/06/2017.06-E-Mobility-Factsheet-1.pdf (accessed May 17, 2024).

[19] IDTechEx, The Role and Demand for Copper in the Future Automotive Market, (2022). https://internationalcopper.org/wp-content/uploads/2022/05/Automotive-Fact-Sheet-updated.pdf (accessed May 17, 2024).

[20] G. Bolger, The selection of automotive connectors, Senior Thesis, Coventry University, 1997.

[21] T.W. Liskiewicz, K.J. Kubiak, D.L. Mann, T.G. Mathia, Analysis of surface roughness morphology with TRIZ methodology in automotive electrical contacts: Design against third body fretting-corrosion, Tribol Int 143 (2020). https://doi.org/10.1016/j.triboint.2019.106019.

[22] P.G. Slade, Electrical Contacts, Second Ed., CRC Press, Boca Raton, 2014. https://doi.org/10.1201/b15640.

[23] Precious Metals Insights, Factors that Determine the Silver Price, 2024.

[24] D.W. Rice, P. Peterson, E.B. Rigby, P.B.P. Phipps, R.J. Cappell, R. Tremoureux, Atmospheric Corrosion of Copper and Silver, J Electrochem Soc 128 (1981) 275–284. https://doi.org/10.1149/1.2127403.

[25] A. Fateh, M. Aliofkhazraei, A.R. Rezvanian, Review of corrosive environments for copper and its corrosion inhibitors, Arabian Journal of Chemistry 13 (2020) 481–544. https://doi.org/10.1016/j.arabjc.2017.05.021.

[26] V. Brusic, M.A. Frisch, B.N. Eldridge, F.P. Novak, F.B. Kaufman, B.M. Rush, G.S. Frankel, Copper Corrosion With and Without Inhibitors, J Electrochem Soc 138 (1991) 2253–2259. https://doi.org/10.1149/1.2085957.

[27] S. Pareek, D. Jain, D. Behera, S. Sharma, R. Shrivastava, A review on inhibitors alleviating copper corrosion in hostile simulated Sea-water (3.5 wt.% NaCl solution), Mater Today Proc 43 (2021) 3303–3308. https://doi.org/10.1016/j.matpr.2021.01.966.

[28] C. Liang, C. Yang, N. Huang, Tarnish protection of silver by octadecanethiol self-assembled monolayers prepared in aqueous micellar solution, Surf Coat Technol 203 (2009) 1034–1044. https://doi.org/10.1016/j.surfcoat.2008.09.034.

[29] C.H. Liang, C.J. Yang, N.B. Huang, B. Wu, Comparison of four antitarnishing self-assembled monolayers on silver coin, Surface Engineering 27 (2011) 199–204. https://doi.org/10.1179/026708410X12786785573599.

[30] A.C. Phillips, A. Cowley, Octadecanthiol for tarnish-resistant silver coatings, in: R. Navarro, C.R. Cunningham, E. Prieto (Eds.), Modern Technologies in Space- and Ground-Based Telescopes and Instrumentation II, 2012: p. 84503W. https://doi.org/10.1117/12.925505.

[31] T. Ying, An Advanced Anti-Tarnish Process for Silver Coins and Silverware—Monomolecular Octadecanethiol Protective Film, Tribology Transactions 64 (2021) 341–349. https://doi.org/10.1080/10402004.2020.1842573.

[32] C.J. Cleveland, M. Ruth, Indicators of Dematerialization and the Materials Intensity of Use, J Ind Ecol 2 (1998) 15–50. https://doi.org/10.1162/jiec.1998.2.3.15.

[33] J. Kirchherr, D. Reike, M. Hekkert, Conceptualizing the circular economy: An analysis of 114 definitions, Resour Conserv Recycl 127 (2017) 221–232. https://doi.org/10.1016/j.resconrec.2017.09.005.

[34] J. Korhonen, A. Honkasalo, J. Seppälä, Circular Economy: The Concept and its Limitations, Ecological Economics 143 (2018) 37–46. https://doi.org/10.1016/j.ecolecon.2017.06.041.

[35] J. Glüge, M. Scheringer, I.T. Cousins, J.C. Dewitt, G. Goldenman, D. Herzke, R. Lohmann, C.A. Ng, X. Trier, Z. Wang, An overview of the uses of per- And polyfluoroalkyl substances (PFAS), Environ Sci Process Impacts 22 (2020) 2345–2373. https://doi.org/10.1039/d0em00291g.

[36] A.O. De Silva, J.M. Armitage, T.A. Bruton, C. Dassuncao, W. Heiger-Bernays, X.C. Hu, A. Kärrman, B. Kelly, C. Ng, A. Robuck, M. Sun, T.F. Webster, E.M. Sunderland, PFAS Exposure Pathways for Humans and Wildlife: A Synthesis of Current Knowledge and Key Gaps in Understanding, Environ Toxicol Chem 40 (2021) 631–657. https://doi.org/10.1002/etc.4935.

[37] Zentralverband Elektrotechnik- und Elektronikindustrie - ZVEI eV, Ausfallraten für Bordnetz-Komponenten im Automobil - Erwartungswerte und Bedingungen, 2021.

[38] W. Rudschies, ADAC Pannenstatistik 2024: Gewinner und Verlierer, Allgemeiner Deutscher Automobil-Club (2024). https://www.adac.de/rund-ums-fahrzeug/unfall-schaden-panne/adac-pannenstatistik/ (accessed May 31, 2024).

[39] A.C. Koumbourlis, Electrical injuries, Crit Care Med 30 (2002) S424–S430. https://doi.org/10.1097/00003246-200211001-00007.

[40] C.F. Dalziel, Dangerous Electric Currents, Transactions of the American Institute of Electrical Engineers 65 (1946) 579–585. https://doi.org/10.1109/T-AIEE.1946.5059386.

[41] ASM International, ASM Specialty Handbook: Copper and Copper Alloys, ASM International, 2001.

[42] M. Braunovic, V. V. Konchits, N.K. Myshkin, Electrical Contacts, 1st ed., CRC Press, Boca Raton, FL, USA, 2017. https://doi.org/10.1201/9780849391088.

[43] G.W. Stachowiak, A.W. Batchelor, Engineering Tribology, 2nd ed., Butterworth-Heinemann Ltd, 2000.

[44] R. Holm, Electric Contacts, 4th Ed., Springer Berlin Heidelberg, Berlin, Heidelberg, Heidelberg, 1967. https://doi.org/10.1007/978-3-662-06688-1.

[45] K. Seki, T. Kubo, N. Ye, T. Shimizu, Quantifying the spreading resistance of an anisotropic thin film conductor, Sci Rep 10 (2020) 10633. https://doi.org/10.1038/s41598-020-66739-7.

[46] T. Tamai, Y. Saitoh, S. Sawada, Y. Hattori, Peculiarities Characteristics Between Contact Trace and Contact Resistance of Tin Plated Contacts, in: 2008 Proceedings of the 54th IEEE Holm Conference on Electrical Contacts, IEEE, 2008: pp. 337–343. https://doi.org/10.1109/HOLM.2008.ECP.65.

[47] M. Leidner, H. Schmidt, M. Myers, H.F. Schlaak, A new simulation approach to characterizing the mechanical and electrical qualities of a connector contact, The European Physical Journal Applied Physics 49 (2010) 22909. https://doi.org/10.1051/epjap/2010002.

[48] E.S. Gadelmawla, M.M. Koura, T.M.A. Maksoud, I.M. Elewa, H.H. Soliman, Roughness parameters, J Mater Process Technol 123 (2002) 133–145. https://doi.org/10.1016/S0924-0136(02)00060-2.

[49] H. Hertz, Über die Berührung fester elastischer Körper, Journal Für Die Reine Und Angewandte Mathematik 92 (1881) 156–171.

[50] I.M. Hutchings, P. Shipway, Tribology: Friction and Wear of Engineering Materials, 2nd Ed., Butterworth-Heinemann, 2017.

[51] A.C. Fischer-Cripps, Introduction to Contact Mechanics, 2nd Ed., Springer US, Boston, MA, 2007. https://doi.org/10.1007/978-0-387-68188-7.

[52] J.A. Greenwood, J.B.P. Williamson, Contact of nominally flat surfaces, Proc R Soc Lond A Math Phys Sci 295 (1966) 300–319. https://doi.org/10.1098/rspa.1966.0242.

[53] J.A. Greenwood, J.H. Tripp, The Contact of Two Nominally Flat Rough Surfaces, Proceedings of the Institution of Mechanical Engineers 185 (1970) 625–633. https://doi.org/10.1243/PIME_PROC_1970_185_069_02.

[54] L. Kogut, I. Etsion, Elastic-Plastic Contact Analysis of a Sphere and a Rigid Flat, J Appl Mech 69 (2002) 657–662. https://doi.org/10.1115/1.1490373.

[55] W.R. Chang, I. Etsion, D.B. Bogy, An Elastic-Plastic Model for the Contact of Rough Surfaces, J Tribol 109 (1987) 257–263. https://doi.org/10.1115/1.3261348.

[56] Y. Zhao, D.M. Maietta, L. Chang, An Asperity Microcontact Model Incorporating the Transition From Elastic Deformation to Fully Plastic Flow, J Tribol 122 (2000) 86–93. https://doi.org/10.1115/1.555332.

[57] S. Shankar, M.M. Mayuram, A Finite Element Based Study on the Elastic-Plastic Transition Behavior in a Hemisphere in Contact With a Rigid Flat, J Tribol 130 (2008). https://doi.org/10.1115/1.2958081.

[58] L.P. Lin, J.F. Lin, A New Method for Elastic-Plastic Contact Analysis of a Deformable Sphere and a Rigid Flat, J Tribol 128 (2006) 221–229. https://doi.org/10.1115/1.2164469.

[59] H. Ghaednia, X. Wang, S. Saha, Y. Xu, A. Sharma, R.L. Jackson, A Review of Elastic–Plastic Contact Mechanics, Appl Mech Rev 69 (2017). https://doi.org/10.1115/1.4038187.

[60] R.L. Jackson, I. Green, A statistical model of elasto-plastic asperity contact between rough surfaces, Tribol Int 39 (2006) 906–914. https://doi.org/10.1016/j.triboint.2005.09.001.

[61] R.L. Jackson, I. Green, On the Modeling of Elastic Contact between Rough Surfaces, Tribology Transactions 54 (2011) 300–314. https://doi.org/10.1080/10402004.2010.542277.

[62] A. la Monaca, J.W. Murray, Z. Liao, A. Speidel, J.A. Robles-Linares, D.A. Axinte, M.C. Hardy, A.T. Clare, Surface integrity in metal machining - Part II: Functional performance, Int J Mach Tools Manuf 164 (2021) 103718. https://doi.org/10.1016/j.ijmachtools.2021.103718.

[63] H.K. Toenshoff, Wear Mechanisms, in: CIRP Encyclopedia of Production Engineering, Springer Berlin Heidelberg, Berlin, Heidelberg, 2019: pp. 1811–1815. https://doi.org/10.1007/978-3-662-53120-4_6415.

[64] R.B. Waterhouse, Fretting Corrosion, PergamonPressLimited, Oxford, 1972.

[65] S. Fouvry, J. Laporte, O. Perrinet, P. Jedrzejczyk, O. Graton, O. Alquier, J. Sautel, Fretting wear of low current electrical contacts: Quantification of electrical endurance, in: 2017 IEEE Holm Conference on Electrical Contacts, IEEE, 2017: pp. 1–11. https://doi.org/10.1109/HOLM.2017.8088056.

[66] G.A. Tomlison, Rusting of Steel Surfaces in Contact, in: Proceedings of the Royal Society, 1927: p. 472.

[67] D. Godfrey, Investigation of Fretting Corrosion by Microscopic Observations, NACA Tech. Note No. 2039, Cleveland, 1950.

[68] I.M. Feng, B.G. Rightmire, The Mechanism of Fretting, Lubrication Engineering 9 (1953) 134.

[69] H.H. Uhlig, Mechanism of Fretting Corrosion, J Appl Mech 21 (1954) 401–407. https://doi.org/10.1115/1.4010940.

[70] I.F. Stowers, E. Rabinowicz, The Mechanism of Fretting Wear, Journal of Lubrication Technology 95 (1973) 65–70. https://doi.org/10.1115/1.3451736.

[71] Oding I. A., Ivanova V. S., Thermoelectric Effects in Fretting Wear, in: Proceedings of the International Conference on Fatigue of Metals, 1956: p. 408.

[72] N. P. Suh, The delamination theory of wear, Wear 25 (1973) 111–124. https://doi.org/10.1016/0043-1648(73)90125-7.

[73] R.B. Waterhouse, D.E. Taylor, Fretting debris and the delamination theory of wear, Wear 29 (1974) 337–344. https://doi.org/10.1016/0043-1648(74)90019-2.

[74] M. Godet, The third-body approach: A mechanical view of wear, Wear 100 (1984) 437–452. https://doi.org/10.1016/0043-1648(84)90025-5.

[75] S. Nöel, D. Alamarguy, S. Correia, P. Laurat, Fretting Behavior of Nickel Coatings for Electrical Contact Applications, in: 2011 IEEE 57th Holm Conference on Electrical Contacts (Holm), IEEE, 2011: pp. 1–8. https://doi.org/10.1109/HOLM.2011.6034784.

[76] E.S. Sproles Jr., D.J. Gaul, D.J. Duquette, A New Interpretation of the Mechanism of Fretting and Fretting Corrosion Damage, in: N.P. Suh, N. Saka (Eds.), Fundamentals of Tribology, MIT Press, Cambridge, 1978: p. 585.

[77] A. Bouzera, E. Carvou, N. Ben Jemaa, R. El Abdi, L. Tristani, E.M. Zindine, Minimum Fretting Amplitude in Medium Force for Connector Coated Material and Pure Metals, in: 2010 Proceedings of the 56th IEEE Holm Conference on Electrical Contacts, IEEE, 2010: pp. 1–7. https://doi.org/10.1109/HOLM.2010.5619557.

[78] J.-M. Kim, S. Lee, C.-W. Baek, Y. Kwon, Y.-K. Kim, Cold- and hot-switching lifetime characterizations of ohmic-contact RF MEMS switches, IEICE Electronics Express 5 (2008) 418–423. https://doi.org/10.1587/elex.5.418.

[79] N. Ben Jemaa, L. Morin, S. Benhenda, L. Nedelec, Anodic to cathodic arc transition according to break arc lengthening, IEEE Transactions on Components, Packaging, and Manufacturing Technology: Part A 21 (2005) 599–603. https://doi.org/10.1109/tcpma.1998.740053.

[80] J. Swingler, J.W. McBride, The net zero erosion phenomena on opening switching contacts with AC loading, in: Electrical Contacts - 1997 Proceedings of the Forty-Third IEEE Holm Conference on Electrical Contacts, IEEE, 1997: pp. 238–245. https://doi.org/10.1109/HOLM.1997.638048.

[81] N. Sato, Some concepts of corrosion fundamentals, Corros Sci 27 (1987) 421–433. https://doi.org/10.1016/0010-938X(87)90086-2.

[82] J.C. Scully, The Fundamentals of Corrosion, 3rd ed., Elsevier Science & Technology Books, 1990.

[83] ASM International, Corrosion: Fundamentals, Testing, and Protection, ASM International, 2003.

[84] R. Winston Revie, ed., Uhlig's Corrosion Handbook, 3rd ed., John Wiley & Sons, 2011.

[85] S. Lilienfeld, C.E. White, A Study of the Reaction Between Hydrogen Sulfide and Silver, J Am Chem Soc 52 (1930) 885–892. https://doi.org/10.1021/ja01366a005.

[86] T. Ying, T. Power, A. Bacon, Applying a Mono-Octadecanethiol Film on Silver and Gold Coin Products, J Tribol 144 (2022). https://doi.org/10.1115/1.4054743.

[87] P. Patnaik, Handbook of Inorganic Chemistry, MacGraw-Hill, New York, 2002.

[88] J.J. Díaz León, D.M. Fryauf, R.D. Cormia, N.P. Kobayashi, Study of the formation of native oxide on copper at room temperature, in: N.P. Kobayashi, A.A. Talin, M.S. Islam, A. V. Davydov (Eds.), Low-Dimensional Materials and Devices 2016, 2016: p. 99240O. https://doi.org/10.1117/12.2238745.

[89] J.-H. Park, K. Natesan, Oxidation of copper and electronic transport in copper oxides, Oxidation of Metals 39 (1993) 411–435. https://doi.org/10.1007/BF00664664.

[90] B.H. Chudnovsky, Lubrication of electrical contacts, in: Proceedings of the Fifty-First IEEE Holm Conference on Electrical Contacts, 2005., IEEE, Chicago, 2005: pp. 107–114. https://doi.org/10.1109/HOLM.2005.1518230.

[91] A. Abdelbary, L. Chang, Lubrication and surface engineering, in: Principles of Engineering Tribology, Elsevier, 2023: pp. 295–343. https://doi.org/10.1016/B978-0-323-99115-5.00012-8.

[92] R. Lohmann, I.T. Cousins, J.C. Dewitt, J. Glüge, G. Goldenman, D. Herzke, A.B. Lindstrom, M.F. Miller, C.A. Ng, S. Patton, M. Scheringer, X. Trier, Z. Wang, Are Fluoropolymers Really of Low Concern for Human and Environmental Health and Separate from Other PFAS?, Environ Sci Technol 54 (2020) 12820–12828. https://doi.org/10.1021/acs.est.0c03244.

[93] European Chemicals Agency, Registry of restriction intentions until outcome: PFAS, (2024). https://echa.europa.eu/registry-of-restriction-intentions/-/dislist/details/0b0236e18663449b (accessed October 31, 2024).

[94] H.O. Pierson, Handbook of Carbon, Graphite, Diamonds, and Fullerenes: Processing, Properties and Applications, Noyes Publications, 1993.

[95] R.C. Haddon, Chemistry of the Fullerenes: The Manifestation of Strain in a Class of Continuous Aromatic Molecules, Science (1979) 261 (1993) 1545–1550. https://doi.org/10.1126/science.261.5128.1545.

[96] D. Sumanth Kumar, B. Jai Kumar, H.M. Mahesh, Quantum Nanostructures (QDs): An Overview, in: Synthesis of Inorganic Nanomaterials, Elsevier, 2018: pp. 59–88. https://doi.org/10.1016/B978-0-08-101975-7.00003-8.

[97] L. Mino, G. Agostini, E. Borfecchia, D. Gianolio, A. Piovano, E. Gallo, C. Lamberti, Low-dimensional systems investigated by x-ray absorption spectroscopy: a selection of 2D, 1D and 0D cases, J Phys D Appl Phys 46 (2013) 423001. https://doi.org/10.1088/0022-3727/46/42/423001.

[98] W. Bollmann, J. Spreadborough, Action of Graphite as a Lubricant, Nature 186 (1960) 29–30. https://doi.org/10.1038/186029a0.

[99] H. Wang, Graphite Solid Lubrication Materials, in: Q.J. Wang, Z.-W. Chung (Eds.), Encyclopedia of Tribology, Springer US, Boston, MA, 2013: pp. 1550–1555. https://doi.org/10.1007/978-0-387-92897-5_1261.

[100] T.W. Scharf, S. V. Prasad, Solid lubricants: a review, J Mater Sci 48 (2013) 511–531. https://doi.org/10.1007/s10853-012-7038-2.

[101] H.E. Sliney, Solid Lubrificants, 1991. https://ntrs.nasa.gov/api/citations/19910013083/downloads/19910013083.pdf.

[102] F.J. Clauss, Solid Lubricants and Self-Lubricating Solids, Elsevier, New York and London, 1972. https://doi.org/10.1016/B978-0-12-176150-9.X5001-0.

[103] E.R. Braithwaite, Solid Lubricants and Surfaces, Elsevier, Oxford, 1964. https://doi.org/10.1016/C2013-0-01729-X.

[104] C.-G. Lee, Y.-J. Hwang, Y.-M. Choi, J.-K. Lee, C. Choi, J.-M. Oh, A study on the tribological characteristics of graphite nano lubricants, International Journal of Precision Engineering and Manufacturing 10 (2009) 85–90. https://doi.org/10.1007/s12541-009-0013-4.

[105] Z. Zhang, D. Simionesie, C. Schaschke, Graphite and Hybrid Nanomaterials as Lubricant Additives, Lubricants 2 (2014) 44–65. https://doi.org/10.3390/lubricants2020044.

[106] H. Liang, Y. Bu, J. Zhang, Z. Cao, A. Liang, Graphene Oxide Film as Solid Lubricant, ACS Appl Mater Interfaces 5 (2013) 6369–6375. https://doi.org/10.1021/am401495y.

[107] A. Senatore, V. D'Agostino, V. Petrone, P. Ciambelli, M. Sarno, Graphene Oxide Nanosheets as Effective Friction Modifier for Oil Lubricant: Materials, Methods, and Tribological Results, ISRN Tribology 2013 (2013) 1–9. https://doi.org/10.5402/2013/425809.

[108] P. Wu, X. Chen, C. Zhang, J. Zhang, J. Luo, J. Zhang, Modified graphene as novel lubricating additive with high dispersion stability in oil, Friction 9 (2021) 143–154. https://doi.org/10.1007/s40544-019-0359-2.

[109] J.A.C. Cornelio, P.A. Cuervo, L.M. Hoyos-Palacio, J. Lara-Romero, A. Toro, Tribological properties of carbon nanotubes as lubricant additive in oil and water for a wheel–rail system, Journal of Materials Research and Technology 5 (2016) 68–76. https://doi.org/10.1016/j.jmrt.2015.10.006.

[110] F. Dassenoy, L. Joly-Pottuz, J.M. Martin, T. Mieno, Carbon Nanotubes as Advanced Lubricant Additives, in: V.N. Popov, P. Lambin (Eds.), Carbon Nanotubes, Kluwer Academic Publishers, Dordrecht, 2006: pp. 237–238. https://doi.org/10.1007/1-4020-4574-3_46.

[111] J. Kałużny, A. Merkisz-Guranowska, M. Giersig, K. Kempa, Lubricating performance of carbon nanotubes in internal combustion engines – engine test results for CNT enriched oil, International Journal of Automotive Technology 18 (2017) 1047–1059. https://doi.org/10.1007/s12239-017-0102-9.

[112] S. Zhu, G. Xu, Single-walled carbon nanohorns and their applications, Nanoscale 2 (2010) 2538. https://doi.org/10.1039/c0nr00387e.

[113] D. Maharaj, B. Bhushan, S. Iijima, Effect of carbon nanohorns on nanofriction and wear reduction in dry and liquid environments, J Colloid Interface Sci 400 (2013) 147–160. https://doi.org/10.1016/j.jcis.2013.03.008.

[114] N. Karousis, I. Suarez-Martinez, C.P. Ewels, N. Tagmatarchis, Structure, Properties, Functionalization, and Applications of Carbon Nanohorns, Chem Rev 116 (2016) 4850–4883. https://doi.org/10.1021/acs.chemrev.5b00611.

[115] N. Nyholm, N. Espallargas, Functionalized carbon nanostructures as lubricant additives – A review, Carbon N Y 201 (2023) 1200–1228. https://doi.org/10.1016/j.carbon.2022.10.035.

[116] X. Fan, Q. Xue, L. Wang, Carbon-based solid-liquid lubricating coatings for space applications-A review, Friction 3 (2015) 191–207. https://doi.org/10.1007/s40544-015-0079-1.

[117] W. Khalil, A. Mohamed, M. Bayoumi, T.A. Osman, Tribological properties of dispersed carbon nanotubes in lubricant, Fullerenes, Nanotubes and Carbon Nanostructures 24 (2016) 479–485. https://doi.org/10.1080/1536383X.2016.1188804.

[118] L. Joly-Pottuz, B. Vacher, N. Ohmae, J.M. Martin, T. Epicier, Anti-wear and Friction Reducing Mechanisms of Carbon Nano-onions as Lubricant Additives, Tribol Lett 30 (2008) 69–80. https://doi.org/10.1007/s11249-008-9316-3.

[119] M.M. Rahman, M. Islam, R. Roy, H. Younis, M. AlNahyan, H. Younes, Carbon Nanomaterial-Based Lubricants: Review of Recent Developments, Lubricants 10 (2022) 281. https://doi.org/10.3390/lubricants10110281.

[120] X. Chen, J. Li, Superlubricity of carbon nanostructures, Carbon N Y 158 (2020) 1–23. https://doi.org/10.1016/j.carbon.2019.11.077.

[121] A. Hirata, M. Igarashi, T. Kaito, Study on solid lubricant properties of carbon onions produced by heat treatment of diamond clusters or particles, Tribol Int 37 (2004) 899–905. https://doi.org/10.1016/j.triboint.2004.07.006.

[122] G. Fugallo, A. Cepellotti, L. Paulatto, M. Lazzeri, N. Marzari, F. Mauri, Thermal Conductivity of Graphene and Graphite: Collective Excitations and Mean Free Paths, Nano Lett 14 (2014) 6109–6114. https://doi.org/10.1021/nl502059f.

[123] E. Planes, L. Flandin, N. Alberola, Polymer Composites Bipolar Plates for PEMFCs, Energy Procedia 20 (2012) 311–323. https://doi.org/10.1016/j.egypro.2012.03.031.

[124] W. Park, J. Hu, L.A. Jauregui, X. Ruan, Y.P. Chen, Electrical and thermal conductivities of reduced graphene oxide/polystyrene composites, Appl Phys Lett 104 (2014). https://doi.org/10.1063/1.4869026.

[125] D.G. Papageorgiou, I.A. Kinloch, R.J. Young, Mechanical properties of graphene and graphene-based nanocomposites, Prog Mater Sci 90 (2017) 75–127. https://doi.org/10.1016/j.pmatsci.2017.07.004.

[126] R. Saito, G. Dresselhaus, M.S. Dresselhaus, Physical Properties of Carbon Nanotubes, PUBLISHED BY IMPERIAL COLLEGE PRESS AND DISTRIBUTED BY WORLD SCIENTIFIC PUBLISHING CO., London, 1998. https://doi.org/10.1142/p080.

[127] M.S. Dresselhaus, G. Dresselhaus, R. Saito, Physics of carbon nanotubes, Carbon N Y 33 (1995) 883–891. https://doi.org/10.1016/0008-6223(95)00017-8.

[128] V. Popov, Carbon nanotubes: properties and application, Materials Science and Engineering: R: Reports 43 (2004) 61–102. https://doi.org/10.1016/j.mser.2003.10.001.

[129] T.W. Ebbesen, Carbon Nanotubes, Annual Review of Materials Science 24 (1994) 235–264. https://doi.org/10.1146/annurev.ms.24.080194.001315.

[130] S. Nasir, M. Hussein, Z. Zainal, N. Yusof, Carbon-Based Nanomaterials/Allotropes: A Glimpse of Their Synthesis, Properties and Some Applications, Materials 11 (2018) 295. https://doi.org/10.3390/ma11020295.

[131] N. Saifuddin, A.Z. Raziah, A.R. Junizah, Carbon Nanotubes: A Review on Structure and Their Interaction with Proteins, J Chem 2013 (2013) 1–18. https://doi.org/10.1155/2013/676815.

[132] M. Moniruzzaman, K.I. Winey, Polymer Nanocomposites Containing Carbon Nanotubes, Macromolecules 39 (2006) 5194–5205. https://doi.org/10.1021/ma060733p.

[133] C. Li, E.T. Thostenson, T.W. Chou, Dominant role of tunneling resistance in the electrical conductivity of carbon nanotube-based composites, Appl Phys Lett 91 (2007) 91–94. https://doi.org/10.1063/1.2819690.

[134] P. Kim, L. Shi, A. Majumdar, P.L. McEuen, Thermal Transport Measurements of Individual Multiwalled Nanotubes, Phys Rev Lett 87 (2001) 215502. https://doi.org/10.1103/PhysRevLett.87.215502.

[135] J.E. Inglesfield, Physics of Graphite, Physics Bulletin 33 (1982) 333–333. https://doi.org/10.1088/0031-9112/33/9/037.

[136] K.Y. Rhee, Electronic and Thermal Properties of Graphene, Nanomaterials 10 (2020) 926. https://doi.org/10.3390/nano10050926.

[137] J.P. Howe, Properties of Graphite, Journal of the American Ceramic Society 35 (1952) 275–283. https://doi.org/10.1111/j.1151-2916.1952.tb13048.x.

[138] K.M.F. Shahil, A.A. Balandin, Thermal properties of graphene and multilayer graphene: Applications in thermal interface materials, Solid State Commun 152 (2012) 1331–1340. https://doi.org/10.1016/j.ssc.2012.04.034.

[139] Z. Yan, D.L. Nika, A.A. Balandin, Thermal properties of graphene and few-layer graphene: applications in electronics, IET Circuits, Devices & Systems 9 (2015) 4–12. https://doi.org/10.1049/iet-cds.2014.0093.

[140] M. Sang, J. Shin, K. Kim, K.J. Yu, Electronic and Thermal Properties of Graphene and Recent Advances in Graphene Based Electronics Applications, Nanomaterials 9 (2019) 374. https://doi.org/10.3390/nano9030374.

[141] J. Renteria, D. Nika, A. Balandin, Graphene Thermal Properties: Applications in Thermal Management and Energy Storage, Applied Sciences 4 (2014) 525–547. https://doi.org/10.3390/app4040525.

[142] E. Pop, V. Varshney, A.K. Roy, Thermal properties of graphene: Fundamentals and applications, MRS Bull 37 (2012) 1273–1281. https://doi.org/10.1557/mrs.2012.203.

[143] A. Hasani, Approaches to Graphene, Carbon Nanotube and Carbon nanohorn, Synthesis, Properties and Applications, Nanoscience & Nanotechnology-Asia 10 (2020) 4–11. https://doi.org/10.2174/2210681208666180904102649.

[144] Arti, Namita, N. Alam, J.R. Ansari, Nanostructures and Fascinating Properties of Carbon Nanohorns, in: Handbook of Functionalized Carbon Nanostructures, Springer International Publishing, Cham, 2024: pp. 351–389. https://doi.org/10.1007/978-3-031-32150-4_10.

[145] J. Hone, M.C. Llaguno, M.J. Biercuk, A.T. Johnson, B. Batlogg, Z. Benes, J.E. Fischer, Thermal properties of carbon nanotubes and nanotube-based materials, Appl Phys A Mater Sci Process 74 (2002) 339–343. https://doi.org/10.1007/s003390201277.

[146] R.S. Ruoff, D.C. Lorents, Mechanical and thermal properties of carbon nanotubes, Carbon N Y 33 (1995) 925–930. https://doi.org/10.1016/0008-6223(95)00021-5.

[147] J. Hone, Carbon Nanotubes: Thermal Properties, in: S.E. Lyshevski (Ed.), Dekker Encyclopedia of Nanoscience and Nanotechnology, 3rd ed., CRC Press, 2011.

[148] G.K. Amudhalapalli, J.K. Devanuri, Synthesis, characterization, thermophysical properties, stability and applications of nanoparticle enhanced phase change materials – A comprehensive review, Thermal Science and Engineering Progress 28 (2022) 101049. https://doi.org/10.1016/j.tsep.2021.101049.

[149] A.A. Balandin, Thermal properties of graphene and nanostructured carbon materials, Nat Mater 10 (2011) 569–581. https://doi.org/10.1038/nmat3064.

[150] J. Kong, C. Zhou, A. Morpurgo, H.T. Soh, C.F. Quate, C. Marcus, H. Dai, Synthesis, integration, and electrical properties of individual single-walled carbon nanotubes, Appl Phys A Mater Sci Process 69 (1999) 305–308. https://doi.org/10.1007/s003390051005.

[151] S.I. Cha, K.T. Kim, K.H. Lee, C.B. Mo, Y.J. Jeong, S.H. Hong, Mechanical and electrical properties of cross-linked carbon nanotubes, Carbon N Y 46 (2008) 482–488. https://doi.org/10.1016/j.carbon.2007.12.023.

[152] J. Bernholc, D. Brenner, M. Buongiorno Nardelli, V. Meunier, C. Roland, Mechanical and Electrical Properties of Nanotubes, Annu Rev Mater Res 32 (2002) 347–375. https://doi.org/10.1146/annurev.matsci.32.112601.134925.

[153] C.-C. Liu, A.B. Walters, M.A. Vannice, Measurement of electrical properties of a carbon black, Carbon N Y 33 (1995) 1699–1708. https://doi.org/10.1016/0008-6223(95)00125-4.

[154] N. Probst, E. Grivei, Structure and electrical properties of carbon black, Carbon N Y 40 (2002) 201–205. https://doi.org/10.1016/S0008-6223(01)00174-9.

[155] S. Garaj, L. Thien-Nga, R. Gaal, L. Forró, K. Takahashi, F. Kokai, M. Yudasaka, S. Iijima, Electronic properties of carbon nanohorns studied by ESR, Phys Rev B 62 (2000) 17115–17119. https://doi.org/10.1103/PhysRevB.62.17115.

[156] A.H. Castro Neto, F. Guinea, N.M.R. Peres, K.S. Novoselov, A.K. Geim, The electronic properties of graphene, Rev Mod Phys 81 (2009) 109–162. https://doi.org/10.1103/RevModPhys.81.109.

[157] A. Maffucci, G. Miano, Electrical Properties of Graphene for Interconnect Applications, Applied Sciences 4 (2014) 305–317. https://doi.org/10.3390/app4020305.

[158] T. Cusati, G. Fiori, A. Gahoi, V. Passi, M.C. Lemme, A. Fortunelli, G. Iannaccone, Electrical properties of graphene-metal contacts, Sci Rep 7 (2017) 5109. https://doi.org/10.1038/s41598-017-05069-7.

[159] G.H. Kinchin, The electrical properties of graphite, Proc R Soc Lond A Math Phys Sci 217 (1953) 9–26. https://doi.org/10.1098/rspa.1953.0043.

[160] M. Yudasaka, S. Iijima, V.H. Crespi, Single-Wall Carbon Nanohorns and Nanocones, in: Topics in Applied Physics, 2007: pp. 605–629. https://doi.org/10.1007/978-3-540-72865-8_19.

[161] P.R. Bandaru, Electrical Properties and Applications of Carbon Nanotube Structures, J Nanosci Nanotechnol 7 (2007) 1239–1267. https://doi.org/10.1166/jnn.2007.307.

[162] A. Kozbial, F. Zhou, Z. Li, H. Liu, L. Li, Are Graphitic Surfaces Hydrophobic?, Acc Chem Res 49 (2016) 2765–2773. https://doi.org/10.1021/acs.accounts.6b00447.

[163] G. Wang, B. Wang, J. Park, J. Yang, X. Shen, J. Yao, Synthesis of enhanced hydrophilic and hydrophobic graphene oxide nanosheets by a solvothermal method, Carbon N Y 47 (2009) 68–72. https://doi.org/10.1016/j.carbon.2008.09.002.

[164] L. Xu, J. Teng, L. Li, H.-D. Huang, J.-Z. Xu, Y. Li, P.-G. Ren, G.-J. Zhong, Z.-M. Li, Hydrophobic Graphene Oxide as a Promising Barrier of Water Vapor for Regenerated Cellulose Nanocomposite Films, ACS Omega 4 (2019) 509–517. https://doi.org/10.1021/acsomega.8b02866.

[165] P. Karfa, S. De, K.C. Majhi, R. Madhuri, P.K. Sharma, Functionalization of Carbon Nanostructures, in: D.L. Andrews, R.H. Lipson, T. Nann (Eds.), Comprehensive Nanoscience and Nanotechnology, Second, Elsevier, 2019: pp. 123–144. https://doi.org/10.1016/B978-0-12-803581-8.11225-1.

[166] S. Bekou, D. Mattia, Wetting of nanotubes, Curr Opin Colloid Interface Sci 16 (2011) 259–265. https://doi.org/10.1016/j.cocis.2011.01.009.

[167] B.A. Kakade, V.K. Pillai, Tuning the Wetting Properties of Multiwalled Carbon Nanotubes by Surface Functionalization, The Journal of Physical Chemistry C 112 (2008) 3183–3186. https://doi.org/10.1021/jp711657f.

[168] E. Dujardin, T.W. Ebbesen, H. Hiura, K. Tanigaki, Capillarity and Wetting of Carbon Nanotubes, Science (1979) 265 (1994) 1850–1852. https://doi.org/10.1126/science.265.5180.1850.

[169] A.H. Barber, S.R. Cohen, H.D. Wagner, Static and Dynamic Wetting Measurements of Single Carbon Nanotubes, Phys Rev Lett 92 (2004) 186103. https://doi.org/10.1103/PhysRevLett.92.186103.

[170] S.-J. Hong, Y.-F. Li, M.-J. Hsiao, Y.-J. Sheng, H.-K. Tsao, Anomalous wetting on a superhydrophobic graphite surface, Appl Phys Lett 100 (2012). https://doi.org/10.1063/1.3697831.

[171] A. Pertsin, M. Grunze, Water−Graphite Interaction and Behavior of Water Near the Graphite Surface, J Phys Chem B 108 (2004) 1357–1364. https://doi.org/10.1021/jp0356968.

[172] J. Driskill, D. Vanzo, D. Bratko, A. Luzar, Wetting transparency of graphene in water, J Chem Phys 141 (2014). https://doi.org/10.1063/1.4895541.

[173] C.-J. Shih, M.S. Strano, D. Blankschtein, Wetting translucency of graphene, Nat Mater 12 (2013) 866–869. https://doi.org/10.1038/nmat3760.

[174] Y. Wang, Y. Zhu, F. Wang, X. Liu, H. Wu, Super-elasticity and deformation mechanism of three-dimensional pillared graphene network structures, Carbon N Y 118 (2017) 588–596. https://doi.org/10.1016/j.carbon.2017.03.092.

[175] F. Scarpa, R. Chowdhury, S. Adhikari, Thickness and in-plane elasticity of graphane, Phys Lett A 375 (2011) 2071–2074. https://doi.org/10.1016/j.physleta.2011.03.050.

[176] A.R. Payne, The elasticity of carbon black networks, J Colloid Sci 19 (1964) 744–754. https://doi.org/10.1016/0095-8522(64)90081-9.

[177] J.P. Lu, Elastic Properties of Carbon Nanotubes and Nanoropes, Phys Rev Lett 79 (1997) 1297–1300. https://doi.org/10.1103/PhysRevLett.79.1297.

[178] I. Palaci, S. Fedrigo, H. Brune, C. Klinke, M. Chen, E. Riedo, Radial Elasticity of Multiwalled Carbon Nanotubes, Phys Rev Lett 94 (2005) 175502. https://doi.org/10.1103/PhysRevLett.94.175502.

[179] V.N. Popov, V.E. Van Doren, M. Balkanski, Elastic properties of single-walled carbon nanotubes, Phys Rev B 61 (2000) 3078–3084. https://doi.org/10.1103/PhysRevB.61.3078.

[180] C. Goze, L. Vaccarini, L. Henrard, P. Bernier, E. Hemandez, A. Rubio, Elastic and mechanical properties of carbon nanotubes, Synth Met 103 (1999) 2500–2501. https://doi.org/10.1016/S0379-6779(98)01071-6.

[181] D. Kumar, V. Verma, K. Dharamvir, H.S. Bhatti, S.K. Tripathi, K. Dharamvir, R. Kumar, G.S.S. Saini, Structure and Strength of Carbon Nanohorns, in: 2011: pp. 207–208. https://doi.org/10.1063/1.3653682.

[182] M.L. Studebaker, The Chemistry of Carbon Black and Reinforcement, Rubber Chemistry and Technology 30 (1957) 1400–1483. https://doi.org/10.5254/1.3542764.

[183] M.-J. Wang, C.A. Gray, S.A. Reznek, K. Mahmud, Y. Kutsovsky, Carbon Black, in: Kirk-Othmer Encyclopedia of Chemical Technology, John Wiley & Sons, Inc., Hoboken, NJ, USA, 2003. https://doi.org/10.1002/0471238961.0301180204011414.a01.pub2.

[184] Y. Butenko, L. Šiller, M.R.C. Hunt, Carbon Onions, in: Nanomaterials Handbook, 2nd ed., CRC Press, 2017.

[185] J.K. McDonough, Y. Gogotsi, Carbon Onions: Synthesis and Electrochemical Applications, Interface Magazine 22 (2013) 61–66. https://doi.org/10.1149/2.F05133if.

[186] M.E. Plonska-Brzezinska, Carbon Nano-Onions: A Review of Recent Progress in Synthesis and Applications, ChemNanoMat 5 (2019) 568–580. https://doi.org/10.1002/cnma.201800583.

[187] C.N.R. Rao, K. Biswas, K.S. Subrahmanyam, A. Govindaraj, Graphene, the new nanocarbon, J Mater Chem 19 (2009) 2457. https://doi.org/10.1039/b815239j.

[188] A.K. Geim, Graphene: Status and Prospects, Science (1979) 324 (2009) 1530–1534. https://doi.org/10.1126/science.1158877.

[189] W. Choi, I. Lahiri, R. Seelaboyina, Y.S. Kang, Synthesis of Graphene and Its Applications: A Review, Critical Reviews in Solid State and Materials Sciences 35 (2010) 52–71. https://doi.org/10.1080/10408430903505036.

[190] A. Jiménez-Suárez, S.G. Prolongo, Graphene Nanoplatelets, Applied Sciences 10 (2020) 1753. https://doi.org/10.3390/app10051753.

[191] C. Botas, P. Álvarez, P. Blanco, M. Granda, C. Blanco, R. Santamaría, L.J. Romasanta, R. Verdejo, M.A. López-Manchado, R. Menéndez, Graphene materials with different structures prepared from the same graphite by the Hummers and Brodie methods, Carbon N Y 65 (2013) 156–164. https://doi.org/10.1016/j.carbon.2013.08.009.

[192] N.I. Zaaba, K.L. Foo, U. Hashim, S.J. Tan, W.-W. Liu, C.H. Voon, Synthesis of Graphene Oxide using Modified Hummers Method: Solvent Influence, Procedia Eng 184 (2017) 469–477. https://doi.org/10.1016/j.proeng.2017.04.118.

[193] Md.S.A. Bhuyan, Md.N. Uddin, Md.M. Islam, F.A. Bipasha, S.S. Hossain, Synthesis of graphene, Int Nano Lett 6 (2016) 65–83. https://doi.org/10.1007/s40089-015-0176-1.

[194] Y. Zhu, S. Murali, W. Cai, X. Li, J.W. Suk, J.R. Potts, R.S. Ruoff, Graphene and Graphene Oxide: Synthesis, Properties, and Applications, Advanced Materials 22 (2010) 3906–3924. https://doi.org/10.1002/adma.201001068.

[195] M. Zeiger, N. Jäckel, M. Aslan, D. Weingarth, V. Presser, Understanding structure and porosity of nanodiamond-derived carbon onions, Carbon N Y 84 (2015) 584–598. https://doi.org/10.1016/j.carbon.2014.12.050.

[196] L. Reinert, M. Zeiger, S. Suárez, V. Presser, F. Mücklich, Dispersion analysis of carbon nanotubes, carbon onions, and nanodiamonds for their application as reinforcement phase in nickel metal matrix composites, RSC Adv 5 (2015) 95149–95159. https://doi.org/10.1039/C5RA14310A.

[197] S.R. Bakshi, D. Lahiri, A. Agarwal, Carbon nanotube reinforced metal matrix composites - a review, International Materials Reviews 55 (2010) 41–64. https://doi.org/10.1179/095066009X12572530170543.

[198] M. Wang, N. Pan, Predictions of effective physical properties of complex multiphase materials, Materials Science and Engineering: R: Reports 63 (2008) 1–30. https://doi.org/10.1016/j.mser.2008.07.001.

[199] N. Pierard, A. Fonseca, J.-F. Colomer, C. Bossuot, J.-M. Benoit, G. Van Tendeloo, J.-P. Pirard, J.B. Nagy, Ball milling effect on the structure of single-wall carbon nanotubes, Carbon N Y 42 (2004) 1691–1697. https://doi.org/10.1016/j.carbon.2004.02.031.

[200] N. Pierard, A. Fonseca, Z. Konya, I. Willems, G. Van Tendeloo, J. B.Nagy, Production of short carbon nanotubes with open tips by ball milling, Chem Phys Lett 335 (2001) 1–8. https://doi.org/10.1016/S0009-2614(01)00004-5.

[201] J.-Y. Lee, K.-H. Cho, D.-P. Lim, Y.-B. Lee, D.-S. Lim, Effect of attrition milling on dispersion of onion like carbon in aqueous medium, Applied Physics A 88 (2007) 693–697. https://doi.org/10.1007/s00339-007-4029-2.

[202] F. Avilés, J.V. Cauich-Rodríguez, L. Moo-Tah, A. May-Pat, R. Vargas-Coronado, Evaluation of mild acid oxidation treatments for MWCNT functionalization, Carbon N Y 47 (2009) 2970–2975. https://doi.org/10.1016/j.carbon.2009.06.044.

[203] N. Karousis, N. Tagmatarchis, D. Tasis, Current Progress on the Chemical Modification of Carbon Nanotubes, Chem Rev 110 (2010) 5366–5397. https://doi.org/10.1021/cr100018g.

[204] G. Tuci, C. Zafferoni, A. Rossin, A. Milella, L. Luconi, M. Innocenti, L. Truong Phuoc, C. Duong-Viet, C. Pham-Huu, G. Giambastiani, Chemically Functionalized Carbon Nanotubes with Pyridine Groups as Easily Tunable N-Decorated Nanomaterials for the Oxygen Reduction Reaction in Alkaline Medium, Chemistry of Materials 26 (2014) 3460–3470. https://doi.org/10.1021/cm500805c.

[205] I. Singh, P. Sabita, V.A. Altekar, Silver tarnishing and its prevention — A review, Anti-Corrosion Methods and Materials 30 (1983) 4–8. https://doi.org/10.1108/eb007223.

[206] K.E. Trinh, F. Mücklich, E. Ramos-Moore, The role of microstructure and surface topography in the electrical behavior of Sn-coated Cu contacts, in: 27th International Conference on Electrical Contacts, ICEC 2014 - Proceedings, IEEE, Dresden, 2014: pp. 243–248.

[207] K.E. Trinh, A. Tsipenyuk, M. Varenberg, A. Rosenkranz, N. Souza, F. Mücklich, Wear debris and electrical resistance in textured Sn-coated Cu contacts subjected to fretting, Wear 344–345 (2015) 86–98. https://doi.org/10.1016/j.wear.2015.10.010.

[208] K.E. Trinh, E. Ramos-Moore, I. Green, C. Pauly, M. Zamanzade, F. Mücklich, Topographical and Microstructural Effects of Laser Surface Texturing on Tin-Coated Copper Electrical Connectors Under Load Cycling, IEEE Trans Compon Packaging Manuf Technol 7 (2017) 582–590. https://doi.org/10.1109/TCPMT.2017.2659224.

[209] A. Thome, C. Schafer, F. Bonner, A. Herges, S.D. Schuetz, D. Britz, F. Mucklich, S. Suarez, Methodical approach for tribo-electrical and topographical tailoring of Cu-Sn connectors with extended direct laser interference patterning, in: 2022 IEEE 67th Holm Conference on Electrical Contacts (HLM), IEEE, 2022: pp. 1–6. https://doi.org/10.1109/HLM54538.2022.9969772.

[210] F.L. LaQue, Protection by Metallic Coatings, Transactions of the IMF 42 (1964) 1–13. https://doi.org/10.1080/00202967.1964.11869905.

[211] F. Presuel-Moreno, M.A. Jakab, N. Tailleart, M. Goldman, J.R. Scully, Corrosion-resistant metallic coatings, Materials Today 11 (2008) 14–23. https://doi.org/10.1016/S1369-7021(08)70203-7.

[212] Metallic Coatings for Corrosion Control, Elsevier, 1977. https://doi.org/10.1016/C2013-0-06266-4.

[213] I. Buresch, Möglichkeiten der Eigenschaftesoptimierung von Zinnoberflächen für Steckkontakt, in: Kontaktverhalten Und Shalten - 22. Fachtagung Albert-Keil-Kontaktseminar, VDE Verlag GmbH, Karlsruhe, 2013: p. 6.

[214] Z. Mei, A.J. Sunwoo, J.W. Morris, Analysis of low-temperature intermetallic growth in copper-tin diffusion couples, Metallurgical Transactions A 23 (1992) 857–864. https://doi.org/10.1007/BF02675563.

[215] I. Buresch, M. Hack, Eigenschaften von Zinnschichten für elektromechanische Bauelemente - Einflussfaktoren und ihre Auswirkungen, in: Kontaktverhalten Und Shalten - 20. Fachtagung Albert-Keil-Kontaktseminar, VDE Verlag GmbH, Karlsruhe, 2009: pp. 23–30.

[216] ASM International, Welding, Brazing, and Soldering, ASM International, 1993. https://doi.org/10.31399/asm.hb.v06.9781627081733.

[217] S.F. Etris, Silver and Silver Alloys, in: Kirk-Othmer Encyclopedia of Chemical Technology, Wiley, 2010: pp. 1–43. https://doi.org/10.1002/0471238961.1909122205201809.a01.pub3.

[218] H. Endres, Praxishandbuch Steckverbinder, 2nd. Ed., Vogel COmmunications Group, Würzburg, 2021.

[219] F. Findik, H. Uzun, Microstructure, hardness and electrical properties of silver-based refractory contact materials, Mater Des 24 (2003) 489–492. https://doi.org/10.1016/S0261-3069(03)00125-0.

[220] C. Wu, D. Yi, W. Weng, S. Li, J. Zhou, F. Zheng, Arc erosion behavior of Ag/Ni electrical contact materials, Mater Des 85 (2015) 511–519. https://doi.org/10.1016/j.matdes.2015.06.142.

[221] J.-H. Chen, S. Chen, M. Xie, J.-Q. Hu, S.-B. Wang, High-speed imaging observation on molten bridges of AgNi10 electrical contact material, Rare Metals 42 (2023) 336–345. https://doi.org/10.1007/s12598-017-0911-z.

[222] X. Yuan, F. Fu, R. He, Graphene-enhanced silver composites for electrical contacts: a review, J Mater Sci 59 (2024) 3762–3779. https://doi.org/10.1007/s10853-024-09473-z.

[223] G. Genchi, M.S. Sinicropi, G. Lauria, A. Carocci, A. Catalano, The Effects of Cadmium Toxicity, Int J Environ Res Public Health 17 (2020) 3782. https://doi.org/10.3390/ijerph17113782.

[224] H. Wang, J. Wang, J. Du, F. Meng, Influence of Rare Earth on the Wetting Ability of AgSnO2 Contact Material, Rare Metal Materials and Engineering 43 (2014) 1846–1849. https://doi.org/10.1016/S1875-5372(14)60143-0.

[225] C. Selzner, F. Mücklich, New microstructure investigations of arc damaged silver/tinoxide electrodes by means of FIB-technique, in: The 27th International Conference on Electrical Contacts, IEEE, Dresden, 2014: pp. 1–5.

[226] A. Verma, T.R. Anantharaman, Internal oxidation of rapidly solidified silver-tin-indium alloy powders, J Mater Sci 27 (1992) 5623–5628. https://doi.org/10.1007/BF00541633.

[227] V. Behrens, Th. Honig, A. Kraus, E. Mahle, R. Michal, K.E. Saeger, Test results of different silver/graphite contact materials in regard to applications in circuit breakers, in: Electrical Contacts - 1995. Proceedings of the Forty-First IEEE Holm Conference on Electrical Contacts, IEEE, 1995: pp. 393–397. https://doi.org/10.1109/HOLM.1995.482896.

[228] R. Michal, K.E. Saegar, Metallurgical aspects of silver-based contact materials for air-break switching devices for power engineering, IEEE Transactions on Components, Hybrids, and Manufacturing Technology 12 (1989) 71–81. https://doi.org/10.1109/33.19015.

[229] P. Wingert, R. Bevington, G. Horn, The effect of graphite additions on the performance of silver-nickel contacts, in: Thirty-Sixth IEEE Conference on Electrical Contacts, and the Fifteenth International Conference on Electrical Contacts, IEEE, 1990: pp. 524–529. https://doi.org/10.1109/HOLM.1990.113053.

[230] E. Shobert, Carbon, Graphite, and Contacts, IEEE Transactions on Parts, Hybrids, and Packaging 12 (1976) 62–74. https://doi.org/10.1109/TPHP.1976.1135101.

[231] P. Jiang, F. Li, Y. Wang, Effect of different types of carbon on microstructure and arcing behavior of Ag/C contact materials, IEEE Transactions on Components and Packaging Technologies 29 (2006) 420–423. https://doi.org/10.1109/TCAPT.2006.875873.

[232] W. Xie, G. Wu, Z. Yang, P. She, H. Wang, H. Zuo, W. Wei, G. Gao, C. Tu, Study on the erosion characteristics of copper-carbon electrode pairs by DC air arc, High Voltage 6 (2021) 674–683. https://doi.org/10.1049/hve2.12124.

[233] K. Sawa, T. Ueno, K. Nakano, Evaluation of Arc Erosion of Cu-graphite Brush Used in Small DC Motors with and without Quenching Device, in: 2020 IEEE 66th Holm Conference on Electrical Contacts and Intensive Course (HLM), IEEE, 2020: pp. 170–175. https://doi.org/10.1109/HLM49214.2020.9307855.

[234] P.C. Wingert, The effects of interrupting elevated currents on the erosion and structure of silver-graphite, in: Electrical Contacts - 1996. Proceedings of the Forty-Second IEEE Holm Conference on Electrical Contacts. Joint with the 18th International Conference on Electrical Contacts, IEEE, 1996: pp. 60–69. https://doi.org/10.1109/HOLM.1996.557180.

[235] B. Fotovvati, N. Namdari, A. Dehghanghadikolaei, On Coating Techniques for Surface Protection: A Review, Journal of Manufacturing and Materials Processing 3 (2019) 28. https://doi.org/10.3390/jmmp3010028.

[236] L. Quintino, Overview of coating technologies, in: Surface Modification by Solid State Processing, Elsevier, 2014: pp. 1–24. https://doi.org/10.1533/9780857094698.1.

[237] A.R. Boccaccini, J. Cho, J.A. Roether, B.J.C. Thomas, E. Jane Minay, M.S.P. Shaffer, Electrophoretic deposition of carbon nanotubes, Carbon N Y 44 (2006) 3149–3160. https://doi.org/10.1016/j.carbon.2006.06.021.

[238] M. Atiq Ur Rehman, Q. Chen, A. Braem, M.S.P. Shaffer, A.R. Boccaccini, Electrophoretic deposition of carbon nanotubes: recent progress and remaining challenges, International Materials Reviews 66 (2021) 533–562. https://doi.org/10.1080/09506608.2020.1831299.

[239] A. Boccaccini, J.A. Roether, B.J.C. Thomas, M.S.P. Shaffer, E. Chavez, E. Stoll, E.J. Minay, The Electrophoretic Deposition of Inorganic Nanoscaled Materials -A Review-, Journal of the Ceramic Society of Japan 114 (2006) 1–14. https://doi.org/10.2109/jcersj.114.1.

[240] J. Cho, K. Konopka, K. Rożniatowski, E. García-Lecina, M.S.P. Shaffer, A.R. Boccaccini, Characterisation of carbon nanotube films deposited by electrophoretic deposition, Carbon N Y 47 (2009) 58–67. https://doi.org/10.1016/j.carbon.2008.08.028.

[241] I. Corni, M.P. Ryan, A.R. Boccaccini, Electrophoretic deposition: From traditional ceramics to nanotechnology, J Eur Ceram Soc 28 (2008) 1353–1367. https://doi.org/10.1016/j.jeurceramsoc.2007.12.011.

[242] B.J.C. Thomas, A.R. Boccaccini, M.S.P. Shaffer, Multi-walled carbon nanotube coatings using Electrophoretic Deposition (EPD), Journal of the American Ceramic Society 88 (2005) 980–982. https://doi.org/10.1111/j.1551-2916.2005.00155.x.

[243] P.L. Dickrell, S.B. Sinnott, D.W. Hahn, N.R. Raravikar, L.S. Schadler, P.M. Ajayan, W.G. Sawyer, Frictional anisotropy of oriented carbon nanotube surfaces, Tribol Lett 18 (2005) 59–62. https://doi.org/10.1007/s11249-004-1752-0.

[244] P.L. Dickrell, S.K. Pal, G.R. Bourne, C. Muratore, A.A. Voevodin, P.M. Ajayan, L.S. Schadler, W.G. Sawyer, Tunable friction behavior of oriented carbon nanotube films, Tribol Lett 24 (2006) 85–90. https://doi.org/10.1007/s11249-006-9162-0.

[245] J. Puetz, M.A. Aegerter, Dip Coating Technique, in: Sol-Gel Technologies for Glass Producers and Users, Springer US, Boston, MA, 2004: pp. 37–48. https://doi.org/10.1007/978-0-387-88953-5_3.

[246] K. Kalantar-Zadeh, B. Fry, Spin Coating and Drop Casting, in: Nanotechnology-Enabled Sensors, Springer US, 2008.

[247] J.F. Taylor, Spin coating: An overview, Metal Finishing 99 (2001) 16–21. https://doi.org/10.1016/S0026-0576(01)80527-4.

[248] L.E. Scriven, Physics and Applications of DIP Coating and Spin Coating, MRS Proceedings 121 (1988) 717. https://doi.org/10.1557/PROC-121-717.

[249] L.E. Scriven, C.V. Sternling, The Marangoni Effects, Nature 187 (1960) 186–188. https://doi.org/10.1038/187186a0.

[250] J. Zhang, J. Milzetti, F. Leroy, F. Müller-Plathe, Formation of coffee-stain patterns at the nanoscale: The role of nanoparticle solubility and solvent evaporation rate, Journal of Chemical Physics 146 (2017). https://doi.org/10.1063/1.4978284.

[251] M. Schmitt, H. Stark, Marangoni flow at droplet interfaces: Three-dimensional solution and applications, Physics of Fluids 28 (2016). https://doi.org/10.1063/1.4939212.

[252] A. Denneulin, J. Bras, F. Carcone, C. Neuman, A. Blayo, Impact of ink formulation on carbon nanotube network organization within inkjet printed conductive films, Carbon N Y 49 (2011) 2603–2614. https://doi.org/10.1016/j.carbon.2011.02.012.

[253] L. BESRA, M. LIU, A review on fundamentals and applications of electrophoretic deposition (EPD), Prog Mater Sci 52 (2007) 1–61. https://doi.org/10.1016/j.pmatsci.2006.07.001.

[254] L. Reinert, F. Lasserre, C. Gachot, P. Grützmacher, T. MacLucas, N. Souza, F. Mücklich, S. Suarez, Long-lasting solid lubrication by CNT-coated patterned surfaces, Sci Rep 7 (2017) 42873. https://doi.org/10.1038/srep42873.

[255] C. Schäfer, L. Reinert, T. MacLucas, P. Grützmacher, R. Merz, F. Mücklich, S. Suarez, Influence of Surface Design on the Solid Lubricity of Carbon Nanotubes-Coated Steel Surfaces, Tribol Lett 66 (2018) 89. https://doi.org/10.1007/s11249-018-1044-8.

[256] L. Reinert, S. Schütz, S. Suárez, F. Mücklich, Influence of Surface Roughness on the Lubrication Effect of Carbon Nanoparticle-Coated Steel Surfaces, Tribol Lett 66 (2018) 45. https://doi.org/10.1007/s11249-018-1001-6.

[257] T. MacLucas, A. Klemenz, P. Grünewald, V. Presser, L. Mayrhofer, G. Moras, S. Suarez, M. Dienwiebel, F. Mücklich, M. Moseler, Multiwall Carbon Nanotubes for Solid Lubrication of Highly Loaded Contacts, ACS Appl Nano Mater 6 (2023) 1755–1769. https://doi.org/10.1021/acsanm.2c04729.

[258] T. MacLucas, P. Grützmacher, S. Husmann, J. Schmauch, S. Keskin, S. Suarez, V. Presser, C. Gachot, F. Mücklich, Degradation analysis of tribologically loaded carbon nanotubes and carbon onions, Npj Mater Degrad 7 (2023). https://doi.org/10.1038/s41529-023-00346-5.

[259] T. MacLucas, P.G. Grützmacher, P. Leonhard-Trautmann, S. Suarez, C. Gachot, F. Mücklich, Combining Carbon Nanoparticle Coatings and Laser Surface Texturing for Enhanced Lubricity Under High Loads, Tribol Lett 72 (2024) 38. https://doi.org/10.1007/s11249-024-01837-5.

[260] T. MacLucas, S. Schütz, S. Suarez, F. Mücklich, Surface protection of austenitic steels by carbon nanotube coatings, Surf Topogr 6 (2018) 014005. https://doi.org/10.1088/2051-672X/aab145.

[261] T. MacLucas, P. Leonhard-Trautmann, S. Suarez, F. Mücklich, Long-Term Lubricity of Carbon Nanoparticle Coatings on Periodically Laser-Patterned Metallic Surfaces, Tribol Lett 70 (2022) 123. https://doi.org/10.1007/s11249-022-01667-3.

[262] T. Maclucas, L. Daut, P. Grützmacher, M.A. Guitar, V. Presser, C. Gachot, S. Suarez, F. Mücklich, Influence of structural depth of laser-patterned steel surfaces on the solid lubricity of carbon nanoparticle coatings, Friction 11 (2023) 1276–1291. https://doi.org/10.1007/s40544-022-0664-z.

[263] T. MacLucas, S. Suarez, On the Solid Lubricity of Electrophoretically Deposited Carbon Nanohorn Coatings, Lubricants 7 (2019) 62. https://doi.org/10.3390/lubricants7080062.

[264] T.W. Ebbesen, H.J. Lezec, H. Hiura, J.W. Bennett, H.F. Ghaemi, T. Thio, Electrical conductivity of individual carbon nanotubes, Nature 382 (1996) 54–56. https://doi.org/10.1038/382054a0.

[265] J. Sánchez-González, A. Macías-García, M.F. Alexandre-Franco, V. Gómez-Serrano, Electrical conductivity of carbon blacks under compression, Carbon N Y 43 (2005) 741–747. https://doi.org/10.1016/j.carbon.2004.10.045.

[266] B. Alderete, T. MacLucas, D. Espin, S.P. Brühl, F. Mücklich, S. Suarez, Near Superhydrophobic Carbon Nanotube Coatings Obtained via Electrophoretic Deposition on Low-Alloy Steels, Adv Eng Mater 23 (2021) 2001448. https://doi.org/10.1002/adem.202001448.

[267] B.C. Kandpal, J. Kumar, H. Singh, Production technologies of metal matrix composites - A review, in: 4th International Conference on Advances in Materials and Manufacturing Technology, Punjab, 2014: pp. 60–67.

[268] N. Kumar, A. Bharti, M. Dixit, A. Nigam, Effect of Powder Metallurgy Process and its Parameters on the Mechanical and Electrical Properties of Copper-Based Materials: Literature Review, Powder Metallurgy and Metal Ceramics 59 (2020) 401–410. https://doi.org/10.1007/s11106-020-00174-1.

[269] P. Rossi, S. Suarez, F. Soldera, F. Mücklich, Quantitative Assessment of the Reinforcement Distribution Homogeneity in CNT/Metal Composites, Adv Eng Mater 17 (2015) 1017–1021. https://doi.org/10.1002/adem.201400352.

[270] S. Suarez, F. Lasserre, O. Prat, F. Mücklich, Processing and interfacial reaction evaluation in MWCNT/Ni composites, Physica Status Solidi (a) 211 (2014) 1555–1561. https://doi.org/10.1002/pssa.201431018.

[271] S. Suárez, L. Reinert, F. Mücklich, Carbon Nanotube (CNT)-Reinforced Metal Matrix Bulk Composites: Manufacturing and Evaluation, in: Mahmood. Aliofkhazraei (Ed.), Diamond and Carbon Composites and Nanocomposites, InTech, 2016: p. 182. https://doi.org/10.5772/63886.

[272] P.C. Angelo, R. Subramanian, B. Ravisankar, Powder Metallurgy: Science, Technology and Applications, 2nd ed., PHI Learning Pvt. Ltd., 2022.

[273] G. Fernlund, J. Wells, L. Fahrang, J. Kay, A. Poursartip, Causes and remedies for porosity in composite manufacturing, IOP Conf Ser Mater Sci Eng 139 (2016) 012002. https://doi.org/10.1088/1757-899X/139/1/012002.

[274] S. Tang, R. Ummethala, C. Suryanarayana, J. Eckert, K.G. Prashanth, Z. Wang, Additive Manufacturing of Aluminum-Based Metal Matrix Composites—A Review, Adv Eng Mater 23 (2021). https://doi.org/10.1002/adem.202100053.

[275] J. Shi, Y. Wang, Development of metal matrix composites by laser-assisted additive manufacturing technologies: a review, J Mater Sci 55 (2020) 9883–9917. https://doi.org/10.1007/s10853-020-04730-3.

[276] A. Mussatto, I.U. Ahad, R.T. Mousavian, Y. Delaure, D. Brabazon, Advanced production routes for metal matrix composites, Engineering Reports 3 (2021). https://doi.org/10.1002/eng2.12330.

[277] D. Gu, X. Rao, D. Dai, C. Ma, L. Xi, K. Lin, Laser additive manufacturing of carbon nanotubes (CNTs) reinforced aluminum matrix nanocomposites: Processing optimization, microstructure evolution and mechanical properties, Addit Manuf 29 (2019) 100801. https://doi.org/10.1016/j.addma.2019.100801.

[278] M. Dadkhah, M.H. Mosallanejad, L. Iuliano, A. Saboori, A Comprehensive Overview on the Latest Progress in the Additive Manufacturing of Metal Matrix Composites: Potential, Challenges, and Feasible Solutions, Acta Metallurgica Sinica (English Letters) 34 (2021) 1173–1200. https://doi.org/10.1007/s40195-021-01249-7.

[279] S. Suárez, E. Ramos-Moore, F. Mücklich, A high temperature X-ray diffraction study of the influence of MWCNTs on the thermal expansion of MWCNT/Ni composites, Carbon N Y 51 (2013) 404–409. https://doi.org/10.1016/j.carbon.2012.09.002.

[280] S. Suárez, F. Soldera, C.G. Oliver, D. Acevedo, F. Mücklich, Thermomechanical Behavior of Bulk Ni/MWNT Composites Produced via Powder Metallurgy, Adv Eng Mater 14 (2012) 499–502. https://doi.org/10.1002/adem.201200100.

[281] W. Zhou, T. Yamaguchi, K. Kikuchi, N. Nomura, A. Kawasaki, Effectively enhanced load transfer by interfacial reactions in multi-walled carbon nanotube reinforced Al matrix composites, Acta Mater 125 (2017) 369–376. https://doi.org/10.1016/j.actamat.2016.12.022.

[282] S. Zhao, Z. Zheng, Z. Huang, S. Dong, P. Luo, Z. Zhang, Y. Wang, Cu matrix composites reinforced with aligned carbon nanotubes: Mechanical, electrical and thermal properties, Materials Science and Engineering: A 675 (2016) 82–91. https://doi.org/10.1016/j.msea.2016.08.044.

[283] S. Suarez, F. Lasserre, F. Mücklich, Mechanical properties of MWNT/Ni bulk composites: Influence of the microstructural refinement on the hardness, Materials Science and Engineering: A 587 (2013) 381–386. https://doi.org/10.1016/j.msea.2013.08.058.

[284] S. Suárez, E. Ramos-Moore, B. Lechthaler, F. Mücklich, Grain growth analysis of multiwalled carbon nanotube-reinforced bulk Ni composites, Carbon N Y 70 (2014) 173–178. https://doi.org/10.1016/j.carbon.2013.12.089.

[285] J.G. Park, D.H. Keum, Y.H. Lee, Strengthening mechanisms in carbon nanotube-reinforced aluminum composites, Carbon N Y 95 (2015) 690–698. https://doi.org/10.1016/j.carbon.2015.08.112.

[286] S. Simões, F. Viana, M.A.L. Reis, M.F. Vieira, Influence of dispersion/mixture time on mechanical properties of Al–CNTs nanocomposites, Compos Struct 126 (2015) 114–122. https://doi.org/10.1016/j.compstruct.2015.02.062.

[287] P.-C. Tsai, Y.-R. Jeng, J.-T. Lee, I. Stachiv, P. Sittner, Effects of carbon nanotube reinforcement and grain size refinement mechanical properties and wear behaviors of carbon nanotube/copper composites, Diam Relat Mater 74 (2017) 197–204. https://doi.org/10.1016/j.diamond.2017.03.012.

[288] H. Deng, J. Yi, C. Xia, Y. Yi, Mechanical properties and microstructure characterization of well-dispersed carbon nanotubes reinforced copper matrix composites, J Alloys Compd 727 (2017) 260–268. https://doi.org/10.1016/j.jallcom.2017.08.131.

[289] A. Bachmaier, A. Katzensteiner, S. Wurster, K. Aristizabal, S. Suarez, R. Pippan, Thermal stabilization of metal matrix nanocomposites by nanocarbon reinforcements, Scr Mater 186 (2020) 202–207. https://doi.org/10.1016/j.scriptamat.2020.05.014.

[290] B. Chen, S. Li, H. Imai, L. Jia, J. Umeda, M. Takahashi, K. Kondoh, Carbon nanotube induced microstructural characteristics in powder metallurgy Al matrix composites and their effects on mechanical and conductive properties, J Alloys Compd 651 (2015) 608–615. https://doi.org/10.1016/j.jallcom.2015.08.178.

[291] L. Reinert, I. Green, S. Gimmler, B. Lechthaler, F. Mücklich, S. Suárez, Tribological behavior of self-lubricating carbon nanoparticle reinforced metal matrix composites, Wear 408–409 (2018) 72–85. https://doi.org/10.1016/j.wear.2018.05.003.

[292] L. Reinert, S. Suarez, T. Müller, F. Mücklich, Carbon Nanoparticle-Reinforced Metal Matrix Composites: Microstructural Tailoring and Predictive Modeling , Adv Eng Mater 19 (2017). https://doi.org/10.1002/adem.201600750.

[293] L. Reinert, S. Suárez, A. Rosenkranz, Tribo-Mechanisms of Carbon Nanotubes: Friction and Wear Behavior of CNT-Reinforced Nickel Matrix Composites and CNT-Coated Bulk Nickel, Lubricants 4 (2016) 11. https://doi.org/10.3390/lubricants4020011.

[294] S. Suárez, A. Rosenkranz, C. Gachot, F. Mücklich, Enhanced tribological properties of MWCNT/Ni bulk composites – Influence of processing on friction and wear behaviour, Carbon N Y 66 (2014) 164–171. https://doi.org/10.1016/j.carbon.2013.08.054.

[295] J.P. Tu, Y.Z. Yang, L.Y. Wang, X.C. Ma, X.B. Zhang, Tribological properties of carbon-nanotube-reinforced copper composites, Tribol Lett 10 (2001) 225–228. https://doi.org/10.1023/A:1016662114589.

[296] L.A. Batista, M.D.V. Felisberto, L.S. Silva, T.H.R. da Cunha, E.M. Mazzer, Influence of multi-walled carbon nanotubes reinforcements on hardness and abrasion behaviour of porous Al-matrix composite processed by cold pressing and sintering, J Alloys Compd 791 (2019) 96–99. https://doi.org/10.1016/j.jallcom.2019.03.265.

[297] D. García, S. Suárez, K. Aristizábal, F. Mücklich, Powder-Metallurgical Fabrication and Electrical Contact Resistance Characterization of Copper–Nickel Composites Reinforced by Multiwalled Carbon Nanotubes, Adv Eng Mater 24 (2022) 2100755. https://doi.org/10.1002/adem.202100755.

[298] S. Suarez, N. Souza, F. Lasserre, F. Mücklich, Influence of the Reinforcement Distribution and Interface on the Electronic Transport Properties of MWCNT-Reinforced Metal Matrix Composites , Adv Eng Mater 18 (2016) 1626–1633. https://doi.org/10.1002/adem.201600216.

[299] S. Suarez, R. Puyol, C. Schafer, F. Mucklich, Carbon Nanotube-reinforced Metal Matrix Composites as Novel Electrodes for Low-voltage Switching Applications: A Surface Degradation Analysis, in: 2019 IEEE Holm Conference on Electrical Contacts, IEEE, 2019: pp. 135–141. https://doi.org/10.1109/HOLM.2019.8923921.

[300] J.W. McBride, E.M. Yunus, S.M. Spearing, Gold Coated Multi-Walled Carbon Nanotube Surfaces As Low Force Electrical Contacts for MEMS Devices: Part 1, in: 2009 Proceedings of the 55th IEEE Holm Conference on Electrical Contacts, IEEE, 2009: pp. 281–287. https://doi.org/10.1109/HOLM.2009.5284389.

[301] J.W. McBride, S.M. Spearing, L. Jiang, C. Chianrabutra, Gold Coated Carbon-Nanotube Surfaces as Low Force Electrical Contacts for MEMS Devices: Part II, Fine Transfer Mechanisms, in: 2011 IEEE 57th Holm Conference on Electrical Contacts (Holm), IEEE, 2011: pp. 1–6. https://doi.org/10.1109/HOLM.2011.6034800.

[302] M.P. Down, R. Cook, L. Jiang, J.W. McBride, Mechanical Characterisation and Optimisation of Carbon Nanotube Composite Surfaces for Electrical Contacts, in: 27th International Conference on Electrical Contacts (ICEC), VDE, Dresden, 2014.

[303] E.M. Yunus, J.W. McBride, S.M. Spearing, Low force electrical switching using gold sputter coated vertically aligned multi-walled carbon nanotubes surfaces, IEICE Technical Report 108 (2008) 61–64.

[304] J.W. McBride, The Wear Processes of Gold Coated Multi-Walled Carbon Nanotube Surfaces Used as Electrical Contacts for Micro-Electro-Mechanical Switching, Nanoscience and Nanotechnology Letters 2 (2010) 357–361. https://doi.org/10.1166/nnl.2010.1109.

[305] F.S.A. Khan, N.M. Mubarak, M. Khalid, M.M. Khan, Y.H. Tan, R. Walvekar, E.C. Abdullah, R.R. Karri, M.E. Rahman, Comprehensive review on carbon nanotubes embedded in different metal and polymer matrix: fabrications and applications, Critical Reviews in Solid State and Materials Sciences 47 (2022) 837–864. https://doi.org/10.1080/10408436.2021.1935713.

[306] N. Silvestre, State-of-the-art Review on Carbon Nanotube Reinforced Metal Matrix Composites, International Journal of Composite Materials 6A (2013) 28–44.

[307] B. Lim, J. Hwang, D. Lee, S. Suh, S. Hong, Fabrication processes and multi-functional applications of carbon nanotube nanocomposites, J Compos Mater 46 (2012) 1731–1737. https://doi.org/10.1177/0021998311424324.

[308] S.C. Tjong, Recent progress in the development and properties of novel metal matrix nanocomposites reinforced with carbon nanotubes and graphene nanosheets, Materials Science and Engineering: R: Reports 74 (2013) 281–350. https://doi.org/10.1016/j.mser.2013.08.001.

[309] W.D.Jr. Callister, Materials Science and Engineering: An Introduction, 7 Ed., John Wiley & Sons, Ltd, 2006.

[310] F.N.H. Robinson, S.B. McGrayne, E.E. Suckling, E. Kashy, electricity, Encyclopedia Britannica (2024). https://www.britannica.com/science/electricity (accessed May 27, 2024).

[311] T.E. of E. Britannica, electron charge, Enyclopedia Britannica (2024).

[312] R.D. Knight, Physics for Scientists and Engineers - A Strategic Approach, 2nd ed., Pearson Addison-Wesley, San Francisco, 2008.

[313] N.W. Ashcroft, N.D. Mermin, Solid State Physics, 1st ed., Holt, Rinehart and Winston, 1976.

[314] R.A. Serway, C.J. Moses, C.A. Moyer, Modern Physics, 3rd ed., Cengage Learning, Belmont, 2004.

LIST OF FIGURES

The figures and tables herein listed correspond to those included in the following sections: MOTIVATION & INTRODUCTION, THEORETICAL FRAMEWORK, STATE OF THE ART, INCLUDED ARTICLES, ANNEX I, and APPENDIX A. Figures and tables corresponding to the appended articles are not included in this section.

Figure 1: a) Global stock of electric vehicles between 2020 and 2023. Copper requirements in b) different passenger vehicle types and c) in power generation. d) Illustration of electrical systems in a BEVs and charging infrastructure. 2

Figure 2: a) Schematic representation of two contacting surfaces. b) Top-down view of the apparent, load-bearing, quasi-metallic, and real contact area between two surfaces at different loads. c) Schematic representation of the current's constriction at a-spots and d) spreading resistance at an a-spot between two bulk conductors (top) and between two thin films (bottom). e) Visualization of constriction and spreading of the current due to differences in the film and bulk materials' resistivity. Subfigure a) was reused and adapted with permission from Gwidon W. Stachowiak and Andrew W. *Batchelor, Engineering* Tribology 2nd Edition, 2000, Butterworth-Heinemann, page 461, Figure 10.12 [43]. Subfigure c), d), and e) were reused and adapted with permission from Paul G. *Slade, Electrical Contacts: Principles and* Applications 2nd Edition, 2017, Taylor & Francis Group, page 5, Figure 1.1, page 19, Figure 1.15, and page 24, Figure 1.19, respectively [22]. 8

Figure 3: Exemplary slope analysis for a tin-plated copper electrode against a hemispherical hard gold coated counter electrode. The shaded areas highlight the different slopes and loading ranges. The slope of regions A and B approach -1, which corresponds to predominantly film resistance and plastic deformation, whereas the slope of region C approaches -1/3, which corresponds to predominantly constriction resistance and elastic deformation. 12

Figure 4. Schematic representation of a) static and b) dynamic adhesive wear, c) two-body and d) three-body abrasive wear. e) Schematic of different types of micro-cutting, micro-plowing, and micro-cracking (from left to right). The arrows indicate the direction in which each body is moving, whereas the dots indicate that the body is moving out of plane. Subfigures a) and e) were reused and adapted with permission from Gwidon W. Stachowiak and Andrew W. Batchelor, Engineering *Tribology 2nd* Edition, 2000, Butterworth-Heinemann, pages 484, Figure 11.1 and page 534, Figure 12.2, respectively [43]. 16

Figure 5. Schematic representation of fretting wear. 19

Figure 6. Schematic representation of the formation of the electrical arc during hot switching. a) Constriction of the current through the a-spots. b) As the moveable electrode retreats, the molten bridges are formed and drawn out. c) Molten bridges become unstable and rupture, emitting metallic vapor into the gap and increasing local pressure. d) The electrical arc ignites, eroding the electrodes through electron and ion bombardment. 21

Figure 7. sp2-hybridized *carbon* nanostructures, classified according to their dimensionality. 0D – Carbon black, onion-like carbon, carbon nanohorns. 1D – Single-walled and multi-walled carbon nanotubes. 2D – Graphene, few-layer graphite, graphene oxide, and graphene nanoplatelets. 3D – Graphite. Schemes made using Nanotube Modeler, © *JCrystalSoft*, Version 1.7.6 (www.jcrystal.com). 27

Figure 8. Schematic representation of HDT/ODT self-assembled monolayer on silver surface, protecting it from sulfidation. Without the passivation layer, silver reacts with atmospheric hydrogen sulfide to produce silver sulfide tarnishing film. 29

Figure 9. Scheme of lubrication between two electrodes and the constriction of the current at the a-spots. 30

Figure 10. Selection criteria for plating material based on connector requirements [213]. 31

Figure 11. Schematic overview of the classifications for each appended article, followed by 41

Figure 12. Schematic overview of appended articles for *materials* classification. 42

Figure 13. Schematic overview of appended articles for *coatings* classification. 43

Figure 14. Schematic overview of appended articles for *composites* classification. 45

Figure A.I.1: Normalized ECR comparing the low-density MMC from ARTICLE XI with the high-density MMC from ARTICLE XII. CNT content: a) 0.5 wt.% and b) 1 wt.%. 308

Figure A.I.2: ECR evolution during fretting wear of low-density silver MMC from ARTICLE XI and high-density MMC from ARTICLE XII. 308

Figure A.I.3: a) SEM and b) magnified macrograph of fretting track i) AgCNT0.5 wt.% and ii) AgCNT1 wt.%. EDS c) carbon, d) silver, and e) gold maps. 309

Figure A.A.1: a) Schematic representation of the sea *of electrons moving* freely in a linear trajectory within a metal in the absence of an electric field. These electrons are bound to the solid, not a particular atom. b) Schematic representation of a conductor within an electric field generated due to a potential difference. Now, the electrons move in a parabolic trajectory, resulting in a net displacement in the opposite direction of the field. The colliding electrons transfer energy to the lattice, thereby increasing the material's temperature. The heat generated Q *is* proportional to the squared current and the resistance of the conductor, known as Joule's law or resistive heating. IV

Figure A.A.2: Resistivity of copper and copper-nickel alloys demonstrating its dependence on purity, deformation state, and temperature. Reused and adapted with permission from William D. Callister, Materials *Science and Engineering: An Introduction 7th* Edition, 2007, John Wiley & Sons, page 675, Figure 18.8 [309]. V

LIST OF TABLES

Table 1 – Electrical resistivity at 20 °C of commonly used metals [22]. 7

Table A.I.1 – Approximate fretting mark dimensions. 309

APPENDIX A

A.1. Electricity

A.1.1. Basic concepts

Electricity is a phenomenon related to the presence and movement of electric charges [310]. Like mass, charge is a fundamental characteristic of matter. All matter is composed of atoms, which are themselves composed of a nucleus consisting of positively charged protons and neutral neutrons. The negatively charged electrons are found in a surrounding orbit around the nucleus. Although protons and electrons have markedly disparate masses, both subatomic particles possess the same and opposite charge: $1.6 \times 10^{-19}\ C$ [311]. In metals, the electrons are weakly bonded to the nuclei, thereby enabling the formation of the so-called *sea of electrons*, which allows these subatomic particles to carry charge [312]. This is based on the semi-classical free electron model of metals proposed by Drude. In this model, the electrons are represented as a gas, where the kinetic theory of gases could be applied to metals [313]. Drude's approach provides an explanation of the electrical conductivity of metals, in which the gas of electrons moves through a fixed lattice of positively charged ion cores [314], with the individual electrons not belonging to any particular atom in the metal.

A.1.2. Conductivity, resistivity, and resistance

The ability of a material to conduct electricity is determined by the strength of the electric field E and the current density J [312]. In a good conductor, an applied electric field will result in a substantial current density within the material. This implies that the field will generate a considerable electron density n_e or a longer mean time between collisions τ_e (analogous to the mean free path between collisions in the kinetic theory of gases). The mean time between collisions is a material property that solely depends on temperature and is not influenced by the strength of the electric field. Conversely, in a poor conductor, the electric field will not generate as large electron density or have a shorter mean time between collisions. This relationship is mathematically expressed in **Equation A.A.1**, where e_c is the charge of an electron and v_d is the drift velocity of electrons. The latter represents the average velocity at which electrons move in the *sea of electrons* due to the presence of an electric field – schematically shown in **Figure A.A.1a**. The drift velocity is superimposed on the thermal motion of electrons. The current density can also be determined using **Equation A.A.1** provided that the electrical current I and the cross section of the conductor A are known. The current is the rate at which charge carriers move within the conductor. This quantity is measured in coulombs per unit area, or amperes (A) in the International System of Units.

$$J = n_e e_c v_d = \sigma E = \frac{I}{A}$$ **Equation A.A.1**

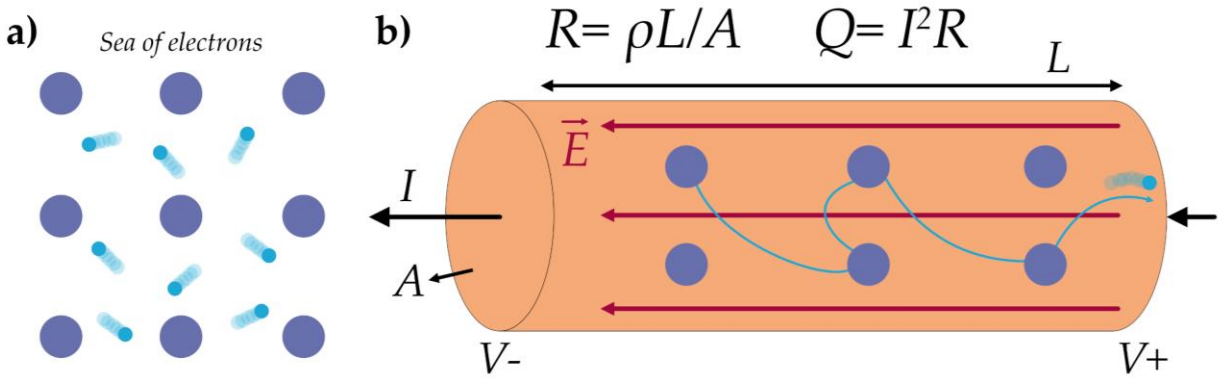

Figure A.A.1: a) Schematic representation of the *sea of electrons* moving freely in a linear trajectory within a metal in the absence of an electric field. These electrons are bound to the solid, not a particular atom. **b)** Schematic representation of a conductor within an electric field generated due to a potential difference. Now, the electrons move in a parabolic trajectory, resulting in a net displacement in the opposite direction of the field. The colliding electrons transfer energy to the lattice, thereby increasing the material's temperature. The heat generated Q is proportional to the squared current and the resistance of the conductor, known as Joule's law or resistive heating.

$$\rho = \frac{1}{\sigma} = \frac{m_e}{n_e {e_c}^2 \tau_e} = \frac{RA}{L}$$ **Equation A.A.2**

Resistivity ρ, defined as the inverse of conductivity, is also a material property. It indicates the difficulty with which an electron moves within a material in the presence of an electric field. The mathematical definition of resistivity is provided in **Equation A.A.2**, where m_e is the mass of an electron and L is the length of the conductor and schematically shown in **Figure A.A.1b**. Resistivity is dependent on the mean time between collisions, thereby meaning that the resistivity of a material is temperature dependent. As the temperature rises, the thermal vibrations of the atoms also increase, which in turn increases the frequency of collisions. This results in a reduction of τ_e and an increase in ρ. Consequently, metals – which are materials where the charge carriers are the electrons – exhibit a lower resistivity at lower temperatures. However, this is not always the case. In semiconductors and other nonmetals, both positive and negative charge carriers (electron-hole pairs) are present. As a consequence of the elevated temperature, the availability of charge carriers rapidly increases, thereby reducing the resistivity [314].

In contrast, resistance R is not a material property but rather a characteristic of the system that depends on the geometry, topography, cleanliness of the contacting electrodes, as well as other design choices, such as the materials' hardness, normal load, coating or plating, etc. As demonstrated by **Equation A.A.2**, the resistance of a conductor can be quantified by utilizing the dimensions and resistivity of the material in question. Nevertheless, this equation is only applicable to pure, defect-free materials

at a known temperature. The incorporation of foreign atoms or deformation into the lattice of a material results in a reduction in the mean time between collisions, thereby

$$\rho_t = \rho_m + \rho_d + \rho_i \qquad \textbf{Equation A.A.3}$$

increasing the material's resistivity. Therefore, the real resistivity of non-ideal materials ρ_{total} is comprised of three components: the intrinsic resistivity of the pure material ρ_m, the resistivity induced by deformation ρ_d, and the resistivity corresponding to foreign atoms ρ_i. These increased scattering effects due to lattice perturbation are known as Matthiessen's rule, mathematically shown in **Equation A.A.3** [309]. ρ_m is caused by thermal oscillations of the crystalline structure. It is typically considered to be the resistivity of pure, ideal materials. ρ_i and ρ_d are generally not temperature dependent since they result from electron scattering due to lattice imperfections [22]. **Figure A.A.2** provides a visual demonstration of Matthiessen's rule.

As shown in **Figure A.A.2**, the resistivity of pure copper undergoes a linear change in response to temperature, exhibiting a resistivity at 25 °C of approximately $\rho_m = 1.7 \times 10^{-8}$ Ωm. The residual components of the total resistance – i.e., ρ_i and ρ_d – are the result of a multitude of factors, including impurities, dislocations, vacancies, grain boundaries, are pores [22]. Pure metals are frequently alloyed with other metals or reinforced with second phases in order to enhance their mechanical properties

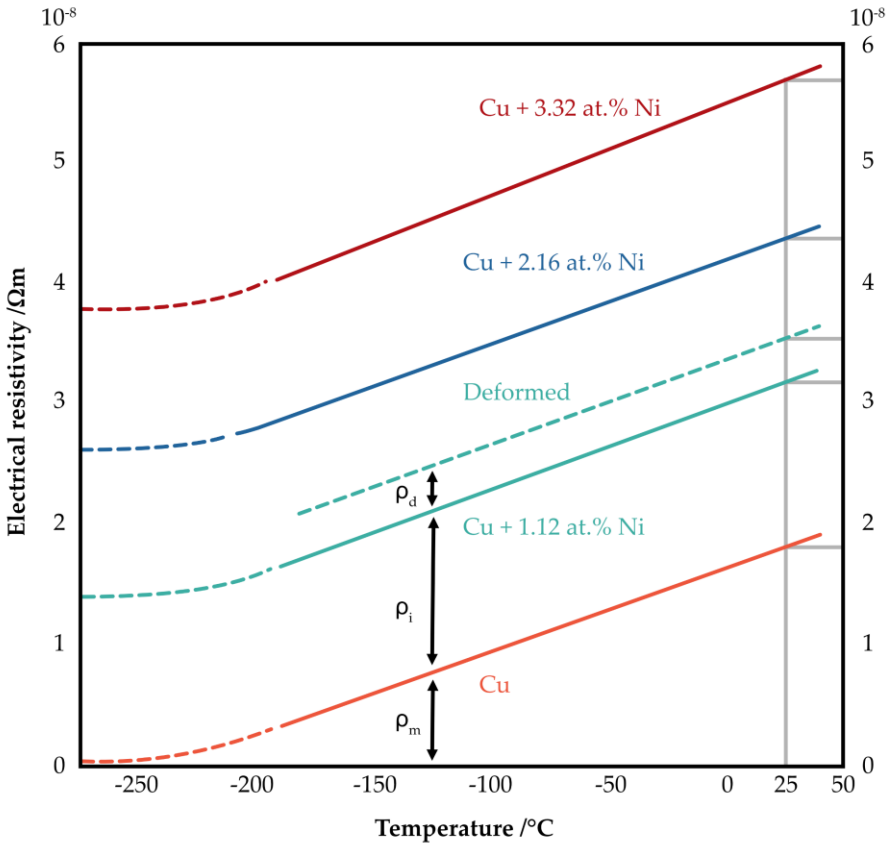

Figure A.A.2: Resistivity of copper and copper-nickel alloys demonstrating its dependence on purity, deformation state, and temperature. Reused and adapted with permission from William D. Callister, *Materials Science and Engineering: An Introduction* 7th Edition, 2007, John Wiley & Sons, page 675, Figure 18.8 [309].

(e.g., increase tensile strength, ductility, wear resistance, etc.) or to reduce costs. However, this is achieved at the expense of electrical conductivity, as the solute or reinforcement phase disrupts the periodicity of the crystalline lattice, thereby increasing the material's resistivity. As the example from **Figure A.A.2** highlights, the rise in resistivity due to alloying is significant. The incorporation of 1.12 at.% of nickel into copper results in a total resistivity of approximately 3.1×10^{-8} Ωm at 25 °C, corresponding to $\rho_i = 1.4 \times 10^{-8}$ Ωm. Further alloying considerably increases the total resistivity to approximately 4.4×10^{-8} Ωm and 5.7×10^{-8} Ωm at 25 °C for 2.16 at.% and 3.32 at.%, respectively. As with alloying and reinforcing, many metals require processing prior to their application. Inducing plastic deformation is used to improve strength and wear resistance. However, the deformation-induced dislocations in the crystalline structure of the material cause electron scattering, which in turn increases its resistivity. This phenomenon is shown in **Figure A.A.2**, which in this example depicts the resistivity of the 1.12 at.% alloy increasing to approximately 3.5×10^{-8} Ωm, corresponding to $\rho_d = 0.4 \times 10^{-8}$ Ωm.

Microstructural imperfections, such as vacancies, affect the conductivity by scattering electrons due to the disruption of the lattice's periodicity, by altering the electron density of the material, and by favoring the diffusion of foreign atoms into the vacancy [22]. In polycrystalline materials, electrons are scattered while crossing grain boundaries, contributing to higher resistivities. Moreover, porosities – i.e., nano- and micro-scale voids within a given material – also impedes the material's conductivity due to the scattering of electrons and the reduction of the conduction volume. These voids may be formed as a result of inadequate sintering, during processing, or due to operational conditions. It is of great importance to prevent or minimize the formation of voids since they not only affect the transport properties of the material, but also its mechanical properties due to stress concentrations or crack propagation. These factors, among others, contribute to the residual resistivity, which in turn leads to a considerable total resistivity of an electrical system.

A.2. Ignition of the electrical arc while breaking

If we consider a switching electrical contact performing a break operation, the mechanisms behind the formation of the electrical arc are as follows. In an initial instance, conduction occurs between the two electrodes due to the contact between the topographic features of each surface (a-spots). The sum of these a-spots forms the real contact between the surfaces, hence realizing the conduction paths, which generate the constriction of the electrical current. The constriction increases the electrical contact resistance and heats up the contacting asperities. During a break operation, the applied force between the contacts decreases (tending to zero), which means that the contact area also tends to zero. Consequently, as the contact area decreases, the constriction

$$T_c^{\,2} = T_0^{\,2} + V_c^{\,2} \times 10^7 K$$ **Equation A.A.4**

resistance will increase, thus leading to a temperature increase at the contacting site according to **Equation A.A.4**, where T_c is the contact temperature, T_0 is the ambient temperature, and V_c is the voltage drop between the electrodes [22]. As T_c increases, the temperature will surpass the melting temperature T_m of the metals, leading to the formation of the molten bridge. It is important to highlight that the molten bridge will always generate during hot switching irrespective of the switching components characteristics (i.e., opening speed, environmental conditions, current level, etc.).

Upon the metals' fusion, coupled with the retraction of the movable electrode, the molten bridge is drawn, thereby elongating it which will considerably increase the current density. At this point, the electrical arc has not yet been established since, as the name suggests, the molten bridges join the two electrodes. However, as the bridges gradually elongate due to the continued retraction of the movable electrode, the bridges become increasingly unstable until they rupture. It is at this point that the electrical arc is established in the vicinity of the ruptured molten bridges. The bridges' instability is caused by colder material from the base of the bridge which flows towards the hotter regions during elongation, in addition to the ejection of the bridges' material towards the gap as the bridges' temperature surpasses the boiling temperature T_b of the metal [22]. Once the molten bridge explodes and the subsequent ignition of the electrical arc, metallic vapor is released into the contact gap. This vapor considerably increases the pressure in the contact gap, which gradually expands into lower pressure regions, establishing a "pseudo arc" where ions are the conductors. When switching at atmospheric conditions (i.e., not under vacuum), there is a sustained reduction in pressure which enables atmospheric gases to flow into the gap. Consequently, the arc undergoes a transition from a metallic phase towards a gaseous phase where electrons are the primary current conductors instead of ions as was the case in the initial stages of the arc. The electrical arc is sustained as long as the cathode provides a constant supply of electrons, which will continually ionize the metallic vapor generated due to the explosion of the molten bridges. However, the cathode's temperature should be sufficiently high in order for enough electrodes to be liberated [22]. Therefore, I_{min} can be defined as the minimum arc current required to sustain electron production in the cathode, thus sustaining the electrical arc. Consequently, when the current is higher than I_{min}, the arc can be extinguished by increasing the interelectrode gap. In this manner, increasing the distance between the electrodes generates a higher arc voltage which consequently reduces the arc's current until it falls below I_{min}, thus extinguishing the electrical arc [22]. The development of the electrical arc's ignition is schematically represented in **Figure 6**.

A.3. Carbon hybridization states

Carbon is a very versatile element due to the fact that it is capable of bonding with itself in different ways due to the formation of hybrid atomic orbitals. Depending on the different carbon-carbon bonds, different molecular and crystalline structures are formed – known as allotropes or polymorphs (i.e., its hybridization state) [94]. In a sp^3-hybridization state, direction (i.e., stereospecific), covalent *sigma* bonds are formed between the carbon atoms, where each atom share an electron pair. This *sigma* bonds are strong due to a maximization of attraction forces between the bonding electrons and the nuclei, while minimizing the mutual repulsion between the nuclei. The result from a sp^3-hybridized carbon molecule, is a three-dimensional, tetrahedron structure that forms a 109.5° angle between each of the four *sigma* bond. As a consequence, sp^3-hybridized materials present exceptional mechanical properties [94], such as in the case of diamond. Other examples of sp^3-hybridized substances are methane and aliphatic compounds.

Similarly, sp^2-hybridized carbon also exhibits strong *sigma* covalent bonds [94]. However, here three sp^2 orbitals are formed in addition to a delocalized non-hybridized p_z-orbital. In this case, the three sp^2-hybridized orbitals can form strong *sigma* bonds. These orbitals are in-plane, forming a 120° angle with each other, and present higher energy and shorter bond length than in a sp^3 hybridization state. The p_z-orbital, on the other hand, is in a perpendicular direction to the sp^2 plane, thereby enabling the formation of weaker *pi* bonds. This enables each sp^2-hybridized carbon atom to form a *sigma* bond in-plane with three other sp^2-hybridized carbon atoms and vertically form *pi* bonds with other bonded planes, thereby forming the typical stacked hexagonal structure observed in graphite. It is the high-mobility, non-hybridized electron (p_z-orbital) that is responsible for the exceptional transport properties of sp^2-hybridized structures. However, the delocalized p_z-orbitals possess the particularity that they can freely move in-plane, while requiring higher amounts of energy to move cross-plane. Therefore, sp^2-hybridized structures generally present anisotropic transport properties [94].

Lastly, *sp*-hybridized structures are made up of a single strong *sigma* bond [94], which accounts for two electrons, and two delocalized *p*-orbitals. Due to the strong repulsion between the two *sp*-orbitals, this structure is linear, forming a 180° angle between each orbital [94]. Carbynes are typical *sp*-hybridized structures.